Transactions of the ASME®

Journal of Turbomachinery

Published Quarterly by The American Society of Mechanical Engineers

VOLUME 122 • NUMBER 2 • APRIL 2000

Technical Editor, **T. H. OKIISHI (2003)**
Associate Technical Editors
Gas Turbine (Review Chair)
D. BALLAL (2000)
Heat Transfer
N. NIRMALEN (2000)
Turbomachinery
R. ABHARI (2002)
R. DAVIS (2002)
C. KOCH (2002)
S. SJOLANDER (2002)
A. STRAZISAR (2000)

BOARD ON COMMUNICATIONS
Chairman and Vice-President
R. K. SHAH

OFFICERS OF THE ASME
President, **R. E. NICKELL**

Executive Director, **D. L. BELDEN**

Treasurer, **J. A. MASON**

PUBLISHING STAFF
Managing Director, Engineering
CHARLES W. BEARDSLEY
Director, Technical Publishing
PHILIP DI VIETRO
Managing Editor, Technical Publishing
CYNTHIA B. CLARK
Managing Editor, Transactions
CORNELIA MONAHAN
Production Coordinator
VALERIE WINTERS
Production Assistant
MARISOL ANDINO

Transactions of the ASME, Journal of Turbomachinery (ISSN 0889-504X) is published quarterly (Jan., Apr., July, Oct.) for $215.00 per year by The American Society of Mechanical Engineers, Three Park Avenue, New York, NY 10016. Periodicals postage paid at New York, NY and additional mailing offices. POSTMASTER: Send address changes to Transactions of the ASME, Journal of Turbomachinery, c/o THE AMERICAN SOCIETY OF MECHANICAL ENGINEERS, 22 Law Drive, Box 2300, Fairfield, NJ 07007-2300.

CHANGES OF ADDRESS must be received at Society headquarters seven weeks before they are to be effective. Please send old label and new address.

PRICES: To members, $40.00, annually; to nonmembers, $215.00. To countries outside the United States and Canada, add $40.00 for surface postage and $60.00 for airmail postage.

STATEMENT from By-Laws. The Society shall not be responsible for statements or opinions advanced in papers or ... printed in its publications (B7.1, Par. 3).

COPYRIGHT © 2000 by the American Society of Mechanical Engineers. For authorization to photocopy material for internal or personal use under those circumstances not falling within the fair use provisions of the Copyright Act, contact the Copyright Clearance Center (CCC), 222 Rosewood Drive, Danvers, MA 01923, tel: 978-750-8400, www.copyright.com. Request for special permission or bulk copying should be addressed to Reprints/Permission Department.

INDEXED by Applied Mechanics Reviews and Engineering Information, Inc. Canadian Goods & Services Tax Registration #126148048

TECHNICAL PAPERS

(Contents continued on inside back cover)

This journal is printed on acid-free paper, which exceeds the ANSI Z39.48-1992 specification for permanence of paper and library materials. ♾™
♲ 85% recycled content, including 10% post-consumer fibers.

Downloaded 01 Jun 2010 to 171.66.16.52. Redistribution subject to ASME license or copyright; see http://www.asme.org/terms/Terms_Use.cfm

(**Contents continued**)

Journal of Turbomachinery **Volume 122, Number 2** **APRIL 2000**

ANNOUNCEMENTS

1999 International Gas Turbine Institute Scholar Lecture

Aerodynamic Analysis of Multistage Turbomachinery Flows in Support of Aerodynamic Design

John J. Adamczyk
NASA Glenn Research Center,
Cleveland, OH 44135

This paper summarizes the state of 3D CFD based models of the time-averaged flow field within axial flow multistage turbomachines. Emphasis is placed on models that are compatible with the industrial design environment and those models that offer the potential of providing credible results at both design and off-design operating conditions. The need to develop models free of aerodynamic input from semiempirical design systems is stressed. The accuracy of such models is shown to be dependent upon their ability to account for the unsteady flow environment in multistage turbomachinery. The relevant flow physics associated with some of the unsteady flow processes present in axial flow multistage machinery are presented along with procedures that can be used to account for them in 3D CFD simulations. Sample results are presented for both axial flow compressors and axial flow turbines that help to illustrate the enhanced predictive capabilities afforded by including these procedures in 3D CFD simulations. Finally, suggestions are given for future work on the development of time-averaged flow models. [S0889-504X(00)02002-X]

Introduction

Turbomachinery aerodynamicists have long realized that the flow within multistage turbomachinery is complex. In addition to the small-scale chaotic unsteadiness due to turbulence, which is nondeterministic, at a large scale the flow is also unsteady and aperiodic from blade passage to blade passage. The flow features associated with these large scales are deterministic. It is because of the unsteady deterministic flow that turbomachinery is able to either impart or extract energy from a flow. The term unsteady deterministic is used to characterized all unsteady behavior linked to shaft rotational speed. The length and time scales associated with the unsteady flow field within turbomachinery are understood. The range of these length and time scales is large and consequently turbomachinery flow modeling is very challenging. The challenge is to develop an analytical model of sufficient fidelity to address key design issues. At the same time, the cost and time of executing a simulation based on the model, and the cost of acquiring and maintaining the empirical database that underpins the model must be compatible with the design environment. The balance point between model resolution and the cost of implementation and execution is constantly changing as the cost of computing comes down and more detailed experimental information is gathered about the nature of the flows within multistage turbomachinery. This change in the balance point with time must also be considered when deciding upon a mathematical modeling strategy.

Figure 1 illustrates a range of mathematical models that can be used to simulate turbomachinery flows. They appear on the figure in the order of their fidelity. At the extreme left are the Navier–Stokes equations, at the extreme right are the equations governing a mean-line model. The other models that appear on the figure will be addressed in the text.

The balance between model resolution and cost of model implementation can be illustrated with the aid of Fig. 1. Apart from the empirical information required to model the physical and thermodynamic properties of a fluid, no other empirical information is required to solve the Navier–Stokes equations. The direct solution of the Navier–Stokes equations for Reynolds numbers typical of aero and industrial turbomachinery configurations would produce a nondeterministic or turbulent flow state. Although the fidelity of such a simulation would be very impressive, the task of extracting information to guide an aerodynamic design would be difficult. In addition, the computer requirements associated with solving the Navier–Stokes equations in support of aerodynamic design, both in terms of CPU speed and memory size, would far exceed the capabilities of today's most advanced computers. Otherwise, the cost of acquiring the empirical database for the physical and thermodynamic properties that underpin the Navier–Stokes equations for working fluids typical of most turbomachinery applications is relatively modest and, for the most part, is readily available today.

At the other extreme, the computer requirements associated with executing a simulation based on a mean-line model of a multistage configuration are well within the capabilities of personal computers. The fidelity of a mean-line model is one dimensional in space and may include time as an additional independent variable. The empirical database underpinning a mean-line model used in turbomachinery aerodynamic design is large. The maintenance and acquisition cost associated with this database is also large.

In the foreseeable future, it is highly unlikely that computers of sufficient power for use in solving the Navier–Stokes equations for a multistage turbomachinery configuration will be readily available. Although mean-line models are very useful in preliminary aerodynamic design, they are insufficient for detailed aerodynamic blade design of advanced configurations. For these reasons, aerodynamicists have evolved models whose resolution lies between these two extremes. A number of these models are noted on Fig. 1.

As of ten years ago, the aerodynamic design of most axial flow multistage turbomachinery was executed using various axisymmetric flow models. The use of these models was iterative. A design was executed based on the existing database. Data obtained from tests of the fabricated hardware were used to update empirical correlations embedded within these models. The updated axi-

---

Contributed by the International Gas Turbine Institute and presented at the 44th International Gas Turbine and Aeroengine Congress and Exhibition, Indianapolis, Indiana, June 7–10, 1999. Manuscript received by the International Gas Turbine Institute February 1999. Paper No. 99-GT-80. Review Chair: D. C. Wisler.

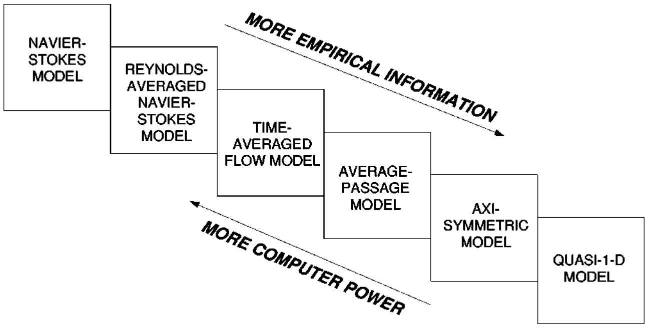

Fig. 1 The range of mathematical models that can be used to simulate turbomachinery flows

symmetric flow model was then used to support the next design of the configuration. This boot-strap approach to the aerodynamic design of axial flow multistage turbomachinery resulted in some truly impressive machines, as evidenced by the aerodynamic performance they achieved. However, because of strong economic forces, the turbomachinery industry was forced to re-examine this iterative approach to aerodynamic design. These economic forces mandated that industry reduce the time and cost of developing a turbomachinery component and, at the same time, required the design of machinery whose performance goals lay outside the then-existing experience base. As a result, a strong need arose for developing a new methodology for executing the aerodynamic design of axial flow multistage turbomachinery. The foundation of this new methodology required aerodynamic models whose resolution was greater than that of the axisymmetric flow models. These models had to allow for overnight turnaround using computer resources compatible with the design environment. Finally, the models had to be capable of addressing the aerodynamic issues associated with the design of advanced configurations.

The objective of this paper is to review the development and application of three-dimensional (3D) computational fluid dynamics (CFD) based models for use in the aerodynamic design of multistage axial flow turbomachinery. More specifically, this review discusses those models that offer the potential of providing credible results at both design and off-design operating conditions without recourse to aerodynamic matching information supplied implicitly or explicitly by existing aerodynamic design systems. The term aerodynamic matching refers to the matching of the inlet flow requirements of a stage to the outlet flow of upstream stages.

The paper is divided into four parts. The first part discusses the historical development of the models currently used in the design of multistage turbomachines. The second part of the paper deals with the issues associated with modeling the time-averaged flow within a typical passage of a blade row embedded in a multistage turbomachine. The third section presents results from numerical simulations of multistage axial flow compressors and turbines based on a three-dimensional flow model that attempts to account for the unsteady flow environment within these machines. The last section summarizes the results presented in the paper and suggests areas for future research. An appendix is included in which a mathematical procedure is outlined for constructing the field equations governing the time-averaged flow within a typical passage of a blade row embedded in an axial flow multistage turbomachine.

Historical Background

Historically, in order to make any headway in analyzing multistage turbomachinery flows, it was necessary to assume that each blade row had an infinite number of blades. If the incoming and exiting flow is axisymmetric and independent of time, the assumption relating to blade count implies that the entire flow field is axisymmetric. The resulting flow field is in general three dimensional, since the radial, tangential, and axial velocity components all exist. This axisymmetric flow representation is described by throughflow models. The individual blade rows are represented by a force distribution (actuator duct model) and an energy source (for compressors) or energy sink (for turbines) distribution. If the chord length of each blade row is allowed to vanish while the aerodynamic loading on the blade row is maintained, the blade row representation is that of an actuator disk. Across each disk, the tangential velocity component undergoes a finite change due to the tangential force generated by the blade row.

The axisymmetric flow field is treated as a core region and two endwall regions. The effect of the endwall regions on the core region is, in part, accounted for by means of a flow blockage. It is assumed that the blade force acting on the core fluid can be obtained from cascade flow theory [1], while the force acting on the fluid within the endwalls is based on empirical correlations [2]. As of ten years ago the throughflow models were the mainstay of aero design systems for multistage axial flow turbomachines. Today their primary use is in preliminary design to generate blade shapes. An excellent review of the development of through-flow and cascade flow theory is given by Serovy [3]. In addition, a thorough discussion of the underlying flow physics being accounted for in throughflow models is presented by Cumpsty [4].

It was not until digital computers were easily accessible to turbomachinery flow modelers and the development of CFD that the throughflow models were replaced by quasi-three-dimensional flow models. The quasi-three-dimensional flow models numerically coupled an axisymmetric flow model to a cascade flow model. The formulation of these quasi-three-dimensional models was influenced by the work of Wu [5]. The axisymmetric flow model provided the stream surfaces on which the cascades were defined. The cascade flow model provided the blade force distribution required as input to the axisymmetric flow model. The development of such a flow model is outlined by Jennions and Stow [6]. Two more recent publications, Howard and Gallimore [7] and Gallimore [8], are representative of the current state of the art of axisymmetric flow models.

The quasi-three-dimensional flow models were an advancement over the throughflow models. However, like the throughflow models, the quasi-three-dimensional models still required a sound estimate of the aerodynamic blockage for the predictions to match data. This limited a new design to regions of design parameter space, which was still relatively close to that of a previous machine. Without a good a priori estimate of the blockage associated with a design, aero designs executed using the quasi-three-dimensional flow model fell short of their performance goals. This led to rebuilds of machinery, a costly and time consuming process.

In Fig. 1, these quasi-three-dimensional flow models are grouped together with the throughflow models under the label axisymmetric flow models. Because the axisymmetric flow models are of higher fidelity, they lie to the left of the mean-line models.

Within the last ten years, there has been a steady infusion of 3D CFD-based models into axial flow multistage turbomachinery design systems. In part this has been due to the useful role these models have played in the analysis of isolated blade rows. The performance level of the fan rotor of the current generation high bypass ratio turbofan engine is directly tied to the advances made in the use of 3D CFD-based models to guide aero design. The initial fan rotor geometry may be provided by a throughflow or a quasi-three-dimensional system, but the final shape of the rotor is evolved exclusively using 3D CFD-based models. The rotor shape is tailored to control the interaction of shock waves with the blade surface boundary layers to avoid separation and to minimize loss. In addition, using these 3D CFD models one is able to resolve the tip clearance flow as well as the stator hub leakage flow, and establish their impact on aerodynamic performance. From this activity guidelines have been established for use in aerodynamic design [9–11].

The 3D CFD-based models that were initially introduced into multistage axial flow turbomachinery design systems ignored the impact of the unsteady, deterministic flow existing within axial flow multistage turbomachines. The unsteady, deterministic flow is produced by the surrounding blade rows and its frequency content is linked to shaft rotational speed. These 3D models have two forms. The first is simply an isolated 3D blade row CFD-based model linked to a throughflow code. The initial geometry and the inlet and exit flow conditions to the blade row being designed are established by the throughflow or quasi-3D system. The established inlet and exit flow conditions to a blade row set the boundary conditions for the 3D model. 3D simulations are executed with geometry updates until a blade configuration is found whose inlet and exit flow closely match that of the throughflow system. The aerodynamic matching of stages within a machine is established by the through-flow system.

The second model pioneered by the work of Denton and Singh [12], employs ''Mixing Planes'' between blade rows to define a steady inlet and exit flow for each blade row within a machine. The mixing plane model produces a series of blade passage flowfields, each of which is independent of time and periodic in the tangential direction, with a period equal to the pitch of the respective blade row. This model is strictly valid in the limit as the axial spacing between blade rows becomes large. Further details on the mixing plane model are provided in the work of Dawes [13], Denton [14], and Hall [15].

In using the mixing plane model in aerodynamic design, the initial geometry is provided by a throughflow system. In addition, data from similar builds are often used to fix aerodynamic modeling constants so that a reasonable prediction of a machine's aerodynamic stage matching is achieved. For a totally new configuration, these aerodynamic modeling constants are adjusted based on information from a throughflow system [16,17]. Simulations of groups of stages or the entire machine are executed with geometry updates to remove any undesirable flow features associated with the initial configuration. However, during this process, the aerodynamic matching of stages within the machine remains essentially that established by the values assigned to the aerodynamic modeling constants.

There are two approaches that account for the unsteady deterministic flow environment within a multistage turbomachine. The first of these approaches directly simulates the unsteady deterministic flow state. The equations associated with this model are the Reynolds-averaged form of the Navier–Stokes equations. The use of this model in design applications where overnight simulation turnaround is mandated must await the development of more powerful computes. However, recent publications [18–24] have shown these models to be very useful in conducting numerical experiments to quantify the impact of the unsteady deterministic flow on turbomachinery aerodynamic performance and durability. They have also proven useful in generating databases for use in the development of models that introduce the effect of the unsteady deterministic flow environment into simulations of the time average flow field within multistage turbomachines [25].

The remaining approach is based on the flow model derived from the work of Adamczyk [26]. This model and its offshoots have proven useful in design applications [27]. The model developed by Adamczyk [26] is referred to as the average-passage flow model. This flow model describes the time-averaged-flow field within a typical passage of a blade row embedded within a multistage configuration. The resulting flow field is periodic over the pitch of the blade row of interest. The average-passage flow model is an analysis model as are all the others that have been referred to thus far. This means that geometry is the input and the output is the flow field generated by the geometry. When using the average-passage flow model in aerodynamic design, the initial geometry is defined by a throughflow system. During the design process, geometry updates are done exclusively based on simulation results from the average-passage model [28,29]. No output from an axisymmetric throughflow system or a data match that implicitly or explicitly sets the aerodynamic matching of stages within a turbomachine is provided to the average-passage simulations. The credibility of an average-passage flow simulation is not tied to aerodynamic matching information provided by a throughflow system or a data match. The credibility is tied to the models used to account for the effects of the unsteady flow environment on the average-passage flow field. The effect of the unsteady deterministic flow field on aerodynamic matching of stages is accounted for by velocity correlations within the momentum equations associated with the average-passage flow field and by a velocity total enthalpy correlation within the energy equation associated with the average-passage flow field. The term unsteady deterministic refers to all time-dependent behavior linked to shaft rotational speed. All unsteady behavior not linked to shaft rotational speed is referred to as nondeterministic. The mathematical steps leading to these correlations are outlined in Appendix A.

There is no doubt that 3D CFD-based models with aerodynamic input from throughflow models have provided credible designs. These models will continue to provide credible designs as long as the design parameters are within the bounds of the database underpinning well-calibrated throughflow or quasi-3D design systems. However, reliance on throughflow or quasi-3D models to set key aerodynamic design parameters such as the aerodynamic matching of stages greatly impedes the utility of these models. Specifically, they are limited in their ability to uncover the fluid mechanics controlling the performance of multistage axial flow turbomachines at design and off-design operating conditions. The objective of 3D CFD-based modeling should be to break free of the dependence on throughflow or quasi-3D design systems except for providing the initial geometry. If such 3D CFD-based models are proven credible, their use will allow aerodynamic designs of machinery whose parameters lay outside the bounds of the database underpinning throughflow systems to be executed with confidence. This would include both design and off-design operation, and in the case of compressors, prediction of stall margin. This author believes that such 3D CFD-based models can be developed within the framework of a time average flow model by correctly accounting for the effects of the unsteady flow environment within a multistage axial flow turbomachine.

This section is concluded by providing a simple example, which illustrates the impact of an unsteady, deterministic flow on the time-averaged flow field. Consider the flow field downstream of an isolated compressor rotor. In the reference frame of the rotor, the flow is steady in time. In the absolute or stator frame of reference the flow is unsteady in time, the result of the rotor flow field being nonaxisymmetric. Figure 2 shows the time-averaged and mass-averaged total temperature distributions in the stator frame of reference at two axial locations downstream of NASA Rotor 37 [30] as a function of span. These results were derived from a simulation at design speed and near peak efficiency. The axial locations Station 3 and Station 4 correspond to stations reported in the ASME blind test case exercise [31]. These two locations are approximately one rotor chord apart. Station 3 would be slightly upstream of a stator had a stator been included in the simulation. The difference between the time-averaged and mass-averaged total temperature distribution down-stream of the rotor is a direct measure of the unsteady total temperature exiting the rotor. At Station 4 the difference is small, indicating that the unsteady flow field is effectively mixed out at this location, while at Station 3 the difference is significant. Figure 3 shows the footprint of fluid particles on an axial plane at Station 4, which were released at Station 3 at 20 percent of span, 50 percent of span, and 80 percent of span. The particles in the rotor wake and in the core fluid are noted in the figure. The particles in the wake have a radial drift velocity relative to the particles in the core fluid. The wake particles also have an excess of total temperature relative to the core fluid particles. The radial drift of the wake particles relative to the core fluid particles is an unsteady deterministic process

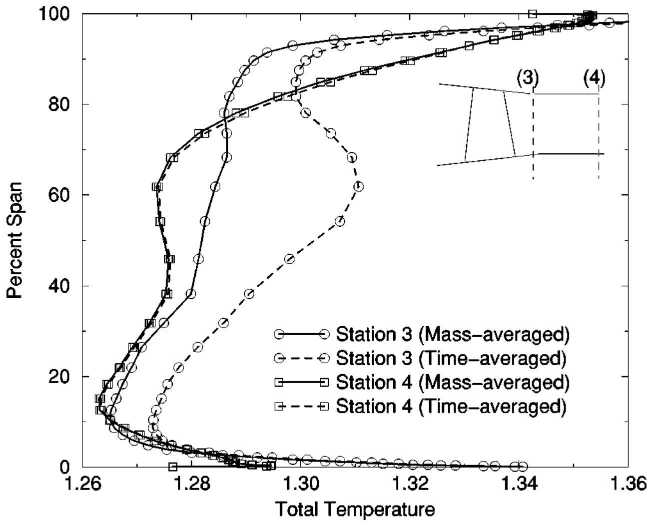

Fig. 2 Spanwise distribution of total temperature down-stream of a high-speed compressor rotor

when viewed in the absolute or stator frame of reference. This process results in a redistribution of the time-averaged total temperature field between Stations 3 and 4. The difference between the time-averaged total temperature distribution at Station 3 averaged over the span and the distribution at Station 4 averaged over span is nearly 7 percent of the total temperature rise across the rotor. This difference is not insignificant.

Figure 2 also shows that there is a difference in the spanwise distribution of the mass-averaged total temperature at Stations 3 and 4 even though the mass-averaged total temperature across the flow annulus is conserved. Note the difference in the two mass-averaged total temperature profiles outboard of 80 percent span. The change in either the time-averaged total temperature profiles or the mass-averaged total temperature profiles between Stations 3 and 4 is not the result of transport by the time-averaged velocity field. Transport of either the time-averaged or mass-averaged total temperature at Station 3 by the time-averaged velocity field would yield a profile only slightly altered from that at Station 3. The change in the total temperature profiles that occurs between Stations 3 and 4 is the direct result of the unsteady deterministic flow exiting the rotor. Had a downstream stator been located in the flow field at an axial location downstream of the rotor typical of core engine compressors, the spanwise redistribution of the time-averaged total temperature field would be taking place within the stator passages. The time-averaged total temperature field exiting the stator would be influenced by the spanwise migration of the rotor wake fluid particles and thus impact the performance of a downstream rotor.

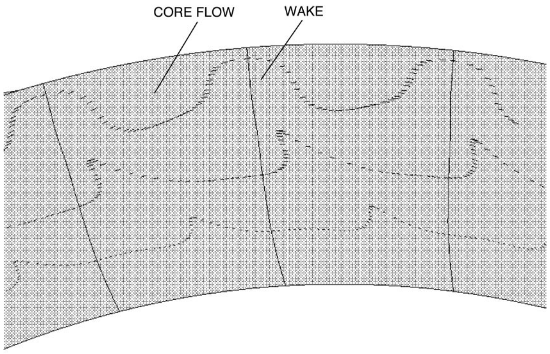

Fig. 3 Radial transport of rotor wake fluid particles

The cumulative effect of spanwise redistribution of total temperature has a significant impact on the predicted aerodynamic performance of axial flow multistage compressors and turbines.

The next section presents a number of models by which one can account for the effects of the unsteady deterministic flow state on the time-averaged flow field and the flow physics being captured by these models.

Flow Physics Associated With the Average-Passage Stress and Total Enthalpy Flux

In Appendix A it is shown that within the framework of the average-passage model, the average-passage stress and total enthalpy flux account in part for the effect of momentum transport and total enthalpy transport attributed to surrounding blade rows. The average-passage stress appears in the average-passage form of the momentum equations, while the average-passage total enthalpy flux appears in the average-passage form of the energy equation. From Appendix A the average-passage stress and total enthalpy flux are:

$$R_{ij}=\overline{\overline{\overline{\rho u_i' u_j'}^{e}}^{t}}^{ap}+\overline{\overline{\bar{\rho}^{e} u_i'' u_j''}^{t}}^{ap}+\overline{\overline{\bar{\rho}^{e}}^{t} u_i''' u_j'''}^{ap} \qquad (A9)$$

and

$$HF_i=\overline{\overline{\overline{\rho H' u_i'}^{e}}^{t}}^{ap}+\overline{\overline{\bar{\rho}^{e} H'' u_i''}^{t}}^{ap}+\overline{\overline{\bar{\rho}^{e}}^{t} H''' u_i'''}^{ap} \qquad (A10)$$

where lower case u_i' is the velocity component in the ith direction, H is the total enthalpy, and ρ is the fluid density. The remaining variables that appear in Eqs. (*A*9) and (*A*10) are defined in Appendix A.

The average-passage stress and the average-passage total enthalpy flux are composed of three terms. With respect to a given blade row, the first term is due to the nondeterministic flow field, the second is due to the unsteady deterministic flow field, and the third is due to the average-passage flow field of blade rows other than the one of interest, which are in the same spatial reference frame. Thus the first term in Eqs. (*A*9) and (*A*10) accounts for the diffusion of total enthalpy and momentum attributed to unsteady flow processes not linked to shaft rotational speed, which includes diffusion due to turbulence. Since in most turbomachines the flow is turbulent, the need to model this portion of the average-passage stress and the corresponding portion of the average-passage total enthalpy flux is self-evident.

The component of the average-passage total enthalpy flux associated with the unsteady deterministic flow field is the result of flow processes directly linked to shaft rotational speed. These flow processes are responsible for the radial redistribution of total temperature previously illustrated. They are also responsible for the circumferential redistribution of total temperature. This redistribution of total temperature leads to the formation of hot spots in turbines, which has a significant impact on turbine blade life.

The component of the average-passage stress associated with the unsteady deterministic flow is responsible for the recovery of wake mixing loss in compressors, flow blockage, and the spanwise redistribution of momentum.

The remaining portion of the average-passage stress and total enthalpy flux accounts for the effect of blade indexing (i.e., the relative circumferential placement of blade rows on the same shaft). It is through these terms that the effect of circumferential placement of hot streaks entering a turbine blade row and the impact of indexing on blade loss are accounted for.

The impact of the unsteady deterministic flow on the aerodynamic performance of an axial flow multistage turbomachine is the main topic of this section. The terms that account for this are the second expressions in Eqs. (*A*9) and (*A*10):

$$R_{ij}^{D} = \overline{\overline{\bar{\rho}^{e} u_i'' u_j''}^{t}}^{ap} \tag{1}$$

and

$$HF_i^{D} = \overline{\overline{\bar{\rho}^{e} H'' u_i''}^{t}}^{ap} \tag{2}$$

The superscript D ascribed to R_{ij}^{D} and HF_i^{D} denotes the deterministic component of the average-passage stress and the deterministic component of the average-passage total enthalpy flux. All the terms that appear on the right-hand side of Eqs. (1) and (2) are associated with the unsteady deterministic flow.

The unsteady flow field is defined with respect to the stator frame of reference, unless otherwise noted. The ensuing discussion is equally applicable to the unsteady flow field with respect to the rotor frame and therefore no separate discussion is warranted. With respect to the stator frame of reference the unsteady deterministic velocity and total enthalpy in Eqs. (1) and (2) may be decomposed as follows:

$$u_i'' = \tilde{u}_i(z,r,\theta-\Omega t) + \hat{u}_i(z,r,\theta-\Omega t) + \tilde{\tilde{u}}_i(z,r,\theta,t) \tag{3}$$

$$\tilde{u}_i = \sum_{n=1}^{N} \left[U_{i_{(n)}}^{ap} - u_i^{axi}(z,r) \right]$$

and

$$H'' = \tilde{H}(z,r,\theta-\Omega t) + \hat{H}(z,r,\theta-\Omega t) + \tilde{\tilde{H}}(z,r,\theta,t) \tag{4}$$

where

$$\tilde{H} = \sum_{n=1}^{N} \left[H_{(n)}^{ap} - H^{axi}(z,r) \right]$$

The subscript n denotes the nth rotor blade row, of which there are N. The first term in Eqs. (3) and (4) is a sum of the nonaxisymmetric component of the average-passage velocity and total enthalpy field attributed to each rotor. The second term in Eqs. (3) and (4), superscript $\hat{}$, denotes the unsteady flow field arising from the circumferential indexing of rotor blade rows. For a single-stage machine this term is absent. The remaining term arises because of unsteady rotor–stator flow interactions. The first two terms in Eqs. (3) and (4) are independent of time in the rotor frame of reference, while the last term is a function of time in both the stator and rotor frame of reference.

The correlation, Eq. (1), is constructed by forming the product of the unsteady deterministic velocity with itself and density. The constructed product is first averaged over time according to Eq. ($A2$) and then averaged according to Eq. ($A4$), which yields its average-passage form. The same procedure is used to construct the correlation in Eq. (2). The development of a scheme to evaluate all of the terms in correlations Eq. (1) and (2) is a formidable task, which is far beyond the objective of this paper. The evaluation of all terms is also unnecessary at the present time. What is necessary, and the focus of this section, is to identify which terms are deemed to be the most important, and address the modeling of these terms. The next section shows what new predictive capability results from including the models developed in this section in the simulation of axial flow multistage turbomachines.

The prioritization of the terms in correlations Eqs. (1) and (2) formed from Eqs. (3) and (4) is based on the premise that the further blade rows are apart, the less their flow interactions contribute to the correlations. This premise appears reasonable, as evidenced by the plots in Fig. 2. At station 4, which is slightly downstream of the trailing edge of a stator had it been placed in the flow path, the unsteady flow is nearly mixed-out as evident by the correspondence between the spanwise distribution of the mass average total temperature and the time average total temperature. Based on the stated premise, the terms deemed most important are the terms that are the self product of the nonaxisymmetric component of the average-passage velocity field of an individual blade row and the corresponding total enthalpy velocity product. The next series of terms involve products that contain the rotor–stator interaction components, $\tilde{\tilde{u}}_i(z,r,\theta,t)$ and $\tilde{\tilde{H}}(z,r,\theta,t)$. These remaining terms at the present time are thought to be of less importance. The resulting unsteady flow field upon which the correlations are estimated is that produced by a single rotor interacting with an upstream stator and a downstream stator. The unsteady flow interactions with the upstream stator are independent of the unsteady flow interactions with the downstream stator. With respect to the unsteady flow field in the rotor frame of reference, the unsteady flow field upon which the correlations would be based is that produced by a stator with a rotor on either side. Similarly, the unsteady interaction with the upstream rotor is assumed to be independent of the unsteady interaction with the downstream rotor.

In the stator frame of reference the resulting contribution from the nth rotor to the correlations Eqs. (1) and (2) simplifies to:

$$R_{ij}^{(n)} = \overline{\overline{\bar{\rho}^{e} \tilde{u}_{i_{(n)}} \tilde{u}_{j_{(n)}}}^{t}}^{ap} + \overline{\overline{\bar{\rho}^{e} \left(\tilde{u}_{i_{(n)}} \tilde{\tilde{u}}_j + \tilde{\tilde{u}}_i \tilde{u}_{j_{(n)}} \right)}^{t}}^{ap} + \overline{\overline{\bar{\rho}^{e} \tilde{\tilde{u}}_i \tilde{\tilde{u}}_j}^{t}}^{ap} \tag{5}$$

and

$$HF_i^{(n)} = \overline{\overline{\bar{\rho}^{e} \tilde{H}_{(n)} \tilde{u}_{i_{(n)}}}^{t}}^{ap} + \overline{\overline{\bar{\rho}^{e} \left(\tilde{H}_{(n)} \tilde{u}_i + \tilde{\tilde{H}} u_{i_{(n)}} \right)}^{t}}^{ap} + \overline{\overline{\bar{\rho}^{e} \tilde{\tilde{H}} \tilde{u}_i}^{t}}^{ap} \tag{6}$$

with $\tilde{u}_{i_{(n)}}$ defined as

$$\tilde{u}_{i_{(n)}} = U_{i_{(n)}}^{ap} - u_i^{axi} \tag{7}$$

The time average of the first term in Eq. (5) is axisymmetric, as is the time average of the corresponding total enthalpy velocity product. A procedure for estimating either of these terms was presented by Adamczyk et al. [32], and a generalization of the procedure is given by Kirtley et al. [33]. A variation of the procedure derived by Adamczyk et al. [32] is presented by Rhie et al. [34]. All three of these research groups have shown the benefits of incorporating their respective procedures for estimating the first term in Eqs. (5) and (6) into 3D CFD codes used in the simulation of axial flow multistage turbomachinery. It is through these terms that the effect of spanwise redistribution of momentum and total enthalpy due to the unsteady deterministic flow field is accounted for in modeling the average-passage flow field. These terms also insure that the time-averaged vorticity field and time-averaged momentum flux entering a stator are consistent with the time-averaged velocity field [35] and by doing so account for the flow blockage of incoming rotor wakes. The second and third correlations in Eqs. (5) and (6) account for rotor–stator unsteady flow interactions such as the transport of a rotor wake across a compressor stator passage and its subsequent pile-up on the stator pressure surface. In the case of a turbine vane, these correlations account for the pile-up of rotor wakes on the vane suction surface.

Spanwise Redistribution of Total Enthalpy and Momentum. In the next three sections the fluid mechanic processes described by the average-passage stress and total enthalpy flux are explored in more detail. The first term in Eq. (6) formed from the product of the nonaxisymmetric portion of the average-passage velocity field and the nonaxisymmetric portion of the average-passage total enthalpy field accounts for the spanwise redistribution of the time average total temperature field shown in Fig. 2. To show this, consider the flow field downstream of the rotor, which includes a stator. Assume that the flow is deterministic, adiabatic, and inviscid, and that the fluid is a nonconducting ideal gas. The energy equation for this unsteady flow is:

$$\frac{DH}{Dt} = \frac{1}{\rho}\frac{\partial p}{\partial t} \tag{8}$$

where H is the absolute total enthalpy of the unsteady deterministic flow field, and $\vec{u}$, p, and ρ are the velocity, pressure, and density of the unsteady deterministic flow field. D/Dt is the material time derivative and t is time. Combining Eq. (8) with the continuity equation,

$$\frac{\partial \rho}{\partial t} + \vec{\nabla}\cdot\rho\vec{u} = 0, \tag{9}$$

yields

$$\left[\frac{\partial \rho H}{\partial t} + \vec{\nabla}\cdot\rho H\vec{u}\right] = \frac{\partial p}{\partial t} \tag{10}$$

The time average of Eq. (10) is

$$\vec{\nabla}\cdot\overline{\rho T_0\vec{u}}^{t} = 0 \tag{11}$$

where H has been replaced by the product of the specific heat at constant pressure, assumed to be a constant, and total temperature T_0. Equation (11) states that the mass-averaged total temperature of the unsteady deterministic flow field is conserved across the stator.

T_0 and $\vec{u}$ can both be decomposed into a time-averaged component and an unsteady component:

$$T_0 = \widetilde{T_0}^{t} + T_0'' \tag{12}$$

$$\vec{u} = \widetilde{\vec{u}}^{t} + \vec{u}'' \tag{13}$$

The total temperature

$$\widetilde{T_0}^{t}$$

and the velocity

$$\widetilde{\vec{u}}^{t}$$

are density weighted [26]. Introducing both decompositions into Eq. (11) yields:

$$\vec{\nabla}\cdot\bar{\rho}^{t}\widetilde{T_0}^{t}\widetilde{\vec{u}}^{t} = -\vec{\nabla}\cdot\overline{\rho T_0''\vec{u}''}^{t} \tag{14}$$

For an ideal gas with constant thermodynamic properties, the correlation on the right-hand side of Eq. (14) multiplied by the specific heat at constant pressure is equal to Eq. (2) (i.e., the portion of the average-passage total enthalpy flux associated with the unsteady deterministic flow field).

If the divergence of the time-averaged total temperature flux associated with the unsteady deterministic flow field (i.e., right-hand side of Eq. (14)) is nonzero, Eq. (14) implies a spatial variation in the time-averaged total temperature will exist even if the incoming time-averaged total temperature field is uniform. The time-averaged total temperature distribution at Stations 3 and 4 in Fig. 2 differ because of the existence of the time-averaged total temperature flux associated with the unsteady deterministic flow field and its spatial variation. For the same reason the mass-averaged total temperature profiles also differ.

To proceed further with this analysis, we assume the time-averaged total temperature distribution entering the stator is that at Station 3 in Fig. 2. Figure 4 shows a snapshot at an instant in time of this total temperature field projected onto an axial plane. The figure shows that a fluid particle in the wake has a higher total temperature than a neighboring fluid particle in the core flow, this being the result of the wake fluid particle having taken longer to pass through the rotor. Figure 4 also shows a sketch of the time history of this total temperature distribution along with the time history of the radial velocity at Station 3. Recall that Fig. 3 showed that the fluid particles in the rotor wake drifted radially relative to neighboring fluid particles in the core flow. With respect to the time history of total temperature sketched in Fig. 4, the unsteady total temperature component, T_0'', may also be written as:

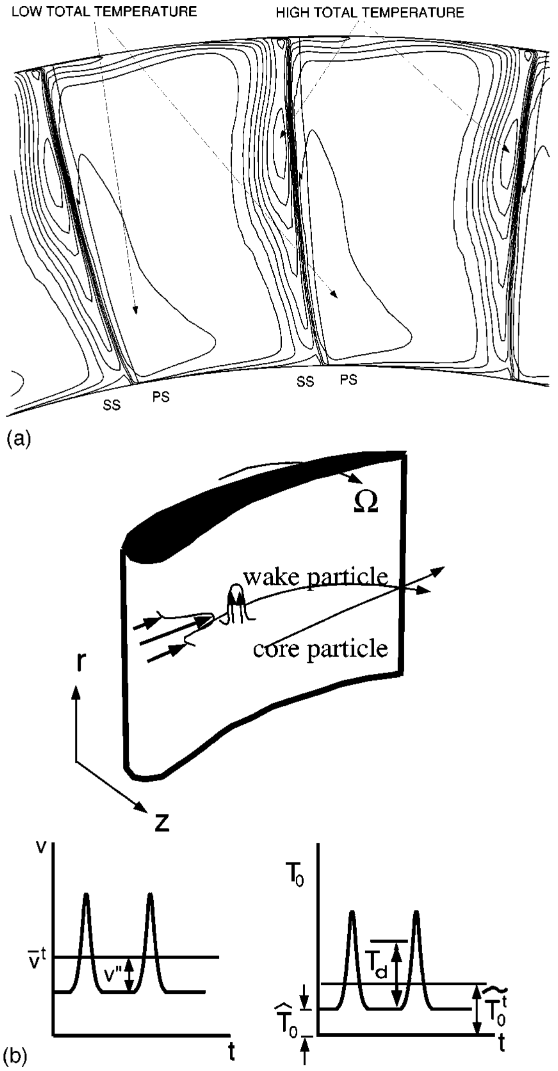

Fig. 4 (*a*) Total temperature exiting a high-speed compressor rotor at an instant of time; (*b*) time history of radial velocity and total temperature downstream of a compressor rotor

$$T_0'' = \widehat{T_0} - \widetilde{T_0}^{t} + T_{0_d} \tag{15}$$

where $\widehat{T_0}$ is the total temperature of the free-stream fluid (assumed to be independent of time) and T_{0_d} is the excess of total temperature within the wake. Introducing Eq. (15) into the right-hand side of Eq. (14) yields:

$$\vec{\nabla}\cdot\bar{\rho}^{t}\widetilde{T_0}^{t}\overline{\vec{u}}^{t} = -\vec{\nabla}\cdot\overline{\rho T_{0d}\vec{u}''}^{t} \tag{16}$$

In deriving Eq. (16), one must note that the time average of the product of the density and the velocity component $\vec{u}''$ is zero. The correlation on the right-hand side of Eq. (14) has been rewritten as a correlation involving the excess of total temperature within the wake and the unsteady velocity.

Equation (16) is valid upstream of the stator but is also valid within the stator passage, provided a fluid particle maintains its total temperature or nearly does so as it convects through the stator. According to Eq. (6), the unsteady velocity that appears in the correlation on the right-hand side of Eq. (16) has two parts, one associated with the nonaxisymmetric component of the average-passage velocity field of the upstream rotor, $\tilde{u}_{i_{(n)}}$, and the other resulting from the interaction of the wake with the stator, $\tilde{\tilde{u}}_i$. Away from the surface of a stator blade $\tilde{u}_{i_{(n)}}$ dominates. Near the surface both are of the same order of magnitude. For an inviscid fluid, their component normal to the stator surface is of equal magnitude but of opposite sign. For a viscous fluid, at the stator surface, these components are of equal magnitude and of opposite sign.

Away from the surface of a stator blade, but near an endwall, the derivative normal to the endwall of the correlation involving the component of $\tilde{u}_{i_{(n)}}$ normal to the endwall and T_{0_d} is the dominant term on the right-hand side of Eq. (16). If the endwalls are right cylindrical surfaces, the resulting term is the radial derivative of the correlation involving the radial component of $\tilde{u}_{i_{(n)}}$ and T_{0_d}. With reference to Fig. 4, T_{0_d} is positive. The time average of the product of the density, T_{0_d}, and the radial component of $\tilde{u}_{i_{(n)}}$ is also positive. At an endwall this correlation is zero, the result of the normal component of $\tilde{u}_{i_{(n)}}$ being zero at the endwall. Thus at the shroud, the radial derivative of the correlation formed by the density, T_{0_d}, and the normal component of $\tilde{u}_{i_{(n)}}$ is negative. At the hub the radial derivative of this correlation is positive. A positive radial derivative implies an energy sink, while a negative radial derivative implies an energy source. The sink and source formed by the radial derivative of the portion of the average-passage total enthalpy flux associated with the unsteady deterministic flow field result in a redistribution of the time-averaged total temperature field in the stator frame of reference. In the present example, it would lead to an increase in the time-averaged total temperature at the shroud and to a decrease at the hub. This would accentuate the total temperature profile, which is opposite to the trend generally associated with turbulent diffusion. With respect to Fig. 2, the radial derivative of the correlation between the radial component of $\tilde{u}_{i_{(n)}}$ and T_{0_d} is negative outboard of 70 percent span and positive from 10 percent of span to 70 percent of span. Thus with respect to the average-passage flow field, there exists an energy sink between 10 percent and 70 percent of span and an energy source outboard of 70 percent of span. The resulting redistribution of total temperature between Stations 3 and 4 as a result of the radial derivative of this correlation is clearly evident. Outboard of 80 percent of span the time-averaged total temperature at Station 4 is greater than that at Station 3, while between 10 percent of span and 80 percent of span the time-averaged total temperature at Station 4 is less than that at Station 3.

In a similar fashion it may be shown that the correlations formed by the radial component of $\tilde{u}_{i_{(n)}}$ and the vector $\tilde{u}_{i_{(n)}}$ account for the spanwise redistribution of momentum with respect to the average-passage flow field attributed to the unsteady deterministic flow state.

As shown by Adkins and Smith [36], accounting for spanwise redistribution of total temperature and momentum attributed to the unsteady deterministic flow state is very important in predicting the aerodynamic performance of multistage axial flow compressors. Likewise Lewis [37,38] showed that accounting for the spanwise redistribution of total temperature and momentum attributed to the unsteady deterministic flow field is very important in predicting the aerodynamic performance of axial flow multistage turbines.

Circumferential Redistribution of Total Enthalpy and Momentum. A topic closely related to spanwise total temperature redistribution is circumferential total temperature redistribution. However, unlike spanwise redistribution, no evidence has come forth suggesting that circumferential redistribution of total temperature (or equivalently total enthalpy) impacts aerodynamic performance. What has been shown is that circumferential redistribution of total temperature leads to the formation of hot spots on the surface of a turbine blade, which impacts turbine life.

Butler et al. [39], showed that circumferential redistribution of an incoming time varying total temperature field can substantially increase the time-averaged temperature of the pressure surface of a turbine rotor. Based on their numerical simulations, temperature spikes of 50 K above a background temperature of 388 K would increase the time-averaged temperature of the pressure surface of a turbine rotor by 38.8 K. Graham [40] stated that an increase in metal temperature of 16.6 K above design intent can reduce the life of a turbine rotor by a factor of two. Thus, even though the increase in pressure side temperature might appear to be small relative to the temperature of the incoming flow, it is large enough to affect the life of a turbine rotor significantly.

Sharma et al. [24] referred to the circumferential redistribution process of converting an unsteady total temperature field into a time-averaged total temperature field as total temperature segregation. The fluid mechanic processes involved with total temperature segregation were first explained by Kerrebrock and Mikolajczak [41] with respect to high-speed compressors. They observed that the absolute total temperature in the wake of a compressor rotor was higher than that outside of the wake, as shown in Fig. 4. As the wake passed through the downstream stator, the wake particles drifted toward the stator pressure surface, carrying with them an excess of total temperature. This redistribution of total temperature resulted in a circumferential variation in the time-averaged total temperature distribution exiting the stator. The total temperature was found to be higher adjacent to the pressure surface than it was near the suction side. In the case of a turbine, when the total temperature excess is the result of a hot streak formed in the rotor, the fluid particles within the hot streak drift toward the pressure surface of the downstream vane. The flow kinematics are shown in Fig. 5. In the frame of reference of the rotor, the fluid particles in the hot streak have the same flow direction as those of the cold fluid particles in the free stream. However, the magnitude of the relative velocity of the fluid particles in the hot streak is less than that of cold fluid particles in the free stream. In the frame of reference of the downstream vane, this difference in the magnitude of relative velocities leads to a drift of the fluid particles in the hot streak toward the pressure surface of the vane. The result is a significant increase in the time-averaged temperature of the vane pressure surface.

Total temperature segregation within the framework of the average-passage model is accounted for by the average-passage enthalpy flux associated with the unsteady deterministic flow field. The flow physics as modeled by Kerrebrock and Mikolajczak [41] is accounted for by the first two terms in Eq. (6). To

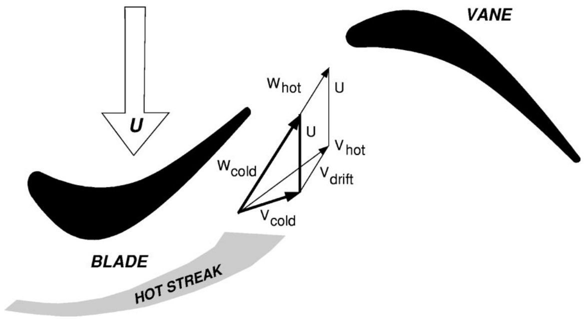

Fig. 5 Kerrebrock and Mikolajczak effect in a turbine stage

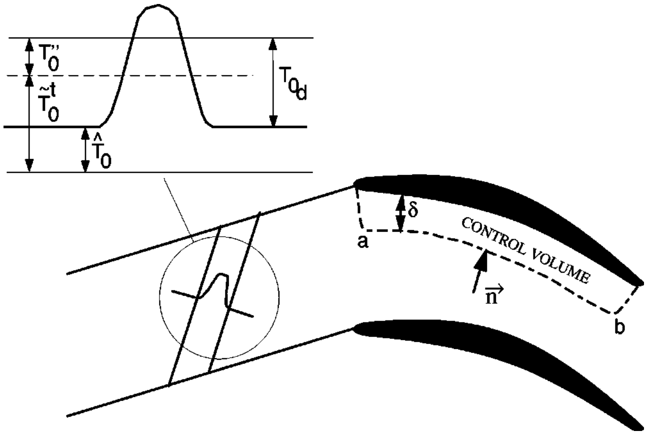

Fig. 6 Convection of a hot streak through a turbine cascade

show this, consider the flow through a vane in which the incoming flow is unsteady in time. Once again the flow field is assumed to be deterministic, inviscid, and adiabatic. The incoming unsteady flow is generated by an incoming nonuniform total temperature field (i.e., a hot streak). The incoming total pressure field is assumed to be independent of time and uniform in the radial and circumferential direction. The working fluid is an ideal gas with constant thermodynamic properties. The energy equation for this unsteady flow is Eq. (8), while the equation governing the time average flow is Eq. (16).

With respect to a control volume (i.e., see Fig. 6) located away from either endwall and adjacent to the pressure surface of a vane, whose boundaries are defined by the streamlines associated with the time-averaged flow, Eq. (16), may be rewritten as:

$$\overline{\rho}^t\widetilde{T_0}^t\widetilde{U}^t\delta|_b-\overline{\rho}^t\widetilde{T_0}^t\widetilde{U}^t\delta|_a=-\int\overline{\rho T_{0d}\overrightarrow{u''}\cdot\vec{n}}^t\,ds \tag{17}$$

whose differential form is:

$$\frac{d}{ds}\overline{\rho}^t\widetilde{T_0}^t\widetilde{U}^t\delta=-\left.\overline{\rho T_{0d}\overrightarrow{u''}\cdot\vec{n}}^t\right|_a^b \tag{18}$$

where δ is the width of the control volume, s is the distance along the pressure surface, $\widetilde{U}^t$ is the axial velocity, and $\vec{n}$ is a unit vector normal to the control volume. Equation (17) is essentially the result derived by Kerrebrock and Mikolajczak [41]. At the surface of the vane

$$-\overline{\rho T_{0d}\overrightarrow{u''}\cdot\vec{n}}^t$$

is zero. At the surface of the control volume labeled $a-b$ in Fig. 6, which is in the flow stream, the total temperature flux

$$-\overline{\rho T_{0d}\overrightarrow{u''}\cdot\vec{n}}^t$$

is positive. This indicates a flow of total temperature into the control volume. This positive flux increases the time-averaged total temperature along the pressure surface. Along the suction surface, the flux is negative, which results in a reduction of the time-averaged total temperature along the suction surface.

As was previously stated, there are no published data, which suggests that total temperature segregation impacts aerodynamic performance. Therefore, introducing models to account for total temperature segregation in simulations where the objective is estimates of aerodynamic performance is deemed unnecessary. If the objective of the simulation is an assessment of the impact of total temperature segregation on turbine blade surface temperature, there appears to be a need for inclusion of models that account for total temperature segregation in the simulation. However, this is not necessary, because it is possible to construct credible estimates of the segregated total temperature field from average-passage simulations, which are devoid of the flow physics associated with segregation as part of a post-processing procedure. This post-processing procedure entails estimating the temporal correlation in Eq. (18) from results obtained from the average-passage flow state of the incoming hot streak. With the temporal correlation known and assuming that the velocity in Eq. (18) can be approximated by the average-passage velocity field of the blade row through which the hot streak is passing, Eq. (18) may be solved to yield the segregated total temperature field produced by the incoming hot streak.

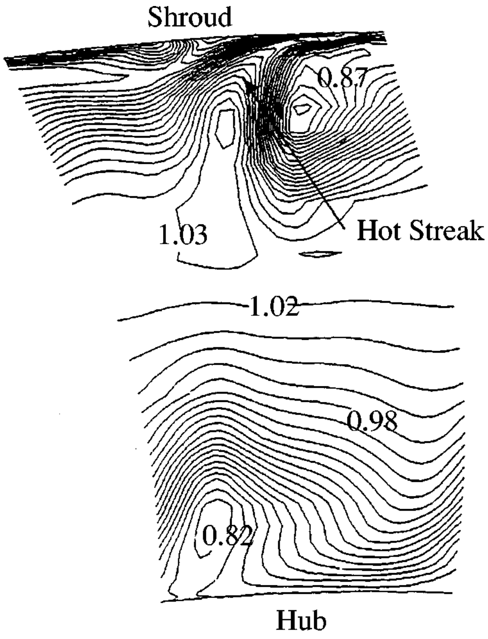

Fig. 7 Snapshot of unsteady total temperature ratio exiting a turbine rotor

To test the validity of the above procedure for estimating hot streak segregation, Kirtley et al. [42] applied the procedure to the passage of a hot streak through a turbine stator. The hot streak was generated by the secondary flow field within the upstream rotor. Kirtley et al. [42] used a code that solved the average-passage flow equations and an unsteady wake–blade-row interaction code. Both codes assumed all metal surfaces to be adiabatic. The simulation based on the average-passage code did not incorporate a model for the segregation of the hot streak as it passed through the stator. In the unsteady simulation, the incoming unsteady flow to the stator was established from the average-passage simulation of the upstream rotor. Figure 7 shows a cross-channel view (i.e., axial plane) of the incoming total temperature distribution to the stator at an instant in time. The hot streak is located near 90 percent of span.

The average-passage simulation of the rotor (i.e., the average-passage flow field in which the incoming hot streak is defined) was used to estimate the temporal correlation on the right-hand side of Eq. (18). Using the velocity and density field associated with the average-passage flow field of the stator, Eq. (18) was solved to determine the time-averaged total temperature distribution along the stator suction and pressure surface. The only empirical information used in the solution of Eq. (18) was the axial

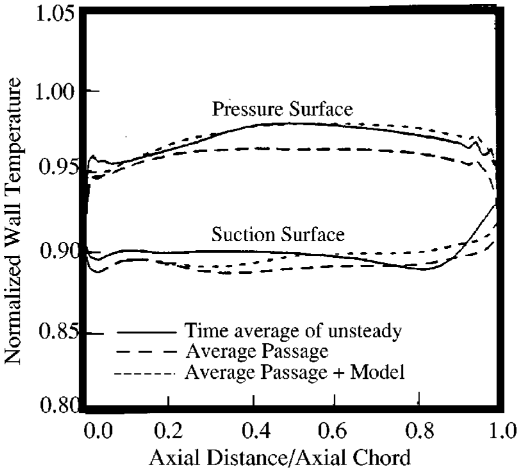

Fig. 8 Turbine blade temperature distribution

location at which the correlation on the right-hand side of Eq. (18) became small. This information was deduced from the unsteady simulation and set at 50 percent of chord.

The chordwise time-averaged temperature distributions along the suction and pressure surface at 90 percent of span from the average-passage simulation of the vane, the vane average-passage simulation as corrected by Eq. (18), and the unsteady simulation are shown in Fig. 8. The temperature has been normalized with respect to the mass-averaged incoming total temperature. The time average surface temperature distribution derived from the unsteady simulation is shown as a solid line in the figure. The chordwise variation of the time-averaged surface temperature is a result of the vane secondary flow field and total temperature segregation. The average-passage simulation of the vane, devoid of the flow physics associated with segregation, only accounts for the redistribution of total temperature due to the vane secondary flow field. On the pressure side the temperature predicted by the average-passage simulation falls short of that predicted by the unsteady simulation. The average-passage result, as corrected by the procedure outlined above, agrees fairly well with that predicted by the unsteady simulation. The increase in temperature along the pressure surface from 20 percent of chord to near 50 percent of chord is captured by the correction procedure. In addition, the cooling of the suction surface as a result of the segregation process is also captured by the procedure.

An alternative procedure to account for total temperature hot streak segregation is outlined by Orkwis and Turner [43].

Closely related to the topic of total temperature segregation is the flow process of circumferential transport of momentum attributed to the unsteady deterministic velocity field. All the terms in Eq. (5) play a role in the circumferential redistribution of momentum.

Both Valkov and Tan [44–46] and Dawes [47] examined the impact of this momentum transport on the performance of a compressor blade row. Dawes concluded that additional loss above that associated with mixing-out of the leakage flow was generated by the unsteady interaction involving the rotor tip leakage flow and the downstream stator. Unfortunately because of the procedure used by Valkov and Tan [45,46] to estimate loss, the significance of their loss estimates is unclear. The significance and fluid mechanics responsible for loss generation in compressors due to unsteady interactions involving two-dimensional wakes and blade boundary layers that are turbulent is unknown at this time.

Fritsch and Giles [48] conducted an analytical and numerical study to assess the impact on performance resulting from the passage of a wake through a turbine cascade. From their simulations it appears that the loss within the turbine passage is increased by having the wake convect through the turbine as compared to having it mix-out prior to entering the turbine. Whether there is an unsteady interaction between the incoming wakes and the blade boundary layers that contributes in a measurable way to loss generation in turbines is unknown at the present time.

Wake Recovery. Another unsteady process whose impact on blade row performance has been studied both analytically and through numerical simulations is wake recovery. Wake recovery, first identified by Smith [49], involves the reduction or amplification of the velocity deficit of a wake by a reversible unsteady process that reduces or increases the mixing loss associated with the wake. Adamczyk [50] has shown that wake recovery is directly tied to the portion of the average-passage stress, Eq. (5), formed by the unsteady deterministic flow field. All the terms in Eq. (5) contribute to the wake recovery process.

A simple example that illustrates the fluid mechanics associated with the wake recovery process was given by Smith [49] and is repeated here. Figure 9 shows a wake entering and exiting a compressor and turbine blade row. The flow field is assumed to be inviscid, two-dimensional, and incompressible. The flow state is deterministic. Evaluating the circulation, Γ, around a circuit whose boundary lies along the centerline of the wake and its edge yields:

$$\Gamma = v_d l \tag{19}$$

where l is the length of the wake filaments bounded by the two stagnation stream lines and v_d is the velocity deficit of the wake, Fig. 9. According to Kelvin's theorem, Batchelor [51], the circulation associated with the incoming wake must remain constant as the wake convects through the cascade. Hence the wake circulation at the inlet to the cascade is equal to that at the exit. This equality yields the following expression for the ratio of the velocity deficit of the wake at the exit of the cascade to that at the inlet:

$$v_d|_{\text{exit}} = \frac{v_d l|_{\text{inlet}}}{l|_{\text{exit}}} \tag{20}$$

If the length of a wake segment is increased as it passes through the cascade, as illustrated in the case of a compressor cascade, its velocity deficit is reduced, leading to a reduction in the wake mixing loss. If the length of a wake segment is reduced, as it is in the turbine illustration, its velocity deficit is increased, enhancing the wake mixing loss. This simple example by Smith [49] based on kinematic arguments illustrates the recovery process in both compressors and turbines.

Valkov and Tan [44] and Deregel and Tan [52] conducted a number of very detailed numerical simulations, which confirmed the kinematic model proposed by Smith [49] for wake recovery in axial flow compressors.

Adamczyk [50] used a perturbation analysis to link wake recovery to wake mixing loss and to the average-passage stress associated with the unsteady deterministic flow field. Adamczyk's [50] analysis, like that of Smith's [49] assumed the flow to be two-dimensional and incompressible. If one neglects the effect of viscosity as the wake passes through the cascade, the loss reduction or increase due to the wake mixing out after it exits the cascade as opposed to mixing out prior to entering the cascade is given as:

$$\chi_{\text{inlet}} - \chi_{\text{exit}} = K_{\text{inlet}} - K_{\text{exit}} \tag{21}$$

where χ is the loss coefficient at the inlet and exit to the cascade, respectively. K_{inlet} is the flux in kinetic energy of the incoming unsteady flow, and K_{exit} is the flux in kinetic energy of the exiting unsteady flow.

Whether the wake mixing loss is reduced by having the wake pass through a cascade prior to being mixed-out is dependent on the reduction of the kinetic energy associated with the unsteady deterministic velocity field across a blade row. This kinetic energy is equal to one half the sum of the diagonal components (i.e., the trace) of the average-passage stress associated with the unsteady deterministic flow field. The sum of the diagonal components of

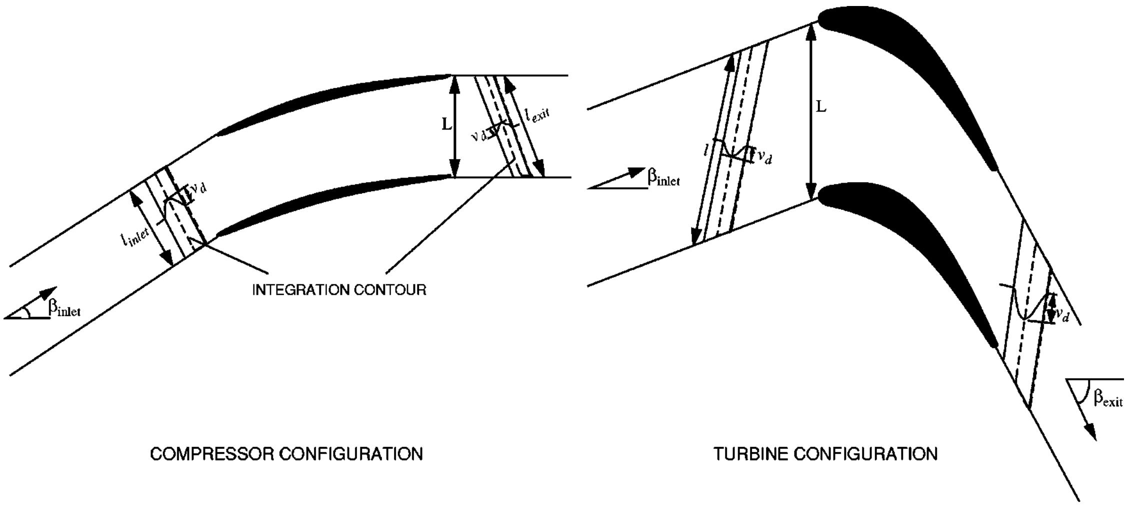

Fig. 9 Wake blade row interactions in a typical turbine and compressor

the average-passage stress associated with the unsteady deterministic flow field is a measure of the magnitude of the velocity field associated with this flow field.

The link between the recovery process and the component of the average-passage stress associated with the unsteady deterministic flow field is established by means of a transport equation formed by the vector dot product of the unsteady deterministic velocity and the linearized inviscid momentum equation it is assumed to satisfy. The time average of the resulting transport equation when integrated across a cascade yields:

$$K_{inlet} - K_{exit} = \frac{1}{L}\int_{vol} \frac{\overline{u_i'' u_j''}^{t}}{2} \frac{\partial U_i^{ap}}{\partial x^j} dVol \qquad (22)$$

where L is the pitch of the cascade. The details can be found in Adamczyk [50].

The integral on the right-hand side of Eq. (22) controls the growth of the wake deficit as it passes through the cascade. This growth is the result of the wake being strained by the time-averaged velocity field within the cascade. If this integral is positive, the wake deficit is reduced and there is a transfer of energy from the unsteady deterministic flow field to the average-passage flow field. A reduction in the wake deficit leads to a reduction in the wake mixing loss. If this integral is negative, energy is transferred from the average-passage flow field to the unsteady deterministic flow field. This transfer of energy increases the wake deficit leading to an increase in wake mixing loss.

Adamczyk [50] noted that in many cases the transfer of energy from the unsteady deterministic flow field to the average-passage flow field is opposite to that that occurs between the nondeterministic flow field (turbulent flow state) and the average-passage flow field. For a turbulent flow, energy flows from the mean flow to the unsteady chaotic flow associated with turbulence where the energy cascades down to fine scale eddies and is dissipated, resulting in an increase in the internal energy (i.e., temperature) of the mean flow. The common practice of using a gradient diffusion model with a positive diffusion coefficient (i.e., positive eddy viscosity) to model this energy transfer process is well justified. However, the use of a gradient diffusion model to account for wake recovery may be questionable. In the case of wake recovery in compressors, the energy associated with the unsteady deterministic flow field of the wakes is reduced by the strain imposed on the wakes as they convect through a blade row. The energy loss by the unsteady deterministic flow field is transferred by a reversible process to the time-averaged flow field. The use of a gradient diffusion model to account for wake recovery in compressors would thus require a negative diffusion coefficient, which is physically difficult to justify.

There are some data that show the need to account for the wake recovery process in simulating multistage turbomachinery flows, especially at off-design operating conditions. To model the recovery process within the context of the average-passage flow model, one must realize that recovery is accounted for through the portion of the average-passage stress associated with the unsteady deterministic flow field. Furthermore, it is the strain imposed on the wakes as they convect through a blade row and the subsequent modification of the average-passage stress that needs to be accounted for. The strain responsible for the wake recovery process can be decomposed into two components. The first component is associated with the axisymmetric flow field of the blade row through which the wake is passing. The other component is associated with the strain imposed by the time-averaged nonaxisymmetric flow field of the blade row through which the wake is passing. The strain imposed by the axisymmetric flow field is accounted for in the procedure outlined by Adamczyk et al. [32]. The strain imposed by the time-averaged nonaxisymmetric flow field is currently not being accounted for in simulations based on the average-passage flow model.

Recent works by Van Zante et al. [53] and van de Wall [54] provide models that account for the strain imposed by the time-averaged nonaxisymmetric flow field on recovery. However, these models remain to be incorporated into simulations of the average-passage flow field. The model developed by Van Zante et al. [53] extended the model of Smith [48] to include the effects of viscosity. The model of Van Zante et al. [53] provides an estimate of the kinetic energy associated with the unsteady deterministic velocity field of the wake as it convects through a blade row. The result of Van Zante et al. [53] was compared to LDV measurements from a single-stage high-speed compressor. The agreement between the predicted decay of the velocity deficit of the rotor wake and that measured was quite good. The results of Van Zante et al. [53] showed that the decay of the rotor wake as it convected through the stator was dominated by the kinematic recovery process as outlined by Smith [49] and not by viscosity.

Van de Wall [54] was able to develop a transport model for the average-passage stress associated with the unsteady deterministic flow field. Van de Wall's model is three dimensional and includes the effects of viscosity. By solving this transport equation, van de Wall [54] was able to estimate the decay of the kinetic energy associated with the unsteady deterministic flow field. For a compressor, van de Wall's [54] findings were similar to those of Valkov and Tan [45] and Van Zante et al. [53]. All these researchers found that wake mixing loss in a compressor is reduced by nearly 70 percent as a result of the wake being strained by the velocity field associated with the average-passage field of the blade row through which it is passing. At the design point of a well-designed machine, the mixing loss of a compressor blade is estimated to be 15 percent of the total loss. The effect of recovery reduces the mixing loss to 4.5 percent of the total, a 10.5 percent reduction in the total loss. At an off-design operating condition of an axial compressor, where there might be significant regions of flow separation, the effect of recovery becomes even more important. Smith [55] estimated that at the design point of a well-designed axial compressor recovery can yield a half point increase in efficiency.

For a turbine, van de Wall [53] found that recovery has a detrimental impact on performance. For an inviscid flow van de Wall [53] showed that the velocity deficit within a stator wake increased as it passed through the downstream rotor. Viscosity was found to limit the growth of the velocity deficit, but because this process is nonreversible, it leads to an increase in the loss of total pressure across the blade row through which the wake is passing. The more the wake decays prior to entering the downstream blade row, the less the loss in total pressure across the blade row through which the wake is passing.

The recovery process can also lead to an increase in the pressure rise across a compressor blade row, and to a reduction in the pressure drop across a turbine blade row. The mathematical details are given in Appendix B. According to Eq. ($B11$) the pressure rise coefficient C_p^{us} resulting from an unsteady incoming vortical flow is:

$$\begin{aligned} C_p^{us} &= \frac{\overline{\overline{p}^{t}}^{y}\big|_{\infty} - \overline{\overline{p}^{t}}^{y}\big|_{-\infty}}{(1/2)q_{ref}^2|_{-\infty}} \\ &= 1 - \frac{\cos^2\beta_{-\infty}}{\cos^2\beta_{\infty}} \\ &\quad + \left[\delta_R\big|_{-\infty} - \delta_R\big|_{\infty}\left(\frac{\cos^2\beta_{-\infty}}{\cos^2\beta_{\infty}}\right)\right] \end{aligned} \tag{B11}$$

where $\beta_{-\infty}$ and β_{∞} are the inlet and exit flow angles of the steady flow, respectively. The first two terms in Eq. ($B11$) are the pressure rise produced by the steady incoming flow while the term in parentheses is that attributed to the incoming unsteady vortical flow. The variable δ_R is the recovery energy thickness defined by Eq. ($B10$). This thickness is a measure of the flow blockage attributed to the unsteady vortical flow. Its relationship to the portion of the average-passage stress associated with the unsteady deterministic flow field is given by Eq. ($B20$).

For a compressor cascade, $\cos^2\beta_{-\infty} < \cos^2\beta_{\infty}$, thus the incoming unsteady flow will increase the pressure rise across the cascade if $\delta_R|_{-\infty} > \delta_R|_{\infty}(\cos^2\beta_{-\infty}/\cos^2\beta_{\infty})$. For a turbine cascade, $\cos^2\beta_{-\infty} > \cos^2\beta_{\infty}$, and the incoming unsteady flow will increase the pressure drop across the cascade if $\delta_R|_{-\infty} < \delta_R|_{\infty}(\cos^2\beta_{-\infty}/\cos^2\beta_{\infty})$.

To provide a quantitative estimate of the impact of incoming wakes on cascade pressure rise, consider first a compressor cascade that turns the flow through 25 deg. The incoming flow is at an angle of 46 deg with respect to the axial direction. The flow exits the cascade at 21 deg. The flow conditions for this compressor and its geometry are those used by Valkov and Tan [45] in their study. The incoming wakes are one-dimensional shear flows, which are assumed to be perpendicular to the incoming flow. As the wakes convect through the cascade, they are strained by the velocity field within the cascade passage. This straining was shown to reduce the wake velocity deficit. This reduction in the wake velocity deficit corresponds to a reduction in the kinetic energy of the unsteady flow associated with the wakes. For this cascade the reduction in the kinetic energy of the unsteady flowfield across the cascade is approximately 61 percent. The reduction of the magnitude of the unsteady axial velocity component across the cascade is approximately 28.5 percent. These values are extracted from the kinematic model put forth by Smith [49] for wake recovery. Based on these values, the pressure rise across the cascade attributed to the steady potential flow according to Eq. ($B11$) is:

$$C_p^{(0)} = 0.446 \tag{23}$$

while that attributed to the unsteady flow (i.e., $C_p^{(2)} = C_p^{us} - C_p^{(0)}$) is approximately:

$$C_p^{(2)} = (0.071)\left.\frac{\overline{\vec{u}^{(1)}\cdot\vec{u}^{(1)}}^{t}}{\vec{u}^{(0)}\cdot\vec{u}^{(0)}}\right|_{-\infty} \tag{24}$$

Equation (24) shows that the pressure rise attributed to the unsteady flow is proportional to the velocity deficit of the incoming wake squared. Assuming the unsteady flow is generated by wakes whose deficit is 25 percent of the incoming flow, the increase in pressure rise attributed to the incoming wakes is approximately 1.0 percent. For this cascade Valkov and Tan [45] reported an increase in static pressure rise of only 0.5 percent Valkov and Tan's [45] estimate was deduced from a numerical simulation, which included the effects of viscosity. Whether the factor of two difference in the estimate of the benefit of recovery is solely related to the effects of viscosity is unclear.

Smith [2] reported the pressure rise per stage of a four-stage compressor was increased by approximately 4 percent as the axial gap between the blade rows was reduced. The midspan geometry of the compressor reported upon by Smith [2] is very similar to the cascade geometry described above. If one assumed this pressure rise was solely due to the recovery process and that the pressure rise is equally split between the rotor and the stator, the 4 percent per stage is equal to 2 percent per blade row. The current analysis and that of Valkov and Tan [45] indicate that the increase in pressure rise resulting from incoming wakes should scale as the relative wake deficit squared (i.e., wake deficit relative to the incoming relative flow). Using Smith's [2] data and assuming the wake deficit in the compressor analyzed by Smith [2] is 25 percent of the incoming flow at the nominal axial spacing and 50 percent at half the nominal spacing (i.e., estimates from Valkov and Tan [45]) the increase in pressure rise across a single blade row attributed to incoming wakes is:

$$C_p^{(2)} = (0.0475)\left.\frac{\overline{\vec{u}^{(1)}\cdot\vec{u}^{(1)}}^{t}}{\vec{u}^{(0)}\cdot\vec{u}^{(0)}}\right|_{-\infty} \tag{25}$$

For a wake deficit of 25 percent of the incoming flow, the increase in pressure rise according to Eq. (25) is nearly 0.7 percent. This number is slightly greater than that given by Valkov and Tan [45] (i.e., 0.5 percent) and less than that given by the current analysis (i.e., 1 percent).

In this example, had the compressor cascade turned the flow to axial, which would imply a flow turning of 46 deg (a value representative of advanced designs) the increase in pressure rise as estimated by Eq. ($B11$) would be:

$$C_p^{(2)} = (0.1)\left.\frac{\overline{\vec{u}^{(1)}\cdot\vec{u}^{(1)}}^{t}}{\vec{u}^{(0)}\cdot\vec{u}^{(0)}}\right|_{-\infty} \tag{26}$$

For this cascade the pressure rise produced by the steady flow according to Eq. ($B11$) is approximately:

$$C_p^{(0)} = 0.5 \tag{27}$$

For a wake deficit of 25 percent of the incoming flow, the increase in pressure rise is 1.25 percent of that produced by the steady flow. If the pressure rise increase were equally split between a rotor and stator, the increase in stage pressure would be 2.5 percent, a number that is not all that insignificant. One may view this number as an upper bound whose value is reduced because of viscosity. The magnitude of the impact of viscosity on the wake recovery processes is not clear.

The significance of the recovery process on aerodynamic performance depends on the design parameters of a machine. As the aerodynamic loading of blade rows is increased in an attempt to design machinery with fewer parts and of reduced weight, the blade wakes will deepen and the recovery process will have to be accounted for. Recovery is also more important at off-design conditions, where large regions of flow separation generate large velocity deficits.

Blade Indexing. This section is concluded with a brief discussion of the components of the average-passage stress and the average-passage enthalpy flux that is associated with the blade rows which are in the same spatial frame of reference. They are the last terms in Eqs. (*A*9) and (*A*10). These components of the average-passage stress and the average-passage enthalpy flux account for the effect of circumferential spatial distortions with length scales unrelated to the pitch of the blade row of interest. These components account for performance changes brought about by circumferential indexing or clocking of blades which are in the same reference frame. The experimental findings of Barankiewicz and Hathaway [56] suggest that the effect of indexing in axial flow compressors is small and therefore need not be addressed. However for turbines, the work of Arndt [57] and Sharma et al. [58] shows that there are performance gains to be had through the indexing of blade rows.

The fact that indexing has a measurable impact on turbine performance and an insignificant impact on compressor performance is an indication the turbine wakes persists far longer than compressor wakes. This observation is consistent with the findings of van de Wall [54].

Stress and total enthalpy flux models, which account for the effect of indexing on the average-passage flow field, have yet to be developed. However, the procedure outlined by Adamczyk et al. [32] may be used to estimate the magnitude of the third term in Eqs. (*A*9) and (*A*10) attributed to the average-passage flow fields other than that of the blade row of interest. The resulting estimate accounts for the straining and rotation of wakes by the axisymmetric flow field and the vorticity generated by this interaction.

Examples of Simulations

The previous section presented a number of examples that illustrate the effects of the unsteady deterministic flow field on the average-passage flow field and how these effects may be accounted for in CFD simulations of multistage axial flow turbomachines. In this section, the results from a number of simulations will be presented to illustrate the predictive capabilities afforded by incorporating these models into a CFD code. The code used to generate these results is referred to as APNASA. Some of the results to be presented are predictions and will be noted as such. A predictive result implies the simulation was done prior to the experiment. Some of the simulations were done by researchers in engine companies who are attempting to assess the predictive capabilities of this code. In all cases no information was provided to APNASA, which set the aerodynamic matching of stages. The aerodynamic matching of stages and the flow blockage associated with that matching is an output of the simulation and not an input.

Low-Speed Research Compressor. Figure 10 shows the measured pressure rise characteristic along with simulation results at a flow coefficient of 0.395 and 0.375 for the Lewis low-speed axial compressor (LSAC). LSAC is a four-stage machine with an inlet IGV, Wellborn and Okiishi [59], which is representative of the rear stages of a high-pressure (H.P.) compressor. The compressor is of a modern design employing hub-shrouded stators with end-bends. The four stages are geometrically identical. The simulation accounted for the rotor tip clearance. The simulation did not include the stator hub cavities nor did the simulations account for stator hub leakage. Two experimental results are shown: one for a baseline leakage with stator hub cavities present, the other with no leakage and no cavities present.

At the flow coefficient of 0.395 (which is near the measured peak efficiency operating point) and at the flow coefficient of 0.375, the simulation results are in good agreement with the measurement. An attempt to simulate an operating condition near peak pressure failed to converge. The simulation did not account for casing treatment over the first rotor present in the experiment. Tests with the casing treatment removed show that the compressor stalls at a flow coefficient near the peak pressure point of the characteristic.

Figure 11 shows the measured static pressure rise characteristic for each stage along with results from the simulations. The agreement between the simulation results and the data is very good. For the flow coefficient of 0.395, Fig. 12 shows plots of the total and static pressure coefficient, the axial and absolute tangential velocity, and the absolute and relative flow angle as a function of span for the simulation and the experiment. The plots are for an axial location behind the second stator. Once again, the agreement between the simulation results and the data is good. The slight difference between the static pressure coefficient derived from the simulation and that measured inboard of 40 percent span is unknown. For the same flow coefficient, Fig. 13 compares the simulated and measured results for an axial location behind the third stage rotor. The agreement between the simulation results and that derived from the measurements is comparable to that shown in Fig. 12. Additional comparisons are presented in Adamczyk et al. [60].

These results clearly show that the APNASA code with its current models that account for the effects of the unsteady deterministic flow field is, to a large extent, capturing the flow features that are setting the performance of the LSAC compressor.

High-Speed Ten-Stage Compressor. The next set of results are for the high pressure (H.P.) compressor of the GE 90 engine series. This compressor has ten stages plus an IGV. At the design point the first three stages of this compressor are transonic. The origin of this compressor dates back to the GE E^3 compressor

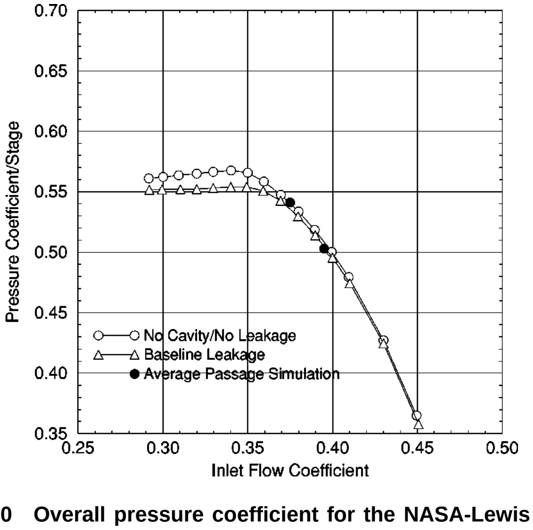

Fig. 10 Overall pressure coefficient for the NASA-Lewis low-speed four-stage axial compressor

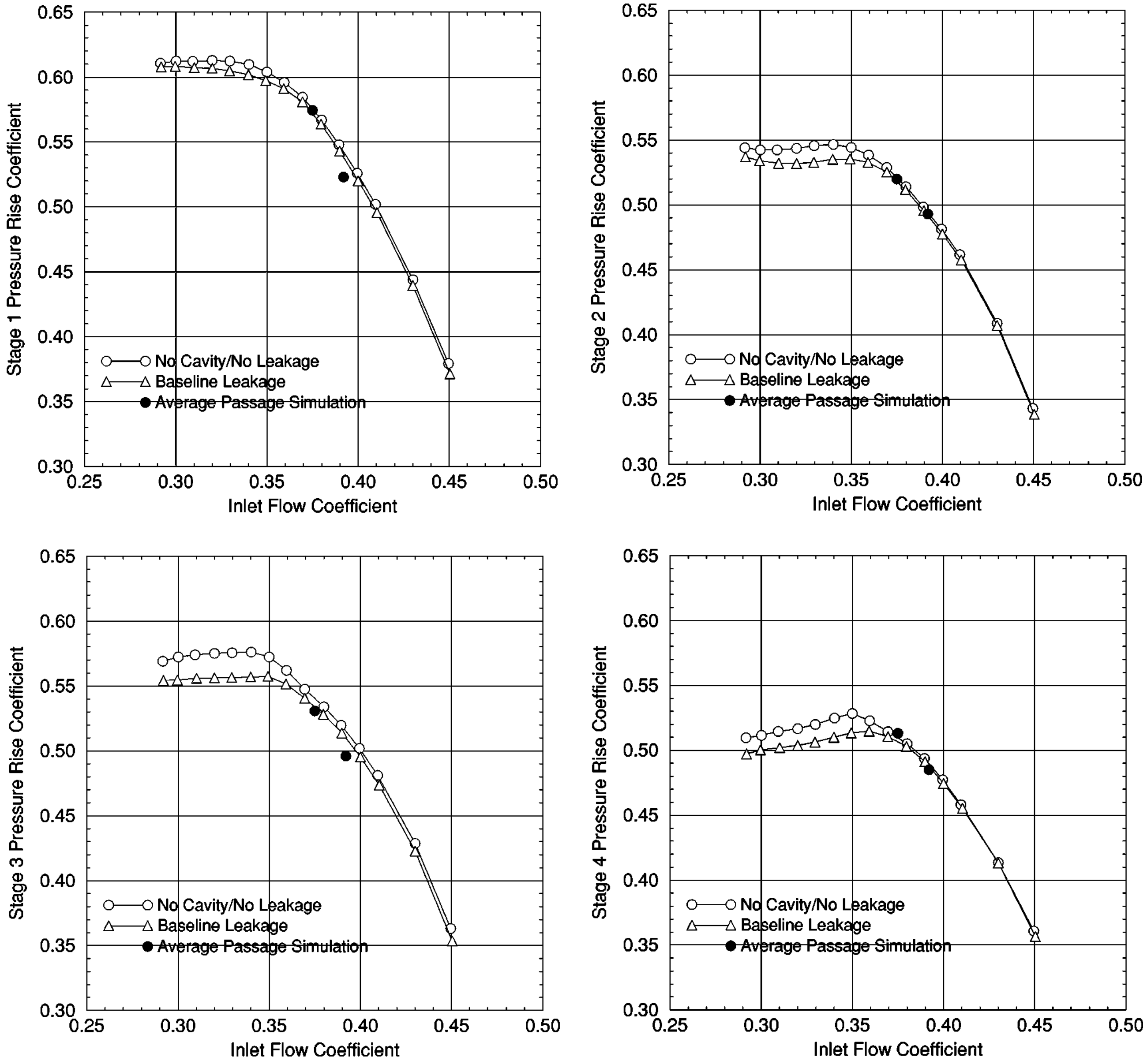

Fig. 11 Individual stage pressure rise coefficient as a function of inlet flow coefficient for the NASA-Lewis low-speed four-stage axial compressor

[61,62]. In simulating this compressor, all known leakage and bleed flows were accounted for. The first set of results, Fig. 14, shows the total temperature and total pressure at the exit of each rotor as predicted by APNASA relative to that predicted by a refined quasi-three-dimensional flow code, CAFMIX II, developed by Smith [63]. The results are presented in terms of a relative difference between the APNASA predictions and those of CAFMIX II. The leakage and bleed flows are the same in both simulations. The simulated operating point of the compressor is near its design point. Figure 14 shows that the results from both models are in good agreement with each other throughout the compressor. The maximum difference in total temperature is less than 0.8 percent, and the difference in total pressure is less than 4 percent. Figure 15 shows spanwise profiles of the normalized total pressure distribution and the normalized total temperature distribution at three axial locations within the compressor. The locations are the exit of the third and seventh stage and at the compressor discharge. Once again the agreement between the two models is quite good. The average-passage model appears to give results very comparable to those of a refined quasi-three-dimensional flow model without the empiricism built into the quasi-three-dimensional model.

An interesting outcome of this study is a comparison between the flow blockage estimates of CAFMIX II and those deduced from the APNASA simulation, Turner [64]. The flow blockage deduced from the APNASA simulation is based on the definition of flow blockage used in the CAFMIX II code. The comparison is shown in Fig. 16. Even though the throughflow results from both codes are nearly the same, the flow blockage estimates are markedly different. For example, for the fifth stage the flow blockage estimate of CAFMIX II is 1.4 times larger than that deduced from the APNASA simulation. In addition, the flow blockage deduced from the APNASA simulation is almost constant throughout the compressor, while the estimate from CAFMIX II increases from the front to the discharge of the compressor. The difference in the two estimates of blockage is nearly equal to the empirical blockage corrections used by CAFMIX II that were derived from a data match of another compressor.

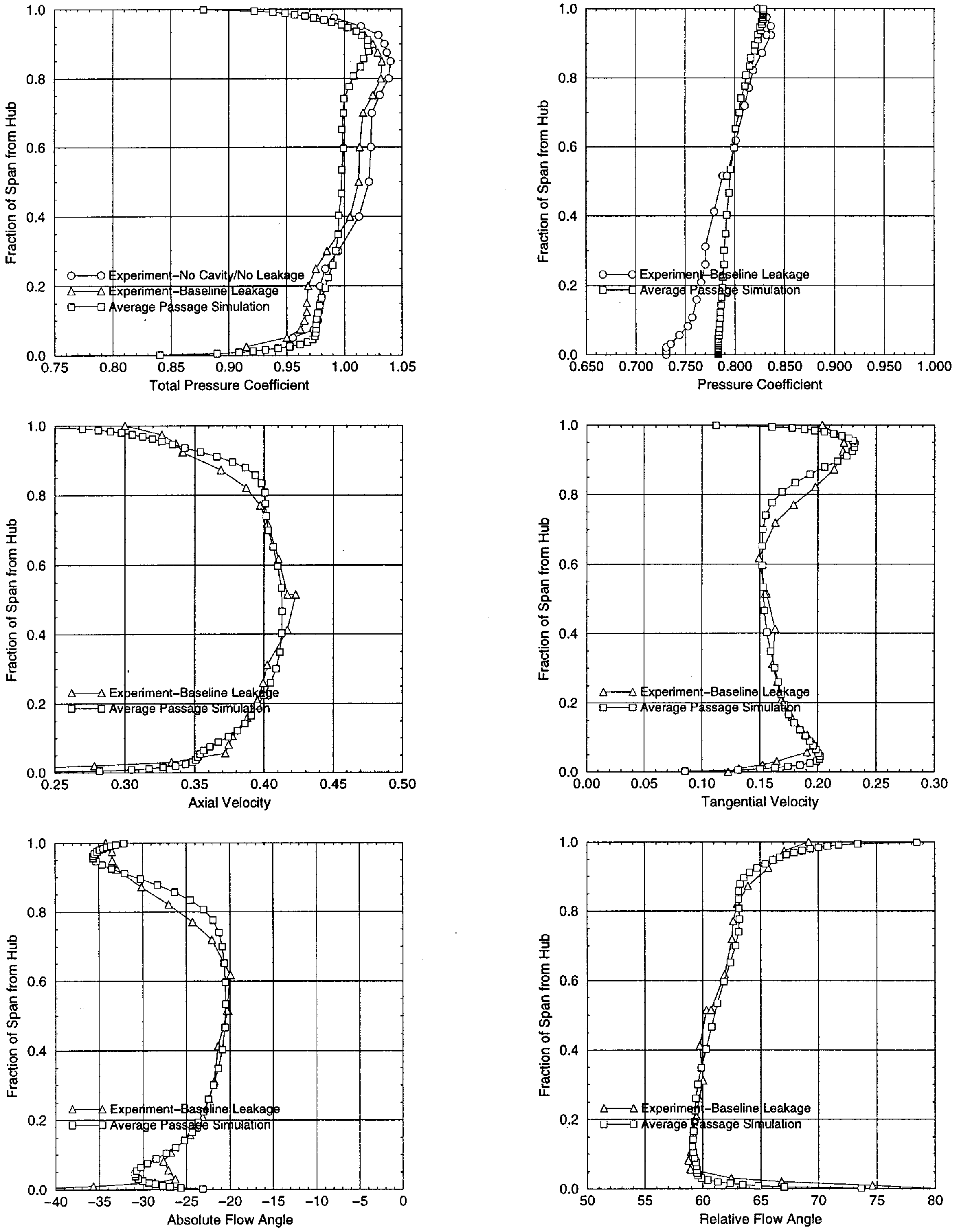

Fig. 12 Axisymmetric flow variables exiting the second-stage stator in the NASA-Lewis low-speed four-stage axial compressor

Since the predicted total temperature and total pressure rise through the compressor by both simulations was nearly the same, one may wonder if the difference in estimated flow blockage is being compensated for by differences in estimates of the flow angle exiting the blade rows. Figure 17 shows the spanwise distribution of the flow angle exiting the third-stage rotor, the third-stage stator, the seventh-stage rotor, and the seventh-stage stator as predicted by both codes. The agreement between the two predictions is good, but there are differences. The sensitivity of total pressure rise or total temperature rise to changes in flow blockage or exit flow angle for this compressor is unknown to the author. Whether the difference in the predicted exit flows seen in Fig. 17

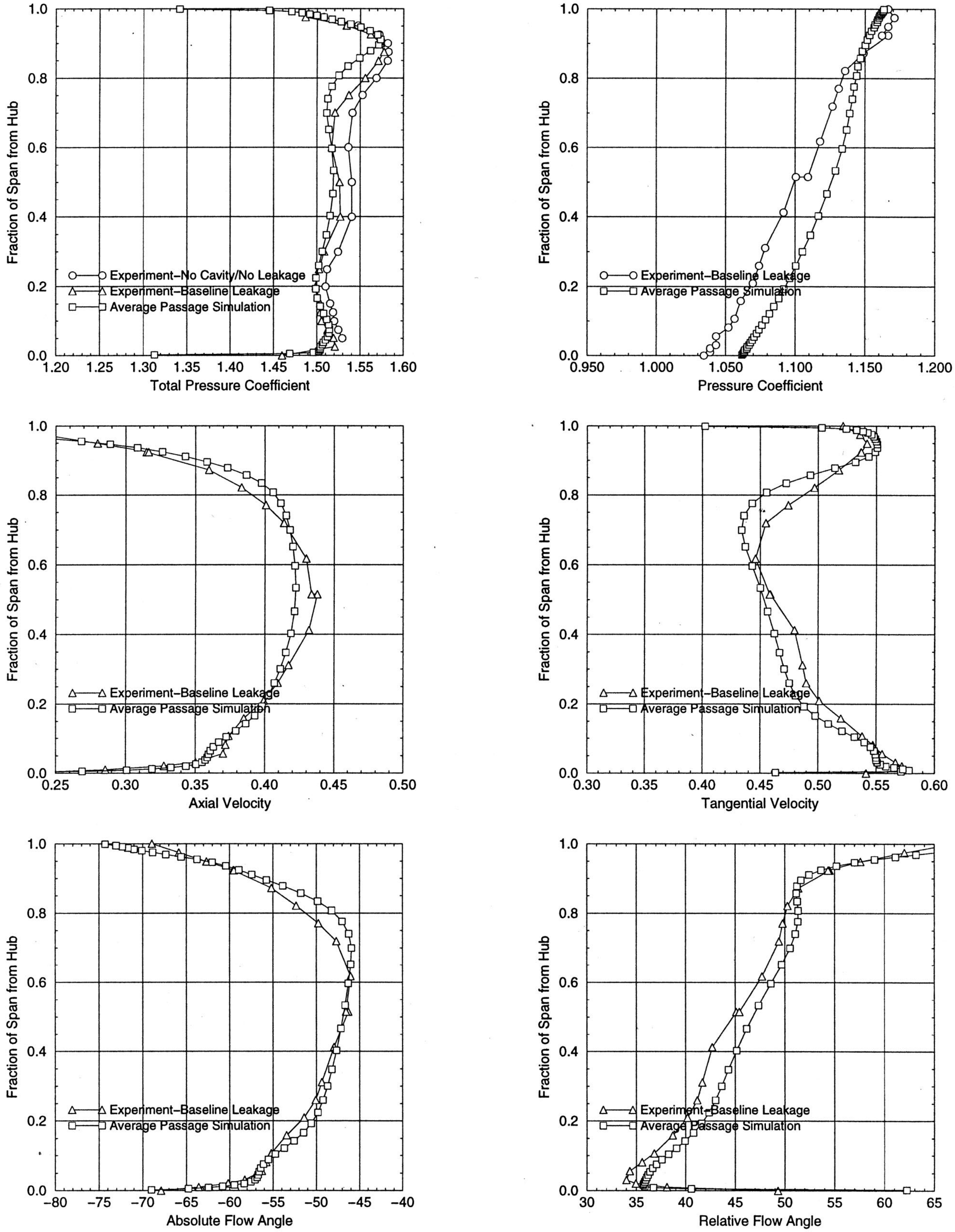

Fig. 13 **Axisymmetric flow variables exiting the third-stage rotor in the NASA-Lewis low-speed four-stage axial compressor**

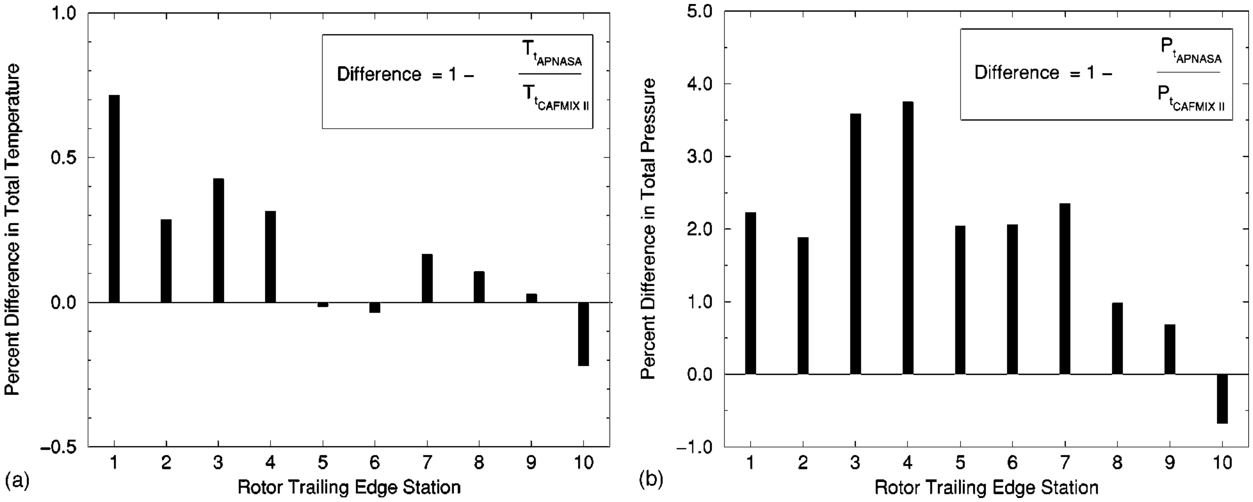

Fig. 14 (***a***) **Comparison of total temperature as predicted by APNASA and CAFMIX II for the ten-stage GE90 compressor; (*b*) comparison of total pressure as predicted by APNASA and CAFMIX II for the ten-stage GE90 compressor**

compensates for the difference in estimated flow blockage seen in Fig. 16 is unknown.

The results presented in Figs. 16 and 17 raise questions as to how best to incorporate the results from a three-dimensional simulation into a throughflow model. If the estimates of flow blockage derived from the APNASA simulation were introduced into CAFMIX II, it is speculated that the outcome would be an increase in the pressure rise across the aft stages, and a decrease in the pressure rise across the front stages for a fixed overall compressor pressure ratio. This would drive the agreement between the two models apart.

Unfortunately the compressor was never tested at the IGV setting, vane settings, and bleed rates corresponding to the APNASA and CAFMIX II simulations. Therefore, no true prediction of the compressor performance is available by which to judge either code. A series of simulations were executed using APNASA with the IGV and vanes set to their test settings in an attempt to match experimental measurements at a point on the operating line near design wheel speed. Additional simulations were executed at this wheel speed in which the compressor was throttled from the operation line to near stall. The first set of results, Fig. 18, shows the relative difference in total pressure ratio between the simulation result and the data for each stage in the compressor. The data were obtained from instrumentation mounted to the leading edge of the stators. The axial location of the simulation results is also the leading edge of stators and the compressor discharge. The agreement between the simulation results and the data is quite good. Figure 19 shows the spanwise distribution of normalized total pressure and total temperature at the leading edge of the third-stage stator, the leading edge of the seventh-stage stator, and at the discharge of the compressor. Both simulation results and data are shown. The profiles resulting from the simulation are in good agreement with that inferred from the data, especially the total temperature profiles. The compressor efficiency as estimated by the simulation agreed very well with the measured efficiency.

The level of agreement shown in Figs. 18 and 19 required an adjustment of the bleed rates from the initial values specified. The initial values were best estimates prior to compressor tests. The final estimates were derived from measurements and a series of data match computations. Figure 20 shows the relative difference in total pressure ratio for each stage based on the simulation used to generate the results in Figs. 18 and 19 (i.e., best estimate of bleed rates, IGV, and vane settings) and two other bleed rate schedules. The first of these bleed rate schedules, annotated by shaded bars, corresponds to that used to generate the results in Figs. 14–17. For this bleed schedule, the front end of the compressor becomes unloaded relative to the back end. The next result, annotated by open bars, was generated by lowering the third-stage bleed rate to that measured. By drawing less third-stage bleed air, the predicted pressure ratio of the front stages increased to near their measured values, while that of the back stages was reduced. Finally, reducing the amount of bleed air being drawn from the seventh-stage bleed to that measured lowered the predicted pressure ratio of stages eight through ten to near that measured. Stages one through four remained unchanged as stage-seven bleed was reduced, while stages five through seven experienced an increase in pressure ratio. The results shown in Fig. 20 are quite significant for they clearly show how bleed can affect the matching of stages within a compressor. The initial simulation using the a priori estimates of bleed rates was judged to be less than satisfactory for design purposes. Clearly, in addition to having sound models to account for the unsteady flow field within axial flow multistage compressors, it is equally important to have credible estimates of the leakage flow rates and the bleed flow rates.

A series of simulations were also performed to ascertain APNASA's ability to compute the impact of throttling on compressor performance. The wheel speed for these simulations corresponds to that used in the previous simulations. Figure 21 shows the percent difference in total pressure ratio of individual stages relative to their predicted total pressure ratio on the operating line (i.e., simulation results used to generate the results in Fig. 18). The pressure ratio is defined from stator leading edge to rotor trailing edge. For the tenth stage the pressure ratio is from the leading edge of the ninth-stage stator to compressor discharge.

A series of simulations were executed for increasing back pressure until the code failed to converge. The highest total pressure ratio for which a converged solution was obtained is less than the total pressure ratio at which the compressor stalled. The first case, labeled Case 1, is for a back pressure slightly greater than the value corresponding to Fig. 18, while Case 4 is for a back pressure setting very close to the numerical stall point. The other two cases are for back pressure settings which lay between these two extremes.

For Case 1, the slight increase in back pressure caused the last six stages to move slightly up their pressure characteristic. The operating point of the first four stages remains unchanged. Case 2 increased the back pressure further and caused all of the stages with the exception of stage 1 to respond. The mass flow, being set by the first stage, is unaffected by this increase in back pressure. The change in the pressure ratio of stages five through nine is significantly greater than that for stage ten. Stage ten shows a

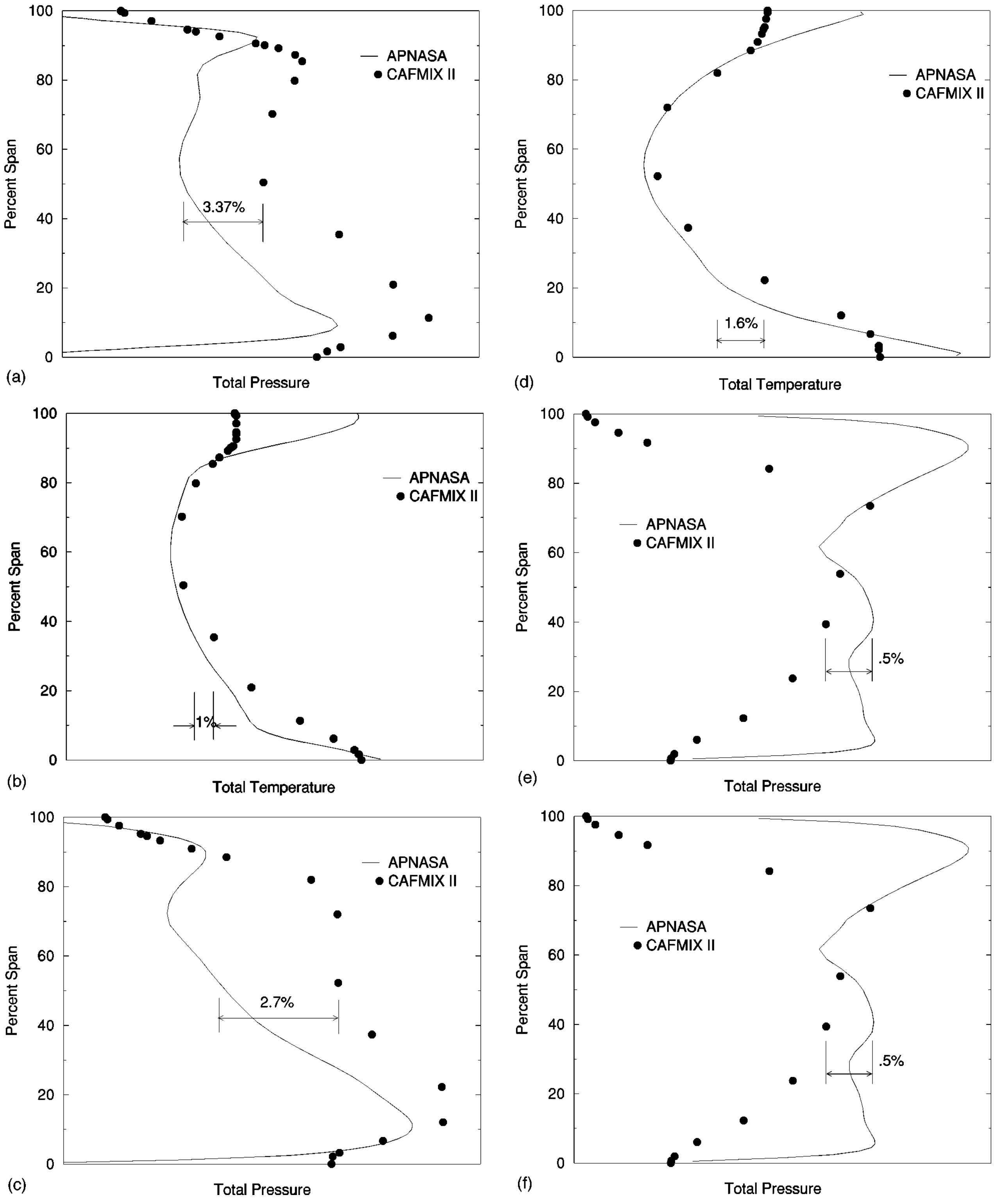

Fig. 15 (*a*) Spanwise distribution of total pressure at the exit of the stage 3 stator in the GE90 compressor; (*b*) spanwise distribution of total temperature at the exit of the stage 3 stator in the GE90 compressor; (*c*) spanwise distribution of total pressure at the exit of the stage 7 stator in the GE90 compressor; (*d*) spanwise distribution of total temperature at the exit of the stage 7 stator in the GE90 compressor; (*e*) spanwise distribution of total pressure at the compressor exit in the GE90 compressor; (*f*) spanwise distribution of total temperature at the compressor exit in the GE90 compressor

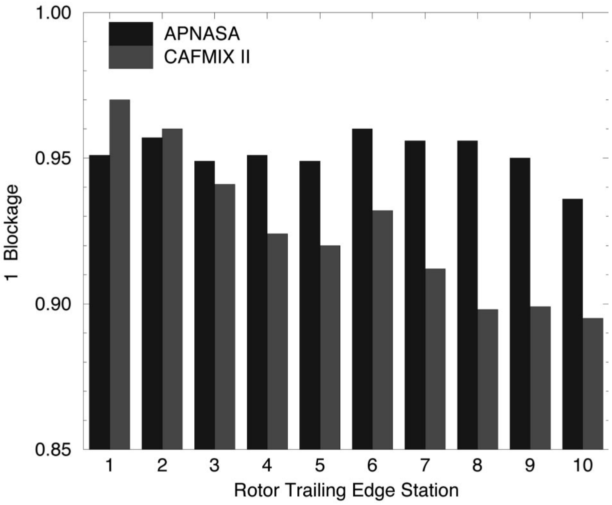

Fig. 16 Flow blockage distribution through the GE90 compressor

modest change in pressure ratio, which implies that it is operating on the flat part of its characteristic. Raising the back pressure still higher, Case 3, further increases the pressure ratio of stages three through nine. Stages one and two remain unchanged, as does the mass flow, while the pressure ratio across stage 10 decreases. Stage ten is operating near the peak of its pressure characteristic (i.e., total pressure coefficient versus incoming corrected mass flow). Throttling the compressor to near its numerical stall point, Case 4, causes an increase in pressure ratio of stages two through eight. The pressure ratio for stage one remains unchanged, as does the mass flow. The pressure ratio for stages nine and ten has decreased. Stage nine is operating near the peak of its pressure characteristic, while stage ten is operating on the positive side of its characteristic. Simulation results show that the pressure characteristic for stage ten rolls over very abruptly after peak pressure. Obtaining a converged solution at still higher back pressures proved difficult because of the extreme sensitivity to back pressure setting. It is thought that stage eight is operating near peak pressure and that any slight increase in back pressure causes its operating point to shift to the positive side of its pressure characteristic. When this occurs, the compressor stalls numerically. At this wheel speed, there is experimental evidence which suggests that stall originates in the eighth stage [65].

High-Speed Three-Stage Compressor. The next set of results are for a small high-speed three-stage plus IGV axial flow

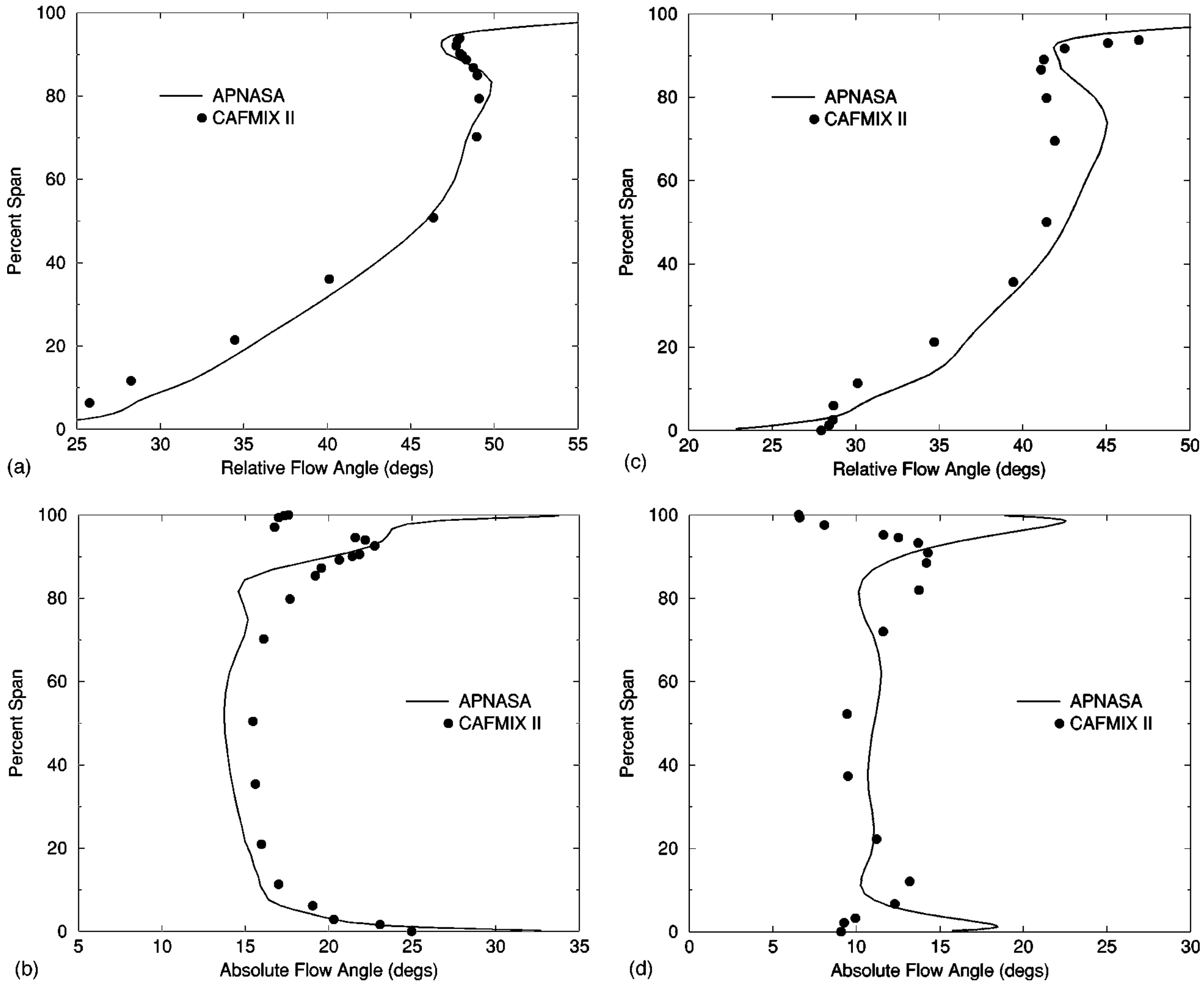

Fig. 17 (***a***) **Relative flow angle at the exit of the stage 3 rotor in the GE90 compressor; (*b*) absolute flow angle at the exit of the stage 3 stator in the GE90 compressor; (*c*) relative flow angle at the exit of the stage 7 rotor in the GE90 compressor; (*d*) absolute flow angle at the exit of the stage 7 stator in the GE90 compressor**

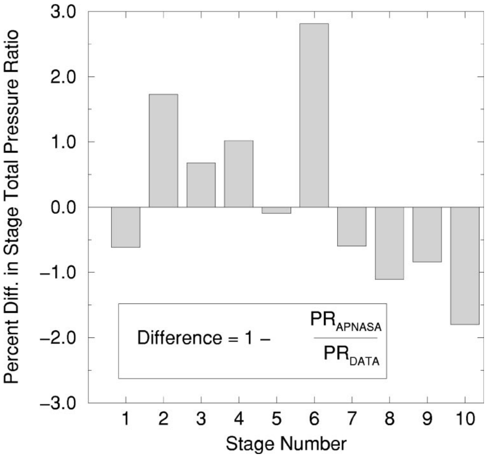

Fig. 18 Percent difference in total pressure ratio through the GE90 compressor near the design speed operating point

compressor. The compressor was designed, tested and simulated by Allied Signal, Mansour [28]. The compressor is of a modern design, employing transonic rotors in all three stages. Although the simulations are not a prediction (the tests predate the simulations) they were executed by a researcher who is not a developer of APNASA but rather a user who is attempting to assess its predictive capabilities. The total pressure characteristics and the total temperature characteristics of the individual stages as derived from the simulations and measurements are shown in Fig. 22. The experimental results were obtained from stator leading edge instrumentation. For the first stage, the total pressure ratio as well as the total temperature ratio is from the inlet to the exit of the first stage rotor. For stage two, the pressure ratio as well as the total temperature ratio is from the inlet of the first-stage stator to the exit of the second-stage rotor. For the third stage, the total pressure ratio as well as the total temperature ratio is from the inlet of the second-stage stator to the exit of the third-stage rotor. The stage total pressure ratios as well as the stage total temperature ratios are plotted as a function of corrected flow exiting each of the rotors. The characteristics are for the design wheel speed. The error between the simulated results and experimental data is also shown on the figure.

Two throttle settings were simulated in an attempt to bracket the design pressure ratio of the compressor. In both the simulation and test, the first-stage operating point remains fixed as the compressor is throttled. This result implies that the second-stage rotor is choked. The corrected mass flows exiting the first-stage rotor, as derived from the simulations, are approximately 1.5 percent greater than that deduced from the experimental measurements. For the second stage, the difference in corrected mass flow is 1.4 percent. For the third stage, the difference between the corrected mass flow deduced from the data and that from the simulation results is 0.4 percent. Overall the agreement is quite satisfactory.

Figure 23 shows the total pressure ratio and the total temperature ratio at the exit of the first-stage rotor as a function of span. Percent differences are also shown on the figure. Only the results from one simulation and one experimental point are shown, since the operating point of the first-stage rotor remained unchanged as the compressor was throttled. With the exception of the region near 90 percent of span, the agreement between the total pressure profiles derived from the simulation and the experiment data is very good. At 90 percent of span, the total pressure profiles differ by less than 3 percent. The total temperature profiles are also in good agreement. The difference between the two total temperature profiles at midspan is less than 1.0 percent. It is encouraging to see that the simulation shows nearly the same rise in total temperature as the experiment outboard of 70 percent of span.

Figure 24 shows the pressure ratio and the total temperature ratio at the exit of the third-stage rotor as a function of span. The pressure ratio associated with the two simulations brackets the experimental pressure ratio. The shape of the total pressure profiles are in reasonable agreement with each other. At midspan, the two simulations differ by less than 5 percent, while the experimental value differs from either simulation result by less than 3 percent.

The shapes of the total temperature profiles shown in Fig. 24 are also in reasonable agreement with each other. However, the spanwise-averaged total temperature from the two simulations is less than that deduced from the experiment. The relative difference between the experiment and simulation point 1 is approximately 1.3 percent.

The agreement between data and simulation was judged to be sufficient for the purposes of using APNASA to guide the aerodynamic design of this multistage axial flow compressor [28].

High-Speed High-Pressure and Low-Pressure Turbine. The final simulation examples are of a high-pressure turbine (HPT) and low-pressure turbine (LPT). The HPT is a 3/4 scale model of the HPT from the GE engine family, while the LPT is a 1/2 scale model of the LPT from the GE engine family. The HPT is a two-stage machine while the LPT is a six-stage machine. The simulations of both machines included the effect of cooling and purge flows as well as variable gas properties. The simulations were set up to match the conditions for which data was available. The details of the simulations are given in Turner et al. [60]. Figure 25 shows the spanwise profiles of total pressure and total temperature exiting the second stage rotor of the HPT. The measurements are represented by solid squares, while the simulation results appear as a solid line. The relative difference between the measurements and the simulation results is also shown on the figure. The agreement between the simulation and the data is very good. A comparison of the overall one-dimensional performance parameters showed that the simulation was 2.5 percent high in mass flow, 0.4 percent high in total pressure ratio, and 1.6 percent low in total temperature ratio. Figure 26 shows a similar set of plots for the LPT. The spanwise profiles are at the exit of the sixth stage rotor. The relative difference between the measurements and the simulation is shown on the figure. The agreement between the two is also very good. For the LPT study, a comparison of the overall one-dimensional performance parameters showed that the simulation was 2.5 percent low in mass flow, 0.3 percent high in total pressure ratio, and 3.5 percent low in total temperature ratio.

The machines whose simulation results were presented in this section cover a broad range of multistage axial flow turbomachinery configurations. The objective of this section was to illustrate to the turbomachinery design community what could be, and what could not be, predicted by a code based on the average-passage flow model with the current procedures to account for the effects of the unsteady flow environment within multistage turbomachines. All the simulations were executed without recourse to information supplied by external models or data that prescribed the aerodynamic matching of stages, this information being an output of the simulations and not an input. Being able to establish the aerodynamic matching of stages reliably in a multistage configuration is critical to ensuring that advanced designs attain their aerodynamic goals in the first build.

In the next section the current state of the art for simulating multistage axial flow turbomachines in support of aerodynamic design using models that are uncoupled from throughflow models is summarized. Suggestions for future work are also presented.

Summary and Suggested Future Work

Before summarizing, it is important to stress the need to have correct geometry and correct inflow and outflow boundary conditions before attempting any simulation. This detail cannot be emphasized enough, as evidenced by the findings of Shabbir et al. [66], Escuret and Veysseyre [67], and Wellborn and Okiishi et al.

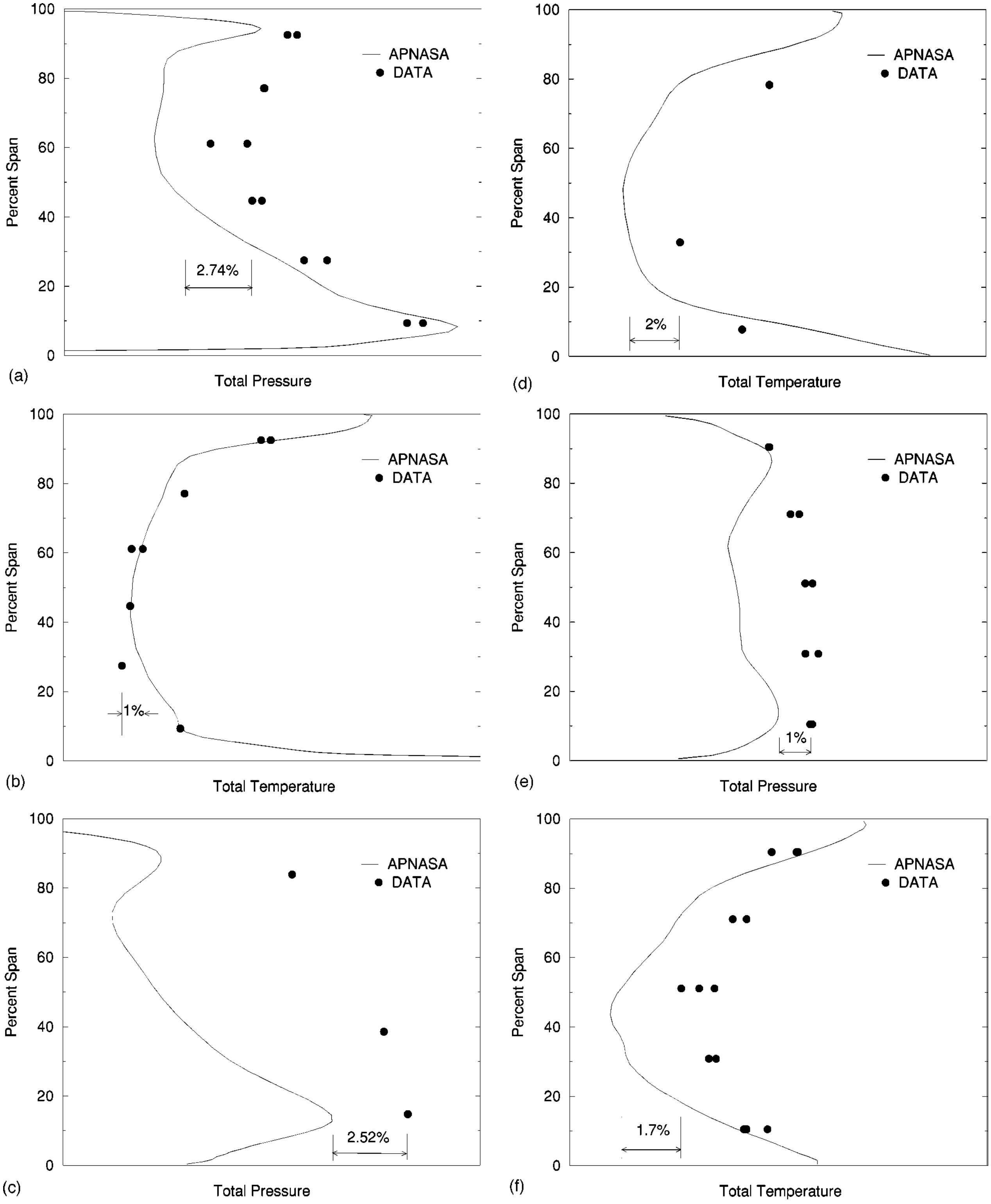

Fig. 19 (*a*) Spanwise distribution of total pressure at the exit of the stage 3 rotor in the GE90 near design speed; (*b*) spanwise distribution of total temperature at the exit of the stage 3 rotor in the GE90 near design speed; (*c*) spanwise distribution of total pressure at the exit of the stage 7 rotor in the GE90 near design speed; (*d*) spanwise distribution of total pressure at the exit of the stage 7 rotor in the GE90 near design speed; (*e*) spanwise distribution of total pressure at the exit of the GE90 near design speed; (*f*) spanwise distribution of total temperature at the exit of the GE90 near design speed

[68], Wellborn et al. [11]. It is important to know the geometry at the flow conditions being simulated. This includes the blade geometry as well as the hub and shroud geometry. Rotor tip clearance, stator hub clearance, variable geometry setting, and variable geometry button configuration must all be known. Blade fillet geometry and surface finish must also be known. All cavities that are opened to the primary flow path must be known. All leakage flows must be known including those associated with shrouded blading, bleed flows, purge flows, and the cooling flows of turbines. If any of these details (geometry, inflow and outflow

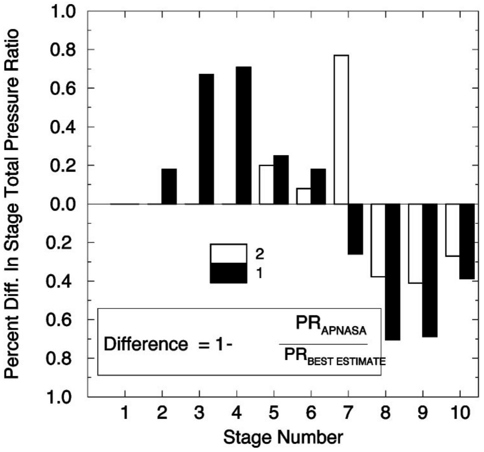

Fig. 20 Percent difference in stage pressure ratio as a function of bleed rates for the GE90 compressor

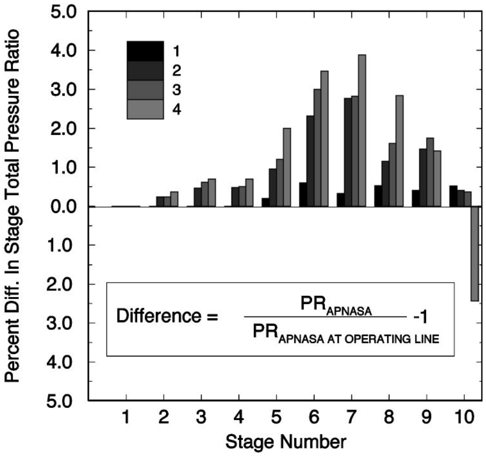

Fig. 21 Percent difference in stage pressure ratio as a function of back pressure for the GE90 compressor

boundary conditions) are unknown, it is important to establish the sensitivity of the simulation results to their assumed values.

Table 1 is a bullet chart that summarizes the fluid mechanics addressed in this paper. At the top of the list is spanwise transport of wake fluid particles, which leads to a redistribution of total temperature and momentum. Although not specifically addressed, the spanwise redistribution of entropy is also implied.

Next on the list is circumferential transport of wake fluid particles, which also leads to a redistribution of total temperature and momentum. The flow physics associated with this redistribution was shown to be equivalent to that associated with spanwise redistribution of total temperature. Although circumferential redistribution of total temperature does not appear to impact aerodynamic performance, it does lead to total temperature segregation resulting in the formation of hot spots. These hot spots have a significant impact on turbine blade life.

Circumferential redistribution of momentum also involves the interaction between a blade and incoming wakes and blade boundary layers. The impact of incoming wakes interacting with turbulent blade boundary layers on aerodynamic performance is not clear. However, when the interaction involves a transitional blade boundary layer, evidence exists that aerodynamic performance is impacted. This subject will be addressed later in this section. There appears to be an indication that the interaction of compressor rotor tip clearance flows with a downstream stator leads to increased loss.

Next on the chart is the straining of wakes as they convect through a blade row. This straining process leads to wake recovery. Wake recovery results in the transfer of energy by a reversible flow process between the unsteady flow generated by wakes and the time average flow field. Wake recovery was shown to impact the mixing loss of wakes as they pass through a downstream blade row. With respect to an axial flow compressor, the mixing loss attributed to two-dimensional wakes is significantly reduced by the wake recovery process. For an axial flow turbine, the mixing loss attributed to two-dimensional wakes is increased by the wake recovery process. Thus, there is a performance benefit to be gained in axial flow compressors by having blade rows closely spaced, while the opposite is true for axial flow turbines.

It was shown that the wake recovery process also impacted the pressure rise across the blade row through which the wakes are passing. The pressure rise was linked to flow blockage defined in terms of an energy recovery thickness. Sample results for an axial flow compressor showed that as the depth of wakes becomes large, the pressure rise associated with the recovery process needs to be accounted for.

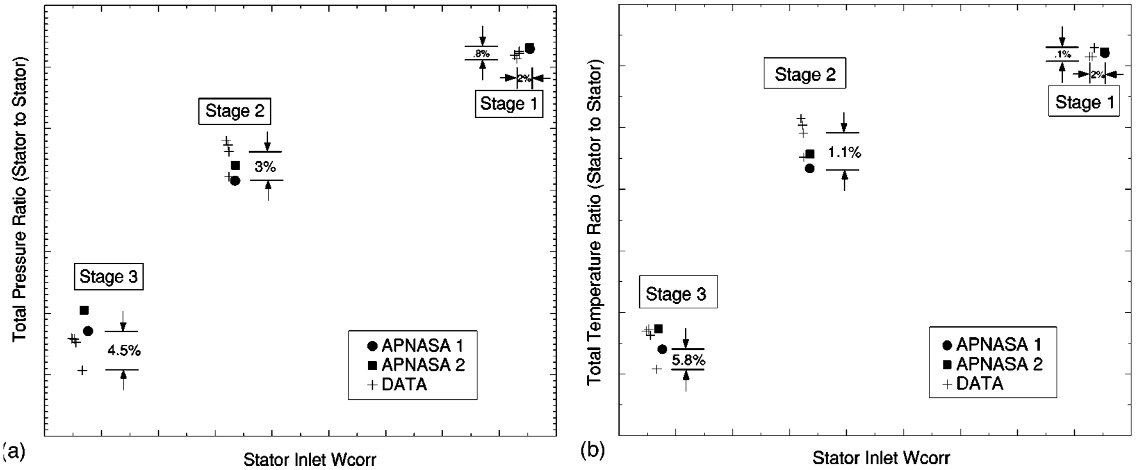

Fig. 22 (*a*) Stage total pressure ratio characteristic as a function of corrected mass flow for a three-stage high-speed compressor; (*b*) stage total temperature ratio characteristic as a function of corrected mass flow for a three-stage high-speed compressor

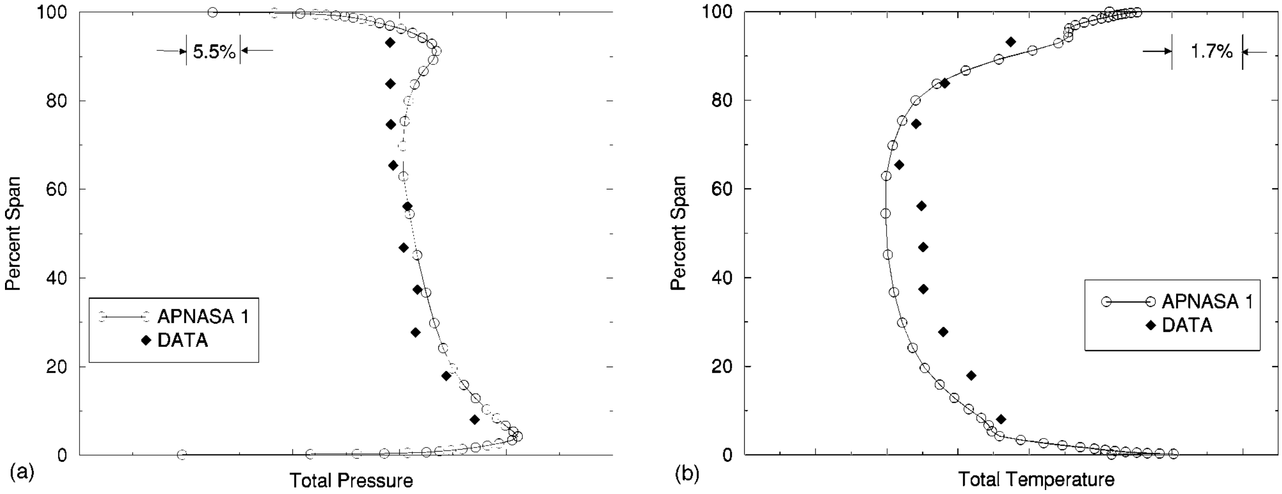

Fig. 23 (***a***) **Spanwise distribution of total pressure at the exit of the stage 1 rotor for a three-stage high-speed compressor; (*b*) spanwise distribution of total temperature at the exit of the stage 1 rotor for a three-stage high-speed compressor**

Models that attempt to account for the unsteady flow processes summarized above were used in generating the results presented in the ''Examples'' section. The results are encouraging, for they show that the average-passage flow model is capturing a good deal of the flow physics controlling the aerodynamic performance of axial flow multistage turbomachinery. However, there are a number of research studies that suggest the need to include additional models of unsteady flow phenomena. To list the key results from all these studies and to attempt to prioritize them in order of importance is beyond the scope of this work. However, there are a few topics that are on the author's short list for further study.

As two blade rows rotate past one another, an unsteady flow field is generated. This unsteady flow field results in an unsteady aerodynamic force, which acts on each blade row. When one blade row's unsteady force is viewed in the reference frame of the other, its time average is nonzero. Thus, within the framework of the average-passage flow model, the time averages of both forces are accounted for by nonaxisymmetric body forces. With respect to the upstream blade row, the flow processes that produce the body force associated with the downstream blade row are similar to those encountered in the interaction of a total pressure distortion with a rotating blade row. The flow physics that produce the body force associated with the upstream blade row is similar to that involving a rotating blade row interacting with a downstream-generated flow distortion. The flow distortion is characterized in terms of a potential field. If the upstream blade row is a rotor, the nonaxisymmetric body force associated with the rotor generates a circumferential variation in the total pressure and total temperature field. The generation of this total pressure and total temperature field and their interaction with the downstream stator was investigated by Shang et al. [69]. Smith [55] also reported experimentally observing a variation in the total pressure field downstream of a rotor embedded within a low-speed multistage axial flow compressor. Smith [55] speculated that if the region of high total pressure were to flow over the suction surface of the downstream stator a performance benefit would be realized.

Smith [55] noted that the body force attributed to the downstream blade row results in a circumferential variation of the pressure field in the inter blade row region of a multistage axial flow compressor. This pressure field could reduce the pressure gradient along the suction surface of the upstream blade row. The reduced pressure gradient would lead to a reduction of the wake deficit and hence a reduction of wake mixing loss. Smith [55] concluded that along with wake recovery, the unsteady flow processes that lead to the development of the nonaxisymmetric body forces contributed nearly equally to the measured efficiency gain of 1.3 percent

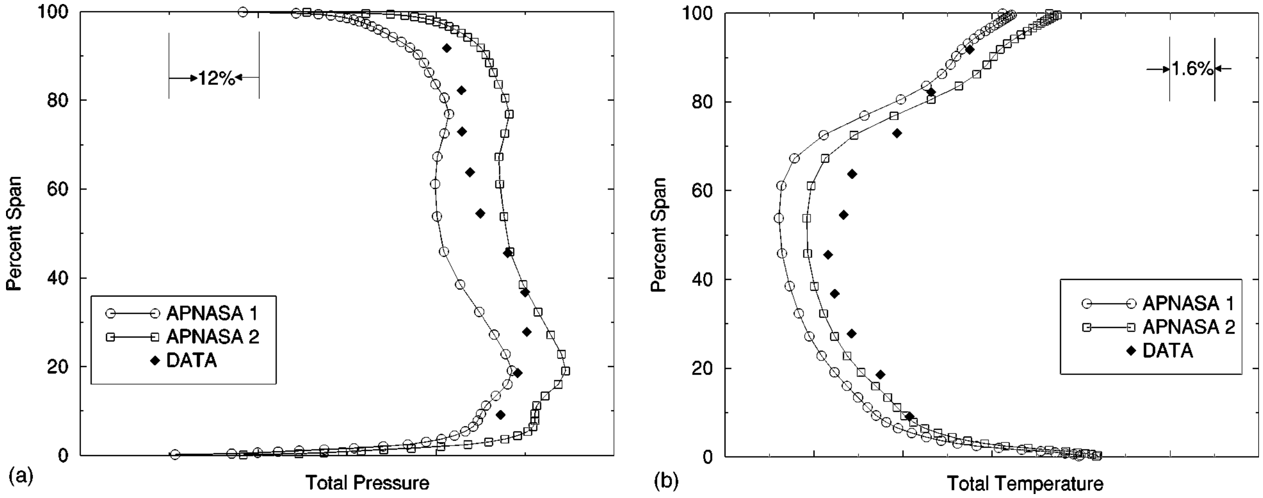

Fig. 24 (***a***) **Spanwise distribution of total pressure at the exit of the stage 3 rotor for a three-stage high-speed compressor; (*b*) spanwise distribution of total temperature at the exit of the stage 3 rotor for a three-stage high-speed compressor**

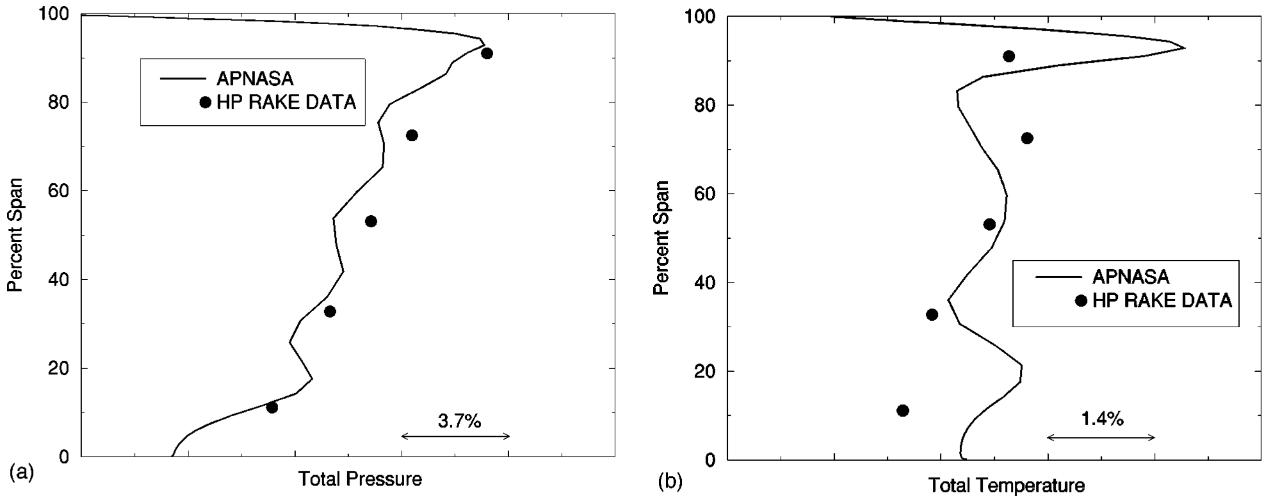

Fig. 25 (***a***) **Total pressure profile at the exit of an HP turbine stage 2 rotor;** (***b***) **total temperature profile at the exit of an HP turbine stage 2 rotor**

brought about by reducing the axial gap between blade rows in a low-speed four-stage axial flow compressor. This is not an insignificant change and there is a need to model the fluid mechanics involved. A procedure for developing such models is presented by Giles [70].

A number of experimental studies [71–74] have shown that flow transition is playing a role in establishing the aerodynamic performance of both axial flow compressors and low pressure turbines. The fluid mechanics involves the interaction between convecting turbulent wakes and transitional blade boundary layers. The impact of this process on the performance of low pressure turbines has recently been factored into their design [75].

The simulation of the NASA Lewis Low-Speed Axial Compressor (LSAC) by Adamczyk et al. [59] clearly showed the need to account for transition in some form in order to match the measured performance. Figure 27 shows the results of a simulation performed using an average-passage form of the Launder and Spalding [76] $k-\epsilon$ model. Plotted is measured pressure rise of this compressor as a function of flow coefficient. The results from two simulations are also shown. The performance of this compressor as estimated by the simulations falls significantly short of that measured. The simulation was repeated with an improved $k-\epsilon$ model developed by Shih et al. [77] and the results are presented in Figs. 10–13. The improved model is not a transition model, but it mimics the transition process. In the stagnation region and in regions where the pressure gradient is favorable, it suppresses the growth of the turbulent eddy viscosity. In regions where the pressure gradient is adverse, the turbulent eddy viscosity increases. For the LSAC, the Launder–Spalding model produces a level of turbulent eddy viscosity along the suction surface of both rotors and stators typical of a high-Reynolds-number flow. At the stagnation region and along the suction surface, where the pressure gradient is favorable, the improved model of Shih produces a level of eddy viscosity that is slightly greater than the molecular viscosity. As flow diffuses along the suction surface, the eddy viscosity grows to a level typical of a turbulent boundary layer. As previously noted, the agreement of the improved model with data is very encouraging.

The improved model was also used to simulate an operating point of the GE 90 compressor. The results were only slightly different from a simulation executed using an average-passage form of the Launder and Spalding $k-\epsilon$ model. All the previously reported simulations of the GE 90 and the Allied Signal compressor used the average-passage form of the Launder and Spalding $k-\epsilon$ model. The reason behind the small difference seen in the simulation of the GE 90 versus the rather large differences seen in the simulation of the LSAC is attributed to the difference in the blade Reynolds numbers and the blade surface finish of these two

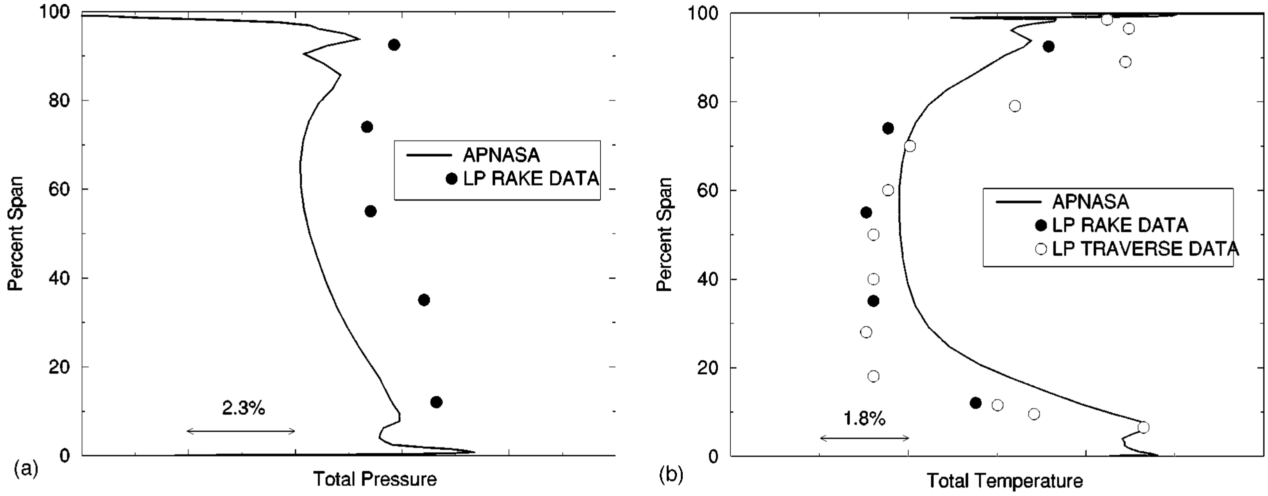

Fig. 26 (***a***) **Total pressure profile at the exit of an LP turbine;** (***b***) **total temperature profile at the exit of an LP turbine**

Table 1

Summary of unsteady deterministic flow processes discussed that impact the time-averaged performance of multistage turbomachinery
• Spanwise transport of wake fluid particles.
• Circumferential transport of wake fluid particles.
• Straining of wakes.

machines. When simulating machines whose blade Reynolds numbers are small, there is clearly a need to account for transition.

The final topic involves unsteady flows that are classified as nondeterministic but are not turbulent in nature. An example of this is the shedding of vorticies from a blade trailing edge, where the shedding frequency is not related to shaft rotational speed. Vortex shedding has been observed in fan rotors, Hathaway et al. [78] and has been shown to lead to spanwise redistribution of entropy, Kotidis and Epstein [79]. There is also an issue associated with the stability of shear flows in adverse pressure gradients. It has been observed that the stretching of vorticies leads to flow instabilities resulting in rapid mixing [80,81]. A related subject is the stability of rotor tip clearance flows. Based on experiments in a water tunnel, Zierke et al. [82] concluded that the tip vortex shed by a rotor meandered as it traveled downstream. Graf et al. [83] conducted a series of numerical simulations of a stage from a high-speed multistage compressor and observed similar phenomena. These unsteady nonturbulent flows appear to lead to the mixing of shear layers and thus generate loss. The magnitude of the impact of such mixing processes on aerodynamic performance of multistage axial flow turbomachines is unknown. An effective means for modeling such mixing processes within the frame work of a time-averaged flow model such as the average-passage flow model is not clear.

Finally, there is a real need for executing well-defined physical and computational experiments that focus on specific fluid mechanic issues related to the impact of unsteady flows on the performance of axial flow multistage turbomachines. Too often results are presented with no clear explanation as to their significance and the question they answer. Information such as this is not very useful in sorting out issues as complex as those involved in the fluid mechanics of multistage turbomachinery.

As computers become more powerful and the resolution capabilities of instrumentation improves, there is no doubt that many of the issues delineated in this section will be resolved. In addition, many new issues will appear that, at the present time, are unknown. One thing is certain, the modeling of multistage turbomachinery flow will remain a challenge for the foreseeable future and economic forces will continue to push the development of improved flow models for the purpose of supporting aerodynamic design.

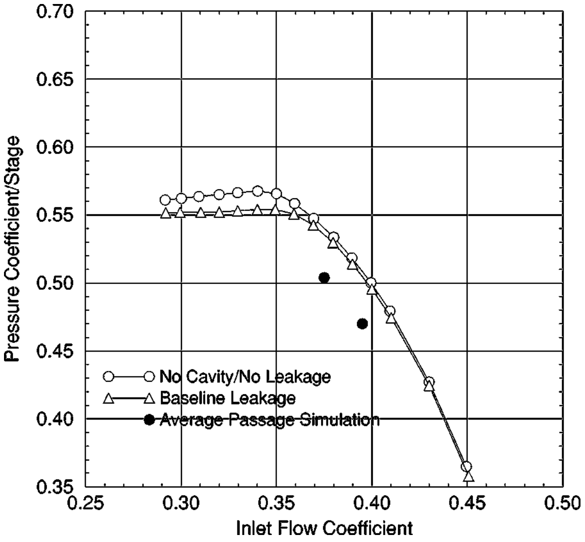

Fig. 27 Overall pressure coefficient as a function of inlet flow coefficient for the NASA-Lewis four-stage axial flow compressor

Acknowledgments

The author wishes to thank the IGTI Scholar Lecture Committee and to those who have reviewed the drafts of this paper. The author wishes to express his gratitude to those managers, in industry and at NASA Glenn Research Center, who have supported the author's research endeavors. The author is also grateful to the many researchers in academia, industry, and at NASA Glenn who have openly shared their research results and thoughts with the author on the fluid mechanics of multistage turbomachinery. Finally, the author wishes to acknowledge the support and contributions of Dr. M. L. Celestina, Mr. R. A. Mulac, Mr. T. A. Beach, Dr. W. M. To, Dr. A. Shabbir, Mr. J. R. Wood, Dr. M. D. Hathaway, and Dr. A. J. Strazisar to the development of the average-passage model and APNASA.

Appendix A

A Three-Dimensional Flow Model for Axial Flow Multistage Turbomachines. The procedure used for constructing the average-passage flow equations is based on the concept of mathematical filtering or averaging. Starting with the Navier–Stokes equations, the continuity equation, the energy equation, and the equation of state, one can construct a sequence of mathematical filtering operations that result in a system of equations that govern the flow state resolved by the filtering operation. The resulting equations only resolve flow structures that are unaltered by the filtering operation. The resulting solution of the filtered equations is identical to that obtained by applying the filtering operation to the solution of the unfiltered equations. For example, the construction of the Reynolds-averaged form of the Navier–Stokes equation involves a filter that removes the nondeterministic flow structures associated with turbulence while retaining the deterministic structures. This is accomplished by using an ensemble-averaging filter. The resulting deterministic flow state as described by the Reynolds-averaged form of the Navier–Stokes equation is identical to that obtained by directly applying the ensemble-averaging filter to the solution of the Navier–Stokes equation.

The filtering operator used in the construction of the Reynolds-averaged form of the Navier–Stokes equations ensemble-averages consecutive samples of data taken over one shaft revolution. The mathematical form of the ensemble-averaging operator is:

$$\overline{f}^{e} = \lim_{M\to\infty} \frac{1}{M} \sum_{m=1}^{M} f(r,\theta,z,\tau)$$

$$\tau = t + \frac{2\pi}{\Omega}(m-1) \qquad (A1)$$

$$t_1 \leqslant t \leqslant \frac{2\pi}{\Omega} + t_1 = T + t_1$$

where m is an integer, M is the number of shaft revolutions over which the data are collected, f, the data being sampled,

$$\overline{f}^{e}$$

its ensemble average. The variable Ω is the shaft rotational speed, t_1 is a reference time, and T is the time for one shaft revolution.

All flow features resolved by Eq. ($A1$) are associated with the deterministic flow field. This includes all time-dependent behavior directly linked to shaft rotational speed, Ω. All flow features filtered out by Eq. ($A1$) are associated with the nondeterministic flow field. Such features include turbulent eddies and shed vortices, which are unrelated to shaft rotational speed. The global effect of the nondeterministic field on the deterministic field is accounted for by means of the Reynolds stress in the momentum equation and a total enthalpy flux in the energy equation. The Reynolds stress accounts for the transport of momentum between the deterministic and nondeterministic flow fields. These terms arise as a result of applying the filtering operator to the nonlinear terms that appear in the momentum and energy equations. The modeling of the Reynolds stress and the total enthalpy flux is the closure problem associated with solving turbulent flows. Equations for these terms must be provided and they form part of the equation system for the deterministic flow field.

As shown in Fig. 1, the Reynolds-averaged flow model has less fidelity than the Navier–Stokes equations. For the purpose of the present work, the Reynolds-averaged flow description of the deterministic flow field is time dependent.

To construct a time-averaged representation of the flow field within a multistage turbomachine requires the use of a time-averaged filtering operation. Two time-averaged flow fields can be defined: one with respect to the rotor frame of reference; and the other with respect to the stator or fixed frame of reference. For the stator frame of reference, the time-average filter is defined by the following integral:

$$\overline{f}^{t}=\frac{1}{T\lambda}\int_{0}^{T}H_{G}(r,\theta,z,t)\overline{f}^{e}(r,\theta,z,t)dt \qquad (A2)$$

where H_G is a gate function whose value is one at an instant in time, t, when the axial position, z, the tangential position, θ, and the radial position, r, define a point lying within the flow domain or on its boundaries. Otherwise the value of H_G is zero. The variable λ is defined as:

$$\lambda\equiv\frac{1}{T}\int_{0}^{T}H_{G}(r,\ \theta,z,\ t)dt \qquad (A3)$$

and is a measure of the metal blockage attributed to the rotors. For the rotor frame of reference, the filter is defined by replacing in both Eqs. ($A2$) and ($A3$), the absolute tangential position, θ, with the relative tangential position, θ_{rel}.

Equation ($A2$), applied to the deterministic form of the continuity equation, the momentum equation, the energy equation, the equation of state, and the closure equations associated with the Reynolds stress and the total enthalpy flux yields a set of equations that govern the time-average flow field in the fixed frame of reference. The resulting system of equations contain additional terms relative to those that appear in the deterministic equation system. This is again the direct result of the averaging operation. The continuity, momentum, and energy equations all contain the metal blockage term λ. The momentum equation contains a body force and a stress tensor involving products of the unsteady deterministic velocity components. The form of this tensor is identical to that for the Reynolds stress and accounts for the transport of momentum between the deterministic flow field and the time-averaged flow field. The body force is the result of the time-averaged pressure and shear force imposed by the rotor blades on the fluid. The energy equation contains an energy source (sink) and a total enthalpy flux correlation. The energy source is associated with the work input attributed to the body force, while the total enthalpy flux accounts for the transfer of total enthalpy between the deterministic and time-averaged flow field.

The time-averaged flow model is also shown in Fig. 1, and because it is of lower fidelity for a multistage turbomachine application than the Reynolds-averaged model, it lies to its right. For the case of a single rotor or stator operating in a stable aero-mode (i.e., free of rotating stall or surge), with uniform circumferential inflow and outflow boundary conditions, the time-averaged flow model and the Reynolds-averaged flow model are mathematically equivalent.

For a single-stage configuration operating in a stable aero-mode with uniform circumferential inflow and outflow boundary conditions, the time-averaged flow field for either the rotor or stator is periodic in the tangential direction with a period equal to the pitch of the respective blade row. Thus the time-averaged equation system for the rotor and stator is by definition the average-passage description for the stage as defined by Adamczyk [26]. However, with respect to the stator frame of reference, if additional stators are present whose blade count is different from that of the reference stator, the resulting time-averaged flow field will have a circumferential periodicity other than that of the reference stator.

Construction of an average-passage description of the flow field in a multistage machine therefore requires an additional averaging operation [26]. For a given stator, this average operation is defined by the equation:

$$\overline{f}^{ap}=\frac{1}{\Lambda N}\sum_{n=0}^{N-1}G\left(r,\theta+\frac{2\pi n}{N},z\right)\overline{f}^{t}\left(r,\theta+\frac{2\pi n}{N},z\right) \qquad (A4)$$

where n is an integer and N is the number of passages in the stator. The variable G is a function composed of the product of L gate functions, g_l,

$$G(r,\ \theta,z)=\Pi_{l=1}^{L}g_{l}(r,\ \theta,z) \qquad (A5)$$

assigned to each blade row in the stator frame of reference. The gate function for the lth stator, g_l, is equal to zero when r, θ, and z lie within the interior of the lth stator, otherwise its value is one. Thus the variable G is a function whose value is one when r, θ, and z lie within the interior or on the boundaries of the time average flow field. Otherwise, the value of G is zero.

For the jth stator, Λ is defined by the equation:

$$\Lambda=\frac{1}{2\pi}\int_{0}^{2\pi}\Pi_{\substack{l=1\\ l\neq j}}^{L}g_{l}(r,\ \theta,z)d\theta \qquad (A6)$$

and is a measure of the metal blockage of the stator blade rows other than the one of interest. Each stator blade row has associated with it a filter as defined by Eqs. ($A4$), ($A5$), and ($A6$).

With respect to a given stator blade row, Eq. ($A4$) forms the average-passage value of $\overline{f}^{t}$ by summing values of $G\overline{f}^{t}$, which are shifted tangentially by the pitch of the given stator. Hence by construction $\overline{f}^{ap}$ is periodic in the tangential direction with a period equal to that of the given stator blade row. $\overline{f}^{ap}$ so constructed is a discontinuous function, and this mathematical outcome of the averaging process described by Eq. ($A4$) must be recognized.

A procedure similar to Eq. ($A4$) is applied to the equations associated with the rotor time-averaged flow description. As in the case of each stator blade row, each rotor blade row is associated with a unique averaging operator. Hence each blade row in a multistage configuration has its own average-passage description, which by construction is independent of time and periodic over the pitch of that blade row. The average-passage flow description is by construction the flow field turbomachinery designers have heuristically thought of when executing an aerodesign. The inlet and exit boundaries of each of these flow descriptions are at the physical inlet and exit of the machine.

Application of the filtering and averaging operations Eqs. ($A1$), ($A2$), and ($A4$) to the axial momentum equation associated with the fixed frame of reference yields:

$$
\begin{aligned}
&\frac{\partial}{\partial r}(\lambda^{ap} r\rho^{ap} V^{ap} U^{ap}) + \frac{\partial}{\partial \theta}(\lambda^{ap} \rho^{ap} W^{ap} U^{ap}) \\
&\quad + \frac{\partial}{\partial z}\lambda^{ap}(r\rho^{ap} U^{ap} U^{ap} + p^{ap}) \\
&\quad = \frac{\partial}{\partial r} r\lambda^{ap}(\tau_{rz}^{ap} - R_{rx}) + \frac{\partial}{\partial \theta}\lambda^{ap}(\tau_{\theta z}^{ap} - R_{\theta z}) \\
&\quad + \frac{\partial}{\partial \tau} r\lambda^{ap}(\tau_{zz}^{ap} - R_{zz}) + f_z^{(R)} + f_z^{(S)}
\end{aligned} \tag{A7}
$$

where λ^{ap} is the product of λ and Λ, p^{ap} is the pressure, ρ^{ap} the density, U^{ap}, V^{ap}, and W^{ap} the velocity components in the axial, radial, and tangential directions, respectively, and τ_{ij}^{ap} the viscous shear stress. The subscripts attached to τ_{ij}^{ap} identify the respective component. The superscript *ap* signifies that the variable is associated with the average-passage flow state. The variable $f_z^{(R)}$ is the axial component of the body force generated by the rotor blade rows, while $f_z^{(S)}$ is the axial component of the body force generated by the stator blade rows other than the one of interest.

The body force whose axial component is $f_z^{(S)}$ is a singular function composed of Dirac delta functions, Lighthill [84]. Because of this singular behavior, the average-passage flow variables are discontinuous at the location where this body force is singular. In dealing with this body force and the corresponding energy source (sink) only their nonsingular axisymmetric component is retained. The nonaxisymmetric component (the singular portion) is omitted because it is nonphysical, the singular behavior being strictly an outcome of the averaging operation Eq. (*A*4). With the omission of the singular portion of the body force and energy source (sink), the average-passage flow variables are no longer discontinuous. They remain periodic in the tangential direction with a period equal to the stator of interest. In addition, there still remains one unique axisymmetric flow state that is common to all the average-passage flow states.

In deriving Eq. (*A*7) the following decomposition for the velocity field was used:

$$
\begin{aligned}
u_i &\equiv \widetilde{u}_i^{\,e} + u'_i, \quad \widetilde{u'_i}^{\,e} = 0 \\
\widetilde{u}_i^{\,e} &\equiv \widetilde{\widetilde{u}_i^{\,e}}^{\,t} + u''_i, \quad \widetilde{u''_i}^{\,t} = 0 \\
\widetilde{\widetilde{u}_i^{\,e}}^{\,t} &\equiv U_i^{ap} + u'''_i, \quad \widetilde{u'''_i}^{\,ap} = 0, \quad U_i^{ap} \equiv \widetilde{\widetilde{\widetilde{u}_i^{\,e}}^{\,t}}^{\,ap}
\end{aligned} \tag{A8}
$$

where ~ denotes a density-weighted average, and the subscript *i* (i.e., index notation) refers, respectively, to the axial, tangential, and radial directions.

Equation (*A*7) also contains the axial component of a generalized Reynolds stress, R_{ij}, which will be referred to as the average-passage stress. It is defined as:

$$
R_{ij} = \overline{\overline{\overline{\rho u'_i u'_j}^{e}}^{t}}^{ap} + \overline{\overline{\rho}^{e}\,\overline{u''_i u''_j}^{t}}^{ap} + \overline{\overline{\overline{\rho}^{e}}^{t} u'''_i u'''_j}^{ap} \tag{A9}
$$

where the product,

$$
\overline{\overline{\overline{\rho u'_i u'_j}^{e}}^{t}}^{ap}
$$

is the contribution from the nondeterministic flow field,

$$
\overline{\overline{\rho}^{e}\,\overline{u''_i u''_j}^{t}}^{ap}
$$

the contribution from the unsteady deterministic flow field, and

$$
\overline{\overline{\overline{\rho}^{e}}^{t} u'''_i u'''_j}^{ap}
$$

the contribution from the average-passage flow field of the stator blade rows other than the one of interest. The use of subscripts *i* and *j* is standard tensor notation for orthogonal coordinate systems. The average-passage stress thus accounts for the effect of momentum transport associated with the nondeterministic flow field, the unsteady deterministic flow field, and the average-passage flow field other than that of the blade row of interest.

Application of the averaging operator in Eq. (*A*4) to the energy equation associated with the time-averaged flow field in the fixed frame of reference results in an additional total enthalpy flux correlation associated with the average-passage flow field of the stator blade rows other than the one of interest. Taken together, the total enthalpy flux associated with the nondeterministic flow field, the unsteady deterministic flow field, and the average-passage flow field of stators other than the one of interest, they form the average-passage total enthalpy flux correlation:

$$
HF_i = \overline{\overline{\overline{\rho H' u'_i}^{e}}^{t}}^{ap} + \overline{\overline{\rho}^{e} H'' u''_i{}^{t}}^{ap} + \overline{\overline{\overline{\rho}^{e}}^{t} H''' u'''_i}^{ap} \tag{A10}
$$

where *H* is the total enthalpy. The decomposition of *H* is identical to that of Eq. (*A*8) for the velocity.

The averaging operator Eq. (*A*4) is also applied to the equations used to estimate the Reynolds stress and total enthalpy flux associated with the nondeterministic flow field and the equations used to estimate their deterministic counterparts. As a result, additional terms may arise in the averaged form of these equations whose values must be estimated.

The closure terms associated with the average-passage equation system are the body force, energy source (sink), the average-passage stress, the average-passage total enthalpy flux, and any additional terms that arise from the application of the averaging operations to the equation used to estimate the Reynolds stress and the total enthalpy flux associated with the nondeterministic flow. Models are needed for the various closure terms that appear in the average-passage equation system, just as models for the Reynolds stress are needed in simulations of the deterministic flow field associated with a turbulent flow state. The development of these models is the closure problem associated with the average-passage equation system. The degree to which the closure models need to be developed is dependent upon the level of accuracy to which the average-passage flow field is to be predicted.

Appendix B

Pressure Rise Resulting From Wake Recovery. The wake recovery process can impact the pressure rise across a cascade of airfoils. To show this consider the passage of two-dimensional wakes through a cascade of airfoils as shown in Fig. 9. The working fluid is assumed to be incompressible and inviscid. The flow field is assumed to be deterministic. The flow variables are nondimensionalized with respect to the incoming fluid density (i.e., assumed to be constant), the axial chord length of the cascade, and the magnitude of the incoming flow velocity. The mechanical energy equation states that the time average of the flux in total pressure entering the cascade must equal that exiting the cascade:

$$
\int_{inlet} \overline{P_0 u}^{t} dl = \int_{exit} \overline{P_0 u}^{t} dl \tag{B1}
$$

where P_0 is the total pressure, *u* the axial velocity component.

The total pressure is related to the pressure and the dynamic head by Bernoulli's equation:

$$
P_0 = p + \frac{1}{2}\vec{u}\cdot\vec{u} \tag{B2}
$$

Combining Eqs. (*B*1) and (*B*2), the time average of the flux in total pressure becomes:

$$\int \overline{P_0 u}^t dl = \int \overline{pu}^t dl + \int \overline{\frac{1}{2} u \vec{u} \cdot \vec{u}}^t dl \qquad (B3)$$

where the product *pu* is the local pressure work, and

$$\overline{\tfrac{1}{2} u \vec{u} \cdot \vec{u}}^t$$

is the flux of the kinetic energy of the flow stream.

Introducing Eq. (*B*3) into Eq. (*B*1) yields the following expression for the mass-averaged pressure rise or decrease across the cascade:

$$\widehat{\overline{p}^t}^y \overline{\overline{U}^t}^y L\Big|_\infty - \widehat{\overline{p}^t}^y \overline{\overline{U}^t}^y L\Big|_{-\infty} = \int \overline{\frac{1}{2} u \vec{u} \cdot \vec{u}}^t dl\Big|_{-\infty} - \int \overline{\frac{1}{2} u \vec{u} \cdot \vec{u}}^t dl\Big|_\infty \qquad (B4)$$

where

$$\widehat{\overline{p}^t}^y$$

the mass-averaged pressure, is defined as

$$\widehat{\overline{p}^t}^y = \frac{1}{\overline{\overline{U}^t}^y L} \int \overline{pu}^t dl \qquad (B5)$$

and

$$\overline{\overline{U}^t}^y$$

is the time average axial velocity averaged over *L*, the pitch of the cascade, Fig. 9:

$$\overline{\overline{U}^t}^y = \frac{1}{L} \int \overline{u}^t dl \qquad (B6)$$

At this point in the analysis, it is constructive to introduce the concept of flow blockage. In order to do so, a reference flow field must be defined. For this analysis, the reference flow field will be steady in time with a mass flow equal to that of the unsteady flow. The pressure rise across the cascade associated with this reference flow is

$$p_{ref}\Big|_\infty \overline{\overline{U}^t}^y L - p_{ref}\Big|_{-\infty} \overline{\overline{U}^t}^y L = \frac{1}{2} q^2_{ref}\Big|_{-\infty} \overline{\overline{U}^t}^y L - \frac{1}{2} q^2_{ref}\Big|_\infty \overline{\overline{U}^t}^y L \qquad (B7)$$

Subtracting Eq. (*B*7) from Eq. (*B*4) yields an equation for the increase or decrease in the pressure rise across the cascade attributed to the unsteady flow. This equation is:

$$\left(\widehat{\overline{p}^t}^y - p_{ref}\right)\Big|_\infty \overline{\overline{U}^t}^y L - \left(\widehat{\overline{p}^t}^y - p_{ref}\right)\Big|_{-\infty} \overline{\overline{U}^t}^y L = \left[\frac{1}{2} \int \overline{u(\vec{u} \cdot \vec{u} - q^2_{ref})}^t \Big|_{-\infty} dl\right] - \left[\frac{1}{2} \int \overline{u(\vec{u} \cdot \vec{u} - q^2_{ref})}^t \Big|_\infty dl\right] \qquad (B8)$$

where

$$\overline{\overline{U}^t}^y$$

in Eq. (*B*7) has been replaced by its integral form, Eq. (*B*6).

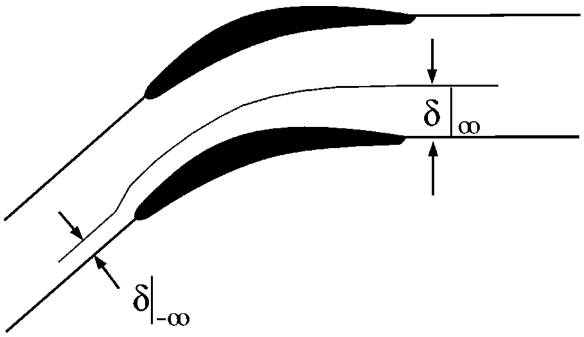

Fig. 28 Steady flow through a cascade with blockage

Each of the bracketed terms on the right-hand side of Eq. (*B*8) may be rearranged into the following form:

$$\frac{L}{2} \int \overline{u(\vec{u} \cdot \vec{u} - q^2_{ref})}^t \frac{dl}{L} = \frac{L}{2} q^2_{ref} \overline{\overline{U}^t}^y \delta_R \qquad (B9)$$

where the recovery energy thickness, δ_R is

$$\delta_R = \int \overline{\frac{u}{\overline{\overline{U}^t}^y}\left[\frac{\vec{u} \cdot \vec{u}}{q^2_{ref}} - 1\right]}^t \frac{dl}{L} \qquad (B10)$$

Note that the recovery energy thickness is similar in form to the energy thickness of boundary layer theory. If the flow is independent of time, δ_R is zero. Whether the recovery energy thickness is positive or negative depends upon the portion of the average-passage stress associated with the unsteady deterministic flow field.

Adding Eq. (*B*8) to Eq. (*B*7) with the bracketed terms in Eq. (*B*8) replaced with Eq. (*B*10) yields:

$$C_p^{us} = \frac{\widehat{\overline{p}^t}^y\big|_\infty - \widehat{\overline{p}^t}^y\big|_{-\infty}}{(1/2) q^2_{ref}\big|_{-\infty}} = 1 - \frac{\cos^2 \beta_{-\infty}}{\cos^2 \beta_\infty} + \left[\delta_R\Big|_{-\infty} - \delta_R\Big|_\infty \left(\frac{\cos^2 \beta_{-\infty}}{\cos^2 \beta_\infty}\right)\right] \qquad (B11)$$

where $q_{\text{ref}}|_\infty / q_{\text{ref}}|_{-\infty} = \cos \beta_{-\infty} / \cos \beta_\infty$ with $\beta_{-\infty}$ and β_∞ being the inlet and exit flow angles of the reference flow, respectively. C_p^{us} is the cascade pressure rise coefficient resulting from an unsteady incoming vortical flow. The first two terms in Eq. (*B*11) is the pressure rise, $C_p^{(0)}$, produced by the steady incoming flow while the term in parentheses is that attributed to the incoming vortical flow.

Consider next a steady flow through a cascade in which the blockage at the inlet is $\delta|_{-\infty}$ and that at the exit is $\delta|_\infty$, Fig. 28. Within the core flow, the total pressure is uniform, hence

$$P_0|_\infty = P_0|_{-\infty} = p|_\infty + \frac{1}{2} q^2|_\infty = p|_{-\infty} + \frac{1}{2} q^2|_{-\infty} \qquad (B12)$$

The pressure rise produced by this steady flow across the cascade is

$$p|_\infty - p|_{-\infty} = \frac{1}{2} q^2|_{-\infty} - \frac{1}{2} q^2|_\infty \qquad (B13)$$

At the inlet:

$$q\Big|_{-\infty} = \frac{\overline{\overline{U}^{t}}^{y} \sec\beta}{(1-\delta)}\Big|_{-\infty} \tag{B14}$$

while at the exit,

$$q\Big|_{\infty} = \frac{\overline{\overline{U}^{t}}^{y} \sec\beta}{(1-\delta)}\Big|_{\infty} \tag{B15}$$

Using Eqs. (B14) and (B15), Eq. (B13) can be rewritten as a pressure rise coefficient,

$$\begin{aligned} C_p =& \frac{p\big|_{\infty} - p\big|_{-\infty}}{(1/2)\overline{\overline{U}^{t}}^{y} \sec\beta_{-\infty}} \\ =& 1 - \frac{\cos^2\beta_{-\infty}}{\cos^2\beta_{\infty}} + \left[2\delta\Big|_{-\infty} - 2\delta\Big|_{\infty}\left(\frac{\cos^2\beta_{-\infty}}{\cos^2\beta_{\infty}}\right)\right] \end{aligned} \tag{B16}$$

where $1/(1-\delta)^2$ has been approximated by $1+2\delta$ (i.e., $\delta \ll 1$).

Comparing Eq. (B11) to Eq. (B16) shows that the pressure rise across a cascade due to an incoming unsteady vortical flow is equal to that produced by a steady flow in which the inlet flow blockage is $(1/2)\delta_R|_{-\infty}$ while that at the exit is $(1/2)\delta_R|_{\infty}$. Had the assumption not been made regarding the magnitude of δ, the flow blockage of the equivalent steady flow would be:

$$\delta = 1 - \frac{1}{\sqrt{1+\delta_R}} \tag{B17}$$

The link between the flow blockage attributed to the unsteady flow and the portion of the average-passage stress associated with the unsteady deterministic flow field is through the expression for the recovery energy thickness, Eq. (B10). To establish this relationship, it is assumed that the pressure and velocity field can be expanded in a perturbation series of the form

$$p = p^{(0)} + \epsilon p^{(1)} + \epsilon^2 p^{(2)} + O(\epsilon^3) \tag{B18}$$

$$\vec{u} = \vec{u}^{(0)} + \epsilon \vec{u}^{(1)} + \epsilon^2 \vec{u}^{(2)} + O(\epsilon^3) \tag{B19}$$

The lowest order term in Eqs. (B18) and (B19) is associated with a steady potential flow. The first-order pressure term is also associated with a potential flow field and thus vanishes far upstream and downstream of the cascade.

The time average of the first-order term in Eqs. (B18) and (B19) is zero. Flow continuity requires that the pitchwise average of the axial component of $\vec{u}^{(2)}$ be zero. Using the perturbation expansions given by Eqs. (B18) and (B19), the expression for the recovery energy thickness to second order is

$$\begin{aligned} \delta_R =& \frac{2\epsilon^2 k_e\big|_{-\infty}}{q^{(0)^2}}\left[\frac{\overline{\overline{v^{(0)}v^{(2)}}^{t}}^{y}}{k_e\big|_{-\infty}}\right] \\ &+ \frac{2\epsilon^2 k_e\big|_{-\infty}}{q^{(0)^2}}\left[\frac{k_e}{k_e\big|_{-\infty}}\right. \\ &+ \left.\frac{\overline{\overline{u^{(1)}u^{(1)}}^{t}}^{y} + \frac{v^{(0)}}{u^{(0)}}\overline{\overline{u^{(1)}v^{(1)}}^{t}}^{y}}{k_e\big|_{-\infty}}\right] \end{aligned} \tag{B20}$$

where

$$k_e = \frac{1}{2}\overline{\overline{\vec{u}^{(1)} \cdot \vec{u}^{(1)}}^{t}}^{y} \tag{B21}$$

and $q^{(0)}$ is the speed of the steady potential flow.

In order to simplify the process for estimating δ_R, it is assumed that the exit flow angle defined in terms of the time-averaged velocity field is unaffected by the incoming unsteady flow. This assumption implies that

$$\overline{\overline{v^{(2)}}^{t}}^{y}$$

at the exit of the cascade is zero.

References

[1] Marble, F. E., 1964, ''Three-Dimensional Flow in Turbomachines,'' *High Speed Aerodynamics and Jet Propulsion* **X**, *Aerodynamics of Turbines and Compressors*. Princeton University Press.

[2] Smith, L. H., Jr, 1969, ''Casing Boundary Layers in Multistage Compressors,'' *Proc. Symp. Flow Research on Blading*, Dzung, L. S., ed.

[3] Serovy, G. K., 1981, ''Axial-Flow Turbomachine Through Flow Calculation Methods,'' AGARD Advisory Report No. 175, *Through Flow Calculations in Axial Turbomachines*, Ch. Hirsch and J. D. Denton, eds.

[4] Cumpsty, N. A., 1989, *Compressor Aerodynamics*, Longman Scientific & Technical, Publisher.

[5] Wu, C. H., 1952, ''A General Theory of Three-Dimensional Flow in Subsonic or Supersonic Turbomachines of Axial-, Radial-and Mixed-Flow Type,'' NACA TN 2604.

[6] Jennions, I. K., and Stow, P., 1986, ''The Importance of Circumferential Non-uniformities in a Passage-Averaged Quasi-Three-Dimensional Turbomachinery Design System,'' ASME J. Eng. Gas Turbines Power, **108**, pp. 240–245.

[7] Howard, M. A., and Gallimore, S. J., 1993, ''Viscous Throughflow Modeling for Multi-Stage Compressor Design,'' ASME J. Turbomach., **115**, p. 296.

[8] Gallimore, S. J., 1998a, ''Viscous Throughflow Modeling of Axial Compressor Bladerows Using a Tangential Blade Force Hypothesis,'' ASME J. Turbomach., **120**, p. 662.

[9] Khalid, S. A., Khalsa, A. S., Waitz, I. A., Tan, C. S., Greitzer, E. M., Cumpsty, N. A., Adamczyk, J. J., and Marble, F. E., 1999, ''Endwall Blockage in Axial Compressors,'' ASME J. Turbomach., **121**, pp. 499–509.

[10] Van Zante, D. E., Strazisar, A. J., Wood, J. R., Hathaway, M. D., and Okiishi, T. H., 1999, ''Recommendations for Achieving Accurate Numerical Simulation of Tip Clearance Flow in Transonic Compressor Rotors,'' ASME Paper No. 99-GT-390, accepted for the ASME J. Turbomachinery.

[11] Wellborn, S. R., Tolchinsky, I., and Okiishi, T. H., 2000, ''Modeling Shrouded Stator Cavity Flows in Axial-Flow Compressors,'' ASME J. Turbomach., **122**, pp. 55–61.

[12] Denton, J. D., and Singh, U. K., 1979, ''Time Marching Methods for Turbomachinery Flow Calculations,'' VKI-LEC-SER-1979-7, VKI.

[13] Dawes, W. N., 1992, ''Toward Improved Throughflow Capability: The Use of Three-Dimensional Viscous Flow Solvers in a Multistage Environment,'' ASME J. Turbomach., **114**, pp. 8–17.

[14] Denton, J. D., 1992, ''The Calculation of Three-Dimensional Viscous Flow Through Multistage Turbomachines,'' ASME J. Turbomach., **114**, pp. 18–26.

[15] Hall, E. J., and Delaney, R. A., 1993, ''Investigation of Advanced Counter Rotation Blade Configuration Concepts for High Speed Turboprop Systems,'' NASA CR 187126.

[16] Gallimore, S. J., 1998b, ''Axial Flow Compressor Design,'' *The Successful Exploitation of CFD in Turbomachinery Design*, IMechE, HQ, London.

[17] Gallimore, S. J., 1999, Rolls Royce plc, private communication, Compressor Design.

[18] Chen, J. P., Celestina, M. L., and Adamczyk, J. J., 1994, ''A New Procedure for Simulating Unsteady Flows Through Turbomachinery Blade Passages,'' ASME Paper No. 94-GT-151.

[19] Dorney, D. J., Davis, R. L., Edwards, D. E., and Madavan, N. K., 1990, ''Unsteady Analysis of Hot Streak Migration in a Turbine Stage,'' AIAA Paper No. 90–2354.

[20] Giles, M. B., 1990, ''Stator/Rotor Interactions in a Transonic Turbine,'' AIAA J. Propulsion Power, **6**, p. 621.

[21] Gundy-Burlet, K. L., Rai, M. M., Stauter, R. C., and Dring, R. P., 1991, ''Temporally and Spatially Resolved Flow in a Two-Stage Axial Compressor: Part 2—Computational Assessment,'' ASME J. Turbomach., **113**, No. 2, pp. 219–226.

[22] Hodson, H. P., and Dawes, W. N., 1998, ''On the Interpretation of Measured Profile Losses in Unsteady Wake-Turbine Blade Interaction Studies,'' ASME J. Turbomach., **120**, p. 276.

[23] Rai, M. M., and Dring, R. P., 1987, ''Navier–Stokes Analysis of the Redistribution of Inlet Temperature Distortion in a Turbine,'' AIAA Paper No. 87–2146.

[24] Sharma, O. P., Pickett, G. F., and Ni, R. H., 1992, ''Assessment of Unsteady Flows in Turbines,'' ASME J. Turbomach., **114**, pp. 79–90.

[25] Hall, E. J., 1997, ''Aerodynamic Modeling of Multistage Compressor Flowfields,'' ASME Papers No. 97-GT-344 and 97-GT-345.

[26] Adamczyk, J. J., 1985, ''Model Equation for Simulating Flows in Multistage Turbomachines,'' ASME Paper No. 85-GT-226.

[27] LeJambre, C. R., Zacharias, R. M., Biederman, B. P., Gleixner, A. J., and Yetka, C. J., 1998, ''Development and Application of a Multistage Navier–Stokes Flow Solver: Part II—Application to a High-Pressure Compressor Design,'' ASME J. Turbomach., **120**, p. 215.

[28] Mansour, M., 1999, AlliedSignal Engines, private communication, Multistage Compressor Simulations.

[29] Wellborn, S. R., 1999, Rolls-Royce Allison, private communication, Multistage Compressor Simulations.

[30] Reid, L., and Moore, R., 1978, ''Design and Overall Performance of Four Highly Loaded, High-Speed Inlet Stages for an Advanced High-Pressure Ratio Core Compressor,'' NASA TP 1337.

[31] Denton, J., 1996, ''Lessons Learned From Rotor 37,'' presented at the Third International Symposium on Experimental and Computational Aerothermodynamics of Internal Flows (ISAIF).

[32] Adamczyk, J. J., Mulac, R. A., and Celestina, M. L., 1986, ''A Model for Closing the Inviscid Form of the Average-Passage Equation System,'' ASME J. Turbomach., **108**, p. 180.

[33] Kirtley, K. R., Turner, M. G., and Saeidi, S., 1999, ''An Average-Passage Closure Model for General Meshes,'' ASME Paper No. 99-GT-077.

[34] Rhie, C. M., Gleixner, A. J., Spear, D. A., Fischberg, C. J., and Zacharias, R. M., 1998, ''Development and Application of a Multistage Navier–Stokes Solver: Part 1—Multistage Modeling Using Body Forces and Deterministic Stresses,'' ASME J. Turbomach., **120**, p. 205.

[35] Adamczyk, J. J., 1991, ''A Mathematical Constraint Placed Upon Inter-Blade Row Boundary Conditions Used in The Simulation of Multistage Turbomachinery Flows,'' AGARD Conf. Proc. 510, *CFD Techniques for Propulsion Applications*.

[36] Adkins, Jr, G. G., and Smith, Jr, L. H., 1982, ''Span-wise Mixing in Multistage Axial Flow Compressors,'' ASME J. Eng. Power, , **104**, p. 97.

[37] Lewis, K. L., 1993, ''Spanwise Transport in Axial-Flow Turbines: Part 1—The Multistage Environment,'' ASME J. Turbomach., **116**, pp. 179–186.

[38] Lewis, K. L., 1994, ''Spanwise Transport in Axial-Flow Turbines: Part 2—Throughflow Calculations,'' ASME J. Turbomach., **116**, pp. 187–193.

[39] Butler, T. L., Sharma, O. P., Joslyn, H. D., and Dring R. P., 1989, ''Redistribution of an Inlet Temperature Distortion in an Axial Flow Turbine Stage,'' AIAA J. Propulsion Power, 5.

[40] Graham, R. W., 1979, ''Fundamental Mechanisms That Influence the Estimate of Heat Transfer to Gas Turbine Blades,'' ASME Paper No. 79-GT-43.

[41] Kerrebrock, J. L., and Mikolajczak, A. A., 1970, ''Intra-Stator Transport of Rotor Wakes and Its Effect on Compressor Performance,'' ASME J. Eng. Power, **92**, p. 359.

[42] Kirtley, K. R., Celestina, M. L., and Adamczyk, J. J., 1993, ''The Effect of Unsteadiness on the Time-Mean Thermal Loads in a Turbine Stage,'' SAE Paper No. 931375.

[43] Orkwis, P. D., and Turner, M. G., 1999, ''An Eulerian/Lagrangian Approach for Analyzing Temperature Segregation Effects in High Pressure Turbines,'' to be published.

[44] Valkov, T., and Tan, C. S., 1993, ''Control of the Unsteady Flow in a Stator Blade Row Interacting With Upstream Moving Wakes,'' ASME J. Turbomach., **117**, pp. 97–105.

[45] Valkov, T. V., and Tan, C. S., 1998, ''Effect of Upstream Rotor Vortical Disturbances on the Time-Average Performance of Axial Compressor Stators: Part 1—Framework of Technical Approach and Wake-Stator Blade Interactions,'' ASME J. Turbomach., **121**, pp. 377–386.

[46] Valkov, T. V., and Tan, C. S., 1999, ''Effect of Upstream Rotor Vortical Disturbances on the Time-Average Performance of Axial Compressor Stators: Part 2—Rotor Tip Vortex/Streamwise Vortex-Stator Blade Interactions,'' ASME J. Turbomach., **121**, pp. 386–396.

[47] Dawes, W. N., 1994, ''A Numerical Study of the Interaction of a Transonic Compressor Rotor Over-tip Leakage Vortex With the Following Stator Blade Row,'' ASME Paper No. 94-GT-156.

[48] Fritsch, G., and Giles, M. B., 1993, ''An Asymptotic Analysis of Mixing Loss,'' ASME J. Turbomach., **117**, pp. 367–374.

[49] Smith, Jr, L. H., 1996, ''Wake Dispersion in Turbomachines,'' ASME J. Basic Eng., **88**, No. 3.

[50] Adamczyk, J. J., 1996, ''Wake Mixing in Axial Flow Compressors,'' ASME Paper No. 98-GT-29.

[51] Batchelor, G. K., 1967, *An Introduction to Fluid Dynamics*, Cambridge University Press.

[52] Deregel, P., and Tan, C. S., 1996, ''Impact of Rotor Wakes on Steady State Performance of Compressor,'' ASME Paper No. 96-GT-253.

[53] Van Zante, D. E., Adamczyk, J. J., Strazisar, A. J., and Okiishi, T. H., 1997, ''Wake Recovery Performance Benefit in a High-Speed Axial Flow Compressor,'' ASME Paper No. 97-GT-535.

[54] van de Wall, A. G., 1999, ''A Transport Model for the Deterministic Stresses Associated With Turbomachinery Blade Row Interactions,'' Ph. D Thesis, Department of Mechanical and Aerospace Engineering, Case Western Reserve University.

[55] Smith, L. H., Jr., 1996, Discussion of ASME Paper No. 96-GT-029 and ASME Paper No. 96-GT-253, Birmingham, United Kingdom.

[56] Barankiewicz, W. S., and Hathaway, M. D., 1997, ''Effects of Stator Indexing on Performance in a Low Speed Multistage Axial Compressor,'' ASME Paper No. 97-GT-496.

[57] Arndt, N., 1993, ''Blade Row Interaction in a Multistage Low-Pressure Turbine,'' ASME J. Turbomach., **115**, pp. 137–146.

[58] Sharma, O. P., Stetson, G. M., Daniels, W. A., Greitzer, E. D., Blair, M. F., and Dring, R. P., 1997, ''Impact of Periodic Unsteadiness on Performance and Heat Load in Axial Flow Turbomachines,'' NASA Contractor Report No. 202319.

[59] Wellborn, S. R., and Okiishi, T. H., 1996, ''Effects of Shrouded Stator Cavity Flows on Multistage Compressor Aerodynamic Performance,'' NASA CR 198536.

[60] Adamczyk, J. J., Hathaway, M. D., Shabbir, A., and Wellborn, S. R., 1998, ''Numerical Simulation of Multi-Stage Turbomachinery Flows,'' presented at the Applied Vehicle Technology Symposium on Design Principles and Methods for Aircraft Gas Turbine Engines, Toulouse, France, May 11–15.

[61] Cline, S. J., Fesler, W., Liu, H. T., Lovell, R. C., and Shaffer, S. J., 1977, ''Energy Efficient Engine, High Pressure Compressor Component Performance Report,'' NASA CR-168245.

[62] Wisler, D. C., Koch, C. C., Smith, L. H., Jr., 1977, ''Energy Efficient Engine, Preliminary Design Study of Advanced Multistage Axial Flow Core Compressors,'' NASA CR 135133.

[63] Smith, L. H., Jr., 1999, GE Aircraft Engines, private communication, CAF-MIX II Development.

[64] Turner, M. G., 1999, private communication, Blockage Estimates.

[65] Liu, H. T., 1999, GE Aircraft Engines, private communication, Compressor Stall.

[66] Shabbir, A., Celestina, M. L., Adamczyk, J. J., and Strazisar, A. J., 1997, ''The Effect of Hub Leakage Flow on Two High Speed Axial Flow Compressor Rotors,'' ASME Paper No. 97-GT-346.

[67] Escuret, J. F., and Veysseyre, P. H., 1997, ''Effect of a Mismatch Between the Buttons of Variable Stator Vanes and the Flowpath in a Highly Loaded Transonic Compressor Stage,'' ASME Paper No. 97-GT-471.

[68] Wellborn, S. R., and Okiishi, T. H., 1998, ''The Influence of Shrouded Stator Cavity Flows on Multistage Compressor Performance,'' ASME J. Turbomach., **121**, pp. 486–497.

[69] Shang, T., Epstein, A. H., Giles, M. B., and Sehra, A., 1993, ''Blade Row Interaction Effects on Compressor Measurements,'' AIAA J. Propulsion Power, **9**, No. 4, p. 569.

[70] Giles, M. B., 1992, ''An Approach for Multi-stage Calculations Incorporating Unsteadiness,'' ASME Paper No. 92-GT-282.

[71] Cumpsty, N. A., Dong, Y., and Li, Y. S., 1995, ''Compressor Blade Boundary Layers in the Presence of Wakes,'' ASME Paper No. 95-GT-443.

[72] Halstead, D. E., Wisler, D. C., Okiishi, T. H., Walker, G. J., Hodson, H. P., and Shin, H., 1997, ''Boundary Layer Development in Axial Compressors and Turbines: Part 1 of 4—Composite Picture,'' ASME J. Turbomach., **119**, p. 114.

[73] Hodson, H. P., 1990, ''Modeling Unsteady Transition and Its Effects on Profile Loss,'' ASME J. Turbomach., **112**, pp. 691–701.

[74] Walker, G. J., 1974, ''The Unsteady Nature of Boundary Layer Transition on an Axial Flow Compressor,'' ASME Paper No. 74-GT-135.

[75] Harvey, N. W., Schulte, V. S., Howell, R. J., and Hodson, H. P., 1999, ''The Role of Research in the Aerodynamic Design of an Advanced Low Pressure Turbine,'' Proc. 3rd European Conf. on Turbomachinery, IMechE, London, Mar.

[76] Launder, B. E., and Spalding, D. B., 1974, ''The Numerical Computation of Turbulent Flows,'' Comp. Math. Appl. Mech., **3**, p. 269.

[77] Shih, T. H., Liou, W. W., Shabbir, A., Zhu, J., and Yang, Z., 1995, ''A New $k-\epsilon$ Eddy Viscosity Model for High Reynolds Number Turbulent Flows,'' Comp. Fluids, **23**, No. 3, p. 227.

[78] Hathaway, M. D., Gertz, J. B., Epstein, A. H., and Strazisar, A. J., 1986, ''Rotor Wake Characteristics of a Transonic Axial-Flow Fan,'' AIAA J., **24**, No. 11, p. 1802.

[79] Kotidis, P. A., and Epstein, A. H., 1991, ''Unsteady Radial Transport in a Transonic Compressor Stage,'' ASME J. Turbomach., **113**, pp. 207–218.

[80] Binder, A., Foster, W., Kruse, H., and Rogge, H., 1985, ''An Experimental Investigation Into the Effect of Wakes on the Unsteady Turbine Rotor Flow,'' ASME J. Eng. Mater. Technol., **107**, p. 458.

[81] van de Wall, A. G., Kadambi, J. R., Boyle, R. J., and Adamczyk, J. J., 1995, ''The Transport of Vorticies Through a Turbine Cascade,'' ASME Paper No. 95-GT-240.

[82] Zierke, W. C., Straka, W. A., and Taylor, T. D., 1993, ''The High Reynolds Number Flow Through an Axial Flow Pump,'' Applied Research Lab. Penn. State Univ. T. R. 93-12.

[83] Graf, M. B., Greitzer, E. M., Marble, F. E., and Sharma, O. P., 1999, ''Effects of Stator Pressure Field on Upstream Rotor Performance,'' ASME Paper No. 99-GT-99.

[84] Lighthill, M. J., 1964, ''Introduction to Fourier Analysis and Generalized Functions,'' Cambridge Monographs on Mechanics and Applied Mathematics, Cambridge University Press.

The Determination of End-Wall Blockage in Axial Compressors: A Comparison Between Various Approaches

J. H. Horlock
Whittle Laboratory,
Cambridge, United Kingdom

The end-wall blockage in axial compressors has been the subject of several investigations over a period of many years. This paper reviews and compares various approaches to determining the blockage, particularly in the ''repeating'' stage, a stage deeply embedded in the compressor where an equilibrium state is reached, the flow through any one stage repeating in the next. These approaches include: (i) correlations of displacement thickness measured in compressor rigs; (ii) a relationship between outlet blockage and the clearance area, based both on an empirical development of a simple model of the flow through the clearance space and full CFD calculations of the flow; (iii) momentum analysis of the flow through the blockage region, developed from the boundary layer analyses of some years ago, but not now relying on boundary layer concepts.
[S0889-504X(00)01502-6]

1.0 Introduction

The end-wall blockage in axial compressors has been the subject of several investigations over a period of many years. This paper reviews various approaches to determining the blockage, particularly in the ''repeating'' stage, a stage deeply embedded in the compressor in which an equilibrium state is reached, the flow through any one stage repeating in the next.

Khalid et al. [1] recently published a new and challenging approach to the problem; they provided realistic descriptions, analytical and experimental, of how the flow through the clearance region is linked with downstream blockage of the mainstream flow. A brief summary of their work is given later in this paper, and it is related and compared to:

(i) previous experimental work, particularly by Smith [2], on the ''equilibrium blockage'' that is developed in repeating stages after a few blade rows in a multistage compressor; and
(ii) momentum analysis of the flow through the ''equilibrium'' blockage region, a development of the work of Stratford [3] and Horlock and Perkins [4].

2.0 The Repeating Stage

In a classic paper, Smith studied the detailed flow in repeating stages. From extensive experimental data he showed that for a well-behaved axial compressor, the flow settled down to an equilibrium form after a couple of stages. The axial velocity and flow angle profiles at entry to a stage (outlet from the previous stator) were more or less unchanged after passage through the repeating stage, i.e., they were repeated at exit from the stator. Thus the (axial) blockage was virtually unchanged across the repeating stage. Figure 1 shows Smith's results, as reproduced by Cumpsty [5], with some additional points obtained by the latter.

Smith drew attention to the wide scatter in the data, emphasizing that his approach was that of a designer, seeking rough guidance on blockage for preliminary design purposes. However, he concluded that in general the blockage (or axial displacement thickness, normalized with respect to the ''staggered spacing,'' $g = s \cos \beta_e$) increased with nondimensional tip clearance (τ/g) and with the stage pressure rise coefficient. This broad conclusion is not entirely dissimilar from that reached by Khalid et al., although the form of the dependency of the blockage on pressure rise coefficient that they derived is different and involves an additional parameter related to the total pressure deficit in the clearance region.

Such repeating flows have been observed in other compressors. An early set of results obtained by McKenzie [6] illustrated that the repeating phenomenon was set up soon after the first-stage stator in a four-stage Rolls Royce compressor and this was confirmed by Cumpsty [5] in his more detailed measurements on the same compressor. The repeating stage phenomenon was also observed by Howard et al. [7] in a four-stage compressor tested at Cranfield. Horlock [8] drew attention to the fact that the secondary flow must also repeat the outlet air angle distributions with radius being identical for deeply embedded stages.

Attempts to calculate a repeating stage flow for the Cranfield compressor were made by Bolger and Horlock [9], using computer codes developed by Dawes [10] and Denton [11]. They took the observed flow at entry to the stage as the input for calculating the leaving flow, which was shown to be close, but not identical, to that at entry. However, a more convincing calculation was subsequently made by Denton [12], who used his code to calculate the whole compressor flow ''ab initio''; he showed that the repeating stage flow developed quickly.

Another approach had been adopted earlier by Horlock and Perkins [4], who developed a method for calculating the ''annulus wall boundary layers'' through Smith's compressor and through industrial axial compressors. Their work indicated that the values of the axial blockage area (A_{bx}), or axial displacement thickness, δ_x^*, did indeed reach equilibrium levels quite quickly.

It must be accepted that compressor design has advanced substantially since these early works. Stage loadings have been increased and the number of stages consequently reduced, so that in LP aircraft engine compressors there will be few repeating stages and the ''equilibrium stage'' concept is less important. Nevertheless, even with modern CFD modeling, estimates of wall blockage may be of value in preliminary design of industrial compressors and possibly the HP compressors of aeroengines.

3.0 A Discussion of Smith's Results

There is another important conclusion to be drawn from the experimental data of Smith, Cumpsty, and Howard. It is that the

---

Contributed by the International Gas Turbine Institute for publication in the JOURNAL OF TURBOMACHINERY. Manuscript received at ASME Headquarters December 6, 1999. Associate Technical Editor: T. H. Okiishi.

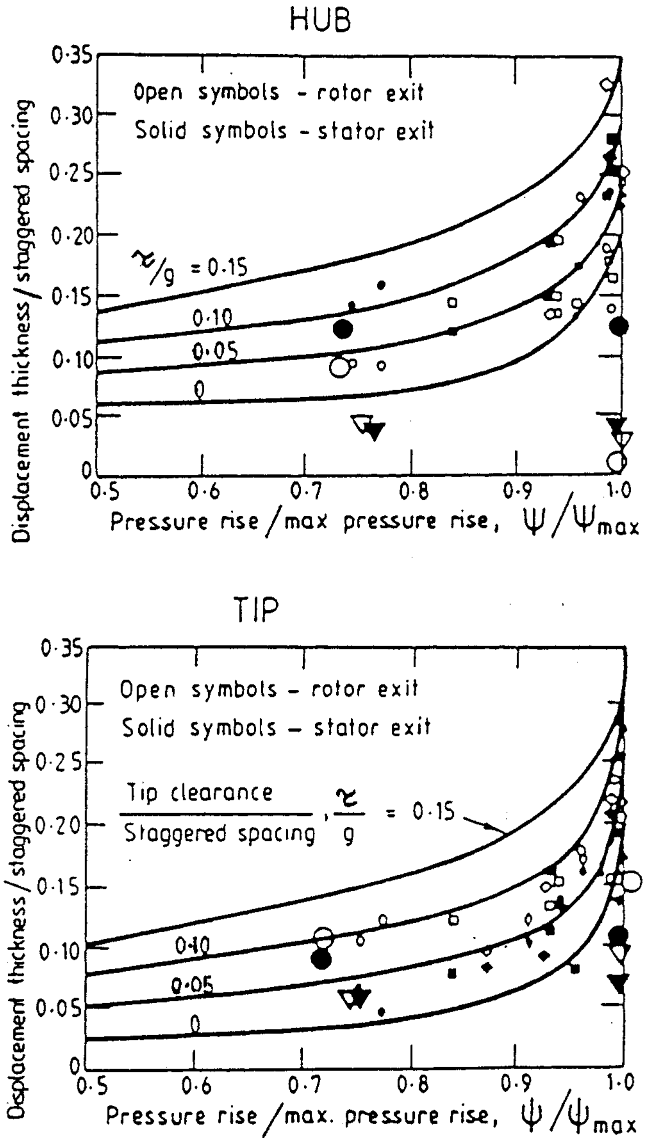

Fig. 1 Smith's experimental data for blockage as presented by Cumpsty, with some of his own data added (shown by larger symbols)

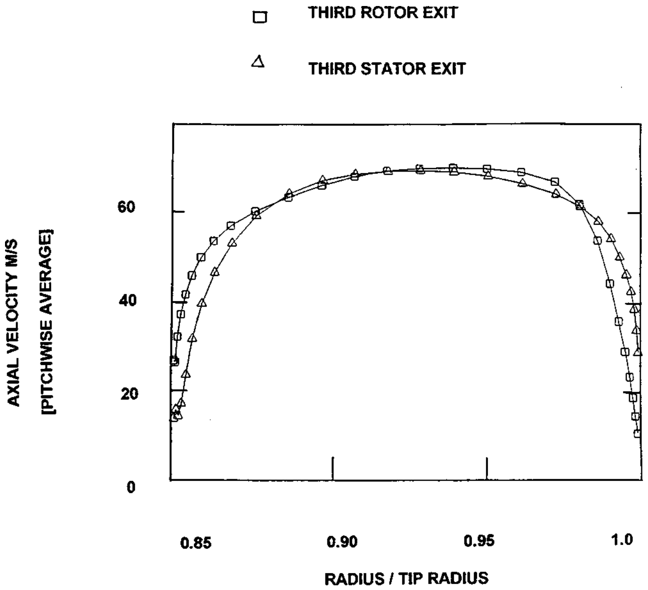

Fig. 2 Denton's calculations of axial velocity profiles in the Cranfield compressor (after third rotor and third stator)

repetition occurs not only after the stators of the repeating stages but also after the rotors, i.e., that the axial velocity profile after, say, the third rotor is the same as that after the fourth rotor. But this repeating axial velocity profile after a rotor is different from the repeating axial velocity profile after a stator, so the blockage after the rotor $[(A_{bx})_R$ or $(\delta_x^*)_R]$ is different from that after a stator $[(A_{bx})_S$ or $(\delta_x^*)_S]$.

Smith's results showed that for the flow near the casing, the displacement thickness increased across the rotor row, which has end-wall or tip clearance, and then decreased across a stator row cantilevered from the casing, which has no such clearance. Further, his data for the hub flows in general showed the converse: the axial blockage decreased across the rotor (with no radial clearance) and increased across the unshrouded stator (with radial clearance).

This effect was confirmed in the boundary layer calculations of Horlock and Perkins, and by Denton in full three-dimensional Navier–Stokes calculations [12]. Figure 2 shows the latter's calculations of the axial velocity profiles at exit from the rotor and stator of the third stage in the Cranfield compressor. The boundary layer thickness clearly increases across the clearance regions (rotor casing and stator hub) and decreases across the nonclearance regions (rotor hub and stator casing).

Table 1 shows calculated values of $(\delta_x^*)/g$ (where $g = c\cos\beta_e$) obtained from Denton's calculations, for hub and tip sections, together with the values of nondimensional clearance (τ/g) used in the calculations. The value of $(\psi/\psi_{\max})$ is not known for the flow condition calculated, but if it is taken as a high efficiency point, with $(\psi/\psi_{\max})=0.95$ say, then Smith's correlation (the full lines shown in Fig. 1) would give values of $(\delta_x^*)/g$ (the bracketed figures in the table) some 10–15 percent less than the calculated values for the two sections.

Bracketed figures show approximate values from Smith's correlation (the full lines of Fig. 1).

Smith's data are used later to obtain the increase in blockage through a blade row with end-wall clearance in a repeating stage. This increase may be shown to be proportional to the clearance itself and to the *stage* loading. Khalid et al. consider a single row with clearance, the resulting blockage at exit being proportional to the clearance and increasing with a loading factor equal to the pressure rise coefficient for the *row* less an additional coefficient that allows for the total pressure deficit in the clearance space (but not specifically the deficit in an entry boundary layer).

Smith's data also yield the change in blockage across the subsequent ''nonclearance'' row, but Khalid et al. [1] do not provide such information. Indeed, the elementary Bernoulli type of analysis from which they develop their work would imply that blockage should increase further as the pressure rises across the following ''nonclearance'' row, whereas Smith's data shows that the opposite occurs in repeating stages.

Table 1 Calculations of equilibrium blockage

Hub
Rotor exit $(\delta_x^*)_R/g=0.153(0.125)$, Clearance $\tau/c\cos\xi=0$
Stator exit $(\delta_x^*)_S/g=0.170(0.150)$, Clearance $\tau/c\cos\xi=0.026$
Casing
Stator exit $(\delta_x^*)_S/g=0.079(0.080)$, Clearance $\tau/c\cos\xi=0$
Rotor exit $(\delta_x^*)_R/g=0.130(0.120)$, Clearance $\tau/c\cos\xi=0.034$

4.0 A Development of Smith's Physical Description of the Repeating Stage

By extending the physical arguments that Smith presented, an explanation can be given for the balancing decrease in blockage across a ''nonclearance'' blade row within the repeating stage.

Smith's interpretation of the flow in a repeating stage is along the lines described briefly below. It is presented here for a ''rectilinear'' casing endwall region, i.e., one in which the blockage area affected is small compared with the total flow area (or displacement thickness small compared with the local radius) and where it is the rotor that has the end-wall clearance. If it is accepted empirically that the flow in a stage repeats, then consideration of the axial momentum flux through a control surface surrounding the stage leads to the conclusion that the sum of the axial component of the blade forces (rotor and stator), the pressure forces at entry and exit, and the viscous forces on the wall should be zero.

There are important limitations on the concept of the equilibrium stage and its application in compressor design. For example:

- (i) strictly the blade force components described above are made up of the pressure forces and viscous forces acting on the two blades;
- (ii) ignoring the viscous forces on the end-walls (as we do below) will mean that the blockage will continue to grow;
- (iii) the effects of radial transport and axial velocity diffusion are ignored;
- (iv) the repeating stage concept is really limited to well-behaved compressors with high aspect ratios and moderately small clearances, operating without significant separations on the blades and end-walls, as both Smith (and Howell before him) observed.

If the viscous forces on the end-walls are ignored, then for the flow to repeat, the axial components of the two blade forces must be equal to the product of the pressure rise times the area considered (the blade spacing times the length of blade). The argument may be applied from previous stator exit to repeating stage stator exit, or from previous rotor exit to repeating stage rotor exit, i.e., across two blade rows in each case. This leads to the conclusion that the *sum* of the axial component of the blade forces, *on rotor plus stator*, is maintained constant through the ''end-wall boundary layer.''

Consider next the flow through a *rotor* with tip clearance, across which the axial velocity profile does change. For the ''rectilinear'' blade row the pressure is still substantially constant along the blade, at entry and at exit. But there is now a difference between the integrated (axial) blade force and the pressure change area product. This difference is negative in the axial flow direction and produces a reduction in the axial momentum. The force on the blade drops off toward its end, falling to zero in the clearance space (this effect is discussed again later).

Application of the same argument to the following *stator* then produces an interesting conclusion. There must be an equal but opposite difference between the axial blade force and the pressure rise term (now an ''incremental'' difference, positive in the axial direction) that will increase the axial momentum of the flow (and reduce the blockage). This is because the sum of the blade forces on the two rows must be equal to the pressure rise across the whole stage (assumed constant along the blade length) and if there is a force deficit on the rotor, there must be a force increment on the stator.

These arguments were also developed in the paper by Horlock and Perkins, on annulus wall boundary layers in turbomachines, and are briefly recapitulated below. Essentially they followed a remarkable (but not well recognized) paper by Stratford. The whole concept of an annulus wall boundary layer has since been justifiably criticized (see Cumpsty [13]); but it was the employment of ''conventional'' boundary layer concepts, such as Coles-type velocity profiles, entrainment, and shear stress functions, where the criticism was most valid. The use of the von Karman momentum equation is not subject to the same criticism, since its application to the blockage or momentum deficit area cannot be questioned, if the assumption by Smith of invariant pressure with radius is accepted (also made in the simple analysis of Khalid et al. [1]).

For the case of mainstream axial velocity constant, and with the wall shear stress neglected, the change in the axial momentum thickness across a [rotor] clearance row is

$$(\Delta \overline{\theta_x})_{SR} = (F_x)_R(\nu_x)_R/s\rho\overline{C}_x^2 \tag{1}$$

where the subscript SR indicates the change from the condition downstream of the preceding stator [S] to downstream of the rotor [R]. The momentum thickness [(θ_x)] in this equation results from area integration: [a] integrating the axial velocity component c_x across the pitch at each radius to give $\overline{c_x}s$ [where $\overline{c_x}$ is the pitch-wise mean axial velocity]; and [b] integrating

$$\int [1-(\overline{c_x}/\overline{C_x})](\overline{c_x}/\overline{C_x})dz = (\overline{\theta_x}).$$

The integral is taken along the blade direction z, into the mainstream where $\overline{c_x} = \overline{C_x}$.

Further $(\nu_x)_R$ is the axial force deficit thickness introduced by Smith and also used by Horlock and Perkins,

$$(\nu_x)_R = \int [1-(f_x/F_x)_R]dz$$

where $(F_x)_R$ is the axial force on the blade per unit length in the mainstream and $(f_x)_R$ is the local blade force in the deficit region. For a rotor blade, outside the boundary layer region, $(F_x)_R = s\Delta p_R$, where Δp_R is the pressure rise across the rotor.

For their calculations, Horlock and Perkins took $(\nu_x)_R$ to be the product of an empirical constant K (of order unity) and tip clearance τ, implying that the blade lift is retained to the end of a cantilevered unshrouded blade (we shall discuss this further below). With that assumption, the change in the axial blockage across a row with tip clearance is given by

$$(\Delta A_{bx})_{SR} = s\Delta(\overline{\delta_x^*})_{SR} = sH\Delta(\overline{\theta_x})_{SR} = H(F_x)_R K\tau/\rho\overline{C}_x^2 \tag{2}$$

where H is the ratio of the displacement thickness to the momentum thickness. The bar superscript will be dropped subsequently, implying that δ^*, θ, c_x, C_x below are all pitch-averaged quantities. Note also that the axial blockage area, $(A_{bx})_R$, and the blockage, $(A_b)_R$, across the mainstream are related by

$$(A_b)_R = (A_{bx})_R \cos\beta_e$$

where β_e is the rotor exit air angle.

For comparison with Smith's measurements of displacement thickness, using his definitions of static pressure coefficient and flow coefficient

$$\psi = \Delta p_{\text{stage}}/1/2(\rho U_{\text{mid}}^2), \quad \phi = C_x/U_{\text{mid}},$$

it follows that

$$\Delta(\delta_x^*)_{SR} = (KH)(\Delta p)_{SR}\tau/\rho C_x^2 \tag{3}$$

$$= (KH)R\psi\tau/2\phi^2 \tag{3a}$$

where $R = (\Delta p_{SR}/\Delta p_{\text{stage}})$ is the stage reaction.

The momentum equation from R to S across the following stator (nonclearance row at the casing) is then

$$\Delta(\delta_x^*)_{RS} = -(KH)R\psi\tau/2\phi^2 \tag{4}$$

since in the repeating stage model the momentum thickness (and the displacement thickness) are restored to their values at entry to the stage [i.e., $\Delta(\delta_x^*)_{\text{stage}} = 0$].

Note from Eqs. (3a) and (4) that the values of $\Delta(\delta_x^*)_{SR}$ and $\Delta(\delta_x^*)_{RS}$ are each individually proportional to the pressure rise across the rotor row with casing clearance, Δp_{SR} in the presentation given above. But the change across the stator hub clearance row will be given by

$$\Delta(\delta_x^*)_{SR} = (KH)(1-R)\psi\tau/2\phi^2 \qquad (5a)$$

and across the following rotor [with no clearance] by

$$\Delta(\delta_x^*)_{RS} = -(KH)(1-R)\psi\tau/2\phi^2 \qquad (5b)$$

5.0 The Axial Force Deficit Thickness

The question of how, and indeed whether, the blade force is retained near the clearance region has been the subject of much discussion in the literature. Lakshminarayana and Horlock [14] reported experimental work in cascades, giving empirical expressions for the amount of the retained lift, as functions of the clearance/chord ratio. Obviously as clearance is increased to a large value, all the lift must be shed, but there appeared to be evidence that some lift was retained as the clearance was reduced progressively toward zero (when all the lift should be retained). Their empirical data has been used by others in design (e.g., Adkins and Smith [15] but the concept of retained lift has been the subject of discussion by others who argue that retention is not possible for a perfect fluid.

The effect of differing assumptions on the force deficit thickness is illustrated diagrammatically in Fig. 3. For the case adopted by Horlock and Perkins (100 percent retention up to the blade end) the force deficit thickness is simply equal to the clearance ($K \approx 1$, $\nu_x = \tau$). For the ''classical'' case of all the lift shed, but progressively toward the tip, the force deficit thickness will be much greater ($K \approx 2$, say). The Lakshminarayana and Horlock results show progressive shedding toward the tip together with some lift retention there, suggesting that the force deficit thickness should be somewhat greater than τ ($1 < K < 2$, say).

An empirical approach suggested here is to take the product of K and H to be about 2 (i.e., to assume that H is of the order 1.4 and K is of the same order). This then yields a value of $(\Delta\delta_x^*)_{SR}$ across a rotor (clearance) row as

$$(\Delta\delta_x^*)_{SR}/\tau = R\psi/\phi^2 \qquad (6a)$$

and across a stator (clearance) row

$$(\Delta\delta_x^*)_{RS}/\tau = (1-R)\psi/\phi^2 \qquad (6b)$$

It is argued that the analysis is valid for an equilibrium stage of any reaction in that the boundary layer increases across the clearance rows [as described by Eq. (6a) for a casing flow and by Eq. (6b) for a hub flow with cantilevered stators] and then decreases across the following (nonclearance) row, giving no net change across the stage. For shrouded stators, the analysis would suggest that the boundary layer would remain unchanged at its equilibrium value along the hub, since none of the hub blade sections would have radial clearance.

For a 50 percent reaction stage, Eqs. (6a) and (6b) become

$$(\Delta\delta_x^*)_{SR}/\tau = (\Delta\delta_x^*)_{RS}/\tau = \psi/2\phi^2 \qquad (7)$$

across each of the two clearance sections.

6.0 Three Sources of Information

There are thus three sources of information available on blockages in repeating stages.

6.1 Smith's Data. Most of Smith's compressors appear to have a reaction somewhat less than 50 percent at the design flow. From his data but using engineering judgement, Smith suggested a general correlation for the displacement thicknesses measured in his repeating stages, (δ_x^*),

$$(\delta_x^*)_{\tau\neq 0}/g = (\delta_x^*)_{\tau=0}/g + (\psi/\psi_{\max})\tau/g \qquad (8)$$

where g is Smith's ''staggered spacing,'' $g = s\cos\beta_e$, with β_e the leaving angle.

If we consider first a casing flow, then the first term on the right-hand side of Eq. (8) would refer to the boundary layer downstream of the stator [i.e., $(\delta_x^*)_S = (\delta_x^*)_{\tau=0}$]. The left-hand side of Eq. (8) would refer to the condition downstream of the rotor with clearance [i.e., $(\delta_x^*)_R = (\delta_x^*)_{\tau\neq 0}$]. Thus, *for casing flows* (rotors with clearance, stators without) we may write Eq. (8) as

$$(\delta_x^*)_R/\tau = (\delta_x^*)_S/\tau + (\psi/\psi_{\max})$$

so that

$$\Delta(\delta_x^*)_{SR}/\tau = (\delta_x^*)_R/\tau - (\delta_x^*)_S/\tau = (\psi/\psi_{\max}) = -\Delta(\delta_x^*)_{RS}/\tau \qquad (8a)$$

Similarly *for hub flows* (stators with clearance, rotors without), $(\delta_x^*)_R$ is taken as equal to $(\delta_x^*)_{\tau=0}$, so that Eq. (8) now yields

$$\Delta(\delta_x^*)_{RS}/\tau = (\delta_x^*)_S/\tau - (\delta_x^*)_R/\tau = (\psi/\psi_{\max}) = -\Delta(\delta_x^*)_{SR}/\tau \qquad (8b)$$

It may be noted from Fig. 1 that $(\delta_x^*)_S$ at the casing (i.e., for $\tau=0$) is somewhat less than $(\delta_x^*)_R$ at the hub (also for $\tau=0$) but that $\Delta(\delta_x^*)_{RS}$ increases with τ at about the same rate as does $\Delta(\delta_x^*)_{SR}$; this would be expected from Eqs. (6) and (7) if the stage reaction $R \approx 0.5$.

6.2 The Work of Khalid et al. [1]. The paper by Khalid et al. presents an entirely novel approach to the blockage problem, relating the blockage to the flow through the tip clearance area. The work starts from a simple analysis of how a wake in a two-dimensional entry flow develops in an adverse pressure gradient (Fig. 4). By assuming that the flow in the entering wake (c_1A_1) is equal to the flow in the exit wake (c_2A_2) and assuming no losses, it is possible to derive an expression for the ratio of the blockage area $A_{b2} = [1-(c_2/C_2)]A_2$ to the area A_1 of the form

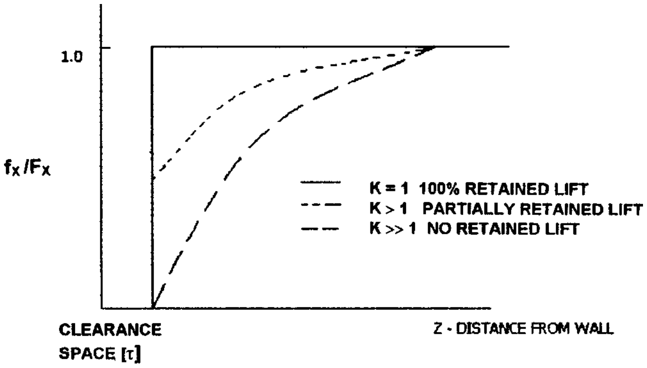

Fig. 3 Retained lift and corresponding values of *K*

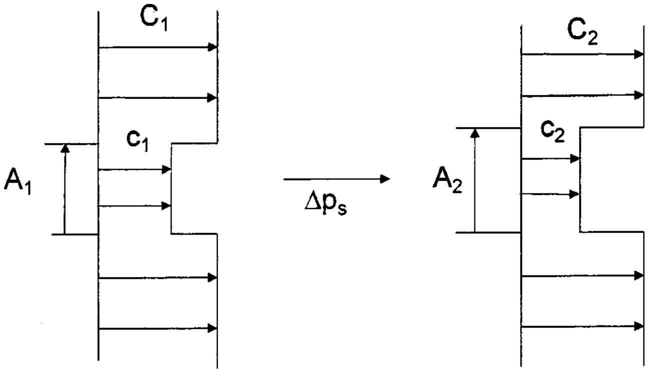

Fig. 4 Simple blockage model used by Khalid et al.

$$A_{b2}/A_1=\alpha_1\{(\alpha_1^2-C_{ps})^{-1/2}-(1-C_{ps})^{-1/2}\} \qquad (9a)$$

where $C_{ps}=\Delta p_s/Q_1$ [with $Q_1=\rho C_1^2/2$], $C_{pt}=[(p_t)_{\text{defect}}-(p_t)_{\text{free-stream}}]/Q_1=\alpha_1^2-1$ with $\alpha_1=c_1/C_1$. A more useful form of this equation is

$$A_{b2}/A_1=(1+C_{pt})^{1/2}\{[1-(C_{ps}-C_{pt})]^{-1/2}-(1-C_{ps})^{-1/2}\} \qquad (9b)$$

where a new loading parameter $X=(C_{ps}-C_{pt})=1-\alpha_2^2=1-(c_2/C_1)^2$ has been introduced. The advantage of this second form of the equation is that it may be shown that the area ratio (A_{b2}/A_1) is strongly dependent on X, with a weak dependence on C_{pt}.

Khalid et al. then generalize this concept for a flow leaving a clearance gap entering the mainstream and turning with it to form the downstream blockage region. Measurements were made of blockage area in single compressor rotors and wind tunnel experiments, together with full CFD calculations of the flows. The blockage area in the flow direction $A_{bx}\cos\beta_e$, corresponding to A_{b2} in the simple analysis described above, was normalized by the entrance ''wake'' (or clearance) area, corresponding to A_1 above, i.e., $A_1=\tau c$. Thus, the nondimensional blockage corresponding to A_{b2}/A_1 above was written as

$$Y=A_{bx}\cos\beta_e/\tau c \qquad (10a)$$

or in terms of the axial displacement thickness δ_x^*, with $A_{bx}=s\,\delta_x^*$,

$$Y=[g/c][\delta_x^*/\tau] \qquad (10b)$$

Khalid et al. then show that this nondimensional blockage, developed across a clearance row, can be virtually uniquely correlated against $X=(C_{ps}-C_{pt})$,

$$Y=[g/c][\delta_x^*/\tau]=Y(X) \qquad (10c)$$

if the loading parameter X is mass averaged across the clearance space.

It should be emphasized that this work refers to a single clearance row and was not presented in relation to deeply embedded equilibrium stages. However, if it were assumed that a casing blockage flow [say $(\delta_x^*)_R=(\delta_x^*)_{\tau\neq 0}$] mixed out in the subsequent nonclearance row [to give $(\delta_x^*)_S=(\delta_x^*)_{\tau=0}=0$] then Khalid's results would refer to the increase in blockage across clearance rows as well as the absolute value. It is clear both from the experimental data of Fig. 1 and from the CFD calculations of Fig. 2 that $[(\delta_x^*)]_{\tau=0}$ does *not* tend toward zero (i.e., that full mixing out does not occur) but for an order of magnitude comparison with the present analysis we shall assume that Eq. (10*c*) refers to the increase in blockage in equilibrium stages, $\Delta(\delta_x^*)$.

6.3 The Present Analysis. The increase in displacement thickness across the clearance rows (together with the subsequent decrease in the following nonclearance rows) were given in Eqs. (6*a*) and (6*b*). Virtually all the available experimental data available to the author (those of Smith, McKenzie, and Howard et al.) refer to stages of roughly 50 percent reaction so for the purposes of comparison we take the simplified form of these equations with $R=0.5$,

$$\{(\Delta\delta_x^*)_{SR}/\tau\}_{\text{CASING}}=\{(\Delta\delta_x^*)_{RS}/\tau\}_{\text{HUB}}=\psi/2\phi^2 \qquad (7a)$$

The decreases across the nonclearance rows are then

$$\{(\Delta\delta_x)_{RS}/\tau\}_{\text{CASING}}=\{(\Delta\delta_x)_{SR}/\tau\}_{\text{HUB}}=-\psi/2\phi^2 \qquad (7b)$$

7.0 Comparisons Between the Three Approaches

7.1 Basis for Comparisons. Two comparisons are made here: Smith with the present analysis [PA]; and Khalid et al. with [PA]. The basis for the comparisons is first briefly discussed and numerical comparisons are given subsequently.

7.1.1 Smith and the Present Analysis [PA]. Smith's experimental correlations, leading to Eqs. (8*a*) or (8*b*), may now be compared directly with [PA], leading to Eqs. (7*a*) and (7*b*), assuming that his test stages were approximately 50 percent reaction. In such a comparison it may be noted that Smith would imply the increase in (δ_x^*/τ) to be linearly dependent upon the stage loading ψ; the analysis outlined above would imply a dependence on ψ/ϕ^2, i.e., a stronger dependence upon ψ, because ϕ decreases as ψ increases.

7.1.2 Khalid and the Present Analysis [PA]. As discussed above, to compare Khalid's correlations with [PA] for the deeply embedded stage, we shall assume that Khalid's results for the growth across a single rotor also give the *increase* in boundary layer thickness across an equilibrium rotor casing section. To make this comparison, we rewrite Khalid's expression for the blockage

$$Y=[g/c][\delta_x^*/\tau]=Y(X) \qquad (10c)$$

as

$$(\Delta\delta_x^*)_R/\tau\approx(\delta_x^*)_R/\tau=(c/g)Y(X) \qquad (10d)$$

with $X=C_{ps}-C_{pt}$.

A comparison with [PA] may then be by writing the basic equation, Eq. (3)

$$(\Delta\delta_x^*)_R\approx(\Delta p)_R\tau/(\rho C_x^2/2)$$

as

$$(\Delta\delta_x^*)_R/\tau=C_{ps}/\cos^2\beta_1=\{C_{ps}s/(1-C_{ps})\cos^2\beta_e\} \qquad (11)$$

where losses have been ignored in eliminating $\cos^2\beta_1$ using $C_{ps}\approx 1-(\cos^2\beta_1/\cos^2\beta_e)$.

Equations (10*d*) and (11) both show a linear dependence of the blockage on the clearance and both indicate rapid increase with pressure rise coefficient (C_{ps}). Both are dependent on the assumption of a constant pressure rise in the mainstream and deficit regions, but then the basic assumptions diverge. The simple analysis of Khalid et al. [which was the guide to the subsequent correlation of Eq. (10*d*)] rests on continuity within the deficit region, whereas the approach outlined in this paper is dependent on the overall momentum equation. Because of these critical differences analytical reconciliation of the two approaches is not possible; but numerical comparisons are given in the following section.

7.2 Numerical Comparisons. Some order-of-magnitude numerical comparisons have been made between the three approaches to end-wall blockage (Smith against PA, and Khalid against PA).

7.2.1 Smith Against PA. First, from Eqs. (7) of [PA], $(\Delta\delta_x^*)/\tau$ was plotted against stage pressure coefficient (Fig. 5), using a mean characteristic to relate ψ and ϕ [that given by Smith for his configuration 5, together with $\psi_{\max}=0.675$]; Smith's correlation as given by Eq. (8) was added. Smith's experimental blockage data (see Fig. 1) were then replotted on this graph, as the difference between the rise in δ_x^* across clearance rows, $\Delta(\delta_x^*)_{SR}=(\delta_x^*)_R-(\delta_x^*)_S$ for the casing and $\Delta(\delta_x^*)_{RS}=(\delta_x^*)_S-(\delta_x^*)_R$ for the hub. The results very near stall, for $(\psi/\psi_{\max})$ greater than 0.96, were difficult to interpret and not included.

As both Smith and Cumpsty [2] have pointed out, the experimental scatter in the data is considerable. The orders of magnitude predicted by Eq. (7) of [PA] for the larger changes in δ_x^* appear reasonable for most of the results, but there are several very low experimental values of δ_x^*, particularly for the casing results. There is insufficient data at low $\psi/\psi_{\max}$ for a fully valid comparison to be made.

The calculations of Fig. 2 gave the boundary layer values given in Table 1. For both sections the increases in nondimensional blockage across the clearance sections are given in Table 2. For

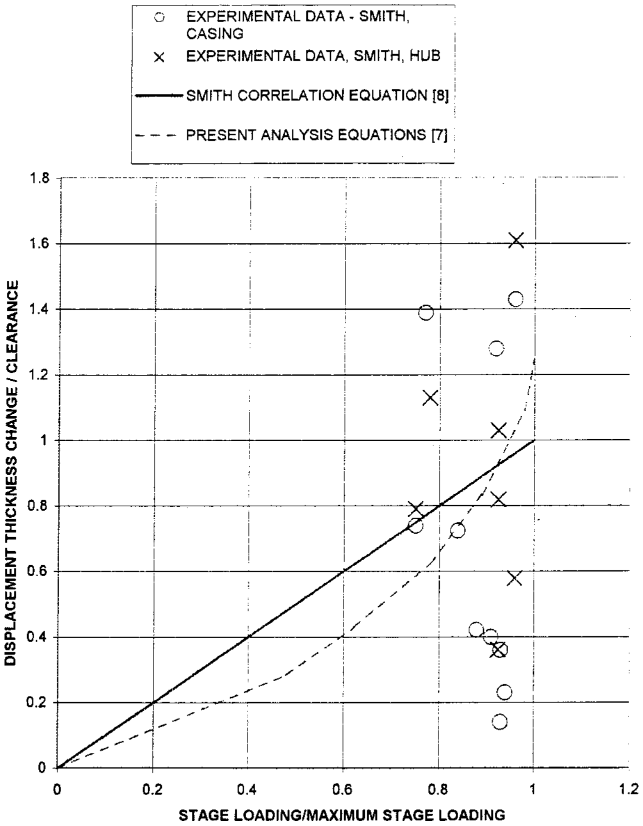

Fig. 5 Predictions of change in displacement thickness compared with Smith's data

both hub and casing this increase is greater than unity and greater than would be expected from the Smith correlation [which would simply predict assuming $\Delta(\delta_x^*)/\tau=(\psi/\psi_{\max})$, about 0.95 if the stage is operating close to the peak efficiency point]. The [PA] prediction gives an even lower figure based on the assumption of 50 percent of reaction, but it should be remembered that for the casing the reaction is likely to be higher than 0.5 and for the hub a lower reaction would also give a higher factor for the growth across the stator clearance row.

7.2.2 Khalid Against PA. Direct comparison between the Khalid correlations and Eq. (10) was not possible since C_{pt} (the total pressure deficit in the clearance space) is not known; it is itself presumably a function of C_{ps}. The authors appear to take local values for each element of clearance in obtaining an overall value. But taking the value of $s/c\approx 0.8$ and $\cos\beta_e\approx 0.8$ ($\beta_e=37$ deg) for Khalid's rotating rig data, his Eq. (10*d*) becomes

$$(\Delta\delta_x^*)_R/\tau\approx(\delta_x^*)_R/\tau=Y(X)/0.64 \tag{10e}$$

The relationship of Eq. (10*e*) is then plotted against $C_{ps}=X+C_{pt}$ in Fig. 6, using Khalid's data for his rotating rig experiments, and with C_{pt} assumed to be given by (*i*) $C_{pt}=-0.1$ [$\alpha_1=(1+C_{pt})^{1/2}\approx 0.95$] and (*ii*) $C_{pt}=-0.2$ ($\alpha_1\approx 0.90$).

Table 2

	Calculations	Smith ($\psi/\psi_{\max}$=0.95)	[PA]
Hub			
$\Delta(\delta_x^*)_{RS}/\tau$	1.3	0.95	0.8
Casing			
$\Delta(\delta_x^*)_{SR}/\tau$	1.22	0.95	0.8

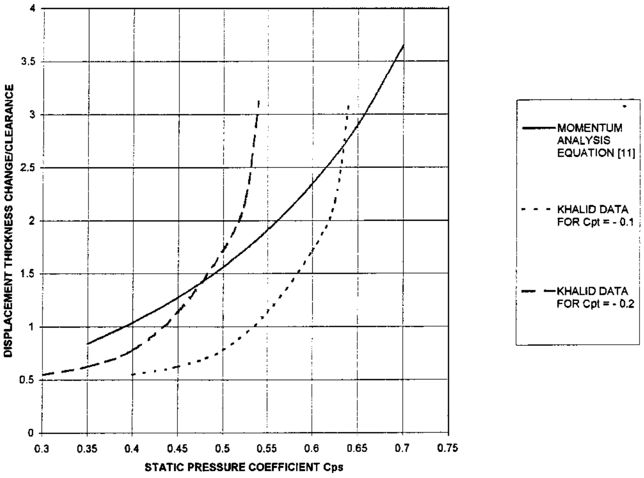

Fig. 6 Predictions of change in displacement thickness as functions of blade row pressure rise coefficient C_{ps} to: present analysis and correlation of Khalid et al.

The present analysis leads to the equation

$$(\Delta\delta_x^*)_R/\tau=C_{ps}/[1-C_{ps}]\cos^2\beta_e \tag{11}$$

and this is also plotted against C_{ps} in Fig. 6.

For the [PA], Eq. (11) yields $(\Delta\delta_x^*)_R/\tau$ about unity for practical values of C_{ps} [0.35–0.4]. Khalid et al. give lower blockage at low C_{ps} but increasing more rapidly with C_{ps} than does Eq. (11). Presumably, α_1 is likely to approach unity for high stagger blading, for which velocity through the clearance space will approach the blade speed and hence the free-stream velocity. Indeed, Khalid et al. refer to the work of Storer and Compsty [16] who take $C_{pt}=0[\alpha_1=1.0]$.

7.2.3. Comparison Between Smith's Experimental Data and Khalid's Correlations. No direct attempt has been made to compare Smith's data with Khalid's correlations, but a comparison is implied if Figs. 5 and 6 are taken together. Bearing in mind the wide scatter of the Smith data and the various assumptions made in deriving the two figures, it may not be unreasonable to conclude that the three approaches give approximately the same final answer for blockage. Indeed, $\Delta(\delta_x^*)/\tau\approx 1.0$ would appear to be a good approximation approach and a good empirical rule of thumb for a compressor designer.

8.0 Discussion

The development of Eq. (9) by Khalid et al. into graphic correlations was based not only on experimental data from compressor and cascade tests but was also backed up by detailed CFD calculations using the Adamczyk code. Such work, based on the detailed fluid mechanics, should be more accurate, but should not invalidate the overall answers for flow through a ''momentum box'' as used in this paper.

As emphasized earlier, the Khalid analysis only gives the *change* in blockage across a clearance row, so if it is to be used in design for equilibrium stages, the following problems would still remain:

(i) how the blockage is to be calculated at entry to a stage deep within a compressor;
(ii) whether increase in blockage determined across the clearance row is to be added to that at entry to give that at exit;
(iii) how C_{pt} within the clearance space is to be determined.

With regard to [*i*], it will be remembered that in the comparisons of the change in blockage across the clearance rows made in Section 7 it was assumed that the entry blockage was small; this is clearly not true as indicated by the Smith data. But a related puzzle on this point lies in the work of Hunter and Cumpsty [17], which showed the displacement thickness at exit from a single rotor to be little different from that at exit from the rotors of Smith's repeating stages.

While the present analysis [PA] gave results for the effect of reaction [Eqs. (6*a*) and (6*b*)] the subsequent comparisons made involved the assumption of $R=0.5$, as in Eq. (7), since virtually all the experimental data are for stages close to 50 percent reaction. If anything, Smith's stages and the Cranfield compressor appear to have reaction somewhat less than $R=0.5$ and Eqs. $(6a)$ and $(6b)$ would then suggest initially that the boundary layer growth across the stator clearance rows would be greater that those leaving the rotor clearance rows. However, reaction usually increases with radius; thus even for a stage with $R=0.5$ at the mean section R will be greater at the casing, less at the hub. Equation (6*a*) then suggests that the nondimensional growth across the rotor clearance at the casing will be greater than $(\psi/2\phi^2)$; at the hub, Eq. (6*b*) suggests that the growth will again be greater than $(\psi/2\phi^2)$. So [PA] is likely to lead to underestimates for both hub and casing.

It would appear that the final answer to these various queries must ultimately lie in applying advanced CFD codes to the whole multistage compressor (as Denton did for the Cranfield compressor). An alternative would be to use CFD until the equilibrium repeating stage is reached (although as was indicated in the introduction this is now likely to occur only in industrial compressors with many stages). The analysis given in this paper [leading to Eqs. (6)] could then give the changes across the repeating stage; alternatively the Smith correlation could still be used, or perhaps the Khalid correlation, restoration of the original entry momentum thickness across the following nonclearance row in the repeating stage being implied.

9.0 Conclusions

Smith's original data showed axial blockage in a repeating stage to be strongly dependent on tip clearance and on stage pressure rise. Khalid et al. have subsequently presented an original and ingenious method of relating the blockage, leaving a single blade row to the clearance chord product, giving experimental and computational evidence for their approach. An alternative approach has been developed here, based essentially on the momentum equation for the blockage area and Smith's arguments about the variation in blade force through a repeating compressor stage.

The approach described in this paper and that of Khalid et al. give the probable *increase* in blockage across a clearance row, but neither gives the *absolute* levels of blockage to be expected downstream of a clearance row and a nonclearance row in a repeating stage. Such information must still rely on data such as Smith's, although it would now appear to be possible to undertake full CFD calculations for multistage machines, which will give reasonable answers. The computational complexity involved is now less daunting than it was.

Nomenclature[1]

A = area
c = chord length
C_{ps} = static pressure coefficient
C_{pt} = defect total pressure coefficient (negative)
c, C = local mainstream velocity
c_x = axial velocity within boundary layer
C_x = mainstream axial velocity
g = staggered spacing $=s\cos\beta_e$
H = boundary layer form or shape factor
K = constant
p = pressure
R = reaction
s = blade spacing
U = blade speed
X = loading factor $=C_{ps}-C_{pt}$
Y = blockage parameter defined by Khalid et al., $A_{bx}\cos\beta_e/\tau c$
z = coordinate along blade
α = ratio of defect velocity to mainstream velocity $=(1+C_{pt})^{1/2}$
β = relative flow angle
δ^* = displacement thickness
θ = momentum thickness
ν = force deficit thickness
ξ = stagger
ρ = density
τ = tip clearance height
ψ = pressure rise coefficient

Subscripts and Superscripts

b = blocked
e = exit from blade row
mid = midspan
s = static
R = downstream of rotor, inlet to stator in repeating stage
S = downstream of stator, inlet to rotor in repeating stage
SR = change across rotor of repeating stage [i.e., from preceding stator exit (S) to rotor exit (R)]
RS = change across stator of repeating stage [i.e., from preceding rotor exit (R) to stator exit (S)]
stage = for complete stage
t = total
1 = inlet, but only for Khalid simple analysis
2 = outlet, but only for Khalid simple analysis
x = axial
– = mean across the blade pitch

References

[1] Khalid, S. A., Khalsa, A. S., Waitz, I. A., Tan, C. S., Greitzer, E. M., Cumpsty, N. A., Adamczyk, J. J., and Marble, F. E., 1999, ''Endwall Blockage in Axial Compressors,'' ASME J. Turbomach., **121**, pp. 499–509.
[2] Smith, L. H., 1970, ''Casing Boundary Layers in Multistage Axial-Flow Compressors,'' in: *Flow Research in Blading*, L. S. Dzung, ed., Elsevier, Amsterdam, p. 275.
[3] Stratford, B. S., 1967, ''The Use of Boundary-Layer Techniques to Calculate the Blockage From the Annulus Boundary Layer in a Compressor,'' ASME Paper No. 67-WA/GT-7.
[4] Horlock, J. H., and Perkins, H. J., 1974, ''Annulus Wall Boundary Layers in Turbomachines,'' AGARDograph AG-185.
[5] Cumpsty, N. A., 1986, ''Annulus Wall Boundary-Layer Measurements in a Four-Stage Compressor,'' ASME J. Eng. Gas Turbines Power, **108**, pp. 2–6.
[6] McKenzie, A. B., 1956, ''Initial Tests on the Four Stage Experimental Compressor,'' Rolls Royce Internal Report No. 43A/101; see also 1981, Proc. Inst. Mech. Eng., **194**, pp. 103–111.
[7] Howard, M. A., Ivey, P. C., Barton, J. P., and Young, K. F., 1994, ''Endwall Effects at Two Tip Clearances in a Multistage Axial-Flow Compressor With Controlled Diffusion Blading,'' ASME J. Turbomach., **106**, pp. 635–647.
[8] Horlock, J. H., 1995, ''Secondary Flow in the Repeating Stages of Axial Turbomachines,'' Proc. Inst. Mech. Eng., **209**, pp. 101–110.
[9] Bolger, J. J., and Horlock, J. H., 1995, ''Predictions of the Flow in Repeating Stages of Axial Compressors Using Navier–Stokes Solvers,'' ASME Paper No. 95-GT-199.
[10] Dawes, W. N., 1987, ''A Numerical Analysis of the Three-Dimensional Viscous Flow in a Transonic Compressor and Comparison With Experiment,'' ASME J. Turbomach., **109**, pp. 83–90.
[11] Denton, J. D., 1992, ''The Calculation of Three Dimensional Viscous Flow Through Multistage Turbomachines,'' ASME J. Turbomach., **114**, pp. 18–26.
[12] Denton, J. D., 1995, private communication.
[13] Cumpsty, N. A., 1989, *Compressor Aerodynamics*, Longman, London.
[14] Lakshminarayana, B., and Horlock, J. H., 1965, ''Leakage and Secondary Flows in Compressor Cascades,'' ARC R&M 3483.
[15] Adkins, G. G., and Smith, L. H., 1982, ''Spanwise Mixing in Axial-Flow Turbomachines,'' ASME J. Eng. Power, **104**, pp. 97–110.
[16] Storer, J. A., and Cumpsty, N. A., 1991, ''Tip Leakage Flow in Axial Compressors,'' ASME J. Turbomach., **113**, pp. 252–259.
[17] Hunter, I. H., and Cumpsty, N. A., 1982, ''Casing Wall Boundary Layer Development Through an Isolated Compressor Row,'' ASME J. Eng. Power, **104**, pp. 805–817.

---

[1] In general the notation used by Khalid et al. (1998) is followed here.

Simulations of the Unsteady Flow Through the Fastrac Supersonic Turbine

Lisa W. Griffin
Fluid Dynamics Analysis Branch,
National Aeronautics and Space Administration,
George C. Marshall Space Flight Center,
Marshall Space Flight Center, AL 35802

Daniel J. Dorney
Department of Mechanical Engineering,
Virginia Commonwealth University,
Richmond, VA 23113

Analysis of the unsteady aerodynamic environment in the Fastrac supersonic turbine is presented. Modal analysis of the turbine blades indicated possible resonance in crucial operating ranges of the turbopump. Unsteady computational fluid dynamics (CFD) analysis was conducted to support the aerodynamic and structural dynamic assessments of the turbine. Before beginning the analysis, two major problems with current unsteady analytical capabilities had to be addressed: modeling a straight centerline nozzle with the turbine blades and exit guide vanes (EGVs), and reducing run times significantly while maintaining physical accuracy. Modifications were made to the CFD code used in this study to allow the coupled nozzle/blade/EGV analysis and to incorporate Message Passing Interface (MPI) software. Because unsteadiness is a key issue for the Fastrac turbine [and future rocket engine turbines such as the Reusable Launch Vehicle (RLV)], calculations were performed for two nozzle-to-blade axial gaps. Calculations were also performed for the nozzle alone, and the results were imposed as an inlet boundary condition for a blade/EGV calculation for the large gap case. These results are compared to the nozzle/blade/EGV results. [S0889-504X(00)02902-0]

Introduction

Flowfield unsteadiness is a major factor in turbine performance and durability. This is particularly true if the turbine is a high work design, compact, transonic, supersonic, counterrotating, or uses a dense drive gas. Most modern rocket engine turbines fall within these categories. For example, the Space Transportation Main Engine (STME) fuel turbine, a high work, transonic design, was predicted to have an unsteady interrow shock that reduced efficiency by two points and increased dynamic loading by 24 percent [1]. The Revolutionary Reusable Technology Turbopump (RRTT) turbine, which uses full flow oxygen as its drive gas, was predicted to shed vortices with such energy as to raise serious concerns about the blade's durability [2]. In both cases, the sources of the problems were uncovered before turbopump testing with the application of validated, unsteady CFD to the designs.

As requirements for smaller and lighter weight components push turbines to more compact, closely coupled designs, flow unsteadiness increases. Current designs such as the Fastrac turbine and future designs like the RLV fuel turbine add the complexities of supersonic flow regimes. The ability to predict this flow unsteadiness accurately in a timely manner is crucial to producing a design that meets program objectives.

In this study, the unsteady aerodynamic environment of the Fastrac turbine has been analyzed. The objective of the Fastrac Engine project is to demonstrate a reliable, low cost turbopump-fed rocket engine. The development strategies included simple engine system design, a simple approach to turbomachinery design, reduced number of parts, the use of commercial manufacturing techniques, and the use of commercial off the shelf components. The engine uses a gas generator cycle and is fueled by a mixture of liquid oxygen and kerosene. Pumps are used to increase the pressure of the propellants. These pumps, one for each propellant, are on a single shaft and are powered by one turbine. A drawing of the cross section of the turbopump is shown in Fig. 1. Modal analysis of the turbine blade indicates possible resonance near a crucial operating speed, as shown in the Campbell diagram (Fig. 2). The diagram shows crossovers of excitations at blade bending modes due to twice the nozzle count, and due to the EGVs within a 10 percent margin of the nominal design speed. Unsteady CFD analysis was used to support the aerodynamic assessments of blade loading and efficiency, and the structural dynamic evaluations by providing unsteady pressures for transient response analysis. The results of the CFD analysis are presented.

To aid in the understanding of the effects of the axial spacing between the nozzle and blade on the flow unsteadiness, calculations were performed for the Fastrac turbine for two different axial spacings. The intent of the analysis was to study the effects of the axial spacing on both flow unsteadiness and on the efficiency of supersonic turbines. This information will benefit future designs, such as for RLV, where turbine performance is a premium. In addition, calculations were performed for the nozzle alone, and the results were imposed as an inlet boundary condition for a blade/EGV calculation for the large axial gap case. These results are compared to the nozzle/blade/EGV results. This calcu-

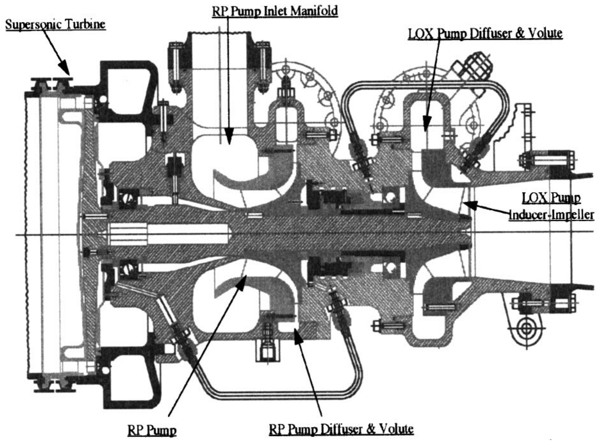

Fig. 1 Cross section of the Fastrac turbopump

Contributed by the International Gas Turbine Institute and presented at the 44th International Gas Turbine and Aeroengine Congress and Exhibition, Indianapolis, Indiana, June 7–10, 1999. Manuscript received by the International Gas Turbine Institute February 1999. Paper No. 99-GT-156. Review Chair: D. C. Wisler.

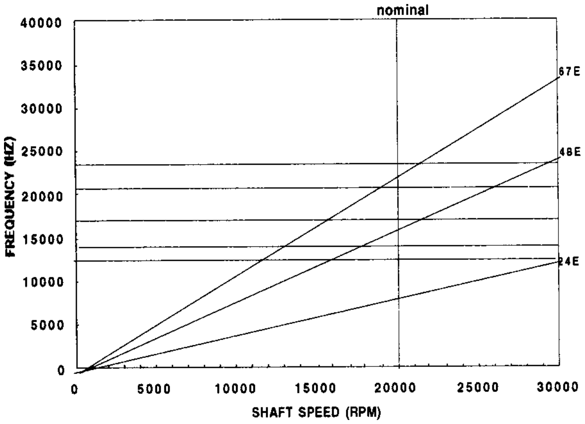

Fig. 2 Fastrac turbine blade Campbell diagram with most responsive modes and excitations (chart by Don Harris)

lation was performed to determine the necessity of coupling the nozzle to the rest of the turbine for the unsteady analysis of supersonic turbines.

Before beginning the analysis of the coupled nozzle/blade/EGV calculation, two major difficulties with the unsteady analysis software used in this study had to be addressed: modeling a straight centerline nozzle with the turbine blades and exit guide vanes (EGVs), and reducing run times significantly while maintaining physical accuracy. Implementing Message Passing Interface (MPI) software into the numerical analysis was the method chosen to enable these calculations with the required speed.

Turbine Description

The Fastrac turbine is a single-stage, full admission supersonic design with exit guide vanes. The turbine is required to produce 895 kW and spins at 20.000 rpm. The nozzle ring contains 24 converging–diverging, straight centerline nozzles with circular cross sections and throat diameters of 0.615 cm. There are 147 impulse-type shrouded blades with heights of 1.045 cm, which is 20 percent larger than the minor axis of the nozzle exit ellipse. They have a mean diameter of 24.46 cm and an axial chord of 0.838 cm. The blades are a two-dimensional design with identical airfoil sections from hub to tip. There are 67 EGVs with heights of 1.045 cm, mean diameter of 24.46 cm, and axial chords of 1.524 cm. The EGVs are also a two-dimensional design. Axial spacing between the nozzles and blades is 0.102 cm and between blades and EGVs is 1.02 cm.

The turbine is driven by a mixture of gaseous kerosene and oxygen with a ratio of specific heats, γ, of 1.108 and a specific heat at constant pressure, c_p, of 2.64 kJ/kg percent K. The gas enters the nozzles with a total pressure, P_{T0}, of 3.79 MPa a total temperature, T_{T0}, of 889 K, and a mass flow rate of 3.24 kg/s. Meanline calculations predict the Mach number at the exit of the nozzle to be 2.11. The total to static pressure ratio, $Pr_{t\text{-}s}$, across the nozzle was designed to be 11.2.

Method of Solution

The flowfield of the Fastrac turbine was numerically analyzed using a parallelized, unsteady, three-dimensional Navier–Stokes code. The methodology, approach, and grid system are discussed in the following sections.

Numerical Algorithm. The governing equations considered in this study are the time-dependent, three-dimensional, Reynolds-averaged Navier–Stokes equations:

$$Q_t+(F_i+F_v)_x+(G_i+G_v)_y+(H_i+H_v)_z=0 \tag{1}$$

The viscous fluxes are simplified by incorporating the thin layer assumption [3]. In the current study, viscous terms are retained in the direction normal to the hub and shroud surfaces. To extend the equations of motion to turbulent flows, an eddy viscosity formulation is used. The turbulent viscosity, μ_T, is calculated using the two-layer Baldwin–Lomax [3] algebraic turbulence model.

The numerical algorithm used in the three-dimensional computational procedure consists of a time-marching, implicit, finite-difference scheme. The procedure is third-order spatially accurate and second-order temporally accurate. The inviscid fluxes are discretized according to the scheme developed by Roe [4]. The viscous fluxes are calculated using standard central differences. An alternating direction, approximate factorization technique is used to compute the time rate of change in the primary variables. Newton subiterations are used at each global time step to increase stability and to reduce linearization errors. For all cases investigated in this study, two Newton subiterations were performed at each time step. Further information on the numerical procedure can be found in Dorney et al. [5,6].

The CFD code used for this study has been widely validated for flows in turbomachinery. Examples of validation cases are given in Dorney and Sondak [7], Dorney and Schwab [8], Dorney and Davis [9,10], and Dorney et al. [5].

Boundary Conditions. The theory of characteristics is used to determine the boundary conditions at the inlet and exit of the computational domain. For subsonic inlet flow, four quantities are specified, and one is extrapolated from the interior of the computational domain. In particular, the total pressure, total temperature, and the v and w components of velocity are specified as a function of the radius. The upstream running Riemann invariant, $R_2=u-2a/(\gamma-1)$, is extrapolated from the interior of the computational domain.

For subsonic outflow, one flow quantity is specified and four are extrapolated from the interior of the computational domain. The v and w velocity components, entropy, and the downstream running Riemann invariant are extrapolated from the interior of the computational domain. The pressure ratio $P_{R\,t\text{-}s}$ is specified at the midspan of the computational exit, and the pressures at all other radial locations at the exit are obtained by integrating the equation for radial equilibrium. For supersonic outflow, all of the flow variables are extrapolated. Periodicity is enforced along the outer boundaries of the **H**-grids in the circumferential direction.

For viscous simulations, no-slip boundary conditions are enforced along the solid surfaces. Absolute no-slip boundary conditions are enforced along the walls of the nozzle, at the hub and tip end walls of the vane passages, and along the surface of the vanes. Relative no-slip boundary conditions are imposed at the hub, shroud, and surfaces of the blades. It is assumed that the normal derivative of the pressure is zero at solid wall surfaces. In addition, a specified (zero) heat flux distribution is held constant in time along the solid surfaces.

The flow variables of Q at zonal boundaries are explicitly updated after each time step by interpolating values from the adjacent grids.

Code Parallelization. The MPI software has been implemented into the numerical analysis. Implementing this software allows the following two advantages: (1) The simulation of a single problem can be run on multiple processors to reduce run times dramatically, and (2) the simulation of multiple problems (each of which can be performed on multiple processors) can be linked through the passing of boundary condition information. In this study, one nozzle from the nozzle ring has been linked with the simulation of a supersonic turbine containing six rotors and three EGVs.

Grid System. The Fastrac turbine has a nozzle-to-blade-to-EGV ratio of 24:147:67. For the current study, the ratio was modeled as 1:6:3. The blades were scaled by a ratio of 147/150 and the EGVs by a ratio of 67/75 to keep the pitch to chord ratio constant.

The grid for the nozzle was an **H**-type grid. The solid walls at the exit plane of the nozzle ring were modeled. The rotor inlet grid is an **H**-grid. The grid around each airfoil consists of an inner and outer zone. The inner zone is discretized with an **O**-grid surrounding the airfoil. The **O**-grids are overlaid onto **H**-grids, which discretize the outer zones. The **H**-grids are patched between blade rows and the rotor **H**-grids slide past the nozzle **H**-grid and the EGV **H**-grids in time. The average value of y^+ was approximately 1.0 for the airfoil surfaces and 4.0 for the endwall surfaces. Figure 3(*a*) shows the grid. Every third point in the grid was plotted, and only a portion of the outflow section of the EGV grid is shown. An axial view showing the exit of the nozzle is shown in Fig. 3(*b*). Grid densities are shown in Table 1. The total number of grid points for each calculation was 1,545,987. The grid densities were chosen based on a compromise between accuracy needed for a design calculation and computational time. Previous simulations suggested that 41 radial planes are adequate.

Table 1 Grid dimensions (per passage) for the small gap and large gap

Grid Type	Nozzle	Rotor Inlet Grid	Rotor (x 6)	EGV (x 3)
O	NA	NA	91x21x41	91x21x41
H	108x38x41	14x51x41	64x21x41	82x31x41
Total	168,264	29,274	800,730	547,719

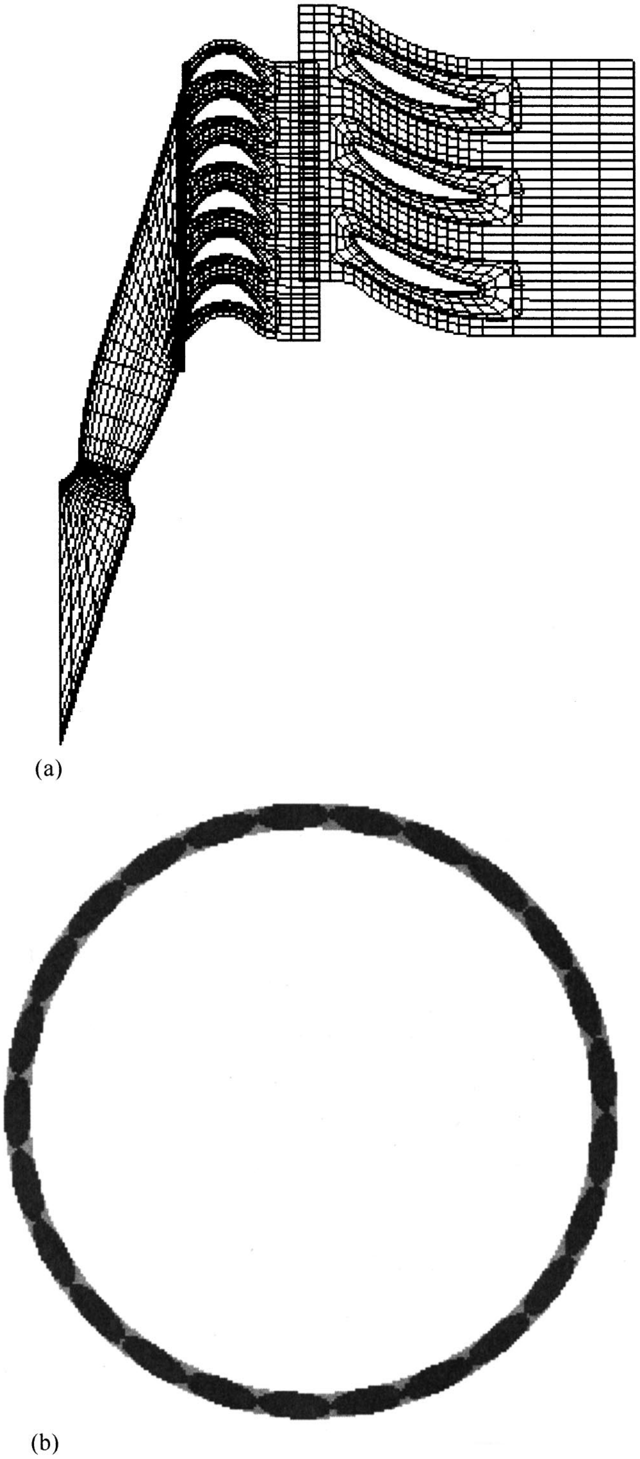

Fig. 3 Computational geometry: (*a*) cross-sectional view (every third point plotted); (*b*) axial view of the nozzle ring exit

Results and Discussion

Results of the unsteady simulations of the Fastrac turbine are presented for the design case (small gap), large axial gap case, and uncoupled case. Results from each case are compared.

Design Case (Small Gap). Predicted flow conditions at the inlet and the exit of the rotor for a nozzle to rotor axial gap of 0.102 cm are given in Table 2. This axial spacing is equal to the actual axial gap in the Fastrac turbine. Work per pound of gas is calculated using

$$\Delta h = c_p (T_{T0} - T_{T2}) \tag{2}$$

Using the predicted flow conditions, the work per pound of flow is calculated to be 276.3 kJ/kg. Power is defined as

$$PW = m \times \Delta h \tag{3}$$

and is calculated to be 890 kW.

Predicted instantaneous Mach number contours at midspan are shown in Fig. 4. Subsonic flow enters the nozzle, chokes at the throat, and becomes supersonic. A Mach disk is seen downstream of the throat. Shock waves form in the diverging section and reflect off the nozzle walls. The fluid expands as it leaves the nozzle. Supersonic flow enters the blade, and a leading edge shock is formed. The boundary layer separates from the suction surface of the blade due to interaction of the bow shock with the suction surface boundary layer. Mach number contours for the blade alone are shown in Fig. 4(*b*) to highlight the shock/boundary layer interaction. The separated region was expected as supersonic turbine blades generally generate large separated regions on the suction side of the blade at design conditions. The size of the separation is dependent upon the blade's circumferential position relative to the nozzle. Because of the large separated region on the blade, the average Mach number at the exit of the blade is subsonic. The boundary layer near the trailing edge of the EGV separates. Separation on the pressure surface of the EGV is dependent on the circumferential position of the blades.

To determine the mechanism of the increased separation on the blade and the separation on the pressure side of the EGV, instan-

Table 2 Predicted rotor conditions, small gap

Variable	Absolute	Relative
M_1	2.01	1.21
M_2	0.44	0.82
T_{T1}	889°K	804°K
T_{T2}	780°K	800°K
P_{T1}/P_0	0.933	0.269
P_{T2}/P_0	0.143	0.186
α_1 and β_1	70.4°	51.0°
α_2 and β_2	-7.7°	-58.9°
ψ_1 and ϕ_1	-0.9°	-0.1°
ψ_2 and ϕ_2	0.0°	0.0°

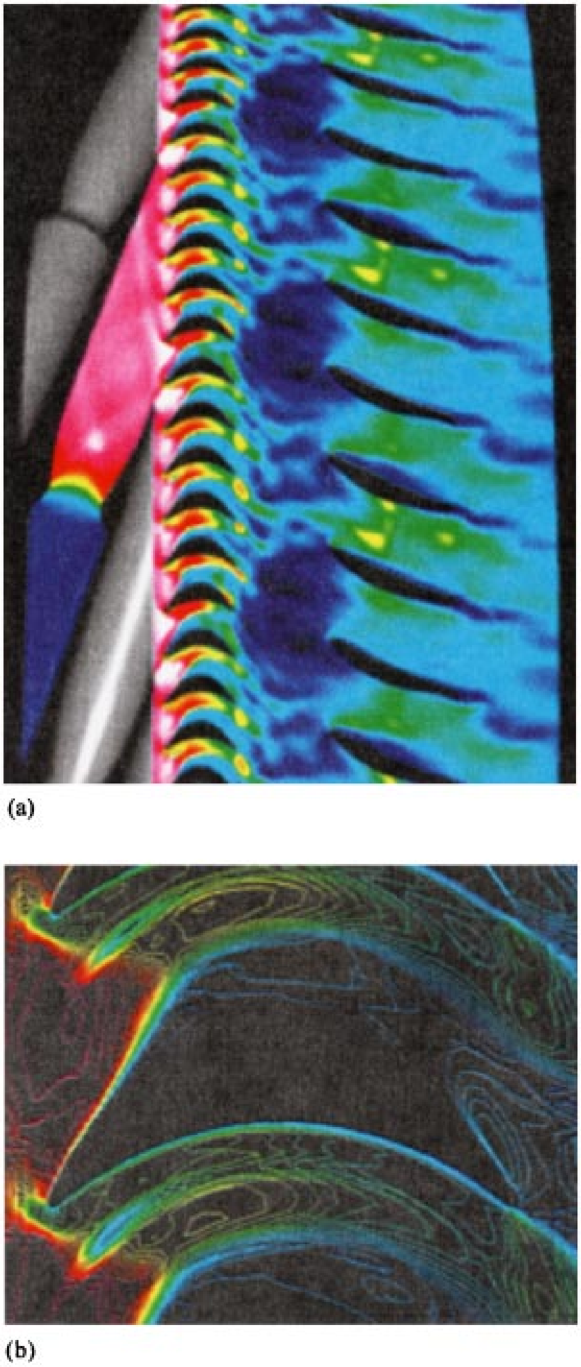

Fig. 4 Instantaneous Mach numbers at midspan: (*a*) turbine; (*b*) blade alone

taneous entropy contours were plotted (Fig. 5). The contours show a wake produced at the lip of each nozzle. This wake is due to the solid wall regions between each nozzle at the exit plane of the nozzle ring. Figure 6 shows an axial view of the total velocity between the nozzle exit and the blade leading edge to highlight the geometry and flow in this region. The nozzle lip wake triggers an earlier separation on the suction surface of the blades than when the blade is fully within the nozzle jet. When this boundary layer sheds, this higher loss flow travels downstream, causing the separation on the pressure side of the EGV.

Pressure envelopes for the blade are shown in Figs. 7(*a*)–(*c*). Large amounts of unsteadiness are predicted, particularly at the blade leading edge. Less unsteadiness is exhibited in the hub and shroud regions than at midspan. Because of the blade is 20 percent taller than the minor axis of the ellipse of the nozzle exit, the jet from the nozzle has not expanded enough to impact these regions near the leading edge of the blade for this small nozzle/blade axial spacing.

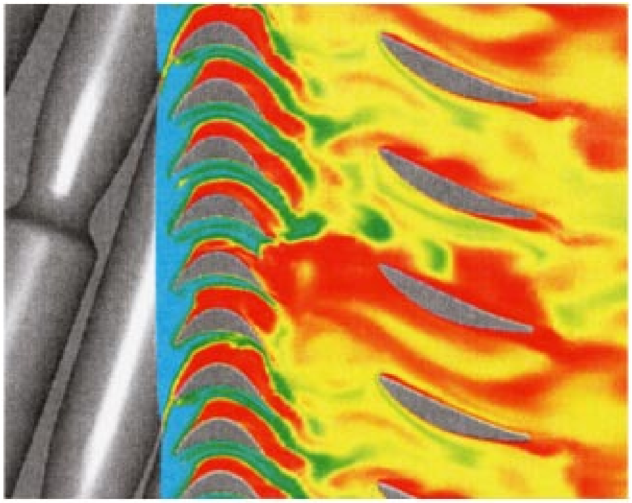

Fig. 5 Instantaneous entropy contours at midspan

Fourier decomposition was performed for the predicted unsteady environment. Figures 8(*a*),(*b*) show the half amplitudes at discrete frequencies for the blade. The nozzle passing frequency is 8000 Hz, and the second harmonic of nozzle passing is at 16,000 Hz. Large amounts of unsteadiness exist at the leading edge for these frequencies. The unsteadiness at the nozzle passing frequency persists as the flow travels over the pressure surface. The pressure fluctuations at the nozzle passing frequency decrease rapidly on the suction surface with distance from the leading edge.

Fig. 6 Total velocity contours between nozzle exit and blade leading edge

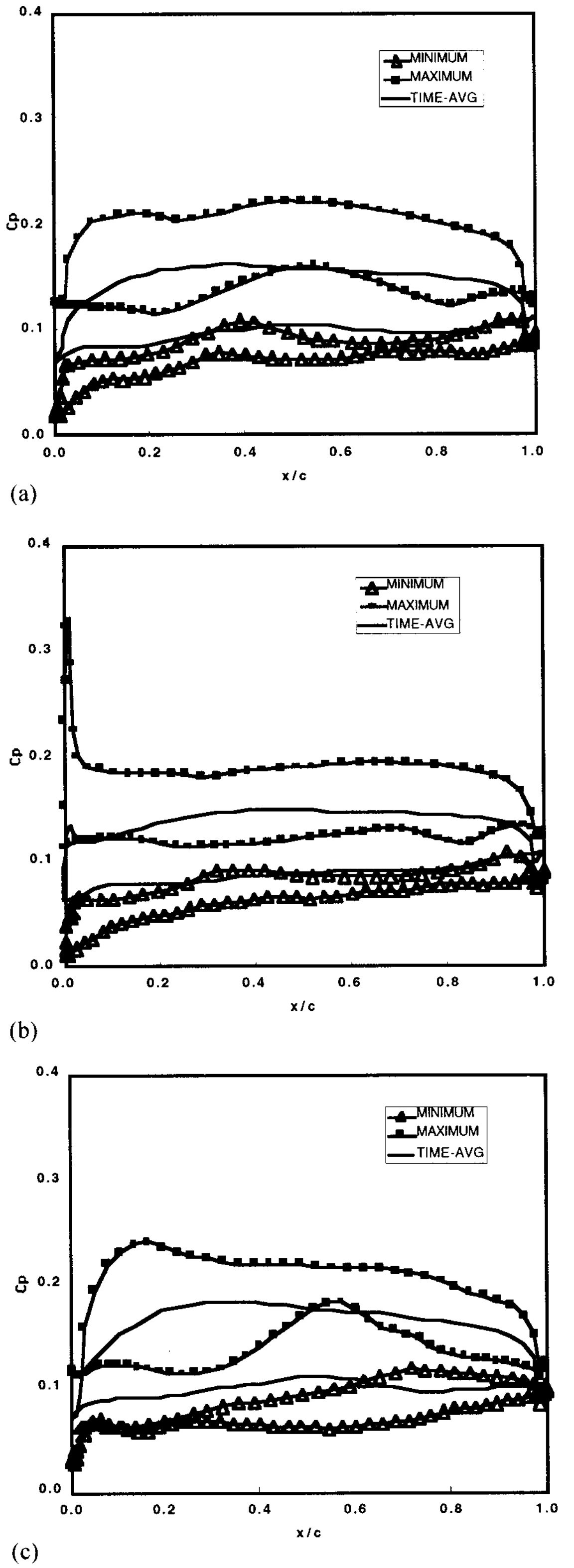

Fig. 7 Blade pressure envelopes, small gap: (*a*) hub; (*b*) midspan; (*c*) tip

However, even after separation, the second harmonic of nozzle passing persists, albeit to a lesser extent than at the leading edge.

A pressure trace at the rotor leading edge at midspan is shown in Fig. 9. The time period for the trace is for one blade to pass one nozzle. The pressure deficit clearly shows the presence of the solid wall regions at the nozzle exit plane.

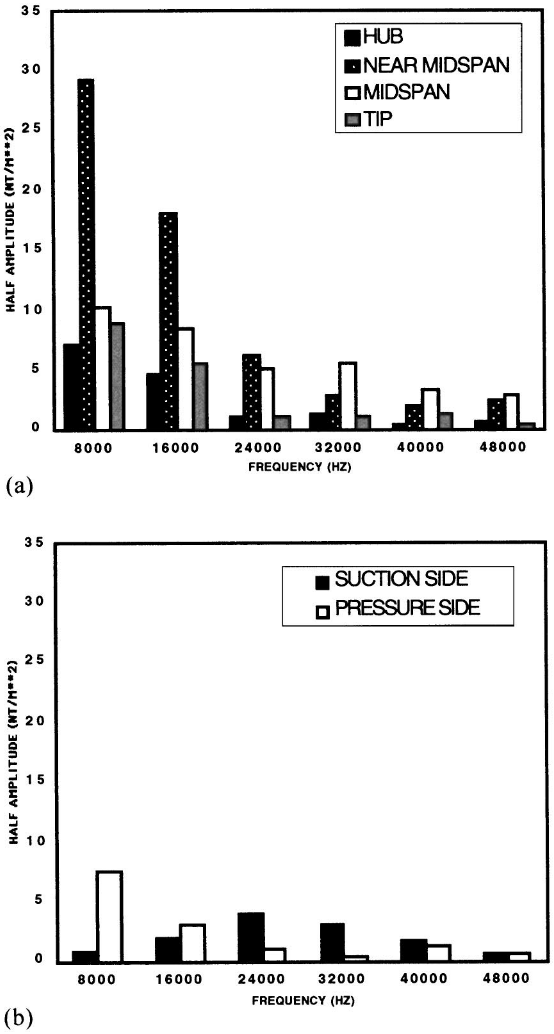

Fig. 8 Fourier decomposition of pressures for blade: (*a*) leading edge; (*b*) 20 percent axial chord

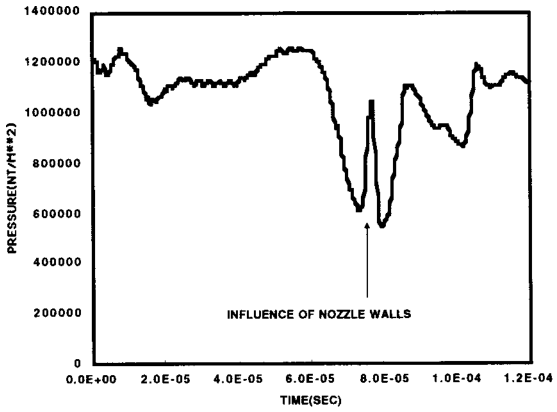

Fig. 9 Pressure trace for blade leading edge, midspan, small gap

Large Gap Case. Because the unsteadiness is large at the leading edge of the blade for the design case, a large axial spacing was considered. The spacing for this large gap case was set at 0.838 cm, or one blade axial chord. Predicted flow conditions at the inlet and the exit of the rotor are given in Table 3. Work per pound of gas is calculated to be 269.1 kJ/kg, and the power output

Table 3 Predicted blade conditions, large gap

Variable	Absolute	Relative
M_1	1.97	1.29
M_2	0.41	0.74
T_{T1}	889°K	802°K
T_{T2}	782°K	800°K
P_{T1}/P_0	0.806	0.271
P_{T2}/P_0	0.146	0.180
α_1 and β_1	74.2°	58.1°
α_2 and β_2	1.6°	-58.9°
ψ_1 and ϕ_1	2.8°	-8.2°
ψ_2 and ϕ_2	-0.4°	2.6°

is 867 kW. These values are lower than those predicted for the small gap case. The nondimensional total pressure, (P_{T1}/P_0), is lower at the inlet to the blade for the large gap case than for the small gap case. The nondimensional total pressures at the exit of the nozzle are comparable for both cases ($P_{\mathrm{TNE}}/P_0 = 1.001$ for the large gap case and 1.005 for the small gap). The increase in total pressure loss ahead of the blade for the large gap case is in the axial gap region. With the increased axial gap, the jet from the nozzle is allowed to expand more fully before reaching the blade. The additional expansion allows for interaction between the jets of successive nozzles. This interaction of supersonic flows creates additional loss.

Pressure envelopes are shown in Fig. 10(*a*)–(*c*). A large amount of unsteadiness is evident on the blade, especially at the leading edge, as was also shown for the small gap case. However, the unsteadiness at the shroud is greater in the large gap case than for the small gap because the jet from the nozzle has had sufficient space to expand into the tip region.

A Fourier decomposition of the unsteady data was performed. Plots are shown in Figs. 11(*a*),(*b*). As the gap was increased, the fluctuating pressures at the blade leading edge at nozzle passing frequency have decreased. However, large pressure fluctuations at the second harmonic of the nozzle passing frequency are exhibited for the large gap case. Unsteadiness due to nozzle passing persists as the flow travels over the pressure side of the blade. The second harmonic is also prominent, as in the small gap case. Unlike the small gap case, however, an increase in fluctuating pressures at nozzle passing frequency was predicted with increasing distance along the suction surface until flow separation. This is believed to be due to the additional expansion of the nozzle jet.

A pressure trace at the leading edge of the blade at midspan is shown in Fig. 12. Although the nozzle wake is still evident, the deficit in pressure is smaller for the large gap case. The second harmonic of the nozzle passing frequency can also be seen in this plot.

Uncoupled Nozzle and Blade/EGV Case. A simpler calculation than coupling the nozzle to the blades and EGVs is to simulate the nozzle flowfield and impose the results from the exit of the nozzle as an inlet boundary condition for a blade/EGV simulation. This procedure poses a numerical problem due to the difficulties in applying a unique incidence boundary condition for the blade. Setting the inlet boundary at the exit of the nozzle will not allow pressure waves to move upstream; therefore, shocks can reflect back into the flow domain. Moving the boundary farther upstream would mitigate this problem, but the nozzle jet would not be properly modeled. However, because of the reduced computer resource requirements, modeling the supersonic turbine in this manner is tempting. This procedure was conducted for the large axial gap. The elliptical nozzle exit was roughly modeled at the inlet of the blade/EGV domain. Work per pound of fluid was calculated to be 244 kJ/kg, and the power produced was 787 kW. These numbers are significantly different from the coupled cases.

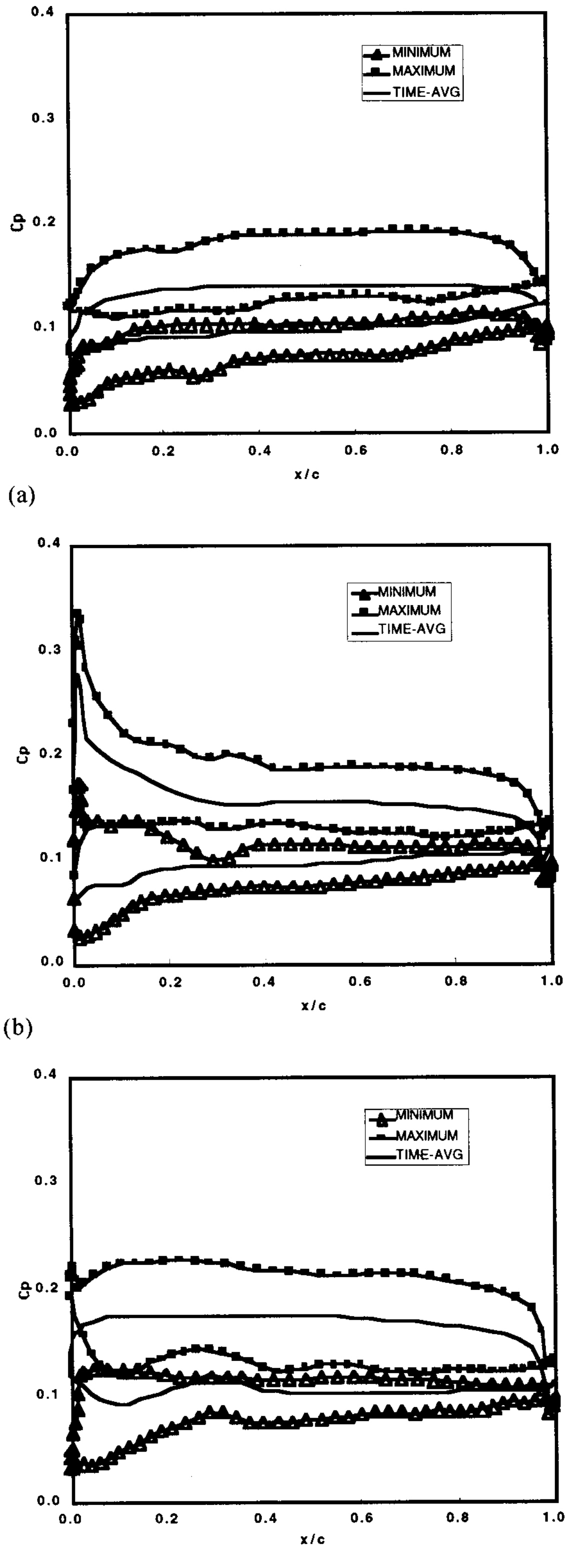

(a)

(b)

(c)

Fig. 10 Blade pressure envelopes, large gap: (*a*) hub; (*b*) midspan; (*c*) tip

Pressure envelopes are shown in Figs. 13(*a*)–(*c*). The pressure envelopes look somewhat similar to those from the large gap coupled simulation, which is not surprising. As the gap between the nozzle and blade increases, the coupled and uncoupled solutions should look increasingly similar. Note, however, that even though the unsteady envelopes (which constitute the sum of all the

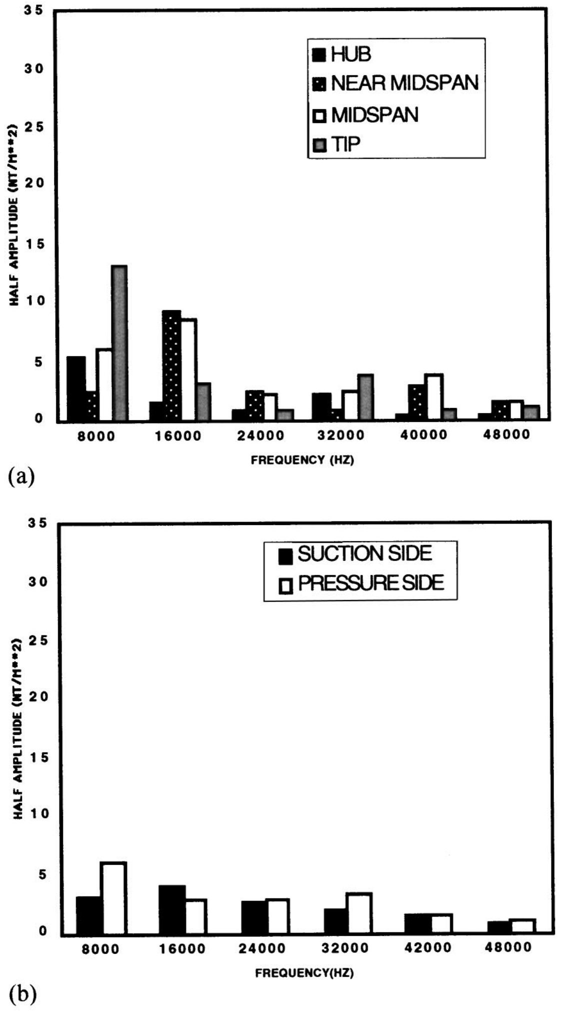

(a)

(b)

Fig. 11 Fourier decomposition of pressure for blade, large gap: (*a*) leading edge; (*b*) 20 percent axial chord

unsteady frequencies) are similar, the amplitudes of the unsteadiness at discrete frequencies are different in the coupled and uncoupled cases.

Comparisons of Radial Profiles. To further illustrate the differences between cases and to improve the understanding of these differences, time-averaged radial profiles of flow variables at the inlet and exit of the blade were plotted for each case. Figures 14(*a*)–(*b*) show circumferential flow angles. At this station, the nozzle jet for the large gap case has had time to expand. The jet has not expanded as fully for the small gap case, and the boundary layers at the hub and tip are larger. The flow angles for the uncoupled case are similar to the coupled large gap case except at

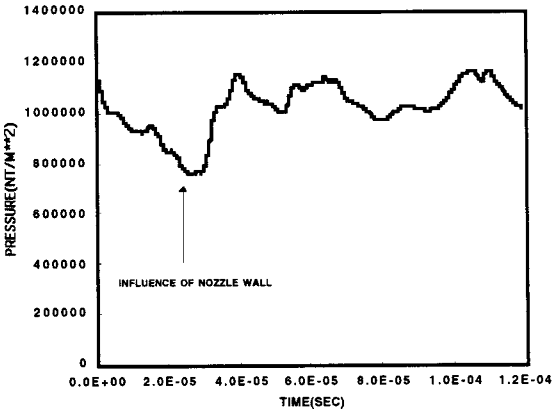

Fig. 12 Pressure trace for blade leading edge, midspan, large gap

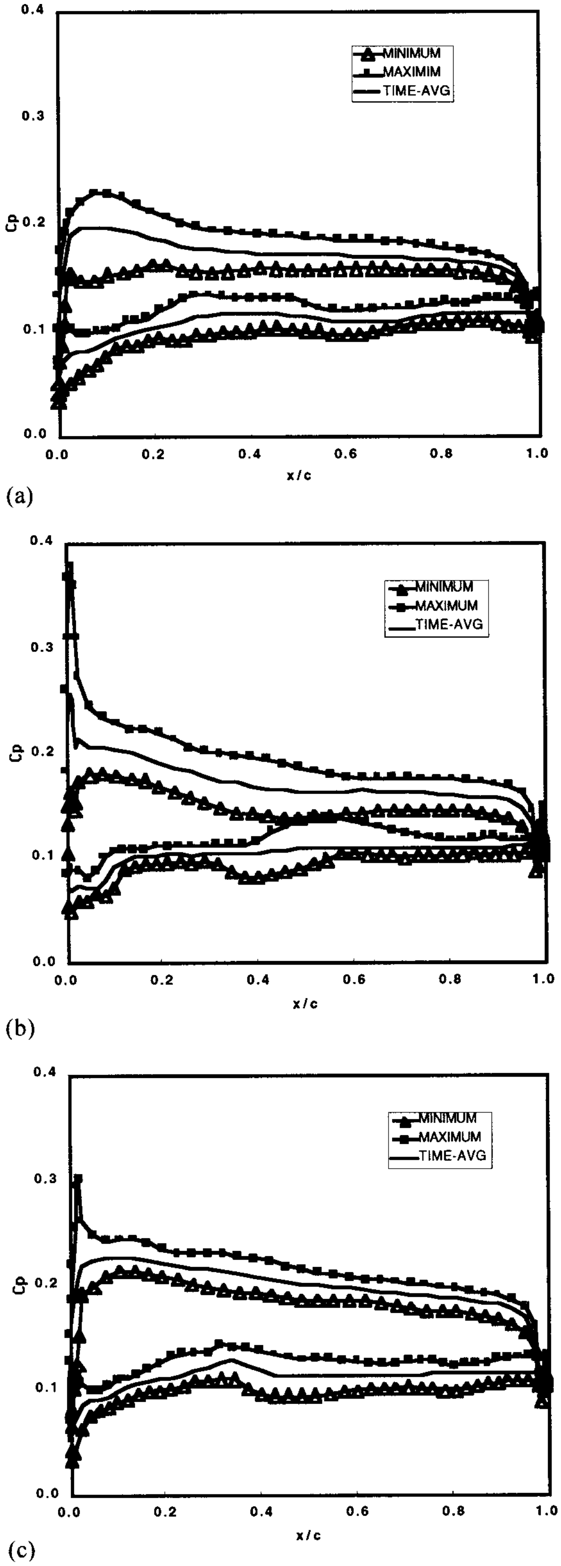

(a)

(b)

(c)

Fig. 13 Blade pressure envelopes, large gap, uncoupled: (*a*) hub; (*b*) midspan; (*c*) tip

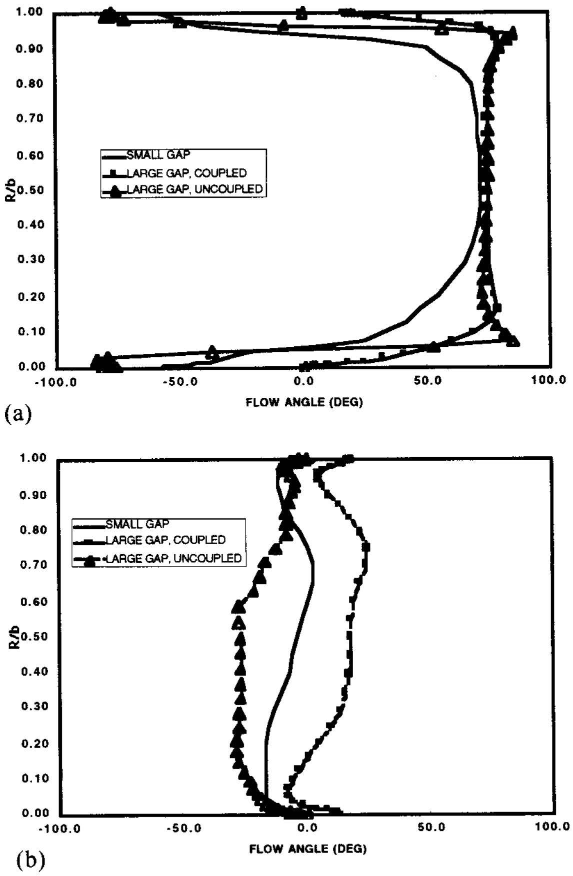

Fig. 14 Circumferential angle profiles: (*a*) blade inlet; (*b*) blade exit

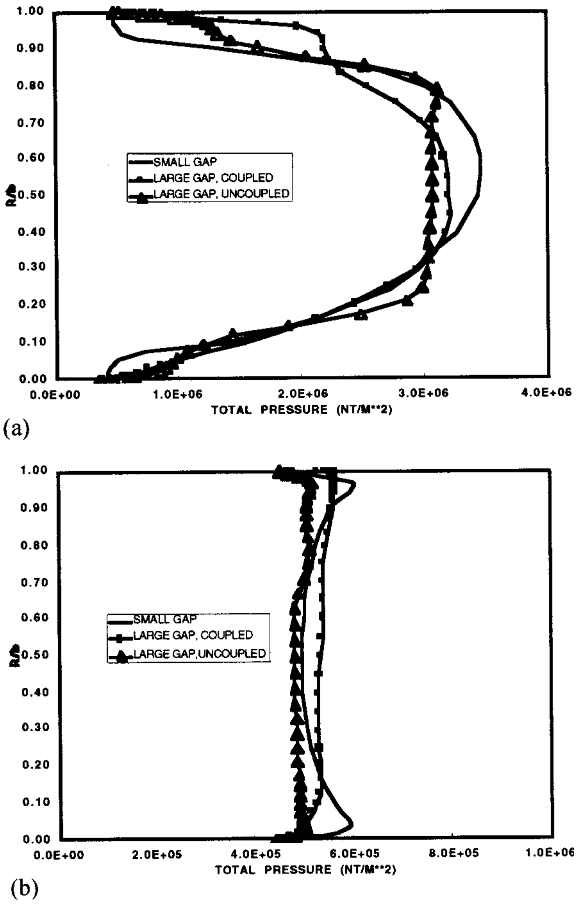

Fig. 15 Total pressure profiles: (*a*) blade inlet; (*b*) blade exit

the endwalls. The jump in flow angle near the endwalls is indicative of an improper prediction of mixing at the nozzle exit (or right at the inlet of the flow domain for the uncoupled case). At the blade exit, the small gap and large gap cases have similar angle profile shapes. However, the exit flow angles for the small gap case are more negative (which is more beneficial). The difference in the magnitudes of the exit flow angles seems to be due to greater airfoil separation for the large gap case, and the differing inlet boundary layer profiles. For the uncoupled case, the flow angles are more negative indicating an under prediction of airfoil separation. The profile shape is dissimilar to those of either of the coupled cases. The difference is not surprising considering the shape of the inlet boundary layer profile.

Figures 15(*a*),(*b*) show total pressure, P_T, at the inlet and exit of the blade. There are regions of higher loss entering the blade for the small gap case than for the large gap case. Because the nozzle jet has not yet expanded into the blade endwall regions, the boundary layers at the inlet section are thick for the small gap case. The profile for this case is nearly symmetric about the midspan. However, the profile shape for the large gap case is not symmetric. The nozzle jet expands into the blade shroud region before entering the hub region, thereby thinning the boundary layer at the shroud. The uncoupled case produces a profile that is nearly uniform with thin boundary layers. The losses for this case are underpredicted. Differences persist at the exit of the blade. For the small gap case, there is a dip in total pressure from both endwalls to midspan. The total pressure at the exit station for the large gap is nearly uniform outside of the boundary layers. The uncoupled case again shows very thin boundary layers.

Conclusions

A numerical study of the unsteady aerodynamic environment of the Fastrac supersonic turbine was conducted. The results were used to support aerodynamic assessments and structural dynamics evaluations. The design case (small gap) calculation showed that the turbine produces the required power. It also shows highly loaded blades, but no severe loading or unloading. However, the calculation also shows a high degree of unsteadiness, a nozzle with reflecting shocks, and a blade with large separation on the suction side. The large separated region is typical of supersonic turbine blades. The goal of a separate effort on which the authors are currently working is to minimize the separation to improve loading and performance characteristics. Relatively high amplitude pressure unsteadiness is predicted at the nozzle passing frequency and its second harmonic, particularly at the blade leading edge. The fluctuating pressures of these harmonics are evident along the pressure surface of the blade and the suction surface of the blade until the boundary layer separates. Thick boundary layers are evident at the inlet of the blade due to the nozzle jet not yet expanding into the endwall regions of the taller blade. The wake produced by the solid wall regions between nozzles interacts with the blade flowfield causing earlier separation, and separation on the pressure side of the EGV.

In order to investigate the effects of nozzle to blade axial spacing, a second case with a larger axial gap was simulated. This case showed higher losses in the region between the nozzle and blade due to jet interaction. However, it also showed less blade unsteadiness and thinner boundary layers entering the blade. Power calculated for the large gap case was lower than for the small gap case. However, this fact in no way implies that the smallest spacing is always optimal. More simulations of different axial spacings must be conducted, and the flowfield in the axial gap region must be studied in detail. The authors plan to perform this study in the future.

An uncoupled nozzle and blade/EGV simulation was run to determine whether the more complicated coupled simulations were necessary. This case showed that the inlet conditions were overspecified, the mixing in the axial gap was not adequately simulated, and the losses were underpredicted. It is the opinion of the authors that the nozzle must be coupled to the blade for unsteady simulations of supersonic turbines.

Acknowledgments

The authors wish to acknowledge the important contributions made to this work by our colleagues. Thomas Zoladz provided expertise in understanding unsteady flow phenomena. His support was most appreciated. The authors also wish to thank the Advanced Space Transportation Program at NASA/MSFC for their support of this activity.

Nomenclature

a = speed of sound
b = blade height
c = axial chord
C_p = coefficient of pressure$=P/P_{T0}$
c_p = specific heat at constant pressure
F, G, H = x, y, z components of flux
i = inviscid quantity
m = mass flow rate
P = pressure
Pr = pressure ratio
PW = power
Q = vector of flow variables
R = radius
$R2$ = Riemann invariant
T = temperature
u, v, w = x, y, z components of velocity
x, y, z = Cartesian coordinates
y^+ = boundary layer parameter
α = circumferential flow angle, absolute
β = circumferential flow angle, relative
Δh = work per unit of fluid
γ = ratio of specific heats
ϕ = yaw angle, absolute
ψ = yaw angle, relative

Subscripts

NE = nozzle exit
T = total (stagnation) quantity
t = time
$t\text{-}s$ = total to static quantity
0 = Nozzle inlet
1 = Rotor inlet
2 = Rotor exit

References

[1] Rangwalla, A. A., Madavan, N. K., and Johnson, P. D., 1992, ‘‘Application of an Unsteady Navier–Stokes Solver to Transonic Turbine Design,’’ J. Propul. Power, **8**, No. 5, pp. 1079–1086.
[2] Griffin, L. W., and Nesman, T., 1996, ‘‘Prediction of the Unsteady Aerodynamic Environment in the RRTT Turbine,’’ presented at the 14th Workshop for Fluid Dynamic Applications in Rocket Propulsion and Launch Vehicle Technology, NASA/Marshall Space Flight Center, Apr. 23–25.
[3] Baldwin, B. S., and Lomax, H., 1978, ‘‘Thin Layer Approximation and Algebraic Model for Separated Turbulent Flow,’’ AIAA Paper No. 78-257.
[4] Roe, P. L., 1981, ‘‘Approximate Riemann Solvers, Parameter Vectors, and Difference Schemes,’’ J. Comput. Phys., **43**, pp. 357–372.
[5] Dorney, D. J., Davis, R. L., Edwards, D. E., and Madavan, N. K., 1992, ‘‘Unsteady Analysis of Hot Streak Migration in a Turbine Stage,’’ J. Propul. Power, **8**, No. 2, pp. 520–529.
[6] Dorney, D. J., 1998, ‘‘Rapid Prediction of Unsteady Three-Dimensional Viscous Flows in Turbopump Geometries,’’ NASA H-28721D Final Report, Mar. 21.
[7] Dorney, D. J., and Sondak, D. L., 1996, ‘‘Study of Hot Streak Phenomena in Subsonic and Transonic Flow,’’ Int. J. Turbo Jet Engines, **13**, No. 2, pp. 131–141.
[8] Dorney, D. J., and Schwab, J. R., 1996, ‘‘Unsteady Numerical Simulations of Radial Temperature Profile Redistribution in a Single-State Turbine,’’ ASME J. Turbomach., **118**, No. 4, pp. 783–791.
[9] Dorney, D. J., and Davis, R. L., 1992, ‘‘Navier–Stokes Analysis of Turbine Blade Heat Transfer and Performance,’’ ASME J. Turbomach., **114**, No. 4, pp. 795–806.
[10] Dorney, D. J., and Davis, R. L., 1993, ‘‘Numerical Simulation of Turbine ‘Hot Spot’ Alleviation Using Film Cooling,’’ J. Propul. Power, **9**, No. 3, pp. 329–336.

Comparison of Different Acceleration Techniques and Methods for Periodic Boundary Treatment in Unsteady Turbine Stage Flow Simulations

Martin von Hoyningen-Huene
Alexander R. Jung
Siemens Power Generation (KWU),
Gas Turbine Development,
D-45466 Mülheim an der Ruhr, Germany

This paper studies different acceleration techniques for unsteady flow calculations. The results are compared with a nonaccelerated, fully explicit solution in terms of time-averaged pressure distributions, the unsteady pressure and entropy in the frequency domain, and the skin friction factor. The numerical method solves the unsteady three-dimensional Navier–Stokes equations via an explicit time-stepping procedure. The flow in the first stage of a modern industrial gas turbine is chosen as a test case. After a description of the numerical method used for the simulation, the test case is introduced. The purpose of the comparison of the different numerical algorithms for explicit schemes is to facilitate the decision as to which acceleration technique should be used for calculations with regard to accuracy and computational time. The convergence acceleration methods under consideration are explicit time-stepping with implicit residual averaging, explicit time-consistent multigrid, and implicit dual time stepping. The investigation and comparison of the different acceleration techniques apply to all explicit unsteady flow solvers. This paper also examines the influence of the stage blade count ratio on the flowfield. For this purpose, a simulation with a stage pitch ratio of unity is compared with a calculation using the real ratio of 78:80, which requires a more sophisticated method for periodic boundary condition treatment. This paper should help to decide whether it is crucial from the turbine designer's point of view to model the real pitch ratio in unsteady flow simulations in turbine stages. [S0889-504X(00)00702-9]

Introduction

While codes that model the steady-state flow in turbine stages have already reached a high degree of maturity, time-accurate flow-solvers are not widely used in an industrial environment at present mainly because of the high computational cost involved. Today's turbines are therefore very well designed with regard to steady-state flow phenomena, but a better understanding of the unsteady flow physics may still reveal a considerable potential for increasing turbine performance and durability. For this reason, it is important to determine the best method to simulate such time-dependent flowfields efficiently.

At Siemens, the Navier–Stokes solver ITSM3D, which was developed at the Institute of Thermal Turbomachinery (ITSM) at the University of Stuttgart is used to predict the unsteady flow in turbine stages. This solver has been specifically designed for application in turbomachines and is very efficient in computational terms. It can be used both for serial and parallel computations because the method is parallelized on a grid block basis using the message passing interface library (MPI).

The computational time needed for three-dimensional calculations of the unsteady flowfield in a turbine stage is still too long for everyday use in an iterative design process. However, different options exist with regard to reduce the computational time required for unsteady calculations significantly. In this paper, the authors present a series of calculations performed with different acceleration techniques, and compare the accuracy of the results. This is intended to encourage engineers to use explicit unsteady flow solvers more efficiently without a significant influence on the quality of the results. The ITSM3D code is subject to continuous improvement by the ITSM in close cooperation with the authors. At present, there is only a very small number of studies that compare the different acceleration techniques in terms of efficiency and accuracy. Davis et al. [1] show that an explicit Lax–Wendroff multiple-grid dual time-stepping procedure predicts the unsteady flowfield significantly faster than an explicit Lax–Wendroff algorithm with implicit residual smoothing. The accuracy, however, cannot be evaluated as the presented explicit results are not yet converged to periodicity in time.

The four different numerical techniques under investigation are a purely explicit time integration without any acceleration technique, an explicit time integration with an implicit residual averaging method applicable to global time-stepping, an explicit time-consistent multigrid method, and a fully implicit dual time-stepping method with multigrid. The latter is investigated in more detail using four different numbers of implicit time steps per rotor blade passing period. For all these comparisons, the original geometry of the test case with a blade count ratio of 78:80 is used.

As another point of interest, the influence of the stage blade count ratio on the flowfield is investigated. For this purpose, a dual time-stepping calculation with a simpler method for the periodic boundary treatment is performed. For this case, the stator is scaled such that the blade count ratio becomes unity (80:80).

Test Case

Description. The three-dimensional flowfield in the first stage of a Siemens Model V84.3A gas turbine is chosen as a test case. It is one of the world's most advanced industrial gas turbines with a single-cycle efficiency of 38 percent and a combined-cycle ef-

---

Contributed by the International Gas Turbine Institute and presented at the 44th International Gas Turbine and Aeroengine Congress and Exhibition, Indianapolis, Indiana, June 7–10, 1999. Manuscript received by the International Gas Turbine Institute February 1999. Paper No. 99-GT-155. Review Chair: D. C. Wisler.

ficiency of 58 percent [2]. While the stator blades are untwisted, the rotor blades are slightly twisted. In order to limit computational time, the spatial resolution in radial direction was chosen to be coarse with only 13 grid planes while the spatial resolution in the azimuthal planes is rather fine. The stator grid comprises 97×49 and the rotor grid 153×57 grid points, giving a grid point total of 175,162. Consequently, the investigation concentrates on the flowfield at midspan. When compared to a two-dimensional or quasi-three-dimensional calculation of a stream surface at midspan, this approach yields additional information about the major three-dimensional effects of the flowfield such as spatial pressure gradients and radial pressure wave propagation. The blade count ratio is 78:80. Using the time-inclining method described below, the simulation can be performed by simulating the flow for only one stator and one rotor passage each. The number of grid points is chosen in accordance with the experience of the authors with other, similar test cases. The computational grid at midspan is shown in Fig. 1.

Flow Regime. Table 1 shows some typical parameters of the test case. Due to the high Reynolds number, the flow is assumed to be fully turbulent from the inlet. According to Zeschky and Gallus [3], the Strouhal number (based on the blade passing frequency) indicates that approximately two wakes can be expected to be found in the rotor channel at a time. The flow medium is flue gas, which is assumed to behave like an ideal gas with a constant ratio of specific heat capacities.

Numerical Method

Governing Equations and Numerical Algorithm. The flow solver ITSM3D allows three-dimensional unsteady viscous flow analysis in multistage turbomachines. It is described in more detail in, e.g., Merz et al. [4] and Merz [5].

The equations solved are the three-dimensional, unsteady, Favre-averaged Navier–Stokes equations. The set of equations is written for a cylindrical coordinate system which rotates at constant angular velocity; see Jung et al. [6]. A modified algebraic Baldwin–Lomax model is used to describe the effects of turbulence. For a wide variety of turbomachinery problems, this implementation of the model has proved to yield reasonable results, see, e.g., Walraevens et al. [7] and Merz et al. [8].

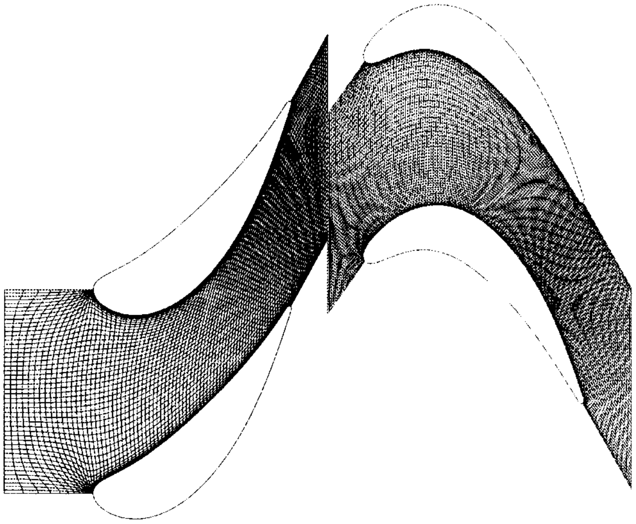

Fig. 1 Computational grid at midspan

Table 1 Flow parameters

Reynolds number at Outflow	10^6
Mach number at Exit	0.81
Mach number of Rotation	0.43
Strouhal number	1.95
pitch/rotor chord	0.75
Aspect Ratio	≈ 1.3

A cell-vertex finite-volume formulation is used for the spatial discretization of the equations on a structured mesh of curved hexahedrals. Artificial dissipation is added to the discretized equations using an extension of the model introduced by Jameson et al. [9]. In order to prevent odd–even decoupling caused by the second-order central difference scheme, fourth-order dissipation is introduced in the entire domain, and in order to improve the shock resolution, second-order dissipation is introduced near shock waves, which is locally activated by a pressure sensor. Scalar damping terms have been chosen for the sake of computational efficiency. In the case of explicit time integration, a five-stage Jameson-type Runge–Kutta time-stepping scheme is used with global time steps in order to allow time-accurate simulations, whereas in the case of implicit time integration, it is used to converge the inner iterations in a pseudo time.

Block-structured *H*-type grids in a multiblock topology are used. The fourth-order artificial dissipation terms are applied continuously across all interblock boundaries of the computational domain. For unsteady flow simulations, the grids at the sliding interfaces between stationary and rotating blade rows are overlapped by one grid cell. An interpolation procedure consistent with the second-order spatial accuracy of the numerical scheme is used to interchange the flow variables during every time step of the integration procedure. As the rotor grid moves relatively to the stator, the position of the rotor is integrated in time in order to track the position of the grid blocks for a time-resolved coupling at the interface regions.

In cases of unsteady simulations in which the stator blade count is different from the rotor blade count, the exact ratio of the blade counts can be modeled since a time-inclining method for three dimensions based on the work of Giles [10] has been implemented in the code [6]. In this approach, time transformations are applied to both the stator and the rotor domains, and different time steps are used in these domains. In this way, simple periodicity conditions can be applied at the boundaries in the pitchwise direction, although these boundaries are not periodic in the physical domain.

Boundary Conditions. At the inlet and exit boundaries, a nonreflecting post-correction method based on the work of Giles [11] and Saxer [12] is applied to prevent spurious reflections from waves that leave the computational domain. The boundary conditions there are taken from a previous calculation of the turbine flowfield performed with a quasi-three-dimensional tool. Total pressure and total temperature are used as boundary conditions at the inlet. In addition, the flow is assumed to be parallel to the machine axis at the inflow, i.e., the flow leaves the combustion chamber without any swirl. The static pressure is imposed at the exit.

Solid surfaces are assumed to be adiabatic, and the no-slip condition is applied. Periodicity in the pitchwise direction is ensured by using phantom cells that keep copies of the periodic values such that the points on these boundaries can be treated like interior points.

Acceleration Techniques

When ITSM3D is used for steady-state calculations, the explicit time-marching method allows several acceleration techniques such as local time-stepping, multigrid cycles, and implicit residual smoothing. When used for unsteady calculations, however, time is not only a numerical parameter, but a meaningful physical quantity, which is why global time steps have to be used. In addition, multigrid cycles are not effective unless they are used together with local time stepping. Thus the only acceleration techniques that can be used for unsteady explicit calculations are implicit residual smoothing and explicit time-consistent multigrid.

Implicit Residual Smoothing. Due to the global time steps, the maximum allowable time step of the basic scheme is limited by the stability limit of the finest grid cells, which are usually found in the boundary layers on solid surfaces or in the very fine viscous grid regions around the blades' leading and trailing edges. In the rather inviscid main portion of the computational domain the grid cells are larger so that they would allow a much larger time step (typically 50 to 100 times larger than in the fine viscous regions). Assuming that in the viscous regions an increase in the time step by a factor of, e.g., 5 would still yield reasonable time accuracy, computational efficiency can be increased by the same factor.

The idea is therefore to use an implicit operator at each stage of the Runge–Kutta scheme in order to stabilize the explicit time integration only at those points where the stability condition is violated as a result of the increased time step. All other points that are well within the stability limit do not need special attention. At the nodes in the fine regions, the residual is replaced by an implicitly calculated weighted average of the residuals of the adjacent points. Thus the residual contains the information of the residuals of all points in the flowfield. The implicit smoothing algorithm for global time steps is based on the method proposed by Jorgenson and Chima [13] but uses directionally weighted smoothing in order to prevent the residuals from being smoothed in those directions which do not determine the stability. This acceleration technique has proved to speed up the calculation considerably, particularly for coarse to medium fine grids.

Time-Consistent Multigrid. He [14] developed a time-consistent multigrid scheme with two global multigrid levels. It avoids the problem of the large influence zone of the implicit residual smoothing and the related error estimation difficulties by using a more straightforward purely explicit method. In this method, the grid is locally coarsed enough to allow for stability when proceeding the given global time-step. Time-consistency is achieved because the coarse grid only contributes to advancing in time so far as necessary to obtain the desired time-step. This method is called time-consistent and not time-accurate as for unsteady problems, it is not fully accurate in time. For a spatial resolution of the coarser grids that is much smaller than the wavelength of the unsteadiness under consideration, however, the error should be rather small. This may not be the case if the unsteady behavior of the boundary layer is examined. The implemented version of this method [15] calculates the number of necessary multigrid levels for each cell at every time step and uses directionally biased grid coarsening rather than employing a sequence of fixed grids as proposed by He. For complex geometries (e.g., when modeling radial blade gaps), this has proved to be not as efficient as for simpler geometries.

Implicit Time Integration (Dual Time-Stepping). The acceleration techniques described so far apply to both time-marching solutions of stationary problems and to explicit calculations of unsteady problems. In contrast to that, the fully implicit time-accurate dual time-stepping method has been developed especially for unsteady calculations. In this method [16], the time-dependent equation is written in the form

$$\frac{\partial u}{\partial t} = -R \tag{1}$$

where u denotes the vector of the flow variable and R the residual vector. The time derivatives are formulated implicitly with second-order backward differences. The equation is rewritten to $\partial u/\partial t + R = R^*$ where the residual R^* has to be driven to zero. A pseudo time τ is introduced, leading to

$$\frac{\partial u}{\partial \tau} = \frac{\partial u}{\partial t} + R = R^* \tag{2}$$

Keeping the physical time t constant, the discretized form of Eq. (2) can be marched forward in the pseudo-time τ. All acceleration techniques applicable to steady-state problems can be used to reduce the number of explicit iterations in the pseudo time as time-accuracy is not needed in the pseudo time. After a number of explicit iterations, the residual R^* will become sufficiently small and the flow variables can be obtained at the time step $t_{i+1} = t_i + \Delta t$ with $\Delta t = T/N$ where T denotes the rotor blade passing period and N the number of dual time steps per period. Unless otherwise indicated, ''period'' denotes the rotor blade passing period. Second-order backward differences are chosen for the implicit discretization of the time-derivative since the explict integration scheme and the spatial discretization are both accurate of second-order. Since implicit methods are unconditionally stable, the time-step to be chosen is determined by the required resolution of the unsteady effects and corresponding frequencies alone.

Unsteady Flow Calculations

The explicit unsteady calculation without acceleration techniques is performed on two Silicon Graphics 195 MHz R10000 processors making use of the parallelized version of the code. All other calculations are performed in serial mode on a 200 MHz HP C200 workstation. The results of a steady-state calculation which needed 500 explicit multigrid cycles for convergence served as initial conditions for the unsteady computations.

Convergence Assessment. For the investigations described in this paper, strict convergence criteria have been chosen in order to allow a fair comparison of the different options. In the time-critical design process however, a turbine design engineer might decide to stop the calculations at an earlier stage when the flowfield remains unchanged in the flow parameters of interest.

In this study, the calculations are terminated after periodicity has been reached in the static pressure fluctuation at eight monitor points representative of the flowfield. The periodicity of the pressure fluctuations at these points (especially in the leading edge and trailing edge regions) turns out to be a more stringent convergence criterion than the other convergence criteria monitored, i.e., the mass-flow at the grid inflow and outflow boundaries, the rms residual of the velocity gradients of all grid points adjacent to a wall, and the entropy distribution along a grid line in pitchwise direction in the rotor near the interface. It is interesting to note that the lower harmonics of the blade-passing frequency converge faster than the higher ones.

For the calculations with implicit dual time-stepping, the number of inner iterations is determined such that the residual reaches an almost constant value. It is found that, according to this criterion, more inner time steps are needed when fewer dual time steps per period are used. It is also discovered that a reduction in the number of inner iterations does not noticeably affect the solution. In order to speed up the computations, the first six periods are calculated with only six inner iterations before increasing their number to the number derived from the criterion mentioned above (see next paragraph).

Computational Time. The explicit calculation without any acceleration method for this grid is stable for CFL numbers up to 1.4, which is far below the theoretical stability limit of the five-stage scheme (CFL*=4.0) so that about 26,500 time steps per period are needed. With implicit residual smoothing, a speed-up of 6 was regarded as appropriate in terms of efficiency and accuracy, allowing for a CFL number of 8.0. The explicit time-consistent multigrid method is stable for a CFL number of 1.0 on the finest grid and 4500 time steps per period yielding a speed-up of 8. In all three explicit cases, approximately twelve periods are needed before convergence is reached. Convergence is defined according to the above-mentioned criteria.

Table 2 Efficiency of different acceleration techniques: method versus number of time-steps and CPU time (in *h*)

Type of calculation	Timesteps	CPU
explicit without acceleration	316,860	1260
implicit residual smoothing	55,451	220
time-consistent multigrid	54,000	220
200 implicit dual time steps	43,200	200
104 implicit dual time steps	29,794	140
56 implicit dual time steps	21,616	100
16 implicit dual time steps	7,776	35

Additionally, four different calculations are performed with dual time stepping, with 16, 56, 104, and 200 dual time steps (dts) per period. In all cases, six periods are calculated with six inner iterations, followed by ten periods with 45, 35, 25, and 18 inner time steps respectively for the calculations with 16, 56, 104, and 200 dual time steps.

The dual time-stepping calculations use three multigrid levels, local time-stepping, and implicit residual smoothing to accelerate the inner iterations.

It is worthwhile to note that the number of blade passing periods needed for convergence is almost constant for a specific method, regardless of the temporal resolution. The number of explicit iterations needed for the different options is summarized in Table 2. For a better comparison, it should be noted that one explicit time step in the dual time-stepping calculations requires approximately 15 percent longer than the calculations with global time-stepping due to the full multigrid cycles with three levels. On the C200, the calculation with 104 dual time steps takes about six days. The dual time-stepping method allows faster computations of the flowfield than implicit residual smoothing. According to the authors, this is mainly due to the fact that the chosen grid is very fine, at least in the $S1$ planes. For computations on coarse grids, however, the overhead due to the implicit dual time steps could become so important that even a moderate implicit residual smoothing or the time-consistent multigrid might take less computing time yielding the same degree of accuracy.

Results With Different Algorithms

The computational results obtained with the different acceleration techniques and parameters described above are compared to the fully explicit calculation with no acceleration technique, which is taken as a reference with the reasonable assumption that it yields the most accurate results.

Pressure and Entropy Distributions. Figure 2 shows the instantaneous pressure and entropy contours at eight different rotor positions, calculated with the fully explicit method without any acceleration technique. The effects of the inviscid potential flow interaction and the viscid wake–blade interaction are obvious. The convection of the wakes toward the suction side of the rotor is due to the ''negative jet'' effect resulting from the velocity deficit in the wake. The physics of the time-resolved flowfield at midspan in the first turbine stage of the Siemens Model V84.3A gas turbine is described in more detail in von Hoyningen-Huene and Hermeler [17,18].

Static Pressure Distribution Over Stator and Rotor. The time-averaged rotor blade pressure distribution is shown in Fig. 3. The plot shows the results of the pure explicit calculation. The pressure distributions obtained when applying acceleration techniques are not depicted because they are practically identical. The unsteady pressure fluctuations are most pronounced close to the rotor leading edge where they amount to approximately 2 percent of the total pressure at inlet p_{t0}. A detailed discussion of the physical background of the pressure fluctuations and their shape, which is found in von Hoyningen-Huene and Hermeler [17,18] is beyond the scope of this paper. The second paper [18] focuses on the differences in the results obtained with different calculation methods. Static pressure fluctuations on the rotor blade at $t = 1/8\,T$ are shown in Fig. 4 as a difference between the instantaneous pressure p and the time-averaged pressure $\overline{p}$. The plot shows the results of the pure explicit calculation, the calculation with implicit residual smoothing, the time-consistent multigrid, and for the implicit calculations with 104 and 16 dual time steps.

The 16 dual time step calculation exhibits significant deviations over the entire profile. All other calculations show good agreement with the reference solution. The best agreement is found for the calculations with 104 and more dual time steps, followed by the explicit calculation with implicit residual averaging. The implicit residual smoothing solution shows considerable differences near the leading edge on the pressure surface. The results are only slightly better than those of the calculation with 56 dual time steps (not shown here).

A good method to investigate the pressure fluctuations that goes beyond mere visual assessment is to analyze the unsteady pressure in the frequency domain. Figure 5 shows the amplitudes of the first and second harmonic of the blade passing frequency over the rotor for the fully explicit and the residual-averaged calculations as well as the implicit calculation with 200 dual time steps. On the left-hand side, the influence of the different smoothing effects and algorithms is shown, and the influence of the temporal resolution on the dual time-stepping solutions is shown on the right. It is found that the largest contribution to the unsteadiness comes from the first harmonic of the blade passing frequency. The maximum amplitudes are found on the suction side close to the leading edge where the potential flow interaction exhibits maximum intensity as well as on the positions where the wake impacts the rotor [18]. These positions are characterized in the phase map by local extrema. The high amplitude values on the pressure side between midchord and the trailing edge are not reflected by local extrema in the phase angle distribution and are therefore assumed to be due to three-dimensional wave interaction.

With the exception of the implicit calculation with 16 dual time steps, all other calculations match the explicit reference solution quite well in amplitude and phase. While the agreement is very good in the first harmonic, it is not as good in the higher harmonics for some of the methods under investigation; see Fig. 5. Especially the calculations with 104 and 200 time steps are in excellent agreement with the explicit calculation. The accuracy of the explicit calculations with implicit residual smoothing and time-consistent multigrid are about as good as for the implicit calculation with 56 dual time steps. The level of absolute deviations remains constant for all harmonics so that the relative deviation is more important for the higher harmonics. Therefore, the second harmonic shows larger relative errors in the results than the first harmonic.

A more detailed examination of the results reveals that the amplitude and phase of the first harmonic are well matched by the dual time-stepping calculations with 56 and more dual time steps. With only 16 dual time steps, however, significant scatter is observed. The time-consistent multigrid calculation also agrees well in both amplitude and phase of the first harmonic. While the explicit calculation using implicit residual smoothing yields good results in terms of predicting the amplitude of the first harmonic, phase deviations up to 11 deg are observed.

As far as the second harmonic is concerned, mainly the implicit residual smoothing calculation but also the time-consistent multigrid exhibit significant scatter in amplitude and phase, amounting to 20 percent of the amplitude and up to 30 and 20 deg, respectively. The calculation with only 16 dual time steps produces even worse results with extremely large errors in phase and an amplitude which amounts locally to only 40 percent of its correct value. The calculations with 56 and more dual time steps represent the amplitude of the second harmonic unexpectedly well. The

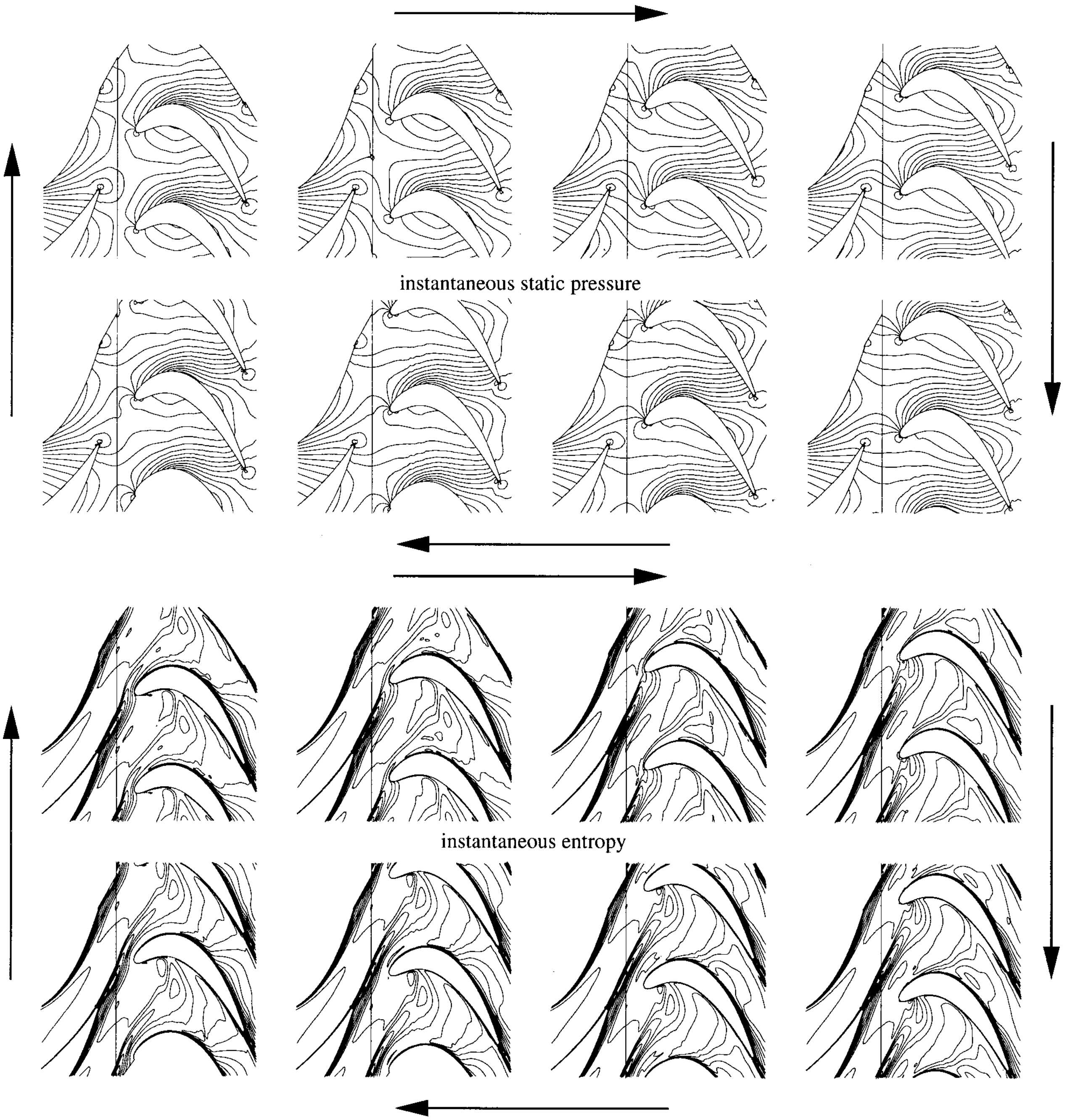

Fig. 2 Contour lines at eight equidistant instants in time; point of reference: $t=0$ at top left corner

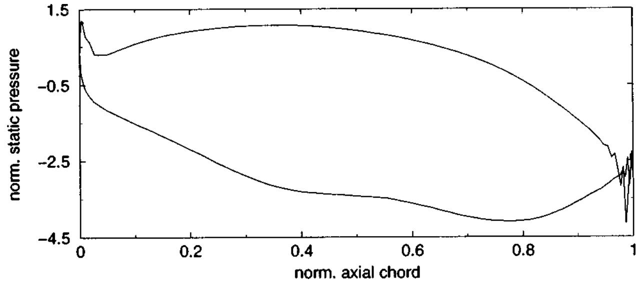

Fig. 3 Time-averaged static pressure distribution over the rotor (explicit calculation)

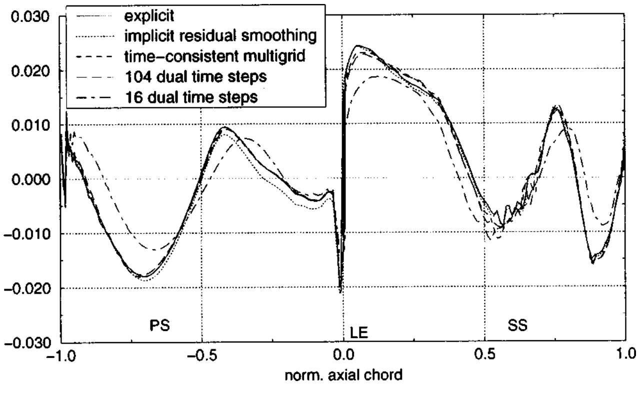

Fig. 4 Instantaneous static pressure deviations $(p-\bar{p})$ on the rotor blade at $t=1/8T$

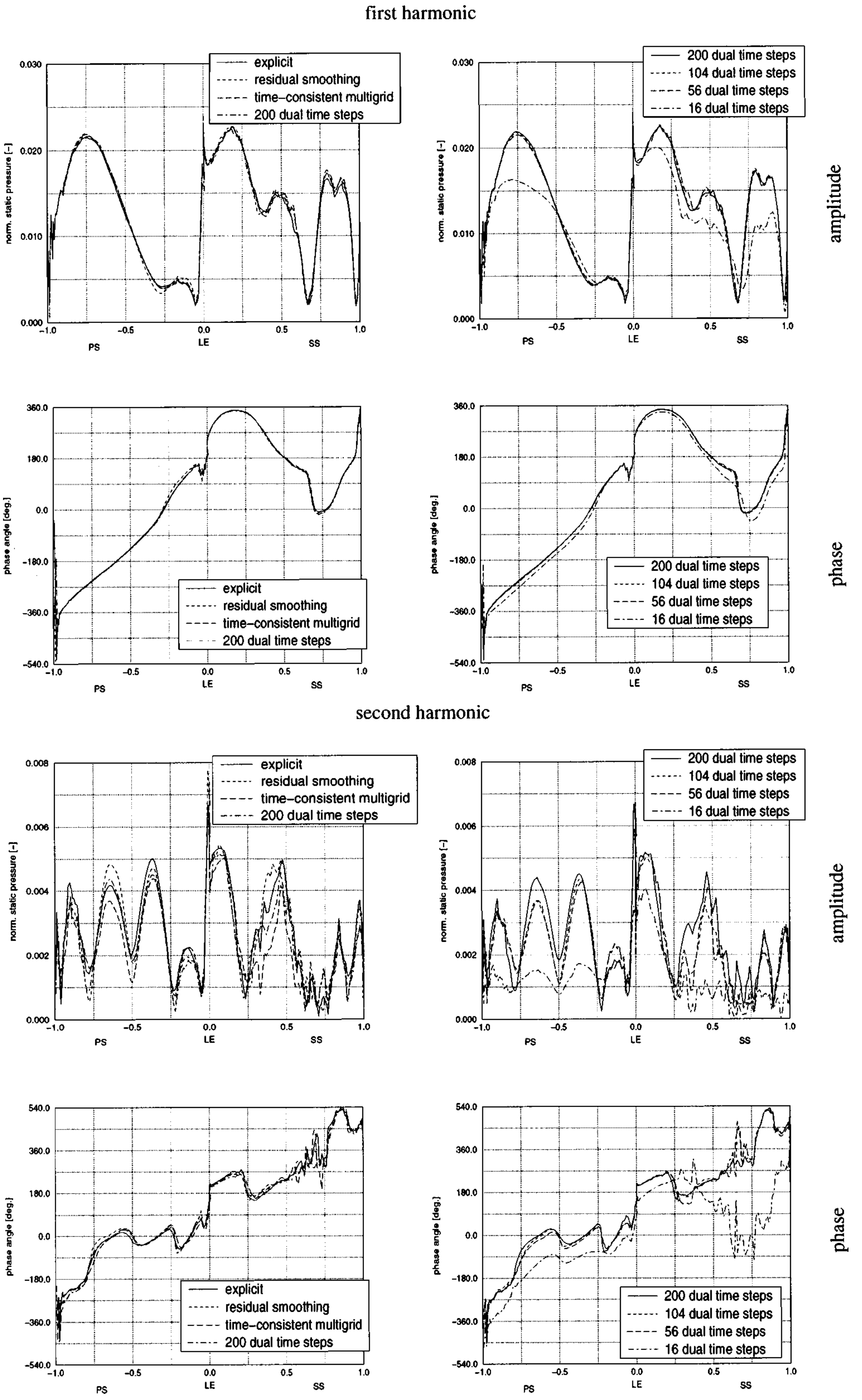

Fig. 5 Rotor blade pressure amplitude and phase at midspan as a function of the axial chord

local deviations in amplitude are below 25 percent, with the exception of a small region on the suction side around 0.7 axial chord.

Figure 6 shows that the stator is subject to similar phenomena. As shown in a companion paper [18], the pressure fluctuations are mainly caused by the potential flow interaction at the stator trailing edge where a pressure wave is induced when the distance to the rotor becomes minimal. However, another, weaker wave is induced by the rotor displacement effect at a distance of approximately 0.2 axial chord upstream from the trailing edge. Again, the

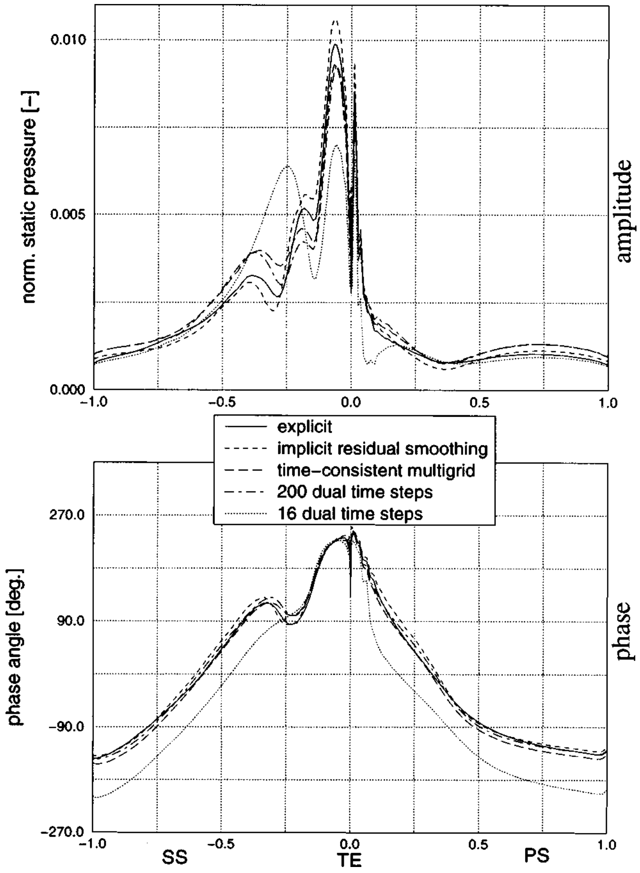

Fig. 6 Pressure amplitude and phase angle of the first harmonic on the stator as a function of the axial chord

origins of both waves are reflected by extrema in the amplitude and phase plots. Figure 6 demonstrates that the phase angle distribution is in very good agreement for all computations with the exception of the implicit calculation with 16 dual time steps. As in the case of the first harmonic on the rotor, a convergence toward the reference solution is observed when the number of dual time steps is increased. While the solution with implicit residual averaging shows slightly higher differences in the phase angle, it yields a better matching in the distribution of the pressure amplitudes. It is surprising that the agreement of the amplitude on the stator is not quite as good as on the rotor, especially near the throat on the suction surface. The results of the implicit residual-averaged calculation are the most accurate in terms of amplitude distribution, but less accurate in terms of phase angle. The dual time-stepping calculations and the time-consistent multigrid calculation slightly overestimate the local maximum, which is caused by the pressure displacement effect. Apart from this position, 104 dual time steps prove sufficient to come very close to the explicit calculation. The calculations with time-consistent multigrid and dual time stepping with more than 16 dual time steps (not plotted) capture the phase angle distribution well.

The second harmonic on the stator (not plotted) exhibits reasonable agreement with all algorithms apart from the calculation with only 16 dual time steps, although the amplitude in the trailing edge region on the suction side is underestimated by all methods by approximately 7 percent.

Pressure Fluctuations in the Flowfield. The calculations are also investigated in terms of the unsteady pressure oscillations at eight monitor points, which are situated one grid point behind the stator and rotor trailing edge, one grid point in front of the stator and the rotor leading edge, and at the inlet and exit of the stator and the rotor grid, respectively.

The two most critical monitor points are the points that are one node point away from the trailing edges of the stator and the rotor blade. Due to the fine grid cells in the boundary layer region, the allowable local time step in these regions is very small so that the effects of the acceleration techniques on the accuracy of the flowfield are expected to be particularly important there. The pressure fluctuations at these points are shown in Fig. 7.

The top graph in Fig. 7 shows the pressure fluctuations near the stator blade trailing edge. Apart from the error in amplitude and phase when using 16 dual time-steps, which can be perceived at this position as well, all other calculations show good agreement as regards amplitude and phase angle. In the stator wake, all dual time-stepping calculations are shifted toward a slightly different mean pressure level, which is approximately 0.002 p/p_{t0} higher than in the reference calculation. The explicit calculation with implicit residual smoothing captures the shape of the oscillations excellently except for a little scatter around $t=0.75$, but the mean pressure value is approximately 0.01 p/p_{t0} higher than for the reference calculation. The calculations with time-consistent multigrid and with 56, 104, or 200 dual time steps are in good overall agreement with the reference solution. However, these calculations smooth out some of the secondary peaks. The fewer dual time-steps are taken, the more the plot is smoothed. This is due to the fact that the temporal resolution of high-frequency harmonics is limited to the number of dual time steps. The pressure fluctuations downstream of the rotor are depicted in the bottom graph in Fig. 7. In this case, there is almost no shift in the mean pressure level. At this point, the fluctuations and the amplitude of the explicit reference solution are best captured by the explicit calculation with implicit residual smoothing and the time-consistent multigrid. The results with 104 and 200 dual time steps capture the overall behavior (described by the phase and amplitude of the lower harmonics) well but again some of the secondary oscillations are smoothed out due to the limited temporal resolution. For 16 and 56 dual time-steps, a considerable mismatch in amplitude and phase is found. The calculation with implicit residual smoothing shows the best agreement with the reference solution.

Entropy Fluctuation in the Flowfield. In addition to the pressure fluctuations, the entropy fluctuations are investigated

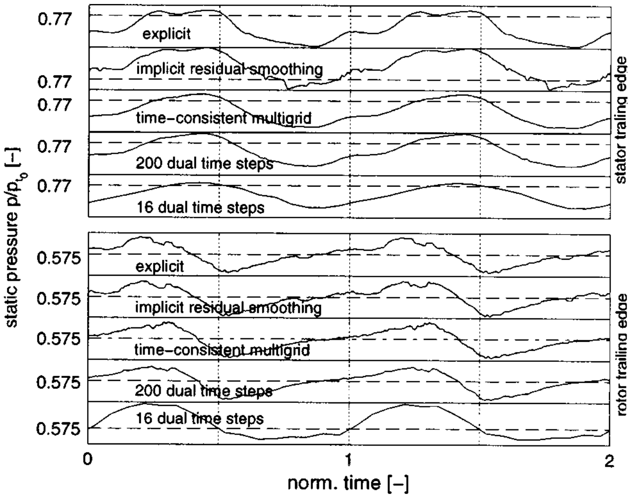

Fig. 7 Unsteady pressure fluctuations at one node downstream of the stator blade trailing edge (top) and one node downstream of the rotor trailing edge (bottom) during two blade passing periods. The height of each plot is chosen to correspond to 0.02.

along a pitchwise gridline in the rotor domain close to the stator/rotor interface plane, which is almost parallel to the interface and can therefore be interpreted as a line of constant axial coordinate with the length of one rotor pitch. The effect of the passing wakes can be investigated along this line.

The top graph in Fig. 8 shows the time-averaged entropy in the rotor frame of reference. Note that the time-averaged entropy is not constant along this line but varies by more than 10 percent of the circumferentially averaged time-mean value. This is due to the nonlinearity of the stator–rotor interaction effects, i.e., the entropy distribution in the wake changes depending on the relative rotor position. All steady calculations that use some sort of mixing plane approach do not account for this phenomenon and therefore produce inaccurate solutions of the time-mean flowfield. All methods result in the same shape of the time-averaged entropy distribution. Compared with the other calculations, the dual time-stepping calculations are slightly shifted toward smaller entropy values. This offset increases with the number of dual time steps used. It amounts to 0.5 percent of the time- and space-averaged entropy value for 104 dual time steps and to 0.2 percent for 16 dual time steps. This means that the dual-time stepping calculations are slightly less dissipative than the other methods.

The temporal fluctuations along this gridline are analyzed in the frequency domain. In the bottom plot on Fig. 8, the maximum amplitudes of the first and second harmonic are shown for the different algorithms. The maximum amplitude of the first harmonic is located at approximately 37 percent pitch and amounts to about 9 percent of the circumferentially averaged time-mean value. The results with the different methods are shown in the graph. The overall agreement is very good. The time-consistent multigrid calculation yields the best results, followed by the calculations with 104 and more dual time steps. The calculation with 16 dual time steps locally underestimates the amplitude by up to 7 percent. The calculation with implicit residual smoothing shows the largest disagreement, deviating in both directions by up to 12 percent of the local amplitude. The corresponding phase angle distribution of the first harmonic is depicted in the top graph in Fig. 9. Again, the overall agreement is very good, and for the time-consistent multigrid calculation, it is perfect. For 104 and more dual time steps, the maximum angle deviation is less than 2 deg, for the calculation with implicit residual smoothing, it amounts to 3 deg. For the calculation with 16 dual time steps, the maximum shift in the first harmonic amounts to about 6 deg.

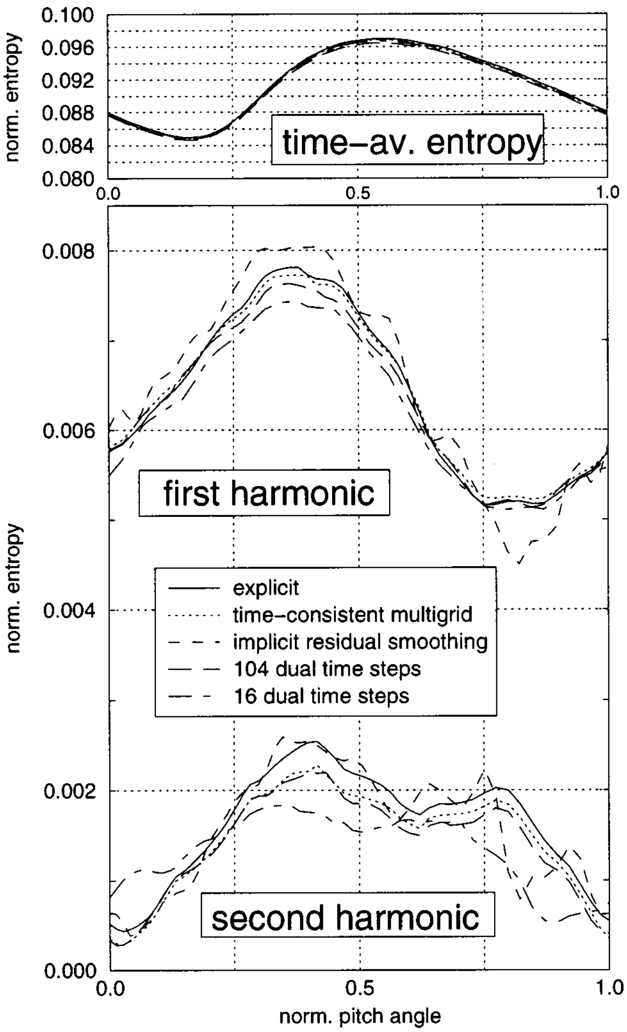

Fig. 8 Entropy distribution in the rotor along a grid line in pitchwise direction (near the interface)

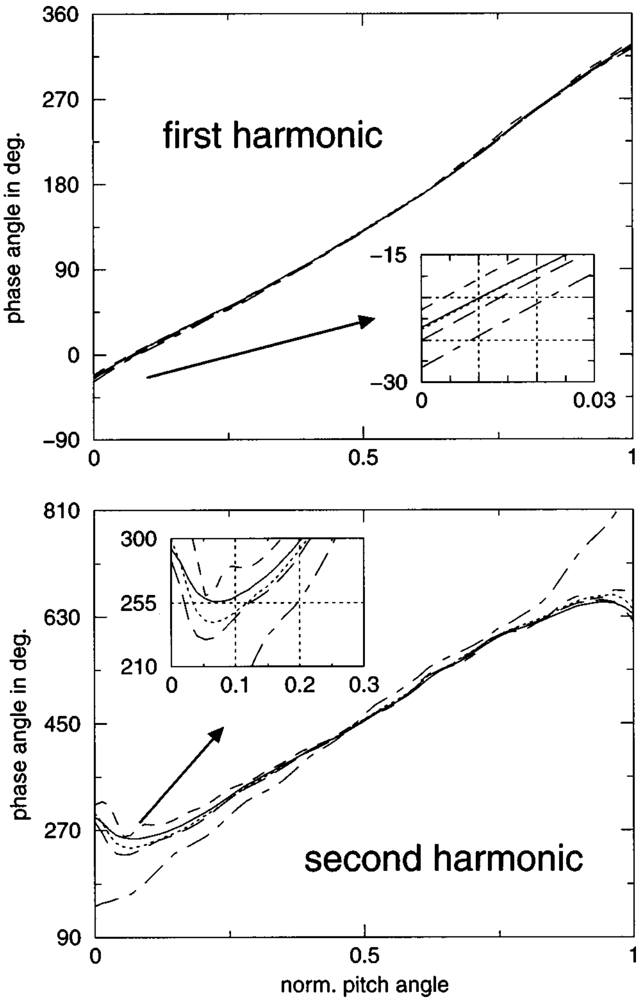

Fig. 9 Phase angle of the first and second entropy harmonic along a gridline in the pitchwise direction (near the interface), legend as in Fig. 8

The amplitude of the second harmonic is depicted in the bottom graph in Fig. 8. The maximum is located at approximately 37 percent pitch. It amounts to about 2.8 percent of the circumferentially averaged time-mean value. The best agreement is obtained using time-consistent multigrid or dual time-stepping with 56 and more dual time-steps. They result in a maximum error of 15 percent. As for the first harmonic, the calculation with implicit residual smoothing produces some wiggles in the amplitude distribution that are not found in the explicit reference calculation leading to large local deviations in amplitude (up to 50 percent of the circumferentially averaged amplitude). The calculation with only 16 dual time steps underpredicts the amplitude of the second harmonic over most of the pitch, deviating from the reference solution by up to 80 percent of the circumferentially averaged amplitude. The phase of the second harmonic is depicted in the lower graph of Fig. 9. Around 50 percent pitch, all calculations are in good agreement, but towards 0 and 100 percent pitch the phase angle deviations between the calculations become obvious. At this position, the calculation with 16 dual time-steps is out of phase by 150 deg. The results with implicit residual smoothing and with 104 dual time steps are both off by 25 deg. The time-consistent multigrid simulation is off by only 15 deg.

It can be summarized that the entropy fluctuations along the chosen grid line are best captured by the time-consistent multigrid. It is also well represented by the dual time-stepping calculations with 56 and more dual time steps. The calculation with implicit residual smoothing and the calculation with 16 dual time steps, however, do not accurately predict the time-resolved entropy distribution.

Wake Convection In the Flowfield. In Fig. 10, the instantaneous entropy contours at $t=0$ are shown in black for the explicit reference calculation; superposed on this, the flowfield at the same instant is depicted in gray for the implicit calculation with 16 dual time steps. The two results show big differences in both the shapes of the lines of constant entropy and the location of the local extreme values. The extreme values in the dual time-stepping calculation are farther upstream of the extreme values in the more accurate explicit calculation by approximately 9 percent of axial chord in the leading edge region (Detail A) and approximately 3 percent farther upstream in the channel. This means that the two simulations show a noticeable phase shift in the time-dependent behavior, which is also indicated in Fig. 9 discussed above. It is interesting to compare this phenomenon to the observations of Walraevens et al. [7] who described a similar effect as the result of a grid refinement study. In the implicit calculation with only 16 dual time-steps, the temporal resolution is too coarse to capture the wake convection correctly in amplitude and phase. By analogy, Walraevens et al. show that a spatial resolution that is too coarse leads to a misprediction of amplitude and phase of the wake convection. The calculations with 56 and more dual time steps do not show a similar phase shift. Therefore, it can be concluded that in order to simulate the wake convection process correctly, the number of dual time-steps required per blade passing period has to be at least equal to the number of grid lines in pitchwise direction. This means that with one implicit iteration, a rotor node at the grid interface must not move farther in circumferential direction than the circumferential distance to the adjacent grid point. For the calculation with 16 dual time-steps, the phase mismatch in the channel is reflected also by the strong phase mismatch of the second pressure harmonic on the rotor, which can be seen in Fig. 5. Finally, in the boundary layer region on the suction side, the static pressure gradients differ as well for the calculation with only 16 dual time steps (not depicted).

Boundary Layer. In order to compare the solutions in the boundary layer region, the skin friction factor on the rotor is plotted. The skin friction factor is defined as

$$c_f = 2\,\frac{\tau_w}{\rho u_\infty^2} \tag{3}$$

where τ_w denotes the wall shear stress, ρ the density, and u_∞ some reference velocity (here taken to be the spatially averaged velocity at rotor entrance), respectively. The time-averaged value of c_f is shown in Fig. 11. All algorithms capture the time-averaged value quite accurately. The calculation with implicit residual smoothing and with time-consistent multigrid match the reference solution almost exactly. The calculation with 200 dual time steps yields a result that is very similar to the one for 104 time steps. All dual time-stepping calculations with 56 and more dual time steps show local deviations of the time-averaged skin friction factor of up to almost 7 percent. With only 16 dual time steps, the results show significant scatter.

The differences in the time-resolved distribution of the skin friction factor are more important. The instantaneous skin friction factor distribution for different algorithms on the rotor at time $t=0$ is shown in Fig. 12. The comparison with the time-averaged c_f and with the flowfield depicted in Fig. 2 shows that at this time step, the wake interacts with the suction side boundary layer at approximately 20–50 percent axial chord leading to a deviation from the time-mean value in this region. The position of the local minimum found in this region is not exactly captured by the dual time-stepping calculations. In this region, the skin friction values differ from the reference solution by up to almost 15 percent. Further downstream on the suction side, near the location where the wake from the previous period has migrated, the deviatons are below 4 percent except for the calculation with 16 dual time steps, which shows larger differences.

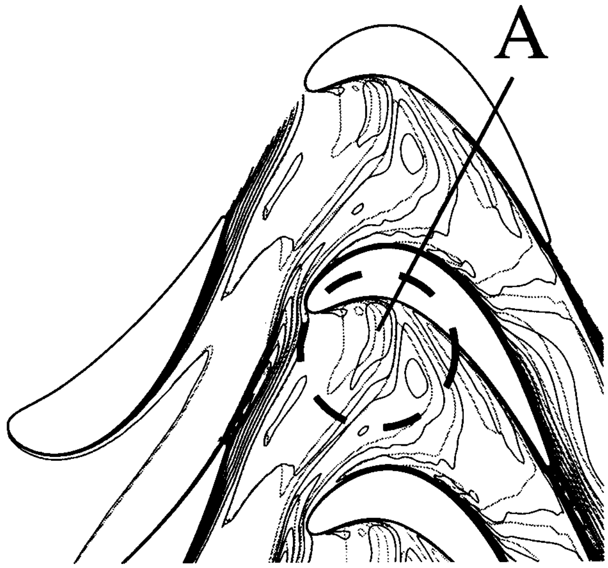

Fig. 10 Entropy contours at $t=0$. The unaccelerated calculation is depicted in black, the implicit calculation with 16 dual time-steps depicted in gray.

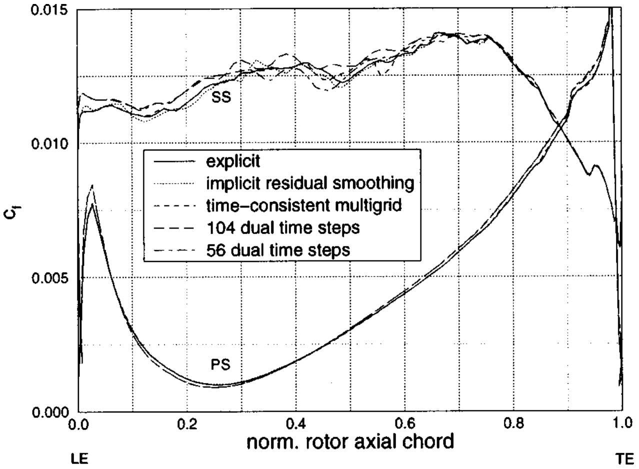

Fig. 11 Time-averaged skin friction factor on the suction side (SS) and the pressure side (PS) of the rotor

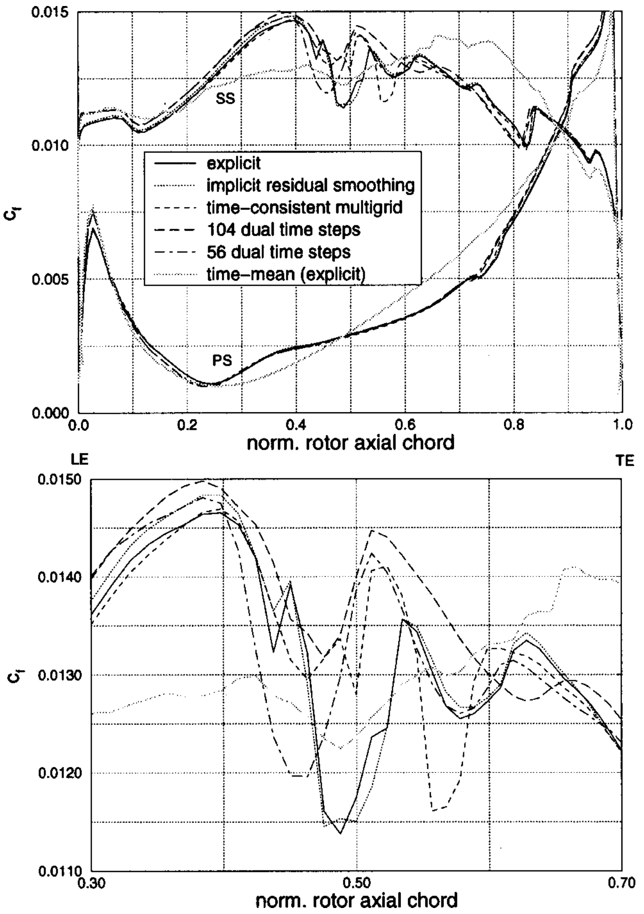

Fig. 12 Comparison of the instantaneous skin friction factor at $t=0$ on the suction side (SS) and the pressure side (PS) of the rotor. The time-averaged skin friction factor from the reference solution is plotted in gray. The enlargement at the bottom shows the region on the suction side where the instantaneous fluctuations are the most pronounced.

On the pressure side, the fluctuation amplitudes are smaller because the wake is convected away from the pressure side due to the negative jet. The local deviation from the time-averaged value at approximately 35 percent axial chord is caused by the stator wake impinging on this position as shown in Fig. 2. As was expected from the time-averaged results, the simulation with implicit residual averaging shows the best agreement also for the time-resolved data. The dual time-stepping calculations show a phase shift of the local minimum on the suction side as can be seen in the enlargement in the lower part of the figure. This time-shift decreases as the number of dual time steps increases. The time-consistent multigrid calculation leads to an even bigger phase shift in the opposite direction. Apart from this region, all calculations except for the calculation with 16 dual time steps are in good agreement with the reference solution.

Different Periodic Boundary Treatment

In industrial applications, unequal pitch ratios are often desired in order to avoid acoustic resonances and noise generation. As mentioned above, all calculations are performed with a time inclination method for the periodic boundary treatment. Using this approach, the exact stage pitch ratio can be modeled while typically only calculating the flowfield in one stator and rotor channel. Many investigators tend to scale the stator or the rotor in order to obtain a pitch ratio of unity (or, e.g., 2:3, 3:4) in order to avoid the problem with the periodic boundaries. In this test case, the blade count ratio is 78:80 and thus very close to unity. It is interesting to investigate the error introduced by such a scaling approach. Therefore, one calculation with 104 dual time steps is performed with a blade count ratio of 80:80 where the stator blades are scaled down by 78:80 while the axial gap between the stator and the rotor remains unchanged.

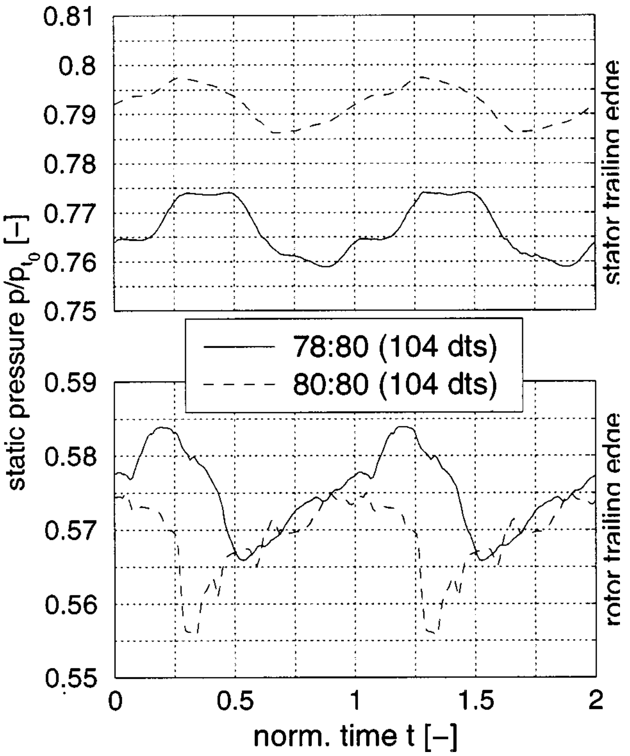

Fig. 13 Unsteady pressure fluctuations one node downstream of the stator trailing edge (top) and one node downstream of the rotor leading edge (bottom) during two blade passing periods

The results are compared with the 104 dual time steps calculation with the real blade count ratio. Since the stator geometry is changed by the scaling, the time-averaged pressure distribution over the stator and also over the rotor deviates from the solution, which simulates the real blade count ratio by up to 3 percent of p_{t0}. It should be noted that the pressure fluctuation amplitudes are underestimated with the 80:80 calculation by more than 20 percent, see Fig. 13. The deviations are especially pronounced on the back section of the stator suction side and the front section of the rotor suction side. The error in time-averaged c_f reaches its maximum at 12 percent chord on the rotor blade and at 7 percent chord on the stator blade. The pressure fluctuations one node downstream of the stator and the rotor differ in shape, amplitude, and phase from the 78:80 calculation, with the phase difference between rotor and stator trailing edge altered by roughly 30 deg.

As for the examination of the different acceleration techniques, the fluctuations are analyzed in the frequency domain. Figure 14 shows the amplitudes of the static pressure harmonics on the rotor.

Although the overall agreement is fairly good, some significant deviations are observed in the first harmonic on the pressure side and over the back section of the suction side. Especially in the first harmonic, it can be perceived that the high-frequency oscillations are underestimated when performing a calculation with unequal pitch ratio. The amplitudes of the harmonics of order three and higher (not plotted) are smaller for the calculation with a blade count ratio of unity due to the fact that only one acoustic frequency exists in the flowfield in this case. For a closer examination of the phase shift, the phase angles of the first harmonic are compared on the stator and the rotor in Fig. 15.

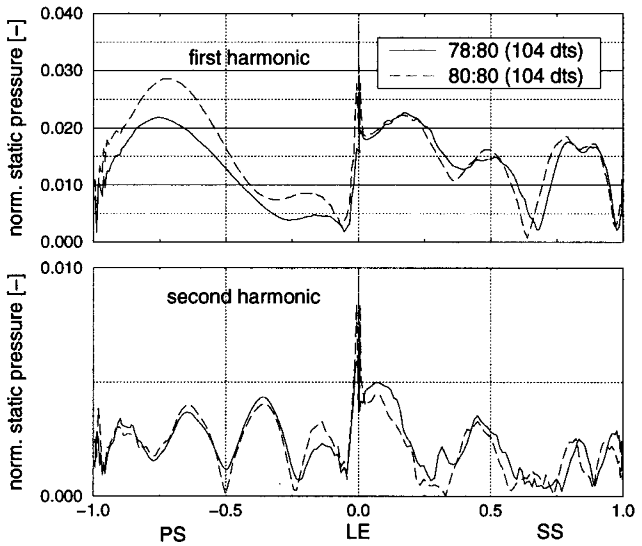

Fig. 14 Pressure amplitudes on the rotor, comparison of the calculation with a blade count ratio of 80:80 with that using the original blade count ratio of 78:80

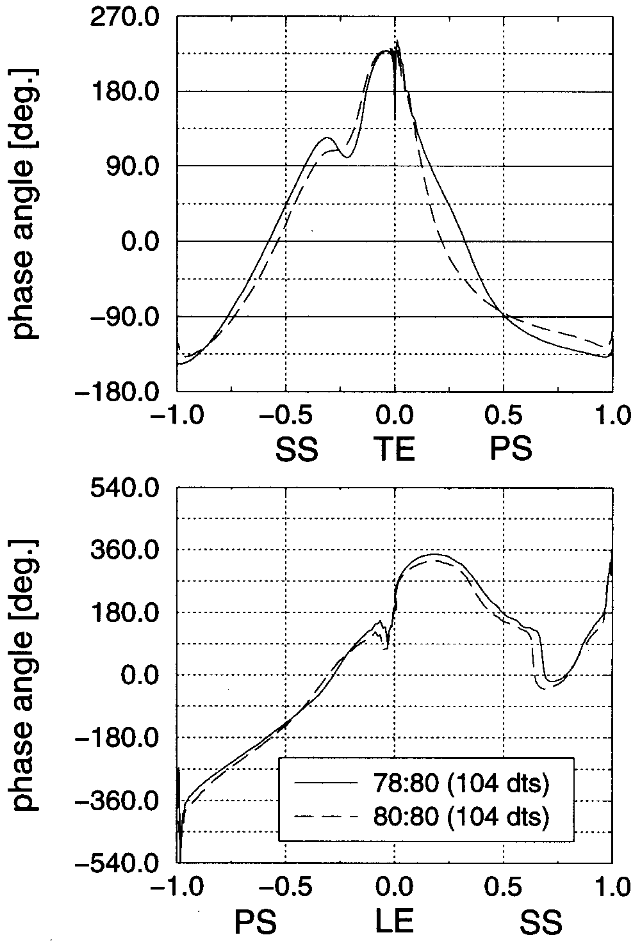

Fig. 15 Phase of the first harmonic on the stator and the rotor, comparison of the calculation with a blade count ratio of 80:80 with that using the original blade count ratio of 78:80. TE: trailing edge, LE: leading edge, PS: pressure side, SS: suction side.

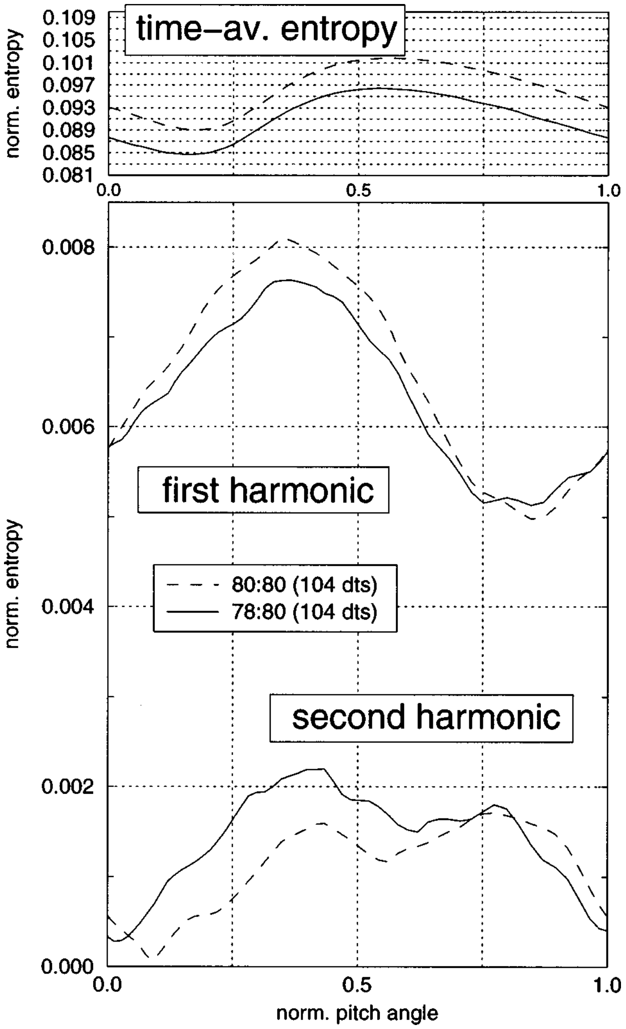

Fig. 16 Entropy distribution in the rotor along a grid line in pitchwise direction (**near the interface**)

Apart from a small region on the stator pressure side where the phase mismatch rises to approximately 60 deg, it remains 20 deg or less on the stator and rotor blades. However, the phase distribution is not simply shifted by a constant amount but also slightly altered in shape. Arnone and Pacciani [19] demonstrated in an extensive study that the stage approximation is clearly deteriorated if the blade pitches are adjusted by more than 1 percent. Since the pitch is adjusted by 2.5 percent in this example, the rather important deviations found agree well with this statement. Additionally, Arnone and Pacciani's results show an increase in amplitude with a better representation of the true blade count ratio as also reported above for this test case. This is caused by the fact that the smaller the greatest common divisor of the blade numbers, the higher the harmonics that interfere, thus causing higher local amplitude peaks. This agrees well with the fact that the amplitudes of the higher harmonics are found to be smaller for a blade count ratio of unity.

By analogy to Figs. 8 and 9, the entropy fluctuations along a pitchwise gridline are compared for the two calculations. In the upper graph of Fig. 16, the time-averaged entropy is depicted in the rotor frame of reference as discussed previously. The entropy level of the 80:80 calculation is higher by 0.04 but the shape of the time-averaged entropy is almost the same. As depicted in the lower part of the figure, however, considerable differences are visible in the amplitude of the first and second harmonic. The average value of the first harmonic is higher at the expense of the

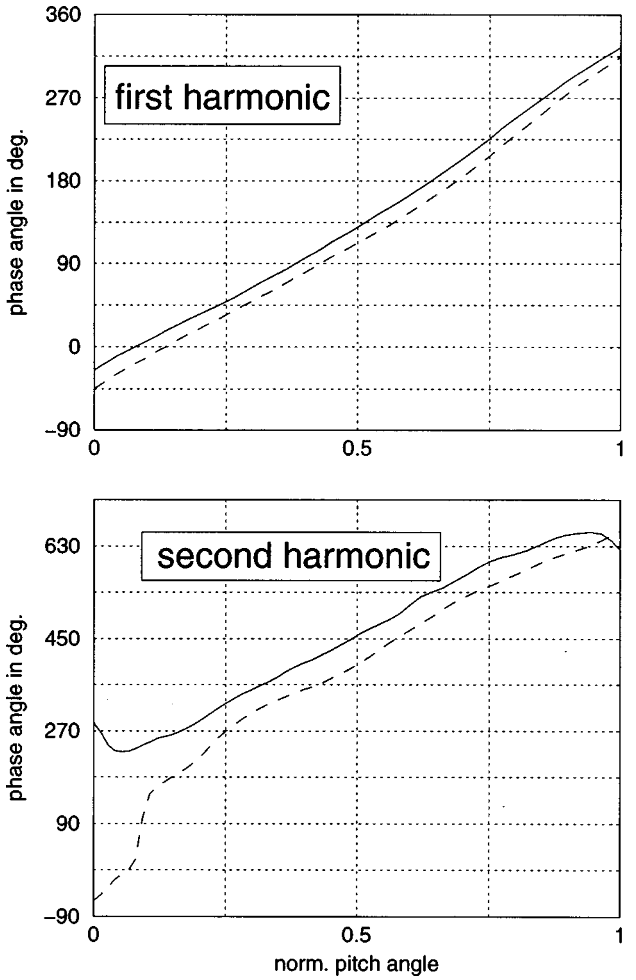

Fig. 17 Phase angle of the first and second entropy harmonic along a gridline in the pitchwise direction (near the interface)

average value of the second harmonic, which is lower. This is a direct effect of the 1:1 periodicity, which does not produce so many high-frequency oscillations as the test case with unequal pitch ratio. Figure 17 shows the phase of the first and second harmonic. While in the first harmonic, an almost constant phase shift is observed, the phase of the second harmonic is also greatly affected in shape by the change in pitch ratio.

Conclusions

Different numerical algorithms, which are used to accelerate unsteady explicit flow solvers, were compared with a purely explicit solution without any acceleration technique.

For the pressure and entropy distributions, with the exception of the calculation with only 16 dual time steps, all calculations showed reasonably good agreement. Explicit calculations with implicit residual smoothing excellently model the boundary layer behavior and can therefore be used for calculations that emphasize on heat transfer or other boundary layer related phenomena. On the other hand, this calculation featured larger deviations when representing the time-resolved flowfield, which is shown for the static pressure fluctuations on the stator and the rotor and the entropy distribution at midspan.

The time-consistent multigrid method proves to model the time-resolved entropy distribution very accurately, but there are some discrepancies in modeling the time-resolved skin friction and the time-resolved pressure distribution on the stator and the rotor blades.

Calculations with dual time-stepping also exhibit some deviations in the skin friction factor distribution on the suction side. The pressure and entropy fluctuations on the stator and rotor blades are modeled sufficiently well by the dual time-stepping calculations, which have the additional advantage to be computationally more efficient for fine grids. However, the number of dual time steps should be larger than the number of grid lines in pitchwise direction in order to correctly model convectional transport.

Periodicity in the higher harmonics of the blade passing frequency as well as pressure fluctuations one grid node downstream of the stator and the rotor have proved to be very sensitive convergence criteria for all algorithms under investigation. For the chosen test case, an implicit dual time-stepping calculation with 104 dual time steps[1] and 25 inner iterations per time step offers the best compromise between computational efficiency and accuracy. It is more than ten times faster than an unaccelerated explicit calculation and will be used for further investigations.

Although a change in the blade count ratio by 2.5 percent does not yield a pronounced change in the general character of the flowfield, an analysis in the frequency domain shows that performance of the calculations with the exact blade count ratio is mandatory in order to represent the pressure fluctuations on the rotor and the stator as well as the time-resolved entropy distribution correctly. Also without modeling the correct pitch ratio, the pressure fluctuation amplitudes in the flowfield may be significantly underestimated. It is therefore reasonable to perform multi-blade-row calculations in turbomachines using the time-inclination method implemented in ITSM3D, which allows the correct blade count ratio to be modeled without significant additional computational effort.

References

[1] Davis, R. L., Shang, T., Buteau, J., and Hi, R. H., 1996, ''Prediction of 3-D Unsteady Flow in Multi-Stage Turbomachinery Using an Implicit Dual Time-Step Approach,'' AIAA Paper No. 96-2565.

[2] Janssen, M., Zimmermann, H., Kopper, F., and Richardson, J., 1995, ''Application of Aero-Engine Technology to Heavy Duty Gas Turbines,'' ASME Paper No. 95-GT-133.

[3] Zeschky, J., and Gallus, H. E., 1993, ''Effects of Stator Wakes and Spanwise Nonuniform Inlet Conditions on the Rotor Flow of an Axial Turbine Stage,'' ASME J. Turbomach., **115**, pp. 128–136.

[4] Merz, R., Krückels, J., Mayer, J. F., and Stetter, H., 1995, ''Computation of Three-Dimensional Viscous Transonic Turbine Stage Flow Including Tip Clearance Effects,'' ASME Paper No. 95-GT-76.

[5] Merz, R., 1998, ''Entwicklung eines Mehrgitterverfahrens zur numerischen Lösung der dreidimensionalen kompressiblen Navier–Stokes Gleichungen für mehrstufige Turbomaschinen,'' Fortschritt-Berichte VDI, Reihe 7—Strömungstechnik, No. 342.

[6] Jung, A. R., Mayer, J. F., and Stetter, H., 1996, ''Simulation of 3D-Unsteady Stator/Rotor Interaction in Turbomachinery Stages of Arbitrary Pitch Ratio,'' ASME Paper No. 96-GT-69.

[7] Walraevens, R. E., Gallus, H. E., Jung, A. R., Mayer, J. F., and Stetter, H., 1998, ''Experimental and Computational Study of the Unsteady Flow in a 1.5 Stage Axial Turbine With Emphasis on the Secondary Flow in the Second Stator,'' ASME Paper No. 98-GT-254.

[8] Merz, R., Meyer, J. F., and Stetter, H., 1997, ''Three-Stage Steam Turbine Flow Analysis Using a Three-Dimensional Navier–Stokes Multigrid Approach,'' 2nd European Conference on Turbomachinery—Fluid Dynamics and Thermodynamics, Antwerpen.

[9] Jameson, A., Schmidt, W., and Turkel, E., 1981, ''Numerical Solutions of the Euler Equations by Finite Volume Methods Using Runge–Kutta Time-Stepping Schemes,'' AIAA Paper No. 81-1259.

[10] Giles, M. B., 1991, ''UNSFLO: A Numerical Method for the Calculation of Unsteady Flow in Turbomachinery,'' GTL Report No. 205, MIT Gas Turbine Laboratory.

[11] Giles, M. B., 1988, ''Non-reflecting Boundary Conditions for the Euler Equations,'' TR 88-1, MIT Computational Fluid Dynamics Laboratory.

[12] Saxer, A. P., 1992, ''A Numerical Analysis of 3-D Inviscid Stator/Rotor Interactions Using Non-reflecting Boundary Conditions,'' GTL Report No. 209, MIT Gas Turbine Laboratory.

[13] Jorgenson, P. C. E., and Chima, R. V., 1989, ''An Unconditionally Stable Runge–Kutta Method for Unsteady Flows,'' AIAA Paper No. 89-0295.

[14] He, L., 1996, ''Time-Marching Calculations of Unsteady Flows, Blade Row Interaction and Flutter,'' von Kármán Institute for Fluid Dynamics, Lecture Series 1996-05, Rhode Saint Genèse, Belgium.

---

[1] That is, approximately 1.8 times the number of grid lines in pitchwise direction.

[15] Jung, A. R., 1997, private notes.
[16] Jameson, A., 1991, ‘‘Time Dependent Calculations Using Multigrid, With Applications to Unsteady Flows Past Airfoils and Wings,’’ AIAA Paper No. 91-1596.
[17] von Hoyningen-Huene, M., and Hermeler, J., 1999, ‘‘Comparison of Three Approaches to Model Stator–Rotor Interaction in the Turbine Front Stage of an Industrial Gas Turbine,’’ Paper No. C 557-18, 3rd European Conference on Turbomachinery—Fluid Dynamics and Thermodynamics, London.
[18] von Hoyningen-Huene, M., and Hermeler, J., 1999, ‘‘Time-Resolved Numerical Analysis of the Aerodynamics in the First Stage of an Industrial Gas Turbine for Different Vane-Blade Spacings,’’ ASME Paper No. 99-GT-102.
[19] Arnone, A., and Pacciani, R., 1996, ‘‘Rotor–Stator Interaction Analysis Using the Navier–Stokes Equations and a Multigrid Method,’’ ASME J. Turbomach., **118**, pp. 679–689.

Numerical and Experimental Study of Unsteady Flow Field and Vibration in Radial Inflow Turbines

T. Kreuz-Ihli
D. Filsinger
A. Schulz
S. Wittig
Lehrstuhl und Institut für Thermische Strömungsmaschinen,
Universität Karlsruhe (TH),
Kaiserstraße 12,
76128 Karlsruhe, Germany

The blades of turbocharger impellers are exposed to unsteady aerodynamic forces, which cause blade vibrations and may lead to failures. An indispensable requirement for a safe design of radial inflow turbines is a detailed knowledge of the exciting forces. Up to now, only a few investigations relating to unsteady aerodynamic forces in radial turbines have been presented. To give a detailed insight into the complex phenomena, a comprehensive research project was initiated at the Institut für Thermische Strömungsmaschinen, at the University of Karlsruhe. A turbocharger test rig was installed in the high-pressure, high-temperature laboratory of the institute. The present paper gives a description of the test rig design and the measuring techniques. The flow field in a vaneless radial inflow turbine was analyzed using laser-Doppler anemometry. First results of unsteady flow field investigations in the turbine scroll and unsteady phase-resolved measurements of the flow field in the turbine rotor will be discussed. Moreover, results from finite element calculations analyzing frequencies and mode shapes are presented. As vibrations in turbines of turbochargers are assumed to be predominantly excited by unsteady aerodynamic forces, a method to predict the actual transient flow in a radial turbine utilizing the commercial Navier–Stokes solver TASCflow3d was developed. Results of the unsteady calculations are presented and comparisons with the measured unsteady flow field are made. As a major result, the excitation effect of the tongue region in a vaneless radial inflow turbine can be demonstrated. [S0889-504X(00)01402-1]

Introduction

Metal fatigue failures in radial inflow turbines, in common with failures in other types of high-speed turbomachinery, are predominantly caused by alternating stress, as a consequence of blade vibration. At present no generally accepted design methodology is available to predict blade vibration and alternating stress in turbochargers. Design work usually concentrates on the calculation of frequencies and stress distribution of particular mode shapes. Consequently, real vibration and stress conditions need to be evaluated by experimental means. Up to now, prediction and understanding of excitation in radial inflow turbines persist in an initial stage. Besides forced vibration due to engine order excitation, aerodynamic excitation and self-exciting mechanisms like flutter, acoustic resonance, and rotating instability may occur in turbomachinery [1]. Alternating forces of self-excited mechanisms are controlled by blade displacements and accompanying velocity changes. As solid turbine blades oscillate with high frequencies and small amplitudes, they are less endangered by self-excitation than, for example, thin flexible compressor blades or lightweight aircraft wings. Blade vibration in radial inflow turbines, therefore, is assumed to be predominantly excited by aerodynamic forces.

Even if we assume steady flow conditions at the entry and exit of a radial turbine, periodically unsteady flows will occur in the turbine casing and in the rotating impeller. The rotating blades pass a flow field that is nonuniform along the circumference. Hence, investigations concerning aerodynamic excitation have to include investigations on transient rotor–stator interactions. The first step in predicting aerodynamically induced vibration is the prediction of the true transient flow interaction in the rotor–stator regime. This leads to a comprehensive approach also concerning turbine performance and, e.g., secondary flows and loss mechanisms in radial inflow turbines. In the present paper a numerical method is used to solve the unsteady flow field in a radial inflow turbine. The exciting forces on the turbine blades, resulting from rotor–stator interactions in the turbine, were calculated for a selected operating point of the turbine.

To understand and predict vibrations of turbine blades, the structural behavior of the turbine rotor has to be examined in detail. Therefore, comprehensive finite element calculations for predicting the eigenfrequencies and the vibrational mode shapes were carried out in the course of this study. The last step in predicting aerodynamically forced vibration is the coupling of the flow field calculations, which provide the exciting forces and loadings and the structural calculations.

Experimental Investigations

A turbocharger test rig was designed and installed in the high-pressure, high-temperature laboratory of the institute. The experimental investigation was carried out at a ZR 140 type turbocharger of the Motoren und Turbinen-Union, Friedrichshafen, due to the conformance of its design parameters and the parameters of the experimental plant. The radial inflow turbine has a 130-mm-dia turbine wheel (Fig. 1) and a vaneless turbine casing with circular cross section. It can be operated up to a turbine inlet temperature of 1020 K. The maximum mass flow rate is 1 kg/s at a pressure ratio of 3.5.

As preheated compressed air is used for running the turbocharger, laser optical investigations of the flow field in the turbine scroll as well as in the impeller can be performed. The compressor of the turbocharger acts as a break controlled by throttling at the inlet and outlet. Using a surge tank, undisturbed incoming flow is attained.

Contributed by the International Gas Turbine Institute and presented at the 44th International Gas Turbine and Aeroengine Congress and Exhibition, Indianapolis, Indiana, June 7–10, 1999. Manuscript received by the International Gas Turbine Institute February 1999. Paper No. 99-GT-341. Review Chair: D. C. Wisler.

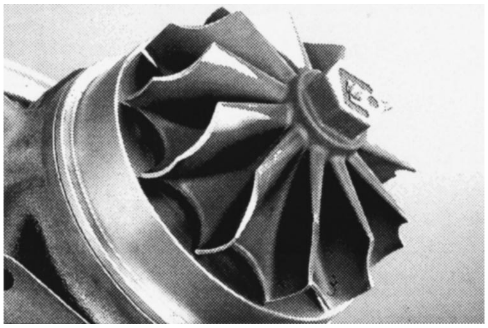

Fig. 1 Turbine rotor of the MTU ZR140

The test rig is equipped with conventional instrumentation to monitor the working conditions of compressor and turbine, respectively. Total temperatures and pressures at the inlet and outlet of compressor and turbine are measured using pitot probes. The air flow rates in both components of the turbocharger are measured using calibrated flat plate orifices. The rotational speed can be measured by using either a magnetic pickup and a magnetized washer on the compressor end of the shaft or a special miniature reflex light barrier mounted on the back of the compressor rotor. Both measurement methods showed negligible deviation. The conventional data acquisition is controlled by a PC using graphic programming software. The characteristic lines of compressor and turbine were measured by variation of the turbine inlet conditions and by throttling the exit of the compressor.

Flow Field Measurements. Flow field measurements in previous studies have proven that laser-Doppler anemometry is well suited for flow mapping in complex geometries and rotating applications (see, e.g., [2,3]). Hence this measuring method was chosen for the present study of the flow field in the radial turbine.

To quantify the three-dimensional unsteady flow field in the volute casing and the exit of the radial turbine, optical access has to be provided. Therefore, the turbine casing was windowed in four meridional planes, including the tongue region (Figs. 2 and 3). At the exit, the axial and circumferential components of velocity are detected through a quartz glass cylinder (Fig. 4). The cylinder is spring loaded to the radial turbine in the axial direction. To avoid expenditure for calibrating of the optical system, the turbine scroll can be rotated to various measuring planes. This is attained by aligning the turbocharger axis and the axis of the outer flanges of the test rig (Fig. 5).

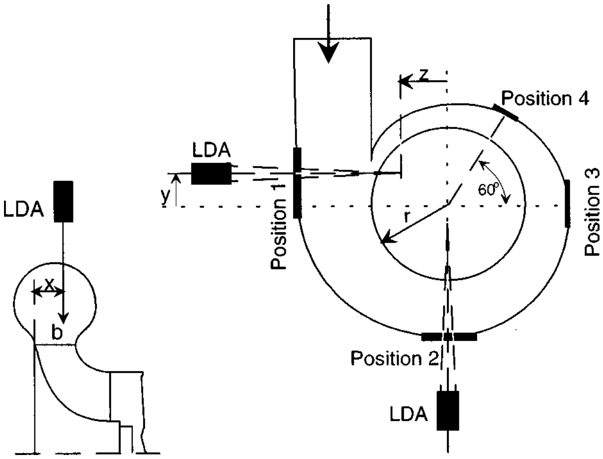

Fig. 2 Schematic of the measuring positions

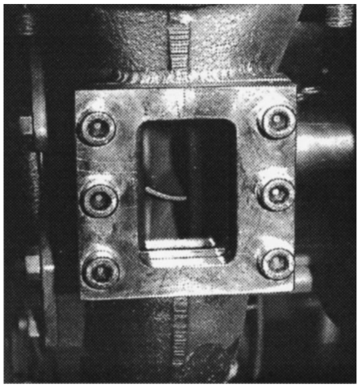

Fig. 3 Measuring window in the turbine scroll

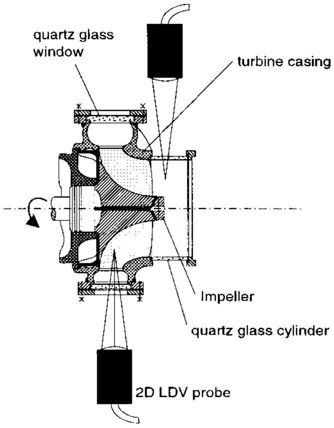

Fig. 4 Schematic of turbine instrumentation

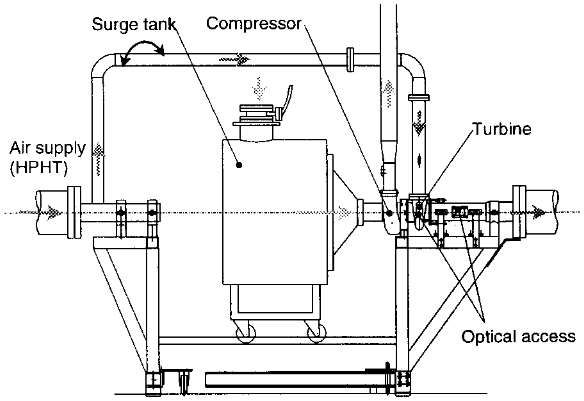

Fig. 5 Turbocharger test rig

To measure the flow velocities, a three-component fiber-optic LDA system from Dantec is used. The LDA comprises a 4 W argon-ion laser in multimode operation, a standard X-optics with 40 MHz Bragg cell, color and beam separators and a one-dimensional and a two-dimensional fiber probe. The signals are detected by a photomultiplier setup in combination with counter-processors. To obtain the time and impeller position dependent velocity distribution, the angular position of the rotor is measured. A trigger signal is detected and recorded simultaneously to the continuously recorded burst signals. Because of the high rotational speed of up to 70,000 rpm and a required high angular resolution, a special miniature reflex light barrier is used to generate a well-defined trigger pulse every shaft revolution. The trigger is used to calculate the angular position of the impeller with respect to the burst signals. By postprocessing, a statistical evaluation of all obtained burst signals corresponding to a discrete angular position in the rotating frame of reference is performed.

A commercial particle generator was used to seed the gas flow in the turbine with oil droplets with a mean diameter of 1 μm. As the oil vaporizes at higher temperatures, unheated air with a temperature of 288 K at the turbine inlet was used for the laser optical measurements. To avoid freezing at the outlet of the turbine, a moderate pressure ratio was chosen. All experimental results presented in this paper were obtained while the turbine was running at a rotational speed of 25,000 rpm. The working conditions are characterized by a pressure ratio of 1.4, total turbine inlet temperature of 288 K, a mass flow rate of 0.38 kg/s, and a total to total efficiency of 67 percent. The inlet loading coefficient was about 0.95; accordingly, the flow enters the turbine rotor in an almost radial direction. This working point represents a typical part load condition and allows investigation of the unsteady flow phenomena.

Additionally, experimental data are essential to verify the unsteady calculations of the flow field in the turbine including volute, impeller, and exhaust channel. Promising that agreement is satisfying, varying operating conditions can be examined by numerical means more efficiently.

Experimental Results. The axial and circumferential components of the flow in the turbine casing were measured in the four measuring positions by use of a two-dimensional laser-Doppler anemometer probe. As the larger window at position 1 allowed use of an additional one-dimensional probe, which was angled to the two-dimensional probe by 20 deg, the three components of the velocity could be measured simultaneously at this position. While the axial position of the probes was fixed, the probes were moved step by step in the radial direction up to the position where the reflections of the passing blades became dominant. To reduce the reflection, the turbine rotor was colored black. At each radial step about 56,000 bursts were sampled to allow a phase-resolved statistical evaluation. Therefore, a special evaluation software was generated. In Figs. 6–9 the time-dependent circumferential and axial velocities are shown with the corresponding position of the turbine blades, which are indicated with pressure side (PS) and suction side (SS). Due to the effect of the passing turbine rotor, the flow field in the turbine scroll shows periodic fluctuations. Its frequency is calculated by multiplying the blade number with the rotational frequency.

The circumferential component of the velocity in the turbine scroll (Figs. 6 and 7) shows only slight dependence on the x/b position. Next to the hub, the circumferential velocity is reduced. Close to the rotor, the influence of the rotating turbine rotor becomes more distinct. In the area above the blades the circumferential velocity of the flow is almost equal to the blade velocity (175 m/s), which is higher than the circumferential velocity of the gas entering the rotor in the middle of the blade channels. Examining the circumferential velocities at the four different measuring positions, a slight reduction was detected from position one to four. The axial component of velocity decreases with distance from the hub. The flow entering the rotor near the shroud is slightly skewed in the axial direction, following the contour of the turbine casing.

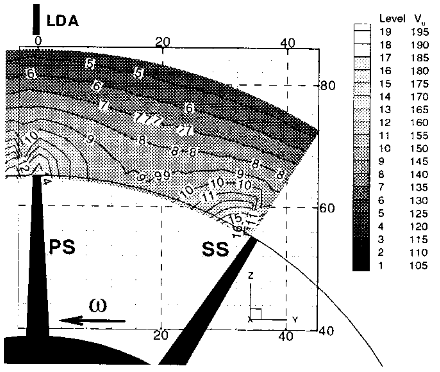

Fig. 7 Position 3, $x/b=0.8$, circumferential velocity (m/s)

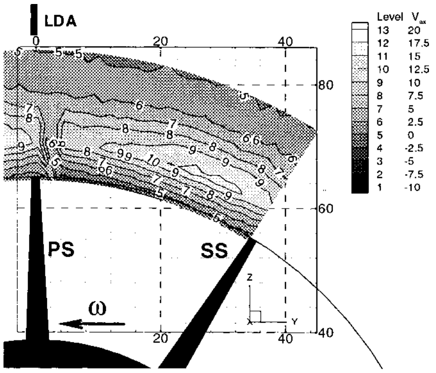

Fig. 8 Position 3, $x/b=0.2$, axial velocity (m/s)

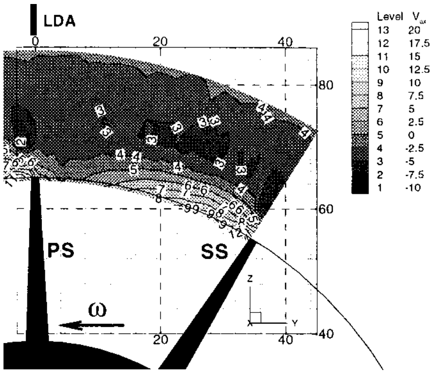

Fig. 9 Position 3, $x/b=0.8$, axial velocity (m/s)

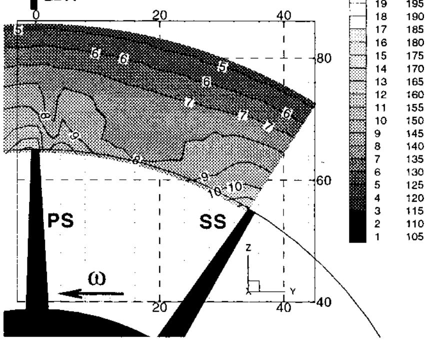

Fig. 6 Position 3, $x/b=0.2$, circumferential velocity (m/s)

The measurements within the impeller were carried out analogously to the measurements in the turbine scroll. The measuring volume was moved by steps of 2–3 mm into the rotating turbine rotor. Single bursts were detected until a sufficient number (56,000 validated bursts) was sampled, to allow a phase-resolved evaluation. Every velocity datum was assigned to the corresponding location in the turbine rotor. For that purpose, the distance between two blades was divided in angular steps of one degree.

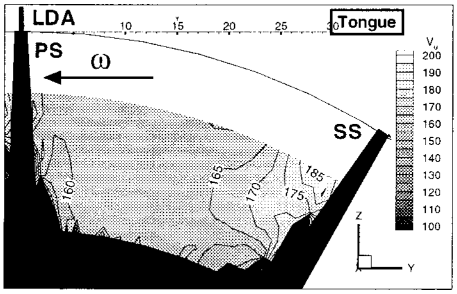

Fig. 10 Position 1, circumferential velocity, $x/b=0.5$, $y/r=0$

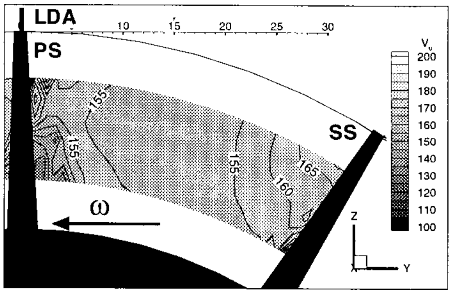

Fig. 12 Position 3, circumferential velocity, impeller, $x/b=0.2$

The bursts according to a one degree area in the rotor were statistically evaluated. Further details of the phase resolved evaluation are given in Jakoby et al. [3].

Analyzing the circumferential velocities at the four different measuring positions, conformity was detected for positions 2 to 4. The velocities gained at position 1 differed noticeably from the other values. The same effect was detected by analyzing the axial velocity. The reason for this discrepancy is obviously the influence of the tongue region (position 1). To analyze the tongue effect in more detail, the probe volume of the laser-Doppler anemometer system was moved step by step closer to the tongue. As a consequence, the two-dimensional laser-Doppler anemometer probe detected the axial velocity and the velocity component whose direction is indicated in the graphs by the omega arrow. The latter component almost equals the circumferential velocity, allowing qualitative analyses of the tongue influence on the circumferential velocity. In Figs. 10 and 11 the measured velocities at varying distances from the tongue are shown. Obviously the velocity decreases the closer the measuring position is moved to the tongue. From this, a high-pressure field in the tongue region can be deducted. Taking into account that the turbine blades are passing this high-pressure area periodically, the exciting effect of the tongue becomes evident. More detailed discussion of the excitation effect detected is given in the numerical results section.

In addition to the blade midheight position, two further x/b positions were investigated (Figs. 12–15). Analyzing the circumferential velocity in the turbine rotor, the highest values were detected next to the hub. The circumferential velocity decreases from the hub to the shroud (Figs. 12 and 13), while the axial velocity increases from the hub to the shroud (Figs. 14 and 15). Obviously, the flow at the shroud area is deflected earlier into axial direction than the flow at the hub. This effect is more pronounced on the suction side than on the pressure side of the blades. As expected, the flow velocities on the suction side are higher than the velocities on the pressure side. This is due to the blade geometry and the acceleration of the flow along the suction side, resulting in a pressure difference across the blades.

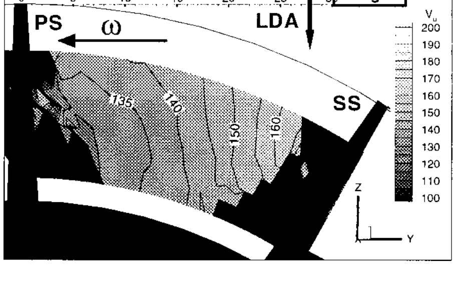

Fig. 11 Position 1, circumferential velocity, $x/b=0.5$, $y/r=0.38$

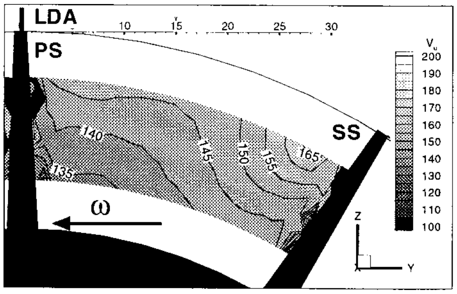

Fig. 13 Position 3, circumferential velocity, impeller, $x/b=0.8$

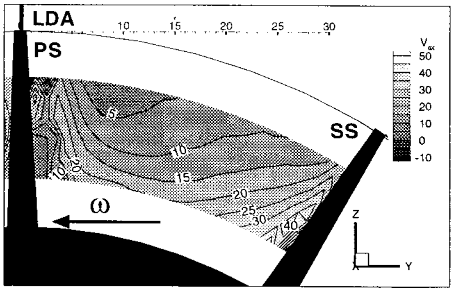

Fig. 14 Position 3, axial velocity, impeller, $x/b=0.2$

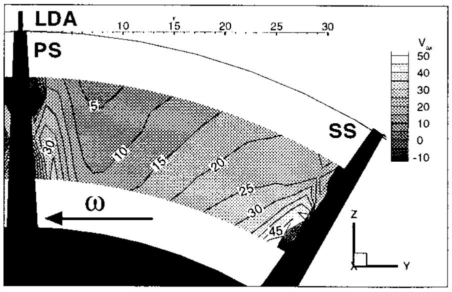

Fig. 15 Position 3, axial velocity, impeller, $x/b=0.8$

Unsteady Flow Field Calculations

A method for simulating unsteady flow while the rotor grid is moved relative to the stator grid was developed. As basis for this work, the commercial Navier–Stokes solver TASCflow3D was used. The code is appropriate for analysis in rotating machinery applications since it uses multiple frames of reference. The unsteady calculation was attained by use of external UNIX scripts, controlling the calculation and the movements of the grids.

Flow Solver. The three-dimensional Reynolds-averaged Navier–Stokes equations are solved in a strong conservative form. The primitive variables, pressure, and Cartesian velocity components in stationary and rotating coordinate system are solved by use of a colocated variable arrangement. Using a finite volume method, the transport equations are discretized. Turbulence is modeled using the standard $k-\varepsilon$ turbulence model. For the determination of the near-wall velocities, the logarithmic wall function is used. The advection terms are represented by a second-order discretization scheme, namely the Mass-Weighted Scheme (MWS) or the Linear Profile Scheme (LPS), combined with physical advection correction terms. An algebraic multigrid method is used, employing coupled solution of mass and momentum equations. The energy equation is solved and the equation of state is solved using the ideal gas law.

Numerical Procedure. Since a turbocharger with a common vaneless turbine casing is examined, spatial periodicity cannot be used to limit the analysis to a single blade passage. Circumferential nonuniformity occurs in the whole turbine scroll. Exciting forces on the turbine blades are due to the unsteady flow in the impeller that is interacting with the unsteady flow in the turbine scroll. Hence, a coincident simulation of the complete unsteady flow field of the whole rotor–stator configuration has to be performed. While executing the CFD analysis, the rotor grid has to be moved relative to the stator grid and local flow quantities have to be transported across the interface. This is attained by successively executing the CFD analysis for single discrete angle time increments. After each physical time step, the rotor grid is turned an angle corresponding to the physical time step. The unsteady coupled rotor–stator simulation described is the only possibility to simulate the real unsteady flow phenomena in turbomachinery, such as the propagation of the wake of the tongue within the rotating impeller.

Solving the Navier–Stokes equations in the rotating frame of reference, additional source terms including Coriolis and centrifugal forces have to be considered [4]. To analyze the coupled rotor–stator configuration, an interface between rotating and fixed components has to be defined. In the present work, neither averaging in the circumferential direction (stage interface of TASCflow3D), nor a permanent attachment between the rotor and stator grids (frozen rotor interface of TASCflow3D) can be applied. For a short instant in time, however, a connection across the interface between turbine scroll and impeller can be made. Therefore, for every time step a new ‘‘frozen rotor interface’’ is defined. For the period of a time step, the interface appears as a steady-state condition to the components on each side of the interface. The numerical procedure described can be considered as a series of snapshots leading to a transient simulation. Numerical details of the standard interface options of TASCflow3D are described in Galpin et al. [5].

To avoid divergence instantly occurring in the transient CFD analysis, an accurate initial guess is essential. It was ascertained that the solution for the attached rotor–stator configuration without rotation has to be computed first. The transient rotating analysis starts with this solution and a low rotational speed. The final result of the first physical time step is used as start solution of the second time step. Before the rotational speed is slightly increased, various time-angle steps have to be executed. This procedure is repeated until the final rotating speed is reached. Dependent on final speed and complexity of the numerical problem, a couple of full rotations of the rotor may be necessary. After reaching the final speed, the transient simulation is carried on until a quasi-stationary, periodically unsteady flow is detected. Consequently, this method leads to the time and angle resolved flow solution of the simultaneous analysis of both stationary and rotating components.

The numerical procedure means expandable expenditure for the user, which was reduced by generating UNIX shell scripts for the automatic preparation of the boundary files for the discrete rotor steps and execution of the unsteady CFD analysis. Additionally, the numerical acceleration process was performed self-acting.

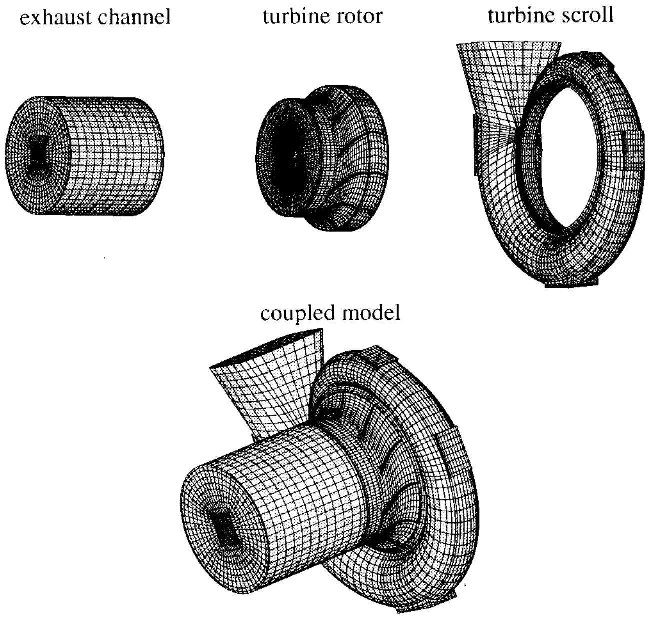

Fig. 16 Numerical model of the radial inflow turbine

Geometry and Boundary Conditions. Unsteady CFD analyses were performed for the radial inflow turbine of the MTU ZR140 turbocharger (Fig. 4). In addition to the whole turbine rotor, the turbine scroll and the exhaust channel were modeled using structured grids. The grid design deals with a refinement in the tongue region. For a first approach a coarse grid of the numerical model was generated (about 100,000 nodes), to keep the calculation time within acceptable limits and to limit the required computing memory. The grid may be too coarse to resolve the boundary regions, but it was assumed that the major effects influencing the pressure distributions on the turbine blades are invoked by the mainflow.

The three grids for scroll, rotor, and exhaust channel (Fig. 16) were coupled using the Generalized Grid Interface (GGI) of TASCflow3D and the frozen rotor interface boundary condition in particular. Hence, the grid of the whole turbine has two interfaces of the type described. The three measuring windows were also modeled in the numerical model to allow for a verification of the numerical method by comparisons with the experimental results. The boundary conditions were specified using experimental data. At the inlet a total pressure of 1.4 bar and a total temperature of 288 K were specified, assuming uniform flow direction. At the exit of the exhaust channel a static pressure of 1 bar was specified. All walls were modeled using a logarithmic wall function. Turbulence was modeled by means of the standard $k-\varepsilon$ model. Compressible air flow was assumed. The final rotor speed was 25,000 rpm.

Comparisons With Experimental Results. For the first unsteady flow field calculations, the verification of the numerical method was crucial. After carrying out an unsteady calculation, for every time step a solution of the whole flow field exists. In contrast the LDA measurements show the time and impeller angle dependent flow field at one special location in the turbine.

For reasons of comparison, the numerical results are shown in the same manner as the LDA results. Therefore, the flow velocities at one special location in the grid, representing the LDA measuring volume, were extracted from the result files of the different time steps. As angle steps of 5 deg were chosen, the resulting

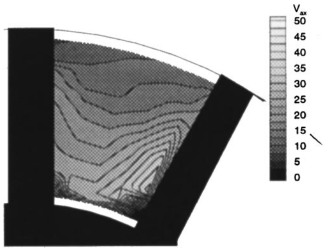

Fig. 17 Position 3, calculated axial velocity

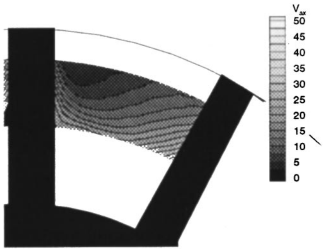

Fig. 18 Position 3, measured axial velocity

graphs show a coarser angular resolution (Figs. 17 and 18). Nevertheless, the comparisons revealed good agreement of the velocities and their gradients. Highest deviation was detected at a position in window 1, where calculated circumferential velocities were about 10 percent lower than measured ones. In summary, the unsteady flow field calculation showed good agreement with the measured values. It is assumed that the results can be improved by refining the grid and by choosing smaller angle and time steps for the unsteady flow calculations, leading, however, to extraordinarily high computing times and demands on memory.

Results of the CFD Analysis. A transient frozen rotor analysis was performed using the described numerical procedure. The rotational speed was increased in 12 steps to the final speed of 25,000 rpm. In total the rotor was turned two full revolutions. Using a serial node of the parallel computer IBM RS/6000 SP of the Universität Karlsruhe, the cumulative CPU time was about 160 hours. Every time step required 13 iterations on the average to converge. Angle steps chosen were 5 deg and physical time steps were given as a function of the rotor speed.

A periodically unsteady flow was detected. From a stationary point of view, the flow oscillates with every turbine passage. Rotating with a turbine blade, the inflow oscillates with the rotational frequency. The time-dependent pressures on the turbine blades were analyzed. As observed with the LDA, a high-pressure area was detected in the tongue region (Fig. 19). The suction side of the blade enters the high-pressure field before the pressure side is influenced by the tongue region, which leads to an unloading of the blade in the tongue region. This is the major reason for the excitation of the blades. At the entry of the rotor even the sign of the loading changes with the consequence of extremely oscillating blade loads (Figs. 20–22).

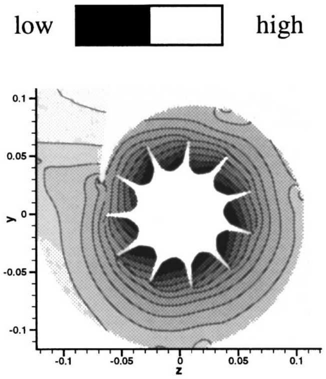

Fig. 19 Static pressure in the turbine (cross section)

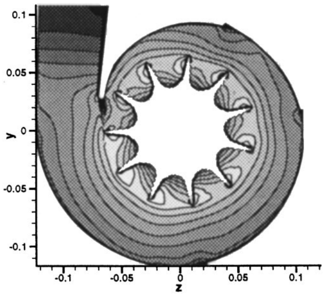

Fig. 20 Turbine Mach number (cross section)

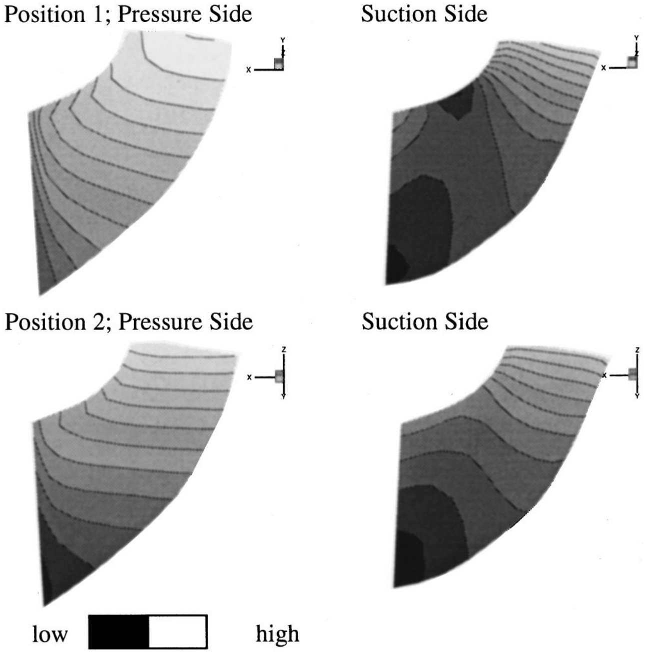

Fig. 21 Pressure distribution on a turbine blade at different positions in the turbine scroll

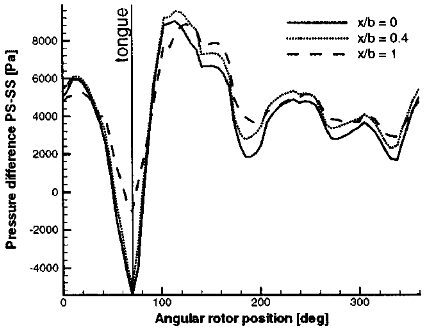

Fig. 22 Pressure difference (pressure-suction side) at three locations on the leading edge versus blade position in the turbine scroll

To verify the calculated pressure distributions on the blades, the resulting torque and power output of the turbine were analyzed.

The difference in the calculated power output, taking the calculated unsteady pressure distribution on the blades into account, and the power output gained from measured thermodynamic was below 5 percent. This, in summary, shows that calculation of the time-dependent pressures on the turbine blades provides reliable results. The excitation effect of the tongue in a radial inflow turbine could be clearly demonstrated.

Structural Analysis

In completion to the CFD analyses and the experimental investigations, finite element analyses were performed to obtain the structure's vibration behavior. The three-dimensional model used for the calculations is shown in Fig. 23. On the left a symmetric segment of the turbocharger rotor is shown. The complete rotor is shown on the right. The finite element grids mainly consist of hexahedral 20-node elements. All calculations were performed using the finite element code ABAQUS by McNeal–Schwendler.

At first, a modal eigenvalue extraction for the determination of the single blade's natural frequencies was performed to learn about the corresponding mode shapes. For this eigenfrequency extraction all displacement degrees of freedom of the nodes on the symmetry planes were restrained. Certainly, this leads to an overestimation of the structure's stiffness, but still predicts the shape of the oscillating blades accurately. Figure 24 illustrates the deformation plots of the first two modes. Due to the high eigenfrequencies of the turbine blades, these modes are assumed to be most relevant, being possibly excited by unsteady aerodynamic forces appearing in the turbine scroll.

In the next step, an eigenfrequency calculation for the entire rotor at rest was performed. To get independence from the rotor support and bearing, the displacement degrees of freedom of the nodes on the rotor axis were fixed for all calculations presented.

Since this study concentrates on turbocharger blade vibrations only, which are highly relevant for damage caused by high cycle fatigue, mode shapes of the spool are not considered. For reason of brevity, the results in Fig. 25 contain only the mode shapes with blades oscillating in mode 1. Corresponding to the number of blades, 11 different mode shapes are detected. The different modes of the entire system can be distinguished by the number of oscillating blades, in-phase or out-of-phase vibrations, and the magnitude of the single blade's deformation. In Fig. 25, arrows with their thickness and direction for each blade indicate the magnitude of deformation and in-phase or out-of-phase vibration, respectively.

There are eight remarkable mode shapes (*iii*–*ix*) in a narrow frequency band with a width of about 100 Hz in which the spool stands motionless and only blade vibrations are observed. These mode shapes are independent from the rotor's support. Pictures (*i*) and (*ii*) in Fig. 25 show modes in which the blades are divided half and half considering the phase of the vibrations. In (*xi*) all blades oscillate in-phase. The implementation of further analyses with varying boundary conditions revealed that the exact values of these frequencies (*i*, *ii*, and *xi*) is dependent on the rotor's support. The vibration behavior of the spool has repercussions on the rotor.

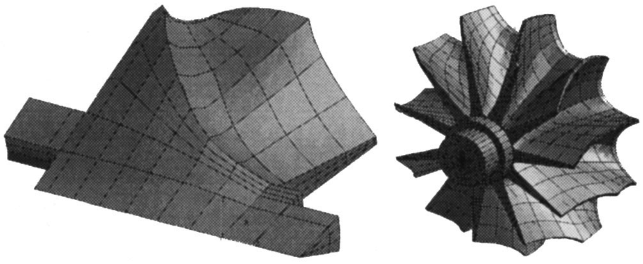

Fig. 23 Finite element models for the modal analysis; left: rotor segment; right: full rotor

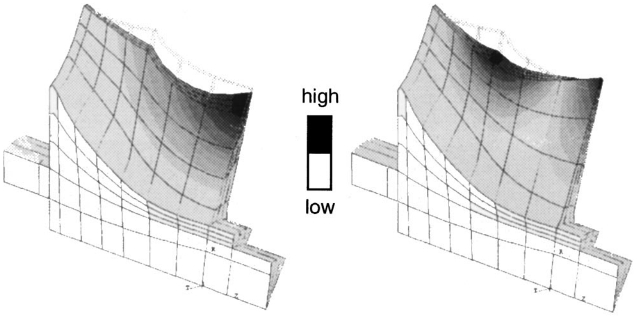

Fig. 24 Deformation plots of the first two modes at 10,005 Hz mode 1 (left) and 16,278 Hz mode 2 (right) for the single blade

It is always favorable to deal with small finite element models, which are more economical with computing memory and computing time. Therefore, to test the suitability of the much smaller symmetric model of the rotor segment, an eigenfrequency calculation was performed. Cyclic and symmetric boundary conditions on the symmetry planes were assumed. The model can reveals the mode shown in Fig. 25, picture (*xi*). In this frequency mode all blades oscillate in-phase. As mentioned before, the support of the rotor has an influence on the calculated frequency value.

Apparently, only in that case are cyclic boundary conditions valid, and this is the only mode that can be detected with the more simple and computationally inexpensive finite element model. Hence, to obtain all mode shapes of the turbocharger rotor, the entire structure has to be modeled and analyzed. This is due to the fact that the oscillating blades do not stand alone but are coupled to the surrounding structure. The surrounding structure, primarily the hub, shows its own vibration behavior and depending on that behavior the blades are either excited or at rest. This strong influence, which is even more pronounced for thin structures like compressor rotors [6], leads to the documented 11 mode shapes in Fig. 25.

The coupled vibration modes of the blade–disk (hub) system can be characterized by node lines lying along the diameter of the rotor and having a constant angular spacing. The maximum number of nodal diameters ND can be calculated with the knowledge of the number of blades n: $\mathrm{ND}=n/2$ (for an odd number of blades

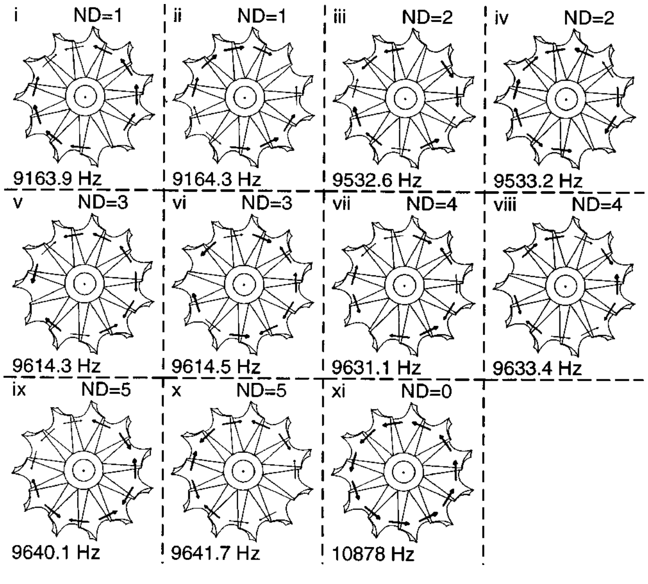

Fig. 25 Calculated rotor eigenmodes, blades oscillate in mode 1

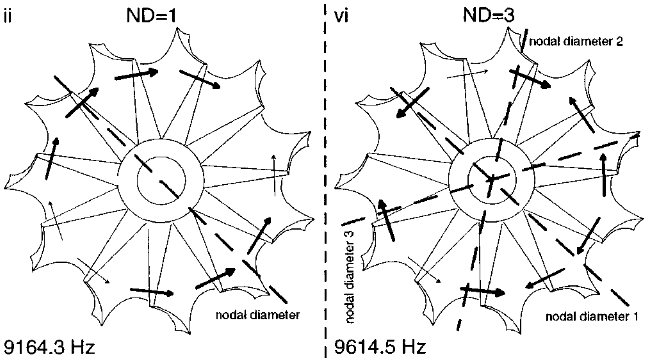

Fig. 26 Diametric modes; left: one nodal diameter; right: three nodal diameters

n is reduced by one). This leads to five diametric modes, which appear in pairs with orthogonal mode shapes. In Fig. 25 the number of nodal diameters is given to identify the diametric modes.

As an example, Fig. 26 illustrates the node lines of two selected mode shapes. The left picture shows one of the one-nodal-diameter modes, the right picture a three-nodal-diameter mode. In the latter there are three node lines intersecting at the center of the disk with an angular spacing of 60 deg between adjacent node lines. The blades close to the nodal points on the disk do experience maximum excitation, whereas the blades at the antinodes are much less excited or stand still.

Summary and Outlook

A new turbocharger test rig has been designed and built at the Institut für Thermische Strömungsmaschinen. The features of the test rig as well as its instrumentation and the measuring techniques applied are described. Laser-Doppler velocimeter measurements were carried out in the turbine scroll and in the turbine rotor. Another main emphasis of this study was to develop a method to predict exciting forces and vibration in radial turbines, particularly in turbochargers with vaneless turbine scrolls. A numerical procedure to predict the true transient interaction of casing and impeller was presented. Besides its importance in predicting blade vibration, the simultaneous transient analysis of both stationary and rotating components is an important tool to optimize flow conditions and efficiency of radial turbines. Analyzing the time-dependent pressure distributions on the turbine blades, the excitation effect of the tongue region in a radial inflow turbine with vaneless turbine casing could be shown. The finite element calculations presented illustrate the expected vibration behavior of the turbine rotor.

A detailed load analysis has not yet been performed, since the exact amplitudes of the vibrations have to be determined first. They are strongly influenced by the exciting forces and pressure distributions on the blade's surfaces. Their values will be determined by detailed CFD analyses described previously. When available, these data will be included into the finite element analysis as boundary conditions. Finally, the numerical calculations have to be validated by a comparison with experimental vibration measurements. In the course of this project an approach to these ambitious goals will be given.

Acknowledgments

The research work described in this paper is funded by the Forschungsvereinigung Verbrennungskraftmaschinen e. V. (FVV). The authors wish to express their gratitude to the partners involved in the project for this support and to Dr. Schmid from MTU Friedrichshafen, who coordinates the project.

References

[1] Baumgartner, M., Kameier, F., and Hourmouziadis, J., 1995, ''Non-Engine Order Blade Vibration in a High Pressure Compressor,'' ISABE Paper No. 95-7094.
[2] Malak, M. F., Hamed, A., and Tabakoff, W., 1987, ''Three-Dimensional Flow Field Measurements in a Radial Inflow Turbine Scroll Using LDV,'' ASME J. Turbomach., **109**, pp. 163–169.
[3] Jakoby, R., Benz, E., Willmann, M., and Wittig, S., 1994, ''Phase Resolved LDV-Measurements in High-Speed Rotating Disk Systems With Orifices,'' presented at the 5th International Symposium on Transport Phenomena and Dynamics of Rotating Machinery (ISROMAC-5), May 8–11, Maui, HI.
[4] Wittig, S., Kim, S., Scherer, T., and Weissert, I., 1996, ''Numerical Study for Optimising Heat Transfer in High Speed Rotating Components,'' *Proc. International Symposium on Transport Phenomena of Rotating Machinery*, **2**, pp. 460–469.
[5] Galpin, P. F., Broberg, R. B., and Hutchinson, B. R., 1996, ''Three-Dimensional Navier–Stokes Predictions of Steady State Rotor/Stator Interaction With Pitch Change,'' presented at the Third Annual Conference of the CFD Society of Canada, Banff, Canada.
[6] Hagelstein, D., Hasemann, H., and Rautenberg, J., 1997, ''Coupled Vibration of Unshrouded Centrifugal Compressor Impellers: Part II—Computation of Vibration Behaviour,'' *Proc. 7th International Symposium on Transport Phenomena and Dynamics of Rotation Machinery (ISROMAC-7)*, pp. 1306–1317.

Flowfield Measurements for a Highly Turbulent Flow in a Stator Vane Passage

R. W. Radomsky[1]
K. A. Thole
Mechanical Engineering Department,
Virginia Polytechnic Institute
and State University,
Blacksburg, VA 24061

Turbine vanes experience high convective surface heat transfer as a consequence of the turbulent flow exiting the combustor. Before improvements to vane heat transfer predictions through boundary layer calculations can be made, we need to understand how the turbulent flow in the inviscid region of the passage reacts as it passes between two adjacent turbine vanes. In this study, a scaled-up turbine vane geometry was used in a low-speed wind tunnel simulation. The test section included a central airfoil with two adjacent vanes. To generate the 20 percent turbulence levels at the entrance to the cascade, which simulates levels exiting the combustor, an active grid was used. Three-component laser-Doppler velocimeter measurements of the mean and fluctuating quantities were measured in a plane at the vane midspan. Coincident velocity measurements were made to quantify Reynolds shear stress and correlation coefficients. The energy spectra and length scales were also measured to give a complete set of inlet boundary conditions that can be used for numerical simulations. The results show that the turbulent kinetic energy throughout the inviscid region remained relatively high. The surface heat transfer measurements indicated high augmentation near the leading edge as well as the pressure side of the vane as a result of the elevated turbulence levels.
[S0889-504X(00)02302-3]

Introduction

High heat transfer augmentations on a turbine blade due to the turbulence levels exiting the combustor continue to be a topic of concern for the gas turbine industry. With this concern comes the need to develop a fundamental understanding of how the highly turbulent flow convects through the turbine vane passage. The turbulence characteristics in the inviscid flow region of the turbine vane passage are typically needed as a boundary condition for boundary layer calculations. Also, when performing a full Navier–Stokes CFD simulation, one of the first benchmarks needed for the various turbulence models is a comparison of the turbulence predictions in the passage.

This paper presents mean and turbulent flowfield measurements in the inviscid region of the turbine airfoil for both a low (baseline) and a highly turbulent flowfield. Several studies presented in the past have measured two of the three velocity components with rms levels in a scarce number of locations in a turbine vane passage. In this study, all three fluctuating velocities were measured to quantify the turbulent kinetic energy variation in the turbine vane passage. Coincident streamwise and cross-pitch velocities were measured to quantify Reynolds shear stress. Energy spectra of the fluctuating velocities were computed to give length scales and estimates of the dissipation at the entrance to the turbine vane. These measurements provide an understanding of the variation of the turbulence throughout the passage as well as a complete set of inlet boundary conditions necessary for a numerical simulation.

Past Studies

There have been a few studies documenting turbulence levels exiting the combustor. Kuotmos and McGuirk [1] measured mean and fluctuating velocity profiles in a can-type combustion chamber and reported local axial turbulence levels up to 30 percent at the exit of the combustor. Moss [2] also measured turbulence levels exiting a variety of gas turbine combustors and reported turbulence levels of 9 percent with a typical length scale being between 5 to 7 mm. Ames [3] studied turbulence levels exiting a scaled-up, two-dimensional representation of an annular combustor and reported turbulence levels as high as 13 percent with a length scale to pitch ratio of $\Lambda_x/P=0.13$.

The characteristics of the turbulent field convecting through the passage have not been completely documented at this time. Bailey [4], Priddy and Bayley [5], Ames [6], Bangert et al. [7], and Radomsky and Thole [8] all reported measurements of some turbulence components inside the turbine vane passage. All of these studies reported that there is a decrease in the streamwise fluctuations in the inviscid region as the flow accelerates along the suction side of the vane. Along the pressure side of the vane, Priddy and Bayley [5] reported streamwise fluctuations that remained nominally constant. Ames [6] reported an increase in the cross-stream fluctuations (normal to the blade surface) as the flow progressed through the passage, while Radomsky and Thole [8] reported similar increases in both the cross-stream and spanwise fluctuations.

In general, there is still not enough information regarding the turbulent flowfield characteristics surrounding a turbine airfoil. To date, there have been some measurements of the streamwise fluctuations and a scarce number of measurements of the cross-pitch velocity fluctuations. Not enough measurements have been made to deduce the turbulent kinetic energy field or the shear stress surrounding a vane. There is a need to have well-documented turbulent flowfield measurements both to gain a better physical understanding and for CFD benchmarking purposes.

Experimental Facility and Instrumentation

A stator vane, scaled up by a factor of nine, was placed in a large-scale wind tunnel for this study. The stator vane geometry was a two-dimensional slice of an engine profile taken at the vane midspan. The construction and the development of the scaled-up stator turbine vane and the test section have been previously documented by Radomsky and Thole [8] and Kang et al. [9]. The wind tunnel used in this study is recirculating with a corner test section,

---

[1] Current address: United Technologies Research Center, 411 Silver Lane, East Hartford, CT 06108.

Contributed by the International Gas Turbine Institute and presented at the 44th International Gas Turbine and Aeroengine Congress and Exhibition, Indianapolis, Indiana, June 7–10, 1999. Manuscript received by the International Gas Turbine Institute February 1999. Paper No. 99-GT-253. Review Chair: D. C. Wisler.

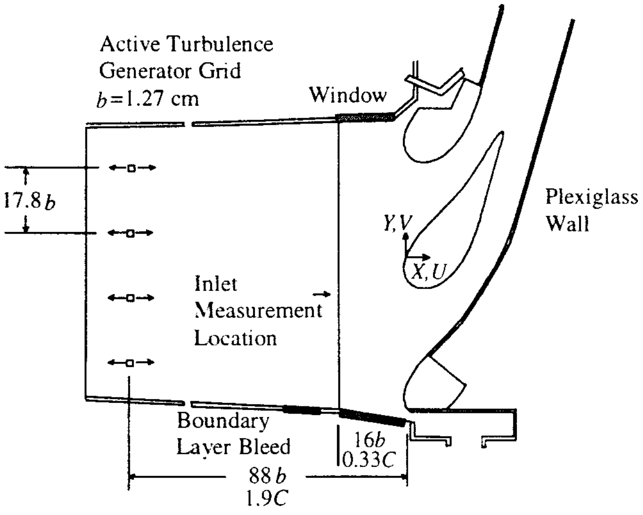

Fig. 1 Schematic of the stator vane test section

shown in Fig. 1. This test section contains a central turbine vane with two adjacent vanes. The outside adjacent vane was constructed by attaching a leading edge to a plexiglass sidewall, allowing for optical access. The placement of the sidewall exactly matches that surface of an adjacent vane. At the point where the adjacent vane geometry stops, the flexible wall was positioned such that the central vane matched a two-dimensional, inviscid pressure distribution computationally predicted for periodic vanes at low-speed conditions. The inlet Reynolds number, based upon approach velocity and chord length, was matched to that of engine conditions. Pressure measurements on the central vane were made to ensure that the sidewall and flow stagnation point were positioned correctly. The upstream sidewall boundary layers were removed by adjustable bleeds while tailboards on the outer vanes ensured that periodic flow occurred in both passages around the central airfoil. A description of the turbine vane itself is given in Table 1.

A fixed Cartesian coordinate system was maintained for these measurements based on a location measured from the flow stagnation point, as shown in Fig. 1. Flowfield measurements, which included all three velocity components and rms velocities, were performed with a two-component laser-Doppler velocimeter (LDV) with digital burst correlator processors. The LDV was positioned both on the top of the test section to measure the streamwise (U) and cross-passage (V) velocity components and on the side of the test section to measure spanwise (W) velocities. A 350 mm focusing lens without a beam expander was used to make measurements of the streamwise and pitchwise components through the top endwall. The spanwise component was measured from the side using the 750 mm focusing lens with a beam expander. The probe volume length and diameter for the 350 mm lens were 1.3 mm and 90 μm whereas the probe volume length and diameter for the 750 mm lens with the beam expander were 0.85 mm and 46 μm. The flow was seeded with 1-μm-dia aluminum dioxide particles. The measured velocities were corrected for bias errors using the residence time weighting correction scheme.

Table 1 Geometrical and flow conditions for the stator vane geometry

Scaling factor	9
Scaled-up chord length (C)	59.4 cm
Pitch / chord (P/C)	0.77
Span / chord (S/C)	0.93
Re_{in}	2.30×10^5
Inlet and exit angles	0° and 78°

Autocorrelation length scales were measured with a single sensor hot-wire having a length of 1.5 mm and diameter of 4 μm. The hot-wire sensor had a frequency response of 200 kHz at 36 m/s, but the analog output was filtered at 10 kHz. The integral length scales were calculated using eight samples with each sample having 80,000 points at a sample frequency of 20 kHz. These single sensor hot-wire measurements were taken at a position where the flow was only in one direction based on the assumption of a Guassian distribution of the turbulence. As will be shown later, good agreement occurred for both the mean and rms levels between the hot-wire measurements and LDV measurements.

As previously described by Radomsky and Thole [8], the central vane as well as the outer leading edges were constructed by stacking rigid polystyrene pieces 5 cm thick that were cut into the shape of the vane using a template and a heated wire. On the outside of the central vane surface, five 50 μm thick type 304 stainless steel foils were attached to the polystyrene. The metal foils provided a constant heat flux boundary condition. Beneath the stainless steel foil and embedded in the styrofoam 58 type E thermocouples were placed. The spanwise position for the thermocouples was at 40 percent of the span measured from the bottom endwall.

The convective heat flux was calculated using the total power supplied to the metal foils minus radiation losses and conduction losses and gains. The radiation correction used a vane surface emissivity of $e=0.22$ (value for typical clean stainless steel given by Incropera and DeWitt [10]) and the measured side wall temperatures, which agreed with the free-stream temperature. The radiation losses ranged between 3–8 percent of the input power for the baseline, low-turbulence cases. A two-dimensional finite element grid was constructed to account for the conduction losses and gains. The worst case was for the baseline case close to the trailing edge, resulting in a 2 percent correction.

The development of the turbulence generator used for the high free-stream turbulence experiments was described in detail by Bangert et al. [7]. This active grid consists of vertical hollow square bars with jets injecting into the mainstream in both the upstream and downstream directions. The bars are 1.27 cm square with the jet holes having a diameter of 1.5 mm and vertically spaced 3.05 cm apart. These hollow bars were installed 88 bar widths upstream of the stator vane stagnation position or, in terms of vane coordinates, at 1.9 chords in front of the stagnation position. A compressed air supply fed a plenum that supplied each of the bars.

Uncertainty Estimates

Each of the mean and rms velocities presented in this paper were averaged over 12,000 points, which took nominally 30 seconds to acquire using the LDV. When performing coincidence measurements for the Reynolds shear stress, a total of 25,000 points were taken at each location. The precision uncertainties for these measurements were estimated using a 95 percent confidence interval. The precision uncertainty for the mean velocities was 0.7 percent for the low turbulence measurements and 0.8 percent for the high turbulence level while the bias uncertainty for both was estimated to be 1 percent. The precision uncertainty for the rms of the velocity fluctuations was 2.0 percent for the high turbulence levels, while the uncertainties in the measured Reynolds stress and turbulent correlation coefficient were estimated to be 12 percent. For the hot-wire measurements, the precision uncertainty for the mean and rms velocities were 2.6 and 2.5 percent, respectively, while the uncertainty in the integral length scale was estimated to be 12.4 percent.

The total uncertainty in Stanton numbers, using the sequential perturbation method discussed by Moffat [11] was 4 percent at the leading edge and 5 percent at the trailing edge on the suction side

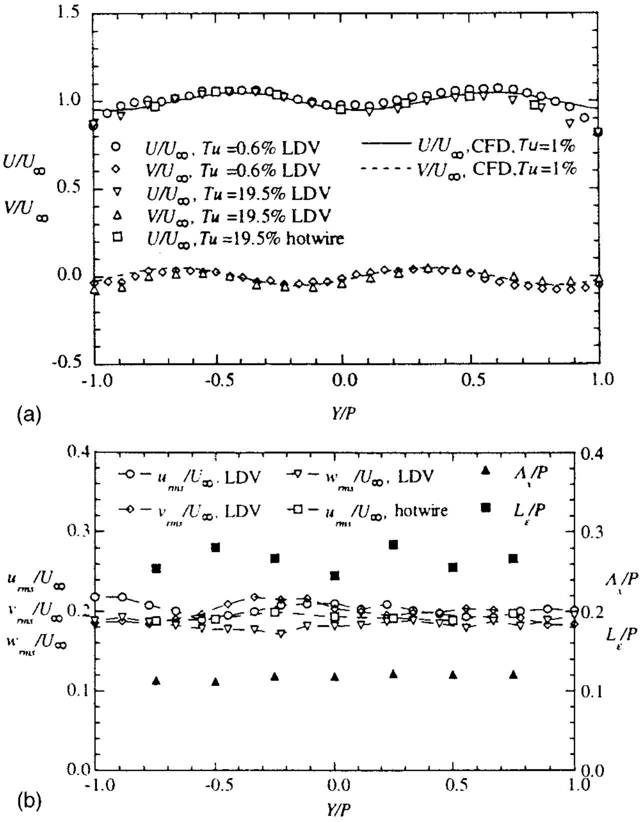

Fig. 2 **(*a*) Inlet mean velocity profiles measured at one-third chord upstream of the vane stagnation; (*b*) Inlet turbulence levels and length scale measured at one-third chord upstream of the vane stagnation**

of the vane. The higher uncertainty at the trailing edge of the suction side is a result of the lower difference between the surface and mainstream temperatures that dominated the uncertainty in the Stanton number.

Inlet Flow Conditions

To insure good flow conditions around the turbine vane, a number of velocity profiles were checked upstream and at the stagnation location. Mean velocity profiles were measured for low and high turbulent flowfields at the inlet using both an LDV and a hot-wire anemometer. In addition, flowfield measurements were compared between the inner and outer passages to insure good periodicity in the two passages surrounding the central vane. The flowfield measurements were compared with CFD predictions made using RAMPANT as described in FLUENT/UNS [12]. These two-dimensional, inviscid, CFD predictions were made using a single passage with periodic boundary conditions. The inlet velocities to the turbine vane for both the low and high turbulence cases were matched.

Figure 2(*a*) compares measured and predicted profiles across the entire pitch of the two passages in terms of the streamwise and cross-stream velocities normalized by the upstream incident velocity, U_∞. The measurement location was one-third of a chord upstream of the vane stagnation. Both the low and high freestream turbulence cases are presented in Fig. 2(*a*). The velocity measurements for both the low and high turbulent cases agree very well with the predicted velocities except near the edge of the test section where there is a sidewall boundary layer. Note that this is upstream of the sidewall suction slot, which is intended to remove the sidewall boundary layer. These measurements are a good indication that the active grid jets have not affected the mean flowfield. Across the vertical span of the turbine vane, the mean velocity uniformity was such that the maximum deviation normalized by the average velocity was 1.6 and 3.5 percent for the low and high turbulence cases. In addition to the LDV data, Fig. 2(*a*) shows good agreement with the hot-wire measurements of the streamwise velocity component for the highly turbulent case. At this location, the vane is already detected by the flow, showing a deceleration in the streamwise velocity component at the center of the passage. As the streamlines turn around the vane, slightly positive cross-span (V/U_∞) velocities occur near the stagnation for $Y/P>0$ and slightly negative cross-span velocities occur near the stagnation for $Y/P<0$.

Figure 2(*b*) shows the normalized rms levels of the streamwise ($u_{\mathrm{rms}}/U_\infty$), cross-stream ($v_{\mathrm{rms}}/U_\infty$), and the spanwise ($w_{\mathrm{rms}}/U_\infty$) velocity fluctuations as well as the normalized integral (Λ_x/P) and dissipation (L_ε/P) length scales for the highly turbulent case. At the inlet location, all three rms levels are close to the same value with only slightly lower spanwise fluctuations, $w_{\mathrm{rms}}/U_\infty$. The average spanwise fluctuations are 91 percent of the average streamwise fluctuations and 93 percent of the cross-stream fluctuations. For the high turbulence case, the maximum deviation of the rms velocities across the vertical span of the turbine vane was 2.8 percent. The average turbulence level at this location is 19.5 percent. The hot-wire measurements of the streamwise fluctuations in Fig. 2(*b*) show good agreement with the LDV measurements.

The integral length scale, also shown in Fig. 2(*b*), is nominally 12 percent of the vane pitch and is relatively uniform across the pitch. The dissipation, used in the dissipation length scale, was determined from a curve fit to the following formula in the inertial subrange of the energy spectra for the streamwise fluctuations [6,13]:

$$E_1(k_1)=1.62(18/55)\varepsilon^{2/3}k_1^{-5/3} \quad (1)$$

The dissipation length scale is nominally two times larger than the integral length scale. Figure 2*b* shows that the level and scale of the turbulence are representative of combustor generated turbulence as measured by Ames [3].

Figure 3(*a*) shows LDV mean velocity measurements across the passages at the vane geometric stagnation for both the low and high turbulence cases as compared with a CFD prediction for the low turbulence case. Note that both the inside and outside passages around the central turbine vane are shown. There is good agreement between the measured and predicted mean velocity components as well as an indication that the flow periodicity between the two passages is quite good. The rms velocities for the highly turbulent flowfield also showed good periodicity for the two passages, as will be shown later.

Streamwise velocity measurements leading up to the flow stagnation and midspan passage locations of the vane are compared with that predicted in Fig. 3(*b*). Note that good agreement between the predicted and measured velocities using both the LDV and hot-wire occur. Figure 4 shows how the streamwise rms levels of the velocity fluctuations as well at the turbulent kinetic energy, normalized by the upstream velocity, vary proceeding up to the leading edge. For each of the velocity fluctuations, an increase starts to occur at $X/C=-0.05$, moving toward the vane. Very close to the vane, the streamwise fluctuations, $u_{\mathrm{rms}}/U_\infty$, again decrease. Note that the hot-wire measurements of the streamwise fluctuations are only presented up to $X/C=-0.1$. Beyond that location the streamlines turn significantly and the velocities are quite low with high turbulence levels making the hot-wire measurements invalid. The turbulent kinetic energy, also shown in Fig. 4, increases to a level that is 1.3 times higher than at the inlet. The rapid increase starts to occur at approximately one integral length scale upstream of the vane stagnation ($X/C\sim-0.1$).

The energy spectra of the streamwise fluctuations at the inlet are shown in Fig. 5 as compared with the von Karman spectra and the unified relation given by Mayle et al. [14]. Also shown in Fig.

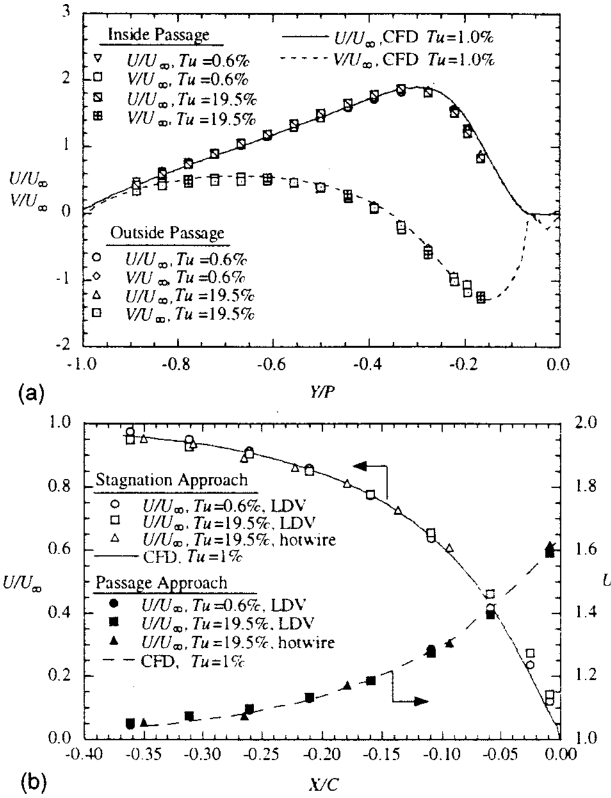

Fig. 3 (***a***) **Velocity components measured at the geometric stagnation and** (***b***) **velocity approaching the vane stagnation and passage**

5 are the spectra taken at the closest position to the stagnation location. The turbulent Reynolds numbers, Re_λ, for these two locations are quite similar. The Taylor microscale was estimated from the following relation:

$$\lambda = \left[\frac{15 \nu u_{\mathrm{rms}}^2}{\varepsilon} \right]^{1/2} \tag{2}$$

In the low wave number region there is good agreement between the measured energy spectra and those given by the von Karman and Mayle et al. [14] relations. As the wave number increases, the drop-off of the inertial subrange is well predicted by the relation given by Mayle et al. [14] for the inlet condition ($X/C = -0.35$). Although the turbulent Reynolds numbers are very similar, closer to the stagnation location ($X/C = -0.09$) the drop-off in the inertial subrange is not predicted by the relation given by Mayle et al. [14] but is much more rapid.

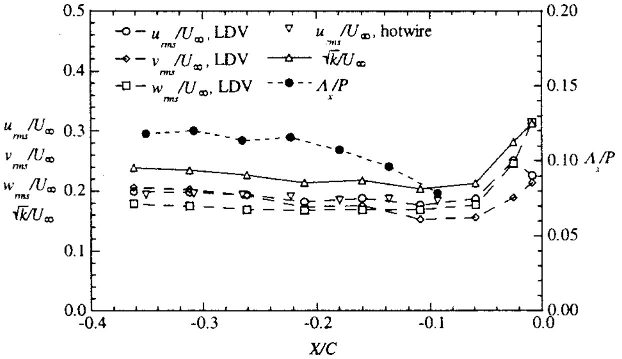

Fig. 4 The rms velocity components, turbulent kinetic energy, and integral length scale approaching the vane stagnation point

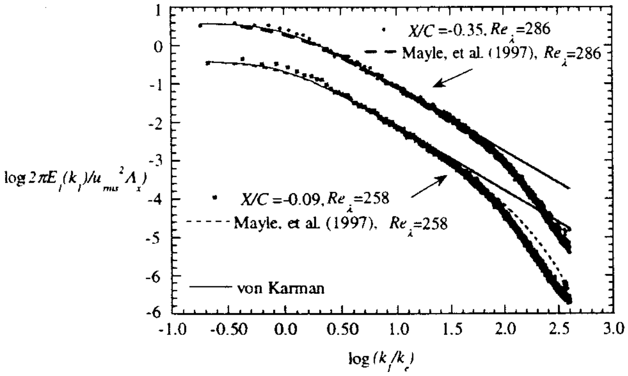

Fig. 5 One-dimensional energy spectra approaching the vane stagnation point

Mean Velocity Flow Field Results

Figures 6(*a*) and 6(*b*) show vectors and normalized total velocity contours for the low free-stream turbulence case measured throughout the passage. Note that all of these flowfield measurements were made in a plane at the midspan between the mid-pitches of the central vane passages. For presentation purposes in this paper, the data were simply numerically shifted to give one full pitch from stagnation to stagnation. Because the data were shifted, the smoothness of the contours are an indication of the good flow periodicity in both passages of the central vane.

As expected with this vane geometry, there is a high acceleration that occurs around the suction side of the vane. The flow stagnation can be clearly seen from both the contours and the velocity vectors. The contour levels indicate that the flow has been accelerated to five times the incident velocity.

Figure 7 gives the normalized total velocity contours for the highly turbulent flow. The largest difference between Figs. 6(*b*) and 7 is along the suction surface where a larger region of high-speed fluid occurs for the highly turbulent flowfield. This larger high-speed region is a result of an acceleration of the inviscid flow due to the transition of a turbulent boundary layer occurring further upstream along the vane. Earlier transition caused a thicker turbulent boundary layer along the suction side of the vane for the highly turbulent case. The difference between the cases can also be seen in Fig. 8 where the local freestream velocity distribution is given for the measured conditions and the inviscid CFD prediction. The effect of the larger boundary layer thickness can be seen at values greater than $s/C = 0.5$.

Turbulent Flow Field Results

Contours of the rms levels of the fluctuations for each of the velocity components were measured for the inviscid region. Figures 9(*a–c*) show contour levels of the normalized rms levels for the 19.5 percent inlet turbulence case. Contour levels are given in increments of 0.04.

For the streamwise fluctuations, shown in Fig. 9(a) the inlet levels are nominally $u_{\mathrm{rms}}/U_\infty = 0.2$. Between the inlet and stagnation region the rms levels are between $u_{\mathrm{rms}}/U_\infty = 0.16$ and 0.20. Near the leading edge, an increase in the streamwise fluctuations occurs with the peak occurring just upstream of the geometric stagnation location toward the suction surface of the vane relative to the flow stagnation location. The peak level rises to a value of $u_{\mathrm{rms}}/U_\infty = 0.24$. Very near the geometric stagnation point, the streamwise fluctuations decrease as a result of being attenuated by the presence of the vane. As the flow progresses along the pressure surface, the $u_{\mathrm{rms}}/U_\infty = 0.20$ contour level moves away from

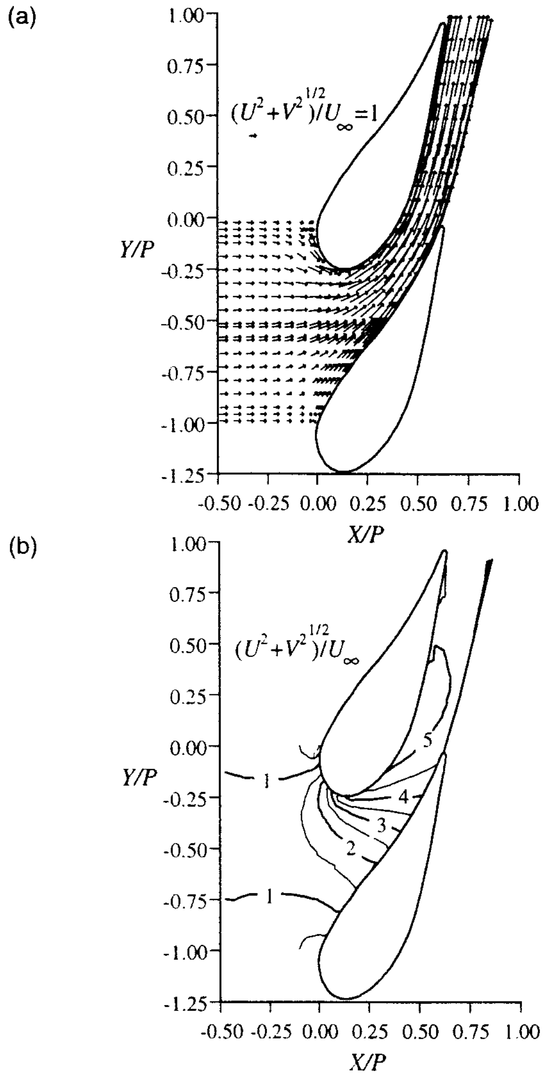

Fig. 6 (*a*) Total velocity vectors and (*b*) total velocity contours at $Tu=0.6$ percent

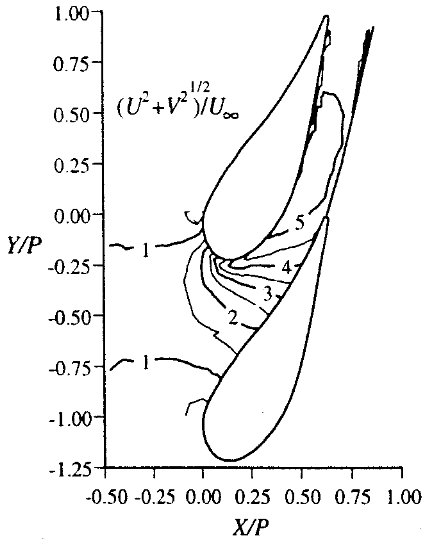

Fig. 7 Total velocity contours at $Tu=19.5$ percent

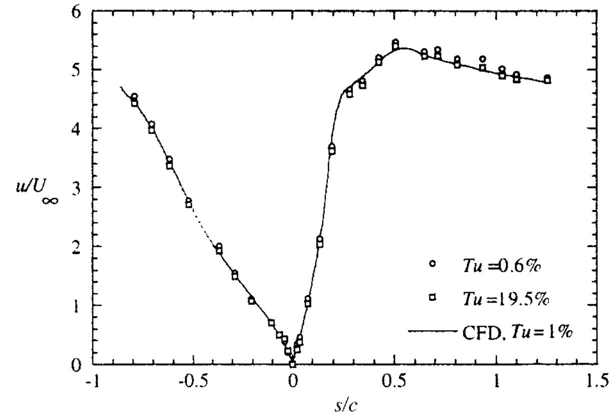

Fig. 8 Vane velocity distribution at $Tu=0.6$ percent and $Tu=19.5$ percent

the pressure surface giving a lower value of $u_{\mathrm{rms}}/U_\infty=0.16$. At the midpitch of the passage, the lowest streamwise rms levels occur at $u_{\mathrm{rms}}/U_\infty=0.16$. This region is where the flow begins to turn and has the highest acceleration in the streamwise velocity component, resulting in a negative production of the streamwise velocity fluctuations.

Progressing through the passage, the streamwise fluctuations again start to increase up to a peak of $u_{\mathrm{rms}}/U_\infty=0.28$. Beyond that peak location, the rms levels stay relatively constant. Note that near the suction surface, the streamwise rms levels are lower than at the midportion of the passage. Keeping in mind that an orthogonal coordinate system was maintained for these measurements, these velocity fluctuations are almost normal to the vane surface. The lower values near the surface can be explained by the fact that the vane surface is attenuating the fluctuations.

The cross-stream rms contours are shown in Fig. 9(*b*). Again, there is good uniformity at the entrance to the test section with a level of $v_{\mathrm{rms}}/U_\infty=0.20$. A high contour of $v_{\mathrm{rms}}/U_\infty=0.24$ occurs near the shoulder of the stator vane in the high acceleration region. This is also the location of the low contours of $u_{\mathrm{rms}}/U_\infty$. Also, a low contour of $v_{\mathrm{rms}}/U_\infty=0.16$ occurs in the middle of the passage, which starts at the location where the high contour of $u_{\mathrm{rms}}/U_\infty$ occurred. Near the suction side of the vane surface, very high $v_{\mathrm{rms}}/U_\infty$ values occur. Unlike the $u_{\mathrm{rms}}/U_\infty$ fluctuations, which were being attenuated at the vane surface, the cross-stream fluctuations are quite high at the suction surface. These high values occur near the end of the turbine vane suction surface since this direction is more parallel with the turbine vane surface.

The spanwise rms contours, shown in Fig. 9(*c*), indicate variations only occurring in the near-wall regions. At the passage inlet the levels are $w_{\mathrm{rms}}/U_\infty=0.20$ with values becoming slightly higher at $w_{\mathrm{rms}}/U_\infty=0.24$ once inside the passage.

The turbulent kinetic energy level contours, which combine all three fluctuations, are shown in Fig. 10. Note that the increment between levels is 0.02. These contours are presented in terms of $\sqrt{k}/U_\infty$ and can be converted to a turbulence intensity through multiplying by a constant factor, i.e. $\sqrt{2/3}\sqrt{k}/U_\infty$. The turbulent kinetic energy is quite uniform at the inlet with values between $\sqrt{k}/U_\infty=0.22$ and 0.24. As the flow progresses toward the geometric stagnation on the suction side of the vane, the turbulent kinetic energy levels increase significantly, reaching as high as $\sqrt{k}/U_\infty=0.32$. At the midpitch region just upstream of the passage, lower turbulent kinetic energy levels occur with values as low as $\sqrt{k}/U_\infty=0.22$. Once inside the vane passage, the turbulent kinetic energy increases to a level of $\sqrt{k}/U_\infty=0.28$, and remains essentially constant throughout the middle of the passage. This result shows that there is not a decay in the turbulent kinetic energy through a turbine vane passage. Near the turbine vane walls high values of the turbulent kinetic energy were measured.

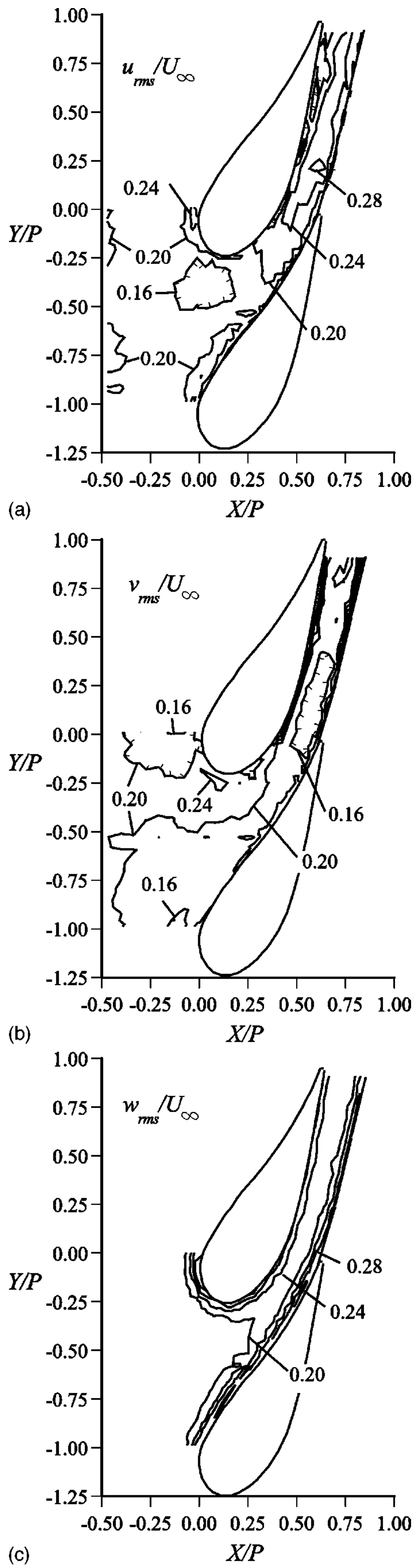

Fig. 9 Contours of (*a*) $u_{\rm rms}/U_\infty$, (*b*) $v_{\rm rms}/U_\infty$, and (*c*) $w_{\rm rms}/U_\infty$ at $Tu=19.5$ percent

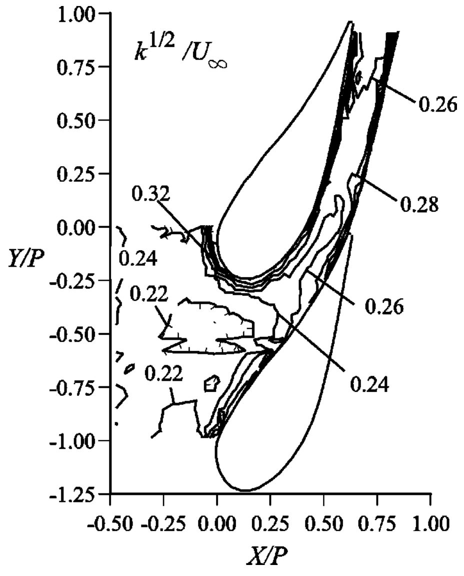

Fig. 10 Contours of $\sqrt{k}/U_\infty$ at $Tu=19.5$ percent

It is clear that there is a very high region along the suction side of the vane beyond $s/C=0.4$ that is approximately where transition to a turbulent boundary layer occurs.

Coincident LDV data were taken for the U and V velocity components to quantify Reynolds shear stress and correlation coefficients. Contours of the Reynolds shear stress normalized by the square of the inlet mean velocity ($\overline{u'v'}/U_\infty^2$) are shown in Fig. 11(*a*) while the correlation coefficients (R_{uv}) are shown in Fig. 11(*b*). Unlike the other turbulent stress components ($u_{\rm rms}^2$, $v_{\rm rms}^2$, and $w_{\rm rms}^2$), the shear stress contours indicate a much different behavior. Positive shear stresses occur along the shoulder of the suction surface starting at the flow stagnation location. A negative shear stress occurs beyond this location. In the center of the passage, the magnitude in shear stress increases up to $|\overline{u'v'}/U_\infty^2|=0.025$, after which a decrease occurs.

For the turbulent shear stress, $\overline{u'v'}$, it is helpful to consider the production mechanism under high free-stream turbulence conditions. As pointed out by Gibson and Rodi [15] and Bradshaw [16] the production term for $\overline{u'v'}$ along a streamline can be written as,

$$P(\overline{u'v'})=(2u_{\rm rms}^2-v_{\rm rms}^2)\frac{u}{R}-v_{\rm rms}^2\left[\left(1+\frac{y}{R}\right)\frac{\partial u}{\partial y}\right] \tag{3}$$

In considering the inviscid region for the high turbulent case, the dominant term in this production equation is the first term whereby streamline curvature effects are included. For Eq. (3), R is the radius of curvature of the streamlines, positive for convex curvature and negative for concave curvature; and u, v, and w are the local mean velocity components along the streamline. In the case where the free-stream turbulence level is low but yet the flow has streamline curvature, the production of $\overline{u'v'}$ shear stress is quite small. In the case where there is no streamline curvature but yet the flow has high free-stream turbulence levels, the production of $\overline{u'v'}$ shear stress is also quite small. This latter case is indicated in the region upstream of the turbine vane and in the center of the vane passage where $\overline{u'v'}=0$ as shown in Fig. 11(*a*). As the flow approaches the turbine vane for the convex curved streamlines ($R>0$) along the suction surface shoulder, a positive production occurs as $2u_{\rm rms}^2>v_{\rm rms}^2$. Much further into the passage where concave curved streamlines occur ($R<0$) and $2u_{\rm rms}^2>v_{\rm rms}^2$, the production of $\overline{u'v'}$ decreases and the $\overline{u'v'}$ values approach zero.

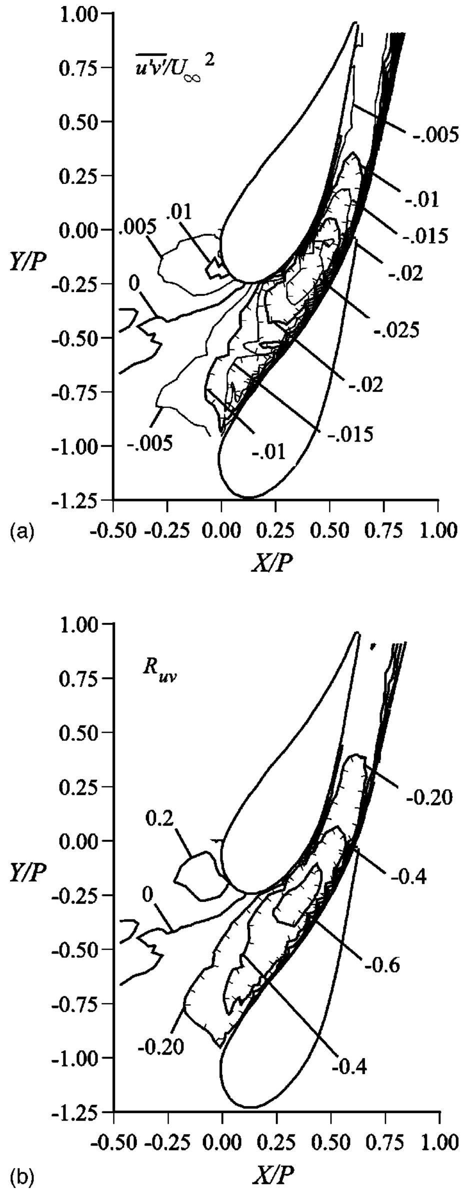

Fig. 11 Contours of (*a*) $\overline{u'v'}/U_\infty^2$ and (*b*) R_{uv}

An understanding of the turbulent kinetic energy contours is better achieved by considering the production terms for a curved streamline along with the shear stress contours. Gibson and Rodi [5] and Bradshaw [16] give the production term for the turbulent kinetic energy along a curved streamline as:

$$P(k) = -\overline{u'v'}\left[\left(1+\frac{y}{R}\right)\frac{\partial u}{\partial y} - \frac{u}{R} + \frac{\partial v}{\partial s}\right] - u_{\mathrm{rms}}^2\left(\frac{\partial u}{\partial s} + \frac{u}{R}\right) - v_{\mathrm{rms}}^2\left(1+\frac{y}{r}\right)\frac{\partial v}{\partial y} \tag{4}$$

Both Gibson and Rodi and Bradshaw point out that the dominating production term is the one that is underlined. For a turbulent boundary layer on flat plate, the production reduces to $\overline{u'v'}\partial u/\partial y$, but where curvature exists there are additional terms such as $\overline{u'v'}(u/R)$. For the convex curvature case (suction side of the vane) where $R>0$ and $\overline{u'v'}>0$, this results in a positive production for the turbulent kinetic energy. For the concave curved streamlines where $R<0$ and $\overline{u'v'}<0$, this also results in a positive production.

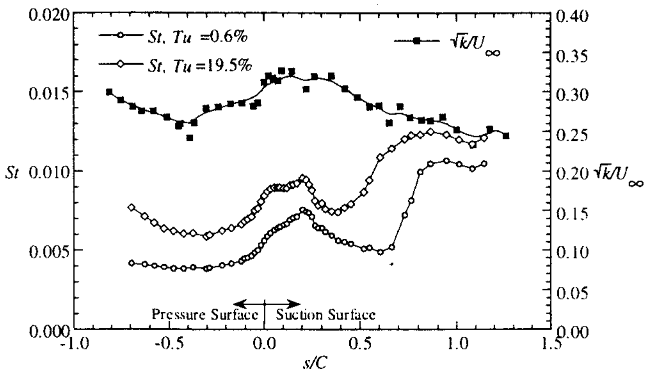

Fig. 12 Stanton number distribution and turbulent kinetic energy outside the vane boundary layer

Referring to Fig. 10, the lowest turbulent kinetic energy levels occur at a location of the midpitch entrance to the turbine vane passage. This location corresponds to the low shear stress values and very little streamline curvature. The high levels of turbulent kinetic energy near the geometric stagnation point (along the suction surface shoulder), can be attributed to the high turning of the streamlines. Progressing through the passage, as the shear stress increases there is an increase in the turbulent kinetic energy due to the increased production.

Figure 11(*b*) shows correlation coefficient contours. At the inlet to the turbine vane, the turbulence structures are uncorrelated, giving a correlation coefficient of $R_{uv}=0$. Except for the suction shoulder of the turbine vane, the correlation coefficients were primarily negative with a peak reaching as high as $|R_{uv}|=0.60$. A negative correlation coefficient implies one of two conditions. The first condition is when a particle with a high *U*-velocity moves in the negative *Y* direction (negative *V*) giving a negative R_{uv} since the instantaneous *U* will be lower than $\overline{U}$. The second condition is when a low *U*-velocity fluid moves in the positive *Y* direction (positive *V*), which is toward the suction surface. Because of the cross-pitch pressure gradient driving the flow from the pressure side toward the suction surface, the streamlines move toward the suction surface. Based on this argument, one would expect negative correlation coefficients to occur inside the turbine vane passage. The correlation coefficient rapidly decreases at the end of the passage. In the leading edge region, the positive correlation coefficients occur because the low streamwise speed fluid is turning in the negative *Y* direction.

Flow Field Relative to Vane Heat Transfer

It has been well-documented that high free-stream turbulence can greatly augment the surface heat transfer. Figure 12 shows the measured heat transfer along the vane surface for low and high free-stream turbulence conditions. For the low free-stream turbulence conditions, the peak heat transfer occurs at $s/C=0.25$, which is where the highest acceleration occurs along the shoulder of the suction side of the turbine vane. For the high free-stream turbulence conditions, the Stanton numbers are relatively constant at elevated values, starting at the stagnation location and extending to $s/C=0.2$ followed by a slight bump at $s/C=0.25$. The transition location has moved significantly upstream on the vane surface for the high free-stream turbulence conditions relative to the baseline low free-stream turbulence. On the pressure side of the vane ($s/C<0$), the Stanton numbers indicate a slight rise near the trailing edge of the vane surface, indicating that transition may be starting.

Also shown in Fig. 12 are the turbulent kinetic energy values along the turbine vane surface just outside of the boundary layer for the $Tu=19.5$ percent case. The highest turbulent kinetic energy levels occur at the stagnation location extending along the suction side of the vane. The turbulence levels start to decrease at $s/C=0.4$ and continue to decrease along the suction surface. After an initial decrease along the pressure surface, there is again an increase in the turbulent kinetic energy levels beyond $s/C=-0.5$. The highest augmentations in heat transfer occur along the pressure side of the vane where the increase in turbulent kinetic energy occurs.

Conclusions

This paper clearly showed that throughout the turbine vane passage, turbulence does not decay but rather it remains quite high throughout the passage. In order to conclude this, it was necessary to do a detailed flowfield mapping of all three velocities to quantify mean and rms levels. The turbulent kinetic energy contours showed increased values at the stagnation location and in the boundary layer after transition. The contours of streamwise and cross-pitch fluctuations showed variations throughout the passage, which, along with the curvature of the streamlines, could be used to explain the production of the shear stress. The contours of spanwise fluctuations showed relatively constant values except near the turbine vane surface. The production mechanisms for the turbulent kinetic energy were also discussed whereby the streamline curvature played a significant role.

The turbulent correlation coefficients in the turbine vane passage indicate that highly correlated turbulent structures exist. The sign of these coefficients are as expected with fluid moving from the pressure side of the vane to the suction side. The turbulent kinetic energy levels in the inviscid region just outside of the boundary layer show values that are very high with the peak levels occurring at the stagnation region and along the shoulder of the suction surface. Other than moving the transition location further upstream along the suction surface, the high free-stream turbulence also greatly augmented the surface heat transfer along the pressure side of the vane.

Acknowledgments

The authors would like to thank the Department of Energy's Advanced Gas Turbine Systems Research Program for supporting this work. In particular, the authors would like to thank Dr. Dan Fant for serving as the contract monitor. The authors would also like to thank Pratt & Whitney, Florida, for supplying the turbine vane geometry.

Nomenclature

b = turbulence generator bar width
C = true chord length
e = emissivity
$E_1(k_1)$ = spectra for streamwise fluctuations
f = frequency
h = convective heat transfer coefficient $=q''_{\text{conv}}/(T_s-T_\infty)$
k = turbulent kinetic energy $=0.5(u_{\text{rms}}^2+v_{\text{rms}}^2+w_{\text{rms}}^2)$
k_1 = wavenumber $=2\pi f/u$
L_ε = dissipation length scale $=1.5\,u_{\text{rms}}^3/\varepsilon$
P = turbine vane pitch
q''_{conv} = convective heat flux $=q''_{\text{input}}-q''_{\text{rad}}-q''_{\text{cond}}$
q''_{cond} = conductive heat flux from finite element analysis
q''_{input} = total heat flux from foils
q''_{rad} = radiative heat flux $=e\sigma(T_s^4-T_\infty^4)$
R = radius of curvature
R_{uv} = turbulent correlation coefficient $=\overline{u'v'}/(u_{\text{rms}}v_{\text{rms}})$
Re_{in} = Reynolds number based on chord length and inlet velocity
Re_λ = Reynolds number based on Taylor microscale and u_{rms}
s = distance measured along vane surface from stagnation
S = full span
St = Stanton number $=h/\rho C_p U_\infty$
T_s = surface temperature
T_∞ = free-stream temperature
Tu = turbulence level
U_∞ = upstream incident velocity
$\overline{u'v'}$ = Reynolds shear stress
u, v, w = local mean velocities along a streamline
U, u_{rms} = local mean and rms velocities in the X direction
V, v_{rms} = local mean and rms velocities in the Y direction
W, w_{rms} = local mean and rms velocities in the Z direction
X, Y, Z = fixed Cartesian coordinate system measured from the flow stagnation, see Fig. 1
ε = turbulent dissipation obtained from Eq. (1)
Λ_x = streamwise integral turbulent length scale
λ = Taylor microscale
ν = kinematic viscosity
σ = Stefan–Boltzmann constant

References

[1] Kuotmos, P., and McGuirk, J. J., 1989, ''Isothermal Flow in a Gas Turbine Combustor—A Benchmark Experimental Study,'' Exp. Fluids, **7**, pp. 344–354.
[2] Moss, R. W., 1992, ''The Effects of Turbulence Length Scale on Heat Transfer,'' University of Oxford, Department of Engineering Science, Report No. OUEL 1924, Ph.D. Dissertation.
[3] Ames, F. E., 1997, ''The Influence of Large Scale High Intensity Turbulence on Vane Heat Transfer,'' ASME J. Turbomach., **119**, pp. 23–30.
[4] Bailey, D. A., 1980, ''Study of Mean- and Turbulent-Velocity Fields in a Large-Scale Turbine-Vane Passage,'' ASME J. Eng. Gas Turbines Power, **102**, pp. 88–95.
[5] Priddy, W. J., and Bayley, F. J., 1988, ''Turbulence Measurements in Turbine Blade Passages and Implications for Heat Transfer,'' ASME J. Turbomach., **110**, pp. 73–79.
[6] Ames, F. E., 1994, ''Experimental Study of Vane Heat Transfer and Aerodynamics at Elevated Levels of Turbulence,'' NASA Contractor's Report 4633.
[7] Bangert, B., Kohli, A., Sauer, J., and Thole, K. A., 1997, ''High Freestream Turbulence Simulation in a Scaled-Up Turbine Vane Passage,'' ASME Paper No. 97-GT-51.
[8] Radomsky, R. W., and Thole, K. A., 1999, ''Effects of High Freestream Turbulence Levels and Length Scales on Stator Vane Heat Transfer,'' ASME Paper No. 98-GT-236.
[9] Kang, M., Kohli, A., and Thole, K. A., 1999, ''Heat Transfer and Flowfield Measurements in the Leading Edge Region of a Stator Vane Endwall,'' ASME J. Turbomach., **121**, pp. 558–568.
[10] Incropera, F. P., and DeWitt, D. P., 1996, *Introduction to Heat Transfer*, 3rd ed., Wiley, New York.
[11] Moffat, R. J., 1988, ''Describing Uncertainties in Experimental Results,'' Exp. Fluid Sci. **1**, pp. 3–17.
[12] FLUENT/UNS User's Guide, 1996, Release 4.2, Fluent, Inc., Lebanon, NH.
[13] Hinze, J., 1975, *Turbulence*, 2nd ed., McGraw-Hill, New York.
[14] Mayle, R. E., Dullenkopf, K., and Schulz, A., 1998, ''The Turbulence That Matters,'' ASME J. Turbomach., **120**, pp. 402–409.
[15] Gibson, M. M., and Rodi, W., 1981, ''A Reynolds-Stress Closure Model of Turbulence Applied to the Calculation of a Highly Curved Mixing Layer,'' J. Fluid Mech., **103**, pp. 161–182.
[16] Bradshaw, P., 1973, ''Effects of Streamline Curvature on Turbulent Flow,'' AGARD-AG-169.

Heat Transfer and Flow on the First-Stage Blade Tip of a Power Generation Gas Turbine: Part 1—Experimental Results

Ronald S. Bunker
Jeremy C. Bailey
General Electric Corp. R&D Center,
Schenectady, NY 12309

Ali A. Ameri
AYT Corporation,
Brook Park, OH 44135

A combined experimental and computational study has been performed to investigate the detailed distribution of convective heat transfer coefficients on the first-stage blade tip surface for a geometry typical of large power generation turbines (>100 MW). This paper is concerned with the design and execution of the experimental portion of the study, which represents the first reported investigation to obtain nearly full surface information on heat transfer coefficients within an environment that develops an appropriate pressure distribution about an airfoil blade tip and shroud model. A stationary blade cascade experiment has been run consisting of three airfoils, the center airfoil having a variable tip gap clearance. The airfoil models the aerodynamic tip section of a high-pressure turbine blade with inlet Mach number of 0.30, exit Mach number of 0.75, pressure ratio of 1.45, exit Reynolds number based on axial chord of 2.57×10^6, and total turning of about 110 deg. A hue detection based liquid crystal method is used to obtain the detailed heat transfer coefficient distribution on the blade tip surface for flat, smooth tip surfaces with both sharp and rounded edges. The cascade inlet turbulence intensity level took on values of either 5 or 9 percent. The cascade also models the casing recess in the shroud surface ahead of the blade. Experimental results are shown for the pressure distribution measurements on the airfoil near the tip gap, on the blade tip surface, and on the opposite shroud surface. Tip surface heat transfer coefficient distributions are shown for sharp edge and rounded edge tip geometries at each of the inlet turbulence intensity levels. [S0889-504X(00)01902-4]

Introduction

The design of high-efficiency, highly cooled gas turbines is achieved through the orchestrated combination of aerodynamics, heat transfer, mechanical strength and durability, and material capabilities into a balanced operating unit. While decades of research have been dedicated to the study and development of efficient aerodynamics and cooling techniques for turbine airfoils, there remain regions that retain a somewhat more uncertain design aspect requiring more frequent inspection and repair. One such region particular to high-pressure turbines is the blade tip area. Blade tips are comprised of extended surfaces at the furthest radial position of the blade, which are exposed to hot gases on all sides, typically difficult to cool, and subjected to the potential for wear or even hard rubs against the shroud. It has long been recognized that the effectiveness of the blade tip design and subsequent tip leakage flows is a major contributor to the aerodynamic efficiency of turbines, or the lack thereof. The derivative of turbine efficiency with blade tip clearance can be significant, signaling a strong desire on the part of the designers to improve efficiency by decreasing tip-to-shroud operating clearances, or by implementing more effective tip leakage sealing mechanisms. There are several blade tip designs in current use within the industry that emphasize various aspects of the total problem. Generally, these designs include flat unshrouded blade tips, which use well-controlled internal cooling to assure thermal stability, unshrouded tips with various forms of squealer rims to reduce hot gas leakage while providing protection against shroud rubs, and shrouded blade tips (attached shrouds), which seek to establish high aerodynamic efficiency but with a penalty on blade stresses. High performance versions of these blade tip designs usually also utilize some amount of film cooling to reduce regional heat loads.

No matter the design choice selected for any particular turbine blade tip, a detailed knowledge of the flow field and tip heat transfer is required to achieve the proper balance of elements for efficiency with durability. The flow in and around turbine blade tips has been under investigation much longer than the heat transfer aspects, spurred by the great impact on efficiency for both turbines and compressors. An early work of Lakshminarayana [1] developed predictive models for stage efficiency and compared these to existing data for several classes of turbomachinery. A comprehensive study by Booth et al. [2] and Wadia and Booth [3] measured overall and local blade tip losses for many configurations of tip geometries, and developed predictive methods based on discharge coefficients. Later work of Moore et al. [4] examined flat tip region flows from laminar to transonic conditions and compared their predictions with available experimental data. More recently, detailed measurements of velocity and pressure fields have been obtained within an idealized tip gap by Sjolander and Cao [5]. The effects of tip clearance, tip geometry, and multiple stages on turbine stage efficiency have lately been quantified by Kaiser and Bindon [6] within a rotating turbine rig environment. Many other works, too numerous to list here, have studied the effects of tip clearances in axial turbines with the primary emphasis on total leakage and efficiency loss prediction.

Heat transfer on turbine blade tips has been a subject of consistent research over the past 15 years, more or less. Even earlier research dealing with flow and heat transfer over cavities, such as Seban [7], relates to certain cases of turbine blade tips. Work directly aimed at blade tip heat transfer began with the study of Mayle and Metzger [8] in which tip-averaged heat transfer coefficients were measured for nominally flat tip models with various

---

Contributed by the International Gas Turbine Institute and presented at the 44th International Gas Turbine and Aeroengine Congress and Exhibition, Indianapolis, Indiana, June 7–10, 1999. Manuscript received by the International Gas Turbine Institute February 1999. Paper No. 99-GT-169. Review Chair: D. C. Wisler.

flow Reynolds number and rotational speeds. For the parameter ranges tested, they found that the average tip heat transfer was only a weak function of the rotational speed; i.e., the average heat transfer was mainly determined by the pressure driven flow through the tip gap. A subsequent study of Metzger et al. [9] examined the local details of tip heat transfer coefficients for both flat and grooved, stationary rectangular tip models as a function of geometry and Reynolds number, based upon the previous finding that the overall tip driving pressure potential controls the heat transfer. Chyu et al. [10] then carried this study one step further by introducing a moving shroud surface over the rectangular cavity. Here again it was determined that the relative motion had a minor influence on the average tip heat transfer, though some local effects were observed. Very limited experimental data have been reported in either stationary or rotating cascade environments. Yang and Diller [11] modeled a turbine blade tip with recessed cavity in a stationary linear cascade, and deduced a local heat transfer coefficient from a heat flux gage placed within the cavity at midchord. Metzger et al. [12] measured several local tip heat fluxes, primarily in the blade forward region, on the flat tips within a rotating turbine rig at two differing tip clearances. No definitive conclusions were drawn from either of these rig studies.

Additional heat transfer experimental studies have focused on other aspects of blade tips, which are equally important to the design of turbines. Metzer and Rued [13] and Rued and Metzger [14] performed fundamental studies showing both the flow field and heat transfer characteristics of the blade pressure side sink flow region as leakage enters the tip gap, and the blade suction side source flow region as leakage exits the tip gap, respectively. The effects of film injection on blade tip local heat transfer and film effectiveness distributions using idealized rectangular models is summarized in Kim et al. [15]. Other aspects of turbines that affect blade tip heat transfer include unsteadiness from upstream wakes and secondary flows, injection of coolant sources from the stationary shroud and casing, surface roughness, radial gas temperature profiles and migration, oxidation, and erosion, all of which can have weak or strong influence, but none of which has been investigated in the open literature on heat transfer.

Numerical investigations are playing an increasingly important role in the study and design of turbine blade tips for both flow and heat transfer considerations. An earlier work of Chyu et al. [16] used a two-dimensional finite difference solver to predict the flow and heat transfer in rectangular grooves modeling blade tips, with and without the effects of rotation. More recently, three-dimensional CFD analyses have been performed by Ameri and Steinthorsson [17,18] and Ameri et al. [19,20] showing the predicted effects of tip clearance, tip geometry, and shroud casing for several blade tip designs. While the details of such CFD analyses are astounding, there are still very few validation data available for comparison.

The present study was undertaken in two parallel paths: Part 1 examines the experimental pressure and heat transfer distributions on a stationary blade tip cascade model, while Part 2 compares these data to CFD predictions performed on the same geometry [21]. This is the first such study to compare detailed blade tip heat transfer distributions to CFD predictions in the same geometry. The blade tip cascade chosen for this study represents a modern first-stage blade of a land-based power turbine. The blade tip geometry is that of a flat tip with a recessed shroud casing and a nominal tip clearance of approximately 1 percent of the blade height. Tip surface heat transfer is presented for sharp edge and radius edge tips, three clearances, and two free-stream approach turbulence levels. Pressure distributions are presented for the blade tip and near-tip surfaces, as well as the shroud surface.

Experimental Apparatus, Test Models, and Test Methodology

The experimental facility used in the present study is a cold-flow, steady-state blade cascade comprised of three airfoils and two airfoil flow passages. The cascade is stationary. Figure 1 shows the overall layout of the facility and cascade test section. The test rig is fed with compressed air from dedicated in-house compressors. Preceding the blade cascade is a flow preparation vessel of 51-cm internal diameter, which contains a front end splash plate to distribute the flow within the vessel and a short section of duct (25 cm length) of the same cross section as the cascade. The vessel also contains a rupture disk for safety against over-pressure. The cascade inlet dimensions are 18.94 cm width by 10.16 cm height (span). The cascade test section is bolted to and sealed against the blind flange face of the vessel. A turbulence generating grid is placed at this juncture, which is composed of 6.35-mm-wide square bars with 12.7-mm openings between bars. Hot-film anemometry measurements using a TSI IFA-100 unit show that the free-stream turbulence intensity level at the cascade blade leading edge plane is 5 percent for the mainstream flow direction; the turbulence length scale was not measured. After flowing through the cascade, air exits into an exhaust duct of larger area and then to an exterior building vent.

The cascade proper is constructed of aluminum walls and airfoils, with the exception of the shroud cover plate, which is 5.08-cm-thick acrylic. The flow channel ahead of the blades contains a splitter plate, which extends from the turbulence grid to within 12.7 mm of the leading edge of the center airfoil, a distance of

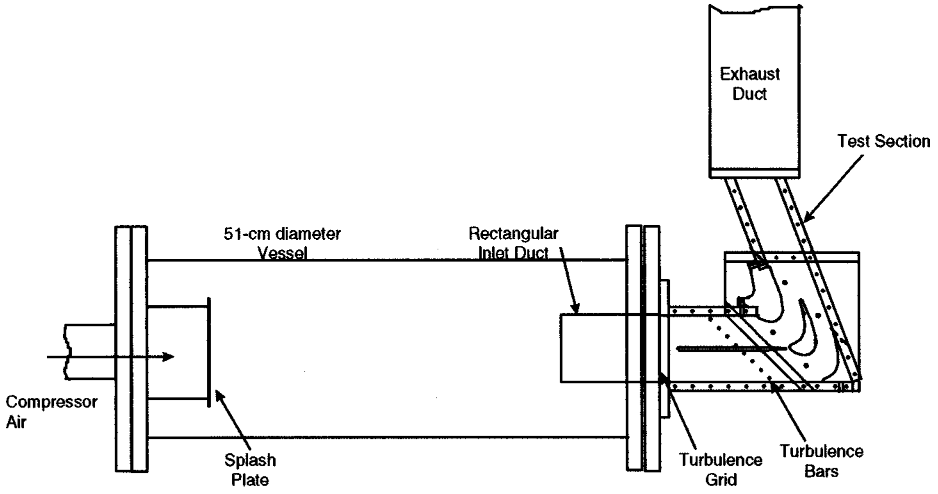

Fig. 1 Blade tip cascade facility

about 35.5 cm. The splitter plate divides the channel into equal halves for the purpose of guaranteeing equal flow to each blade cascade passage. Without this device, a substantially greater percentage of the total flow would proceed through the shorter flow passage due to less resistance in that overall path. Pressure traverses made in each of the two channels ahead of the blades verified the 50/50 flow split. These measurements also showed that typical turbulent flow profiles are present downstream of the turbulence grid. The splitter plate is 9.53 mm wide and extends over the entire span. The upstream end of the plate is rounded to minimize flow disturbance, and the downstream end is tapered to a thickness of 3.18 mm and rounded. It is realized that this splitter plate will present some disturbance to the flow field at the very leading edge of the blade, as well as the leading edge of the blade tip gap. The CFD analyses of Part 2 of this study are used to show the effect of this splitter plate on tip flow and heat transfer, thereby providing the necessary aid to interpretation of the present data. Also placed upstream of the blades are optional turbulence bars for use when a higher turbulence intensity is desired. When in use there are four 1.27-cm-diam round bars placed spanwise in each channel at a distance of 10.2 cm ahead of the blade leading edge plane. In this configuration, hot-film measurements show a turbulence intensity of 9 percent at the blade leading edge plane.

Cascade instrumentation, which is common to all of the present tests, includes an inlet air thermocouple placed midway between the inlet flange and blades, a total pressure wedge probe at the blade leading edge plane midway between two blades, and blade inlet and exit endwall static pressure taps along each passage centerline in the wall opposite the shroud. The total flow for the cascade is measured by an ASME standard orifice station placed in the air supply pipe lines ahead of the test rig. The nominal operating conditions for this cascade are an inlet total pressure of 160 kPa, an exit static pressure of 110.3 kPa, giving an overall blade pressure ratio of 1.45 when no tip gap is present ($C=0$). While the inlet flow and total pressure to each of the two cascade passages are equal, the exit conditions are not quite periodic. This is due to the differing exit lengths and the interactions with boundaries. When $C=0$, the upper passage (concave side of the center airfoil) has a pressure ratio of 1.47, while the lower passage is 1.43, based upon exit static pressures measured in the endwall at the blade root. For the average tip clearance tested, $C=2.03\,\mathrm{mm}$, the passages each have lower individual pressure ratios of 1.41 and 1.33, for upper and lower passages, respectively. This change is due to the leakage of air over the tip from upper to lower passage, and the existence of a flow gap over the airfoil trailing edge base. Experimentally this is not a problem, as long as the blade tip pressures are known and are representative of a typical pressure distribution driving the tip leakage. The nominal total flow rate for the cascade section is 3.4 kg/s, and the typical inlet air total temperature is 22°C. The inlet air velocity approaching the blades is 101 m/s and the corresponding Mach number is 0.30.

The definition of the airfoil placement is depicted in Fig. 2. The airfoils are constant cross section for the entire span (linear cascade) and represent the tip section of an aerodynamic blade design. The inlet flow angle to the test airfoil is 44.9 deg and the exit angle is 65.75 deg, giving a total turning of 110.65 degrees. The blade leading edge pitch is 13.37 cm. The axial chord length of the blade is 12.45 cm. The throat diameter at the point of minimum distance between two blades is 5.19 cm, which with a span of 10.16 cm gives a throat aspect ratio of about 2. The center airfoil is the test airfoil and as such is designed to allow variable insertion depths into the cascade to change the tip gap clearance beneath the acrylic shroud cover. Figure 2 also shows the shroud surface relative to the airfoils. The shroud contains a 2 mm step placed 3.43 cm ahead of the blade leading edge plane, which models a similar feature found in the turbine shroud. Additionally, a boundary layer trip is placed on the shroud wall 1.27 cm ahead of the step to ensure a fresh boundary layer approaches the blade tip and shroud flow region.

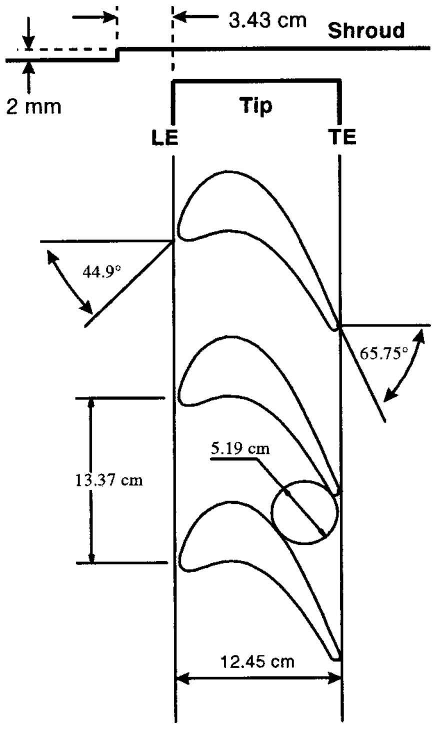

Fig. 2 Airfoil and shroud definition

The tip clearances used in the present study vary from 1.27 to 2.79 mm and are constant over the entire blade tip. Only the center airfoil contains this tip clearance to allow leakage flow from the pressure side to the suction side of the airfoil. An aluminum test airfoil having pressure taps around the entire perimeter of the airfoil was first placed in the center location of the cascade. Surface holes of 0.5 mm diameter were located 3.2 mm down from the blade tip to measure the near-tip airfoil pressure distribution without a tip clearance, and also with a clearance of 2.03 mm. These two pressure distributions are shown together in Fig. 3, where the airfoil local surface axial positions have been normalized by the axial chord length. These distributions show the effect of the gap leakage in modifying the pressure field, which ultimately drives the local leakage strengths and the resulting heat transfer. With the tip gap present, the Mach distribution is shifted ''toward'' the aft portion of the airfoil, which is consistent with expected leakage paths and strengths. At the tip section then, the exit Mach number for the test airfoil is 0.75. The corresponding airfoil Reynolds number is 2.57×10^6, based upon axial chord length and exit flow conditions. A separate blade having pressure measurement taps located on the tip surface, as well as a shroud plate with pressure taps opposite the blade tip surface, were used to obtain pressure field surveys within the tip gap. These surfaces and distributions will be shown in a later section of this paper.

For blade tip heat transfer testing, another central blade model was fabricated with specific features. Figure 4 shows the basic construction of this model. The lower half of the blade is made of aluminum for structural rigidity against the aerodynamic forces present during tests. This lower blade section is affixed to the bottom endwall; shims allow adjustment of the tip clearance. The upper half of the blade model is fabricated mainly of acrylic for good insulation against heat losses. The tip itself is comprised of a 6.35-mm-thick tip cap made of G7 (an insulating material), which is fit into a recess within the acrylic and sealed around all edges of the recess shelf. The width of the remaining edge of acrylic outside the G7 is 3.18 mm. The aft-most portion of the narrow trailing edge tip surface, which does not contain the recess, is about 19 mm in length. Between the G7 cap and the body

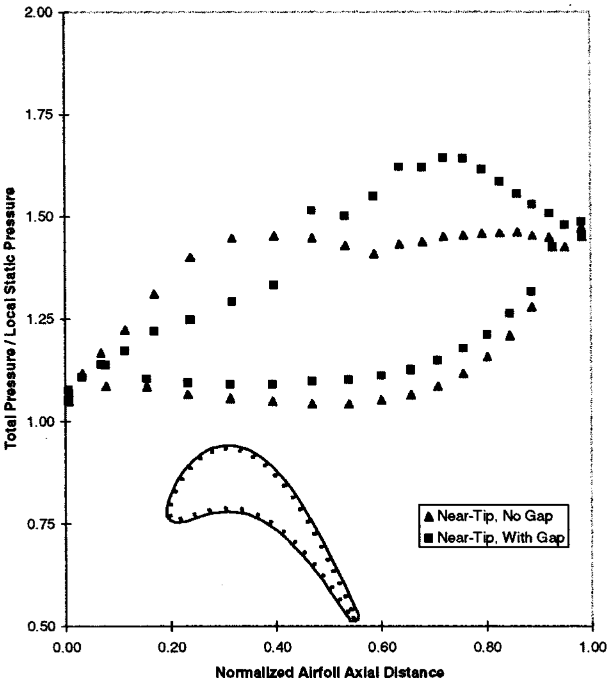

Fig. 3 Airfoil near-tip pressure distributions

of the acrylic blade is an air gap of 6.35 mm depth. This air gap serves as insulation, as well as giving access for the placement of monitoring thermocouples on the underside of the G7, which are routed out through a hole in the blade root. Two such tip models were made for this study, one with sharp tip edges (shown in figure), and the other with rounded edges of 2.54 mm radius. The extent of the tip cap is the same for each of these models.

The top surface of the G7 is covered by an etched thin-foil heater encased in Kapton, which was custom manufactured in the shape of the blade cross section. The heater is then covered by a 0.05-mm-thick layer of copper to assist in spreading the heat source from the etched foil circuit to form a uniform heat flux condition. The copper layer is covered with a sheet of liquid crystals. The liquid crystals used in this study are wide band 40°C to 45°C crystals made by Hallcrest (R40C5W). The liquid crystals are located beneath a 0.127-mm-thick Mylar encapsulation layer. This Mylar layer is constant in thickness, with a thermal conductivity of 0.145 W/m/K.

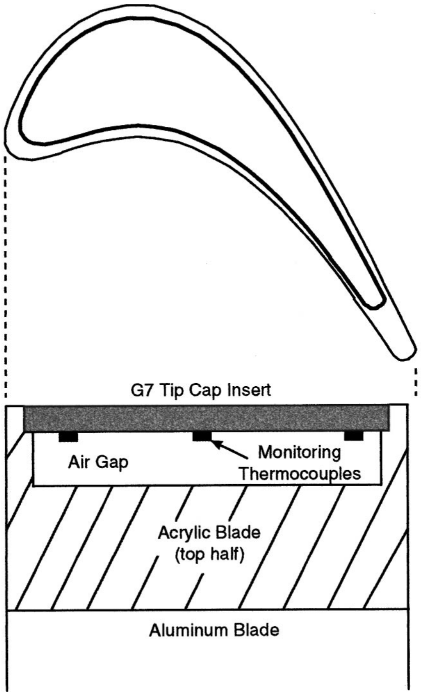

Fig. 4 Heat transfer blade tip construction

The temperature drop across the Mylar layer is accounted for in determining the tip surface temperature seen by the flow. All tests were run by maintaining a steady mainstream flow at the noted Reynolds number, and varying the heater power to allow various regions of the liquid crystals to display color as viewed through the clear shroud wall. The typical heater input power ranged from 40 to 150 W over a total surface area of 46.5 cm^2 for the sharp edge tip, or 33.7 cm^2 for the radius edge tip. Note that in all tests performed, only the tip cap portion of the cascade received a surface heat flux; all other surfaces remained unheated. In this respect, the cascade operates differently from an actual turbine in that the cascade blade tip does not attain the same heat flux direction or wall-to-gas temperature ratios as a turbine blade tip, hence additional adjustments must be made to apply such data to turbine conditions. Such adjustments must also be made to account for the reality of work extraction in a rotating turbine. All cascade model surfaces were smooth.

The general hue intensity method as described by Hollingsworth et al. [22] and Farina and Moffat [23] was used to deduce temperature from the liquid crystal responses. A separate calibration test stand was utilized for each sheet of liquid crystals as applied to the tip models, to determine the hue–temperature calibration curves. Liquid crystal calibrations followed the illuminant invariant method of Farina et al. [24]. Each blade tip heat transfer contour plot shown in this study is the result of some six or seven images obtained with differing heat fluxes, which are combined. The agreement in data within the overlapping regions of individual images is always found to be excellent.

The primary heat loss present during operation of the cascade amounts to the energy that is not going into the air, but rather is lost via conduction into the blade model and eventual convection into the air of the blade passage flows. This loss was estimated by running the cascade at nominal flow with a zero clearance gap. The tip was pushed up against the shroud with a small amount of perimeter sealing to avoid tip flow leakage and thermal conduction into the shroud. The heater power was adjusted until the liquid crystal layer and the several underside monitoring thermocouples gave the same temperature reading. The heat loss determined in this manner was 4 percent of the average total heater power. Heat transfer data shown account for this loss. Thermal radiation loss is estimated to be less than 1 percent of the total power for all conditions and is considered negligible.

The definition of the local heat transfer coefficient in this study is

$$h = Q_{\mathrm{wall}}/(T_{\mathrm{surface}} - T_{\mathrm{air\ inlet}})$$

where Q_{wall} is the input heater power per unit area, and T_{surface} is the liquid crystal indicated temperature adjusted for the Mylar layer. In the present results, $T_{\mathrm{air\ inlet}}$ is the total cascade inlet air temperature. The experimental uncertainty in local heat transfer coefficient defined in this manner is estimated to be ±8 percent or better using the methods of Kline and McClintock [25]. The controlling factor in the uncertainty is the driving temperature potential between the total air temperature and the local tip surface temperature of the Mylar. In all cases, a minimum value of 14°C was maintained for this temperature difference.

Tip and Shroud Pressure Measurements

In addition to the static pressure measurements obtained on the airfoil pressure and suction side surfaces, pressure measurements were also made on both the shroud surface opposite the blade tip and on the blade tip surface. A separate acrylic shroud cover was fabricated with over 100 holes located above the central blade tip region. All of the pressure holes were 1.59-mm-dia holes machined into the acrylic, with short-length 0.51-mm-dia through-holes to the flow path surface. A 48-channel automated Scanivalve system was used to record the pressures for various groups of measurement locations. On this shroud surface, one set of pressure holes was located around the airfoil tip perimeter and 2.54 mm outside the tip edge, while a second set of holes was located 2.54 mm inside the tip edge. Other pressure holes were placed over the interior region above the tip. Figure 5 shows the shroud pressure distribution, in the form of pressure ratios for consistency, over the sharp edge blade tip model with a clearance of 2.03 mm. The inset figure shows the locations of the pressure holes relative to the tip. The ''outer'' pressure side (*P*/*S*) and suction side (*S*/*S*) data represent the measurements just prior to flow entry into the gap or just after exit from the gap, respectively. Likewise, the ''inner'' data represent measurements just inside the tip edges. The ''mean camber'' data are located above the blade mean chord line. As the data show, there is little difference in pressures over the forward 30 percent of the airfoil, but over the remaining portion there is a large pressure drop associated with the pressure side entry into the gap clearance. Some recovery is observed as the mean camber line is reached, and a bit more as the suction side exit is approached. The final difference in pressure ratios from the pressure side outer to the suction side outer locations is nearly the same as that shown for the near-tip, with gap, airfoil measurements of Fig. 3. The same measurements were made for the blade tip model with perimeter radius edge, leading to very similar results.

For the blade tip surface pressure measurements a separate aluminum tip model was made with similar pressure holes arrayed in the tip surface. In this case, a set of holes was placed around the perimeter and offset 5.08 mm to the interior of the sharp tip edge. Additional pressure holes were located in the interior region to measure the mean camber line pressures. Figure 6 shows the pressure distributions for the sharp edge tip model for each of three tip gap clearances. The suction side pressures are for the most part essentially the same for each clearance. The pressure side data also show no effect of clearance over the forward 40 percent of the tip. The aft portion of the tip, however, shows an increasing pressure differential between *P*/*S* and *S*/*S* as the clearance is increased, and this change is primarily due to a large decrease in *P*/*S* gap inlet pressure. This decreasing pressure has an associated higher local flow velocity which will be reflected in the tip heat transfer data shown later. Also of note is the downturn in *P*/*S* pressure ratios towards the trailing edge region of the tip. In this region there is less direct *P*/*S* to *S*/*S* gap leakage as the passage flow streams come to similar velocities.

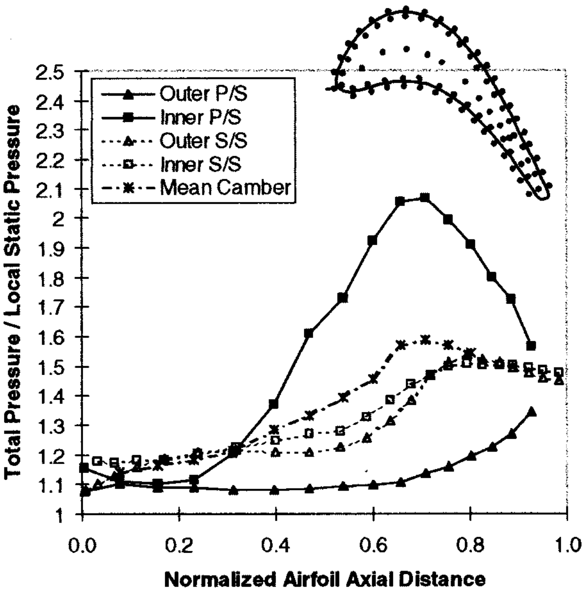

Fig. 5 Shroud surface pressure distribution with sharp-edge blade tip and clearance of 2.03 mm

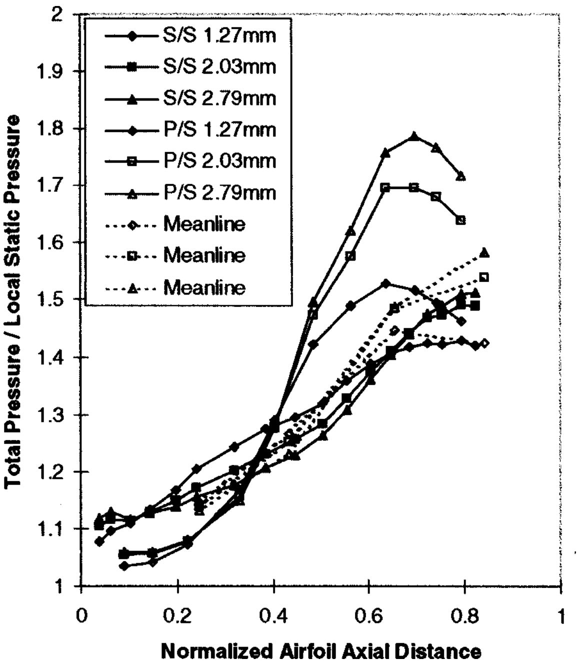

Fig. 6 Blade tip surface pressure distribution with sharp-edge tip and variable clearance

The bulk of direct tip gap leakage is then in the 40–90 percent axial chord range, though leakage also occurs from forward locations on the pressure side to midchord locations on the suction side. These tip surface pressure distributions were also measured for a radius edge tip having a 2.54 mm radius around the perim-

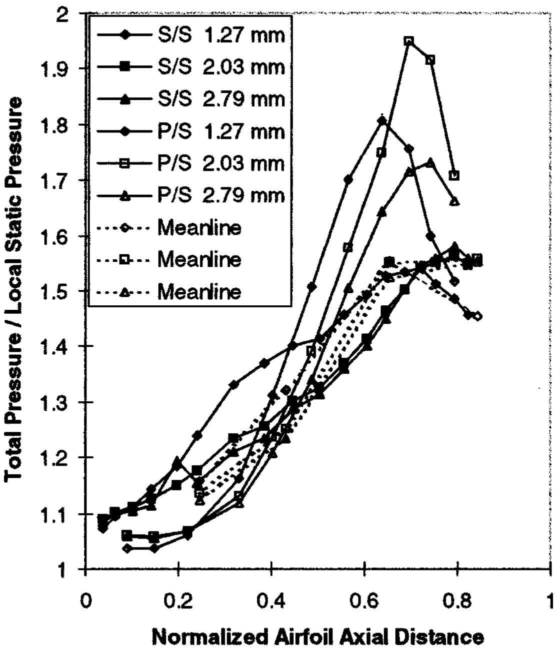

Fig. 7 Blade tip surface pressure distribution with radius-edge tip and variable clearance

eter of the tip. The effect of this tip edge radius is shown in Fig. 7, where the P/S entry pressure loss is clearly more dependent upon the clearance height. A distinction in P/S measurements is seen beginning as far forward as 30 percent axial chord location. The smaller clearances of 1.27 and 2.03 mm show higher P/S pressure ratios than their sharp edge counterparts, and each of the three P/S distributions peak at differing locations. The radius appears to have a definite effect in some redistribution of flow and flow strength into the gap. Little effect is observed on the S/S pressures.

Heat Transfer Results

Tip surface heat transfer coefficient contour plots are shown for both sharp edge and radius edge tip models. In the case of the sharp edge tip model, the surface heater and liquid crystal layer extend to very nearly the edge of the blade tip. Data for the far edges of the tip surface should be considered less reliable since there does exist some two-dimensional conduction here, as well as slightly less heat flux uniformity. In the case of the radius-edge tip model, the surface heater and liquid crystal layer cover less area, being offset to the interior to allow for the edge radius; i.e., the heater does not extend into the radius. Hence, the extent of data is less for the radius tip model. Approximate blade profile overlays are provided in the figures to help in judging these differences. Additionally, regions of very high heat transfer coefficients tend to be more difficult to acquire with a single liquid crystal type, since these regions may require heat fluxes resulting in temperatures that exceed material capabilities. Such limitation is most notable in the absence of full data in the trailing edge regions of some tests.

Figure 8 shows the tip heat transfer coefficient contour map for the sharp edge tip model with a nominal tip clearance gap of 2.03 mm and an approach free-stream turbulence intensity of 5 percent. The distribution of heat transfer coefficient seen here is typical in overall aspects for every case tested in this study; number labels are provided for the following description. Most apparent in this distribution is the development of a low heat transfer region within the thickest portion of the tip, what one might refer to as the ''sweet spot'' (1). This region emanates from the airfoil pressure side location associated with the diffusion zone in Fig. 3, at about 20–30 percent axial chord location (2). The low heat transfer region extends into the central area of the tip and appears to extend aft and toward the suction side. This sweet spot is the area of lowest convective velocity on the tip as seen in the tip pressures of Fig. 6. At about 30–35 percent axial chord the P/S and S/S tip pressures are nearly equal. The tip flow forward of this location proceeds across the leading edge region from P/S to S/S essentially at right angles to the tip meanline, producing high heat transfer coefficients there (3). The tip flow aft of the P/S diffusion location encounters a large entry region pressure loss, clearly seen in Fig. 6, as it enters the P/S of the gap. This entry loss is seen in the bending of the heat transfer coefficient contours near the P/S midchord, creating high local heat transfer gradients (4). The sweet spot conforms around this heavy entry loss area, channeling flow down the mean camber line to the suction side (5). It is postulated that there is a separation vortex in this P/S entry region of the midchord, with similar roll up and bending toward the airfoil trailing edge as seen in Sjolander and Cao [5]. The portion of the tip suction side from the leading edge around the sweet spot exhibits increasing heat transfer from the center of the tip outward with isopleths of the same shape as the suction side profile. The high thermal gradients here are a result of the accelerating leakage flow exiting the tip gap (6). In the trailing edge region of about 50 percent axial chord and aft, leakage flow proceeds mostly straight across from P/S to S/S, except as modified by the entry region separation. Suction side heat transfer coefficients in the trailing edge are observed to be increasing with regularity as one proceeds aft, with the isopleths (lines of constant heat transfer coefficient) aligned at right angles to the suction side exit (7).

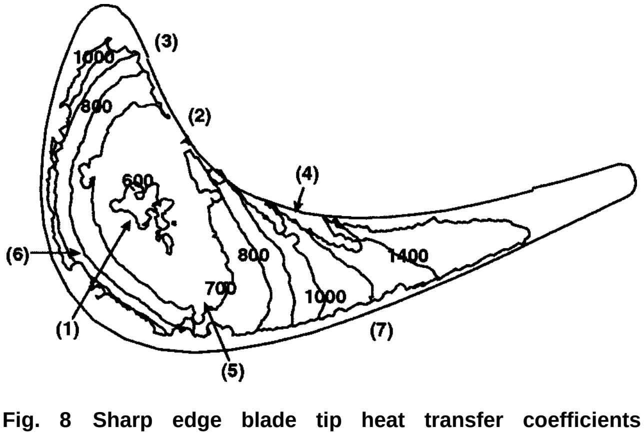

Fig. 8 Sharp edge blade tip heat transfer coefficients (W/m^2/K) for clearance of 2.03 mm and Tu=5 percent

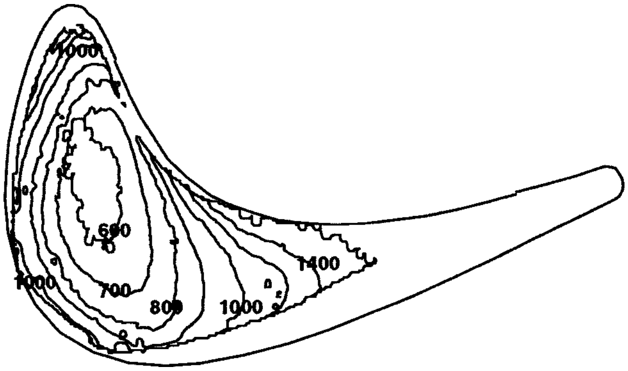

Fig. 9 Sharp edge blade tip heat transfer coefficients (W/m^2/K) for clearance of 2.03 mm and Tu=9 percent

Altering the approach free-stream turbulence intensity level from 5–9 percent by means of the circular rods installed upstream of the airfoils results in the tip heat transfer coefficient distribution shown in Fig. 9. The pattern of heat transfer is seen to be the same as that of Fig. 8. The heat transfer magnitude in the central sweet spot is about 10 percent greater in this case. Heat transfer in the leading edge region is altered but little over the $Tu=5$ percent result; however, that in the trailing edge region aft of the sweet spot is as much as 20 percent higher. The increase in approach Tu level is not expected to change the magnitude of tip leakage flow, but only to adjust the tip local heat transfer. It appears that the increased Tu level has had little effect on tip heat transfer over the forward 50 percent of the tip, but has a not insubstantial effect on the high leakage portion of the blade tip.

Using this tip heat transfer result as more representative of a turbine blade, i.e., higher Tu, a portion of the tip heat transfer was compared to existing literature results. Figure 10 shows the heat transfer coefficients along a single trajectory starting at about 40 percent axial chord on the P/S and ending at about 60 percent axial chord on the S/S. This trajectory follows a line from P/S to S/S within the midchord region which experiences an entry separation followed by reattachment and flow to the exit. Recalling that this is a sharp edge tip, the result is compared to two cases from the work of Boelter et al. [26] as presented in Kays and Crawford [27]: (1) the case of heat transfer in the entry of a sudden contraction, and (2) the case of heat transfer with fully developed flow prior to a heated section. For the blade tip, the hydraulic diameter is taken to be clearance C. Using the overall driving pressure for this trajectory from Fig. 3, the resulting Re_C is 38,750. The correlation for fully developed turbulent channel flow heat transfer, $\mathrm{Nu}_o = 0.023\,\mathrm{Re}^{0.8}\,\mathrm{Pr}^{0.4}$, yields a developed heat transfer coefficient for this location of 1050 W/m^2/K. This heat

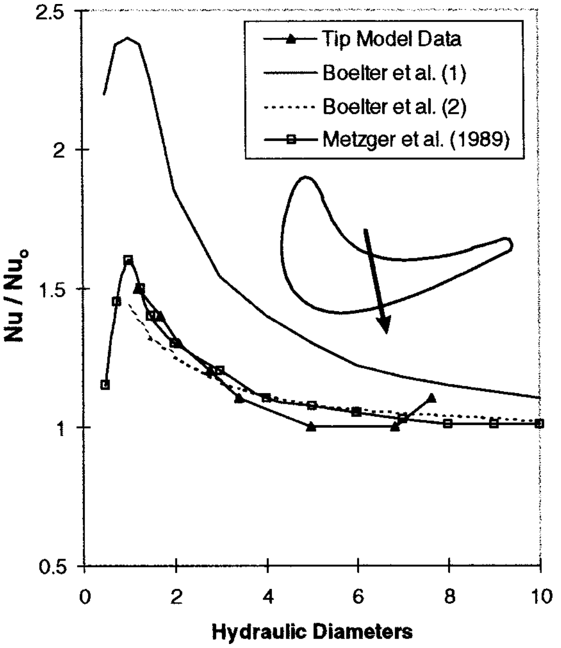

Fig. 10 Comparison of selected tip data with pipe entry region data of Boelter et al. [26] and tip model data of Metzger et al. [9]

transfer level is within 5 percent of the measured value on the blade tip where the isopleth begins to level out at a minimum (refer to the H=1000 isopleth in Fig. 9). The present example of data has insufficient resolution in the entry region to define the heat transfer within $x/C<1$, but the data do lie between cases (1) and (2) of Boelter et al. The present geometry can be expected to lie between these extremes since the entry flow is not strictly normal to the tip edge, but swept into the gap with a streamwise component of flow. Also, the tip model has a sudden contraction on only one side. The exiting region of the tip flow shows an increase over fully developed heat transfer due to the modification of acceleration and turning. This example shows that certain regions of the present blade tip model do conform to the simple pressure-driven heat transfer behavior demonstrated in previous research such as that of Metzger et al. [9]. It is interesting to note that Metzger et al. [9] also found flat tip heat transfer in their rectangular model geometry to be lower than that of the sudden contraction entry of Boelter et al. (case 1); in fact their result was nearly the same as the present study.

The second blade tip geometry tested in this study was that with a simple radius tip edge. A constant radius of 2.54 mm was formed around the entire perimeter of the blade tip. The purpose of the radius is to provide some casement to the sharp edged entry which the P/S leakage flow sees, as well as providing a better representation of expected blade tip features in service. Figure 11 shows the radius edge tip heat transfer coefficient distribution with a clearance gap of 2.03 mm and approach Tu of 5 percent. Compared to the sharp edge case of Fig. 8, the tip heat transfer is here is about 10 percent higher in most regions. This increase might be attributed to the reduced resistance to tip leakage caused by the radius edge, thereby allowing more total leakage flow and subsequently higher heat transfer, though the effects of tip pressure distributions as shown in Fig. 7 can be somewhat subtle in redistributing leakage flows. Figure 12 shows heat transfer for the same tip with an approach Tu of 9 percent. Here too, the tip heat transfer has been increased by 10–15 percent over that of the sharp edge shown in Fig. 9. The relation between radius edge tip heat transfer at Tu of 5 percent and 9 percent is the same as that previously described for the sharp edge cases, a moderate increase in the sweet spot and a somewhat higher increase in the midchord and aft regions.

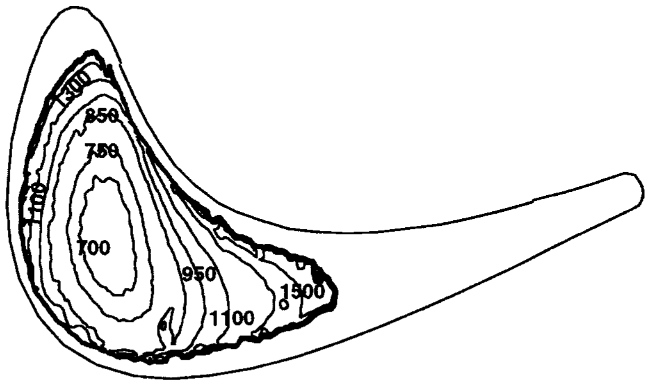

Fig. 12 Radius edge blade tip heat transfer coefficients (W/m^2/K) for clearance of 2.03 mm and Tu=9 percent

Finally, Figs. 13 and 14 show tip heat transfer coefficient distributions for the radius edge model with altered tip gap clearances of 1.27 mm and 2.79 mm, respectively, both at Tu of 9 percent. These changes to the clearance amount to ±38 percent of the nominal gap height of 2.03 mm, or on the basis that nominal clearance is 1 percent of total blade height in a typical turbine then this change is ±0.38 percent of blade height. Tightening the tip clearance serves to decrease heat transfer by about 10 percent due to a reduced tip leakage flow. The sweet spot of Fig. 13 appears to be broader, especially in its extent into the midchord region on the

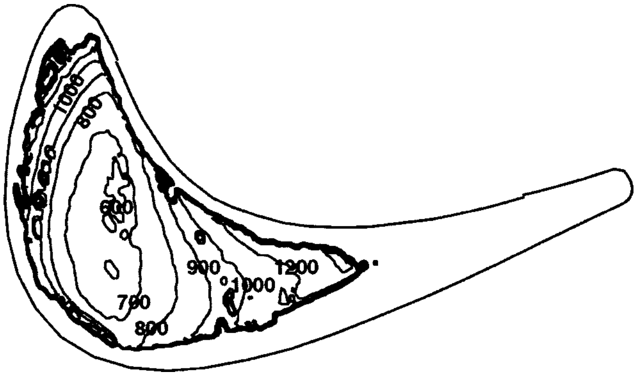

Fig. 11 Radius edge blade tip heat transfer coefficients (W/m^2/K) for clearance of 2.03 mm and Tu=5 percent

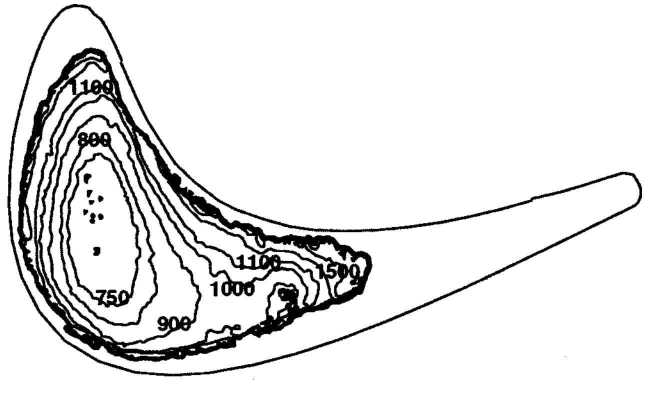

Fig. 13 Radius edge blade tip heat transfer coefficients (W/m^2/K) for clearance of 1.27 mm and Tu=9 percent

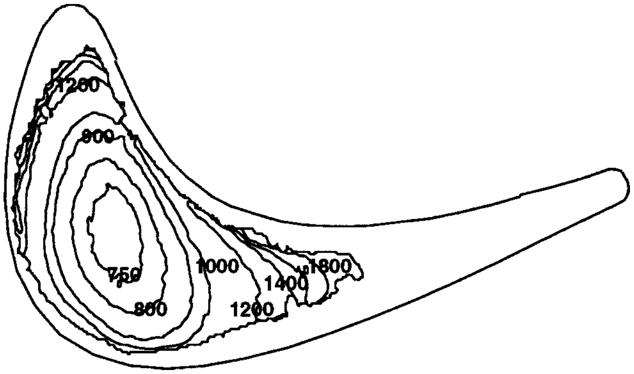

Fig. 14 Radius edge blade tip heat transfer coefficients (W/m^2/K) for clearance of 2.79 mm and *Tu*=9 percent

suction side of meanline. Increasing the tip clearance serves to increase tip heat transfer by about the same amount of 10 percent due to more tip leakage flow.

Conclusions

The present study has utilized a linear airfoil cascade for the express purpose of examining the detailed heat transfer coefficient distributions on the tip surface of a blade model. This is the first reported study of this type that obtains nearly full surface information on heat transfer coefficients within an environment that develops an appropriate pressure distribution about an airfoil blade tip and shroud model. The blade tip model employed is representative of a typical power turbine, having an airfoil Reynolds number of 2.57×10^6 and an overall pressure ratio of 1.45. The major findings of this study may be summarized as follows:

- In this stationary cascade model, the pressures measured on the airfoil in the near-tip region form a good basis for determining the overall pressure driven tip leakage flows. Details of the pressure field on the tip surface are required to fully explain the heat transfer results, even for the simple case of a flat blade tip.
- Shroud pressure measurements agree well with the tip surface pressures in this setting, showing much the same local characteristics.
- Tip entry flow for the sharp edge case exhibits differing character at various positions along the pressure side, with a marked high entry loss region in the midchord-to-aft region. Addition of a small tip edge radius serves to redistribute this entry effect and lead to greater leakage at nominal clearance (as deduced from higher tip heat transfer levels).
- The present tip geometry and flow field demonstrate a characteristic central sweet spot of low heat transfer which extends into the midchord region and toward the suction side. A pressure side entry separation vortex aft of the sweet spot creates a significant enhancement to heat transfer aft of the sweet spot. Large heat transfer coefficient gradients are observed at outlying suction side peripheral areas in the forward half of the airfoil tip.
- An increase in the approach freestream turbulence intensity level from 5 to 9 percent raises the overall tip heat transfer by about 10 percent more so in the aft portion of the tip (~ 20 percent) and less in the forward areas (~ 0 percent).
- The addition of a small edge radius to the tip perimeter causes the tip heat transfer to increase by about 10 percent in most areas, presumably due to higher allowed tip leakage flow.
- Decreasing the tip clearance C by 38 percent of the nominal value results in a decrease of some 10 percent in heat transfer, while an equivalent increase in tip clearance results in a 10 percent increase in heat transfer.
- Certain regions of the present tip model appear to conform to a simple pressure driven heat transfer behavior similar to that of entry flow into a sudden contraction, but with significant local modifications due to the three-dimensional nature of the flow.

For all of the cases studied here, the blade tip heat transfer coefficient distributions show similar features. The variety of regional effects though points to a very three-dimensional problem even for this stationary case. The data obtained under these simplified conditions is used for comparison to three-dimensional CFD predictions of the flow and heat transfer in the blade tip region, which is the subject of Part 2 of this study.

Acknowledgments

This study was prepared with the support of the U.S. Department of Energy, under Cooperative Agreement No. DE-FC21-95MC31176. However, any opinions, findings, conclusions, or recommendations expressed herein are those of the author and do not necessarily reflect the views of the DOE.

Nomenclature

C = tip gap clearance, mm
h = convective heat transfer coefficient, W/m^2/K
k = thermal conductivity W/m/K
LE = airfoil leading edge designation
Nu = Nusselt number $= hC/k_{\mathrm{air}}$
P/S = pressure side of airfoil (concave side)
Q_{wall} = tip surface applied heat flux, W
Re = cascade Reynolds number based on airfoil axial chord length and exit conditions
S/S = suction side of airfoil (convex side)
TE = airfoil trailing edge designation
$T_{\mathrm{air\ inlet}}$ = cascade inlet total air temperature °C
T_{surface} = mylar surface temperature °C
Tu = approach free-stream turbulence intensity

References

[1] Lakshminarayana, B., 1970, ''Methods of Predicting the Tip Clearance Effects in Axial Flow Turbomachinery,'' ASME J. Basic Eng., **92**, pp. 467–482.
[2] Booth, T. C., Dodge, P. R., and Hepworth, H. K., 1982, ''Rotor-Tip Leakage: Part I-Basic Methodology,'' ASME J. Eng. Power, **104**, pp. 154–161.
[3] Wadia, A. R., and Booth, T. C., 1982, ''Rotor-Tip Leakage: Part II—Design Optimization Through Viscous Analysis and Experiment,'' ASME J. Eng. Power, **104**, pp. 162–169.
[4] Moore, J., Moore, J. G., Henry, G. S., and Chaudhry, U., 1989, ''Flow and Heat Transfer in Turbine Tip Gaps,'' ASME J. Turbomach., **111**, pp. 301–309.
[5] Sjolander, S. A., and Cao, D., 1995, ''Measurements of the Flow in an Idealized Turbine Tip Gap,'' ASME J. Turbomach., **117**, pp. 578–584.
[6] Kaiser, I., and Bindon, J. P., 1997, ''The Effect of Tip Clearance on the Development of Loss Behind a Rotor and a Subsequent Nozzle,'' ASME Paper No. 97-GT-53.
[7] Seban, R. A., 1965, ''Heat Transfer and Flow in a Shallow Rectangular Cavity With Subsonic Turbulent Air Flow,'' Int. J. Heat Mass Transf., **8**, pp. 1353–1368.
[8] Mayle, R. E., and Metzger, D. E., 1982, ''Heat Transfer at the Tip of an Unshrouded Turbine Blade,'' *Proc. Seventh Int. Heat Transfer Conf.*, Hemisphere Pub., pp. 87–92.
[9] Metzger, D. E., Bunker, R. S., and Chyu, M. K., 1989, ''Cavity Heat Transfer on a Transverse Grooved Wall in a Narrow Flow Channel,'' ASME J. Lubr. Technol., **111**, pp. 73–79.
[10] Chyu, M. K., Moon, H. K., and Metzger, D. E., 1989, ''Heat Transfer in the Tip Region of Grooved Turbine Blades,'' ASME J. Heat Transfer, **111**, pp. 131–138.
[11] Yang, T. T., and Diller, T. E., 1995, ''Heat Transfer and Flow for a Grooved Turbine Blade Tip in a Transonic Cascade,'' ASME Paper No. 95-WA/HT-29.
[12] Metzger, D. E., Dunn, M. G., and Hah, C., 1991, ''Turbine Tip and Shroud Heat Transfer,'' ASME J. Turbomach., **113**, pp. 502–507.
[13] Metzger, D. E., and Rued, K., 1989, ''The Influence of Turbine Clearance Gap Leakage on Passage Velocity and Heat Transfer Near Blade Tips: Part I—Sink Flow Effects on Blade Pressure Side,'' ASME J. Turbomach., **111**, pp. 284–292.
[14] Rued, K., and Metzger, D. E., 1989, ''The Influence of Turbine Clearance Gap Leakage on Passage Velocity and Heat Transfer Near Blade Tips: Part II—Source Flow Effects on Blade Suction Sides,'' ASME J. Turbomach., **111**, pp. 293–300.
[15] Kim, Y. W., Abdel-Messeh, W., Downs, I. F., Soechting, F. O., Steuber, G. D., and Tanrikut, S., 1995, ''A Summary of the Cooled Turbine Blade Tip Heat

Transfer and Film Effectiveness Investigations Performed by Dr. D. E. Metzger,'' ASME J. Turbomach., **117**, pp. 1–11.
[16] Chyu, M. K., Metzger, D. E., and Hwan, C. L., 1987, ''Heat Transfer in Shrouded Rectangular Cavities,'' J. Thermophys., **1**, No. 3, pp. 247–252.
[17] Ameri, A. A., and Steinthorsson, E., 1995, ''Prediction of Unshrouded Rotor Blade Tip Heat Transfer,'' ASME Paper No. 95-GT-142.
[18] Ameri, A. A., and Steinthorsson, E., 1996, ''Analysis of Gas Turbine Rotor Blade Tip and Shroud Heat Transfer,'' ASME Paper No. 96-GT-189.
[19] Ameri, A., Rigby, D. L., and Steinthorsson, E., 1998, ''Effect of Squealer Tip on Rotor Heat Transfer and Efficiency,'' ASME J. Turbomach., **120**, pp. 753–759.
[20] Ameri, A. A., Steinthorsson, E., and Rigby, D. L., 1999, ''Effects of Tip Clearance and Casing Recess on Heat Transfer and Stage Efficiency in Axial Turbines,'' ASME J. Turbomach., **121**, pp. 683–693.
[21] Ameri, A. A., and Bunker, R. S., 2000, ''Heat Transfer and Flow on the First-Stage Blade Tip of a Power Generation Gas Turbine: Part 2—Simulation Results,'' ASME J. Turbomach., **122**, pp. 272–277.
[22] Hollingsworth, D. K., Boehman, A. L., Smith, E. G., and Moffat, R. J., 1989, ''Measurement of Temperature and Heat Transfer Coefficient Distributions in a Complex Flow Using Liquid Crystal Thermography and True-Color Image Processing,'' *Collected Papers in Heat Transfer*, ASME pp. 35–42.
[23] Farina, D. J., and Moffat, R. J., 1994, ''A System for Making Temperature Measurements Using Thermochromic Liquid Crystals,'' Report No. HMT-48, Thermosciences Division, Stanford University.
[24] Farina, D. J., Hacker, J. M., Moffat, R. J., and Eaton, J. K., 1994, ''Illuminant Invariant Calibration of Thermochromic Liquid Crystals,'' Exp. Therm. Fluid Sci., **9**, pp. 1–9.
[25] Kline, S. J., and McClintock, F. A., 1953, ''Describing Uncertainties in Single Sample Experiments,'' *Mechanical Engineering*, Vol. 75, Jan., pp. 3–8.
[26] Boelter, L. M. K., Young, G., and Iversen, H. W., 1948, ''An Investigation of Aircraft Heaters XXVII—Distribution of Heat Transfer Rate in the Entrance Region of a Tube,'' NACA TN 1451.
[27] Kays, W. M., and Crawford, M. E., 1980, *Convective Heat and Mass Transfer*, 2nd ed., McGraw-Hill, p. 269.

Heat Transfer and Flow on the First-Stage Blade Tip of a Power Generation Gas Turbine: Part 2—Simulation Results

A. A. Ameri
AYT Corporation,
Brook Park, OH 44135

R. S. Bunker
General Electric Corp. R & D Center,
Schenectady, NY 12309

A combined experimental and computational study has been performed to investigate the detailed distribution of convective heat transfer coefficients on the first-stage blade tip surface for a geometry typical of large power generation turbines (>100 MW). This paper is concerned with the numerical prediction of the tip surface heat transfer. Good comparison with the experimental measured distribution was achieved through accurate modeling of the most important features of the blade passage and heating arrangement as well as the details of experimental rig likely to affect the tip heat transfer. A sharp edge and a radiused edge tip was considered. The results using the radiused edge tip agreed better with the experimental data. This improved agreement was attributed to the absence of edge separation on the tip of the radiused edge blade. [S0889-504X(00)01802-X]

Introduction

Blade tips are susceptible to burnout and oxidation due to high thermal loading associated with flow through blade tip gaps. Efficient internal or film cooling schemes are necessary to protect the blade against damage. The design of such schemes requires detailed knowledge of heating patterns on and near the tip, which could be gained by predictive methods. The quality of the predictive method can only be assessed through comparison with relevant experimental data. In the absence of comprehensive data on tip heat transfer, in order to validate computations relating to tip and casing treatments and their effects on heat transfer, the available data on various aspects not directly related to the blade tip heat transfer have been relied upon. For example, for the assessment of the effect of tip recess on the tip heat transfer and efficiency, Ameri et al. [1] used the data of Metzger et al. [2] for modeled tip recess to verify the applicability of the numerical scheme and especially the turbulence model. Numerical prediction of the effect of the casing recess on the blade and tip heat transfer and efficiency [3] was deemed reliable on the basis of the good experiences of the past with the numerical scheme and favorable comparison of the calculated efficiency as a function of tip clearance height with experimental correlations.

There are in fact some heat transfer data available on blade tips, but these are limited to discrete point measurements on locations mainly along the mean camber line of the tip of rotating blades [4–6]. The data do provide a useful check on the numerical prediction of heat transfer, as was done by Ameri and Steinthorsson [7,8]. As the variation of the rate of heat transfer on the tip can be large, the complete map of the tip heat transfer would of course be more useful and agreement with such data more reassuring.

The complete measured heat transfer map of the blade tip as presented in Part 1 of this paper provides the valuable test case that can engender confidence in the numerical solutions. The results reported in this paper constitute the first reported direct comparison between the experimental and numerical calculation of blade tip heat transfer. It is also the first time a computation on a radiused edge tip is presented.

The paper is organized as follows: In the ensuing section a brief description of the experimental setup will be provided. Following this the numerical method used in the simulations will be described. Subsequently the results of the numerical simulations will be presented and finally a summary and the conclusions of the work will be presented.

Experimental Setup

The experimental setup and conditions will be briefly discussed in this section. A detailed description can be found in Part 1 of this paper.

Figure 1 shows the definition of the airfoils and the shroud. The blade profiles are typical of a large power generation turbine. The cascade is linear and the span is 10.16 cm. As can be seen, the shroud contains a step or a recess ahead of the blades to model a similar feature found in an actual turbine shroud. The tip clearance varies from 1.27 to 2.79 mm. However, in this paper we will exclusively address the nominal gap width of 2.03 mm. Figure 2 shows the design of the actual two-passage blade cascade.

The experiments were conducted using two types of blade tips namely, a sharp edged tip and a radiused tip with a radius of 2.54 mm around the perimeter of the tip. The measurements were taken on the tip of the middle blade. The adjacent blades are simulated by the use of contoured walls. A splitter plate was placed ahead of the blade to help force equal mass flow rate in the two passages.

Table 1 lists the run conditions for the cascade and input to the numerical simulations. Our calculations were limited to the 5 percent turbulence intensity.

Computational Method

The simulations in this study were performed using a multiblock computer code called LeRC-HT, previously known as TRAF3D.MB [9] which is based on a single block code designed by Arnone et al. [10]. This code is a general purpose flow solver designed for simulations of flows in complicated geometries. The code solves the full compressible Reynolds-averaged, Navier–Stokes equations using a multistage Runge–Kutta based multigrid method. It uses the finite volume method to discretize the equations. The code uses central differencing together with artificial dissipation to discretize the convective terms. The overall accuracy of the code is second order. The present version of the code [1,11,12] employs the $k-\omega$ turbulence model developed by Wilcox [13,14] with modifications by Menter [15]. The model integrates to the walls and no wall functions are used. For heat trans-

---

Contributed by the International Gas Turbine Institute and presented at the 44th International Gas Turbine and Aeroengine Congress and Exhibition, Indianapolis, Indiana, June 7–10, 1999. Manuscript received by the International Gas Turbine Institute February 1999. Paper No. 99-GT-283. Review Chair: D. C. Wisler.

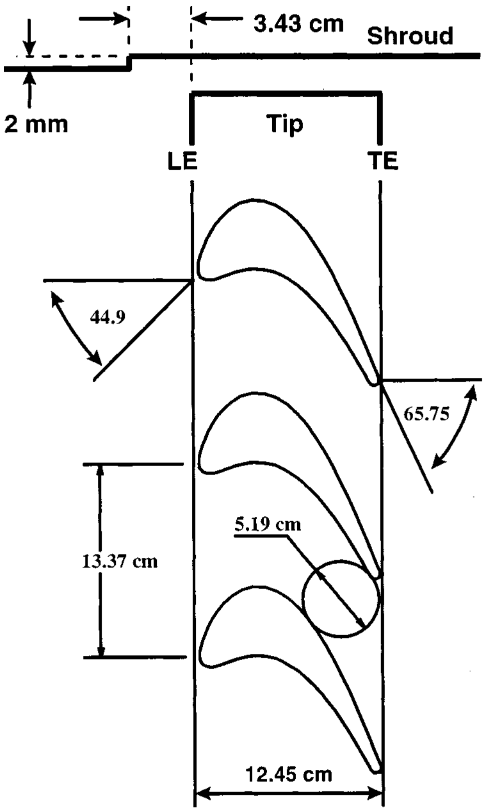

Fig. 1 Airfoil and shroud definition

fer a constant value of 0.9 turbulent Prandtl number, Pr_t, is used. A constant value for Prandtl number (Pr) equal to 0.72 is used. Viscosity is a function of temperature through a 0.7 power law [16] and *Cp* is taken to be a constant.

Geometry Modeling and Grids

Two types of modeling were utilized for the present problem: (*a*) modeling of the flow using a periodic blade cascade as shown in Figs. 3 and (*b*) modeling using the complete flow path including the splitter plate. For both of these the casing recess is included. Details of the casing recess can be seen more closely in Fig. 4(*b*). The casing recess also extended over the splitter plate as was the case in the experiment. Sharp and radiused edged tips were used. Figure 5 shows a radiused edge blade. The same grid topology was used with the radiused and the sharp edge grid. The grid is generated using a commercially available computer program called GridPro™. The sharp edge case was run with the side walls modeled using slip and no-slip boundary conditions. It was decided that since the heat transfer and pressure results did not differ significantly, the slip boundary condition for the side walls be used for the radiused edge case in order to conserve CPU time. The model in Fig. 3 consisted of 1.2 million cells. The model of Fig. 4 consisted of 1.4 or 1.8 million cells depending on whether slip or no-slip side walls were used. The viscous grid is generated by embedding grid lines where needed, including the grid around the splitter. The stretching ratio did not exceed 1.25 for the viscous grid away from the no-slip surfaces. The distance to the first cell center adjacent to solid wall is such that the distance in wall units, (y^+), is near or below unity. To resolve the boundary layers 33–35 grid points are used. This does not include the ''inviscid'' blade-to-blade grid which is also quite fine. Within the tip 65–69 grid points are used in the spanwise direction. At the inlet patch the number of grid points is 85 in the pitchwise and 97 in the spanwise direction.

Table 1 Run conditions

Pressure ratio across the blade row	0.69
Exit Reynolds number	2.57E6
Inlet Mach number	0.30
Turbulence intensity	5% and (9%)
Inlet angle	44.9 deg.

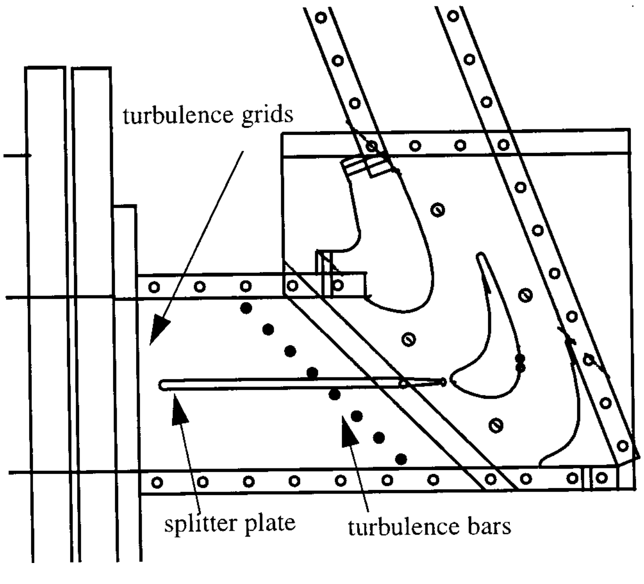

Fig. 2 Cascade

Results and Discussion

General Remarks. All the cases presented herein have been converged to better than 0.002 percent mass flow error between the inlet and the exit of the computational domain. The residual for all the cases dropped six to seven orders of magnitude. Typically 2000 fine grid iterations with two levels of multigrid were necessary for convergence. The heat transfer results have been checked for convergence by comparing solutions after consecutive runs of 300 iterations.

A number of calculations were made to help determine the proper way of modeling the geometry. The choices were a linear cascade with periodic boundary conditions and modeling the channels as in the experimental rig. The results as relates to the pressure distribution is presented in the next section. The heat transfer results are presented in the subsequent section.

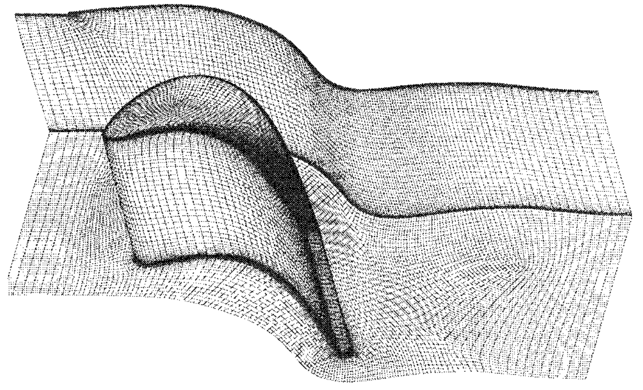

Fig. 3 Overall grid using periodic flow assumption

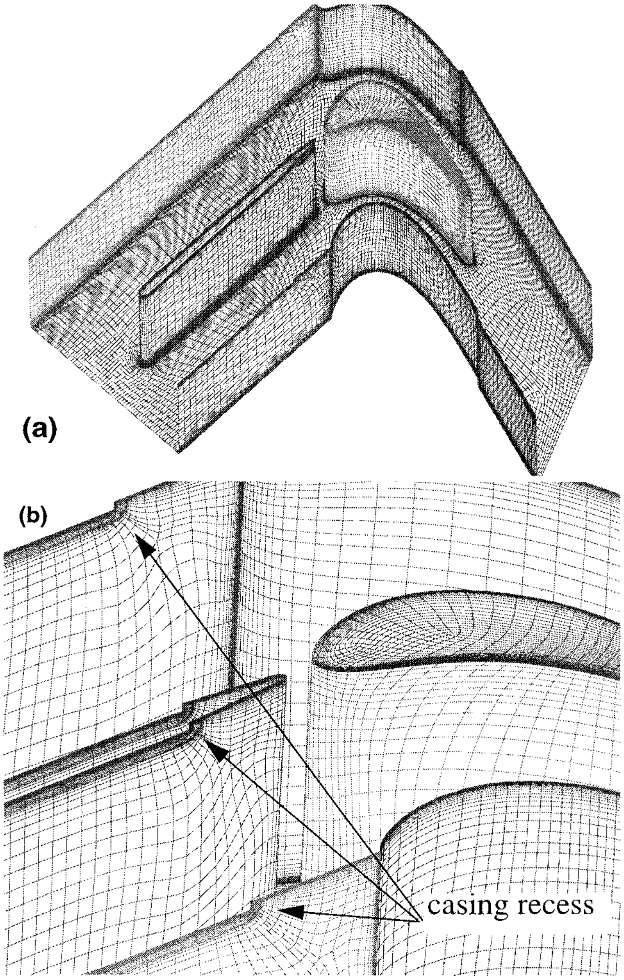

Fig. 4 Model of complete passage: (*a*) overall geometry and grid; (*b*) close-up near leading edge

Pressure Distribution. As described in Part 1, the experimental blade passage consists of one blade with variable clearance and two shaped walls representing the adjacent blades. It might be expected that any similarity to a periodic flow in the two passages is quickly lost as one approaches the tips of the blade, since the flow passes over only the center blade. Figure 6 shows the pressure distribution at the midspan and near the tip of the blade for an experimental run for which the tip gap is closed. The numerical prediction in that figure is done using a periodic setup as in Fig. 3. The calculated midspan pressure distribution matches the characteristics of the experimental measurements leading to the conclusion that the midspan flow is quite periodic. Near the tip the agreement between the experimental and the numerical results is lost. This indicates that the assumption of periodic flow is not a realistic option for calculation of quantities in the endwall region.

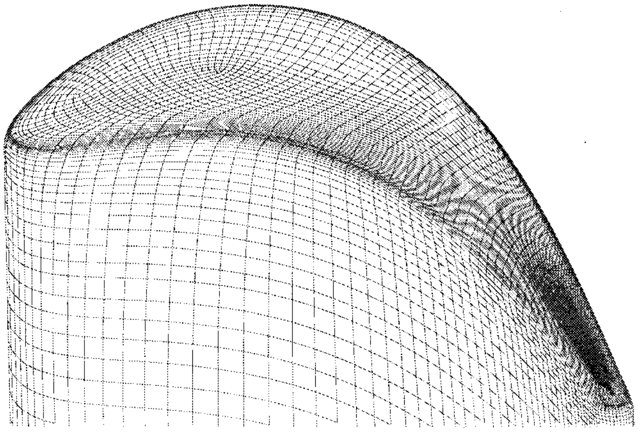

Fig. 5 Radiused edge tip and surface grid

Figure 7 shows the calculated near tip pressure distribution for periodic and complete passage simulations. The agreement with the near-tip pressure distribution appears to improve considerably by accounting for the side walls and the splitter plate. Figure 8 shows the pressure distribution on the tip of the blade. The pressure tap locations are near the edge of the blade, as shown on the inset. The agreement appears to be good. As expected the agreement with the results obtained using periodic boundary conditions was quite bad and is not shown here. Good agreement with the measured data was also obtained, as shown in Fig. 9 for the blade tip pressure when a radiused tip blade is used.

The analysis performed led us to the conclusion that the experimental data do not lend themselves to predictions using periodic modeling of the flow and at least the side walls need to be incorporated in the computational domain. A run without the splitter

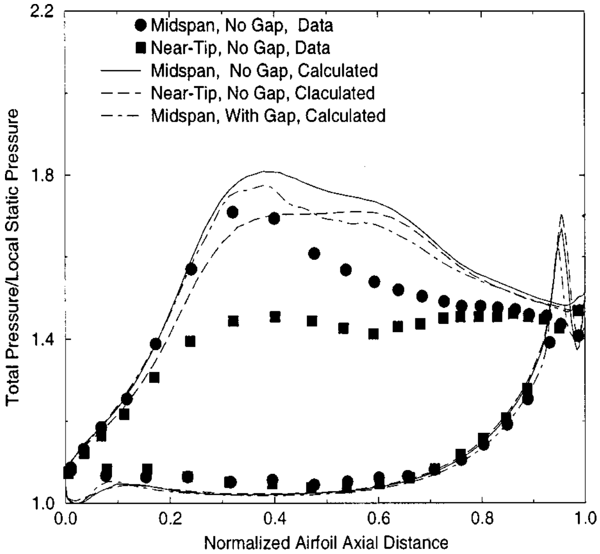

Fig. 6 Blade pressure distribution data and computed pressure distribution using periodic conditions

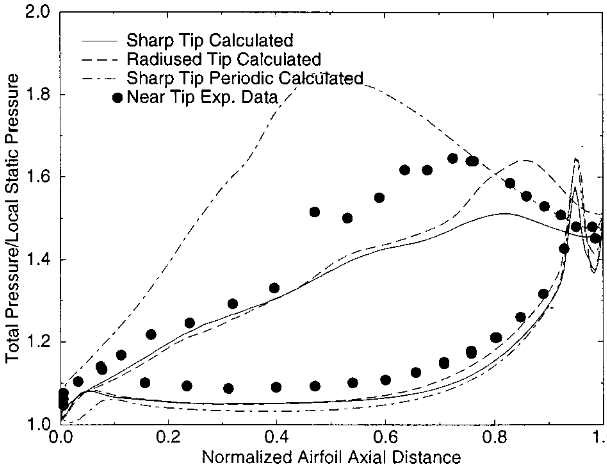

Fig. 7 Near-tip pressure distribution data and computed pressure distribution using the complete passage and periodic cascade

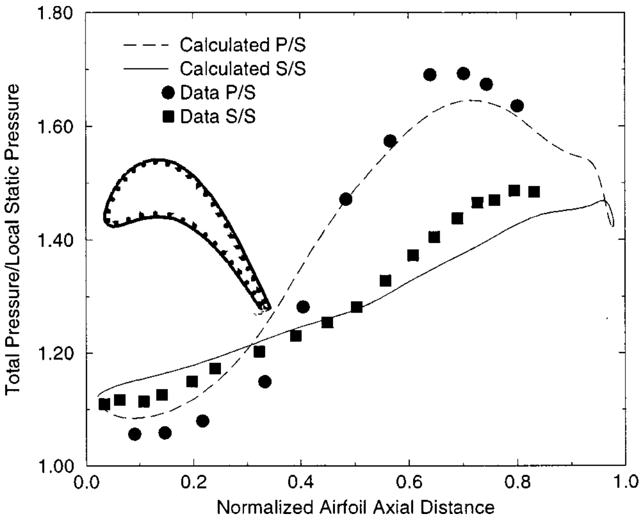

Fig. 8 Blade tip surface pressure distribution with sharp edged tip and baseline clearance of 2.03 mm

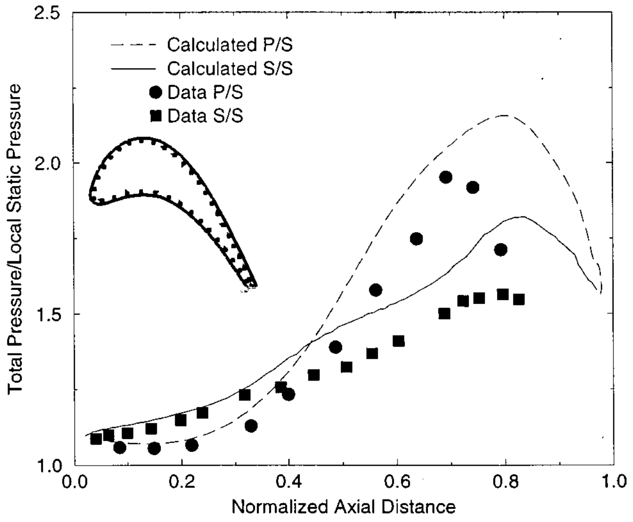

Fig. 9 Blade tip surface pressure distribution with round edged tip and baseline clearance of 2.03 mm

plate was not attempted but it is safe to assume that the existence of the splitter is necessary as it was in the experiments to help with equalizing the flow rate between the two channels.

Heat Transfer. The present computational method has been applied to a variety of turbine heat transfer problems both using an algebraic turbulence model [7,8] and as with the present calculations using a low-Reynolds-number two-equation model. The present turbulence model was tested against the heat transfer data of Metzger et al. [2] for flow over a cavity to show suitability of the model for blade tip recess flows in Ameri et al. [1]. Very good comparison using the current method for blade surface heat transfer with experimental data was achieved by Garg and Rigby [17].

The rate of heat transfer is presented in terms of the heat transfer coefficient, which is defined as:

$$h=\frac{Q_{\text{wall}}}{(T_{\text{wall}}-T_{\text{inlet}})} \tag{1}$$

T_{inlet} is the inlet total temperature and T_{wall} is the wall temperature. T_{wall} was determined from the experimental measurements and found to be 1.06 times the inlet total temperature. The heat transfer coefficient was calculated on the blade tip in the gridded area shown in Fig. 10(*a*), where a constant-temperature boundary condition is imposed. A constant-temperature boundary condition results in a much faster convergence than a constant heat flux boundary condition. Although the experiment was run using a constant heat flux boundary condition, it is expected and was found to be true that the constant heat flux and constant temperature boundary condition yield similar results in the present fully turbulent flow regime. Also, the assumption of constant wall boundary condition is justifiable on the grounds that the experimental variation in the wall temperature was quite small. An effectively adiabatic boundary condition was imposed on all the other surfaces. The experimental measuring area is shown in Fig. 10(*b*). The areas are quite equivalent with the exception of the trailing edge where the computational heated area extends further back on the blade.

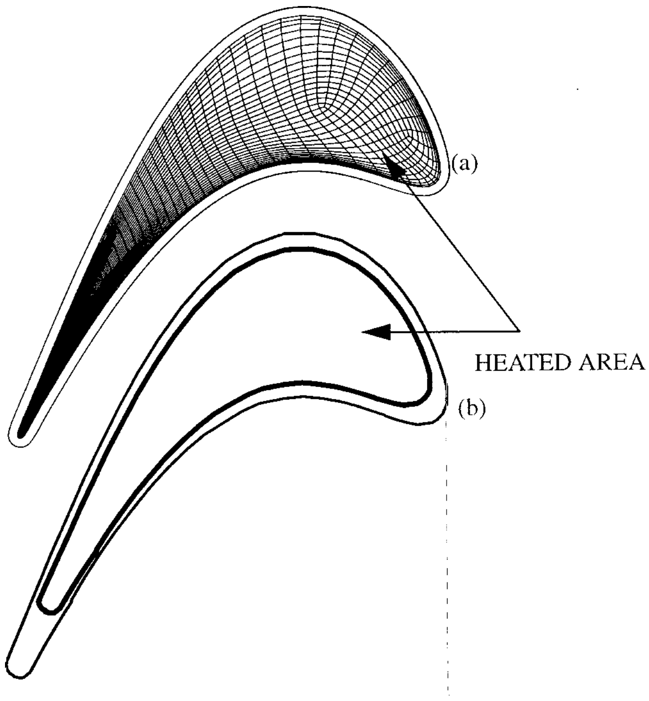

Fig. 10 Heat transfer blade tip: (*a*) computational domain; (*b*) measuring area

The definition of heat transfer coefficient in Eq. (1) was chosen to be consistent with the experimental data. Use of adiabatic wall temperature instead of inlet total temperature leads to a more general definition. The present definition is more convenient computationally, as it does not require the calculation of adiabatic wall temperature. In the present study, the experimental variables are matched as much as possible to make the comparison and thus the conclusions valid.

Both the sharp edge and radiused edge cases with the tip gap of 2.03 mm and a 5 percent turbulence intensity at the inlet were studied. A very thin boundary layer thickness of 0.1 percent of the passage height was imposed at the inlet to the computational domain. Also a turbulence intensity of 10 percent with a length scale of 1 percent of blade chord were imposed at the inlet. This yielded a turbulence intensity of 4 percent at the inlet to the blade cascade.

Figures 11 and 12 show the measured and computed heat transfer coefficient for the sharp edge tip and radiused edged cases. For the sharp edge case, it might be said that the general agreement is good. The largest relative difference between the experimental and calculated values is in the area of the ''sweet spot'' (see Part 1) where the error reaches 30 percent. However, the agreement is good elsewhere and is generally below 15–20 percent of the measured value. In addition, the region of high heat transfer rate, which was marked as area (4) in Part 1 of this paper, correspond-

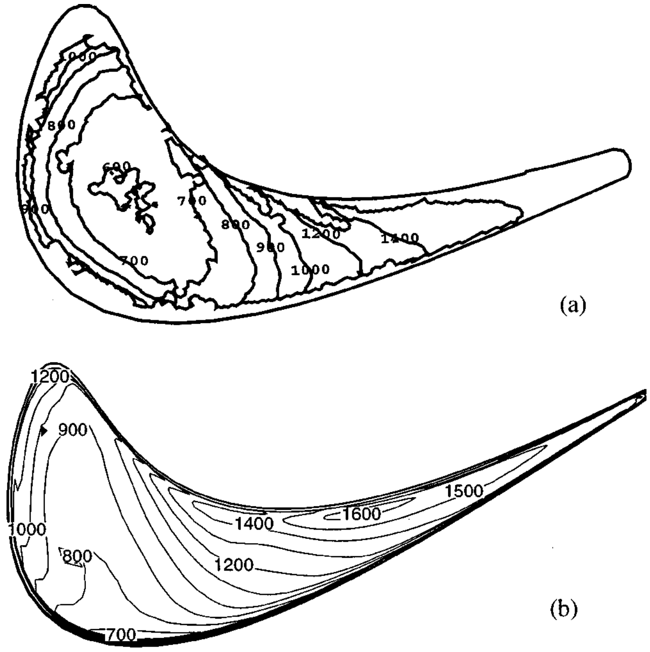

Fig. 11 Sharp edged blade tip heat transfer coefficient (W/m^2/K) for clearance of 2.03 mm and *Tu*=5 percent: (*a*) measured; (*b*) calculated

ing to the high entry loss region, is captured. The experimental measurements show the highest heat transfer rate under the present conditions to take place in the trailing edge region. This is backed up by the numerical calculation.

Figure 12 shows experimental and calculated tip heat transfer for the radiused edge blade. The agreement in this case is much improved over the sharp edge case above, and is consistently better than 15 percent over the entire tip. Apparently the prediction is helped by rounding of the edges, which eliminates the separation and reattachment on the blade tip. Figures 13(*a*) and 13(*b*) show the flow streamlines over the tip of the blade with the sharp and radiused edges. The separation vortex is present everywhere along the pressure side of the sharp edge blade tip and becomes quite large starting from the maximum loss region. On the other hand the flow over radiused edge tip is quite smooth and there is no sign of any vortical structures present on the blade tip.

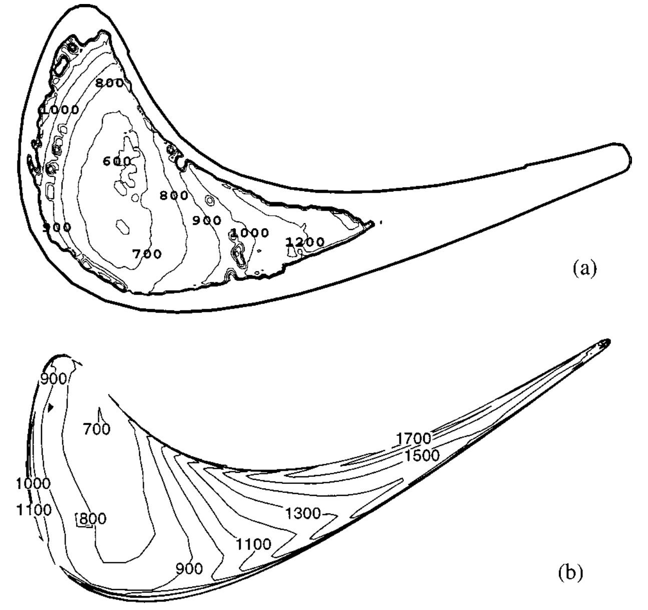

Fig. 12 Radiused edge blade tip heat transfer coefficient (W/m^2/K) for clearance of 2.03 mm and *Tu*=5 percent: (*a*) measured; (*b*) calculated

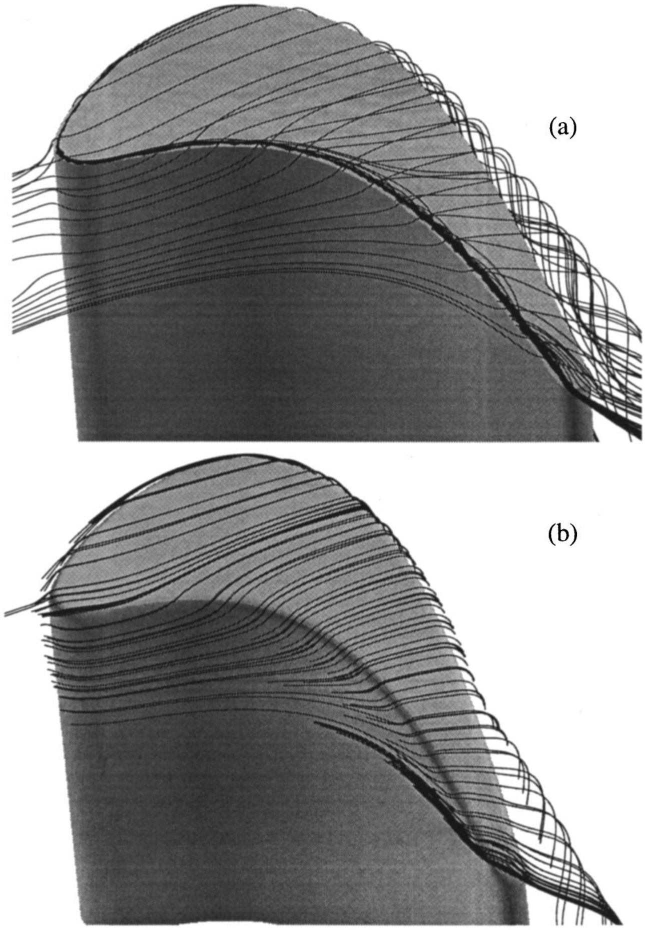

Fig. 13 Flow streamlines over the blade tip for: (*a*) sharp edged blade; (*b*) radiused edge blade

The agreement between the calculations and the measured results is quite good, especially if one considers the fact that the flow over the tip is also influenced by the upstream casing recess.

Figures 14(*a*) and 14(*b*) show the magnitude of the velocity over the blade tip at the mid gap location. The relative magnitude of the velocity between the two cases and the respective tip heat transfer rates are well correlated. This is especially true downstream of the midchord. Ameri et al. [3] showed that the most influential factor in raising the rate of tip heat transfer is the magnitude of the velocity. This was shown by noting the change in the magnitude of the velocity as well as the turbulence intensity and the total temperature as the gap was widened.

Summary and Conclusions

In this paper the numerical prediction and comparison with the experimental data of tip heat transfer for a blade representing a first-stage blade of a large power generation turbine were undertaken. The casing upstream of the blade tip was recessed. It was found that for the calculation of blade tip heat transfer for the present experimental model of the tip, assumption of periodic flow was invalid and the entire passage had to be modeled. It was found that a good representation of the tip heat transfer can be made by our numerical method consisting of a cell-centered finite volume scheme and a $k-\omega$ low-Reynolds-number turbulence

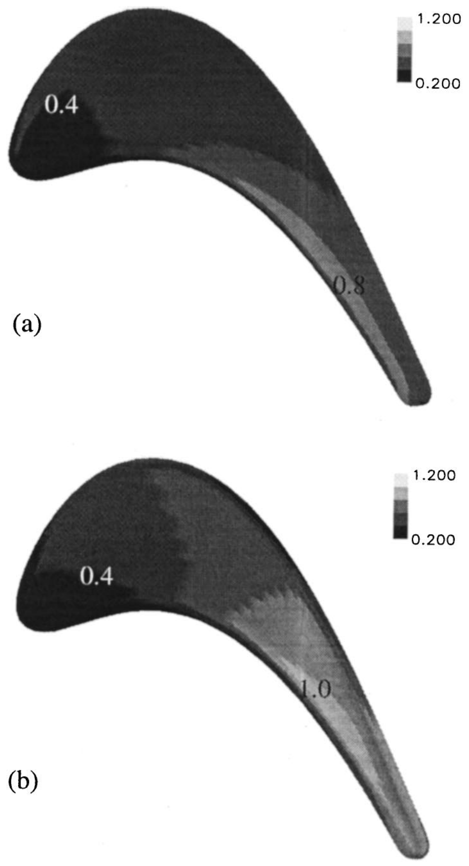

Fig. 14 Magnitude of the velocity, *V*, at the midgap height of the blade tip for: (*a*) sharp edged blade; (*b*) radiused edge blade

model. The numerical results for the radiused edge blade agreed better with the experimental data. This could be due to the absence of separation on the blade tip for the radiused edge blade.

Acknowledgment

This work was sponsored by the Smart Green Engine Project managed at NASA Lewis Research Center by Mr. Kestutis Civinskas. The authors wish to express their gratitude to Dr. Raymond Gaugler, chief of the Turbine Branch, and Mr. Ned Hannum, chief of the Turbomachinery and Propulsion Systems Division of NASA Lewis Research Center, for their support and encouragement of this work. Helpful suggestions offered to the first author by his colleagues Mr. Robert Boyle, Dr. David Rigby, and Dr. Erlendur Steinthorsson are hereby acknowledged. Some of the computations were performed on the CRAY-C90 of NAS at NASA Ames Research Center.

Nomenclature

C_p = constant pressure specific heat
h = heat transfer coefficient
Pr = Prandtl number
R = gas constant
Re = Reynolds number
T = temperature/T_0
Tu = turbulence intensity
V = magnitude of the velocity/$(RT_0)^{1/2}$
y^+ = dimensionless distance from a wall
γ = specific heat ratio

Subscript

t = total conditions
0 = total inlet condition

References

[1] Ameri, Ali A., Steinthorsson, E., and Rigby, David L., 1998, ''Effect of Squealer Tip on Rotor Heat Transfer and Efficiency,'' ASME J. Turbomach., **120**, pp. 753–759.
[2] Metzger, D. E., Bunker, R. S., and Chyu, M. K., 1989, ''Cavity Heat Transfer on a Transverse Grooved Wall in a Narrow Channel,'' ASME J. Heat Transfer, **111**, pp. 73–79.
[3] Ameri, A. A., Steinthorsson, E., and Rigby, D. L., 1999, ''Effects of Tip Clearance and Casing Recess on Heat Transfer and Stage Efficiency in Axial Turbines,'' ASME J. Turbomach., **121**, pp. 683–693.
[4] Dunn, M. G., Rae, W. J., and Holt, J. L., 1984, ''Time Measurement and Analyses of Heat Flux Data in a Turbine Stage: Part I—Description of Experimental Apparatus and Data Analysis,'' ASME J. Turbomach., **106**, pp. 229–233.
[5] Dunn, M. G., Rae, W. J., and Holt, J. L., 1984, ''Time Measurement and Analyses of Heat Flux Data in a Turbine Stage: Part II—Discussion of Results and Comparison With Predictions,'' ASME J. Turbomach., **106**, pp. 234–240.
[6] Dunn, M. G., and Kim, J., 1992, ''Time-Averaged Heat Flux and Surface Pressure Measurements on the Vanes and Blades of the SSME Fuel Side Turbine and Comparison With Prediction for a Two Stage Turbine,'' ASME J. Turbomach., **116**, pp. 14–22.
[7] Ameri, Ali A., and Steinthorsson, E., 1995, ''Prediction of Unshrouded Rotor Blade Tip Heat Transfer,'' ASME Paper No. 95-GT-142.
[8] Ameri, Ali A., and Steinthorsson, E., 1996, ''Analysis of Gas Turbine Rotor Blade Tip and Shroud Heat Transfer,'' ASME Paper No. 96-GT-189.
[9] Steinthorsson, E., Liou, M. S., and Povinelli, L. A., 1993, ''Development of an Explicit Multiblock/Multigrid Flow Solver for Viscous Flows in Complex Geometries,'' Paper No. AIAA-93-2380.
[10] Arnone. A., Liou, M. S., and Povinelli, L. A., 1991, ''Multigrid Calculation of Three Dimensional Viscous Cascade Flows.'' AIAA Paper No. 91-3238.
[11] Rigby, David L., Ameri, Ali A., and Steinthorrson, E., 1996, ''Internal Passage Heat Transfer Prediction Using Multiblock Grids and $k-\omega$ Turbulence Model,'' ASME Paper No. 96-GT-188.
[12] Rigby, D. L., Ameri, A. A., and Steinthorrson E., 1997, ''Numerical Prediction of Heat Transfer in a Channel With Ribs and Bleed,'' ASME Paper No. 97-GT-431.
[13] Wilcox, D. C., 1994, *Turbulence Modeling for CFD*, DCW Industries, Inc., La Canada, CA.
[14] Wilcox, D. C., 1994, ''Simulation of Transition With a Two-Equation Turbulence Model,'' AIAA J., **32**, No. 2, pp. 247–255.
[15] Menter, Florian R., 1993, ''Zonal Two-Equation $k-\omega$ Turbulence Models for Aerodynamic Flows,'' Paper No. AIAA-93-2906.
[16] Schlichting, H., *Boundary Layer Theory*, 7th ed., McGraw-Hill, New York, pp. 312–313.
[17] Garg, Vijay K., and Rigby, David L., ''Heat Transfer on a Film-Cooled Blade-Effect of Hole Physics,'' ASME Paper No. 98-GT-404.

Nonaxisymmetric Turbine End Wall Design: Part I—Three-Dimensional Linear Design System

Neil W. Harvey
Martin G. Rose
Mark D. Taylor
Turbine Engineering,
Rolls-Royce plc,
Derby, United Kingdom

Shahrokh Shahpar
Aerothermal Methods,
Rolls-Royce plc,
Derby, United Kingdom

Jonathan Hartland
David G. Gregory-Smith
School of Engineering,
Durham University,
Durham, United Kingdom

A linear design system, already in use for the forward and inverse design of three-dimensional turbine aerofoils, has been extended for the design of their end walls. This paper shows how this method has been applied to the design of a nonaxisymmetric end wall for a turbine rotor blade in linear cascade. The calculations show that nonaxisymmetric end wall profiling is a powerful tool for reducing secondary flows, in particular the secondary kinetic energy and exit angle deviations. Simple end wall profiling is shown to be at least as beneficial aerodynamically as the now standard techniques of differentially skewing aerofoil sections up the span, and (compound) leaning of the aerofoil. A design is presented that combines a number of end wall features aimed at reducing secondary loss and flow deviation. The experimental study of this geometry, aimed at validating the design method, is the subject of the second part of this paper. The effects of end wall perturbations on the flow field are calculated using a three-dimensional pressure correction based Reynolds-averaged Navier–Stokes CFD code. These calculations are normally performed overnight on a cluster of work stations. The design system then calculates the relationships between perturbations in the end wall and resulting changes in the flow field. With these available, linear superposition theory is used to enable the designer to investigate quickly the effect on the flow field of many combinations of end wall shapes (a matter of minutes for each shape). [S0889-504X(00)00902-8]

Introduction

The turbine designer is always trying to improve the aerodynamic performance of turbine blading, either by increasing the efficiency at a given aerodynamic duty, or trying to maintain efficiency levels at higher duties (higher stage loading or stage work).

A major source of loss of efficiency in a turbine is secondary loss, whose importance relative to other sources, such as profile loss, increases as the aerodynamic duty increases or aspect ratio decreases. Inside a turbomachine blade row a number of vortical flow features will be present, which are collectively known as the secondary flows. A comprehensive review of these is given in Sieverding [1]. Their loss arises in part from dissipation of their kinetic energy of rotation, little of which is recovered in subsequent blade rows.

This paper shows how nonaxisymmetric end wall profiling can reduce these secondary flows. A design of end wall is presented for the large-scale, low-speed rotor profile in the linear cascade at Durham University. This is calculated to reduce the secondary kinetic energy, exit angle deviations, and (to a small extent) the secondary loss.

The Durham cascade has already been the subject of a study of end wall profiling by Hartland et al. [2]. This study was aimed at controlling the end wall static pressure field at the platform trailing edge, rather than the secondary flows, as a means of reducing turbine disk coolant leakage flow, as proposed by Rose [3]. Details of this cascade are given in Hartland et al. [2] and the second part of this paper. The aerofoil is representative of a modern HP turbine rotor profile and runs at an exit Reynolds number of about 400,000.

Overview of Previous Work. A number of researchers have investigated end wall profiling in the past, as a means of reducing secondary flows and losses.

A large part of this work has been on axisymmetric profiles applied to HP NGVs, based on the findings of [4], and most of this has resulted in a small reduction in secondary loss and an increase in overall performance. The majority of researchers have attributed this to a redistribution of pressure and hence loading near the end wall of the blade although some, [5,6], attributed the gain to improved flow at inlet to the rotor downstream of the NGV. In cases where detailed internal measurements were made within cascades, the main decrease in loss has been adjacent to the unprofiled wall with some results [6–9] showing an increase in loss near the profiled end wall. The end wall geometries of these four sets of researchers all incorporated a strong contraction of the passage (often known as a ‘‘Russian kink’’), and the additional increase in velocity ratio through the passage contributes in part to the performance improvements, especially those seen near the unprofiled wall. Most results show that adverse effects downstream of the profiled wall cancel out any positive effects local to it, while not significantly affecting the benefits arising at the unprofiled wall.

Moustapha and Williamson [10] studied two styles of axisymmetric end wall with the same overall passage contraction. They found that a sharp, late contraction of the NGV passage at the casing gave lower turbine losses than an even, linear contraction through the passage. This is a different result to that of Haas and Boyle [11] who found that two such geometries gave the same performance improvement in stage efficiency (0.7 percent) for their highly loaded, low aspect ratio turbine. Not all studies of such end wall profiling have been positive; Arts [12] in a study of a sharp contraction came to no definite conclusion about its benefits.

Most recently, Schnaus Fottner [13] and Duden et al. [14], applied an axisymmetric profile to the inclined end wall of a rotor

---

Contributed by the International Gas Turbine Institute and presented at the 44th International Gas Turbine and Aeroengine Congress and Exhibition, Indianapolis, Indiana, June 7–10, 1999. Manuscript received by the International Gas Turbine Institute February 1999. Paper No. 99-GT-337. Review Chair: D. C. Wisler.

blade in linear cascade. Unlike much previous work, the inlet-to-exit passage area ratio was not changed by the profiling. On its own the profiling resulted in a small reduction in exit flow angle deviations and no change in loss. When combined with compound leaning and thickening of the aerofoil near the end wall, there was a significant reduction in secondary loss. This was counterbalanced by higher profile losses unfortunately, but there was a still significant reduction in the exit angle deviations.

Only three previous researchers, Morris and Hoare [15], Atkins [8], and Rose [3], have attempted to use three-dimensional profiles. The profile of Rose [3] has been shown to achieve significant control of end wall static pressure distributions [2]. Atkins tried two nonaxisymmetric profiles, both based on a bump adjacent to one blade surface reducing to no profile near the opposite surface. The intention was to reduce the maximum or minimum pressure on the relevant blade surface. Both profiles resulted in an overall increase in losses due to adverse effects on the flow near the profiled end wall causing separation and strong twisting of the blade wake. Morris and Hoare [15] used the same profile as their axisymmetric case, but with the profile following and perpendicular to the midpassage streamline. The loss decrease at the unprofiled wall was found to be greater than in the axisymmetric case, but these advantages were canceled by the adverse effects close to the profiled wall and very strong twisting of the blade wake.

Turbine Secondary Flows

The origin and development of turbine passage secondary flows is now well understood; see [1]. Figure 1 shows a diagrammatic representation of turbine end wall secondary flows taken from Takeishi et al. [16]. The principal features are:

(*a*) Rolling up of the inlet boundary layer into the horseshoe vortex at the aerofoil leading edge. The pressure surface side leg of this becomes the core of the passage vortex. The passage vortex is the dominant part of the secondary flow and beneath it on the end wall a new boundary layer is formed, referred to as crossflow ''B'' in Fig. 1, which starts in the pressure side end wall corner.

(*b*) Upstream of this the inlet boundary layer is deflected across the passage (overturned), referred to as crossflow ''A.'' The end wall separation line marks the furthest penetration of the bottom of the inlet boundary layer into the passage and divides it from the new boundary layer forming downstream of it.

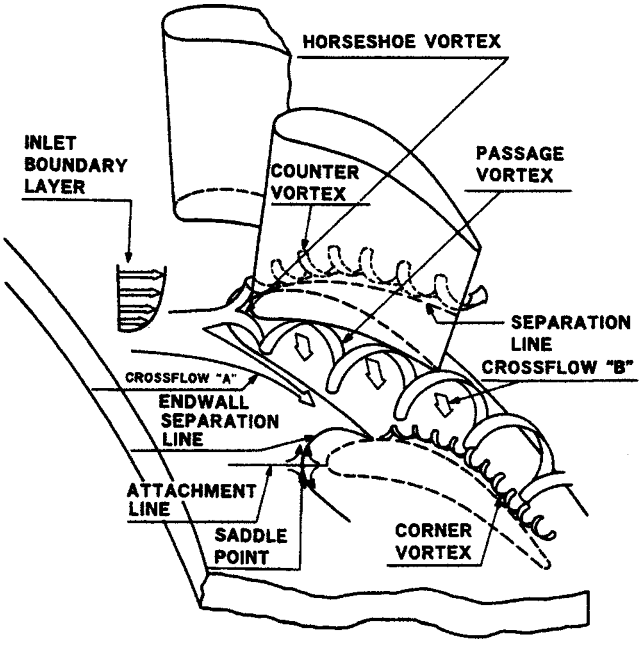

Fig. 1 Secondary flow model after [16]

(*c*) The new end wall boundary layer, crossflow ''B,'' carries up onto the aerofoil suction surface until it separates (along the aerofoil ''separation line'') and feeds into the passage vortex. The suction side leg of the horseshoe vortex, referred to as the countervortex in Fig. 1, remains above the passage vortex and moves away from the end wall as the passage vortex grows.

(*d*) A small corner vortex may occur in the suction surface/end wall corner rotating in the opposite sense to the passage vortex. This has the effect of opposing the overturning at the end wall, although at the cost of additional loss.

In addition to being a loss source in their own right, these secondary flows have a further deleterious effect. Their vortical motion causes the exit angles of the flow to depart from their nominal (two-dimensional) design values. Typically a passage vortex will cause an increase in the exit angle at the end wall (overturning) with a compensatory reduction in angle away from the wall (underturning). These secondary flow deviations cause positive or negative incidence locally at inlet to the next blade row and thus reduce its efficiency.

Design Methodology

From this model, it can be seen that it is the cross-passage pressure gradient and its action on the incoming end wall boundary layer that most often gives rise to secondary flow in turbomachinery blade rows. Thus the primary design methodology adopted here has been to reduce this pressure gradient, in particular where the overturning (of the inlet boundary layer) is strongest.

In his profiled end wall design, Rose [3] laid out the basic principles of controlling the local static pressures by means of streamline curvature. These are straightforward: Convex wall curvature locally accelerates the flow relative to the datum and thus reduces the static pressure while concave curvature causes a (relative) diffusion, raising the static pressure. The results of Hartland et al. [2] have validated this approach, and also the CFD tools used to predict the static pressure field in the design process.

To apply this design methodology, some means of systematically investigating the design space was needed, as recommended by Atkins [8]. An accurate predictor of the flow field: static pressures, flow angles, and (ideally) losses, was required and also the means of defining and verifying design options in a realistic time scale. These are discussed in the next sections.

Linear Design System

Shahpar and Lapworth [17] and Shahpar et al. [18] describe a forward and inverse three-dimensional linear design system for turbomachinery aerofoils. The elements of this approach are:

(*a*) Generate a systematic set of perturbations to the aerofoil geometry at up to seven sections. The design parameters were defined by Rose and Taylor [19] to be: skew, re-camber, re-stagger, and scale and translation in the axial and circumferential directions.

(*b*) Compute the (viscous) flow field for all these perturbations.

(*c*) Construct a linear sensitivity matrix using numerical differentiation.

(*d*) Use the theory of (linear) superposition to construct new geometries and flow fields.

(*e*) Apply inverse design through matrix inversion and quasi-Newton techniques, to generate aerofoil shapes to satisfy chosen design criteria, such as minimizing secondary flow deviation or loss.

This method has now been extended for the design of nonaxisymmetric end walls. However, there are no standard geometric parameters, such as skew or re-camber for the aerofoil, by which to define the end wall shape. A novel approach has been adopted where the perturbation to the axisymmetric end wall surface is created by the product of two curves in axial and circumferential directions. Since the static pressure field is sensitive to the curvature of the end wall, the axial profile of the perturbation is defined

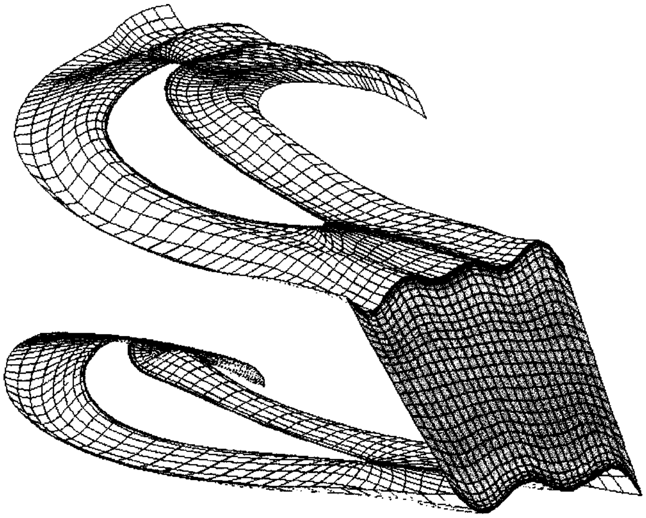

Fig. 2 Example of perturbed end wall and calculation grid

by a *B*-spline curve through six control points. A *B*-spline was chosen because its response to a change in a control point is more local than other parametric curves. The six control points can be specified in the domain rather than at the grid inlet or exit locations. In this case the end-points are clamped, to achieve local axisymmetry.

The first three terms in the Fourier series are used to produce the perturbations in the circumferential direction:

$$\delta r(\theta)=\frac{1}{C}\sum_{i=1}^{3}\left(a_i\sin\left(\frac{2\pi\vartheta}{p}\right)+b_i\cos\left(\frac{2\pi\vartheta}{p}\right)\right) \qquad (1)$$

where p is the blade pitch, a_i and b_i are related to the amplitudes and phase of each harmonic, and C is a normalizing coefficient. Since all the perturbation terms are summed linearly, the sine and cosine functions are treated as individual perturbations. Therefore six are created at each control point, a total of 36 perturbations for each wall.

This has many advantages. First, the circumferential area of the passage remains constant. This helps limit throat area errors, important for compressible flows. Also, since the pressure field in a blade row is often of a sinusoidal form, it is useful to have a general definition using sine and cosine functions. Third, the summation of the first three terms in the Fourier series is generally enough to allow almost any shape to be generated.

A viscous calculation has to be performed for each perturbed geometry, 36 in total. This is achieved overnight on a cluster of workstations. Run times are kept down by taking the solution for the datum case as the starting flow field for each calculation.

Since a body-fitted grid coordinate system is used here, the Fourier curves must be interpolated onto the computational mesh rather than being mapped directly. The mesh is perturbed at each radial plane to accommodate the end wall profiling, linearly reducing the amplitude of the waves from the wall to the grid midheight.

Figure 2 shows a complex end wall shape, and some details of the grid, to illustrate the flexibility of this method. In this case the profiling at grid exit has been chosen to demonstrate a third-order perturbation.

Calculation Method

The computational method was a standard turbomachinery CFD code used within Rolls-Royce. The code is a steady flow solver using a pressure correction method based on the algorithm of Moore [20]. The important feature of this algorithm is the use of upwinded control volumes for the momentum and rothalpy equations, thus allowing the equations to be discretized with second-order accuracy without the need to introduce smoothing to achieve numerical stability. A minimum of numerical mixing is essential for a code that is to be used for estimating aerodynamic losses. The iterative method used is based on the SIMPLER pressure correction scheme. The calculations use a structured ''letter-box'' type of body fitted **H**-grid, which enables accurate representation of the full blade shape. Previous work has shown the capability of this numerical method for the prediction of turbomachinery aerodynamics, e.g., Moore and Gregory-Smith [21] and Robinson and Northall [22].

The grid was Cartesian with 89 axial and 39 tangential points and 29 spanwise planes from the end wall to midheight where a plane of symmetry was specified. Examples of the grid are shown in Figs. 5, 6, 7, and 9.

Measured inlet total pressure and velocity profiles were specified. An adiabatic wall condition was used with fully turbulent boundary layers on the end walls and aerofoil. The exit condition was a circumferentially averaged static pressure profile one axial chord downstream, interpolated between the measured end wall values assuming radial equilibrium. Acceptable convergence was achieved when the residuals in all three velocity components and the static pressure had fallen by at least two orders of magnitude from their initial values. This was typically achieved after 150 iterations.

An algebraic mixing length model is used, based on Prandtl's formulation for the length scale within a shear layer, together with a wall function which is valid for y^+ values up to 100 and above. More details are given in Moore and Gregory-Smith [21] and Harvey et al. [23].

Design Study

As discussed previously, the linear design method generates perturbations at six axial locations on the end wall. The ones chosen are shown in Fig. 4 (stations 1 to 6), aimed at providing an even spread of perturbations over the end wall. Although harmonics up to third order are available in the method, in practice only first harmonic options were investigated in the design. At the time, only a forward mode was available and the shapes, and flows, produced by using second and third-order harmonics were too complex to work with.

The design study focused on controlling the surface static pressures and improving the exit whirl angle distribution (reducing the secondary flow deviations). This was because there was most confidence in the ability of the CFD code to predict these two parameters, more so than the loss. It was also noted that in the design of modern turbines, one approach is to reduce secondary flow deviations, and improve the flow into the next blade row, rather than reduce loss directly. Two such methods are compound leaning, comprehensively investigated by Harrison [24], and skewing blade profile sections open near the end walls to compensate for the overturning. Harrison specifically concluded that compound leaning, extensively applied to turbomachinery blading today, provides no reduction in loss within the blade row it is applied to.

At the outset it was not clear what level of improvements to aim at; reducing flow deviations to zero was very likely to involve extreme end wall shapes, if possible at all. First a limit was set on the maximum radial amplitude of the end wall perturbations, at approximately 25 percent of axial chord. This was, generally, what could be sensibly manufactured in engine terms (without further detailed mechanical studies). In addition, a brief exercise was undertaken to determine the effects of compound lean and differential blade section skewing. This was carried out on a linear cascade profile similar to the Durham cascade. The geometries investigated were:

1 Compound lean, 20 deg lean from the vertical, pressure side toward the end wall, reducing to zero at 25 percent height (''LEAN'').

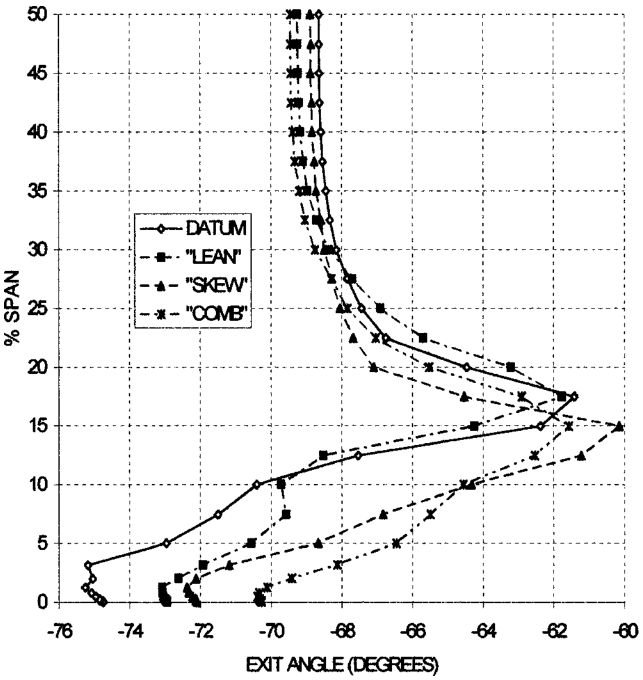

Fig. 3 Calculated exit angles for different aerofoil geometries

2 Profiles skewed open by 6 deg at the end wall, the skew angle reducing linearly to zero at 15 percent span from the wall (''SKEW'').
3 Combination of (1) and (2) (''COMB'').

Figure 3 compares the calculated exit angle distributions at a plane 29 percent axial chord downstream of the trailing edge for these geometries. Compound lean reduces the overturning at the wall by 2 deg. The maximum underturning of the flow (at the edge of the passage vortex farthest from the end wall) has not changed. The small change in midheight exit angle is due to redistribution of mass flow in the blade passage. Compound lean increases the blade loading, and thus the turning, at midheight.

Skewing of the sections near the end wall reduces the overturning, by almost 3 deg from a maximum of about 7 deg. However, the underturning has increased, indicating that the radial extent of the skewing is too great and that it should be more local to the end wall.

The combined geometry significantly reduces the overturning to only 1 deg, with the underturning increased by about 1 deg (noting the increase in midheight exit angle). Unfortunately the row efficiency is reduced by about 6 percent, and in fact all of these geometries are calculated to increase row loss, largely due to increased wetted area.

Although more could have been done, this exercise was sufficient to set the design targets: reduce overturning at the end wall from 7 to 1 deg and reduce the underturning if possible.

First Profiled End Wall. The first design study focused on reducing the cross-passage pressure gradient by applying streamwise curvature in the early part of the passage, where the inlet boundary layer is overturned. Figure 4 shows the blade and profiled end wall in plan view. Two approximate streamwise sections are indicated through it, A–A and B–B (Figs. 5 and 6), as well as approximate axial sections C–C and D–D (Figs. 7 and 9, both of which show two passages). Also indicated in Fig. 4 are the control planes, labeled (1)–(6), on which the perturbations were defined.

Section A–A is close to the pressure side of the passage. For the first study this was the streamwise section with maximum convex curvature, near the aerofoil leading edge plane. (Figure 5 also shows additional curvature downstream of this, applied in the second study; see the next section.) The end wall is locally raised so that the flow over it sees a region of convex curvature, lowering the static pressure.

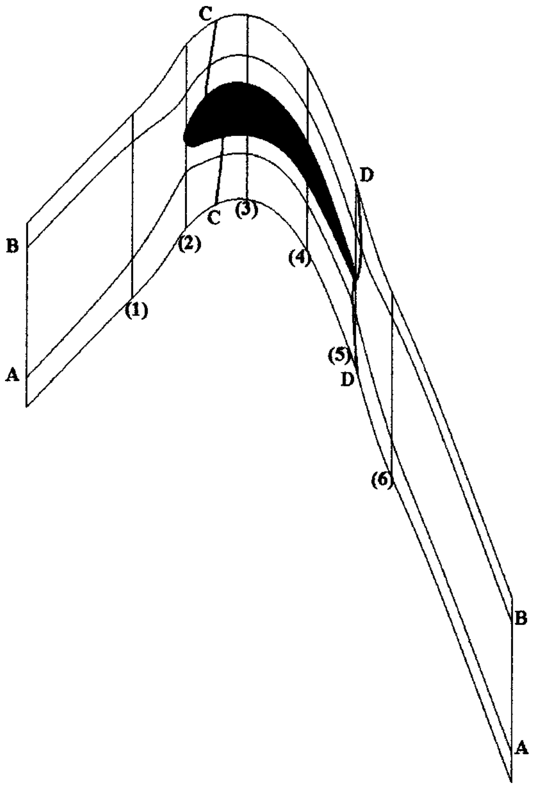

Fig. 4 Plan view of Durham cascade with calculation planes

Section B–B is close to the suction side of the passage. For the first study this was the streamwise section with maximum concave curvature, again in the region of the leading edge plane. The end wall is locally lowered to produce a trough such that the flow over it sees a region of concave curvature, raising the static pressure.

Each area of curvature has to blend back into the datum end wall line, by introducing curvature of the opposite sign. This is done as gently as possible to minimize any adverse effects.

Section C–C shown in Fig. 7 is drawn through the points of maximum and minimum amplitude of sections A–A and B–B (for the first study). This shows the shape in the circumferential direction with the raised surface close to the pressure side of the passage and the trough on the suction side.

Figure 8 shows the resulting exit whirl angle distribution. The maximum underturning has been reduced by about 1 deg and its location has moved closer to the end wall, indicating the passage

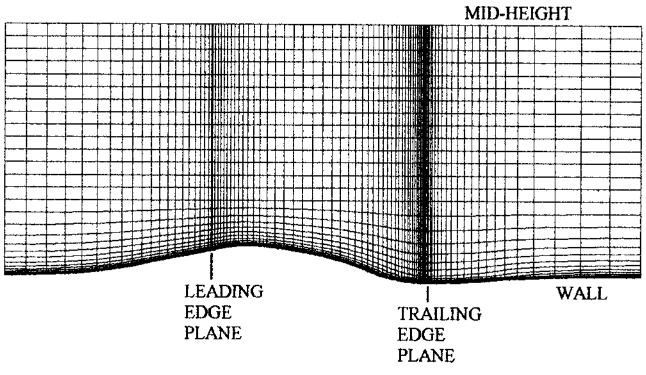

Fig. 5 Streamwise section A–A (pressure side) of end wall

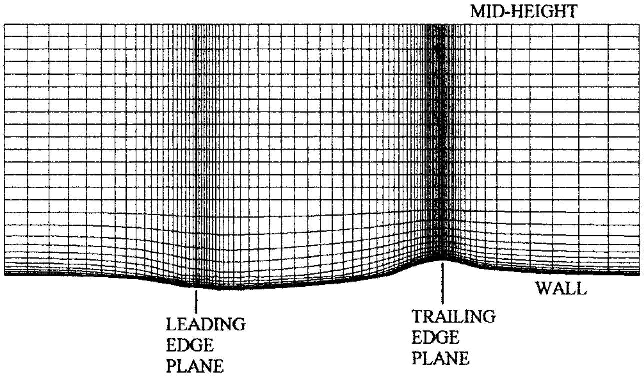

Fig. 6 Streamwise section B–B (suction side) of end wall

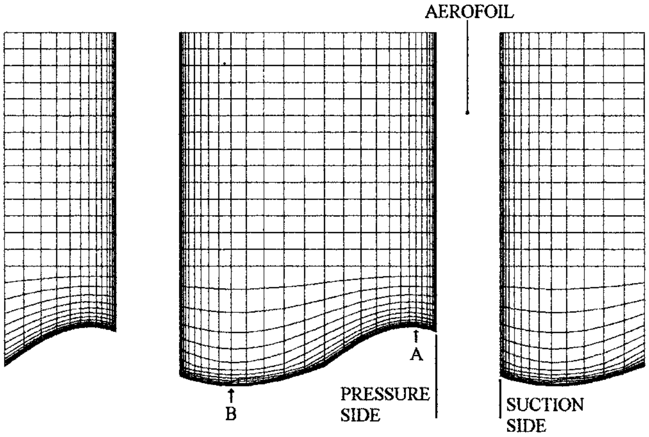

Fig. 7 Approximate axial section C–C of end wall

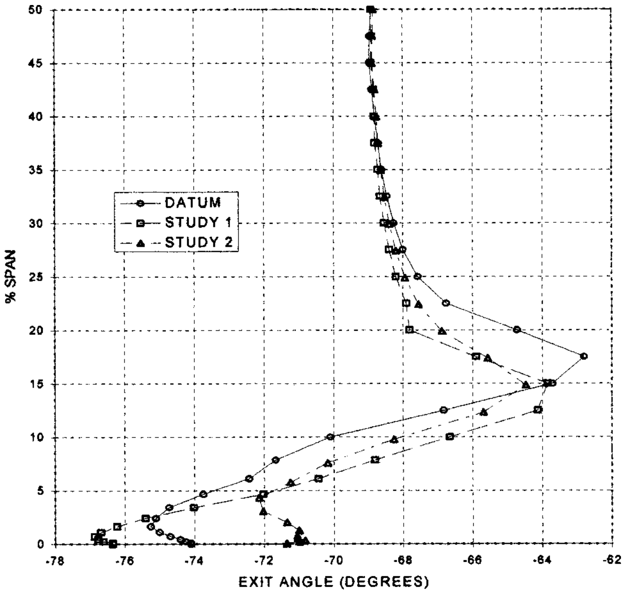

Fig. 8 Calculated exit angles for profiled end walls

vortex is smaller. However, the overturning at the wall is almost 2 deg worse. Referring back to the model of Fig. 1, this is seen to be a direct result, paradoxically, of reducing the cross-passage pressure gradient. The overturning of the end wall boundary layer *within* the passage is delayed, less of it rolls up into the passage vortex and thus a more overturned boundary layer is seen on the end wall at the blade exit.

A further study was undertaken to mitigate this effect.

Second Profiled End Wall. The second study, with the aim of reducing the extra overturning incurred by the first design, has demonstrated the power of the linear design method. For the first end wall there was a clear rationale of reducing the early cross-passage pressure gradient, and local streamline curvature was applied to achieve this. For this study there was no such rationale, so a systematic investigation was undertaken of the effect of the end wall perturbations (first harmonic only) on the overturning. It should be emphasized that by making use of the linear approach, a large number of possibilities could be investigated, a matter of minutes for each one.

Applying additional profiling in the aerofoil trailing edge region was found to be very effective. The resulting end wall shapes are shown in the approximate streamwise sections A–A (Fig. 5) and B–B (Fig. 6) together with the approximate axial section D–D (Fig. 9). Their locations on the end wall are shown in Fig. 4.

The arrangement of the streamline curvature is the opposite of that in the first design. Convex curvature near the suction side (section B–B) further lowers the static pressure in this region while a gentle concave curvature near the pressure side (section A–A) slightly raises the pressure locally. The effect of this on the circumferentially averaged exit flow angles is shown in Fig. 8. The overturning is significantly reduced and is now 3 deg less than the datum, planar end wall. The improved underturning achieved with the first design is retained. The profiling in the trailing edge region seems to have achieved this by the following mechanisms:

1 Flow is encouraged from the pressure surface side of the trailing edge over to the suction side, thereby setting up a crossflow, which opposes overturned boundary layer.
2 An acute corner is formed between the aerofoil suction surface and the end wall, which encourages the formation of a corner vortex, as described in Fig. 1, which counterrotates with the passage vortex and opposes the overturning at the wall.

This design appears to have one drawback in that the axial cross-passage pressure gradient is increased, which might be expected to enhance the overturning. However, it is the orthogonal pressure gradient that drives the overturning, specifically here that in the throat plane. This is only affected by the change in static pressure on the pressure side of the passage, which is slight. The biggest change in the end wall static pressure is on the suction side of the trailing edge which, in terms of orthogonals, is at the passage exit.

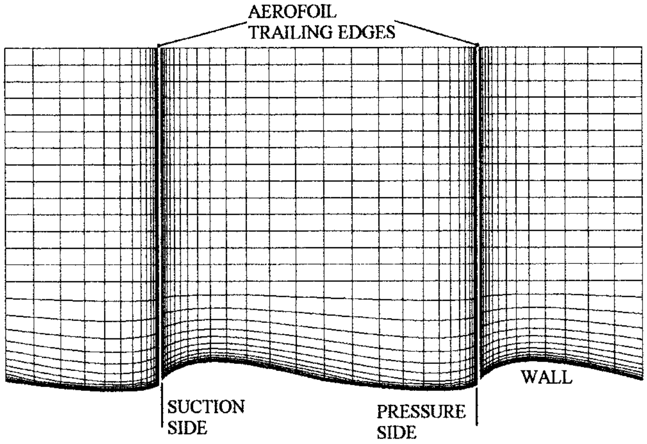

Fig. 9 Approximate axial section D–D through end wall

Discussion of Results

The profiled end wall that has resulted from the design studies, shown in perspective view in Fig. 15, is calculated to achieve slightly over half the target reduction in secondary flow deviations. For the aerofoil with combined lean and skew the maximum angle variation (under-to-overturning) was reduced from 13.5 to 8.5 deg, see Fig. 3, and was largely due to reduced overturning. For the profiled end wall, the calculated reduction in maximum angle variation was from 12 to 8 deg (see Fig. 8) and was more evenly split between under and overturning.

Overall the row loss is calculated to be reduced by about 4 percent, but both this and the loss increases calculated for the skewed and leant profiles are well within the accuracy of the CFD code. Examination of the circumferentially averaged exit loss profiles, Fig. 10, shows there is a reduction in loss in the region of the passage vortex and additional loss close to the wall. A further insight is provided by Fig. 11, which compares the circumferentially averaged profile of secondary kinetic energy (also at the 29 percent axial chord downstream plane) for the datum and profiled end walls. There is a general reduction in secondary kinetic energy up the span, a 40 percent reduction in total, which may indicate a greater potential for reducing loss than shown by the mixed out loss values. The CFD code is being used to determine the reduction in loss of the passage vortex, set against the extra loss due to the counterrotating corner vortex at the wall, which is a difficult balance to calculate accurately.

The behavior of the final profiled end wall design can be described in detail:

1 The profiling in the leading edge region lowers the static pressure on the pressure side of the passage and raises it on the suction side. Figure 12 compares the static pressures at section C–C for the datum and final profiled end wall. There is a more pronounced effect on the suction side because the dynamic head of the free-stream flow is greater, thus making the wall curvature more effective.

2 The reduced cross-passage pressure gradient delays the overturning of the inlet boundary layer (crossflow A in Fig. 1) and its rolling up into the passage vortex. The flow visualization of Fig. 13 compares calculated streaklines in the near wall grid plane for the datum case (Fig. 13(*a*)) and the final profiled end wall (Fig. 13(*b*)) and shows the separation line has moved downstream for the latter.

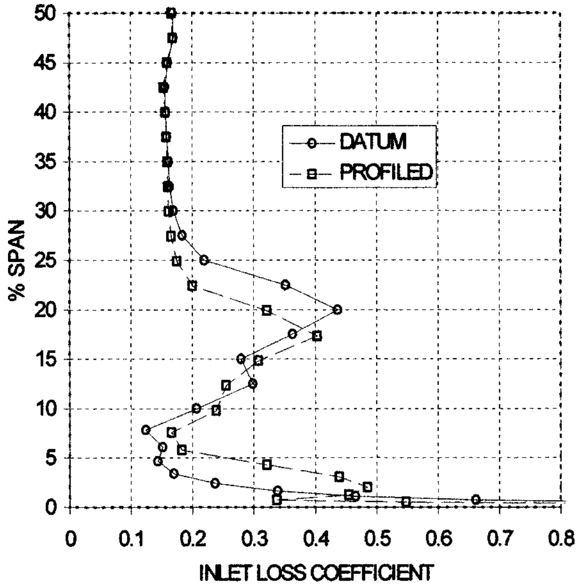

Fig. 10 Calculated losses for profiled end walls

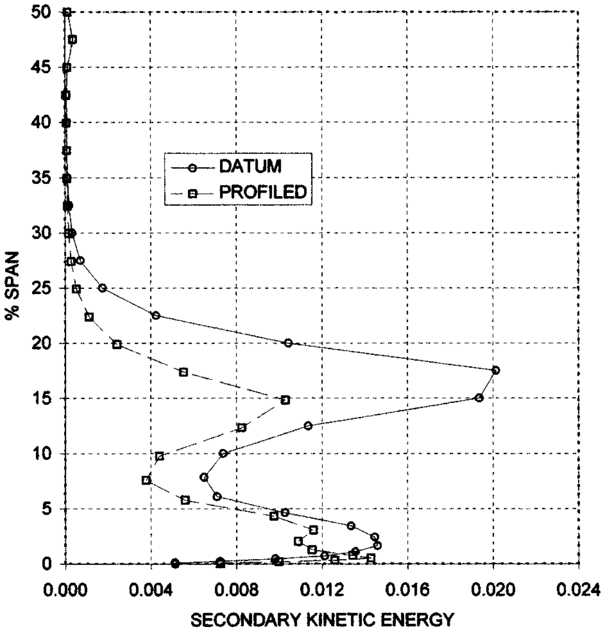

Fig. 11 Calculated secondary kinetic energy profiles

3 The velocity and secondary kinetic energy of the overturned end wall boundary layer flows, both the inlet one (crossflow A) and the new boundary layer formed on the end wall (crossflow B in Fig. 1), are reduced, resulting in the reduced secondary kinetic energy of the passage vortex.

4 Figure 13(*b*) shows the flow at the trailing edge, from pressure to suction side, for the profiled end wall. Its effect of reducing the (circumferentially averaged) overturning is at a cost. The two opposing flows separate from the end wall and set up a vortex rotating in the opposite direction to the passage vortex. This has its own secondary kinetic energy and is thus a source of loss. This appears as the increased loss near the end wall, seen in Fig. 10.

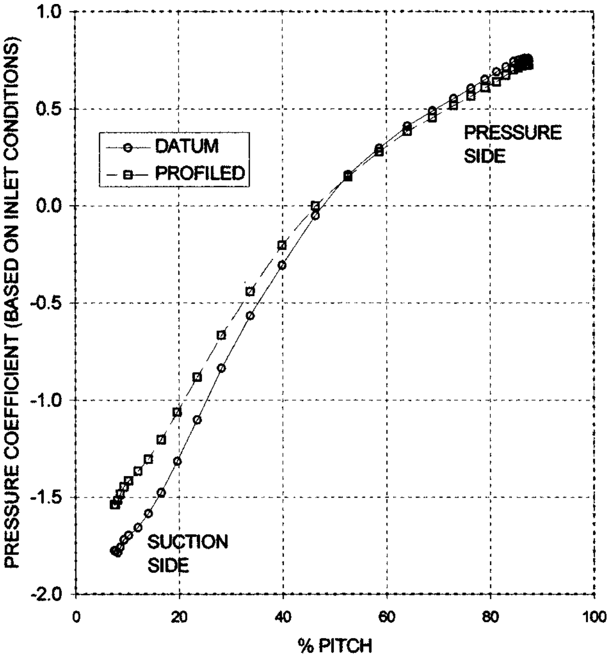

Fig. 12 Static pressures at end wall section C–C

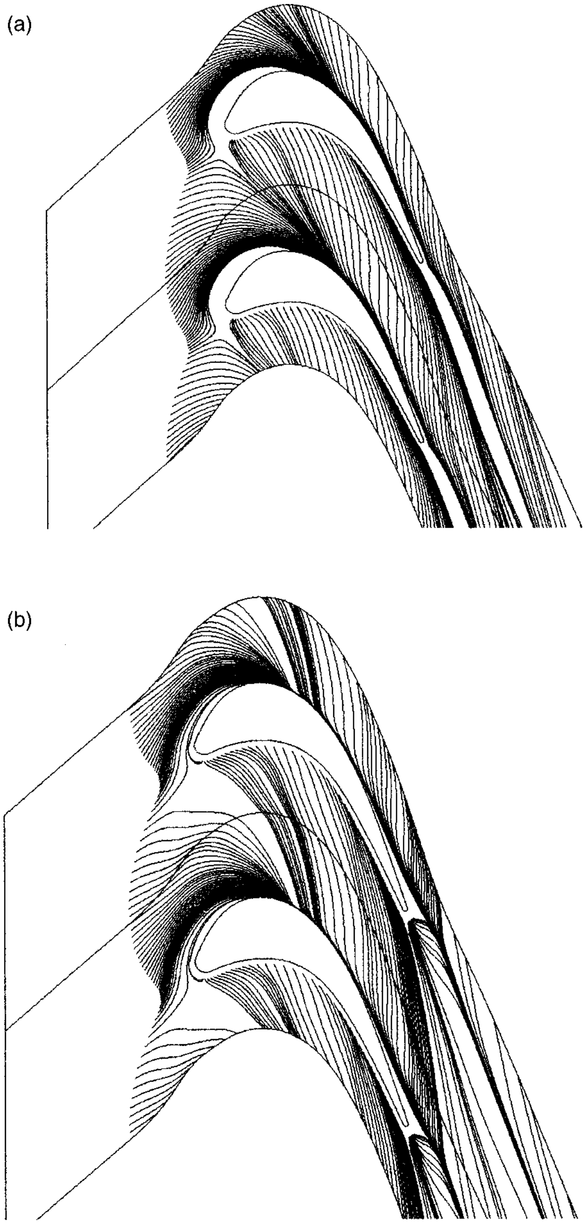

Fig. 13 Surface flow visualization for: (*a*) planar end wall; (*b*) profiled end wall

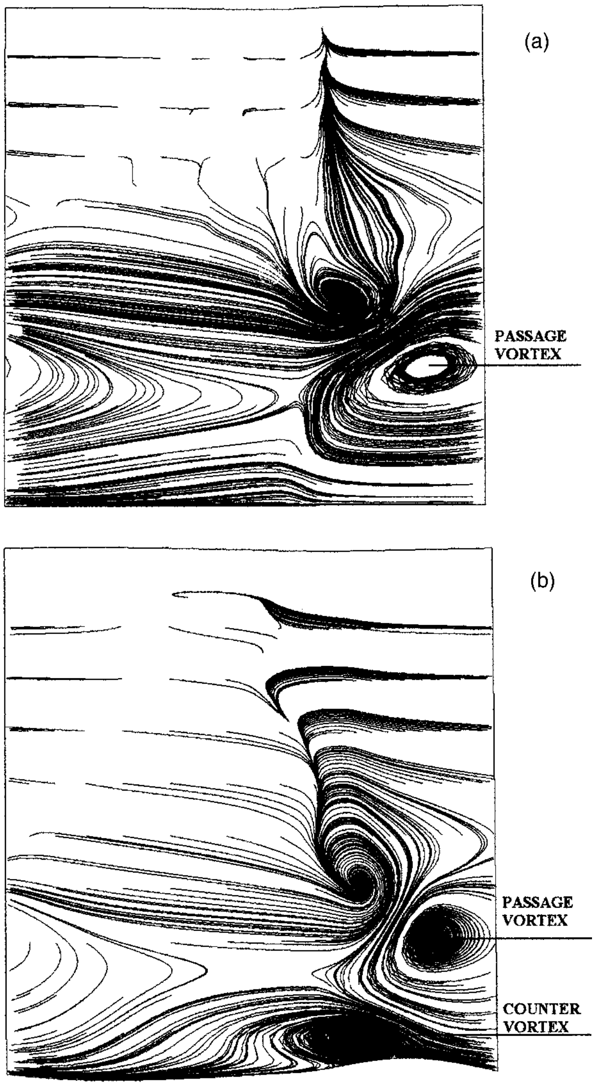

Fig. 14 Exit plane streaklines: (*a*) planar end wall; (*b*) profiled end wall

5 Figure 14 shows calculated streaklines in the 29 percent chord downstream plane for the planar (Fig. 14(*a*)) and final profiled end walls (Fig. 14(*b*)). This plot highlights the secondary flows in this plane. It shows the reduced size of the passage vortex and the presence of the new counterrotating (corner) vortex for the final profiled end wall.

Final Comments

The final profiled end wall (Fig. 15) is calculated to reduce secondary flow deviations significantly. Bigger reductions would have been achievable using larger perturbation amplitudes than the (conservative) design limit of 25 percent of the axial chord. Although larger reductions in secondary flow deviations were achieved with combined aerofoil lean and skew, the end wall profiling does have two advantages. The first is that the midheight exit angle and loading do not change (Fig. 8); the changes in static pressures at the end wall quickly decay up the span. The second is that it may not be mechanically feasible to lean or skew the aerofoil, for instance in a cooled rotor, where end wall profiling could still be applied. End wall profiling should be easily applied to a rotor hub, although rotating shrouds will be more challenging.

The profiled end wall design was judged to be acceptable for experimental verification in the Durham cascade, despite having one unwanted feature. At the time the linear design code applied perturbations to the whole axial extent of the computational mesh. As a result the axial extents of the wall curvature are too large for practical turbomachinery blading. This was corrected after the design was completed, and future studies will be on profiles with limited axial extents of the wall curvature (equivalent to keeping within blading platform leading and trailing edges).

Conclusions

1 A nonaxisymmetric profiled end wall has been defined for testing in the linear cascade at Durham University.

2 CFD predicts this end wall will significantly reduce the secondary flows, and in particular exit angle deviations. Reduced secondary kinetic energy is also expected, but the overall reduction in loss is only predicted to be small.

3 The profile has been generated using a new linear design tool used here for the first time for the design of end walls. Once the 36 perturbation files have been generated, it can be used to very

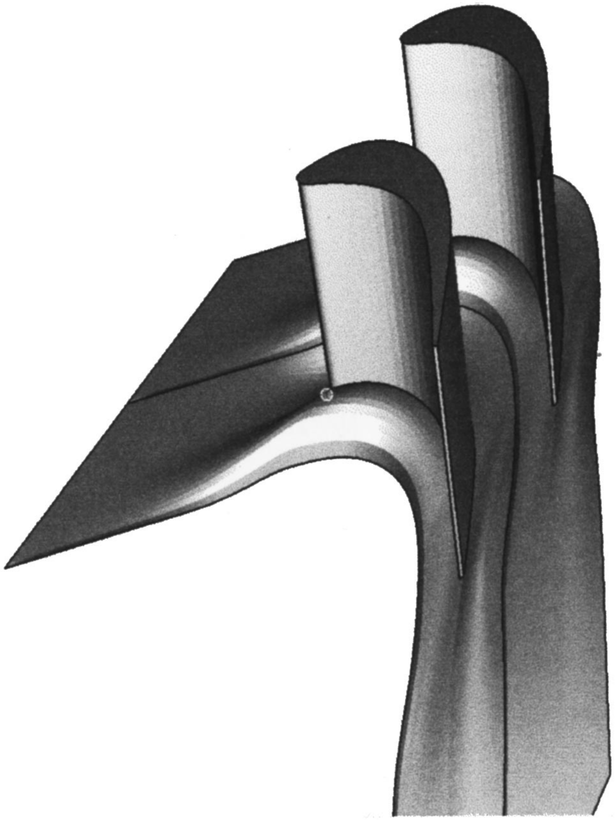

Fig. 15 Perspective view of final profiled end wall design

quickly investigate many options. Although only used in its forward mode so far, it has already helped define a profile not previously imagined. It is anticipated that in its inverse design mode it will enable even better profiles to be defined in future, in terms of reducing secondary flow and loss, by making the second and third harmonics of wall shape available in a practical way to the designer.

4 The effects of nonaxisymmetric end wall profiling are comparable with those of the existing techniques of lean and skew. Although not demonstrated here, end wall profiling can be combined with these where appropriate. An important advantage of end wall profiling is that it may be used on blading where lean and skew may not be mechanically feasible.

5 It is expected that nonaxisymmetric end wall profiling will come to be as widely used as aerofoil lean and skew in the future.

Acknowledgment

This work has been carried out with the support of Rolls Royce plc and the Defence Evaluation and Research Agency (MoD and DTI), Pyestock. The authors would like to thank them for funding it and for their permission to publish this paper.

Nomenclature

a, b = Fourier series coefficients
c = true chord
C = normalizing coefficient
CFD = Computational Fluid Dynamics
DERA = Defence Evaluation and Research Agency
NGV = Nozzle Guide Vane
p = aerofoil pitch
r = end wall radius (or height)
Re = Reynolds number $= \rho V c / \mu$
V = cascade midheight exit velocity
y = distance from wall
y^+ = near-wall Reynolds number $= \rho U \nu / \mu$
δ = boundary layer thickness
μ = viscosity
ρ = gas density
θ = circumferential position on end wall

References

[1] Sieverding, C. H., 1985, ''Secondary flows in straight and annular turbine cascades,'' Ucer, Stow, and Hirsch, eds., *Thermodynamics & Fluids of Turbomachinery*, NATO, Vol. II, pp. 621–624.

[2] Hartland, J. C., Gregory-Smith, D. G., and Rose, M. G., 1998, ''Non-Axisymmetric Endwall Profiling in a Turbine Rotor Blade,'' ASME Paper No. 98-GT-525.

[3] Rose, M. G., 1994, ''Non-axisymmetric Endwall Profiling in the HP NGVs of an Axial Flow Gas Turbine,'' ASME Paper No. 94-GT-249.

[4] Deich, M. E., and Zaryankin, A. E., 1960, ''Methods of increasing the efficiency of turbine stages,'' *Teploenergetica*, No. 2, pp. 18–24 [AEI Translation No. 2816].

[5] Ewen, J. S., Huber, F. W., and Mitchell, J. P., 1973, ''Investigation of the Aerodynamic Performance of Small Axial Turbines,'' ASME Paper No. 73-GT-3.

[6] Boletis, E., 1985, ''Effects of Tip Endwall Contouring on the Three-Dimensional Flow Field in an Annular Turbine Nozzle Guide Vane: Part 1—Experimental Investigation,'' J. Eng. Gas Turbines Power, **107**, pp. 983–990.

[7] Kopper, F. C., Milano, R., and Vanco, M., 1980, ''An Experimental Investigation of Endwalls Profiling in a Turbine Vane Cascade,'' Paper No. AIAA-80-1089.

[8] Atkins, M. J., 1987, ''Secondary Losses and End-Wall Profiling in a Turbine Cascade,'' I Mech. E C255/87, pp. 29–42.

[9] Dossena, V., Perdichizzi, A., and Savini, M., 1999, ''The Influence of Endwall Contouring on the Performance of a Turbine Nozzle Guide Vane,'' ASME J. Turbomach., **121**, pp. 200–208.

[10] Moustapha, S. H., and Williamson, R. G., 1985, ''Investigation of the Effect of Two Endwall Contours on the Performance of an Annular Nozzle Cascade,'' Paper No. AIAA-85-1218.

[11] Haas, J. E., and Boyle, R. J., 1984, ''Analytical and Experimental Investigation of Stator End Wall Contouring in a Small Axial-Flow Turbine,'' NASA Technical Paper 2309, AVSCOM report 84-C-5.

[12] Arts, T., 1985, ''Effects of Tip Endwall Contouring on the Three Dimensional Flow Field in an Annular Turbine Nozzle Guide Vane: Part 2—Numerical Investigation,'' ASME Paper No. 85-GT-108.

[13] Schnaus, J., and Fottner, L., 1997, ''Experimental and Numerical Investigation of the Influence of Endwall Inclination and Contouring on the Flow Field in a Turbine Cascade,'' ISABE 97-7117.

[14] Duden, A., Raab, I., and Fottner, L., 1999, ''Controlling the Secondary Flow in a Turbine Cascade by Three-Dimensional Airfoil Design and Endwall Contouring,'' ASME J. Turbomach., **121**, pp. 191–199.

[15] Morris, A. W. H., and Hoare, R. G., 1975, ''Secondary Loss Measurements in a Cascade of Turbine Blades With Meridional Wall Profiling,'' ASME Paper No. 75-WA/GT-13.

[16] Takeishi, K., Matsuura, M., Aoki, S., and Sato, T., 1990, ''An Experimental Study of Heat Transfer and Film Cooling on Low Aspect Ratio Turbine Nozzles,'' ASME J. Turbomach., **112**, pp. 488–496.

[17] Shahpar, S., and Lapworth, B. L., 1998, ''A Forward and Inverse Three-Dimensional Linear Design System for Turbomachinery Applications,'' *4th ECCOMASS Computational Fluid Dynamics Conference*, Athens, 7–11 Sept.

[18] Shahpar, S., Lapworth, B. L., De Pablos, T., and Taylor M. D., 1999, ''A Linear Approach to the Multi-Parameter Design of Three-Dimensional Turbomachinery Blades,'' AIAA Paper No. 99-0363.

[19] Rose, M. G., and Taylor, M. D., 1997, private communication.

[20] Moore J. G., 1985, ''Calculation of 3D Flow Without Numerical Mixing,'' *AGARD-LS-140 on 3D Computation Techniques Applied to Internal Flows in Propulsion Systems*, pp. 8.1–8.15.

[21] Moore, H., and Gregory-Smith, D. G., 1996, ''Transition Effects on Secondary Flows in a Turbine Cascade,'' ASME Paper No. 96-GT-100.

[22] Robinson, C. J., Northall, J. D., and McFarlane, C. W. R., 1989, ''Measurement & Calculation of the Three-Dimensional Flow in Axial Compressor Stators, With & Without End Bends,'' ASME Paper No. 89-GT-6.

[23] Harvey, N. W., Rose, M. G., Coupland, J., and Jones, T. V., 1999, ''Measurement and Calculation of Nozzle Guide Vane End Wall Heat Transfer,'' ASME J. Turbomach., **121**, pp. 184–190.

[24] Harrison, S., 1992, ''The Influence of Blade Lean on Turbine Losses,'' ASME J. Turbomach., **114**, pp. 184–190.

Nonaxisymmetric Turbine End Wall Design: Part II—Experimental Validation

J. C. Hartland
D. G. Gregory-Smith
University of Durham,
Durham, United Kingdom

N. W. Harvey
M. G. Rose
Rolls-Royce plc,
Derby, United Kingdom

The Durham Linear Cascade has been redesigned with the nonaxisymmetric profiled end wall described in the first part of this paper, with the aim of reducing the effects of secondary flow. The design intent was to reduce the passage vortex strength and to produce a more uniform exit flow angle profile in the radial direction with less overturning at the wall. The new end wall has been tested in the linear cascade and a comprehensive set of measurements taken. These include traverses of the flow field at a number of axial planes and surface static pressure distributions on the end wall. Detailed comparisons have been made with the CFD design predictions, and also for the results with a planar end wall. In this way an improved understanding of the effects of end wall profiling has been obtained. The experimental results generally agree with the design predictions, showing a reduction in the strength of the secondary flow at the exit and a more uniform flow angle profile. In a turbine stage these effects would be expected to improve the performance of any downstream blade row. There is also a reduction in the overall loss, which was not given by the CFD design predictions. Areas where there are discrepancies between the CFD calculations and measurement are likely to be due to the turbulence model used. Conclusions for how the three-dimensional linear design system should be used to define end wall geometries for improved turbine performance are presented. [S0889-504X(00)01002-3]

Introduction

Turning the sheared flow due to the hub or casing boundary layers at inlet to a blade row causes secondary flows to be produced. In essence, the cross-passage pressure gradient set up by the mainstream flow sweeps the low-momentum boundary fluid from pressure to suction surface on the end wall, with a compensating counterflow at a distance from the wall. Other phenomena are associated with secondary flow, which has been studied extensively. A comprehensive review was made by Sieverding [1]. The secondary flow gives rise to increased loss within the blade row and produces a nonuniform flow at exit, which may cause extra loss in succeeding blade rows.

Part I of these papers describes the design of a nonaxisymmetric end wall profile to counteract the secondary flow. By introducing curvature on the end wall, the static pressure field can be modified, thus affecting the secondary flow. The idea of end wall profiling to reduce secondary flows is not new and Part I reviews some of the literature over the past four decades. However, recent advances in computational techniques have allowed the development of design techniques to optimize the three-dimensional shape of an end wall to reduce the effects of secondary flows.

This paper describes the experimental testing of the end wall profile whose design was described in Part I. The immediate predecessor to this work was that of Rose [2] who suggested a design of the end wall for a nozzle guide vane to reduce the pressure nonuniformity at the platform trailing edge, as a means of reducing disk cooling leakage flow. His design was modified for a rotor blade, which is used in the large-scale low-speed cascade at Durham University. This work was reported by Hartland et al. [3], who showed that the designed reduction in pressure nonuniformity was achieved very well, and that there was some effect on the secondary flow, as was expected. A simple and quick method for machining an arbitrary end wall profile from polyurethane foam had been evolved. Thus it was a relatively straightforward task to take the profile coordinates of the new end wall from the design data and manufacture it for testing in the cascade.

Experiments

Durham Cascade. The cascade contains rotor blades of some 110 deg of turning; similar to those of a high-pressure axial flow turbine. The cascade geometry is described by Gregory-Smith and Cleak [4] and is illustrated in Fig. 1. The blading design details are given in Table 1.

There is an upstream turbulence grid to give high inlet turbulence as indicated in Table 2. There are three slots one axial chord upstream of the cascade, used to determine the inlet flow conditions, as described by Moore and Gregory-Smith [5]. There are also 11 traverse slots, one upstream, seven within the cascade, and three downstream. The flow is low speed with the Reynolds number less (about half) than that for a typical HP rotor blade and so the flow shows significant transitional effects as described by Moore and Gregory-Smith [6].

Instrumentation. The instrumentation is described in some detail by Hartland et al. [3], and only the most significant features are mentioned here. To measure the endwall pressure distributions, the existing planar endwall of the cascade (made from Perspex) had been fitted with pressure tappings (~0.8 mm internal diameter). The profiled endwall was machined in sections from polyurethane foam and the sections were coated with Melamine varnish and sanded smooth to give a hard surface with a good finish. Pressure tapping locations were as for the planar wall. The pressure tappings are polythene tubes (~0.76 mm internal diameter) set through the endwall and sanded off to give a smooth finish.

For the investigation of the flow field, measurements were made upstream at slot 1 (9 percent C_{ax} upstream of the leading edge, i.e., -109 percent), within the blade passage at slots 6 and 8, and at slot 10 (at -29, -3, and 28 percent C_{ax} from the trailing edge respectively). A five-holed cobra type probe was used to measure velocities and total pressure. These traverses were carried

---

Contributed by the International Gas Turbine Institute and presented at the 44th International Gas Turbine and Aeroengine Congress and Exhibition, Indianapolis, Indiana, June 7–10, 1999. Manuscript received by the International Gas Turbine Institute February 1999. Paper No. 99-GT-338. Review Chair: D. C. Wisler.

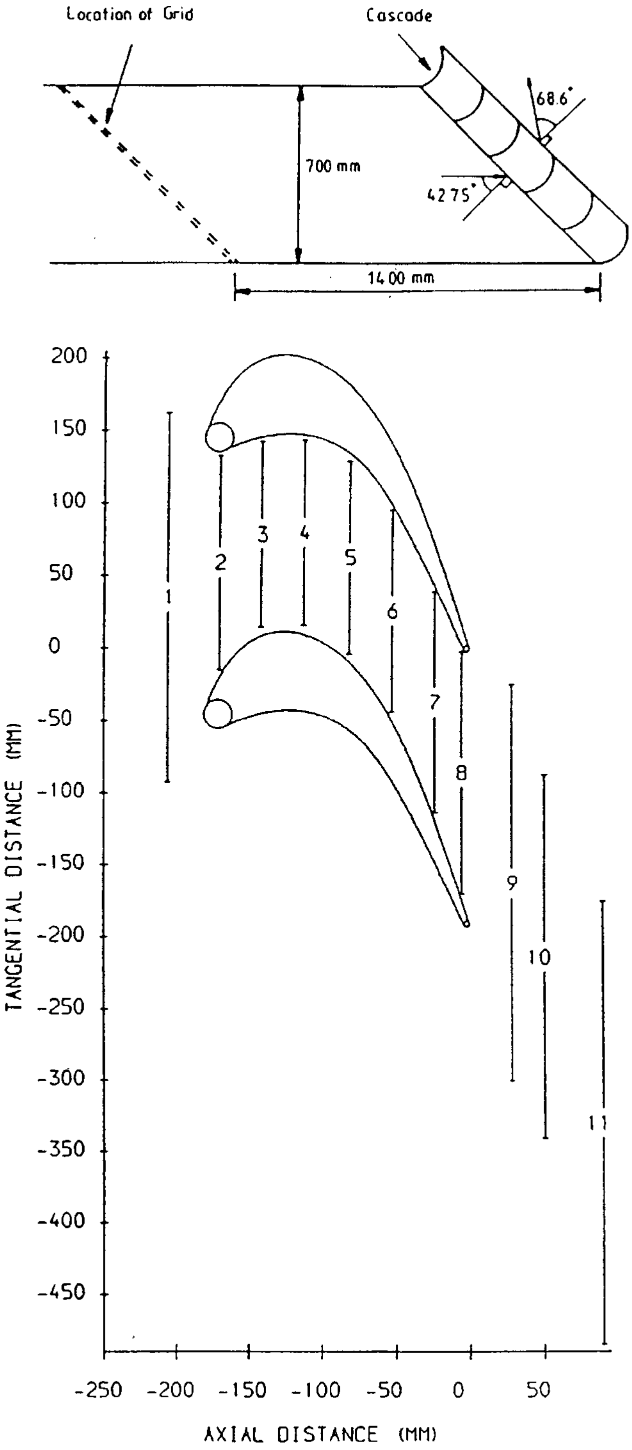

Fig. 1 Cascade and measurement slots

Table 1 Cascade design data

Inlet Flow Angle	42.75°
Blade Exit Angle	-68.7°
Blade Axial Chord, C_{ax}	181 mm
Blade Half-Span	200 mm
Reynolds Number (C_{ax} & V_{ex})	4.0×10^5
Exit Mach Number	0.1

Table 2 Inlet flow, one axial chord upstream

Free Stream	
Inlet Angle	43.5°
Streamwise Turbulence Intensity	5.1%
Spanwise Turbulence Intensity	5.6%
Normal Turbulence Intensity	5.0%
Turbulent k.e. Coefficient	0.0083
Turbulent Dissipation Rate	32.6 m^2/s^3
Mixing Length Scale	9.4mm
End Wall Boundary Layer	
99% Thickness	40 mm
Displacement Thickness	2.8 mm
Momentum Thickness	2.3 mm
Shape Factor	1.22

out with the profiled end wall in position, but also with a planar end wall made from the polyurethane, to ensure that the roughness difference between Perspex and the polyurethane did not affect the results.

Flow visualization was carried out on the end walls using fluorescent dye in diesel oil.

Results

Static Pressures. The shape of the end wall is described in Part I, and illustrated in Fig. 2. It can be seen that the profiling extends upstream of the cascade, so that by the leading edge there is a significant variation in height across the pitch. There is a high

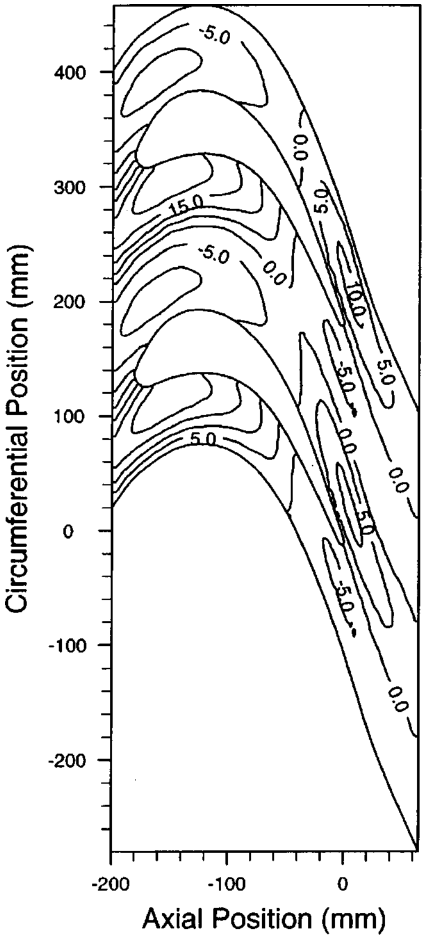

Fig. 2 End wall height contours

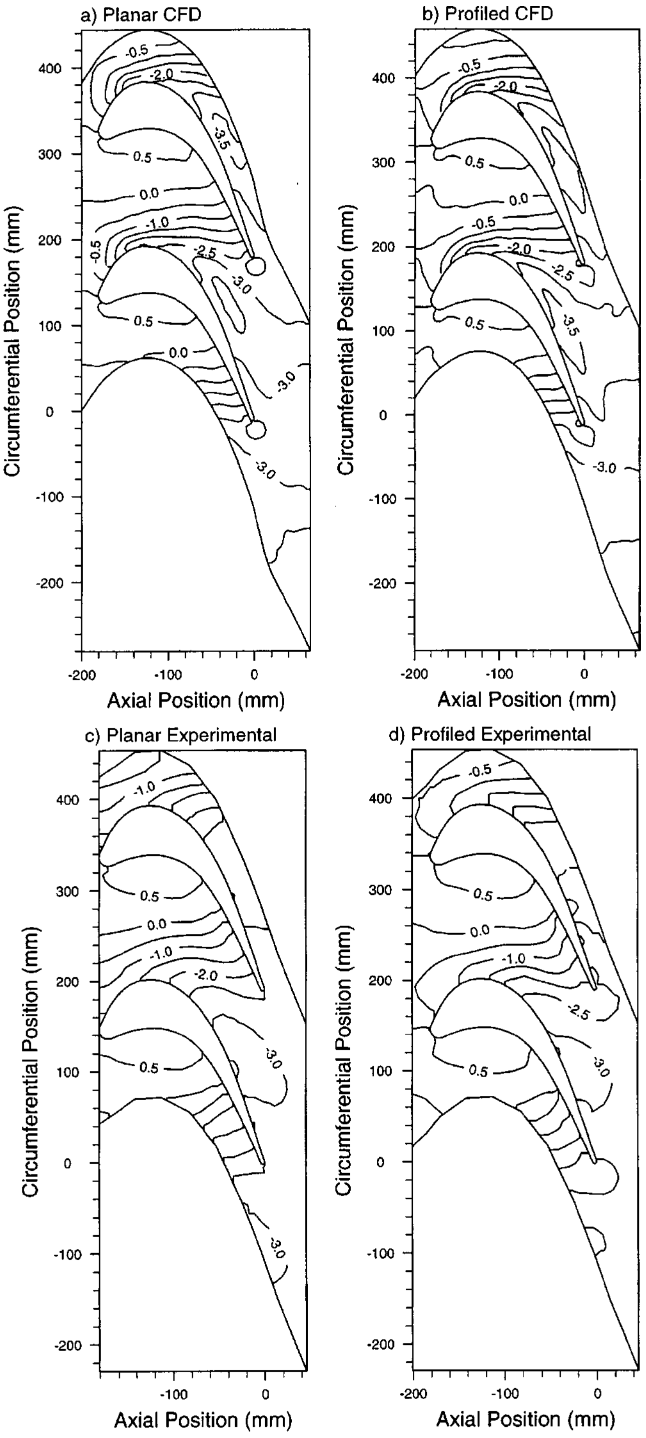

Fig. 3 End wall static pressures

region near the pressure surface, giving convex curvature and so lowering the pressure, and a low region near the suction surface with concave curvature raising the pressure there. The contour levels are in millimeters, so the maximum height near the pressure surface is between 20 mm and 25 mm, and the minimum near the suction surface between −10 mm and −15 mm. In the design, a limitation in end wall perturbation was set at 25 percent of axial chord, i.e., 45 mm.

Figure 3 shows the end wall static pressures for both the CFD and the experiments for the planar and profiled end walls. The contours are of static pressure coefficient, C_p, defined as the (upstream-local static pressure)/upstream dynamic pressure. The effect of the profiling on the pressure distribution in the early part of the passage seems to be rather more evident in the experimental than the CFD results. If the −1.0 contour is followed, it leaves the pressure surface at about −30 mm axial position for both walls. For the planar wall it goes across the plotting area, leaving it at 195 mm circumferential position, and coming back at 165 mm to meet the suction surface just downstream of the leading edge. However, for the profiled wall it curves round and meets the suction surface much further downstream, at about −150 mm axial position. Thus near the suction surface, the pressure has been raised significantly. The effects of curvature on the static pressure magnitude are much greater near the suction surface because the velocity is higher there. The CFD results show the same effects but not so clearly.

Figure 4 shows a static pressure plot around the blade profile for the CFD at the end wall and at 4.65 percent height (17 mm). At the end wall the pressure has been reduced a little on the pressure surface up to 60 percent axial chord, with a more significant raising of the pressure on the suction surface up to 40 percent axial chord. The effects are similar, although reduced at 4.65 percent height, but here the higher pressure on the suction surface extends to about 80 percent axial chord. By 10 percent height (40 mm), the differences are almost zero. Experimental plots corresponding to those of Fig. 4 were not obtained because of the problem of the tappings having to vary in spanwise position, depending on the shape of the end wall.

Toward the exit of the passage, the CFD results in Figs. 3 and 4 show a lowering of pressure near the suction surface due to the convex curvature there indicated by the hump in Fig. 2. This feature, as was explained in Part I, gives rise to a strengthened counter vortex in the design, so reducing the overturning on the end wall downstream. The effect is also seen in the experimental static pressures (Fig. 3), although not so clearly.

Traverse Results: Area Plots. A selection of the traverse results using the five-hole probe is made here; fuller details are given by Hartland [7]. Figure 5 shows the results at slot 6, −29 percent C_{ax}. The planar end wall secondary vectors show the passage vortex well formed and convected toward the corner of the suction surface and end wall. The vortex is convected by its ''image'' in the end wall and then away from the end wall by its ''image'' in the suction surface, as will be seen later. This process

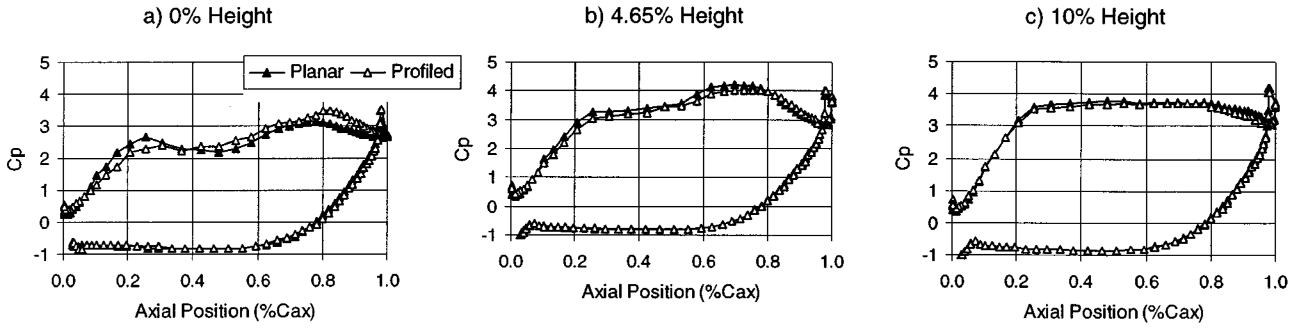

Fig. 4 CFD predictions of blade pressure distributions

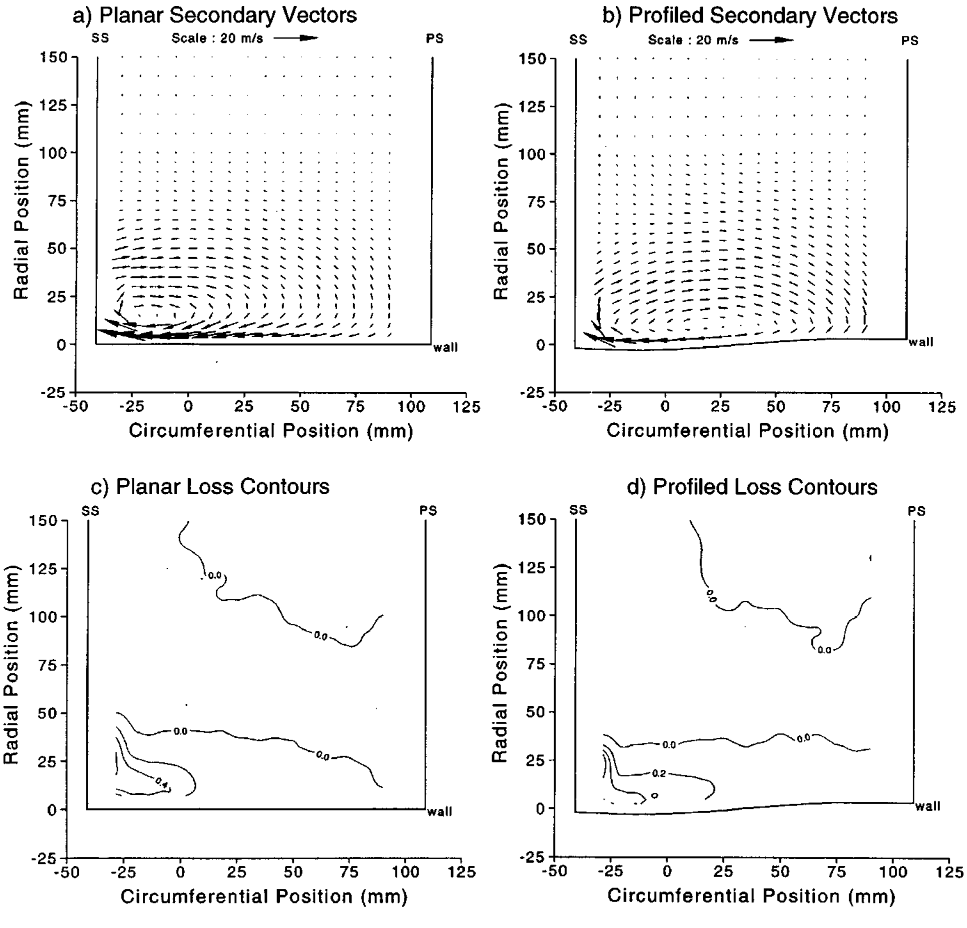
a) Planar Secondary Vectors

b) Profiled Secondary Vectors

c) Planar Loss Contours

d) Profiled Loss Contours

Fig. 5 Secondary vortices and loss at slot 6 (−29 percent C_{ax})

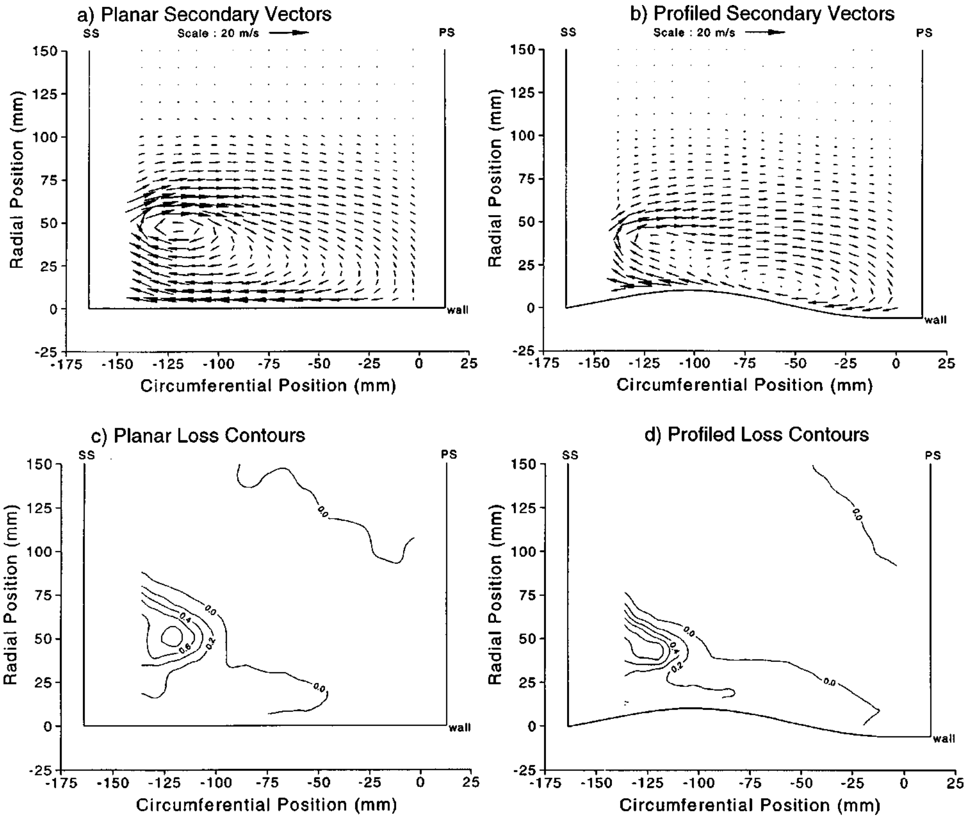
a) Planar Secondary Vectors

b) Profiled Secondary Vectors

c) Planar Loss Contours

d) Profiled Loss Contours

Fig. 6 Secondary vectors and loss at slot 8 (−3 percent C_{ax})

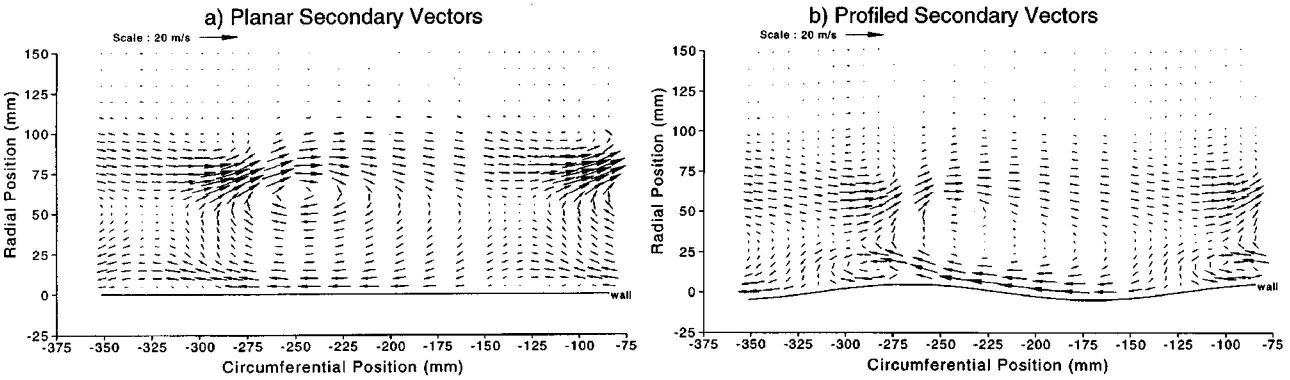

a) Planar Secondary Vectors

b) Profiled Secondary Vectors

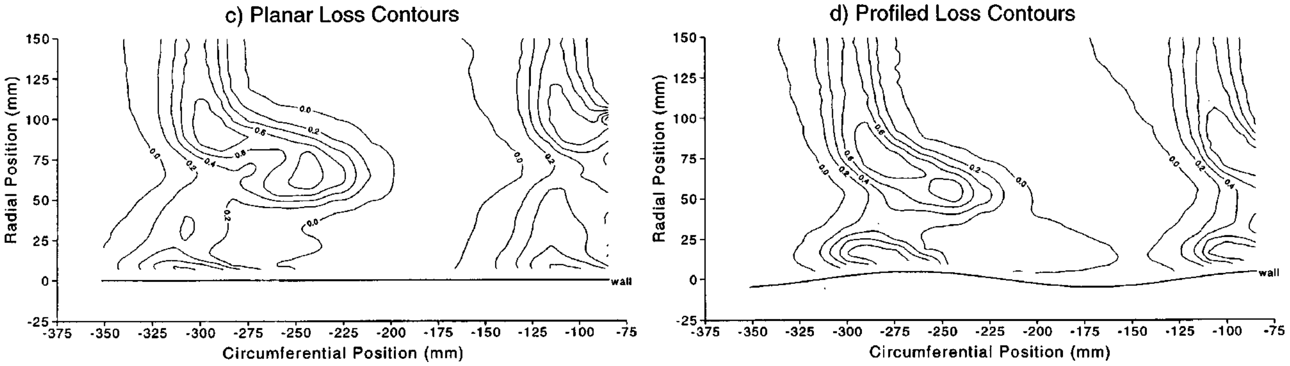

c) Planar Loss Contours

d) Profiled Loss Contours

Fig. 7 Secondary vectors and loss at slot 10 (28 percent C_{ax})

has been observed by other workers, e.g., Gregory-Smith and Graves [8], who describe it in detail. The rate of convection and its final position downstream is an indication of the strength of the secondary flow. The profiled end wall vortex appears weaker and it is centered approximately midpitch. The overturning close to the end wall appears significantly less, and is due to the reduction of the cross-passage pressure gradient in the earlier part of the passage as seen by the static pressures. The secondary kinetic energy overall is reduced by about 10 percent (see Fig. 11 later). Also in Fig. 5 are the contours of total pressure loss. These are expressed as a loss coefficient, C_{p0}, defined as (upstream−local total pressure)/(inlet dynamic pressure). With the planar end wall most of the inlet boundary layer has been convected toward the suction surface, forming a high loss region, which develops into the loss core later. Due to the lower crossflow close to it, the profiled end wall shows less convection of the boundary layer, and a smaller high loss region near the suction surface.

By slot 8 (-3 percent C_{ax}), just upstream of the trailing edge, for the planar wall the vortex has strengthened and has been convected away from the end wall, as shown in Fig. 6. The profiled end wall shows a significantly weaker vortex, which has divided into two parts. The larger but weaker part is centered close to the wall and nearer the pressure surface, and the smaller part, which is more intense, is closer to the suction surface and further from the end wall. In the re-entrant corner between the suction surface and end wall, there is evidence of the strong countervortex. The size of the probe prevented traversing closer into the corner. With respect to the loss contours, the planar end wall shows that the rolling up of the inlet boundary layer is well advanced, forming a loss core away from the end wall. The high-energy fluid has been convected close to the end wall over the pressure side half of the pitch. The profiled wall gives less rolling up of the boundary layer and convection of high-energy fluid, as a consequence of the lower secondary flows. The overall loss appears somewhat reduced.

The exit flow has been measured at slot 10 at 28 percent C_{ax} downstream. This is a little different from the exit plane used in the design process (29 percent C_{ax}). The secondary vectors as

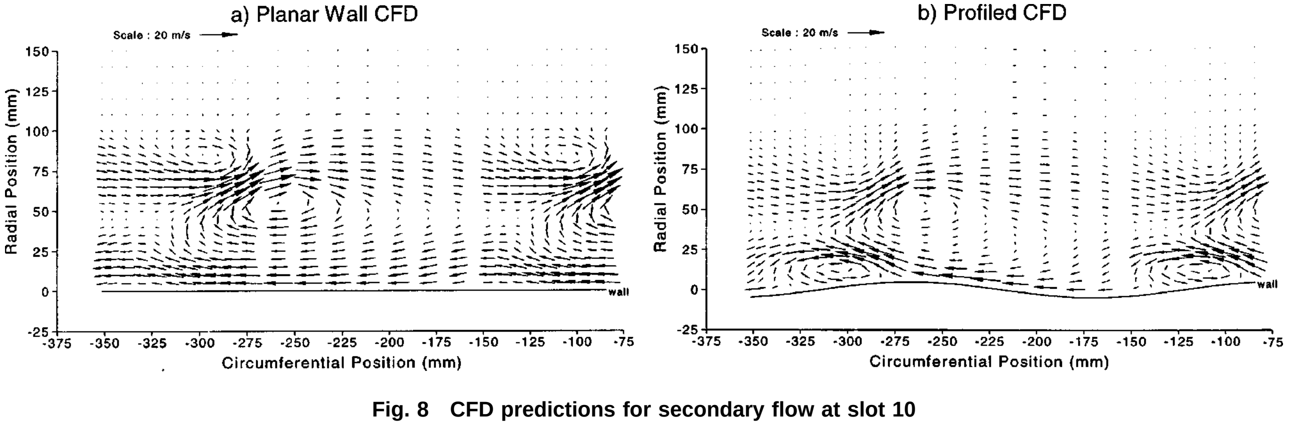

a) Planar Wall CFD

b) Profiled CFD

Fig. 8 CFD predictions for secondary flow at slot 10

measured are shown in Fig. 7, and the CFD predictions are shown in Fig. 8 for comparison. The planar end wall shows the passage vortex (clockwise) further from the end wall, with a countervortex (anti-clockwise) situated above it to the left, which stems from the trailing vorticity from the blade. On the end wall the small countervortex is seen by low (zero) cross flow on the end wall. The profiled end wall has a less intense passage vortex, but the crossflow close to the end wall seems a little stronger, especially in the region on the hump close to the suction surface near the exit seen in Fig. 2. The most significant difference with the profiled end wall is the strong countervortex close to the end wall to the left of the hump, caused by the low pressure on its top. The CFD vectors (Fig. 8) with the planar end wall shows the main features, but the vortex center is not so far from the end wall as in the experiment. As Gregory-Smith [9] has shown, this is quite common for CFD computations using a turbulence model that assumes turbulent flow through the blade passages, whereas in fact the flow on the blade surfaces and end wall is transitional [5]. The CFD results for the profiled end wall again show the main features, and in particular the strong countervortex. The loss contours in Fig. 7 show that the end wall profile does not give the double loss peak of the loss core with the planar end wall, and the core is generally closer to the end wall. The distortion of the wake is less, and these features result from the generally lower secondary flow. The loss associated with the stronger countervortex is a little greater, as might be expected.

Pitch-Averaged Results. The inlet flow profile is shown in Fig. 9 as a total pressure loss coefficient. The two end walls have nearly identical flow, as would be expected, but there is a region of negative loss between 25 mm and 125 mm from the end wall. This was found to be due to the arrangement of the upstream turbulence grid, giving less pressure drop near the edge of the grid. This is important when the loss of the cascade is assessed, but to a first approximation the effect can be allowed for if ''net'' loss is considered, i.e., the difference in loss between exit and inlet.

The legend is given for all the pitch-averaged results, with planar end wall data signified by full symbols and profiled data by open ones. The experimental data are squares and the CFD data, triangles. Figure 10 shows the pitch-averaged data at the downstream slot 10. The yaw angle shows an error at midspan of about 1.5 deg, which may be due partly to a systematic angle error in the measurement. For the planar end wall the CFD data have the underturning peak closer to the end wall, although its value is accurate allowing for the midspan difference. The profiled end wall gives a reduction in the underturning peak of about 2 deg similar to that predicted by the CFD, but the peak is moved inward by about 15 mm, to the same position as the design CFD prediction. Inboard of the peak, the profiled end wall gives less overturning, both compared to the CFD and to the planar end wall, although the values on the wall are similar. In Fig. 10(*b*), the secondary kinetic energy coefficient, C_{ske}, defined as the local secondary kinetic energy divided by upstream mainstream kinetic energy, shows a large reduction in the peak with the profiled end wall. This is also shown by the CFD, although the peak values are slightly higher, and the movement inward is not so great. Near the end wall, the profiled wall gives much more secondary kinetic energy, due to the strong countervortex, and somewhat more than the CFD design.

Figure 10(*c*) shows that the pitch-averaged loss peak is reduced significantly by the profiling, and is moved much closer to the end

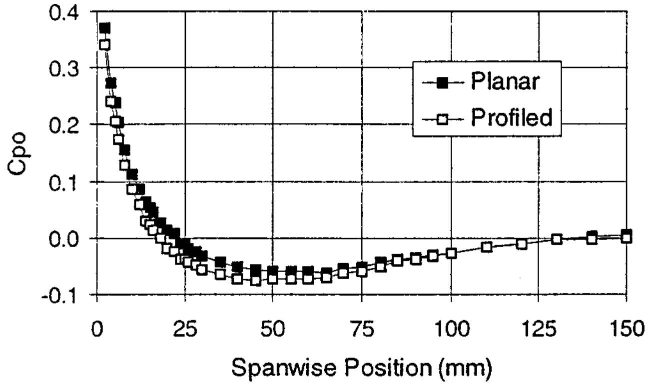

Fig. 9 Pitch-averaged loss coefficient at inlet

a) Yaw Angle

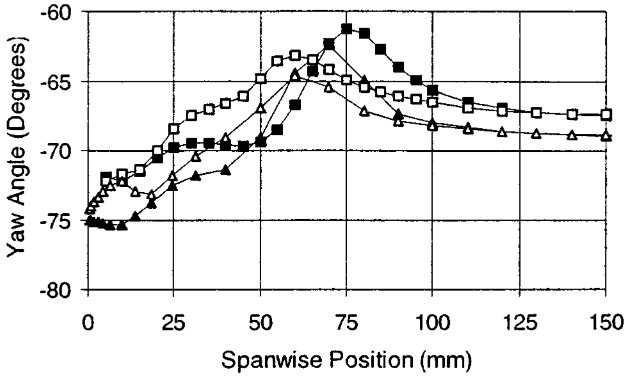

b) Secondary Kinetic Energy Coefficient

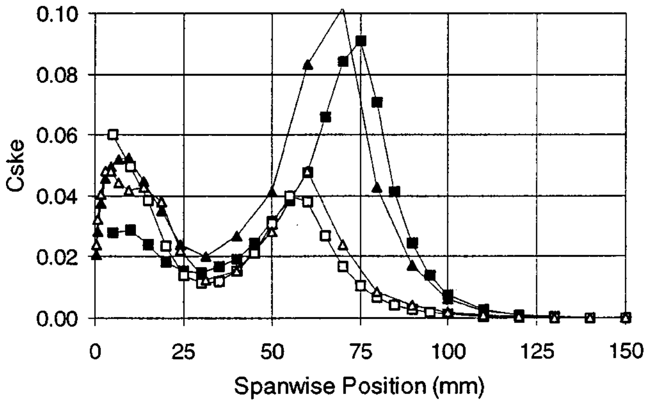

c) Loss Coefficient

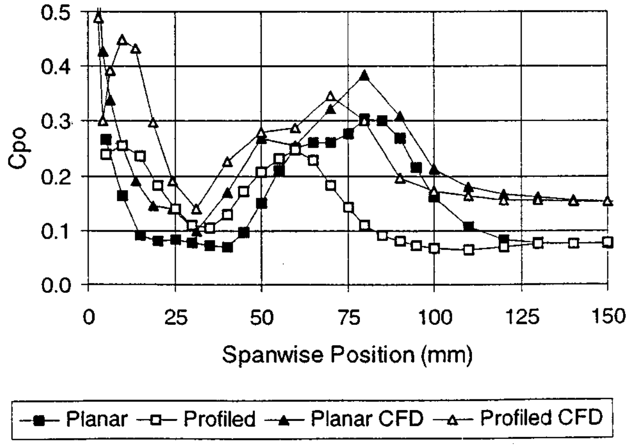

Fig. 10 Pitch-averaged results at slot 10

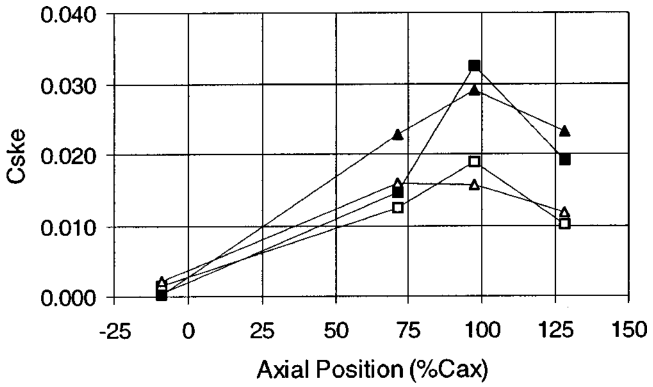

Fig. 11 Growth of secondary kinetic energy through the cascade

Fig. 12 End wall flow visualization

wall. The CFD shows only a slight reduction and not much movement inward. Nearer in, the profiled end wall gives more loss (apart from the closest point to the end wall). This extra loss is mainly associated with the stronger countervortex, which is also seen in the loss contours of Fig. 7. However, some of the ''higher'' loss is due to low-energy fluid still being near to the end wall. Because of the delayed overturning, less of this fluid has been convected into the loss core at this point.

The growth in secondary kinetic energy through the cascade is shown in Fig. 11, where the mass-weighted average across each traverse plane is plotted against axial position. The significant reduction with the profiled end wall is very evident, with the peak value at slot 8 (−3 percent) being reduced by about 40 percent for both the experiment and CFD. It may be noted that the CFD predicts slightly low values at slot 8, but high values at slot 10 (28 percent). This means the secondary velocities are being dissipated too slowly by the turbulence model, and this has been observed by other workers, e.g., [10].

A qualitative picture of the end wall flow is given by the flow visualization, where dye has been injected through some of the pressure tappings; see Fig. 12. It can be seen that the streaks at about 50 percent axial chord are displaced downstream for the profiled end wall due to the lower cross flow velocities. Toward exit, the crossflow seems as strong with the profiled end wall, but there is some evidence of the countervortex near the suction surface trailing edge.

Table 3 Net losses at slot 10

	C_{p0}		
	Full	Mid-Span	Secondary
Profiled	0.1108	0.0557	0.0551
Planar	0.1377	0.0598	0.0780
CFD Profiled	0.1937	0.1518	0.0419
CFD Planar	0.1926	0.1512	0.0414
	Mixed Out C_{p0}		
Profiled	0.1345	0.0709	0.0636
Planar	0.1588	0.0627	0.0961

Table 3 shows the net losses at slot 10. The midspan loss is subtracted from the total loss to give the net secondary loss. It can be seen that the measured net total loss is reduced by 20 percent and the net secondary loss by 30 percent. The CFD losses show little change, and both giving total loss much too high due to high midspan loss. Again this is a common error with CFD predictions because of the very fine grid that would be required for accurate profile loss prediction and the lack of any transition model in this transitional flow. Table 3 also shows the experimental mixed-out losses, where the reductions with the profiled end wall are 15 percent in net total loss and 34 percent in secondary loss.

Design Discussion

Overall the experiments largely confirm the design predictions for static pressure on the end wall. This is to be expected, because the static pressure distribution is largely due to the inviscid flow field, and modern CFD techniques should predict this well. Errors are only likely to arise if there are separations or large boundary layer growth, when the turbulence model is likely to perform poorly.

The traverse results also confirm the design reduction in secondary flow. In fact the experimental results seem to produce rather more improvement than the design predictions, with more general reduction in the passage vortex. This appears to be due to the slightly larger decrease in cross-passage pressure difference observed in the experiments. The experiments confirm the much stronger corner countervortex, which was part of the design. Again, since the production of secondary flow from a sheared flow upstream is an inviscid effect, it is expected that the CFD should give good predictions. However, some of the details will be affected by the generation of loss (and hence shear) within the passage, and so the turbulence model may cause some error, but this should be small.

Where an unexpected benefit arises is the significant reduction observed in net loss across the cascade. The design was aimed primarily at reducing over- and underturning at exit, with the object of improving the performance of a succeeding blade row. However, the significant reduction of secondary flow has resulted in a reduction in loss. This intuitively might be expected due to lower scraping velocities on the end wall and suction surface from the passage vortex, and reduced mixing loss from the secondary velocities. The CFD predicts the secondary kinetic energy well, but the mixing length turbulence model is not adequate to translate this into accurate losses. The modeling required to improve on this is not clear, however. Moore and Gregory-Smith [6] found that for the code used in this design, a $k-e$ turbulence model performed rather worse than a mixing length model, especially if laminar and transitional regions are allowed for in the latter. More work in this area is needed.

The strong countervortex is a source of extra loss as expected from the design, see Figs. 10 and 7. It appears likely that the hump near the suction surface at exit, which causes this vortex, may not be desirable, since it also induces overturning flow on its other side (Fig. 7 vectors). In the design the countervortex was calculated to improve overturning at the wall. Its specific effect on whirl angle cannot be determined from the measurements directly, although the earlier slot traverses show reduced overturning (stemming from the reduced cross passage pressure difference) in the earlier part of the passage. If in fact this strong countervortex is not necessary to reduce the overturning on the end wall, then it could be omitted, resulting in an even larger reduction in loss.

Conclusion

This paper has tested experimentally a profiled end wall designed to reduce secondary flows. The following points may be concluded:

(*a*) The static pressure field agrees well with the design prediction, and in fact seems to show a greater reduction in cross-passage pressure difference in the early part of the passage than that for the design.

(*b*) The resulting secondary flows are significantly reduced in the earlier part of the passage, and this reduction is convected downstream to give reduced secondary flow at exit. The profiled end wall gives significantly less angle variation at exit.

(*c*) A strong corner countervortex is observed according to the design prediction.

(*d*) The net reduction in secondary loss is significant: 30 percent at the downstream exit plane, 34 percent in mixed-out terms.

(*e*) If the strong corner countervortex is not needed to reduce the overturning on the end wall, then greater loss reduction can be achieved if it is omitted.

From the whole investigation on end wall profiling covered by both Part I and Part II papers, the following conclusions may be drawn:

1 A new linear design tool has been successfully developed for the design of nonaxisymmetric end walls.

2 A first design of profiled end wall has achieved significant reductions in exit whirl angle deviations, secondary kinetic energy and secondary loss.

3 Future designs, making use of the inverse mode of the design code, higher order harmonics of wall shape and larger perturbation amplitudes, will seek to reduce secondary flow and loss further.

4 Nonaxisymmetric end wall profiling is a powerful new tool available to the turbomachinery designer, and it is expected that it will come to be as widely used as aerofoil lean and skew in the future.

Acknowledgments

This work has been carried out with the support of Rolls-Royce plc and the Defence Evaluation and Research Agency (MoD and DTI), Pyestock. The authors would like to thank them for funding it and their permission to publish this paper.

Nomenclature

C_{ax} = axial chord
C_p = (upstream-local) static pressure coefficient
C_{p0} = (upstream-local) total pressure coefficient
C_{ske} = secondary kinetic energy coefficient
V_{ex} = nominal exit velocity
Coefficients are made dimensionless by *inlet* velocity.

References

[1] Sieverding, C. H., 1985, ''Recent Progress in the Understanding of Basic Aspects of Secondary Flows in Turbine Blade Passages,'' ASME J. Eng. Gas Turbines Power, **107**, pp. 248–252.
[2] Rose, M. G., 1994, ''Non-axisymmetric Endwall Profiling in the HP NGVs of an Axial Flow Gas Turbine,'' ASME Paper No. 94-GT-249.
[3] Hartland, J. C., Gregory-Smith, D. G., and Rose, M. G., 1998, ''Non-axisymmetric End Wall Profiling in a Turbine Rotor Blade,'' ASME Paper No. 98-GT-525.
[4] Gregory-Smith, D. G., and Cleak, J. G. E., 1992, ''Secondary Flow Measurements in a Turbine Cascade With High Inlet Turbulence,'' ASME J. Turbomach., **114**, pp. 173–183.
[5] Moore, H., and Gregory-Smith, D. G., 1995, ''Turbulence and Transition in Secondary Flows in a Turbine Cascade,'' AGARD-CP571, *PEP Loss Mechanisms and Unsteady Flows in Turbomachines*, Paper No. 8.
[6] Moore, H., and Gregory-Smith, D. G., 1996, ''Transition Effects on Secondary Flows in a Turbine Cascade,'' ASME Paper No. 96-GT-100.
[7] Hartland, J. C., 1999, Ph.D. thesis, University of Durham, to be submitted.
[8] Gregory-Smith, D. G., and Graves, C. P., 1983, ''Secondary Flows and Losses in a Turbine Cascade,'' AGARD-CP351, Paper No. 17.
[9] Gregory-Smith, D. G., 1995, ''Calculations of the Secondary Flow in a Turbine Cascade,'' *Computational Fluid Dynamics in Aeropropulsion*, ASME AD-49, p. 77.
[10] Cleak, J. G. E., and Gregory-Smith, D. G., 1992, ''Turbulence Modeling for Secondary Flow Prediction in a Turbine Cascade,'' ASME J. Turbomach., **114**, pp. 590–598.

An Implicit Scheme for Cascade Flow and Heat Transfer Analysis

C. Xu
R. S. Amano[1]
Department of Mechanical Engineering,
University of Wisconsin,
Milwaukee, WI 53201

A new efficient implicit scheme, based on the second-order time and spatial difference algorithm for solving steady flow by using time-marching Navier–Stokes equations, was developed for predicting turbine cascade flows and heat transfer. The difference scheme comprises an explicit part in the intermediate time-step and an implicit part in the local time-step. The viscous flux vectors are decomposed to simplify the flow calculation in the explicit step. The time difference terms are expressed in terms of the viscous dependent terms that appear in the diffusion terms in the form by adding eigenvalues of viscous flux matrices into the time derivation term. In the presently proposed scheme, the two-sweep procedure is used in the implicit step instead of employing a traditional matrix operation to save the computational time. This method has been used to calculate the flow around C3X and VKI cascades. The computed results were compared with experimental data as well as with other published computations. The comparisons for both surface pressure and heat transfer coefficient showed good agreement with the experiments.
[S0889-504X(00)01702-5]

Introduction

Time-marching algorithms [1–5] have been mostly used in gas turbine cascade flow and heat transfer analyses. The basic principle of a time-marching method is to consider a stationary problem as the solution after sufficiently many time-steps of computation of the time-dependent equations. The computation starts with a rough perturbation, which develops under certain boundary conditions. In this approach, the governing equations are replaced by a robust time difference approximation with which steady or time-dependent flows of interest can be solved at each time level. The time-marching algorithms can be categorized into two types: explicit and implicit schemes. An explicit method is in general easier to program and vectorize allowing simpler accommodations of boundary conditions and turbulence models. One of the main shortcomings of the explicit method is its lack of numerical robustness, resulting in severe constrains of the time step size. An implicit scheme, on the other hand, is generally unconditionally stable so that a relatively large time-step can be used.

There are generally two methods to solve the implicit algorithm. One is the implicit approximate factorization (AF) method [2,6–9] and the other omits any approximate factorization by solving the difference equations using an algebraic method, such as an iteration method reported by Beam and Warming [9]. The implicit AF method for the compressible two-dimensional Navier–Stokes equations, originally derived by Beam and Warming [9] and Ames [10] are characterized by treating the higher dimensional problem as a lower dimensional one. Lee [11] simplified the Beam–Warming scheme and made a mathematical alternative simplification. In the standard AF method, in order to factorize the second-order, time-difference terms are added in the scheme. This second-order time will increase with the time-step increase. This will increase the truncation error when employing a large time-step by using AF method, thereby affecting the stability and accuracy of the scheme. The iteration method has good compatibility and is easy to program but requires a great deal of computational time. In view of these features associated with an implicit method, one of the purposes of this research is to develop a new numerical scheme that can avoid the factorization but simplify the computational procedure. This paper proposes an implicit scheme that uses the spectral radii technique and avoids the approximate factorization to form an efficient scheme.

In general, artificial dissipation terms were used in order to extend the stability and permit a higher CFL number in most of the present interactive schemes for the compressible flow computation [5]. It is well known that the artificial dissipation will influence the accuracy of the numerical computation. Essentially grid-converged solutions for the high-speed viscous flows over aerodynamic shapes should be obtained with sufficiently fine meshes. The computation based on fine meshes is very time consuming; long computational time is required to obtain grid-converged solutions, and makes it difficult to assess the numerical accuracy of the solution. In the present research the dissipation term was presented in the matrix-valued dissipation term, which is similar to the form proposed by Turkel and Vatsa [5] except that the present model does not treat the artificial dissipation terms through modifying the convective fluxes as proposed by Turkel and Vatsa. Instead, the matrix-valued dissipation terms were incorporated into the time-derivative terms to form a new time-discretization scheme.

The effect of eigenvalue stiffness on the convergence of both explicit and implicit schemes is well known and two distinct methods have been suggested for controlling the eigenvalues to enhance convergence. One method is to premultiply the time-derivative by a suitable matrix and the other is to use a perturbed form of the equations in which specific terms are dropped such that the physical acoustic waves are replaced by pseudo-acoustic modes. The present method follows the first idea and incorporated the matrix-valued dissipation terms in time-derivative terms. These terms prevent the eigenvalues of the time-derivative terms from becoming stiff when the calculations are performed in the flow where the Mach number is relatively small. This characteristic can partly control the effect of eigenvalue stiffness that is well known on the convergence of both explicit and implicit schemes. Furthermore, the present scheme employs a hybrid algorithm, which combines the advantages of the implicit and explicit schemes. The present scheme also processes a spectral radii technique to simplify the calculation and avoid the approximate factorization, thus increasing the stability. This new method is a second-order time and spatial derivative scheme permitting a high CFL number.

Mathematical Model

The two-dimensional time-dependent Reynolds-averaged Navier–Stokes equations can be written as:

---

[1] Corresponding author.

Contributed by the International Gas Turbine Institute and presented at the 44th International Gas Turbine and Aeroengine Congress and Exhibition, Indianapolis, Indiana, June 7–10, 1999. Manuscript received by the International Gas Turbine Institute February 1999. Paper No. 99-GT-262. Review Chair: D. C. Wisler.

$$Q_t+E_x+F_y=R_x+S_y \tag{1}$$

where

$$Q=\begin{bmatrix}\rho\\ \rho u\\ \rho\nu\\ e\end{bmatrix},\quad E=\begin{bmatrix}\rho u\\ p+\rho u^2\\ \rho u\nu\\ (e+p)u\end{bmatrix},\quad F=\begin{bmatrix}\rho\nu\\ \rho u\nu\\ p+\rho\nu^2\\ (e+p)\nu\end{bmatrix}$$

$$R=\begin{bmatrix}0\\ \tau_{xx}\\ \tau_{xy}\\ \beta_x\end{bmatrix},\quad S=\begin{bmatrix}0\\ \tau_{xy}\\ \tau_{yy}\\ \beta_y\end{bmatrix}$$

and where

$$\tau_{xx}=2\mu u_x+\lambda(u_x+\nu_y)$$

$$\tau_{xy}=\mu(u_x+\nu_y)$$

$$\tau_{yy}=2\mu u_y+\lambda(u_x+\nu_y)$$

$$\beta_x=u\tau_{xx}+\nu\tau_{xy}+\gamma\mu P_r^{-1}\overline{e_x}$$

$$\beta_y=u\tau_{xy}+\nu\tau_{yy}+\gamma\mu P_r^{-1}\overline{e_y}$$

$$\overline{e}=RT/(\gamma-1)$$

where the energy caloric equation can be written as

$$e=p/[\rho(\gamma-1)]$$

Here γ is specific heat ratio and $\lambda=-2\mu/3$ where the viscosity is the sum of the molecular viscosity and turbulent viscosity, i.e.,

$$\mu=\mu_t+\mu_l$$

According to the idea of Beam and Warming [9], the flux vector can be decomposed into two subvectors consisting of the positive and negative eigenvalues. One can compute the Jacobians, $A=\partial E/\partial Q$ and $B=\partial F/\partial Q$, to show that

$$E=AQ \tag{2}$$

$$F=BQ \tag{3}$$

where Q is the vector in the N–S equations.

The governing equations can be written as

$$Q_t+AQ_\xi+BQ_\eta=R_\xi+S_\eta \tag{4}$$

We have the following transformation relations:

$$P^{-1}AP=\Lambda(A) \tag{5}$$

$$P^{-1}BP=\Lambda(B) \tag{6}$$

where $\Lambda(A)$ and $\Lambda(B)$ are diagonal matrices and can been written as

$$\begin{aligned}\Lambda(A)&=\mathrm{diag}[\tilde{u},\tilde{u},\tilde{u}+aL(\xi),\tilde{u}-aL(\xi)]\\&=\mathrm{diag}[\lambda_{A1},\lambda_{A2},\lambda_{A3},\lambda_{A4}]\end{aligned} \tag{7}$$

$$\begin{aligned}\Lambda(B)&=\mathrm{diag}[\tilde{\nu},\tilde{\nu},\tilde{\nu}+aL(\eta),\tilde{\nu}-aL(\eta)]\\&=\mathrm{diag}[\lambda_{B1},\lambda_{B2},\lambda_{B3},\lambda_{B4}]\end{aligned} \tag{8}$$

where λ's are the eigenvalues of the flux vectors E and F, and a the speed of sound in the physical domain. The transformation between the physical domain (x, y) and computational domain (ξ, η) can be written as

$$\tilde{u}=u\partial\xi/\partial x+\nu\partial\xi/\partial y \tag{9}$$

$$\tilde{\nu}=u\partial\eta/\partial x+\nu\partial\eta/\partial y \tag{10}$$

$$L(\xi)=\sqrt{\xi_x^2+\xi_y^2} \tag{11}$$

$$L(\eta)=\sqrt{\eta_x^2+\eta_y^2} \tag{12}$$

According to the vector splitting method, the eigenvalues of the flux vector can be expressed in the positive and negative forms in order to split the flux vector into two subvectors, i.e.,

$$E=(A^++A^-)Q=E^++E^- \tag{13}$$

$$F=(B^++B^-)Q=F^++F^- \tag{14}$$

The flux vector splitting form of Eq. (4) can be written as

$$Q_t+E_x^++E_x^-+F_y^++F_y^-=R_x+S_y \tag{15}$$

By using the second-order time differencing algorithm, we have

$$\frac{Q^{n+1}-Q^n}{\Delta t}=\frac{1}{2}\left[\left(\frac{\partial Q}{\partial t}\right)^{n+1}+\left(\frac{\partial Q}{\partial t}\right)^n\right] \tag{16}$$

and

$$\begin{aligned}\Delta Q_{i,j}^{n+1}=&-\Delta t\left[\frac{\nabla_\xi E^+}{\Delta\xi}+\frac{\Delta_\xi E^-}{\Delta\xi}+\frac{\nabla_\eta F^+}{\Delta\eta}+\frac{\Delta_\eta F^-}{\Delta\eta}\right]^n\\&+\Delta t\left(\frac{\Delta_c R}{\Delta\xi}+\frac{\Delta_c S}{\Delta\eta}\right)^n\end{aligned} \tag{17}$$

$$\delta Q_{i,j}^{n+1}=Q_{i,j}^{n+1}-Q_{i,j}^n \tag{18}$$

where ∇ and Δ are the second-order backward and forward difference operators and Δ_c the second-order center difference operators, respectively.

According to Turkel and Vatsa, the dissipation terms were written in the matrix-valued dissipation. However, in this study, the dissipation term was not incorporated into the convection flux term. Instead, the idea to overcome the effect of eigenvalue stiffness on the convergence of compressible flow calculation was incorporated into the computational procedure. The dissipation term was incorporated into the time-derivative term. The dissipation terms can play a role to increase the eigenvalue of time-derivative terms when calculation is performed in low Mach number flow regions. Upon incorporation of this idea into Eqs. (15)–(18) along with Eqs. (11) and (12), we can obtain the following difference scheme (for the details see appendix):

$$\begin{aligned}&A_W\delta Q_{i-1,j}^{n+1}+A_S\delta Q_{i,j-1}^{n+1}+A_P\delta Q_{i,j}^{n+1}+A_N\delta Q_{i,j+1}^{n+1}\\&+A_E\delta Q_{i+1,j}^{n+1}=\Delta Q_{i,j}^{n+1}\end{aligned} \tag{19}$$

where

$$A_W=-\frac{\Delta t}{2\Delta\xi}(\Lambda_E^+)_{i-1,j}^n-\frac{\Delta t}{2\Delta\xi}(A_{i-1,j}^+)^n$$

$$A_S=-\frac{\Delta t}{2\Delta\eta}(\Lambda_F^+)_{i,j-1}^n-\frac{\Delta t}{2\Delta\eta}(B_{i,j-1}^+)^n$$

$$\begin{aligned}A_P=I&+\frac{\Delta t}{2\Delta\xi}(\Lambda_E^+)_{i,j}^n-\frac{\Delta t}{2\Delta\xi}(\Lambda_E^-)_{i,j}^n+\frac{\Delta t}{2\Delta\eta}(\Lambda_F^+)_{i,j}^n\\&-\frac{\Delta t}{2\Delta\eta}(\Lambda_F^-)_{i,j}^n+\frac{\Delta t}{2\Delta\xi}(A_{i,j}^+)^n-\frac{\Delta t}{2\Delta\xi}(A_{i,j}^-)^n\\&+\frac{\Delta t}{2\Delta\eta}(B_{i,j}^+)^n-\frac{\Delta t}{2\Delta\eta}(B_{i,j}^+)^n\end{aligned}$$

$$A_N=\frac{\Delta t}{2\Delta\eta}(\Lambda_F^-)_{i,j+1}^n+\frac{\Delta t}{2\Delta\eta}(B_{i,j+1}^-)^n$$

$$A_E=\frac{\Delta t}{2\Delta\xi}(\Lambda_E^-)_{i+1,j}^n+\frac{\Delta t}{4\Delta\xi}(A_{i+1,j}^-)^n$$

Since Eq. (19) is an implicit scheme, it can improve the numerical stability even with a large time step. In this numerical scheme, A_W, A_S, A_P, and A_E are all scalars, which are calculated directly from flux vectors. In this way, the computational efforts are greatly reduced as compared with other coefficient matrix implicit schemes for all time-steps [12].

It is found that the implicit part, Eq. (19), can be solved by using two sweeps similar to the hopscotch sweeps but along the i (i.e., ξ) and j (i.e., η) directions. Equation (19) can be written in the form of the two sweeps as followings

$$\begin{aligned} &A_S \delta Q_{i,j-1}^{n+1} + A_P \delta Q_{i,j}^{n+1} + A_N \delta Q_{i,j+1}^{n+1} \\ &\quad = \Delta Q_{i,j}^{n+1} - A_W \delta Q_{i-1,j}^{n+1} - A_E \Delta Q_{i+1,j}^{n} \end{aligned} \tag{20}$$

Within the same time-step, calculation starts from $i=1$ to $i_{\max}$ ξ direction. At each i direction with the time step $n+1$, the variables $\delta Q_{i,j-l}$, $\delta Q_{i,j}$, and $\delta Q_{i,j+1}$ can be obtained along η direction, since the present scheme consists of an explicit part to calculate ΔQ_{ij} and an implicit part to calculate $\delta Q_{i,j}$.

In this study, the time-step is selected according to the CFL number constraints as:

$$\Delta t = \min(\Delta t_\xi, \Delta t_\xi) \tag{21}$$

where

$$\Delta t_\xi \leqslant \frac{\mathrm{CFL} \cdot \Delta \xi}{|\tilde{u}| + a\sqrt{\xi_x^2 + \eta_y^2} + \dfrac{2\omega}{\Delta \xi \rho}(\xi_x^2 + \eta_y^2)} \tag{22}$$

$$\Delta t_\eta \leqslant \frac{\mathrm{CFL} \cdot \Delta \eta}{|\tilde{v}| + a\sqrt{\xi_x^2 + \eta_y^2} + \dfrac{2\omega}{\Delta \eta \rho}(\xi_x^2 + \eta_y^2)} \tag{23}$$

where $\omega = \max(\mu_l/\mathrm{Re}, \mu_t + 2\mu_l/\mathrm{Re}, \mu_l/\mathrm{Pr}\,\mathrm{Re})$. Usually CFL for an explicit scheme is limited to be less than 1, and this time step constriction is the restriction of typical explicit scheme. However, the CFL for the present scheme can be chosen up to 15. Thus the present scheme is considered to be more efficient than explicit schemes.

Boundary Conditions and Mesh Generation

The boundary conditions play an important role in determining accurate solutions and rapid numerical convergence. The boundary conditions used in the present scheme are similar to those of Liu and Jameson [4]. The additional boundary condition for the present scheme is as $\delta Q_{i,j} = 0$ at inlet, outlet, and solid implicit boundary conditions. The periodical boundary condition in the present scheme is set $\delta Q_{i,1} = \delta Q_{i,j\,\max}$. The boundary conditions for the energy equation are specified as total temperature is constant at upper stream, the surface temperature distribution is specified, and the conditions on periodic and downstream boundaries are treated similarly to other variables at the same boundaries.

The robust mesh generation procedure is needed for obtaining high-quality numerical results in the computations of viscous flows in turbomachinery cascades. In general, the mesh should control the grid point distributions in the boundary layers while achieving periodicity between the upper and lower parts of the outer boundary of the computational domain. An **H**-mesh meets these conditions and has been successfully used in many cascade flow calculations [1,4,13]. Two kinds of **H**-mesh were considered in the present computations. One is the body-fitted **H**-mesh [14] and the other the algebraic **H**-mesh [15].

Results and Discussion

In the calculation of turbine cascade flow analysis, the comparisons of most calculations [2,4,16] were made primarily between calculated and measured surface pressure distributions. The pressure distributions are one of the most important parameters to test the accuracy of the computations. In the present calculations, comparisons are made primarily between calculated and measured surface pressure distributions and surface heat transfer rates together with illustrative calculations for cascade flows. The comparison shows that the predications are in favorable agreement with measurements, indicating that the present scheme is reasonable. It is necessary to point out, however, the present calculations do not intend to simulate the details of the flow futures such as boundary structure and vortex structure of the trailing edge wakes. If a detailed flow structure needs to be investigated, a very fine grid should been used. For example, for investigation the trailing edge flow structure of the blade, Kiss et al. [17] used 437×45 grids in the trailing edge region to simulate the vortex structure of the trailing edge region. However, the more detailed investigations are still limited by the computer power.

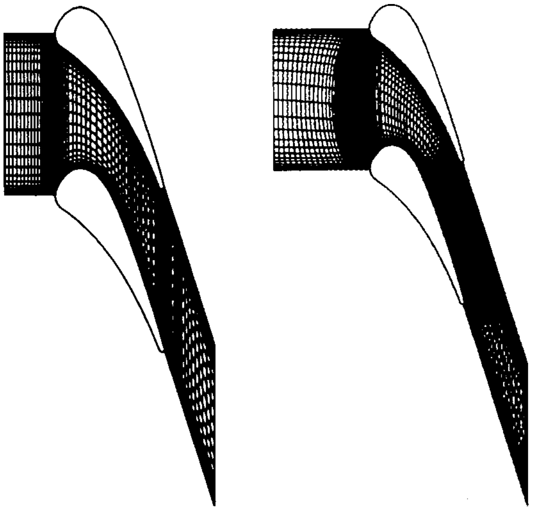
(a) Algebraic H-mesh (b) Body-fitted H-mesh

Fig. 1 Computational meshes

(A) C3X Turbine Cascade. The present numerical model was tested for a two-dimensional C3X turbine cascade [16] by using two types of **H**-meshes as shown in Fig. 1. Figure 1(*a*) shows the algebraic **H**-mesh (M1 Model) and Fig. 1(*b*) shows the body fitted **H**-mesh (M2 Model). The flow conditions correspond to the case 144 of the experiment conducted by Hylton et al. [16]. The geometric inlet and exit angles of the blade are approximately 0 and 72 deg, respectively. The flow conditions at the inlet are total pressure, $p_{T1} = 7.899$ kPa, total temperature, $T_{T1} = 815$ K, and inlet Reynolds number based on the chord length, $\mathrm{Re} = 6.3 \times 10^5$. The ratio of exit static to inlet total pressure was 0.59. The flow was assumed to be fully turbulent in the entire computation domain.

In order to assess the impact of the present scheme, the study of the influence of the CFL number was extensively conducted. Figure 2 shows the typical convergent histories with different CFL number (CFL = 1, 5, 7, 9, and 11, respectively) by using M1 Model with 86×24 meshes. Our research showed that as the CFL number increases, the convergence rate improves. For example, for the rms error to be reduced by four orders of magnitude the case with CFL = 5 requires approximately 500 time steps and the case with CFL = 11 only requires 250 time steps. The results also show that when the CFL number is greater than 7, the rate of convergent improvement becomes smaller than that of CFL numbers less than 7. When the CFL = 1, the computational performance is similar to the case of explicit scheme. In the present computation, the CFL number is selected in the range of 5 to 11.

It is commonly known that the high grid aspect ratios influence the convergence of the calculation. Therefore, the mesh refinement study for case 144 was conducted prior to the computations.

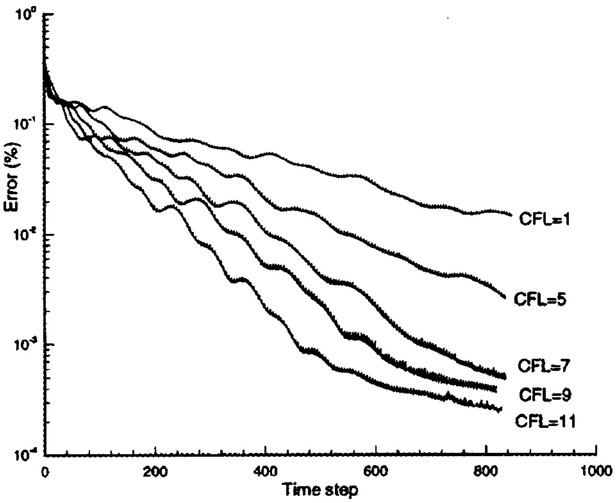

Fig. 2 Computational convergent histories

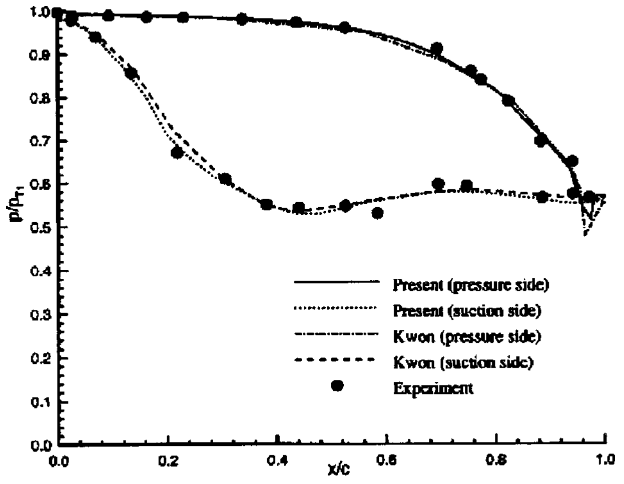

Fig. 4 Blade surface static pressure distributions

The different levels of the magnification factor based on the basic size 43×12 are shown in Fig. 3 where the mass flux residual is shown to reach a certain level by increasing mesh size. It was concluded that the mesh of 86×24 is sufficient for the present flow computations.

Figure 4 shows the comparison of the predictions of the blade surface static-pressure distribution with the experimental data obtained by Hylton et al. [16] and the N–S computations by Kwon [3]. As shown in this figure, both computations are in good agreement with the experiment. It is also noted that the present computation produces less trailing edge singularity, as depicted by the spike of Kwon's computation.

Figure 5 shows the pressure distributions obtained from the different types of **H**-mesh as shown in Figs. 1(*a*) and 1(*b*). Younis and Camarero [14] showed that the advantage of the body-fitted curvilinear mesh (M2 Model) concerns the discretization of the leading edge and trailing edge regions. However, this study shows that the surface pressure distributions are almost the same when using body-fitted mesh and algebraic **H**-mesh. Figure 6 shows the convergent history when using these two types of **H**-mesh. There are slight differences appearing between the two mesh models. It seems that the algebraic **H**-mesh has a better convergent property than the body-fitted **H**-mesh.

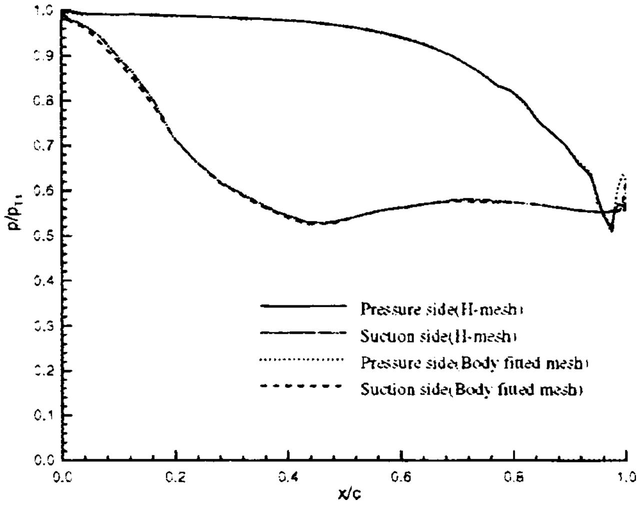

Fig. 5 Pressure distributions by using different meshes

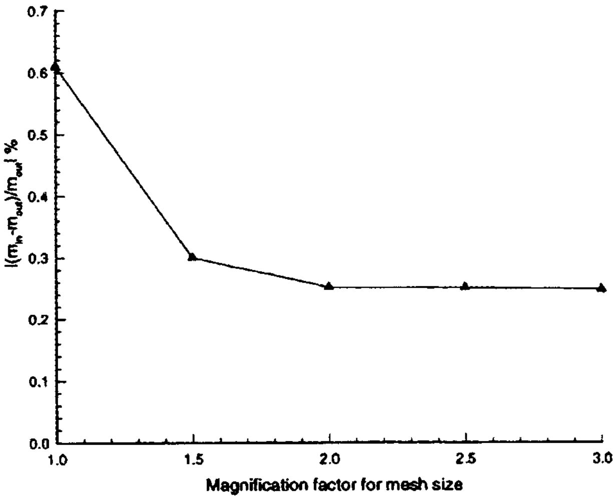

Fig. 3 Mesh refinement study

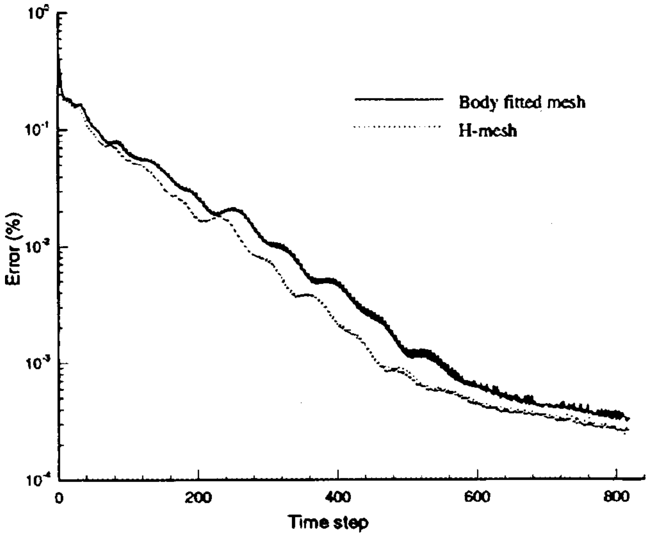

Fig. 6 Mesh influence of the convergent histories

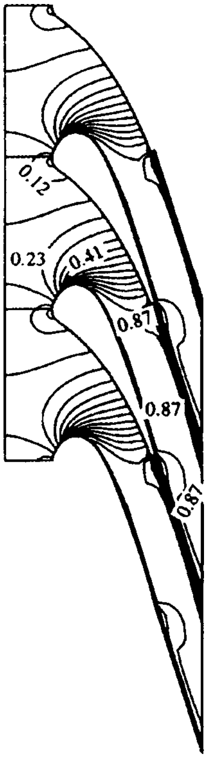

Fig. 7 Contour of computed Mach numbers

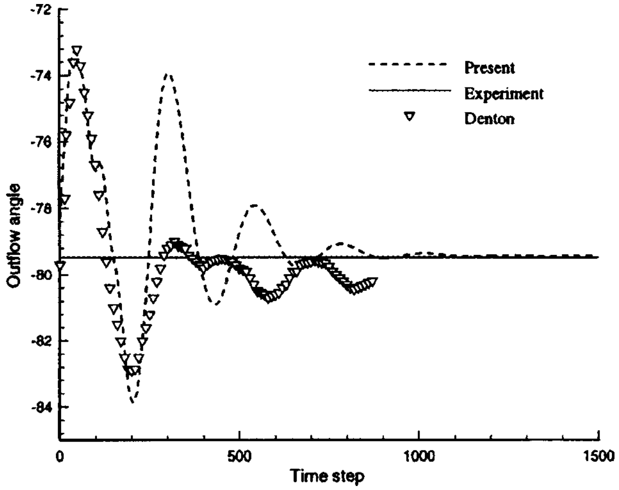

Fig. 9 Convergent histories of the outflow angle

Figure 7 presents the computed Mach number contours by using the algebraic **H**-mesh (M1 Model). The result shows that the flow is entirely subsonic with the computed maximum Mach number being about 0.87. Wakes are clearly seen downstream of the trailing edge. It is shown that the stagnation point forms near the nose of the blade surface. These features are consistent with those expected in actual operation.

The computed heat transfer coefficient was compared with the experiment and shown in Fig. 8. As can be seen, the heat transfer coefficient is in good agreement with the experiment on the pressure surface except in the trailing edge range. However, the heat transfer was overpredicted on the stagnation zone in the immediate vicinity of the leading edge on the suction surface. This discrepancy may be attributed to the fact that the energy equation was coupled with the momentum equations during the calculation. Use of a fully turbulent mixing length in the region of leading edge [18], particularly on the suction surface, due to the large pressure gradient the heat flux was overpredicted. In another aspect, in the practical flow of the experiment [16], the flow field starts from laminar at the upper stream and then undergoes transition to become fully turbulent. However, in this calculation, the flow was assumed as fully turbulent, which may be the main reason for the overprediction of the heat transfer coefficient near the leading edge of the suction surface.

(B) VKI Turbine Cascade. Another test case of the present algorithm is the flow around the VKI turbine cascade. A 77×21 **H**-mesh (M1 Model) was employed with the same surface definition as proposed by Sieverding [13]. For comparison with other computational results, the mesh points as well as the flow conditions were also selected to be the same as those proposed by Sieverding [13].

Figure 9 presents the convergence history of the computed average outflow angle compared with the experimental data and the computed result demonstrated by Denton [1]. After about 1000 steps of iterations, the present computation reaches a steady value that is almost the same as the experiments. However, convergent history of Denton's computation with the multigrid method did not seem to be stabilized at this time-step. The computed outflow angle with different isentropic exit Mach numbers is shown in Fig. 10. The results show that the present calculation agrees well

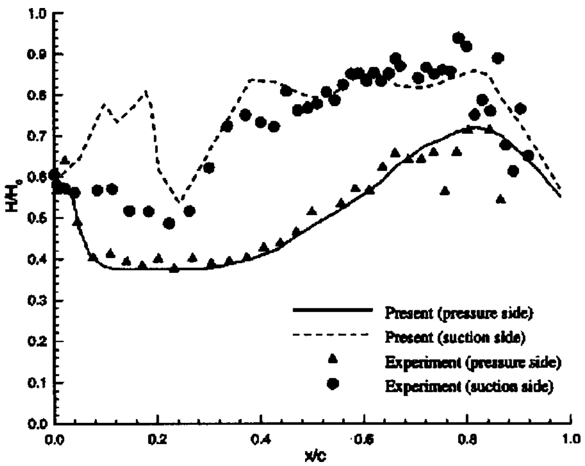

Fig. 8 Heat transfer coefficient distribution on blade surface

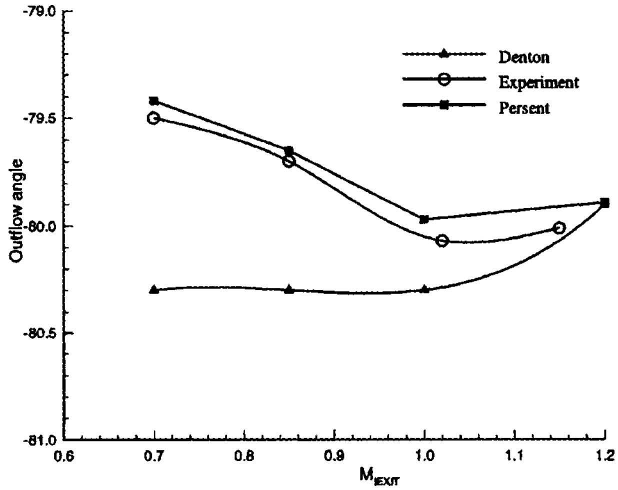

Fig. 10 Outflow angle with Mach number

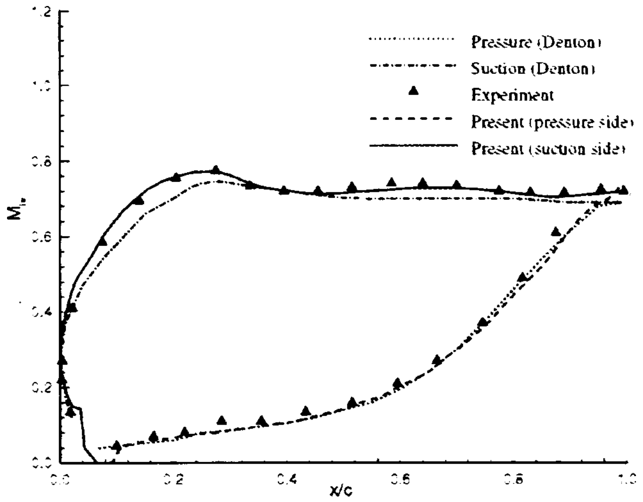

Fig. 11 Isentropic Mach number distributions on the blade surface

with the experiment. The present calculated exit angle when the exit isentropic Mach number is 1.2 was almost the same as that of Denton. Figure 11 shows the computed blade surface isentropic Mach number distributions by comparing with both experiment and computed results by Denton [13]. As shown in Fig. 11, the present results agree better with the experimental data in comparison with Denton's. The computed Mach number in the entire flow region is shown in Fig. 12. The results show that the calculations reflect the proper physics of the flow.

Conclusions

A new numerical scheme was proposed and demonstrated in this study. The study shows that the present method has several-advantages: a good convergence, overall accuracy for predicating the flow field and heat transfer around the turbine cascades.

The features of the present scheme are summarized as follows:

1 The present scheme successfully avoids the coefficient matrix operation and omits the iteration within the same time-step calculation. Therefore, less computation effort is needed for the calculation in comparison with an implicit scheme. Due to the large CFL number that can be used in the computation, the present scheme is also more economical than the usual explicit scheme.

2 The present scheme has a good convergent rate similar to the multigrid method of Denton.

3 The present scheme employs the upwind scheme in the flux-vector-splitting scheme. Therefore, the present scheme is stable

4 The matrix-valued dissipation terms were incorporated into the time-derivative term. This makes the scheme more accurate by avoiding eigenvalue stiffness for low Mach number flow. This also accelerates the convergence of the calculation. This characteristic enables the present scheme to be more advantageous over common implicit or explicit schemes.

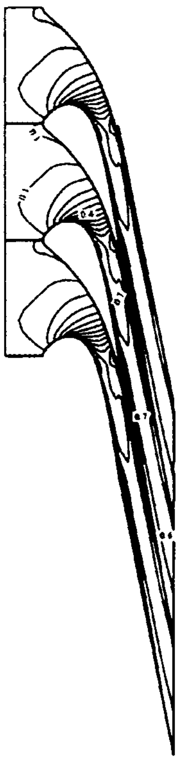

Fig. 12 Contour of computed Mach numbers

Appendix

Formation of the Implicit Scheme. The two-dimensional time-dependent Reynolds-averaged Navier–Stokes equations can be written as,

$$Q_t + E_x + F_y = R_x + S_y \qquad (A\text{-}1)$$

According to the vector splitting method, the eigenvalues of the flux vector can be expressed using positive and negative forms in order to split the flux vectors into two subvectors as shown in Eqs. (13) and (14), i.e.,

$$E = (A^+ + A^-)Q = E^+ + E^- \qquad (A\text{-}2)$$

$$F = (B^+ + B^-)Q = F^+ + F^- \qquad (A\text{-}3)$$

The subvectors E^+, E^-, F^+, and F^- can be expressed according to the positive and negative eigenvalues. The flux vector splitting form of Eq. (A-1) can be written as

$$Q_t + E_x^+ + E_x^- + F_y^+ + F_y^- = R_x + S_y \qquad (A\text{-}4)$$

In the practical computation, the artificial dissipation is usually required to avoid spurious oscillations and stabilize the scheme. The convenient manner to add dissipation term is to modify the convective fluxes as follows:

$$F_{i+1/2,j} = 0.5*(F_{i,j} + F_{i+1,j}) - d_{i+1/2,j} \qquad (A\text{-}5)$$

$$E_{i,j+1/2} = 0.5*(E_{i,j} + E_{i,j+1}) - d_{i+1/2,j} \qquad (A\text{-}6)$$

The terms $d_{i+1/2\,j}$, $d_{i+1/2\,j}$ represent the dissipative terms in i and j directions respectively. There are two forms of artificial dissipation models can be used. One is the scalar dissipation model and another is Matrix-valued dissipation model [5]. In the present research, the concept of the matrix-valued dissipation model was adapted and modified to form a new numerical scheme.

Following Eqs. (5)–(13), the spectral radius for the ξ direction is

$$\lambda_\xi = |\tilde{\mathbf{u}}| + aL(\xi) \qquad (A\text{-}7)$$

To form the present scheme and optimal the dissipation model in the sense that the same dissipation scaling is used for all the governing equations in a given coordinate direction, the matrix-valued dissipation term in ξ direction can be written as

$$D_E = \Lambda_E \cdot \frac{\partial Q}{\partial t} \Delta t \qquad (A\text{-}8)$$

Following the matrix-value dissipation concept, matrix Λ in ξ direction can be written as

$$\Lambda_F=\lambda_3\mathbf{I}+\left(\frac{\lambda_1+\lambda_2}{2}-\lambda_3\right)\left(\frac{\gamma-1}{a^2}E_1+\frac{E_2}{L(\xi)^2}\right)+\frac{\lambda_1-\lambda_2}{2aL(\xi)}$$
$$\times[E_3+(\gamma-1)E_4] \qquad (A\text{-}9)$$

where

$$E_1=[1,\ u,\ \nu,\ c_pT]^T[q^2/2,\ -u,\ -\nu,\ 1]$$
$$E_2=[0,\ \xi_x,\ \xi_y,\ \tilde{u}]^T[-\tilde{u},\ \xi_x,\ \xi_y,\ 0]$$
$$E_3=[1,\ u,\ \nu,\ c_pT]^T[-\tilde{u},\ \xi_x,\ \xi_y,\ 0]$$
$$E_4=[0,\ \xi_x,\ \xi_y,\ \tilde{u}]^T[q^2/2,\ -u,\ -\nu,\ 1] \qquad (A\text{-}10)$$

where q is the total velocity and defined as

$$q^2=u^2+v^2 \qquad (A\text{-}11)$$

and

$$\lambda_1=\tilde{\mathbf{u}}+aL(\xi)$$
$$\lambda_2=\tilde{\mathbf{u}}-aL(\xi)$$
$$\lambda_3=\tilde{\mathbf{u}} \qquad (A\text{-}12)$$

However, in the calculation, we can not choose the λ_1, λ_2, λ_3 according to Eqs. (A-12) because near the stagnation points λ_3 approach zero, whereas near sonic lines λ_1 or λ_2 approach zero. For solving this problem, we limit these values in the following manner:

$$\lambda_1=\max(\tilde{\mathbf{u}}+aL(\xi),\ \tilde{\mathbf{u}}/\mathrm{M}_\mathrm{r}^2)$$
$$\lambda_2=\max(\tilde{\mathbf{u}}-aL(\xi),\tilde{\mathbf{u}}/\mathrm{M}_\mathrm{r}^2)$$
$$\lambda_3=\max(\tilde{\mathbf{u}},\ \tilde{\mathbf{u}}/\mathrm{M}_\mathrm{r}^2) \qquad (A\text{-}13)$$

where

$$\mathrm{M}_\mathrm{r}=\begin{cases}0.001 & M\leqslant 0.001\\ M^2 & 0.001<M\leqslant 1\\ 1 & M>1\end{cases} \qquad (A\text{-}14)$$

where M is the calculated Mach number.

The matrix Λ_E can be represented into the form $\Lambda_E^{\pm}$ according to the positive or negative value of λ_1, λ_2, λ_3, i.e.,

$$\Lambda_E=(\Lambda_E^{+}-\Lambda_E^{-})/2 \qquad (A\text{-}15)$$

Similar expression can be derived for the $\mathrm{D_F}$ by replacing the contravariant velocity $\tilde{\mathbf{u}}$ by $\tilde{\boldsymbol{\nu}}$ and ξ by η in Eqs. (A-7) to (A-15).

By adding the matrix form of the dissipative terms in the governing Eqs. (A-4), we obtain:

$$\left[\Delta t\left(\frac{\partial\Lambda_A^{+}}{2\partial\xi}-\frac{\partial\Lambda_A^{-}}{2\partial\xi}+\frac{\partial\Lambda_B^{+}}{2\partial\eta}-\frac{\partial\Lambda_B^{-}}{2\partial\eta}\right)+I\right]Q_t+E_x^{+}+E_x^{-}+F_y^{+}+F_y^{-}$$
$$=R_x+S_y \qquad (A\text{-}16)$$

By using the second-order time-difference algorithm, we have

$$\frac{Q^{n+1}-Q^n}{\Delta t}=\frac{1}{2}\left[\left(\frac{\partial Q}{\partial t}\right)^{n+1}+\left(\frac{\partial Q}{\partial t}\right)^{n}\right] \qquad (A\text{-}17)$$

and

$$\Delta Q_{i,j}^{n+1}=-\Delta t\left[\frac{\nabla_\xi E^{+}}{\Delta\xi}+\frac{\Delta_\xi E^{-}}{\Delta\xi}+\frac{\nabla_\eta F^{+}}{\Delta\eta}+\frac{\nabla_\eta F^{+}}{\Delta\eta}\right]^n$$
$$+\Delta t\left(\frac{\Delta_c R}{\Delta\xi}+\frac{\Delta_c s}{\Delta\eta}\right) \qquad (A\text{-}18)$$

We let

$$\delta Q_{i,j}^{n+1}=Q_{i,j}^{n+1}-Q_{i,j}^{n} \qquad (A\text{-}19)$$

Substituting Eqs. (13) and (14) into Eq. (A-18), one can obtain

$$A_W\delta Q_{i-1,j}^{n+1}+A_S\delta Q_{i,j-1}^{n+1}+A_P\delta Q_{i,j}^{n+1}+A_N\delta Q_{i,j+1}^{n+1}$$
$$+A_E\delta Q_{i+1,j}^{n+1}=\Delta Q_{i,j}^{n+1} \qquad (A\text{-}20)$$

where

$$A_W=-\frac{\Delta t}{2\Delta\xi}(\Lambda_E^{+})_{i-1,\,j}^{n}-\frac{\Delta t}{2\Delta\xi}(A_{i-l,j}^{+})^n$$

$$A_S=-\frac{\Delta t}{2\Delta\eta}(\Lambda_F^{+})_{i,j-1}^{n}-\frac{\Delta t}{2\Delta\eta}(B_{i,j-1}^{+})^n$$

$$A_p=I+\frac{\Delta t}{2\Delta\xi}(\Lambda_E^{+})_{i,j}^{n}-\frac{\Delta t}{2\Delta\xi}(\Lambda_E^{-})_{i,j}^{n}+\frac{\Delta t}{2\Delta\eta}(\Lambda_F^{+})_{i,j}^{n}$$
$$-\frac{\Delta t}{2\Delta\eta}(\Lambda_F^{-})_{i,j}^{n}+\frac{\Delta t}{2\Delta\xi}(A_{i,j}^{+})^n-\frac{\Delta t}{2\Delta\xi}(A_{i,j}^{-})^n$$
$$+\frac{\Delta t}{2\Delta\eta}(B_{i,j}^{+})^n-\frac{\Delta t}{2\Delta\eta}(B_{i,j}^{+})^n$$

$$A_N=\frac{\Delta t}{2\Delta\eta}(\Lambda_F^{-})_{i,j+1}^{n}+\frac{\Delta t}{2\Delta\eta}(B_{i,j+1}^{-})^n$$

$$A_E=\frac{\Delta t}{2\Delta\xi}(\Lambda_E^{-})_{i+1,\,j}^{n}+\frac{\Delta t}{4\Delta\xi}(A_{i+1,\,j}^{-})^n$$

Acknowledgments

The computations were performed on SGI Power Challenge Array at NCSA, University of Illinois, Urbana-Champaign. The fund is provided by NSF under Grant NSF CTS970045N. The authors wish to thank Professor F. Liu for providing VKI blade information.

References

[1] Denton, J. D., 1983, ''An Improved Time Marching Method for Turbomachinery Flow Calculation,'' ASME J. Eng. Gas Turbines Power, **105**, pp. 514–521.

[2] Weinberg, B. C., Yang, R.-J., McDonald, H., and Shamroth, S. J., 1986, ''Calculations of Two and Three Dimensional Transonic Cascade Flow Fields Using the Navier–Stokes Equations,'' ASME J. Eng. Gas Turbines Power, **108**, pp. 93–102.

[3] Kwon, O. K., 1988, ''Navier–Stokes Solution for Steady Two-Dimensional Transonic Cascade Flows,'' ASME J. Turbomach., **110**, pp. 339–346.

[4] Liu, F., and Jameson, A., 1993, ''Cascade Flow Calculations by a Multigrid Euler Method,'' J. Propul. Power, **9**, pp. 90–97.

[5] Turkel, E., and Vatsa, V. N., 1994, ''Effect of Artificial Viscosity on Three-Dimensional Flow Solutions,'' AIAA J., **32**, pp. 39–45.

[6] Douglass, J., and Gunn, J. E., 1964, ''A General Formulation of Alternating Direction Method,'' Numer. Math., **6**, pp. 428–453.

[7] Briley, W. R., and McDonald, H., 1975, ''Solution of the Three-Dimensional Compressible Navier–Stokes Equations by an Implicit Technique,'' *Proc. 4th Int. Conf. on Numerical Methods in Fluid Dynamics*, **35**, pp. 105–110.

[8] Briley, W. R., and McDonald, H., 1977, ''Solution of the Multidimensional Compressible Navier–Stokes Equations by a Generalized Implicit Method,'' J. Comput. Phys., **24**, pp. 372–397.

[9] Beam, R. M., and Warming, R. F., 1976, ''An Implicit Finite Difference Algorithm for Hyperbolic Systems in Conservation-Law Form,'' J. Comput. Phys., **22**, pp. 87–110.

[10] Ames, W. F., 1977, *Numerical Method for Partial Differential Equations*, 2nd ed., Academic, New York.

[11] Lee, J., 1992, ''Simplification of Beam and Warming's Implicit Scheme for Two-Dimensional Compressible Flow,'' AIAA J., **30**, pp. 266–268.

[12] Chakravarthy, S. R., Anderson, D. A., and Salas, M. D., 1980, ''The Split Coefficient Matrix Method for Hyperbolic Systems of Gasdynamics Equations,'' AIAA Paper No. 80–0268.

[13] Sieverding, C., ed., 1982, ''Test Case 1: 2-D Transonic Turbine Nozzle Blade,'' Von Karman Inst. for Fluid Dynamics Lecture Series, 1982-05, Rhode-Saint-Genese, Belgium.

[14] Younis, M. E., and Camarero, R., 1981, ''Finite Volume Method for Blade to Blade Flow Using a Body Fitted Mesh,'' AIAA J., **19**, No. 11, pp. 1500–1502.

[15] Maruszewski, J. P., and Amano, R. S., 1992, ''Grid Generation and Its Application to Separated Flows,'' Numer. Heat Transfer, Part B, **21**, pp. 183–197.

[16] Hylton, L. D., Mihelc, M. S., Turner, E. R., Nealy, D. A., and York, R. E., 1983, ''Analytical and Experimental Evaluation of Heat Transfer Distribution Over the Surfaces of Turbine Vanes,'' NASA-CR-168015.

[17] Kiss, T., Schetz, J. A., and Moses, H. L., 1996, ''Experimental and Numerical Study of Transonic Turbine Cascade Flow,'' AIAA J., **34**, pp. 104–109.

[18] Baldwin, B. S., and Lomax, H., 1978, ''Thin Layer Approximation and Algebraic Model for Separated Turbulent Flows,'' AIAA Paper No. 78-257.

Effect of Two-Scale Roughness on Boundary Layer Transition Over a Heated Flat Plate: Part 1—Surface Heat Transfer

Mark W. Pinson[1]
Ting Wang[2]
Department of Mechanical Engineering,
Clemson University,
Clemson, SC 29634-0921

An experimental study was conducted to investigate surface heat transfer and boundary layer development associated with flow over a flat test surface covered with two roughness scales. Two-scale roughness was used because in-service aeroengines commonly display larger roughness concentrated at the leading edge with smaller roughness distributed downstream. The first scale, covering up to the first 5 cm of the test surface, was in the form of a sandpaper strip, an aluminum strip, or a cylinder. The second roughness scale covered the remainder of the test surface (2 m) in the form of sandpaper or a smooth surface. In Part 1, the surface heat transfer results are examined. Even though the roughness scales were hydraulically smooth, they induced significantly earlier transition onset, with the two-dimensional roughness causing earlier transition than three-dimensional roughness. All of the rough/smooth cases unexpectedly triggered earlier transition than rough/rough cases. This indicated that the scale of the step-change at the joint between two roughness scales was predominant over the downstream roughness on inducing early transition. Reducing the overall height of the step change was shown to have a greater effect on transition than the specific geometry of the roughness scale. [S0889-504X(00)00701-7]

Introduction

Recent experiments (e.g., [1,2]) conducted within turbines have demonstrated that significant portions of the boundary layer flow surrounding the vanes and blades can be transitional even with the presence of unsteady wake passage and high turbulence levels. Although prediction of boundary layer flows has steadily improved, Kleiser and Zang [3] and Halstead et al. [2] have shown that prediction of transitional flow situations needs improvement. One of the many factors that can influence the transition process is surface roughness.

Surface roughness alters both aerodynamic and thermal performance of turbine systems. These effects are a consideration for the design of new turbine systems as well as for the maintenance of in-service systems. In a new engine, thermal barrier coatings are applied to extend blade life, but the surface finish specification represents a trade-off between manufacturer guaranteed new engine performance and manufacturing cost. For in-service engines the generally corrosive and erosive turbine environment can cause significant variation in blade surface finish on used blades. The structure of the roughness can be a combination of pitting due to localized erosion and protrusions as a result of deposition. Surface measurements on 50 different turbine blades (both new and used) were made by Tarada [4], which indicated that a roughness range of 2 to 160 μm rms is typical. Taylor [5] documented the nonuniform roughness distribution along blade contours, and the leading edge was found to be the roughest area of the blade. Bammert and Sandstede [6] measured a 14 percent decrease in turbine efficiency with the addition of 580 μm roughness, and later measurements made by Bammert and Sandstede [7] with a roughened linear cascade indicated earlier boundary layer transition and increased drag associated with the addition of roughness. Boynton et al. [8] showed that an increase in surface roughness from 0.76 to 10.16 μm decreased overall turbine performance by 2.1 percentage points. With tests involving coated compressor blades, Suder et al. [9] found that decreasing the roughness of the finished coating from 3.1 to 0.6 μm increased overall compressor efficiency three percentage points. Blair [10] reported that a tenfold increase in surface roughness doubled the rate of heat transfer from a turbine blade geometry and that current correlations overpredicted suction side blade heat transfer and underpredicted heat transfer on the pressure side. Tarada and Suzuki [11] also reported heat transfer enhancement resulting from increased roughness. Bunker [12] showed that a tenfold increase in roughness can cause a 30 percent increase in surface heat transfer in the presence of free-stream turbulence levels of 12 percent. The increases in blade heat transfer due to surface roughness will degrade turbine performance and reliability through increased thermal fatigue on the blades and increased blade cooling requirements necessary to offset the heat transfer enhancement.

Many researchers have investigated the effects of surface roughness on turbulent boundary layer flows, but the effects of roughness on the transition region have primarily been limited to isolated roughness elements tripping the flow or single-scale distributed roughness.

Nikuradse [13] provided the first significant contribution to the study of roughness in turbulent flow. The roughness effect was classified according to three regimes: (1) aerodynamically smooth ($k^+ < 4$, where k is a roughness length scale), (2) transitionally rough ($4 < k^+ < 60$), and (3) fully rough ($k^+ > 60$). The first condition, as its name implies, represents the situation where the roughness is within the viscous sublayer, and no significant departure from smooth-wall behavior is observed. The second condition occurs when the roughness elements protrude from the viscous sublayer in such a way that the flow is affected. The fully rough regime is an extention of the effects observed in regime 2, but the effects are a function of the roughness geometry alone and are independent of the Reynolds number. Nikuradse's experiments were conducted using sand grains attached to the interior of round

---

[1] Current address: General Electric Company (Power Systems), Greenville, SC.

[2] Current address: University of New Orleans, New Orleans, LA 70148-2220.

Contributed by the International Gas Turbine Institute and presented at the 44th International Gas Turbine and Aeroengine Congress and Exhibition, Indianapolis, Indiana, June 7–10, 1999. Manuscript received by the International Gas Turbine Institute February 1999. Paper No. 99-GT-158. Review Chair: D. C. Wisler.

pipes. Schlichting [14] introduced the equivalent sand-grain roughness parameter, k_s, as a means of converting roughness data obtained from other roughness types and other flow configurations (e.g., turbulent boundary layer flow) into a roughness measure equivalent to the roughness magnitudes presented by Nikuradse. Coleman et al. [15] provided corrections compensating for assumptions made during Schlichting's data reduction and correlations have been developed by Simpson [16] and Sigal and Danberg [17] to extend the consideration of equivalent sandgrain roughness to many different types of rough surfaces.

A limited amount of data has been obtained regarding the behavior of the transition region under the influence of distributed roughness. Studying flow over an airfoil geometry, Doenhoff and Horton [18] demonstrated that distributed roughness from the stagnation point to a specified location downstream did hasten the transition process, but it was also evident that a very similar effect on the flow could be achieved when small (in the streamwise direction) strips of roughness were located in the laminar layer where the roughness height was on the same order as the boundary layer thickness. For relatively low free-stream velocity values, Pinson and Wang [19] demonstrated that maximum roughness height, not specific roughness geometry, was the primary indicator of the roughness effect. As the velocity was increased, the observed hastening of transition onset and subsequent heat transfer enhancement in the turbulent boundary layer was roughness dependent. Gibbings and Al-Shukri [20] reported limited intermittency data over a surface roughened with sandpaper, but no information regarding the structure of the transitional boundary layer was included. Ligrani and Moffat [21] studied thermal boundary layers on a rough surface downstream of steps. Bogard et al. [22] tried to characterize the turbine airfoil roughness and investigated the heat transfer on a surface with simulated turbine roughness. More detailed literature search can be found in Pinson's dissertation [23].

Due to the significance of surface roughness and boundary layer transition in the turbine blade environment, an experimental study was conducted to examine the flow and heat transfer situation where boundary layer transition occurs over a rough surface. The global objective of the current study was to obtain greater understanding of the effect that variations in protrusion-type surface roughness has on the boundary layer transition process in a controlled environment. To achieve this objective, the present study experimentally investigated flow over a flat, heated surface with two roughness scales placed on the instrumented test surface. The first roughness scale was placed at the leading edge and extended up to 5 cm downstream. The second roughness scale, placed immediately downstream of the first, covered the remainder of the test surface. The first roughness scale was larger than the second because Taylor's [5] measurements showed decreases in roughness level downstream of the leading edge on used turbine blades. Different types of roughness were used at the leading edge to test for geometric dependencies on downstream effects. The use of hot-wire and cold-wire sensors allowed for further classification of the roughness effect through the measurements of fluctuating velocity, Reynolds shear stress, Reynolds heat flux, and intermittency.

The effect of roughness on an actual blade is undoubtedly a function of many parameters that are significant to the environment (high turbulence intensity, strong acceleration, and film-cooling, to name a few). To understand fundamentally the roughness effect on the transition process, this study focused on the low-FSTI, flat-plate roughness condition with zero pressure-gradient flow. Although this study did not simulate the complexity of the gas turbine environment, the results presented can serve as a reference for future study of more complicated situations, and it has the potential for improving the understanding of the roughness effect on heat transfer and fluid mechanics within the transition region of a reference flow condition. Subsequent studies that may consider roughness with additional parameters may find the result of this study useful for gaging the relative contribution of multi-scale roughness to the flow situation.

Experimental Program

Four leading edge conditions were combined with two boundary conditions to form a total of eight surface conditions to be studied. The leading edge conditions were comprised of a 1 mm diameter cylinder, a 0.6 mm by 50 mm metal step, a 50 mm wide strip of 60-grit sandpaper, and a 50 mm wide strip of 40-grit sandpaper. The boundary condition for the rest of the test surface was either smooth or uniformly covered with 100-grit sandpaper. All of these roughness conditions protrude from the test surface into the boundary layer flow. The cylinder and step represent single, two-dimensional flow obstacles, while the sand grains of the sandpaper strips represent multiple three-dimensional obstructions distributed over the test surface area. Various leading edge and boundary conditions were combined and tested with several free-stream velocities. The dimensions and roughness measurements of the surface conditions are provided in Table 1. Each surface condition is identified using ''first roughness scale at leading-edge''/''second roughness scale downstream'' notation. For example, ''60/0'' represents a surface condition with the 50 mm strip of 60-grit sandpaper at the leading edge with smooth conditions downstream, and ''STEP/100'' represents the surface with the 1 mm by 50 mm metal piece attached to the leading edge with 100-grit sandpaper covering the rest of the surface (see Fig. 1). All of the rough-wall data are presented relative to smooth-wall data (referred to as ''baseline'') obtained at the same free-stream velocity.

Table 1 Experimental conditions

Surface Conditions	Roughness Level	
100-grit sandpaper	37 μm (R_a)	122 μm (R_z)
60-grit sandpaper	77 μm (R_a)	202 μm (R_z)
40-grit sandpaper	119 μm (R_a)	360 μm (R_z)
Cylinder	1 mm (diameter)	
Step (aluminum strip)	0.6 mm	

Note: k^+ was calculated and lies between the values 0.35 and 0.94 for all the distributed roughness cases (see part 2).

Average Freestream Conditions

U_∞ (m/s)	FSTI(%)	Integral Length (cm)	v'/u'(ave)
16.1	0.62	1.2	1.89
8.6	0.50	1.9	0.41
5.9	0.40	N/A	N/A
4.6	0.30	2.1	0.32

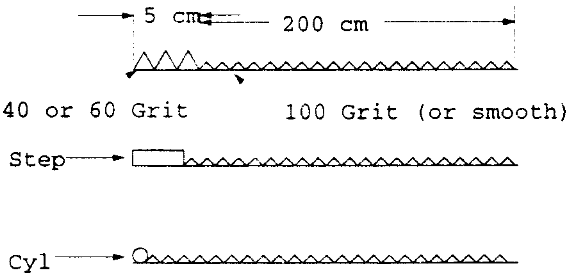

Fig. 1 Layout of roughness conditions

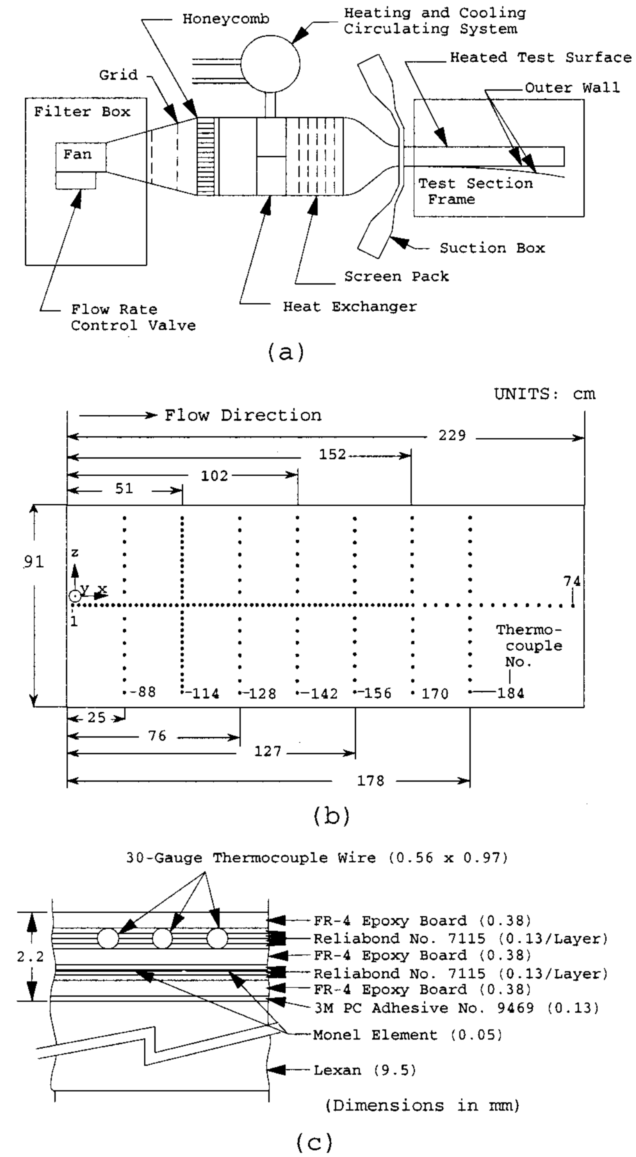

Fig. 2 Schematic diagram of experimental facility

The test facility shown in Fig. 2(*a*) is an open circuit, blowing-type wind tunnel. Air enters the system by passing through a filter designed to remove all particles larger than 5 μm. A honeycomb passage is used to straighten the flow, and a heat exchanger is used to control the steadiness of the free-stream temperature to within 0.04°C over a 20-hour period. Suction is employed upstream of the test surface to facilitate the formation of a boundary layer from zero thickness at an elliptic leading edge. The test section itself is a channel that measures 2.4 m in the streamwise (x) direction, 0.92 m in the spanwise (z) direction (parallel to the leading edge), and 0.15 m in the cross-stream (y) direction (perpendicular to the heated test surface). One side of the test section channel is a flexible acrylic sheet that can be adjusted to provide the pressure gradient desired within the flow area. The opposite side of the test section channel is the heated test surface. The heated test surface itself is a composite design comprised of several layers that are depicted in Fig. 2(*c*). At its lowest level, a layer of Lexan provides structural support, and the upper portions of the test surface contain the monel heating elements and a series of *E*-type thermocouples that are positioned along the length and height of the surface as shown in Fig. 2(*b*). A total of nine monel sheets (0.05 mm thick, 25 cm×91 cm pieces spaced 0.8 mm apart) were connected in series to form the active heating elements within the surface. Layers of epoxy resin board sandwich the heating elements and the thermocouples. The entire unit was cured at elevated temperatures during construction to allow the epoxy board to soften and mold itself around both the heater and the thermocouples. The typical range of heat flux convected into the free stream during experiment was between 88 to 210 W/m^2, and the wall surface temperature was typically 3 to 13°C above the free-stream value.

A custom-designed three-wire probe was used to acquire velocity and temperature data simultaneously within the developing boundary layer above the test surface. Two of the wires were made of platinum-coated tungsten. The 2.5 μm diameter wires were arranged orthogonal to each other and positioned to measure streamwise and cross-stream velocity components. The two velocity wires were operated with an overheat ratio of 1.5 to limit cross-talk among the sensors as suggested by Zhou and Wang [24]. The third sensor of the three-wire probe is a 1.2 μm platinum wire that was operated in constant current (operating current=0.1 mA) mode to permit temperature measurement with the sensing material maintained at a temperature approximately the same as that of the flow. The temperature sensor is placed 0.35 mm to one side of the x-array and is normal to the streamwise flow direction. Additional details on the probe design and qualification are documented by Shome [25]. For the present study, the velocity and temperature fluctuations were sampled simultaneously at 10 kHz for 30 s. An analog low-pass filter with a cutoff frequency of 5 kHz was applied upstream of the analog-to-digital conversion to prevent aliasing.

Uncertainty Analysis

A detailed uncertainty analysis (95 percent confidence level) of the data presented was performed by Pinson [23]. The Stanton number has an experimental uncertainty of 5.2 percent. The primary contributors were temperature measurement and a correction for radiation losses from the test surface.

Results and Discussion

Stanton number distributions, which were based on centerline thermocouple measurements for the smooth-wall case at three different free-stream velocities, are shown in Figs. 3(*a*), 3(*b*), and 3(*c*). The data are observed to follow correlations for laminar and turbulent flow reasonably well. The correlations for a uniformly heated smooth surface from Kays and Crawford [26] including a correction for the unheated starting length of the test surface, are

$$\mathrm{St}_{\mathrm{lam}}=0.453\,\mathrm{Pr}^{-0.67}\,\mathrm{Re}_x^{-0.5}\left[1-\left(\frac{x_{\mathrm{UHSL}}}{x}\right)^{0.75}\right]^{-0.333} \tag{1}$$

and

$$\mathrm{St}_{\mathrm{turb}}=0.028\,\mathrm{Pr}^{-0.4}\,\mathrm{Re}_x^{-0.2}\left[1-\left(\frac{x_{\mathrm{UHSL}}}{x}\right)^{0.9}\right]^{-0.111}, \tag{2}$$

respectively. The Stanton number distribution of the 4.6 m/s baseline case in Fig. 3(*a*) suggests that the flow was laminar for almost the entire length of the test surface. A larger increase in heat transfer for the 8.6 m/s baseline case shown in Fig. 3(*b*) that begins approximately 30 cm ($\mathrm{Re}_x=1\times10^6$) from the test section exit suggests the onset of boundary layer transition. The laminar portions of the distributions are within an average of 5 percent of the correlation. The 4.6 m/s baseline case has the largest deviation at an average of 6.5 percent below; while the 16.1 m/s baseline case ranges from 2.7 percent below to 3.6 percent above the correlation. Overall, the agreement is considered acceptable in light of the 5.2 percent uncertainty estimated for the smooth-wall heat transfer data reduction. A few moderate ripples in the Stanton number distribution are attributed to residual effects of the heat flux nonuniformity discovered during qualification of the test surface. A series of smooth-wall tests were run at different flow

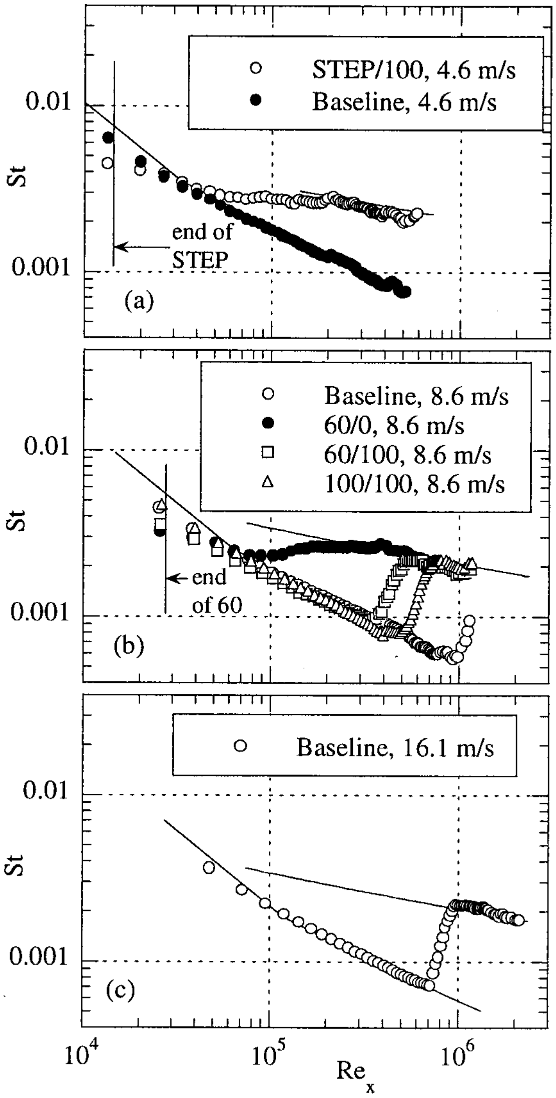

Fig. 3 Comparison of heat transfer data obtained for different roughness conditions at free-stream velocities of 4.6, 8.6, and 16.1 m/s

velocities and heater power input levels to develop a correlation to correct the flux nonuniformity. All of the heat transfer data presented have been corrected using this correlation. Generally, the wall heat flux is less uniform at low free-stream velocity. The small variations in Stanton number observed at low speed (i.e., 4.6 m/s) coincide with the edges of the heating elements within the test surface. The edge effect of each heating element was reduced as air speed increased. Details on the development of this correction are documented in Pinson [23].

The heat transfer results of four rough surface conditions are shown in Figs. 3(*a*) and 3(*b*). At 8.6 m/s, roughening the surface with a uniform layer of 100-grit sandpaper (100/100) with an R_a roughness level of 37 μm caused the onset of transition (observed by a minimum Stanton number) to occur at a Re_x of 4.94×10^5, which is 50 percent earlier than the transition onset of the corresponding smooth-wall case. When the leading-edge roughness was increased by replacing the first 5 cm of 100-grit sandpaper with 60-grit sandpaper ($R_a = 77\,\mu$m) (the 60/100 case) an earlier transition onset was induced at a Re_x of 3.5×10^5. This was expected since the addition of a rougher leading edge would induce earlier transition as a result of the additional source of instability triggered by the 60 grit. *However, an examination of the 60/0 case, obtained by removing the downstream 100-grit sandpaper unexpectedly showed that transition occurred much earlier at a* Re_x *of* 7.67×10^4 *than either the 60/100 or the 100/100 cases.* It was originally thought that the 60/100 case would have the earliest transition because both the leading edge 60-grit and the downstream 100 grit were thought to contribute to the triggering of earlier onset and completion of transition.

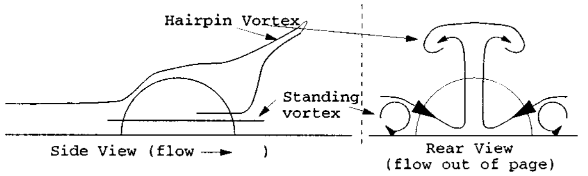

(a) - Acarlar and Smith (1987)

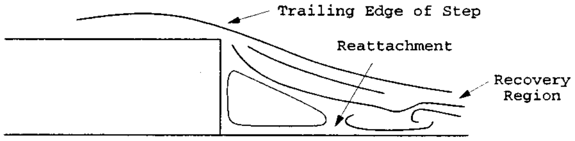

(b)

Fig. 4 Conceptual flow past a hemisphere and a backward-facing step

Based on the flow visualization work performed by Acarlar and Smith [27] downstream of isolated roughness elements, it was speculated that the step change at the joint between the 100-grit and 60-grit sandpaper could be the source of increased instability in the flow. Conceptual drawings of flow past a backward-facing step and a hemispherical disturbance are shown in Fig. 4(*a*). As the flow moves around the hemisphere, Acarlar and Smith [27] documented that a standing vortex forms near its base, and the two halves come together behind the hemisphere to initiate the formation of a hairpin-type vortex. The addition of roughness around the base of the object would at least reduce the size of these interactions because there would be less room for them to form. If the small roughness around the base is significantly three dimensional, it is also possible that the vortex formations associated with flow past the smaller roughness may alter or even prevent the formation of some of the flow structure associated with the larger hemisphere.

In a related situation, a sketch of the flow downstream of a two-dimensional, backward-facing step as visualized by Ruderich and Fernholz [28], is shown in Fig. 4(*b*). A review by Eaton and Johnston [29] suggests that the major features of the flow past the step are a separation bubble and a recovery region. The separation bubble forms immediately downstream of the trailing edge of the step, and the separation shear layer reattaches downstream of the bubble. The exact streamwise location of reattachment is unsteady, and turbulent structures may be shed downstream. Following reattachment, the boundary layer undergoes a recovery from the effects of the upstream step, and eventually regains the characteristics of an unseparated boundary layer condition. It would seem that the addition of small roughness behind a backward-facing step could alter the behavior of the separation bubble and the reattachment point of the shear layer even if only as a result of the reduction in step scale. As a result, disturbances that may propagate downstream of the shear layer may be smaller in magnitude causing less disturbance to the surrounding boundary-layer flow. Applying this concept to the data of the present study suggests that the 60/0 situation represents a larger flow disturbance than the 60/100 situation. Apparently, placement of 100-grit downstream of the 60-grit sandpaper strip reduces the step height, which, in turn, reduces the disturbance that will trigger an earlier transition. In addition to the size and geometry of the sand-grain roughness, the height of the step-change between the larger and

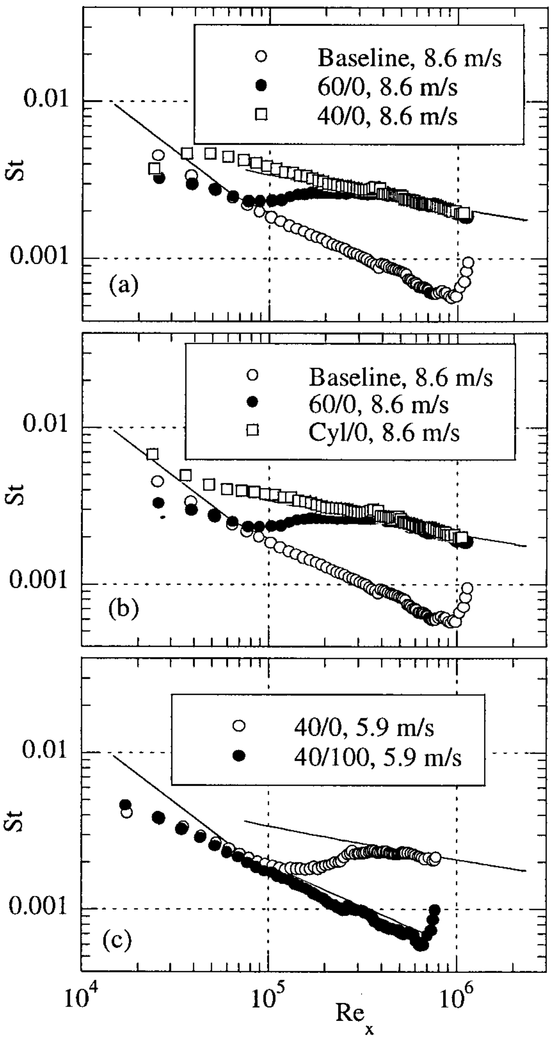

Fig. 5 Comparison of heat transfer data obtained for different roughness conditions at free-stream velocities of 8.6 and 5.9 m/s

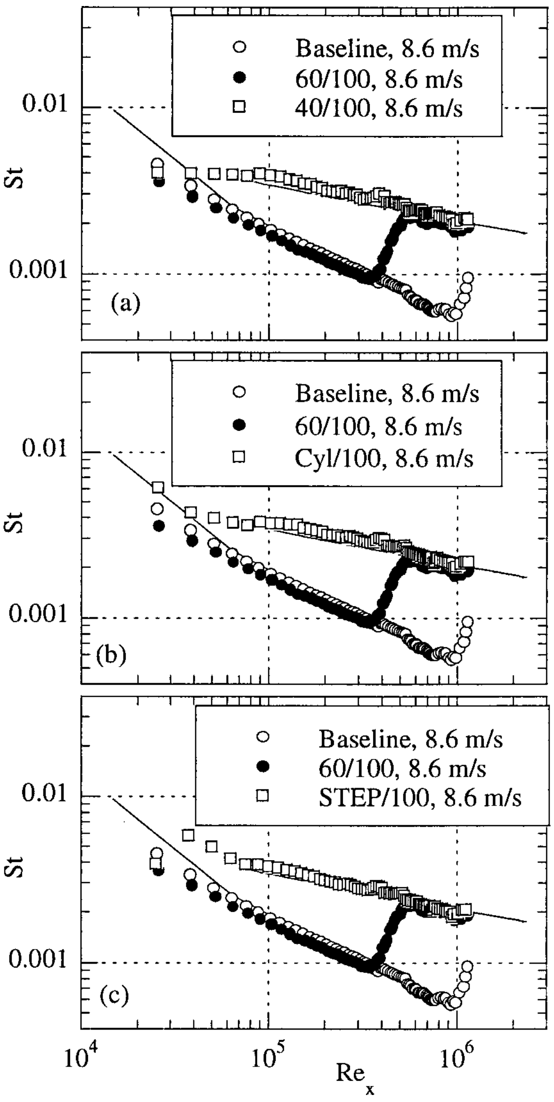

Fig. 6 Comparison of heat transfer data obtained for different roughness conditions at a free-stream velocity of 8.6 m/s

smaller grain-sizes seems to play an important role as the primary scale that triggers additional instability in the present studies.

To verify this behavior, three other surface conditions were used to examine the importance of the step effect discussed above: a rougher grit of sandpaper (40 grit, $R_a = 119\ \mu$m), a 1 mm diameter cylinder, and a smooth aluminum strip (height: 0.6 mm, streamwise width: 50 mm) were used as leading-edge conditions. If the step height is a dominant factor in triggering primary instabilities, then the roughness shape would not be critical and would have a secondary effect. Therefore, a long circular cylinder and a smooth aluminum strip were selected as test conditions. Both the thickness of the aluminum strip (STEP) and the diameter of the cylinder (CYL) were selected to isolate the effect of the sandpaper's backward-facing step from the influences of its roughness. Comparison between a two-dimensional step with a three-dimensional step of similar step height, such as the STEP/100 case in Fig. 7(*c*) and the 40/0 case in Fig. 7(*d*), indicates that *the two-dimensional disturbance of the metal step triggered earlier transition than the three-dimensional sand grains of the sandpaper*. This observation was consistent with the findings of Braslow [30]. He compared the results of several roughness experiments showing that two-dimensional disturbances are more effective in destabilizing a laminar layer than three-dimensional disturbances (also see Figs. 5(*b*), 6(*b*), and 6(*c*)). Generally, it was observed that increasing leading-edge roughness caused earlier transition. For example, the 40-grit and cylinder leading-edge conditions tripped the flow to turbulence almost immediately after the leading-edge roughness as is shown in Figs. 5(*a*), 5(*b*), 6(*a*), 6(*b*), and 6(*c*).

A comparison of the 40/0 and 40/100 cases at 8.6 m/s shown in Figs. 5(*a*) and 6(*a*) suggests that the addition of 100-grit sandpaper downstream of the 40-grit strip lengthens the recovery region downstream of the step in roughness level. The 40/0 case appears to have achieved a fully turbulent condition at $Re_x = 5\times10^4$, but the addition of the 100 grit increases the Re_{tr} (or delays onset of transition) to a value of 9×10^4. This may imply that the decrease in step-height resulting from the addition of 100-grit sandpaper was more effective in reducing the disturbance to the flow than the increase in downstream roughness. On the other hand, a comparison of the Cyl/0 and Cyl/100 cases at 8.6 m/s (Fig. 5(*b*)) and 6(*b*) does not show any significant difference, which suggests that the two-dimensional cylindrical leading-edge geometry is dominant for triggering early transition. The diameter of the cylinder (1 mm) is larger than the thickness (0.6 mm) of the step; therefore, the addition of downstream roughness is not effective in delaying transition onset.

Although the 40-grit, cylinder, and step cases appear somewhat similar at 8.6 m/s (in Figs. 5(*a*), 5(*b*), and 6), a reduction of the

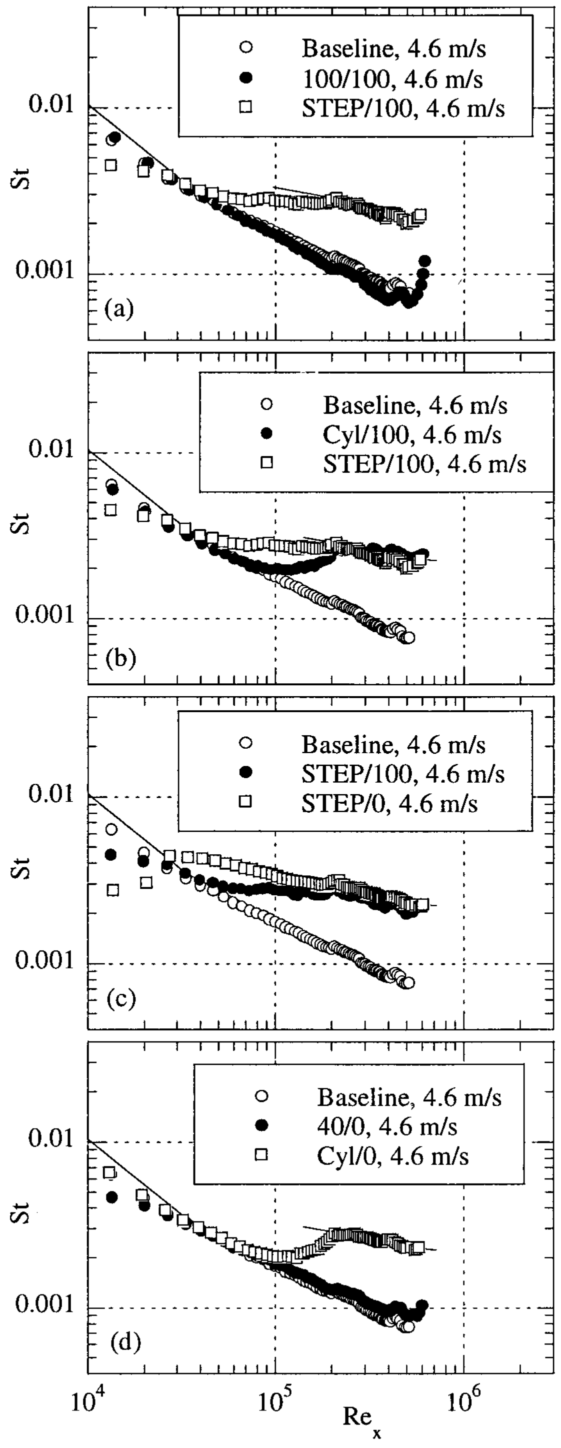

Fig. 7 Comparison of heat transfer data obtained for different roughness conditions at a free-stream velocity of 4.6 m/s

free-stream velocity to 5.9 and 4.6 m/s permitted identification of the different effects caused by each condition. A comparison of the 40/0 case with a corresponding 40/100 case at 5.9 m/s as shown in Fig. 5(*c*) suggests behavior similar to that observed with the comparison of the 60/0 and 60/100 cases at 8.6 m/s. The addition of the 100-grit sandpaper condition downstream of the 40-grit leading-edge condition delays the occurrence of the minimum Stanton number (transition onset) from a Re_x of 1.25×10^5 to 7×10^5. Similarly, a comparison of the STEP/0 case with the STEP/100 case at 4.6 m/s as shown in Fig. 7(*c*) also indicates a similar delay in the onset of turbulence as a result of adding the 100-grit sandpaper downstream. The comparative influence of the 40 grit, cylinder, and step can be observed in Figs. 7(*a*), 7(*b*), and 7(*d*). Apparently, neither the 40 grit (40/0; Fig. 7(*d*)) nor 100 grit (100/100; Fig. 7(*a*)) had much effect on the flow at 4.6 m/s when put in place by themselves. The step appears to present a stronger disturbance to the flow than the cylinder because Fig. 7(*b*) shows that the transition onset was delayed from an Re_x of 7.27×10^4 to 1.1×10^5 by replacing the step with the cylinder at the leading edge even though the cylinder (1 mm in diameter) is higher than the step (0.6 mm). This behavior may be a result of differences in the vortex shedding behind a cylinder versus that behind a backward-facing step. A comparison of the corresponding 4.6 m/s case for the Cyl/0 and Cyl/100 cases (Figs. 7(*b*) and 7(*c*)) does not show any appreciable difference in location of transition onset which, similar to the 8.6 m/s case discussed earlier, suggests that the cylinder leading edge condition is also predominant over the downstream roughness at 4.6 m/s. This hypothesis of vortex shedding caused by the step change at the joint between lead-edge and downstream roughness has been verified by the spectral analysis to be discussed in Part 2.

Conclusions

The heat transfer distributions obtained from the different roughness conditions discussed above suggest several effects caused by two different roughness scales and geometries present on the test surface.

1 The presence of roughness, even though hydraulically smooth, triggers earlier onset of transition.

2 Generally, the two-dimensional leading edge disturbances (cylinder and aluminum strip) were shown to be more effective at hastening the transition onset than the three-dimensional sandpaper roughness.

3 The scale of the step-change between roughness levels of sandpaper was shown to have a significant effect on the location of transition onset. When the leading-edge roughness scale was large in comparison to the downstream condition as in the cylinder/100 case, the downstream roughness was observed to have little effect on the flow. However, when the two roughness levels were closer together, as in the 60/100 and 40/100 cases depending on free-stream velocity, the addition of 100-grit roughness downstream was observed to delay the location of transition onset. This effect apparently resulted from the reduced step height and the downstream roughness acting to limit the formation and amplification of flow disturbances immediately downstream of the larger roughness condition.

4 At lower speeds, a rectangular strip is more effective in triggering the onset of transition than a cylinder. At higher speeds there is little difference between them. At the higher velocity, both conditions may generate similar separation and reattachment situations, which produce similar results in surface heat transfer downstream. When the velocity is reduced, the effect of vortex shedding characteristics of each step geometry on transition becomes more apparent.

Acknowledgment

The experimental study received partial funding through the EPSCOR program of the U.S. Department of Defense (Grant No. F49620-92-J-0459).

Nomenclature

C_f = skin-friction coeffcient
$C_{p,\infty}$ = free-stream specific heat
CWT = continuous wavelet transform
$E(k)$ = power spectral density
FSTI = free-stream turbulence intensity

k = roughness height or roughness scale or wave number depending on context
k^+ = kU_τ/ρ = nondimensional roughness
k_s = equivalent sand grain roughness height
L = length of surface profile
Pr = Prandtl number
PSD = power spectral density function
q''_{conv} = convective heat flux to free stream
R_a = $1/L\int_{x=0}^{x=L}|y(x)|dx$ = average roughness level; $y(x)$ is measured from the midpoint between the average peak and valley heights
R_z = average peak-valley roughness level
Re = xU_∞/ν = Reynolds number
$\mathrm{Re}_{\theta t}$ = Reynolds number based on momentum thickness at x_t
$\mathrm{Re}_{\theta T}$ = Reynolds number based on momentum thickness at x_T
St = Stanton number = $q''_{\mathrm{conv}}/\rho_\infty C_{p,\infty}U_\infty(T_W-T_\infty)$
t' = rms temperature fluctuation
t_{St} = onset of transition based on Stanton number
T_{St} = end of transition (or onset of turbulence) based on Stanton number
T_W = wall surface temperature
T_∞ = free-stream temperature
u' = rms streamwise velocity fluctuation
$u'_{\max}$ = maximum value of u' measured in the boundary layer at a streamwise location
$\overline{uv}$ = Reynolds shear stress
$\overline{ut}$ = Reynolds streamwise heat flux
U^+ = U/U_τ
U_τ = $\sqrt{\tau_w/\rho}$
U_∞ = mean free-stream velocity
v' = rms cross-stream velocity fluctuation
$X1-12$ = streamwise measurement location number
x_{UHSL} = unheated starting length of test surface (2.5 cm)
$x_{25\Gamma}$ = streamwise location where $\Gamma=0.25$
$x_{75\Gamma}$ = streamwise location where $\Gamma=0.75$
x_t = streamwise location of transition onset
x_T = streamwise location of onset of turbulent flow
Y^+ = yU_τ/ν
Γ = intermittency
δ = boundary layer thickness ($0.99U_\infty$)
θ = momentum thickness
ν = kinematic viscosity
ξ = $(x-x_t)/(x_{25\Gamma}-x_{75\Gamma})$
ζ = $(x-x_t)/(x_T-x_t)$
ρ_∞ = free-stream air density
τ_w = wall shear stress

References

[1] Hodson, H. P., Huntsman, I., and Steele, A. B., 1994, ''An Investigation of Boundary Layer Development in a Multistage LP Turbine,'' ASME J. Turbomach., **116**, pp. 375–383.
[2] Halstead, D. E., Wisler, D. C., Okiishi, T. H., Walker, G. J., Hodson, H. P., and Shin, H.-W., 1997, ''Boundary Layer Development in Axial Compressors and Turbines: Part 1 of 4—Composite Picture,'' ASME J. Turbomach., **119**, pp. 114–127.
[3] Kleiser, L., and Zang, T. A., 1991, ''Numerical Simulation of Transition in Wall-Bounded Shear Flows,'' Annu. Rev. Fluid Mech., **23**, pp. 495–537.
[4] Tarada, F. H. A., 1987, ''Heat Transfer to Rough Turbine Blading,'' Ph.D. dissertation, University of Sussex, England.
[5] Taylor, R. P., 1990, ''Surface Roughness Measurements on Gas Turbine Blade.'' ASME J. Turbomach., **112**, pp. 175–180.
[6] Bammert, K., and Sandstede, H., 1972, ''Measurements Concerning the Influence of Surface Roughness and Profile Changes on the Performance of Gas Turbines,'' ASME J. Eng. Power, **94**, pp. 207–213.
[7] Bammert, K., and Sandstede, H., 1980, ''Measurements of the Boundary Layer Development along a Turbine Blade With Rough Surfaces,'' ASME J. Eng. Power, **102**, pp. 978–983.
[8] Boynton, J. L., Tabibzadeh, R., and Hudson, S., 1993, ''Investigation of Rotor Blade Roughness Effects on Turbine Performance,'' ASME J. Turbomach., **115**, pp. 614–620.
[9] Suder, K. L., Chima, R. V., Strazisar, A., and Roberts, W., 1995, ''The Effect of Adding Roughness and Thickness to a Transonic Axial Compressor Rotor,'' ASME J. Turbomach., **117**, pp. 491–505.
[10] Blair, M. F., 1994, ''An Experimental Study of Heat Transfer in a Large-Scale Turbine Rotor Passsage,'' ASME J. Turbomach., **116**, pp. 1–13.
[11] Tarada, F., and Suzuki, M., 1993, ''External Heat Transfer Enhancement to Turbine Blading Due to Surface Roughness,'' ASME Paper No. 93-GT-74.
[12] Bunker, R. S., 1997, ''Separate and Combined Effects of Surface Roughness and Turbulence Intensity on Vane Heat Transfer,'' ASME Paper No. 97-GT-135.
[13] Nikuradse, J., 1933, ''Stomungsgesetz in Rahen Rohren,'' Forschg. Arb. Ing.-Wes., **361** (English Trans. NACA Tech. Memo 1292).
[14] Schlichting, H., 1936, ''Experimentelle Untersuchungen zum Rauhigkeitsproblem,'' Ingenieur-Archiv, **7**, pp. 1–34 (English Trans. NACA Tech. Memo 823).
[15] Coleman, H. W., Hodge, B. K., and Taylor, R., 1984, ''A Re-Evaluation of Schlichting's Surface Roughness Experiment,'' ASME J. Fluids Eng., **106**, pp. 60–65.
[16] Simpson, R. L., 1973, ''A Generalized Correlation of Roughness Density Effects on the Turbulent Boundary Layer,'' AIAA J., **11**, pp. 242–244.
[17] Sigal, A., and Danberg, J. E., 1990, ''New Correlation of Roughness Density Effect on the Turbulent Boundary Layer,'' AIAA J., **28**, pp. 554–556.
[18] Doenhoff, A. E. V., and Horton E. A., 1958, ''A Low-Speed Experimental Investigation of the Effect of a Sandpaper Type of Roughness on Boundary-Layer Transition,'' NACA Report 1349.
[19] Pinson, M. W., and Wang, T., 1997, ''Effects of Leading-Edge Roughness on Fluid Flow and Heat Transfer in the Transitional Boundary Layer Over a Flat Plate,'' Int. J. Heat Mass Transf., **40**, pp. 2813–2823.
[20] Gibbings, J. C., and Al-Shukri, S. M., 1997, ''Effect of Sandpaper Roughness and Stream Turbulence on the Laminar Layer and Its Transition,'' Aeronaut. J., **101**, pp. 17–24.
[21] Ligrani, P. M., and Moffat, R. J., 1985, ''Thermal Boundary Layers on a Rough Surface Downstream of Steps in Wall Temperature,'' Boundary-Layer Meteorol., **31**, pp. 127–147.
[22] Bogard, D. G., Schmidt, D. L., and Tabbita, M., 1998, ''Characterization and Laboratory Simulation of Turbine Airfoil Surface Roughness and Associated Heat Transfer,'' ASME J. Turbomach., **120**, pp. 337–342.
[23] Pinson, M., 1998, ''Effect of Two-Scale Roughness on Boundary Layer Transition Over a Heated Flat Plate,'' Ph.D. Dissertation, Department of Mechanical Engineering, Clemson University, Clemson, SC.
[24] Zhou, D., and Wang, T., 1996, ''Combined Effects of Elevated Free-Stream Turbulence and Streamwise Acceleration on Flow and Thermal Structures in Transitional Boundary Layers,'' Exp. Therm. Fluid Sci., **12**, pp. 338–351.
[25] Shome, B., 1991, ''Development of a Three-Wire Probe for the Measurement of Reynolds Stresses and Heat Fluxes in Transitional Boundary Layers,'' M.S. Thesis, Department of Mechanical Engineering, Clemson University, Clemson, SC.
[26] Kays, W. M., and Crawford, M. E., 1993, *Convective Heat and Mass Transfer*, 3rd ed. McGraw-Hill, pp. 175, 179, 181.
[27] Acarlar, M. S., and Smith, C. R., 1987, ''A Study of Hairpin Vortices in a Laminar Boundary Layer. Part 1, Hairpin Vortices Generated by a Hemisphere Protuberance,'' J. Fluid Mech., **175**, pp. 1–41.
[28] Ruderich, R., and Fernholz, H. H., 1986, ''An Experimental Investigation of a Turbulent Shear Flow With Separation, Reverse Flow, and Reattachment,'' J. Fluid Mech., **163**, pp. 283–322.
[29] Eaton, J. K., and Johnston, J. P., 1981, ''A Review of Research on Subsonic Turbulent Flow Reattachment,'' AIAA J., **19**, pp. 1093–1100.
[30] Braslow, A. L., 1960, ''Review of the Effect of Distributed Surface Roughness on Boundary-Layer Transition,'' Advisory Group for Aeronautical Research and Development, Report 254.

Effect of Two-Scale Roughness on Boundary Layer Transition Over a Heated Flat Plate: Part 2—Boundary Layer Structure

Mark W. Pinson[1]
Ting Wang[2]
Department of Mechanical Engineering,
Clemson University,
Clemson, SC 29634-0921

Velocity and temperature measurements made within transitional boundary layers over a surface roughened by two roughness scales were examined. The variation of intermittency through the transition region was shown to be consistent with a smooth-wall model of transition, but the prediction of transition onset was not well represented by momentum thickness for cases with strong surface disturbances. During transition, distributed roughness was shown to reduce the growth of velocity fluctuation, possibly through stronger dissipation, and to enhance wallward transport of momentum significantly without a corresponding increase in thermal transport. The step change between the two roughness scales was shown to notably affect boundary layer behavior. Spectral analysis supported the hypothesis in Part 1 that the separated region downstream of the step shed vortices into the downstream flow. The wavelet analysis suggested that transition over rough surfaces may be in bypass mode because the disturbances were shown to be amplified in a broad spectral band. [S0889-504X(00)00302-0]

Introduction

Part 1 documented the variations in surface heat transfer resulting from two roughness scales placed on the flat test surface. The results of the heat transfer experiments indicated that the step change between the two roughness scales could be a significant factor in the downstream onset of boundary layer transition. It was further shown that two-dimensional and three-dimensional roughness scales had different effects on the location of transition onset. A conceptual flow situation was introduced to explain the effect of the step-change on the downstream flow. Essentially, the step change seems to dominate the downstream flow development because the overall step height appears to permit or restrict the formation of shedding vortices downstream of the step. Part 2 provides detailed analysis of five selected boundary layer data sets. These five cases were chosen to be representative of the flow behaviors observed in Part 1. The cases discussed include: baseline (smooth wall flow at a free-stream velocity of 16.1 m/s), 60/0 (60-grit sandpaper at leading edge, free-stream velocity of 8.6 m/s), 60/100 (60-grit sandpaper at leading edge and 100 grit sandpaper covering the rest of the test surface, free-stream velocity 8.6 m/s), 100/100 (100-grit sandpaper covering entire test surface, free-stream velocity of 8.6 m/s), and STEP/100 (metal strip at leading edge and 100-grit sandpaper covering rest of the test surface, free-stream velocity of 4.6 m/s). The boundary layer data were analyzed, and the mean and rms measurements are presented and discussed. In light of the transitional nature of the boundary layer flows being investigated, the results of an intermittency and spectral analysis are included. All the rough surface results are presented relative to the smooth-wall data to highlight the effects of the different roughness scales present on the test surface.

Results and Discussion

Intermittency Distributions. The intermittency values were obtained following the methodology suggested by Keller and Wang [1]. The square of the first derivative of instantaneous shear stress, $(d(uv)/dt)^2$, was used as the criterion function. The threshold values for separating turbulent from laminar flow were determined by using the cumulative probability function method originally proposed by Corrsin and Kistler [2] and later extended by Kuan and Wang [3], implemented a ''two-slope'' methodology that can more systematically and unambiguously determine threshold values. Distributions of the intermittency evaluated at $y/\delta\sim 0.1$ are shown in Fig. 1(*a*). In each case, the data have been plotted with a best-fit curve to the intermittency model proposed by Narasimha [4]. The intermittency distribution of the baseline case does not appear to fit the model well for low values of intermittency, but in the range of the worst disagreement, $0.023<\Gamma<0.071$, the magnitude of the intermittency is on the same order as the uncertainty level (± 0.038). The presence of roughness does not seem to affect the applicability of Narasimha's model.

Since the agreement between the rough surface cases and Narasimha's smooth-wall model was fair, transition onset and length data were compared with smooth-wall correlations suggested by Mayle [5]. Good agreement for transition length was observed between the present study and the smooth-wall correlation as shown in Fig. 1(*c*). For the baseline, 60/100, and 100/100 cases, the momentum thickness at transition onset, θ_t, appears to be a useful indicator of boundary layer development as demonstrated in Fig. 1(*b*), but momentum thickness is not as useful when transition begins just a short distance from a relatively large disturbance such as that used in the 60/0 and STEP/100 cases. The lack of correlation with boundary layer momentum thickness may be a result of the step-induced separated shear layer and shedding vortices (see model introduced in Part 1), which triggers the onset of transition rather than via viscous, linearly amplified instabilities through the growing boundary layer. Therefore, the momentum thickness, which is indicative of the viscous effect of the boundary layer, did not correlate the data well. The interaction between laminar–turbulent transition and the separated flow was discussed in detail by Hatman and Wang [6,7].

---

[1] Current address: General Electric Company (Power Systems), Greenville, SC.

[2] Current address: University of New Orleans, New Orleans, LA 70148-2220.

Contributed by the International Gas Turbine Institute and presented at the 44th International Gas Turbine and Aeroengine Congress and Exhibition, Indianapolis, Indiana, June 7–10, 1999. Manuscript received by the International Gas Turbine Institute February 1999. Paper No. 99-GT-159. Review Chair: D. C. Wisler.

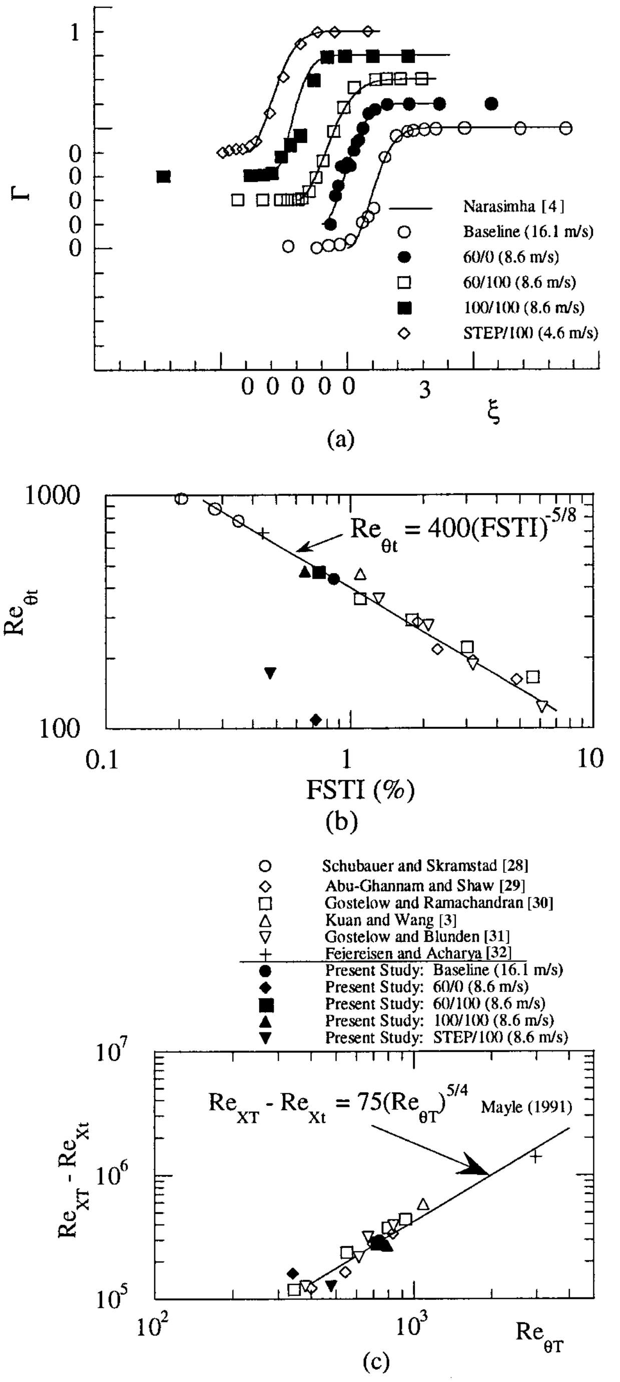

Fig. 1 Comparisons with intermittency models: (*a*) with Narasimha intermittency distributions; (*b*) and (*c*) with Mayle's smooth-wall correlations. Data from Refs. [28–32].

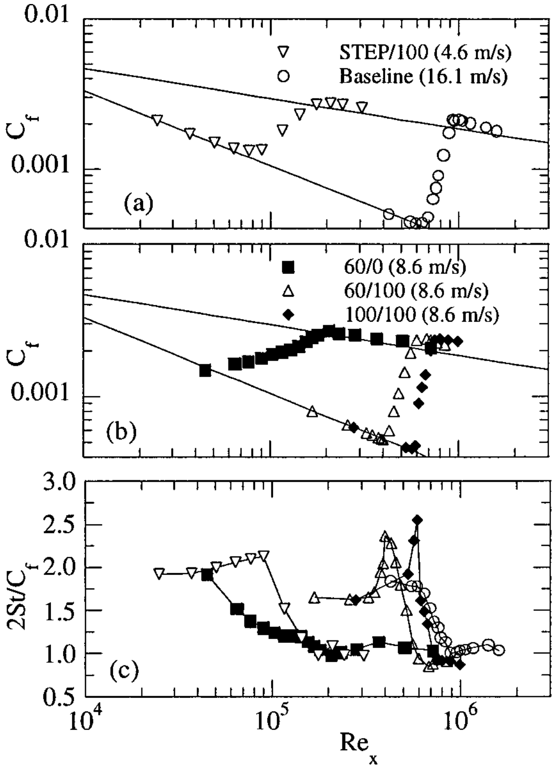

Fig. 2 Skin-friction distributions and Reynolds analogy factor

Wall Shear. The skin-friction data were obtained using the same method employed by Wang et al. [8]. The mean velocity profiles in the laminar and transitional flow regions were fit to the viscous linear region of the near-wall flow behavior ($U^+=Y^+$). Although no mean velocity correlation is available for the transitional flow regime, it is assumed that the viscous sublayer ($Y^+ < 10$) is unaffected by the transition process. The turbulent flow profiles clearly exibit the expected ''law-of-the-wall'' flow behavior, and the method suggested by Clauser [9] was used to evaluate C_f for the turbulent data.

The distributed roughness cases do not exhibit much wall shear increase over the smooth-wall situation as is shown in Fig. 2. The roughness scale parameter, k^+, was calculated to range from 0.35 to 0.94 for all the distributed roughness cases. These values are well within the aerodynamically smooth ($k^+ < 4$) range for turbulent boundary layers, so these roughness levels did not cause a significant increase in C_f or St in the turbulent portion of the boundary layer. The uniform roughness condition, 100/100, suggests that k^+ must be below 0.4 to prevent roughness-induced early transition in a laminar boundary layer from causing substantial increases in heat transfer and skin-friction. *Even though the roughness level is within the aerodynamically smooth regime of a turbulent boundary layer, the transition process is evidently affected by even small changes in surface condition.*

A comparison of skin-friction and Stanton number distributions in terms of the Reynolds analogy factor ($St(C_f/2)$) is shown in Fig. 2(*c*). In the turbulent region of the 60/100 and 100/100 cases, Stanton number data are reduced to about 0.9, while the smooth surface data of the baseline and the 60/0 cases exhibit values of 1.05. The turbulent region in the STEP/100 case shows a value of approximate unity. The low Reynolds analogy factor on the roughened surface implies that the surface roughness affects fluid mechanics, C_f, more than heat transfer, St. These results are consistent with the turbulent flow study performed by Dipprey and Sabersky [10], which indicated that the addition of roughness increases C_f more than St.

Mean and rms Boundary Layer Data. A detailed description of the evolution of mean and fluctuating velocity and temperature quantities over a smooth surface can be found in many previous publications, such as Sohn et al. [11], Wang et al. [8], and Blair [12]. Only a short description is made here as a reference for comparison with the rough surface results. The evolution of the smooth-wall mean velocity and rms velocity fluctuation profiles are shown in Figs. 3(*a*) and 4, respectively. The onset and completion of transition, as determined from the mean velocity profiles, are consistent (within 5 percent) with those indicated by the skin-friction shown in Fig. 2(*a*) and Stanton number data

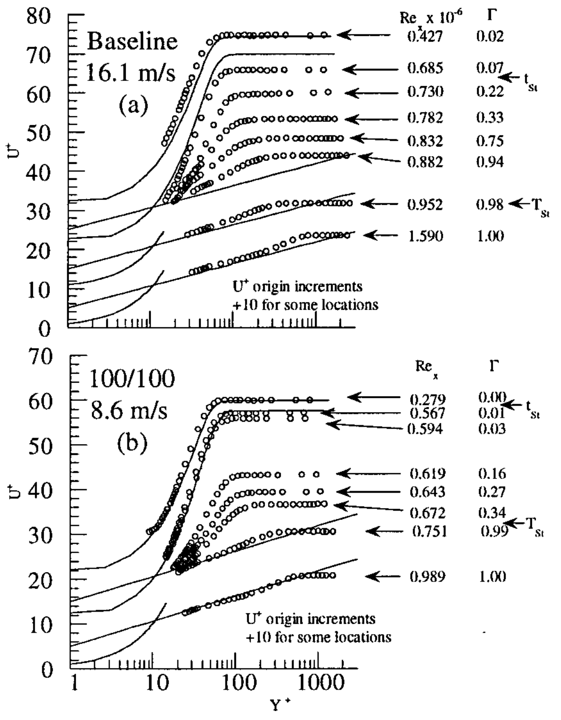

Fig. 3 Selected normalized velocity profiles: (*a*) baseline; (*b*) 100/100

shown in Part 1. Increases in u' (rms fluctuation) and t' were observed after Γ exceeded 0.07 as is shown in Figs. 4(*a*) and 4(*c*) ($\mathrm{Re}_x > 6.41 \times 10^5$). The peak values of both u' and t' observed within the transition are substantially above their respective turbulent values. The single, near-wall value of u'/U_∞ peaked during transition at a value of 0.15 and gradually decreased to 0.08 as the flow became turbulent. Both the u' and t' profiles continue to change downstream of the onset of turbulent flow ($\mathrm{Re}_x > 1 \times 10^6$). In a somewhat similar manner, the normalized Reynolds streamwise heat flux, $-\overline{ut}/(q_w''/\rho C_p)$, was observed to amplify in the transition region to a peak value that was 12 times the wall heat flux and asymptotically decreased to unity in the early turbulent region of the flow. The measurements of $\overline{vt}$ contained large uncertainties and are not shown here.

The amplification of Reynolds shear stress began about the same location ($\mathrm{Re}_x > 6.41 \times 10^5$) in Fig. 4(*d*) where the mean velocity profiles deviated from the Blasius solution. When Γ was 0.03, the peak was located at a $y/\delta = 0.5$ with a value of 0.4 relative to the wall shear, but the peak exceeded the wall shear when Γ reached about 0.07. At an $\Gamma = 0.98$ the region has reduced to approximate unity with the wall shear. Up to $\mathrm{Re}_x = 9.52 \times 10^5$, the results are consistent with data obtained by Kuan and Wang [3]; however, the normalized Reynolds shear stress was observed to decrease from 1 to 0.65 in the Re_x range above 9.52×10^5. An examination of the free-stream velocity suggests that a local acceleration $(K = (\nu/U_\infty^2)(dU_\infty/dx) = 1.6 \times 10^{-7})$ in the region just upstream of the region caused the decrease in $\overline{uv}$. Keller and Wang [13] showed that a favorable pressure gradient reduces $\overline{uv}$ magnitude relative to the local wall shear.

Some aspects of the rough-wall boundary layer measurements were observed to be quite similar to the baseline behavior, but several significant differences were observed in the data. The mean velocity data were consistent with the baseline behavior. For example, selected mean and rms data from the 100/100 case are shown in Figs. 3(*b*) and 5, respectively. During the transition region, the mean velocity profiles are observed to shift gradually from the Blasius correlation to the turbulent correlation. In the turbulent flow, the wake region of the U^+ profile for the rough case is weaker than for the baseline case. The cross-stream development of the u', t', and $\overline{uv}$ distributions are similar to but have lower values than the smooth-wall situation. The v' distributions of the 100/100 case do not show a near-wall peak for $y/\delta < 1$ as the baseline case does. The $\overline{uv}$ distributions exhibit a cross-stream development similar to that of the baseline, but the local $\overline{uv}$ variations within the transition region are shown not to exceed the local wall shear. The primary differences between smooth and rough-wall behavior are more easily observed through an inspection of the streamwise development of the maximum values of the rms data.

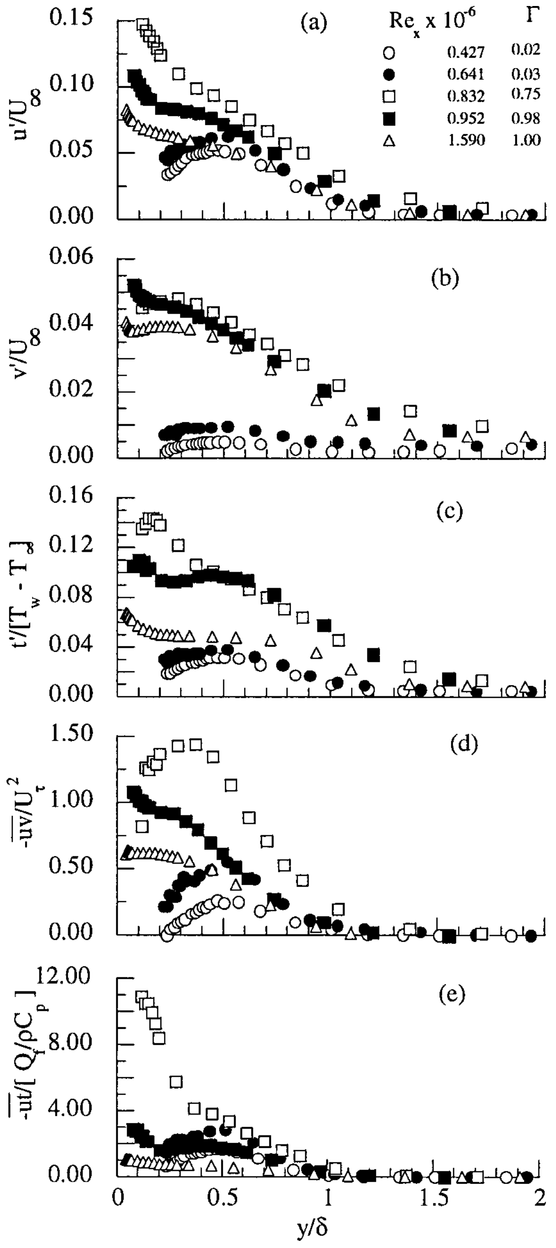

Fig. 4 Selected distributions of turbulent quantities for baseline case at 16.1 m/s

The streamwise development of $u'_{\max}$ in the boundary layer at each streamwise measuring station is shown in Fig. 6(*a*) as a function of normalized distance through the transition region. Both the STEP/100 and 60/0 cases show significant increase in $u'_{\max}$ prior to the smooth-wall case. In both situations, the $u'_{\max}$

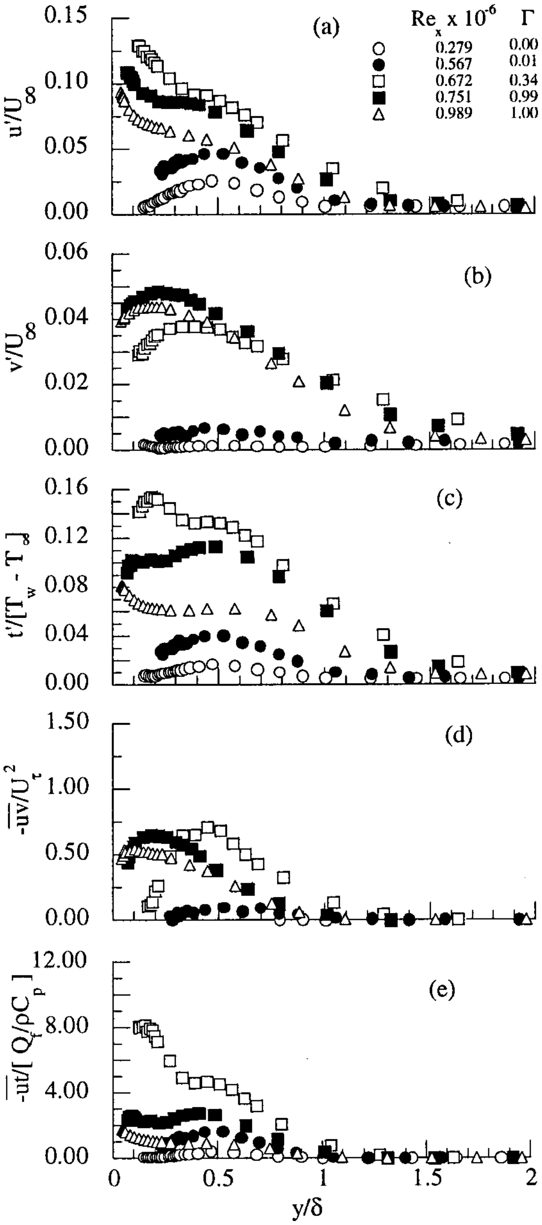

Fig. 5 Selected distributions of turbulent quantities for 100/100 case at 8.6 m/s

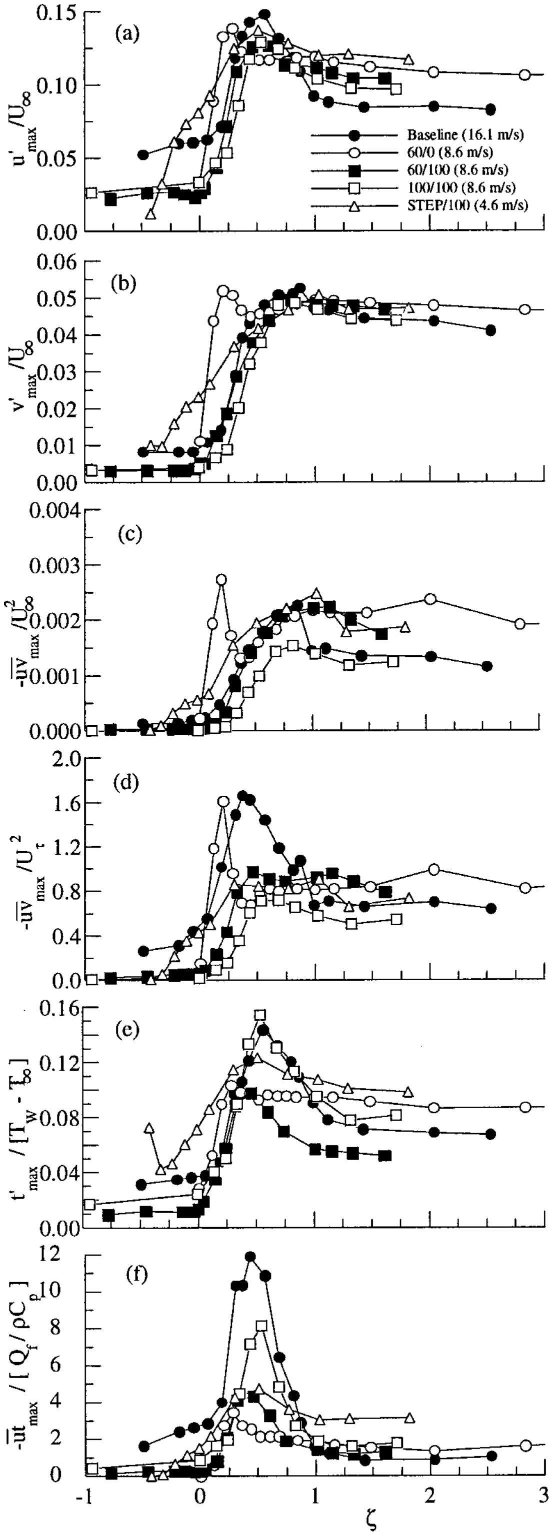

Fig. 6 Streamwise development of peak turbulent quantities in the boundary layer

increases beginning with the first measurement location. The 60/100 and 100/100 cases almost match the baseline in the region, $0.2<\zeta<0.4$ where $\zeta=(x-x_t)/(x_T-x_t)$. Since the 60/100 case is similar to the baseline in the early transition region, the early increase in u'_{max} for the 60/0 and STEP/100 cases is believed to be a result of the disturbance induced by the step change in roughness level. As discussed in Part 1, the backward-facing step change may induce vortex shedding in the shear layer behind the step and triggers the early onset of transition.

All of the roughness cases have u'_{max} peaks in transition that are less than that of the baseline. The 60/0 case has a u'_{max}/U_∞ peak of 0.14 that is nearest to the baseline value of 0.15. However, the peak of the 60/0 case occurs when $\zeta=0.25$, and the peak region grows and decays over a much shorter distance of the transition region than the baseline. Kuan and Wang [3] attributed the decline of smooth-wall u'_{max} variation during transition mainly to the increase in dissipation in the late transition region ($\zeta>0.5$). The earlier decline of u'_{max} in the transition region of the 60/0 case is an indication that the disturbance introduced into the flow by the 60/0 surface condition dissipated faster, due to low Reynolds number effect, than during the natural transition process on a smooth wall. The other roughness cases had lower u'_{max} values in the transition region than either the 60/0 or the baseline case, but the peak locations of these other roughness cases were in the same vicinity of the peak ($\zeta\sim0.5$) as in the baseline case. Evidently, the other roughness cases do trigger early transition relative to the baseline, but once underway, the amplification mechanism and the development of turbulent production proceeds in a manner similar to the smooth-wall case. However, the distributed roughness on the surface evidently introduces an increase in dissipation in the transitional boundary layer either by introducing more resistance to the flow or by confining the lateral growth rate of the hairpin vortices. As a result, $u'_{\max}$ is kept lower than the smooth-wall case within the transition region. The STEP/100 case at 4.6 m/s is evidently not generating a flow disturbance as significant as the 60/0 case at 8.6 m/s because the STEP/100 case exhibits a $u'_{\max}$ peak halfway through transition just like the baseline case, but the step geometry is significant enough to induce earlier increases in $u'_{\max}$ than the baseline.

Although the roughness cases have lower $u'_{\max}/U_\infty$ values in the transition region, all of the roughness cases have higher $u'_{\max}/U_\infty$ values than the baseline in the early turbulent region $(\zeta>1.2)$. This result is consistent with the rough-wall data obtained by Antonia and Luxton [14] and Perry and Lee [15] in turbulent boundary layers. Experiments conducted by Grass and Mansour-Tehrani [16] indicate that the spanwise spacing of low-speed streaks in the fully developed turbulent boundary layer scale according to roughness height as opposed to the wall shear in rough-wall flows. It is thought that the small-scale roughness used in the present study may cause the spanwise spacing of the low-speed streaks to be closer together. If so, the longitudinal development of the bursting process may be influenced in such a way as to enhance overall local production in a turbulent boundary layer. Dissipation in the fully developed turbulent boundary layer may partially balance and prevent the increase in u' from becoming significant even when the surface becomes very rough $(k^+>200)$, as was the case in the studies by Antonia and Luxton [14] and Perry and Lee [15]. In the turbulent region, the level of $u'_{\max}/U_\infty$ seems inversely correlated with the disturbance levels at the leading edge, as shown in Fig. 6(*a*). *This implies that the leading-edge roughness has a longer lasting effect on the turbulent boundary layer than what is usually recognized*. This observation also implies that if leading-edge disturbances are employed to trip boundary layers to study fully turbulent flow behavior, due consideration of the lasting effects introduced by the tripping device should be incorporated into the experimental design. This observation is similar to that reported by Klebanoff and Diehl [17].

The trends in $v'_{\max}$ are consistent with the observed $u'_{\max}$ distributions. The $v'_{\max}$ distributions for most of the roughness cases are similar to that of the baseline in that $v'_{\max}/U_\infty$ gradually increases through the transition region without a large peak during transition. As discussed by Kuan and Wang [3] the cross-stream fluctuation of smooth-wall transition develops in response to the growth of $u'_{\max}$ magnitude via the return-to-isotropy terms, $2\overline{p(\partial u/\partial x)}$ and $2\overline{p(\partial v/\partial y)}$, in the turbulence kinetic-energy balance. In addition, the cross-stream dissipation develops in tandem with $v'_{\max}$, and $v'_{\max}$ achieved equilibrium in midtransition. As with the $u'_{\max}$ distributions, the roughness conditions involving the larger step have more significant deviations from the baseline behavior. The STEP/100 case, for example, develops larger $v'_{\max}$ earlier than the baseline, but the data clearly indicate that $v'_{\max}$ lags $u'_{\max}$ development. For the first two measurement locations $(\zeta\sim-0.5)$ of the STEP/100 case shown in Fig. 6(*b*), $v'_{\max}/U_\infty$ remains approximately constant, and $v'_{\max}$ does not significantly increase until the third measurement location. In contrast, the $u'_{\max}/U_\infty$ of the second measurement location is 1.7 times that of the first location (Fig. 6(*a*)) indicating that $u'_{\max}$ develops prior to $v'_{\max}$ for the STEP/100 condition. The backward-facing step effect in the 60/0 case apparently has a strong disturbance that induces higher values of $v'_{\max}$ simultaneously with $u'_{\max}$, which can be an indication of the effect of vortex dynamics. The discussion of spectral content in the next section indicates that a strong concentration of spectral energy is present in a specific frequency range immediately downstream of the step. This behavior suggests that the step is introducing vortex dynamics that may include both vortex shedding and induced wall-bound vortices that are causing disturbances in both $u'_{\max}$ and $v'_{\max}$ simultaneously. The net result is the observed increase in $v'_{\max}$ in the early transition region with a narrow peak to match that of the $u'_{\max}$ behavior discussed earlier. The effect of vortex dynamics generated by the backward-facing step of the sandpaper roughness is reduced downstream as indicated by the 15 percent decrease in $v'_{\max}/U_\infty$ after the peak value of 0.052.

The streamwise development of Reynolds shear stress is shown in Figs. 6(*c*) and 6(*d*). The variation (normalized by U_∞) of the roughness cases during transition is generally consistent with the baseline data with the 100/100 case being lower and the STEP/100 case being higher. However, the 60/0 case exhibits a peak in $\overline{uv}_{\max}/U_\infty^2$ similar to that observed in the $u'_{\max}$ and $v'_{\max}$ data. In a transitional boundary layer, Wang and Zhou [18] considered the occurrence of $\overline{uv}$ variation indicative of the active turbulent transport, although not necessarily active turbulent production, via breakdown of vortices (e.g., hair-pin vortices). In the 60/0 case, the peak of $\overline{uv}_{\max}/U_\infty^2$, occurring almost immediately after the step change in roughness (X3), is an indication of vigorous turbulent transport produced by vortex dynamics downstream of the separated flow behind a backward-facing step. The narrowness of the peak in $\overline{uv}_{\max}$ suggests that although the step geometry represents a strong disturbance to trigger the onset of early transition, it is not strong enough to alter the transition process involving both linear and nonlinear instabilities. This observation is based on the fact that downstream $(0.5<\zeta<1)$, $\overline{uv}_{\max}$ development matched that of the other cases.

When $\overline{uv}_{\max}$ is compared to the local wall shear in terms of $\overline{uv}_{\max}/U_\tau^2$ as shown in Fig. 6(*d*), the effects of roughness within the transition region become apparent. Both the baseline and the 60/0 cases exhibit $\overline{uv}_{\max}$ behavior in the boundary layer that exceeds the local wall shear $(\overline{uv}_{\max}/U_\tau^2>1)$. This type of behavior has been attributed by Wang et al. [8] to the breakdown near the tips of growing hairpin-type vortices, which occurs away from the near-wall region at $0.2<y/\delta<0.3$ or $70<Y^+<100$. The small vortices generated from these breakdowns may propagate toward the wall to stimulate increases in wall shear until the mean flow gradients adjust accordingly to become fuller near the wall, which gives rise to the characteristic constant shear-stress region over the log-linear region of the wall profiles $(y^+<200)$. It is interesting to observe that none of the roughness cases that have distributed roughness within the transition region have $\overline{uv}$ in the boundary layer that exceeds the local wall shear $(\overline{uv}_{\max}/U_\tau^2<1)$. As discussed above, comparisons of $\overline{uv}_{\max}/U_\infty^2$ magnitudes suggest that the roughness does not significantly alter the magnitudes of $\overline{uv}$ within the transition region. However, the fact that the 60/100, 100/100, and STEP/100 cases exhibit $\overline{uv}$ magnitudes less than the wall shear in the transition region suggests that the presence of distributed roughness during transition may produce higher shear stress at the wall and may also stimulate a more rapid communication between the rough wall and/or the turbulent shear production away from the wall in the transitional boundary layer. In the turbulent region, all of the cases except the 100/100 case show higher $\overline{uv}_{\max}$ values than the baseline case, although $u'_{\max}$ of the 100/100 case is higher than the baseline case.

The presence of roughness significantly affects the variation of t' and $\overline{ut}$ in the transitional boundary layer, which suggests that the thermal transport is different during transition than the momentum transport. As shown in Fig. 6(*a*), the $u'_{\max}/U_\infty$ of the 60/0 case is similar in magnitude to the baseline case during transition, but the $t'_{\max}/(T_W-T_\infty)$ of the 60/0 case is 40 percent below that of the baseline, and the magnitude of the 60/0 peak in $t'_{\max}$ is less than all the other roughness cases during transition. A similar situation is observed for $\overline{ut}_{\max}$ variations. The baseline Reynolds streamwise heat flux peaks about midtransition ($\zeta=0.5$) with a value 12 times the local wall heat flux, and the corresponding peak in $-\overline{ut}_{\max}/(q_w''/\rho C_p)$ for the 60/0 case is only 3 (at $\zeta=0.25$). As the relative size of the step geometry decreases (60/100 and STEP/100), the peaks of $\overline{ut}_{\max}$ and $t'_{\max}$ increase, but they are still well below that of the smooth-wall results during early transition. The 100/100 case appears to be the one most similar to the baseline case as indicated by the significantly larger peaks in t' and $\overline{ut}_{\max}$ (Figs. 6(*e*) and 6(*f*)), but an examination of $\overline{uv}_{\max}$ in Figs. 6(*c*) and 6(*d*) indicate that $\overline{uv}_{\max}$ of 100/100 case that is the farthest away from the baseline. The fully turbulent values of $t'_{\max}$ and $\overline{ut}_{\max}$ are consistent with $u'_{\max}$ in that higher values are generally associated with the roughness cases. The strong contrast between the momentum and thermal transport in the 60/0 case indicated by very high values for $u'_{\max}$, $v'_{\max}$, and $\overline{uv}_{\max}$ and very low values of $t'_{\max}$ and $\overline{ut}_{\max}$ *implies that the vortex dynamics and separation induced by the step change in roughness mainly imposes rigorous turbulent momentum transport toward the wall without significantly enhancing heat transfer from the surface to the free stream*. Therefore, it is clear that momentum and thermal transport for rough wall situations is different than that of the smooth wall during transition.

Spectral Analysis. Two analysis techniques were used to gain insight into the spectral content of the experimental data. The first of these two methods involved determination of the power spectral density function, PSD, obtained through a transformation of the streamwise velocity data into the Fourier domain via a radix-2 FFT algorithm. Comparisons of the relative energy content as a function of wave number can more easily be observed if the data is normalized using wave number and $(u')^2$ in the relation:

$$\frac{1}{(u')^2}\int E(k)dk=\frac{1}{(u')^2}\int kE(k)d\log k=1. \tag{1}$$

If the PSD data are plotted on logarithmic coordinates, then $kE(k)$ represents the local energy content per unit length (not the energy density at a given wave number), and division by $(u')^2$ makes the value a fraction of the total. The second technique that was used to gage the spectral content of the data was a continuous-time wavelet transform (CWT) of the same velocity data using the Morlet wavelet as a mother-function of the transform. Farge [19] provides an overview of the mathematical concept along with a review of previous work on the application of wavelet analysis to turbulent flow (a more recent review is also available in Farge et al. [20]).

The continuous wavelet transform, CWT, is a convolution-type integration that has the general form:

$$w(\kappa,t)=\sqrt{\kappa}\int_{-\infty}^{\infty}f(\tau)g^*(\kappa(\tau-t))d\tau \tag{2}$$

The Morlet wavelet was chosen as the wavelet function to analyze the present results. Lewalle and Ashpis [21] and Volino [22] used the ''mexican hat'' wavelet to analyze transitional boundary layer data, but Farge [19] suggested the Morlet wavelet for processing turbulence data due to its similarity to the eddy used in the spectral energy cascade model suggested by Tennekes and Lumley [23]. The mathematical form of the Morlet function used during the present study is:

$$g(t)=e^{-t^2/2}\cos(5t). \tag{3}$$

The duration of the wavelet function is varied during the actual computation of the transform. The present study presents this duration (or ''scale'') parameter in terms of the equivalent cosine frequency of the wavelet function at a given scale. Classification of κ via an equivalent cosine frequency was done because the central frequency band of the wavelet function in the Fourier domain is a function of the cosine frequency, and this approach allows for easier comparison between PSD and CWT results.

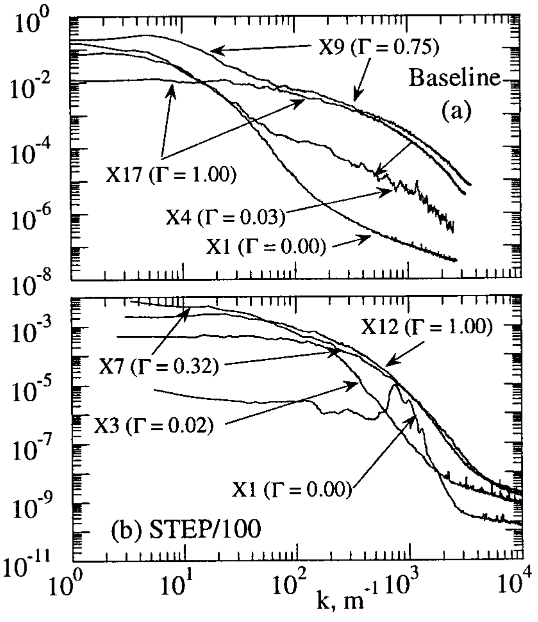

Fig. 7 Power spectral density: (*a*) baseline, 16.1 m/s; (*b*) STEP/100, 4.6 m/s

Most of the spectral content of the baseline laminar region is below a wave number of 100 m^{-1} as shown in Fig. 8(*a*). The same information is plotted in Fig. 7(*a*) in terms of $E(k)$. While Fig. 7(*a*) does show the gradual increase of energy density as transition progresses, the relative energy content at the different scales is not clearly represented. The representation shown in Fig. 8(*a*) shows more clearly the concentrations of energy due to the use of $kE(k)$. The higher total energy levels at large wave number are more clearly represented because even though $E(k)$, the energy density at wave number *k*, is low, the high wave number value implies that a large number of eddies of size 1/*k* are present per unit length, and more energy is present per unit length.

With the onset of transition in the baseline, the X4 measurement location ($\Gamma=0.03$ in Fig. 8(*a*)) indicates that a small fraction of the total energy has moved to a higher wave number range. The higher wave number amplification continues with more energy content developing within $200\,\text{m}^{-1}<k<300\,\text{m}^{-1}$. Within the midtransition region ($0.22<\Gamma<0.75$) there seems to be a demarcation between the low wave number energy and that of the upper region as indicated by the local minimum near 100 m^{-1}. This division may represent the relatively large, low frequency fluctuations ($k\sim10\,\text{m}^{-1}$) induced in the nonturbulent fluid that surrounds the smaller, higher frequency ($k\sim200\,\text{m}^{-1}$) fluctuations within the turbulent wave packets.

The growth of the disturbances in the early transition region ($\Gamma=0.22$) of the baseline case are illustrated in Fig. 9(*b*) in the form of a continuous wavelet transform. Several turbulent wave packets are evident from inspecting the instantaneous velocity signal associated with the CWT. The wave packets are shown in the CWT to have the broad-band spectral nature that is characteristic of turbulentlike flow. In the immediate vicinity of the wave packets, small-amplitude disturbances are evident that, according to the CWT, have a limited wave number range of spectral content. Gad-El-Hak et al. [24] conducted a detailed study of turbulent spot structure, which suggests that the wave packets grow by destabilizing the surrounding fluid. Wygnanski et al. [25] documented the presence of Tollmein–Schlichting type disturbances in

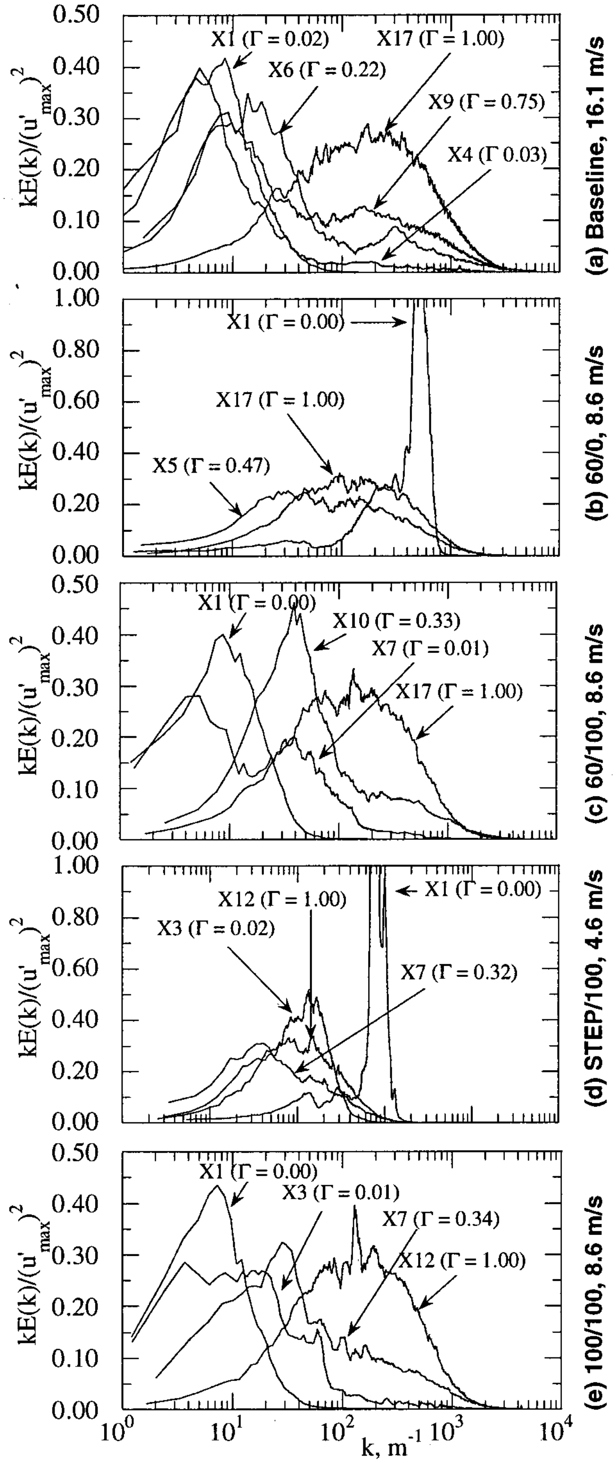

Fig. 8 Selected power spectral distributions: (*a*) baseline, 16.1 m/s; (*b*) 60/0, 8.6 m/s; (*c*) 60/100, 8/6 m/s; (*d*) STEP/100; (*e*) 100/100, 8.6 m/s

the vicinity of turbulent spots. The unstable wave number range predicted by linear instability theory for this region of the baseline case is from 175–350 m^{-1}. Inspection of earlier boundary measurement locations of the baseline case (see Fig. 9(*a*)) indicate disturbances that are exclusively within the wave number range predicted by linear instability theory. When taken in combination with the data in Fig. 9(*b*), the early transition region of the present baseline case appears to be a result of the amplification of small disturbances that began as Tollmein–Schlichting waves.

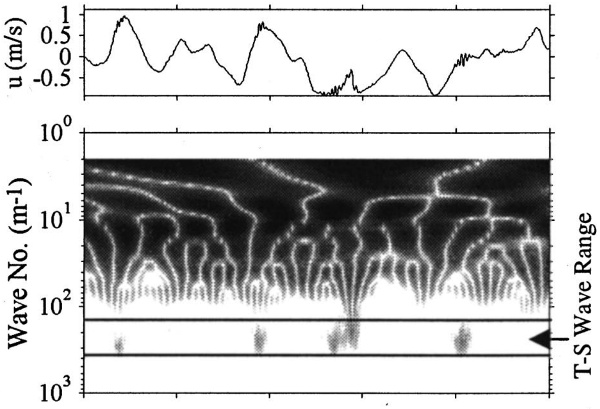

(a) Baseline, Γ = 0.02, 16.1 m/s

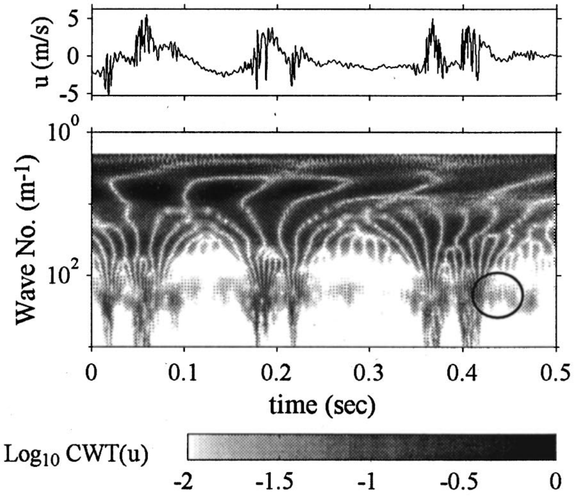

(b) Baseline, Γ = 0.22, 16.1 m/s

Fig. 9 Selected results of wavelet transformations of baseline data using Morlet wavelet function

The step-change in roughness for both the 60/0 and STEP/100 cases, as previously shown in the rms data, causes a significant disturbance downstream. In both cases, the initial normalized PSD distribution shows strong concentration of spectral energy at medium wave numbers just downstream of the step. The 60/0 case (shown in Fig. 8(*b*)) exhibits a spectral peak at 520 m^{-1}, while the STEP/100 case (shown in Figs. 7(*b*) and 8(*d*)) shows a similar one at 800 m^{-1}. This high concentration of spectral energy in a narrow wave number range suggests that the separated region in the vicinity of the step is periodically shedding vortices into the downstream flow even though the step is small (0.6 mm). For flow downstream of backward-facing steps, Eaton and Johnston [26] indicated that the streamwise location of reattachment can be unsteady, and structures with length scales on the order of the step height are shed into the downstream flow. The results of the 60/0 and STEP/100 data are consistent with this observation, given the wave number range of the spectral peak and the size of the step height. Details of shedding frequencies observed downstream of backward facing steps were not located in the literature for the step Reynolds number range of the present results, but using the step height and local mean velocity (at $y/\delta=0.2$), *the Strouhal numbers*, $S=fD/U$, *are 0.038 to the 60/0 case and 0.076 for the STEP/100 case*. By considering local mean velocity and approximate step height, the step Reynolds numbers were estimated to be

88 (60/0) and 45 (STEP/100), respectively. This Strouhal number range is somewhat lower (same order of magnitude) than Strouhal numbers associated with flow separation around a cylinder placed in a free-stream flow. However, Hwang and Yao [27] showed that shedding frequency downstream of a cylinder decreased with proximity to a wall in a numerical simulation. This suggests that a similar shedding to that behind a cylinder occurs downstream of the step for the roughness cases. In marked contrast to the 60/0 case, the 60/100 data, shown in Fig. 8(*c*) does not contain a strong energy concentration indicative of a shedding phenomenon and the gradual shift of energy to the higher wave numbers is similar to that of the baseline case.

Examination of Fig. 8(*b*) suggests that a trend of *reversed transition* from turbulent flow back to more organized flow exists for the 60/0 case. Following the first measurement location (with its associated peak energy level due to shedding), the peak energy level shifts to lower wave numbers for the range from X1 to X5. Then, the peak energy region begins to shift to the higher wave number range. An examination of the intermittency distribution (Γ), v', and $\overline{uv}$ (Figs. 1(*a*), 6(*b*), and 6(*c*), respectively) also suggests a reversal in the development of transitional flow behavior. This behavior downstream of the step could be caused by a quick dissipation of a weak separated shear layer in a region of low Reynolds number flow that has a more stable environment. To some extent the STEP/100 is similar to that of the 60/0 case, but the lower free-stream velocity did not immediately force the onset of transition in the vicinity of the roughness step. The shift of spectral energy back to low wave numbers due to the reversed transition occurs within the low Reynolds number laminar portion of the flow downstream of the step.

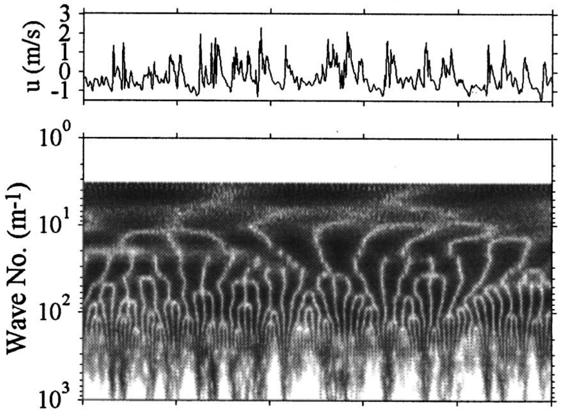

(a) 60/0, Γ = 0.23, 8.6 m/s

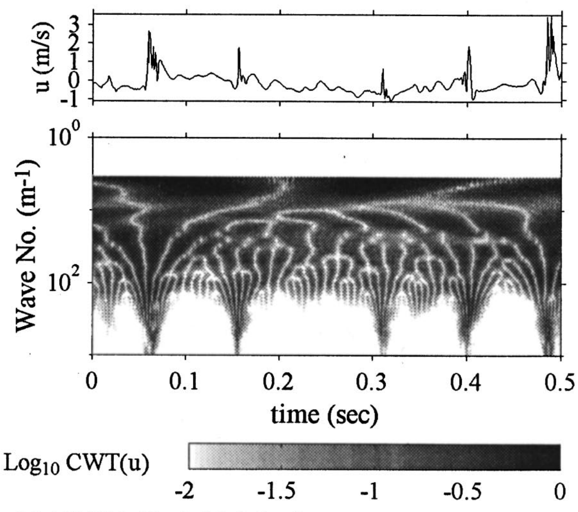

(b) 100/100, Γ = 0.16, 8.6 m/s

Fig. 10 Selected results of wavelet transformations using Morlet wavelet function: (*a*) 60/0 case; (*b*) 100/100 case

The absence of a step-change in surface roughness in the 100/100 case makes the spectral characteristics more similar to that of the baseline case. The spectral distribution shown in Fig. 8(*e*) indicates a gradual shift of energy content from low to high wave numbers, but no clear demarcation between low and high wave number energy was observed in the midtransition region as was seen in the baseline data. The unstable wave number range predicted by linear instability theory is between 50 and 80 m^{-1}, but inspection of the CWT distribution shown in Fig. 10(*b*) does not show clear disturbances amplified in this range. An examination of the early to midtransitional CWT data for all of the roughness cases indicates a similar trend. *The growth of disturbances in the presence of rough surface conditions appears to be spread over a larger spectral range than the baseline. This spectral behavior suggests that the transition process associated with rough surfaces may be classified as bypass transition.*

Uncertainty Analysis

Table 1 Summary of measurement uncertainties

Parameter	Relative Uncertainty	Parameter	Relative Uncertainty
u’	7.1 %	U^+	5 %
v’	8.4 %	T^+	3 %
t’	1.8%	$\overline{uv}$	12 %
Γ	17 %	$\overline{ut}$	3.7 %
C_f	5 %		

The major uncertainties associated with the experimental measurements described in the preceding are summarized in Table 1. The analysis was performed with 95 percent confidence level. The relatively large values of uncertainty associated with the rms boundary layer values are primarily a result of off-axis velocity component effects, and the uncertainty in intermittency results from determining the appropriate threshold value.

Conclusions

Surface roughness was shown to have several effects on the structure of transitional boundary layer flow:

1 During transition, $u'_{\max}$ magnitudes are generally reduced as a result of roughness. The stronger dissipation or restriction of hairpin vortex growth due to surface roughness may have caused the reduction in peak u' values in the early transition.

2 Unlike the transitional boundary layer, the $u'_{\max}$ magnitudes of the rough-wall cases are observed to be higher than the smooth-wall flow in the turbulent boundary layer possibly as a result of the effect of near-wall augmentation of the bursting process induced by the roughness or from unstable flow produced by the leading-edge roughness.

3 The u', v', and $\overline{uv}$ variations for the 60/0, STEP/100, and 60/100 cases support the backward-facing step flow situation proposed in Part 1. In contrast to the baseline case in which the development in v' lags behind u', the relatively large step height of the 60/0 case appears to be shedding vortices which cause significant simultaneous peaks in u', v', and $\overline{uv}$ in the early transition region. As the step height is reduced (as with the STEP/100 and 60/100) cases, these effects are reduced to the point where the flow variations become similar to that of the baseline.

4 The presence of distributed roughness in the transition region appears to stimulate earlier increase of wall shear during transition because $-\overline{uv}_{\max}/U_\tau^2$ of the distributed roughness cases (60/100, 100/100, STEP/100), in contrast to the baseline case, did not exceed unity during the transition region.

5 The values of u' and t' are affected differently by the different roughness conditions tested. The roughness appears to stimulate better momentum transport toward the wall, but the thermal transport is not increased in a corresponding manner.

6 Reverse transition was observed downstream of the step in the 60/0 case as a result of the quick dissipation of separated flow in low Reynolds number laminar flow. The disturbances induced by the step were insufficient to maintain the early increases in u', v', and $\overline{uv}$ observed just downstream of the step.

7 All of these differences were obtained from flow situations where k^+ was small (0.35–0.94) and would be considered hydrodynamically smooth in the turbulent flow region, but early transition was triggered.

Acknowledgment

The experimental study received partial funding through the EPSCOR program of the U.S. Department of Defense (Grant No. F49620-92-J-0459).

Nomenclature

The nomenclature used in the present paper has been included with Part One.

References

[1] Keller, F. J., and Wang, T., 1995, ''Effects of Criterion Functions on Intermittency in Heated Transitional Boundary Layers With and Without Streamwise Acceleration,'' ASME J. Turbomach., **117**, pp. 154–165.

[2] Corrsin, S., and Kistler, A. L., 1955, ''Free-Stream Boundaries of Turbulent Flows,'' NACA, Report 1244.

[3] Kuan, C. L., and Wang, T., 1990, ''Investigation of the Intermittent Behavior of a Transitional Boundary Layer Using a Conditional Averaging Technique,'' Exp. Therm. Fluid Sci., **3**, pp. 157–170.

[4] Narasimha, R., 1985, ''The Laminar–Turbulent Transition Zone in the Boundary Layer,'' Prog. Aerosp. Sci., **22**, pp. 29–80.

[5] Mayle, R. E., 1991, ''The Role of Laminar–Turbulent Transition in Gas Turbine Engines,'' ASME J. Turbomach., **113**, pp. 509–537.

[6] Hatman, A., and Wang, T., 1998, ''Separated-Flow Transition, Part 1—Experimental Methodology and Mode Classification, Part 2—Experimental Results, Part 3—Primary Modes and Vortex Dynamics,'' ASME Paper Nos. 98-GT-461, 98-GT-462, 98-GT-463.

[7] Hatman, A., and Wang, T., 1999, ''A Prediction Model for Separated-Flow Transition,'' ASME J. Turbomach., **121**, pp. 594–602.

[8] Wang, T., Keller, F. J., and Zhou, D., 1996, ''Flow and Thermal Structures in a Transitional Boundary Layer,'' Exp. Fluid Therm. Sci., **12**, pp. 352–363.

[9] Clauser, F. H., 1956, ''The Turbulent Boundary Layer,'' in: *Advances in Applied Mechanics*, H. L. Dryden and T. von Karman, eds., Vol. 4, Academic Press Inc., pp. 1–51.

[10] Dipprey, D. F., and Sabersky, R. H., 1963, ''Heat and Momentum Transfer in Smooth and Rough Tubes at Various Prandtl Numbers,'' Int. J. Heat Mass Transf., **6**, pp. 329–353.

[11] Sohn, K. H., Reshotko, E., and Zaman, K., 1991, ''Experimental Study of Boundary Layer Transition on a Heated Flat Plate,'' ASME FED-**114**, pp. 167–172.

[12] Blair, M. F., 1992, ''Boundary Layer Transition in Accelerating Flows With Intense Free-Stream Turbulence; Part 1—Disturbances Upstream of Transition Onset; Part 2—The Zone of Intermittent Turbulence,'' J. Fluids Eng., **114**, pp. 313–332

[13] Keller, F. J., and Wang, T., 1996, ''Flow and Heat Transfer Behavior in Transitional Boundary Layers With Streamwise Acceleration,'' ASME J. Turbomach., **118**, pp. 314–326.

[14] Antonia, R. A., and Luxton, R. E., 1971, ''The Response of a Turbulent Boundary Layer to a Step Change in Surface Roughness: Part 1. Smooth to Rough,'' J. Fluid Mech., **48**, pp. 721–761.

[15] Perry, A. E., and Lee, J. D., 1990, ''Experimental Support for the Attached-Eddy Hypothesis in Zero-Pressure Gradient Turbulent Boundary Layers,'' J. Fluid Mech., **218**, pp. 405–438.

[16] Grass, A. J., and Mansour-Tehrani, M., 1996, ''Generalized Scaling of Coherent Bursting Structures in the Near-Wall Region of Turbulent Flow Over Smooth and Rough Boundaries,'' in: *Coherent Flow in Open Channels*, P. J. Ashworth, S. J. Bennett, J. L. Best, and S. J. McLelland, eds., Wiley, pp. 41–61.

[17] Klebanoff, P. S., and Diehl, Z. W., 1951, ''Some Features of Artificially Thickened Fully Developed Turbulent Boundary Layers With Zero Pressure Gradient,'' NACA Report 1110.

[18] Wang, T., and Zhou, D., 1996, ''Spectral Analysis of Boundary-Layer Transition on a Heated Flat Plate,'' Int. J. Heat Fluid Flow, **17**, pp. 12–21.

[19] Farge, M., 1992, ''Wavelet Transforms and Their Applications to Turbulence,'' Annu. Rev. Fluid Mech., **24**, pp. 395–457.

[20] Farge, M., Kevlahan, N., Perrier, V., and Goirand, E., 1996, ''Wavelets and Turbulence,'' Proc. IEEE, **84**, pp. 639–669.

[21] Lewalle, J., and Ashpis, D. E., 1995, ''Transport in Bypass Transition: Mapping Active Time Scales Using Wavelet Techniques,'' *Proc. Tenth Symposium on Turbulent Shear Flows*, Vol. 2, pp. 2:37–2:42.

[22] Volino, R. J., 1998, ''Wavelet Analysis of Transitional Flow Data Under High Free-Stream Turbulence Conditions,'' ASME Paper No. 98-GT-289.

[23] Tennekes, H., and Lumley, J. L., 1972, *A First Course in Turbulence*, The MIT Press.

[24] Gad-El-Hak, M., Blackwelder, R. F., and Riley, J., 1981, ''On the Growth of Turbulent Regions in Laminar Boundary Layers,'' J. Fluid Mech., **110**, pp. 73–95.

[25] Wygnanski, I., Haritonidis, J. H., and Kaplan, R., 1979, ''On a Tollmien–Schlichting Wave Packet Produced by Turbulent Spot,'' J. Fluid Mech., **92**, pp. 505–528.

[26] Eaton, J. K., and Johnston, J. P., 1981, ''A Review of Research on Subsonic Turbulent Flow Reattachment,'' AIAA J., **19**, pp. 1093–1100.

[27] Hwang, R. R., and Yao, C.-C., 1997, ''A Numerical Study of Vortex Shedding from a Square Cylinder with Ground Effect,'' ASME J. Fluids Eng., **119**, pp. 512–518.

[28] Schubauer, G. B., and Skramstad, H. K., 1948, ''Laminar-Boundary-Layer Oscillations and Transition on a Flat Plate,'' NACA Report 909.

[29] Abu-Ghannam, B. J., and Shaw, R., 1980, ''Natural Transition of Boundary Layers—The Effect of Turbulence, Pressure Gradient and Flow History,'' J. Mech. Eng. Sci., **22 pp**, 213–228.

[30] Gostelow, J. P., and Ramachandran, R. M., 1983, ''Some Effects of Free-Stream Turbulence on Boundary Layer Transition,'' *Proc. Eighth Australian Fluid Mechanics Conference*.

[31] Gostelow, J. P., and Blunden, A. R., 1989, ''Investigations of Boundary Layer Transition in an Adverse Pressure Gradient,'' ASME J. Turbomach., **111**, pp. 366–375.

[32] Feiereisen, W. J., and Acharya, M., 1986, ''Modeling of Transition and Surface Roughness Effects in Boundary-Layer Flows,'' AIAA J., **24**, pp. 1642–1649.

D. J. Jackson[1]
Graduate student.

K. L. Lee
Graduate student.

P. M. Ligrani[2]
Professor.
Mem. ASME

Convective Heat Transfer Laboratory,
Department of Mechanical Engineering,
University of Utah,
Salt Lake City, UT 84112

P. D. Johnson[3]
Engineering Manager,
Turbines and Mechanical Components,
Pratt & Whitney—Florida,
United Technologies, Inc.,
West Palm Beach, FL 33410
Mem. ASME

Transonic Aerodynamic Losses Due to Turbine Airfoil, Suction Surface Film Cooling

The effects of suction surface film cooling on aerodynamic losses are investigated using an experimental apparatus designed especially for this purpose. A symmetric airfoil with the same transonic Mach number distribution on both sides is employed. Mach numbers range from 0.4 to 1.24 and match values on the suction surface of airfoils from operating aeroengines. Film cooling holes are located on one side of the airfoil near the passage throat where the free-stream Mach number is nominally 1.07. Round cylindrical and conical diffused film cooling hole configurations are investigated with density ratios from 0.8 to 1.3 over a range of blowing ratios, momentum flux ratios, and Mach number ratios. Also included are discharge coefficients, local and integrated total pressure losses, downstream kinetic energy distributions, Mach number profiles, and a correlation for integral aerodynamic losses as they depend upon film cooling parameters. The contributions of mixing and shock waves to total pressure losses are separated and quantified. These results show that losses due to shock waves vary with blowing ratio as shock wave strength changes. Aerodynamic loss magnitudes due to mixing vary significantly with film cooling hole geometry, blowing ratio, Mach number ratio, and (in some situations) density ratio. Integrated mixing losses from round cylindrical holes are three times higher than from conical diffused holes, when compared at the same blowing ratio. Such differences depend upon mixing losses just downstream of the airfoil, as well as turbulent diffusion of streamwise momentum normal to the airfoil symmetry plane.
[S0889-504X(00)02202-9]

Introduction

In recent years, designers have devoted increased attention to the aerodynamic penalties associated with film cooling of turbine airfoils in gas turbine engines. This is because of increased awareness of the drops in efficiency associated with such penalties, and because the improvements in thermal protection provided by newest film hole configurations may be offset by the total pressure losses, which accumulate downstream of the airfoils. Thus, it is paramount that such aerodynamic losses be quantified, especially for transonic turbine airfoils, where total pressure losses often develop from shock waves, boundary layers, and wake mixing. Of recent investigations in this area, Denton [1] indicates that total pressure losses are connected to entropy creation. Consequently, mixing across gradients in the flow can result in increased losses even without the action of frictional forces. Additional entropy increases and losses of stagnation pressure also often result due to separation bubbles, which act to thicken boundary layers. Because boundary layer losses depend upon the cube of the ratio of the blade surface velocity to the upstream reference velocity integrated over the surface of an airfoil, losses originating in the suction surface boundary layer are dominant [1].

A number of recent studies focus on aerodynamic losses downstream of *subsonic* turbine airfoils with no film cooling. Of these investigations, Hoheisel et al. [2], Gregory-Smith and Cleak [3], and Ames and Plesniak [4] examine the influences of inlet turbulence on losses across turbine cascades. Hohisel et al. [2] also consider the effects of blade boundary layers, and Ames and Plesniak [4] demonstrate important connections between wake growth and level of free-stream turbulence. Moore et al. [5] indicate that more than one third of total losses develop downstream of airfoil trailing edges. The authors attribute total pressure losses to deformation work and dissipation of secondary kinetic energy.

Xu and Denton [6], Mee et al. [7], Izaak and Chiang [8], Michelassi et al. [9], and Joe et al. [10] present aerodynamic loss results for *transonic* turbine airfoils with no film cooling. Xu and Denton [6] investigate mixing losses from turbine blades with different trailing edge thicknesses, including the influences of blade boundary layers on downstream mixing. According to Mee et al. [7] boundary layers, shock waves, and wakes mixing all contribute to overall losses in relative amounts which depend upon the Mach number. In addition, most of the mixing losses are generated immediately downstream of the trailing edge of blades where gradients in properties across the wake are largest. Izaak and Chiang [8] present experimental data and numerical predictions which account for turbulence, transition, as well as transonic expansion fans. Michelassi et al. [9] test turbulence and transition models, which include the effects of separation bubbles, for a cascade flow with shock-boundary layer interactions. Joe et al. [10] present aerodynamic loss data measured downstream of a vane at different Reynolds numbers and exit Mach numbers.

A number of other investigators consider the influences of film cooling on aerodynamic losses from turbine blades and vanes. Of these, Ito et al. [11] indicate that total pressure losses in incompressible flow can increase or decrease due to film injection from a single row of holes placed either on the suction surface or the pressure surface. Haller and Camus [12] measured losses due to film cooling from five separate cooling hole locations on a transonic airfoil, with carbon dioxide to simulate density ratios. According to the authors, ejection downstream of the passage throat does not necessarily give higher losses than injection upstream of the throat. Kollen and Koschel [13] also employ carbon dioxide and a transonic airfoil, and indicate that losses increase with blow-

---

[1] Present address: Rocketdyne Division, BNA—Boeing North America, Canoga Park, CA 91309.

[2] Corresponding author.

[3] Present address: Competitive Design Company, Juno Beach, FL 33408.

Contributed by the International Gas Turbine Institute and presented at the 44th International Gas Turbine and Aeroengine Congress and Exhibition, Indianapolis, Indiana, June 7–10, 1999. Manuscript received by the International Gas Turbine Institute February 1999. Paper No. 99-GT-260. Review Chair: D. C. Wisler.

ing ratio for film cooling from the leading edge. Losses decrease with blowing ratio when the film originates on the suction side, except when blowing ratios are very small.

Mee [14], Michelassi et al. [15], Bohn et al. [16], Kapteijn et al. [17], Vlasic et al. [18], Sieverding et al. [19], and Tanuma et al. [20] investigate losses downstream of transonic airfoils with trailing edge ejection. Mee [14], Day et al. [21], and Osnaghi et al. [22] all indicate that density ratio influences are well correlated using the momentum flux ratio. According to Day et al. [21], film cooling causes thickening of airfoil wakes, as well as changes to the flow field near the hub in an investigation of aerodynamic losses from a transonic airfoil with multiple rows of film cooling holes on the leading edge and suction surface. Hong et al. [23] examine the effects of film cooling from a single row of holes located separately either on the suction surface, pressure surface, or leading edge. Results indicate that suction surface film cooling has the largest influence on total pressure losses, and that pressure surface film cooling has the smallest influence. Kubo et al. [24] compare numerical predictions with total pressure losses measured downstream of a low-speed cascade containing a vane with film cooling holes located on the leading edge, suction surface, pressure surface, and trailing edge. As the mass flow rate ratio varies, the largest loss increases relative to the flow with no film cooling are due to injection from holes located near the passage throat on the suction surface and from holed on the leading edge. In another experimental and numerical investigation that employs transonic airfoils, Urban et al. [25] also show that losses are greatly increased by film cooling from the suction surface, whereas pressure side and trailing edge ejection produces only small changes to aerodynamic loss magnitudes. These investigators show that density ratio variations have insignificant influences on loss magnitudes.

The present study employs a test section especially designed to investigate the effects of suction surface film cooling on aerodynamic losses because of their dominating importance in relation to overall downstream loss magnitudes [1,23–25]. A symmetric airfoil is employed with the same transonic Mach number distribution on both sides. Mach numbers along the airfoil surface range from 0.4 to 1.24 and match values on the suction surfaces of airfoils from operating aeroengines. Film cooling holes are located on one side of the airfoil near the passage throat where the free-stream Mach number is nominally 1.07. Two different film cooling configurations are investigated with density ratios from 0.8 to 1.3 over a range of blowing ratios, momentum flux ratios, and pressure ratios. Also included are discharge coefficients, local and integrated total pressure losses, downstream kinetic energy distributions. Mach number profiles, and a correlation for integral aerodynamic losses as they depend upon film cooling parameters. The results thus provide insight into the mechanisms for total pressure losses due to suction surface film cooling beyond that provided by earlier investigators. To the authors' knowledge, the present study is the first one to isolate these phenomena without the complicating influences of flow turning or the collection of vortices ordinarily present in turbine passages due to this turning.

Test Section and Film Cooling Hole Geometries

A schematic diagram of the non-turning airfoil cascade test section is shown in Fig. 1(*a*). The test section is made up of two acrylic side walls, and top and bottom walls made of steel and acrylic. The two side walls are flat, whereas the top and bottom walls are contoured to form a converging–diverging shape, which produces the desired Mach number distribution along the symmetric test airfoil. Because significant flow turning is not included, the camber curvature, present in many cascades with multiple airfoils, is not present.

A schematic diagram of the cross section of one symmetric airfoil tested is shown in Fig. 1(*b*). The airfoil chord length c is 7.62 cm. The effective pitch p is 5.08 cm. The trailing edge of the symmetric airfoil is a 1.14 mm radius round semicircle, designed to produce the wake flows of turbine airfoils employed in operating engines. The symmetric airfoil shape is employed to provide sufficient interior space for a plenum for film cooling injection, while maintaining appropriately scaled injection hole diameter and trailing edge thickness. Geometric dimensions of the contoured test walls and airfoil are given by Jackson [26] and Lee [27].

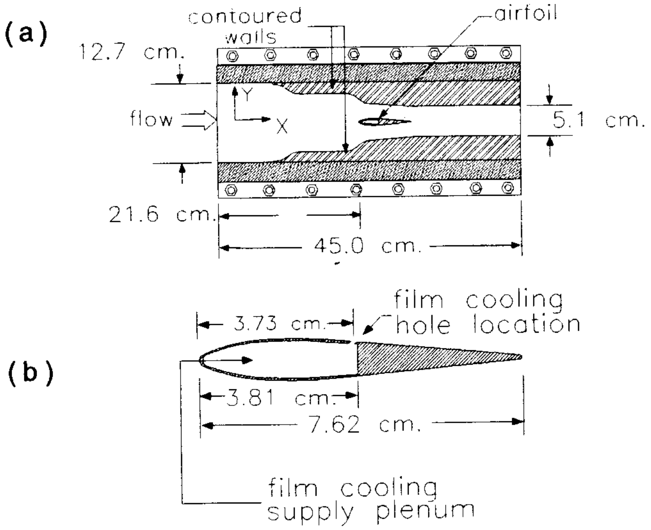

Fig. 1 Schematic diagrams of: (*a*) the test section, and (*b*) the test airfoil

The geometric characteristics of the two hole configurations studied (CDH—conical diffused holes, and RCH—round cylindrical holes) are shown in Fig. 2. In each case, one row of 21 holes is employed with 4 d spanwise spacing at a location 3.73 cm or 0.49 c from the airfoil leading edge. Each hole in the CDH geometry is diffused axisymmetrically about its axis. The entrance diameter, and length-to-entrance diameter ratio of both types of hole are the same 0.068 cm and 2.26, respectively.

The present test section is useful and advantageous over cascade arrangements with multiple airfoils and significant flow turning because: (*i*) the test section produces Mach numbers, pressure variations, Reynolds numbers, passage mass flow rates, and physical dimensions, which match values along airfoils in operating

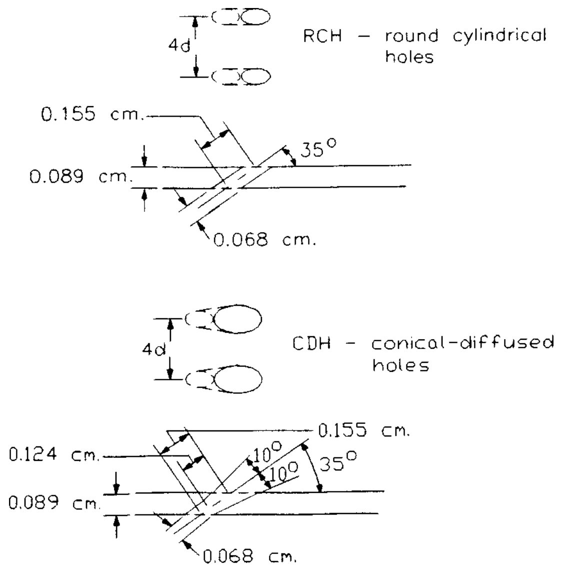

Fig. 2 Film cooling hole geometries

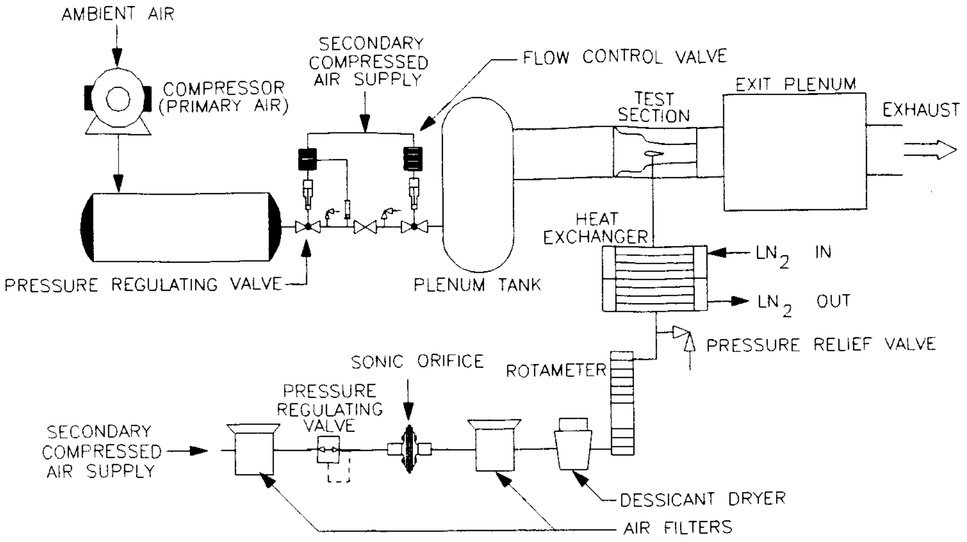

Fig. 3 University of Utah Transonic Wind Tunnel (TWT) including film injection system

engines, (*ii*) the airfoil provides the same suction surface boundary layer development (in the same pressure gradient without flow turning) as exists in operating engines, (*iii*) aerodynamic loss data are obtained on airfoil surfaces without the complicating influences of vortices present near airfoil leading edges, in the blade passages, and along airfoil pressure surfaces, (*iv*) results obtained with the arrangement are not configuration dependent, (*v*) only one airfoil is needed to obtain representative flow characteristics, and (*vi*) the entire airfoil surface is accessible to optical, surface temperature measurement schemes such as infrared thermography (results from which are reported elsewhere). Thus, the present experiment is designed to isolate the effects of suction surface film cooling on wake aerodynamic losses, while matching Reynolds numbers, Mach numbers, pressure gradients, passage flow rates, boundary layer development, and physical dimensions of airfoils in operating engines.

Experimental Apparatus and Procedures

Transonic Wind Tunnel. A schematic diagram of the University of Utah Transonic Wind Tunnel (TWT) is shown in Fig. 3. The blow-down type facility consists of two main parts: (*i*) compressor and storage tanks, and (*ii*) wind tunnel. The wind tunnel consists of five major subsections: (*i*) flow rate management apparatus, (*ii*) plenum tank, (*iii*) inlet ducting and test section, (*iv*) plenum, exit ducting, and ejector, and (*v*) control panel. A Gardner Denver Co. model RL-1155-CB compressor is used to pressurize the array of eight tanks, whose total capacity volume is 11.9 m^3. A VanAir VAS93039 model D16-5 Deliquescent desiccant dryer, a Pall Corp. 5EHG-4882-207 oil filter, and two Permanent Filter Corp. No. 13846 particulate filters are located just downstream of the compressor to remove particulates and moisture from the air. A Fisher pressure regulator with a 6X4 EWT design sliding gate valve, a Fisher type 667 diaphragm actuator, a 3582 series valve positioner, and a Powers 535 1/4 DIN process controller is used to regulate the pressure in the test section as the storage tanks discharge. A plenum tank, a 30.48-cm-ID pipe, a circular-to-square transition duct, a nozzle, and the test section then follow. The free-stream turbulence intensity at the test section inlet is about 0.5 percent. Relative humidity at this location is typically 20–30 percent. The test section is connected to a large 92.71 cm by 91.44 cm by 91.44 cm plenum with a square plastic flange at its inlet. The plenum diffuses high-speed air from the test section exit into a reservoir of low-velocity air. This plenum is then connected to two ducts, which are subsequently connected to the atmosphere.

Secondary Air Injection System. The injectant flow conditions are given in Table 1. The injection system is also shown in Fig. 3. From the building air supply, the air used for film cooling first enters a Norman Filters 5 micron ABS particulate filter, a Fairchild No. 10282 pressure regulator, a sonic orifice, a Wilkerson M16-02 F00B E95 coalescing filter, a Wilkerson X03-02-00A J96 Desiccant dryer, a Dwyer Model RMC series rotameter, and a pressure relief valve. For every experimental test condition, the injectant mass flow rate measured with the sonic orifice is in excellent agreement with the flow rate measured with the rotameter. The dryers and filters are required to avoid frost build since an Xchanger, Inc., TV-050 heat exchanger uses liquid nitrogen to cool injectant air to temperature as low as −120°C.

Pressure and Temperature Measurements. As tests are conducted, Validyne Model DP15-46 pressure transducers (with diaphragms rated at either 345 kPa or 1380 kPa), and calibrated copper-constantan thermocouples are used to sense pressures and temperatures at different locations throughout the facility. Signals from the transducers are processed by Celesco Model CD10D carrier demodulators. All pressure transducer measurement circuits are calibrated using a Wallace and Tiernan FA145 bourdon tube pressure gage as a standard. A United Sensor PLC-8-KL pitot-static probe with an attached copper-constantan thermocouple, and a four-hole conical-tipped pressure probe with an attached copper-constantan thermocouple are used to sense total pressure, static pressure, and recovery temperature at the inlet and exit of the test section, respectively, during each blow down. The conical probe is aligned using two yaw ports placed on either side of the probe. As a blowdown is underway, the probe is located one chord length downstream of the airfoil. It is traversed using a two-axis traversing sled with two Superior Electric M092-FF-206 synchronous stepper motors, connected to a Superior Electric Model SS20001 programmable motion controller and a Superior Electric Model SS2000D6 driver. These are interfaced and controlled by a Hewlett-Packard 362 series computer.

Data Acquisition System. Voltages from the carrier demodulators and thermocouples are read sequentially using Hewlett-Packard HP44222T and HP44222A relay multiplexer card assemblies, installed in a Hewlett-Packard HP3497A low-speed Data Acquisition/Control Unit. This system provides thermocouple compensation electronically such that voltages for type T thermocouples are given relative to 0°C. A Hewlett-Packard HP362 se-

Table 1 Film injection experimental conditions

Hole Configuration	Coolant Temperature	ρ_c/ρ_∞	M_c/M_∞	m	P_{oc}/P_∞	u_c/u_∞	I	IAL (N/cm)
RCH	-	-	-	0.000	-	0.000	0.000	0.634
RCH	ambient	0.839	0.497	0.230	1.212	0.275	0.063	0.853
RCH	ambient	0.858	0.590	0.301	1.304	0.351	0.106	0.892
RCH	ambient	0.953	0.931	0.638	1.871	0.669	0.427	0.909
RCH	cold	1.015	0.295	0.270	1.068	0.265	0.072	0.828
RCH	cold	1.073	0.404	0.291	1.133	0.272	0.079	0.927
RCH	cold	1.166	0.647	0.571	1.370	0.490	0.280	0.968
CDH	-	-	-	0.000	-	0.000	0.000	0.634
CDH	ambient	0.825	0.381	0.221	1.119	0.268	0.059	0.656
CDH	ambient	0.853	0.546	0.352	1.257	0.413	0.145	0.698
CDH	ambient	0.926	0.833	0.644	1.668	0.695	0.448	0.739
CDH	cold	1.010	0.397	0.234	1.130	0.232	0.054	0.644
CDH	cold	1.090	0.545	0.369	1.255	0.339	0.125	0.714
CDH	cold	1.230	0.742	0.605	1.510	0.528	0.319	0.749

ries computer processes signals from all transducers and thermocouples to give pressure and temperature readings, as well as other flow parameters.

Schlieren Images. The Edmund Scientific Corp. Schlieren system is arranged around the test section so that flow visualization may be conducted as blowdown tests are conducted. The Schlieren system consists of a light source, two circular concave mirrors in adjustable stands, a knife edge, and a projection screen. A platform with the light source is positioned near the test section so that the reflected light, originating from the mirror, shines through the test section to illuminate the flow around and between the test blade trailing edge, traversing probe tip, and test section walls. Schlieren images are recorded on video tape using a Dage-MT1 CCD72 video camera attached to a Panasonic AG-1960 video cassette recorder.

TWT Qualifying Characteristics. At the inlet of the test section, the total pressure and static pressure show excellent spatial uniformity [26,27]. Total pressure and static pressure values vary by less than 1.38 kPa (or 0.7 percent of $P_{oi\infty}$) as measurements are made at nine different probe locations. Mach numbers determined from these data then vary by less than 0.002. Steady conditions are maintained in the test section for 45 second long time intervals [27]. Such characteristics are not only due to the TWT design but also to the excellent performance characteristics of the TWT pressure regulator and its controller. Measurements of particulates in the test section flow, checked for size and number, show that they are not plentiful enough to damage any of the instrumentation employed.

Experimental Uncertainties. Uncertainty estimates are based on 95 percent confidence levels, and determined using procedures described by Kline and McClintock [28]. Mach number uncertainty is ±0.002. Uncertainty of temperatures is ±0.15°C. Pressure uncertainty is ±0.25 kPa. Uncertainties of C_P, $M_e/M_{e\infty}$, and KE are ±0.0013 (0.07), ±0.0023 (0.96), and ±0.03 (0.90), respectively, where typical nominal values of these quantities are given in parentheses. Discharge coefficient C_D uncertainty is ±0.035 (0.80). IAL uncertainty is ±0.04 N/cm (0.800 N/cm). Magnitudes of IAL, determined from replicate runs, are repeatedly within IAL uncertainty magnitudes.

Experimental Results

Test Section Flow Characteristics. The airfoil Mach number distribution is measured using a symmetric airfoil with eleven pressure taps located along the midspan line of the airfoil at various positions along its length. Eight of these taps lie on the top surface of the airfoil, and three taps are located on the bottom surface of the airfoil. Figure 4 shows measured Mach numbers along the airfoil surface, which range from about 0.4 to 1.14. Trailing edge shock wave angles and total pressure changes indicate that the experimental Mach number at the airfoil trailing edge is about 1.24. Figure 4 also shows that values from both sides of the airfoil are in agreement, and also match a distribution determined from numerical computations. Results from these numerical computations are presented in a different form in Fig. 5.

Two Schlieren images are shown in Fig. 6, arranged so that flow moves from left to right in each. The conical pressure probe is placed 0.75 *c* downstream of the airfoil, and is evidenced by a dark horizontal pattern on the right-hand side of each image. The top image is obtained with the probe stationary and no flow, and no trailing edge shock waves are evident at the downstream end of the blade. The subsequent image shows a pair of trailing edge oblique shock waves when flow is passing through the test section. From these and other results [26,27]. It is evident that: (*i*) no shock waves are present just in front of the probe, (*ii*) the only shock waves present in the test section are a pair at the trailing edge of the symmetric airfoil, and these do not reflect off of the top and bottom walls of the test section, (*iii*) the presence of the probe does not affect the trailing edge shock waves, even when it moves, and (*iv*) the trailing edge shock waves remain stationary and in place for the entire test sequence. The angle produced by

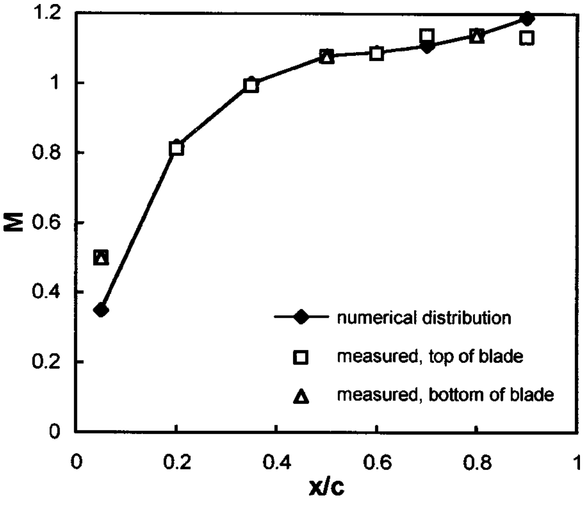

Fig. 4 Airfoil Mach number distribution

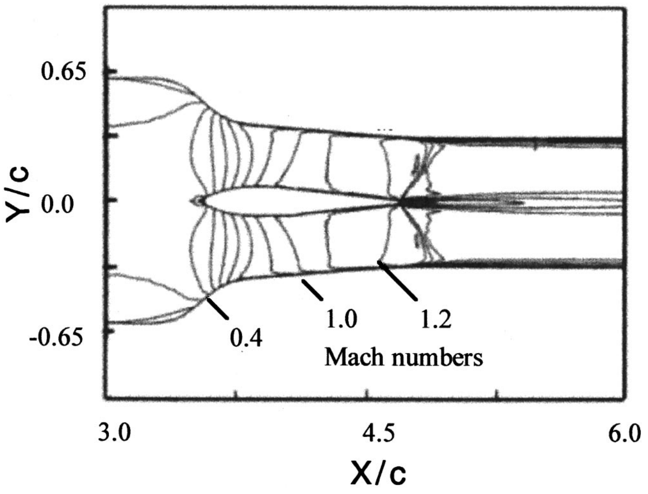

Fig. 5 Numerically computed Mach number distribution through the test section

the strong oblique shock waves at the airfoil trailing edge is about 73 deg (measured from the airfoil symmetry plane). This value and measured total pressures downstream of the oblique shock waves are in good agreement with theoretical values for a 5 deg flow deflection angle from Anderson [29]. The positions and shapes of the oblique shock waves in Fig. 6 also show good qualitative agreement with the Mach number distribution shown in Fig. 5.

Discharge Coefficients. Discharge coefficients are determined using

$$C_D = \dot{m}/\dot{m}_{\text{ideal}} \tag{1}$$

where the ideal mass flow rate is obtained using

$$\frac{\dot{m}_{\text{ideal}}}{A} = \sqrt{\frac{k}{R}}\frac{P_{oc}}{\sqrt{T_{oc}}}\left[\mathrm{M}_c \Big/ \left(1+\frac{k-1}{2}\mathrm{M}_c^2\right)^{k+1/2(k-1)}\right] \tag{2}$$

Here, A is the total cross-sectional area of the holes at their round inlets, and M_c is the isentropic Mach number of the injectant at the exits of the film cooling holes. This Mach number is determined using the isentropic relation based on the ratio of the stagnation pressure in the injection plenum P_{oc}, and the static pressure at the exits of the film cooling holes, P_∞.

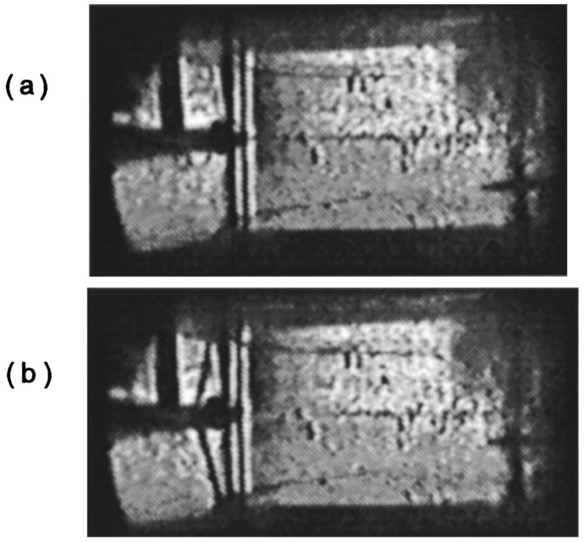

Fig. 6 Schlieren images showing: (*a*) no trailing edge shock waves with no flow, and (*b*) a pair of oblique shock waves at the airfoil trailing edge. Flow moves from left to right in each image.

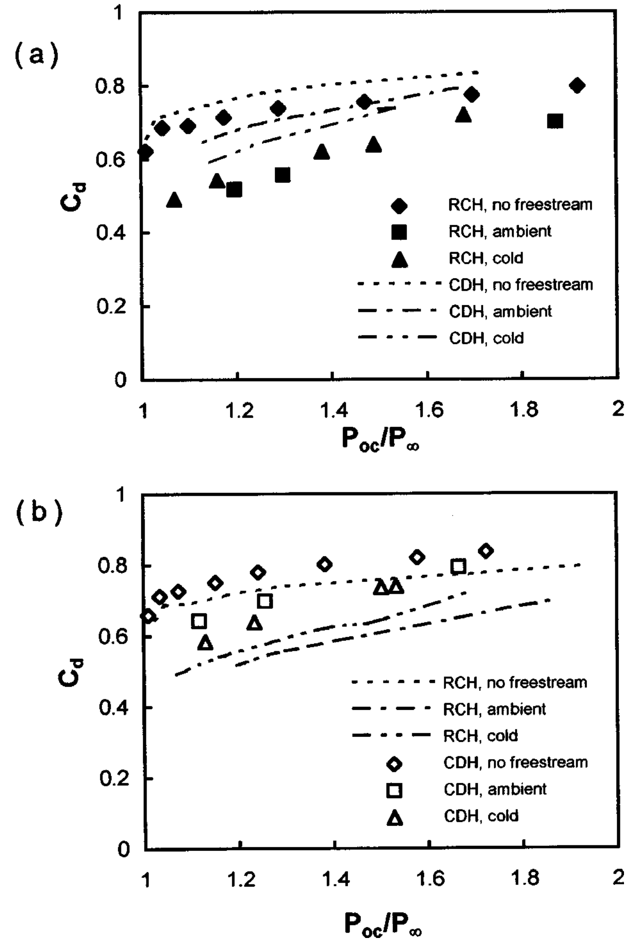

Fig. 7 Discharge coefficients, both with and without free-stream crossflow, as dependent upon coolant to free-stream pressure ratio for: (*a*) round cylindrical holes (RCH), and (*b*) conical diffused holes (CDH)

Discharge coefficients, measured at different injectant to free-stream pressure ratios, are presented in Figs. 7(*a*) and 7(*b*). Data are given with and without free-stream external flow, for both hole configurations, RCH and CDH. With no free-stream external flow, RCH discharge coefficients range from 0.60 to 0.78, whereas CDH values (also with no external flow) are slightly higher when compared at the same pressure ratio. With free-stream external flow, CDH discharge coefficients are higher than RCH values when compared at the same pressure ratio. Differences between ''cold'' and ''ambient'' data sets evidence some dependence on ρ_c/ρ_∞ in these coordinates.

Local Aerodynamic Loss, Mach Number, and Kinetic Energy Distributions—RCH Configuration. Figures 8(*a–c*) and 9(*a–c*) present profiles of normalized inlet total pressure minus exit total pressure C_P, normalized exit Mach number $\mathrm{M}_e/\mathrm{M}_{e\infty}$, and normalized exit kinetic energy KE, where exit refers to values measured one chord length downstream of the airfoil trailing edge. Results for RCH are given in Fig. 8(*a–c*) and results for CDH are given in Figs. 9(*a–c*). As mentioned, film injection test conditions are given in Table 1, where ''cold'' film cooling corresponds to ρ_c/ρ_∞ from 1.01 to 1.23, and ''ambient'' film cooling corresponds to ρ_c/ρ_∞ from 0.82 to 0.95. Note that all film cooling parameters in Table 1 are based on hole *inlet* areas, and that the

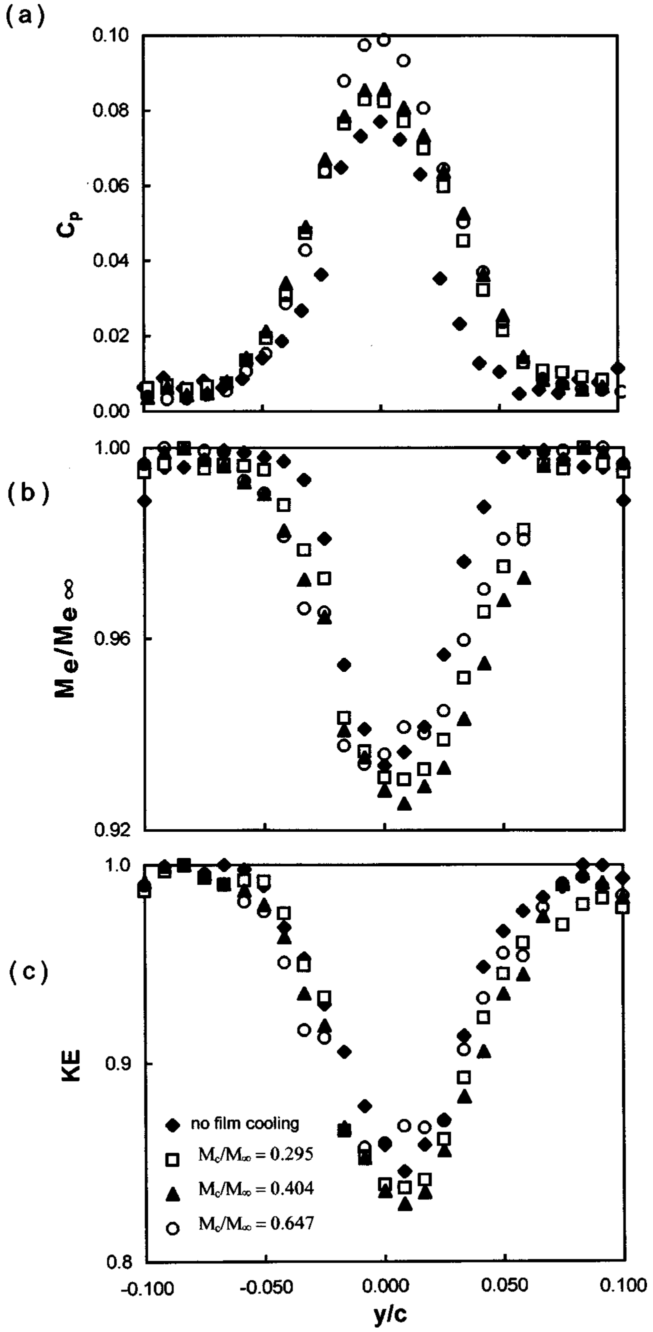

Fig. 8 Profiles measured one chord length downstream of the airfoil for "cold" film injection at $\rho_c/\rho_\infty = 1.0-1.2$ from round cylindrical holes (RCH): (*a*) normalized local total pressure losses, (*b*) normalized Mach number, and (*c*) normalized kinetic energy.

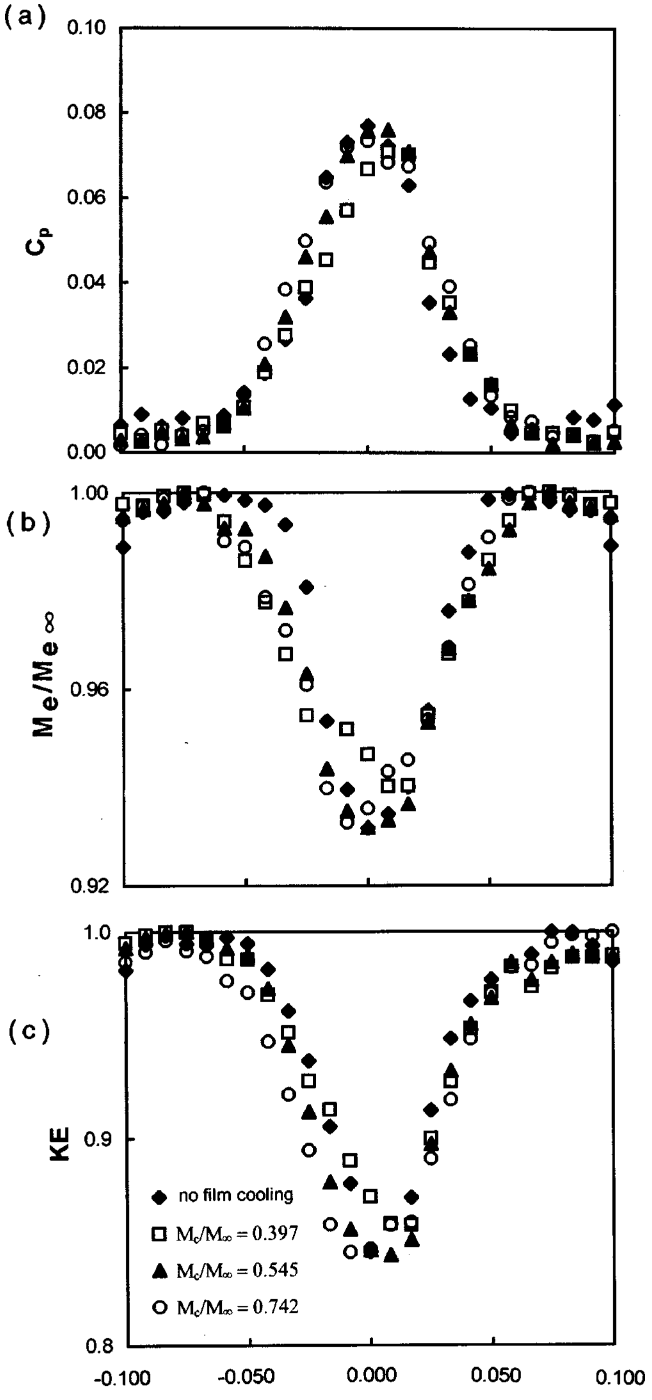

Fig. 9 Profiles measured one chord length downstream of the airfoil for "cold" film injection at $\rho_c/\rho_\infty = 1.0-1.3$ from conical diffused holes (CDH): (*a*) normalized local total pressure losses, (*b*) normalized Mach number, and (*c*) normalized kinetic energy

inlet free-stream stagnation pressure $P_{oi\infty}$ is 196.1 kPa. Results in Figs. 8(*a–c*), and 9(*a–c*) are obtained with "cold" film cooling over a range of film injection conditions.

The nondimensional aerodynamic loss profiles in Figures 8(*a*) and 9(*a*) include contributions from shock waves and mixing. The profiles in Fig. 8(*a*), measured downstream of the RCH configuration, are roughly symmetric with respect to $y/c = 0$, even though the film is ejected only from the top (or positive *y*) side of the airfoil. Such symmetry results because of mixing losses generated immediately downstream of the trailing edge of the airfoil, where gradients in properties across the wake are largest. Turbulent diffusion of streamwise momentum normal to the airfoil symmetry plane is also responsible. As the film injectant Mach number ratio M_c/M_∞ increases from 0 to 0.65, magnitudes of aerodynamic loss increase continuously at $y/c = 0$ and in the middle part of the wake between $y/c = -0.02$ and $y/c = +0.02$. Outside of this region, the most important C_P increase occurs as M_c/M_∞ increases from 0 to 0.30. Thus, the profile measured with no film cooling has the lowest C_P magnitudes of the different wakes investigated.

In addition, changes of wake total pressure profiles in the outer portions of the wakes (at $y/c < -0.02$ and $y/c > +0.02$) are quite small as M_c/M_∞ increases from 0.30 to 0.65.

Normalized Mach number profiles, measured downstream of round cylindrical holes (RCH), are shown in Fig. 8(*b*). $M_e/M_{e\infty}$ values generally decrease with increasing M_c/M_∞ at each y/c. Here, $M_{e\infty}$ is about 0.97–0.98 (with no film cooling), which is consistent with numerical predictions in Fig. 5, and the slight Mach number increase with streamwise distance that occurs at locations *downstream* of the trailing edge shock waves.

Normalized kinetic energy profiles for RCH in Fig. 8(*c*) are also roughly symmetric with respect to $y/c=0$. In the middle parts of the wakes at y/c from -0.05 to $+0.05$, KE magnitudes generally decrease as M_c/M_∞ increases. The only data set with a different trend in Fig. 8(*b*) and 8(*c*) corresponds to $M_c/M_\infty = 0.65$, which, for some positive y/c values only, lies between the $M_c/M_\infty=0$ and $M_c/M_\infty=0.40$ data sets. Such behavior is due to the slightly greater energizing influence of the film at $M_c/M_\infty = 0.65$.

Local Aerodynamic Loss, Mach Number, and Kinetic Energy Distribution—CDH Configuration. Figure 9(*a*) shows an aerodynamic loss profile measured with no film cooling $(M_c/M_\infty=0)$, which is roughly symmetric, and several loss profiles, measured with film cooling, which are somewhat less symmetric with respect to the airfoil symmetry plane at $y/c=0$. These results are obtained using conical diffused holes (CDH) at Mach number ratios from 0 to 0.74. At positive y/c, C_P magnitudes with film cooling are generally greater than the $M_c/M_\infty=0$ profile, and increase with M_c/M_∞ at each location. At negative y/c from 0 to -0.025, C_P magnitudes with film cooling are either about the same as values measured with no film cooling for $M_c/M_\infty=0.74$, or are somewhat less at each y/c for $M_c/M_\infty = 0.40$ and $M_c/M_\infty=0.55$. At other negative y/c, C_P values increase with M_c/M_∞ at each y/c. Recall that the film cooling holes are located on the $+y$ side of the air foil. Overall profile shapes and quantitative magnitudes indicate that losses measured with CDH film cooling are not substantially greater than losses measured with no film cooling. Comparison with results measured downstream of RCH thus shows that the aerodynamic losses have a strong dependence on film cooling hole geometry. Evidence of different mixing losses is also provided by the different levels of symmetry in the aerodynamic loss profiles. Greater profile symmetry at one chord length downstream of the airfoil results from increased mixing. Also important is turbulent diffusion of streamwise momentum in a direction normal to the air foil symmetry plane.

Normalized profiles of kinetic energy KE in Fig. 9(*c*), measured downstream of film cooling with CDH, also show interesting nonsymmetric behavior. Profiles measured with film cooling are about the same as or just less than the no film cooling profile at $y/c>0$. However, at $y/c<0$, profiles are either about the same as the $M_c/M_\infty=0$ profile for $M_c/M_\infty=0.40$, or are increasingly lower than the $M_c/M_\infty=0$ profile as M_c/M_∞ increases, for M_c/M_∞ of 0.55 and 0.74.

Normalized Mach number profiles in Fig. 9(*b*) show similar qualitative trends. Values are in rough agreement with the $M_c/M_\infty=0$ profile at $y/c>0$, and substantially different from the $M_c/M_\infty=0$ profile at $y/c<0$. Thus, even though the film cooling holes are located on the top (or $+y/c$ side) of the airfoil, the largest changes to the Mach number and kinetic energy profiles occur on the $-y/c$ side. This is believed to be due to slight changes to $M_{e\infty}$ and $(P_{oe}-P_e)_\infty$ produced by the film. Also affecting profile shapes are the film trajectories from the CDH configuration, particularly the locations of the largest film concentrations very near to the airfoil surface. As these concentrations approach the trailing edge, they alter the strengths and orientations of the trailing edge shock waves. Additional details are provided in the next section.

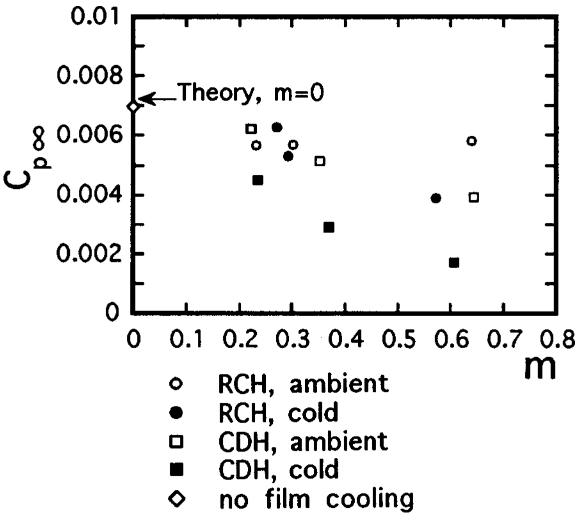

Fig. 10 Normalized total pressure losses in the free stream due to trailing edge, oblique shock waves as dependent upon blowing ratio for round cylindrical holes (RCH) and conical diffused holes (CDH)

Aerodynamic Losses Due to Trailing Edge Shock Waves. In Figs. 8(*a*) and 9(*a*), wake total pressure deficits extend to $y/c = \pm 0.07$ from the airfoil symmetry line at $y/c=0$. Outside of this region, in the free stream, magnitudes of $P_{oi\infty}-P_{oe\infty}$ are nonzero, ranging from 0.3–1.6 kPa (which correspond to C_P from 0.002 to 0.007) because of the pair of trailing edge oblique shock waves shown in Figs. 5 and 6.

Magnitudes of free-stream pressure coefficient $C_{p\infty}$, deduced from these free-stream pressures, are given as dependent upon blowing ratio in Fig. 10. These data thus represent aerodynamic losses due to the trailing edge oblique shock waves only. Even though experimental uncertainties are relatively high relative to the magnitudes of these data, consistent trends are apparent. The most important of these is the decrease of $C_{p\infty}$ with *m* for ''ambient'' and ''cold'' CDH injection as well as for ''cold'' RCH injection. Values with film cooling are also lower than the $m=0$ no film cooling value, which is in agreement with oblique shock wave theory given by Anderson [29]. As $C_{p\infty}$ decreases with increasing *m*, shock wave angles (measured relative to the airfoil symmetry plane) become increasingly larger than 73 deg (the no film cooling value evidenced by the Schlieren results in Fig. 6). This happens because the film increases the effective thickness of the airfoil trailing edge, which results in less expansion through the airfoil passage. As a result, the flow deflection angle at the trailing edge decreases, along with Mach numbers downstream of film hole locations. The trailing edge shock waves are thus weakened by CDH film cooling and ''cold'' RCH film cooling as blowing ratio increases since normalized total pressure drops across them are smaller. Eventually, the oblique shock waves disappear as shock wave angles approach 90 deg. Figure 10 shows that the largest $C_{p\infty}$ decreases with blowing ratio occur with CDH films rather than with RCH films. This is because larger concentrations of CDH film remain closer to the surface as the film advects to the airfoil trailing edge. Lower $C_{p\infty}$ values and weaker oblique shock waves also result as the density ratio increases since lower momentum flux ratios enhance this effect.

Integrated Aerodynamic Loss Distributions. In determining magnitudes of the integrated aerodynamic losses, IAL contributions from the oblique shock waves in the free stream are removed from total pressure profiles, such as the ones presented in Figs. 8(*a*) and 9(*a*). This is accomplished by subtracting off the constant free-stream value of $(P_{oi\infty}-P_{oe\infty})/P_{oi\infty}$ throughout each C_P profile. This gives corrected profiles of $(P_{oe\infty}-P_{oe})/P_{oi\infty}$,

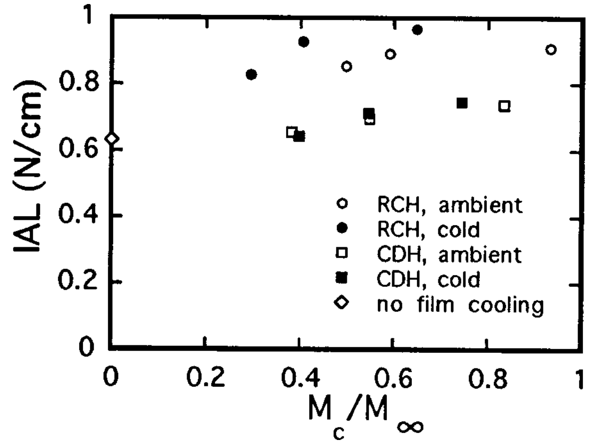

Fig. 11 **Comparison of integrated aerodynamic losses as dependent upon Mach number ratio from round cylindrical holes (RCH) and conical diffused holes (CDH), after correction for the presence of trailing edge oblique shock waves**

which, of course, equal zero in the free stream. Profiles of $(P_{oe\infty}-P_{oe})$ are then integrated with respect to y to determine IAL values at each film injection flow condition. IAL magnitudes thus represent mixing losses only without the contributions of the shock waves.

Such IAL magnitudes are presented in Fig. 11 as dependent upon Mach number ratio, M_c/M_∞, for all test conditions tabulated in Table 1. Included is the integrated aerodynamic loss magnitude for no film cooling at $M_c/M_\infty=0$. In all cases, values measured with film cooling are higher than the no film cooling value.

Figure 11 also shows important variations with film cooling hole geometry since integrated losses measured downstream of RCH are substantially higher than CDH magnitudes (when compared at the same Mach number ratio M_c/M_{oc}). The two hole configurations additionally show different dependencies on the density ratio. IAL values measured downstream of CDH increase continuously with M_c/M_∞ with about the same magnitudes for "ambient" and "cold" film injection. In contrast, RCH integrated aerodynamic losses increase with density ratio at each M_c/M_∞. When compared at the same momentum flux ratio I in Fig. 12, changes with density ratio for both hole configurations are somewhat less.

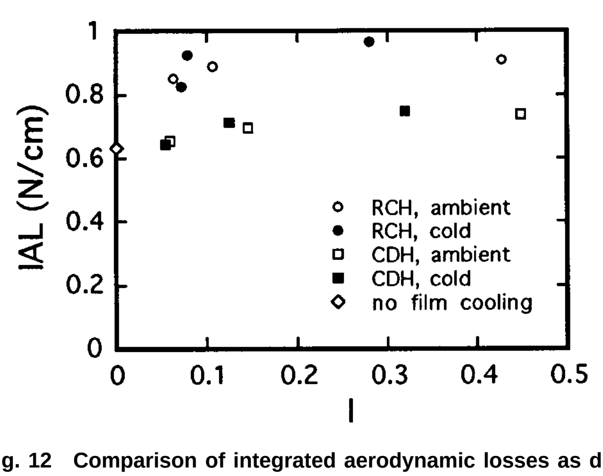

Fig. 12 **Comparison of integrated aerodynamic losses as dependent upon momentum flux ratio from round cylindrical holes (RCH) and conical diffused holes (CDH), after correction for the presence of trailing edge oblique shock waves**

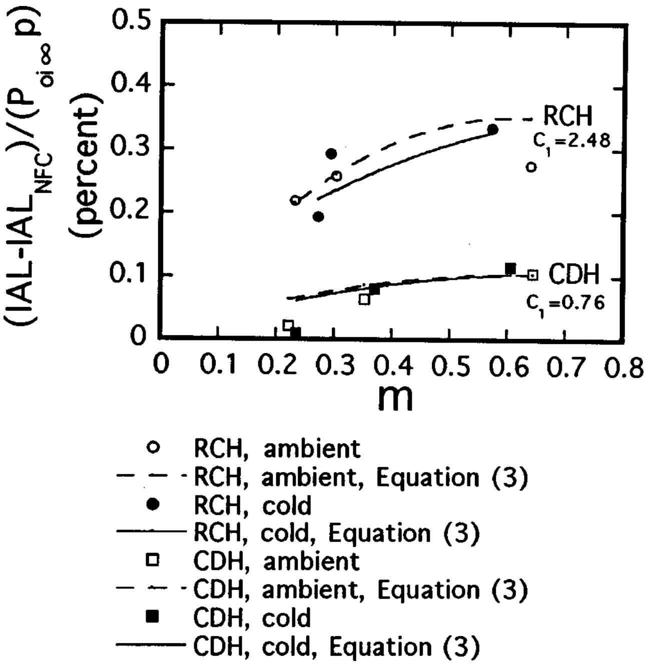

Fig. 13 **Comparison of normalized integrated aerodynamic losses relative (minus integrated aerodynamic losses with no film cooling) at different blowing ratios (after correction for the presence of trailing edge oblique shock waves) with correlating Eq. (3)**

The same data are shown in normalized form after subtracting off the IAL value for no film cooling in Fig. 13. Values are compared with the one-dimensional mixing loss equation given by

$$(\mathrm{IAL}-\mathrm{IAL}_{\mathrm{NFC}})/pP_{oi\infty}=C_1[kM_\infty^2/2](\dot{m}_c/\dot{m}_\infty)B \qquad (3)$$

where $C_1=0.76$ for CDH and $C_1=2.48$ for RCH, and

$$B=[1+T_{oc}/T_{oi\infty}-[2(u_c/u_\infty)\cos\theta]] \qquad (3)$$

In this equation, M_∞, $\dot{m}_\infty$, and u_∞ are free-stream values at the streamwise locations of the film cooling holes. Equation (3) shows good agreement with CDH data in Fig. 13, including its dependence on density ratio, for blowing ratios m greater than 0.3. The correlating equation also shows agreement with most of the RCH data, including its dependence on density ratio since "ambient" values are higher than "cold" values at each m. The decrease of RCH "ambient" data as m increases (for $m>0.6$ in Fig. 13) is consistent with data presented by Kubo et al. [24] as well as the C_P profiles in Fig. 8(*a*).

Summary and Conclusions

Local and integrated aerodynamic losses, Mach number profiles, and kinetic energy distributions are given for Mach number ratios from 0.3 to 0.9, coolant stagnation to free-stream static pressure ratios from 1.1 to 1.9, and density ratios from 0.8 to 1.3. These are measured using symmetric turbine airfoils with two different film cooling hole configurations located just downstream of the passage throat where the free-stream Mach number is nominally 1.07: (*i*) simple angle, round cylindrical holes (RCH), and (*ii*) simple angle, conical diffused holes (CDH). The University of Utah Transonic Wind Tunnel is employed for the tests. This facility provides excellent test section inlet uniformity, steady flow properties over time intervals as long as 45 seconds, and a Mach number distribution over the airfoil ranging from 0.4 to 1.24, which matches the distribution on the suction surface of airfoils from operating gas turbine engines.

Comparing Figs. 8(*a*) and 9(*a*) to Fig. 10 shows that the aerodynamic losses due to mixing are significantly greater than those due to oblique trailing edge shock waves. Contributions to total pressure coefficient profiles from the two types of losses are separated by assuming that shock losses are the same magnitude at all y/c throughout the wake and adjacent free-stream flows. In some cases, the cooling films reduce the strength of the shock waves (and the associated aerodynamic losses) by greater amounts as the blowing ratio increases, particularly with higher density ratio films from the CDH configuration. Such decreases are evidenced by reduced free-stream pressure coefficients, which are accompanied by increased shock wave angles and smaller flow deflection angles.

Integrated aerodynamic mixing losses, measured one chord length downstream of the airfoil (and with the effects of the trailing edge oblique shock waves removed) are higher with film cooling than without. For each hole configuration investigated, integrated losses generally increase with injectant Mach number ratio as the film to free-stream density ratio is approximately constant. Integrated aerodynamic losses are significantly lower with conical diffused holes than with cylindrical holes (three times when compared at the same blowing ratio), which illustrates the strong dependence of aerodynamic mixing losses on film hole geometry. Such behavior is due to different amounts of mixing just downstream of the airfoils and different turbulent diffusion of streamwise momentum in a direction normal to the airfoil symmetry plane, both of which are evidenced by different aerodynamic loss profile magnitudes and levels of symmetry. Much of the normalized integrated aerodynamic loss data are well represented by correlating Eq. (3), including their dependence on film cooling hole geometry, blowing ratio, and density ratio.

For the RCH hole configuration, integrated aerodynamic mixing losses increase somewhat with injectant-to-free-stream density ratio at each Mach number ratio. Much smaller changes with density ratio are present with the CDH configuration. When compared at the same momentum flux ratio, changes due to density ratio are somewhat less for both film hole configurations, which is consistent with Mee [14], Day et al. [21], and Osnaghi et al. [22].

Discharge coefficients with free-stream crossflow are lower than values measured with no free-stream flow. The CDH configuration is again advantageous in this respect over the RCH configuration, since CDH discharge coefficients at particular coolant-to-free-stream pressure ratios are higher.

Acknowledgments

This work was sponsored, in part, by Pratt & Whitney—Florida. Dr. F. O. Soechting is acknowledged for his support.

Nomenclature

A = area
c = airfoil chord
C_1 = correlation constant
C_D = discharge coefficient
C_P = pressure coefficient $=(P_{oi\infty}-P_{oe})/P_{oi\infty}$
d = diameter of the film cooling hole entrances
I = momentum flux ratio
IAL = integrated aerodynamic losses
k = ratio of specific heats
KE = normalized kinetic energy $=(P_{oe}-P_e)/(P_{oe}-P_e)_\infty$
M = Mach number
m = blowing ratio
$\dot{m}$ = mass flow rate
p = airfoil passage effective pitch
P = pressure
R = gas constant
T = temperature
u = velocity
x = linear distance along airfoil centerline from airfoil leading edge
X = streamwise coordinate from test section inlet
y, Y = normal coordinate measured from airfoil centerline
θ = film cooling holes inclination angle
ρ = density

Subscripts

c = injectant or film coolant value at exit planes of film cooling holes
∞ = local free-stream value
i = inlet of test section
e = exit of test section
NFC = no film cooling
o = total or stagnation
ideal = ideal isentropic value

References

[1] Denton, J. D., 1993, ‘‘Loss Mechanisms in Turbomachines,’’ ASME J. Turbomach., **115**, pp. 621–656.
[2] Hoheisel, H., Kiock, R., Lichtfuss, H. J., and Fottner, L., 1987, ‘‘Influence of Free Stream Turbulence and Blade Pressure Gradient on Boundary Layer and Loss Behavior of Turbine Cascades,’’ ASME J. Turbomach., **109**, pp. 210–219.
[3] Gregory-Smith, D. G., and Cleak, J. G. E., 1992, ‘‘Secondary Flow Measurements in a Turbine Cascade With High Inlet Turbulence,’’ ASME J. Turbomach., **114**, pp. 173–180.
[4] Ames, F. E., and Plesniak, M. W., 1997, ‘‘The Influence of Large-Scale, High-Intensity Turbulence on Vane Aerodynamic Losses, Wake Growth, and the Exit Turbulence Parameters,’’ ASME J. Turbomach., **119**, pp. 182–192.
[5] Moore, J., Shaffer, D. M., and Moore, J. G., 1987, ‘‘Reynolds Stress and Dissipation Downstream of a Turbine Cascade,’’ ASME J. Turbomach., **109**, pp. 258–266.
[6] Xu, L., and Denton, J. D., 1988, ‘‘The Base Pressure and Loss of a Family of Four Turbine Blades,’’ ASME J. Turbomach., **110**, pp. 9–17.
[7] Mee, D. J., Baines, N. C., Oldfield, M. L. G., and Dickens, T. E., 1992, ‘‘An Examination of the Contributions to Loss on a Transonic Turbine Blade in Cascade,’’ ASME J. Turbomach., **114**, pp. 155–162.
[8] Izsak, M. S., and Chiang, H.-W. D., 1993, ‘‘Turbine and Compressor Wake Modeling for Blade Forced Response,’’ ASME Paper No. 93-GT-238.
[9] Michelassi, V., Rodi, W., and Giess, P.-A., 1997, ‘‘Experimental and Numerical Investigation of Boundary-Layer and Wake Development in a Transonic Turbine Cascade,’’ ASME Paper No. 97-GT-483.
[10] Joe, C. R., Montesdeoca, X. A., Soechting, F. O., MacArthur, C. D., and Meininger, M., 1998, ‘‘High Pressure Turbine Vane Annular Cascade Heat Flux and Aerodynamic Measurements With Comparisons to Predictions,’’ ASME Paper No. 98-GT-430.
[11] Ito, S., Eckert, E. R. G., and Goldstein, R. J., 1980, ‘‘Aerodynamic Loss in a Gas Turbine Stage With Film Cooling,’’ ASME J. Eng. Power, **102**, pp. 964–970.
[12] Haller, B. R., and Camus, J. J., 1984, ‘‘Aerodynamic Loss Penalty Produced by Film Cooling Transonic Turbine Blades,’’ ASME J. Eng. Gas Turbines Power, **106**, pp. 198–205.
[13] Kollen, O., and Koschel, W., 1985, ‘‘Effect of Film-Cooling on the Aerodynamic Performance of a Turbine Cascade,’’ AGARD CP-390.
[14] Mee, D. J., 1992, ‘‘Techniques for Aerodynamic Loss Measurement of Transonic Turbine Cascades With Trailing-Edge Region Coolant Ejection,’’ ASME Paper No. 92-GT-157.
[15] Michelassi, V., Martelli, F. and Amecke, J., 1994, ‘‘Aerodynamic Performance of a Transonic Turbine Guide Vane With Trailing Edge Coolant Ejection: Part II—Numerical Approach,’’ ASME Paper No. 94-GT-248.
[16] Bohn, D. E., Becker, V. J., Behnke, K. D., and Bonhoff, B. F., 1995, ‘‘Experimental and Numerical Investigations of the Aerodynamical Effects of Coolant Injection Through the Trailing Edge of a Guide Vane,’’ ASME Paper No. 97-GT-23.
[17] Kapteijn, C., Amecke, J., and Michelassi, V., 1996, ‘‘Aerodynamic Performance of a Transonic Turbine Guide Vane With Trailing Edge Coolant Ejection: Part I—Experimental Approach,’’ ASME J. Turbomach., **118**, pp. 519–528.
[18] Vlasic, E. P., Girgis, S., and Moustapha, S. H., 1996, ‘‘The Design and Performance of a High Work Research Turbines,’’ ASME J. Turbomach., **118**, pp. 792–799.
[19] Sieverding, C. H., Arts, T., Denos, R., and Martelli, F., 1996, ‘‘Investigation of the Flow Field Downstream of a Turbine Trailing Edge Cooled Nozzle Guide Vane,’’ ASME J. Turbomach., **118**, pp. 291–300.
[20] Tanuma, T., Shibukawa, N., and Yamamoto, S., 1997, ‘‘Navier–Stokes Analysis of Unsteady Transonic Flows Through Gas Turbine Cascades With and Without Coolant Ejection,’’ ASME Paper No. 97-GT-479.
[21] Day, C. R. B., Oldfield, M. L. G., and Lock, G. D., 1999, ‘‘The Influence of Film Cooling on the Efficiency of an Annular Nozzle Guide Vane Cascade,’’ ASME J. Turbomach., **121**, pp. 145–151.
[22] Osnaghi, C., Perdichizzi, A., Savini, M., Harasgama, P., and Lutum, E., 1997, ‘‘The Influence of Film-Cooling on the Aerodynamic of a Turbine Nozzle Guide Vane,’’ ASME Paper No. 97-GT-522.
[23] Hong, Y., Fu, C., Cunzhong, G., and Zhongqi, W., 1997, ‘‘Investigation of Cooling-Air Injection on the Flow Field Within a Linear Turbine Cascade,’’ ASME Paper No. 97-GT-520.

[24] Kubo, R., Otomo, F., Fukuyama, Y., and Nakata, T., 1998, ''Aerodynamic Loss Increase Due to Individual Film Cooling Injections From Gas Turbine Nozzle Surface,'' ASME Paper No. 98-GT-497.

[25] Urban, M. F., Hermeler J., and Hosenfeld H.-G., 1998, ''Experimental and Numerical Investigations of Film-Cooling Effects on the Aerodynamic Performance of Transonic Turbine Blades,'' ASME Paper No. 98-GT-546.

[26] Jackson, D. J., 1998, ''Aerodynamic Mixing Losses and Discharge Coefficients Due to Film Cooling From a Symmetric Turbine Airfoil in Transonic Flow,'' M. S. Thesis, Department of Mechanical Engineering, University of Utah.

[27] Lee, K. L., 1998, ''Aerodynamic Losses and Discharge Coefficients for a Transonic Turbine Blade With Film Cooling,'' M. S. thesis, Department of Mechanical Engineering, University of Utah.

[28] Kline, S. J., and McClintock, F. A., 1953, ''Describing Uncertainties in Single Sample Experiments,'' Mech. Eng., **75**, Jan., pp. 3–8.

[29] Anderson, J. D., 1990, *Modern Compressible Flow*, McGraw-Hill, New York.

Influence of Internal Flow on Film Cooling Effectiveness

Günter Wilfert[1]
ABB Corporate Research Ltd.,
CH-5405 Baden-Dättwil, Switzerland

Stefan Wolff
Institut für Strahlantriebe,
Universität der Bundeswehr München,
D-85577 Neubiberg, Germany

Film cooling experiments were conducted to investigate the effects of internal flow conditions and plenum geometry on the film cooling effectiveness. The film cooling measurements show a strong influence of the coolant inlet conditions on film cooling performance. The present experiments were carried out on a flat plate with a row of cylindrical holes oriented at 30 deg with respect to a constant-velocity external flow, systematically varying the plenum geometry and blowing rates ($0.5 \leqslant M \leqslant 1.25$). Adiabatic film cooling measurements using the multiple narrow-banded thermochromic liquid crystal technique (TLC) were carried out, simulating a flow parallel to the mainstream flow with and without crossflow at the coolant hole entry compared with a standard plenum configuration. An impingement in front of the cooling hole entry with and without crossflow was also investigated. For all parallel flow configurations, ribs were installed at the top and bottom coolant channel wall. As the hole length-to-diameter ratio has an influence on the film cooling effectiveness, the wall thickness has also been varied. In order to optimize the benefit of the geometry effects with ribs, a vortex generator was designed and tested. Results from these experiments show in a region $5 \leqslant X/D \leqslant 80$ downstream of the coolant injection location differences in adiabatic film cooling effectiveness between +5 percent and +65 percent compared with a standard plenum configuration.
[S0889-504X(00)01102-8]

Introduction

Rising turbine inlet temperatures have led to extensive use of film cooling technology and research work within this area. The review by Goldstein [1] delineates much of the physics of film cooling, especially the jet in crossflow behavior. In film cooling literature a large number of parameters have been investigated with numerical and experimental methods, for example, Ardey and Fottner [2], Chernobrovkin and Lakshminarayana [3], Leylek and Zerkle [4], Papell [5], Sinha et al. [6], and Walters and Leylek [7] but most of them used a classical plenum for hole supply. Modern cooled turbine vane (Fig. 1) cooling configurations combine convective impingement and film cooling. Therefore, a classical plenum configuration is hardly used, but hole configurations supply parallel flow at the cooling hole entrance. The inlet flow conditions to the film cooling holes are different for nearly every hole position.

Wilfert [8] and Vogel [9,10] investigated vortex generation and mixing behavior on a scaled airfoil at real turbomachinery flow conditions. Their experimental and numerical results showed a significant influence of inner contouring on mixing behavior and film cooling performance. Thole et al. [11], Wittig et al. [12], and Gritsch et al. [13] varied hole supply Mach number, flow angle, hole geometry, and inclination angle, and showed a significant influence on the hole exit and downstream flow field and on the film cooling performance. They used a two-dimensional coolant channel with $H/D=2$. Berhe and Patankar [14] found an influence of the internal flow for $H/D \leqslant 2$. Burd and Simon [15] determined differences up to 20 percent in lateral averaged adiabatic effectiveness between a plenum and a parallel crossflow configuration ($H/D=2$; $VR=1$).

The present study is based on a development that intensifies the positive effects of parallel cross flow shown in Fig. 2 with ribs at the top and bottom wall of the coolant supply channel. In order to get valuation criteria for actual hole supply configuration designs, an investigation on four different internal flow configurations, and a classical plenum as a reference were carried out, systematically measuring adiabatic film cooling effectiveness. Low and high turbulent coolant flows were simulated with and without crossflow. Additionally the length of the film cooling hole was varied.

Experimental Apparatus

The adiabatic film cooling experiments were conducted in a subsonic open-circuit wind tunnel with a straight channel test sec-

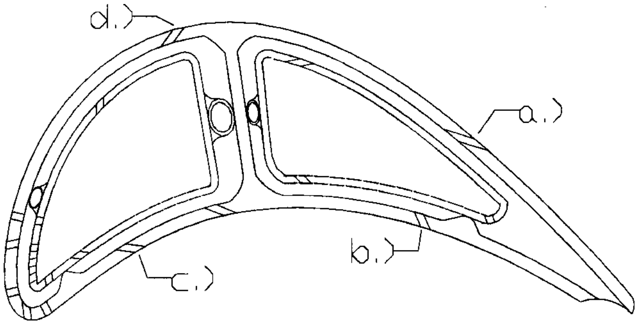

a.) parallel & cross flow
b.) parallel & no cross flow
c.) impingement & cross flow
d.) impingement & no cross flow

Fig. 1 Cross section of a combined cooled turbine blade

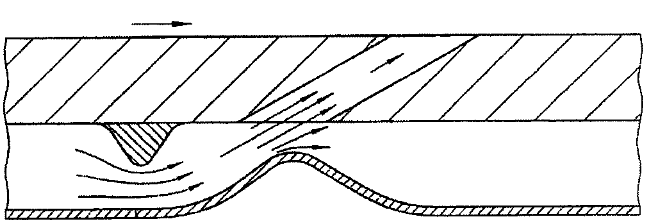

Fig. 2 Internal geometry for improved vane cooling

---

[1] Present address: MTU Motoren- und Turbinen-Union, München, Germany.

Contributed by the International Gas Turbine Institute and presented at the 44th International Gas Turbine and Aeroengine Congress and Exhibition, Indianapolis, Indiana, June 7-10, 1999. Manuscript received by the International Gas Turbine Institute February 1999. Paper No. 99-GT-258. Review Chair: D. C. Wisler.

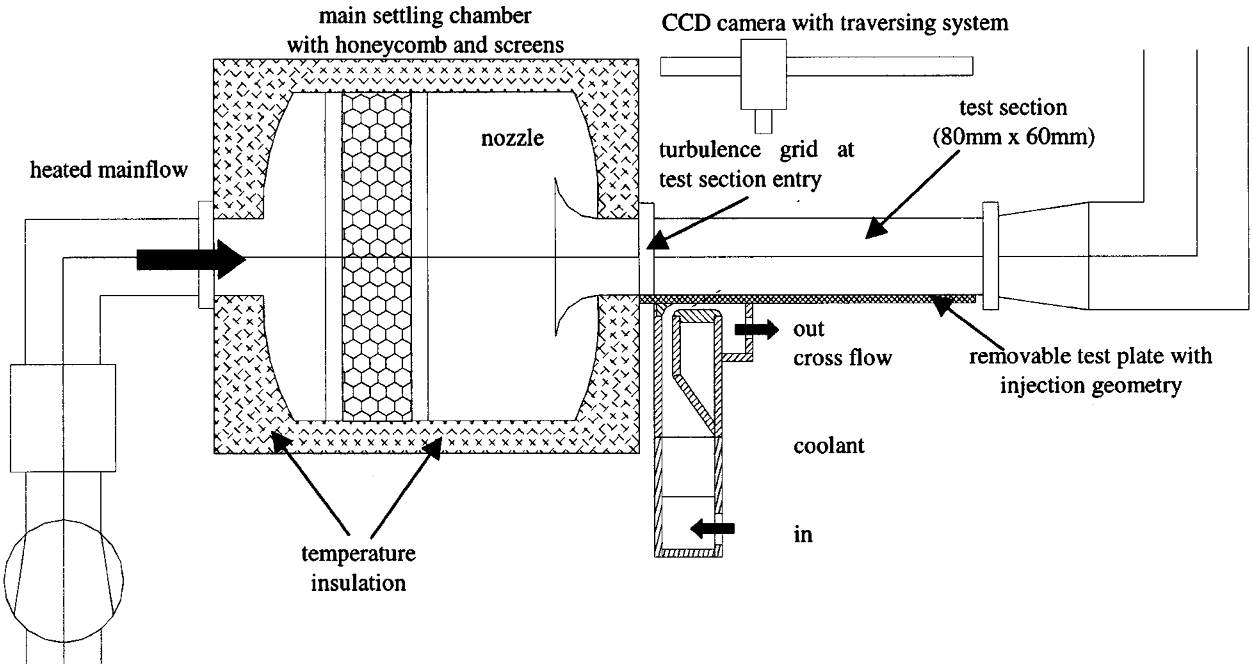

Fig. 3 Straight channel test facility

tion shown in Fig. 3. Ambient air was compressed by an electrical blower. Free-stream air was heated in a range of 60°C to 70°C by an electrical heater before it entered the settling chamber. The hot air path and the settling chamber were insulated in order to minimize temperature differences of the incoming flow. An assembly of honeycomb and a series of screens homogenized the flow inside the settling chamber. The flow accelerated through the nozzle with a 10:1 contraction ratio into the test section.

A turbulence grid was placed at the test section entrance to increase the free-stream turbulence intensity. This turbulence grid consisted of 3×3 mm rectangular holes that were spaced 4 mm in width and height from one hole center to the next hole center. The streamwise decay of the free-stream turbulence intensity was determined in previous measurements on this test facility ($Tu_\infty = 5.0$ percent at $X/D = 18$, $Tu_\infty = 3.5$ percent at $X/D = 0$, and $Tu_\infty = 2.0$ percent at $X/D = 40$). The approaching boundary layer was turbulent with a boundary layer thickness of about 4 mm at the injection location. The displacement thickness at this location was determined to be 0.5 mm. The free-stream velocity level was about $U_\infty = 115$ m/s.

A second pressurized air supply system of the lab delivered the cooling mass flow at an ambient temperature level of about 20°C. The incoming cooling mass flow was accurately determined by means of a turbine wheel meter (1 percent measurement uncertainty) and piped into the cooling air settling chamber, where the air passed through a set of flow-straightening devices to minimize flow disturbances. Thereafter, the coolant flow was accelerated into a vertical channel of $H/D = 3$ and turned into horizontal direction by a bend with another contraction of the channel to $H/D = 2$. Ribs are placed on the top and bottom side of the coolant passage (Fig. 5(*a*)) in order to optimize the inflow into the cooling holes. The cooling air was injected into the heated free-stream flow through a single row of cylindrical holes at selected blowing rates in the range of $0.5 \leqslant M \leqslant 1.25$. To simulate crossflow conditions at the hole entry, a part of the mass flow was sucked off at the end of the coolant channel and measured by means of a second turbine wheel. The injected cooling mass flow was determined by the difference between the incoming and outgoing mass flow with an accuracy of better than 4 percent.

The typical density ratio for all experiments conducted was DR = 1.15. For the impingement configurations, the bend was replaced by a row of 10 holes ($D_i = 1.25D$; $P_i/D_i = 2$) to impinge the cooling gas $20D$ upstream on the top wall of the coolant channel (Fig. 4, right side).

The dimensions of the hot gas flow channel in the straight test section were 80 mm in width and 60 mm in height with top and side walls constructed of polycarbonate material. The polycarbonate walls allowed optical access to the test surface. A color CCD camera was arranged to observe the test surface through the top wall of the test section. Secondary air was injected after 90 mm of the total test section length of 600 mm. The bottom wall of the straight channel, the actual test surface, held the different injection configurations investigated. The use of low conductivity material (Necurom, $k = 0.1$ W/m/K) and additional thermal insulation applied below this test surface kept the heat losses to low values. Temperature measurement errors due to heat losses were determined to be less than 0.05°C by a two-dimensional heat conduction analysis.

Figure 5 shows the top and side view of the removable test plate and illustrates the injection configurations. All configurations consisted of a single row of five cylindrical holes. The hole spacing in lateral direction corresponded to a pitch-to-diameter ratio of $P/D = 4$. The hole channels were inclined at $\alpha = 30$ deg with respect to the free-stream flow direction. The hole length-to-diameter ratio of the injection channels was varied from $L/D = 4$ (Fig. 5(a)) to $L/D = 8$ (Fig. 5(b)), by increasing the test plate thickness from 8 to 16 mm.

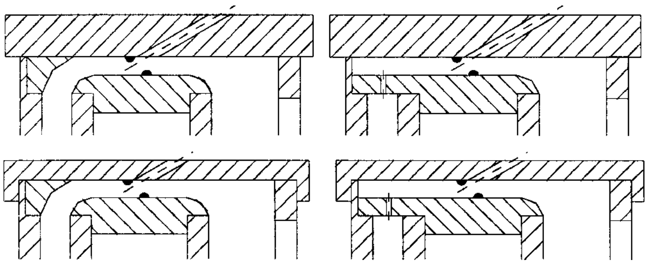

Fig. 4 Injection configurations

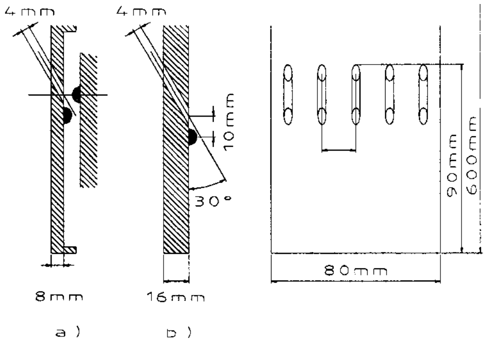

Fig. 5 Injection configurations ($P/D=4$): (a) $L/D=4$; (b) $L/D=8$

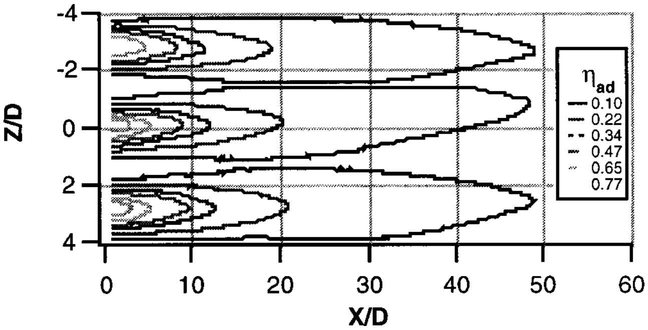

Fig. 6 Typical TLC contours of film cooling effectiveness values at a low blowing rate

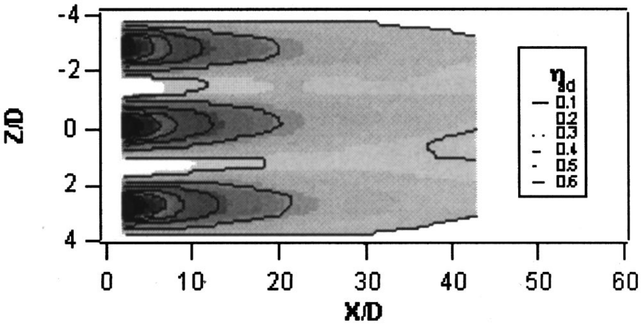

Fig. 7 Typical interpolated film cooling effectiveness data at a low blowing rate

Data Analysis

Adiabatic film cooling data were obtained using the well-established thermochromic liquid crystal technique (TLC) to measure the adiabatic wall temperature distribution. Isothermal temperature patterns due to film cooling on the adiabatic test plate were indicated by a mixture of four narrow-banded thermochromic liquid crystals and were recorded by a color CCD camera in conjunction with a color image processing system. All additional experimental data, i.e., temperature, pressure, and mass flow information of the main and secondary flow, was stored by a separate data acquisition system for later data reduction purposes.

To achieve an accurate measurement of the wall temperature using the TLC's, a special apparatus was built to conduct temperature calibration of the TLC indication temperatures inside the film cooling test section. The calibration was conducted by interchanging the test plate with a copper calibration plate. A linear temperature distribution was achieved by heating one end of this plate and cooling the other end. Determination of the TLC temperature indications on the copper surface was obtained with the same color image processing system used for the film cooling measurements. Thermocouples, embedded in the copper surface, were used to measure the temperature distribution over the plate length. The experimental uncertainty of the local film cooling effectiveness values was determined by an uncertainty analysis to be less than 0.01 [16]. To investigate the influence of the backside flow on the test surface, two-dimensional heat flux calculations were performed. Only for the results up to $X/D=7$ for the thin test surface ($L/D=4$) was an influence of the increased convective heat flux due to the coolant crossflow determined.

During the experiments, the TLC data were captured using a color CCD camera in conjunction with a color image processing system. A complete data set was compiled using up to six adjacent smaller images. The camera was mounted above the experimental apparatus on a traverse system controlled by a stepping motor, allowing all pictures to be taken with the same reference points. Using multiple images to build up the final picture allowed higher resolution and better isothermal definition of the adiabatic wall temperature distributions. The temperature indications of the TLC's were assumed to be the adiabatic wall temperatures. The free-stream temperature was measured by a total temperature probe at $X/D=-10$ upstream of the injection location. The coolant temperature was measured by a thermocouple in the coolant settling chamber. With the additional information of the coolant and free-stream temperatures, these isothermal contour lines were recalculated to adiabatic film cooling effectiveness contours as shown in Fig. 6 by the following equation:

$$\eta_{ad}=\frac{T_{\infty}-T_{\mathrm{TLC}}}{T_{\infty}-T_{c}} \tag{1}$$

For the calculation of the lateral averaged film cooling effectiveness values, a special interpolation technique was used. The field of interpolation was determined over a range of two pitches (three holes) in the lateral direction. In the streamwise direction it was depending on the input data set, respectively (Fig. 7). For details see Lutum and Johnson [16].

Finally, an integration in the lateral direction was performed to determine the lateral averaged film cooling effectiveness data at each streamwise position. The estimated integration error based on the experimental and interpolation uncertainty was about 1 to 3 percent of the streamwise local lateral averaged film cooling effectiveness. The uncertainty depends on the effectiveness level, with the higher uncertainty corresponding to lower effectiveness values.

Present Results

The test program comprises five configurations (Table 1) with different inlet flow conditions. Configuration 1 is a classical plenum. where the coolant is sucked in from a chamber, whereas the other configurations have a supply channel parallel to the mainstream direction. For configurations 2 and 3 a bend is used to direct the coolant in horizontal direction, whereas for configurations 4 and 5 the coolant impinges on the upper wall of the coolant supply channel. To simulate crossflow conditions (configurations 2 and 4), a part of the cooling gas is sucked off downstream of the supply channel. The crossflow Mach numbers inside of the supply channel ($\mathrm{Ma}_{c,cr}$) upstream and downstream of the cooling hole entrance are given in Table 1. The various blowing ratios were investigated for $L/D=4$ and $L/D=8$. Additional investigations were performed without guiding ribs.

In Fig. 8 the results for $L/D=8$ and $L/D=4$ of configuration 1 (plenum) are compared with the results of Lutum and Johnson [16]. The film cooling effectiveness is in the expected range considering that Lutum and Johnson used a film cooling configuration with an inclination angle α=35 deg and a blowing rate of $M=1.15$ (configuration 1, α=30 deg, $M=1.0$). Detailed validation of the test facility can be found in Lutum and Johnson [16].

Table 1 Measurement program

Sketch	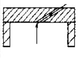	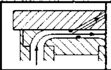	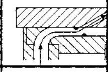	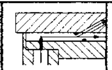	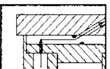
Nr.:	Conf. 1	Conf. 2	Conf. 3	Conf. 4	Conf. 5
$Ma_{c,cr}$ up/ downstream	0.00 0.00	0.12 0.08	0.02 0.00	0.12 0.08	0.02 0.00
M =	0.5 – 1.25				
Ribs	-	With & without ribs			
L/D =	8 & 4				

Measurements of adiabatic film cooling effectiveness for selected hole supply configurations ($L/D=8$), are presented in Figs. 9–14. All results are shown with the dimensionless streamwise coordinate X/D. Configuration 4 with a simulated impingement flow and a crossflow is used to show the differences to the plenum configuration. The film cooling effectiveness distributions for these two configurations are shown in Figs. 9 and 10. The adiabatic film cooling distribution for configuration 1, given in Fig. 9 ($L/D=8$), shows a typical pattern of effectiveness with high values just behind the injection location and a lateral spreading of the cooling film further downstream. The distribution of the impingement with crossflow configuration (configuration 4) indicates a higher maximum value of 0.5 up to $X/D=9$ and larger areas in lateral and streamwise directions with effectiveness values over 10 percent. However this kind of graphic presentation is not useful when attempting to create quantitative performance comparisons between different film cooling setups. Therefore, the lateral averaged film cooling effectiveness is used to appraise all configurations. These values and variations from a reference case give an easy way to compare different configurations.

The plenum configuration (Fig. 11) shows rapidly decreasing film cooling effectiveness downstream of the injection location for $M=0.5$. The higher blowing ratios start with lower effectiveness, but level off at higher values further downstream, especially at $M=1.0$ and $M=0.75$.

The impingement with crossflow configuration (Fig. 12) shows the same performance for $M=0.5$, but different progressions for higher blowing ratios. The effectiveness near the hole is higher for $M=1.0$ and $M=1.25$, and for $M=1.0$ the decrease in effectiveness in streamwise direction is less rapid than for the plenum configuration. All configurations level off at higher effectiveness at $X/D=80$.

Comparisons of the tested configurations are represented by the improvement of lateral averaged film cooling effectiveness, setting the plenum configuration at 100 percent as a reference.

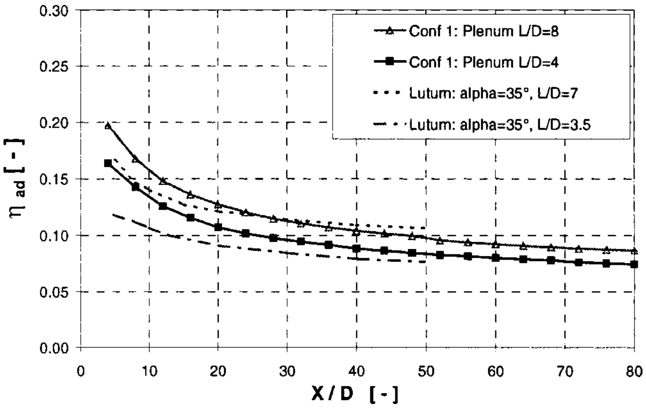

Fig. 8 Lateral averaged film cooling effectiveness for configuration 1 ($M=1.0$) and Lutum ($M=1.15$)

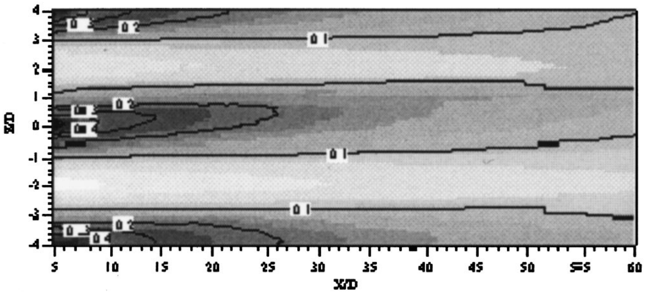

Fig. 9 Adiabatic film cooling effectiveness distribution for $M=1$, configuration 1 ($L/D=8$)

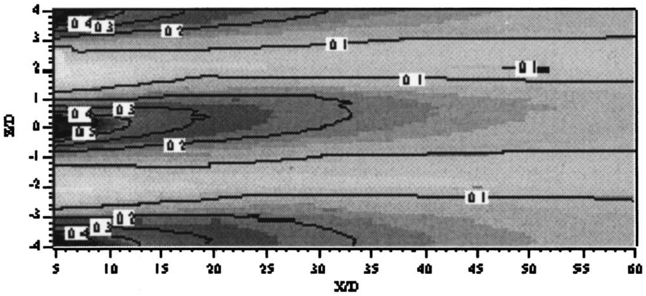

Fig. 10 Adiabatic film cooling effectiveness distribution for $M=1$, configuration 4 ($L/D=8$, with ribs)

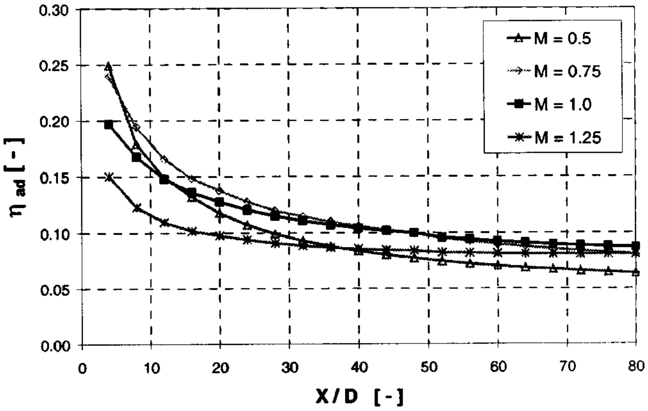

Fig. 11 Influence of blowing rate on lateral averaged adiabatic film cooling effectiveness for configuration 1 ($L/D=8$)

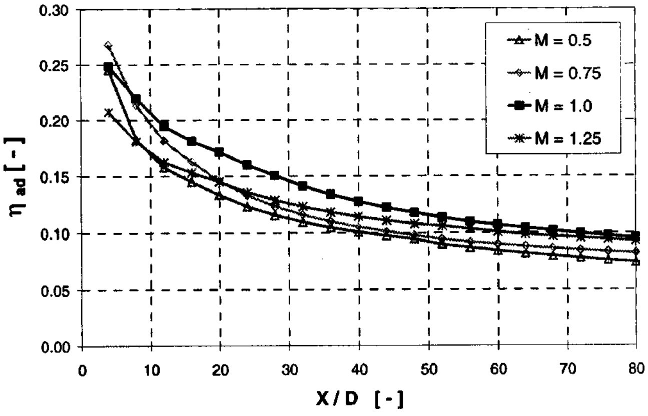

Fig. 12 Influence of blowing rate on lateral averaged adiabatic film cooling effectiveness for configuration 4 ($L/D=8$, with ribs)

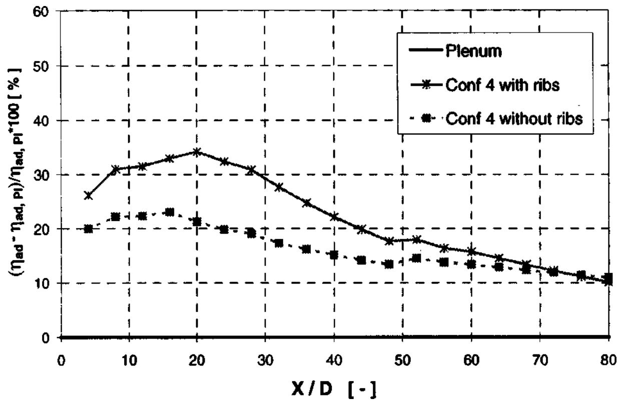

Fig. 13 Influence of guiding ribs on improvement of lateral averaged adiabatic film cooling effectiveness ($M=1$, $L/D=8$)

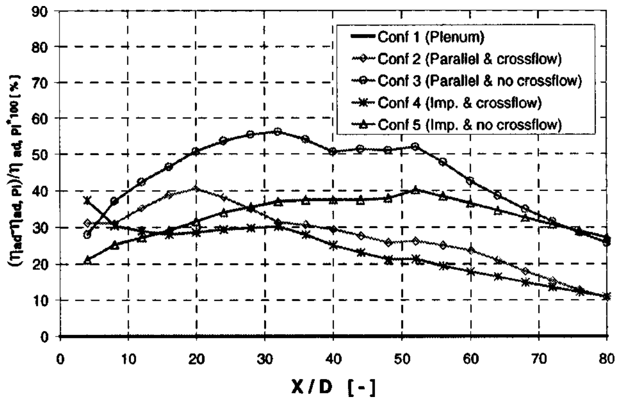

Fig. 15 Improvement of lateral averaged adiabatic film cooling effectiveness ($M=1$, $L/D=4$, with ribs)

$$\text{Improvement}=\frac{\eta_{ad}-\eta_{ad\ \mathrm{Pl}}}{\eta_{ad\ \mathrm{Pl}}}*100\ [\text{percent}] \tag{2}$$

To be able to separate the influence of internal flow parallel to the mainstream and the ribs for guiding the flow into the film cooling hole, tests were conducted without ribs. Figure 13 shows the improvement of film cooling effectiveness for configuration 4 with and without ribs at the blowing rate $M=1.0$. For the near-hole field, an increase of about 10 percent was measured for the configuration with ribs.

The improvement in lateral averaged film cooling effectiveness for configurations 2–5, given in Fig. 14, shows less than 10 percent differences between the plenum configuration and the configurations with no cross flow. Nevertheless, for the crossflow configurations, an improvement up to 34 percent is determined. Furthermore, for the impingement with crossflow configuration (configuration 4), an improvement of about 22 percent up to $X/D=80$ in average can be observed. The increasing improvement up to $X/D=20$ may be caused by an additional pair of vortices [17]. The pair of vortices is conserved further downstream than the kidney-shaped vortex and is transporting the hot gas through the jet to the surface and not sucking the hot gas between the holes to the surface and underneath the jet.

Effects of the internal flow decrease for longer holes. Therefore, measurements were performed for shorter holes at $L/D=4$. In Fig. 15 the improvements for configurations 2–5 are shown again referenced against the plenum configuration. As expected, the influence is increasing for shorter holes. Configuration 4 with impingement and crossflow has about the same effectiveness as for $L/D=8$. All other configurations show an improvement of more than 30 percent. Especially configurations 3 and 5 without crossflow now have the highest values. For configuration 3 an improvement up to 56 percent maximum and 43 percent in average is determined. For the long holes, the influence of the ribs was also investigated. Figure 16 shows the influence for configuration 3. For this case without crossflow, the improvement with the ribs is about 30 percent up to $X/D=40$ compared to the case without ribs.

These results lead to the conclusion that the exit flow distribution and its vortices have a strong influence on the mixing behavior and therefore on the film cooling effectiveness. The above-mentioned counterrotating vortices measured by Wilfert [17] are very stable and have a positive influence on the mixing. To intensify this pair of vortices, a prevortex generator was developed and tested (Fig. 17). The vortex generator uses the mechanism of secondary flow production. If the coolant flow is redirected from horizontal direction into the cooling holes, a pressure gradient is induced. The radial equilibrium for the flow in a bend is defined as follows:

$$\frac{\partial p}{\partial r}=\rho_\infty\frac{U^2}{R_\infty} \tag{3}$$

The interaction of pressure gradient and the side wall boundary layer of the vortex generator results in a counter-rotating pair of vortices inside the hole.

The film cooling effectiveness distribution for configuration 3 with ribs and with vortex generator is shown in Figs. 18 and 19. The values on the centerline are higher for the case with the vor-

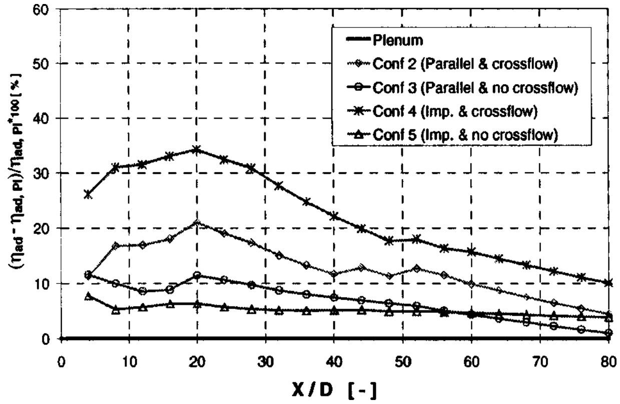

Fig. 14 Improvement of lateral averaged adiabatic film cooling effectiveness ($M=1$, $L/D=8$, with ribs) configurations ($M=1$, $L/D=8$)

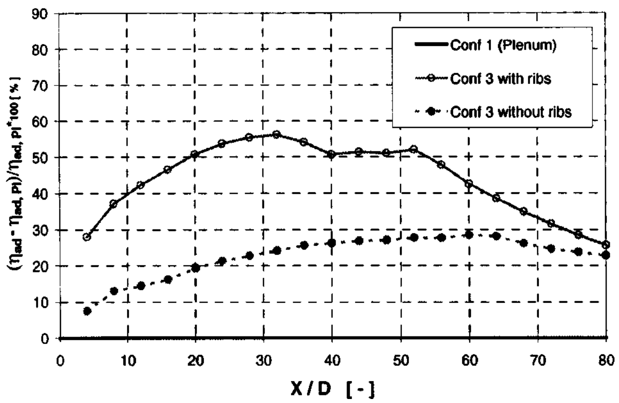

Fig. 16 Influence of guiding ribs on improvement of lateral averaged adiabatic film cooling effectiveness ($M=1$, $L/D=4$)

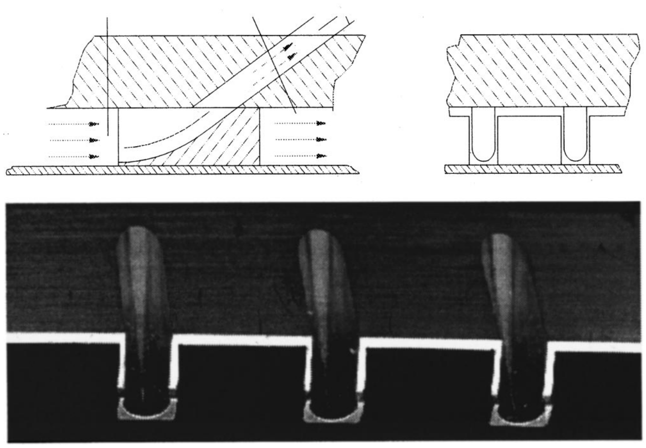

Fig. 17 Sketch and photo of vortex generator setup

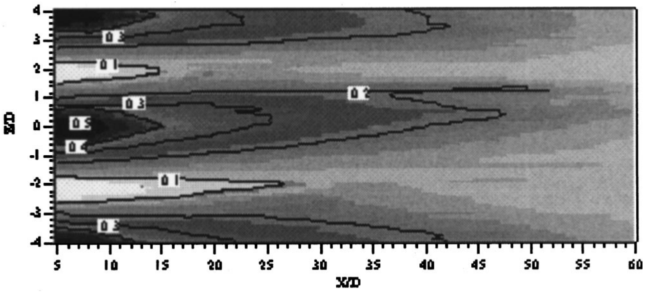

Fig. 18 Adiabatic film cooling effectiveness distribution for $M=1$, $L/D=4$, configuration 3 with vortex generator

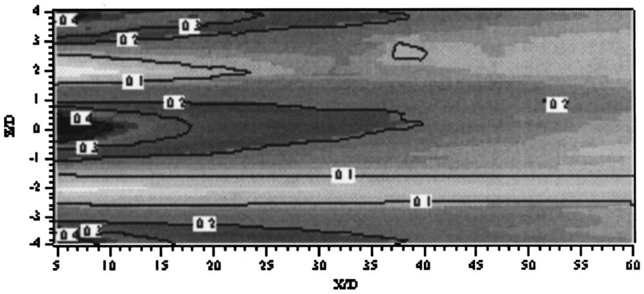

Fig. 19 Adiabatic film cooling effectiveness distribution for $M=1$, $L/D=4$, configuration 3 with ribs

tex generator and the low effectiveness regions between two holes are smaller. The improvement of lateral averaged adiabatic film cooling effectiveness to the configuration with vortex generator, as well as the best configuration with parallel flow and ribs, shown in Fig. 20, are again referenced to the plenum configuration. The benefit of the vortex generator is quite obvious, improvements above 80 percent maximum value and above 65 percent in average up to $X/D=80$ are determined compared to the standard plenum configuration. Furthermore, an improvement up to 15 percent in average between configurations with the vortex generator and the best configuration with ribs could be observed.

Conclusions

The present measurements demonstrate the influence of the inner contouring of the coolant channel and the hole supply on lateral averaged film cooling effectiveness. Compared to plenum configurations, deviations in adiabatic film cooling effectiveness of up to 30 percent can be observed. The lateral averaged film cooling effectiveness increases up to 56 percent maximum and 43 percent in average when using guiding ribs to redirect the coolant into the holes. Furthermore, some interesting observations are made:

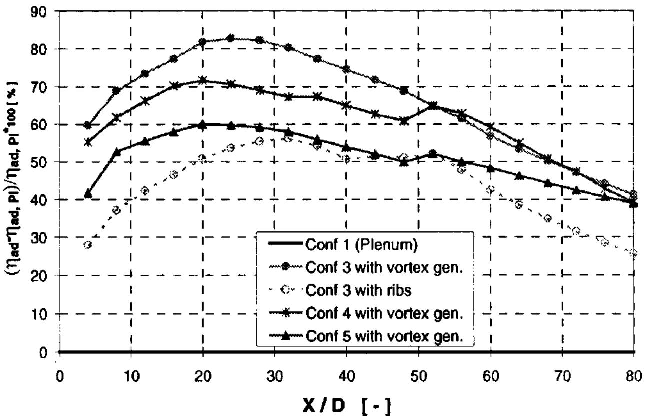

Fig. 20 Improvement of lateral averaged film cooling effectiveness for configurations 3, 4, and 5 with vortex generator and configuration 3 with ribs ($M=1$, $L/D=4$)

- Plenum geometry and hole supply have a stronger influence for low L/D ratios than for high L/D ratios.
- For high L/D ratios, the coolant channel velocity (crossflow) has a strong influence whereas the guiding ribs have just a small effect.
- Small L/D ratios show a different trend: Small influence of coolant crossflow and a strong influence of the redirection by means of the guiding ribs.

In order to optimize the benefit due to the geometry effects on the lateral averaged film cooling effectiveness, a vortex generator was designed and tested.

- The vortex generator leads to better lateral spreading of the cooling gas on the cooled surface.
- The vortex generator shows the best results for lateral averaged film cooling effectiveness of all tested configurations with an improvement of up to 83 percent maximum and about 65 percent in average compared to the classical plenum configuration for an internal parallel flow without crossflow.

To get usable predictions for modern film cooled turbine vanes, the plenum geometry and the hole supply have to be taken into account for future film cooling investigations. Very often cylindrical holes are used at high blowing rates instead of shaped holes because shaped holes have higher manufacturing costs. The effects presented for $M=1$ are increasing with increasing blowing rate. Especially for higher blowing rates, an important improvement in film cooling effectiveness can be achieved with optimized internal flow conditions.

Acknowledgments

The authors wish to acknowledge the help of E. Lutum, C. Herrmann, and H. Schär for conducting the film cooling experiments described in this paper.

Nomenclature

D = coolant hole diameter, m
DR = density ratio $=\rho_c/\rho_\infty$
H = coolant channel height, m
H/D = dimensionless height of coolant channel
VR = velocity ratio $=U_c/U_\infty$

I = momentum flux ratio $=\rho_c U_c^2/\rho_\infty U_\infty^2$
L = length of coolant passage, m
M = blowing rate $=\rho_c U_c/\rho_\infty U_\infty$
P = hole pitch, distance between holes in lateral direction, m
P/D = dimensionless lateral spacing, pitch to diameter ratio
R = radius, m
T = temperature, °C
Tu = turbulence intensity, percent
U = mean velocity, m/s
X = streamwise coordinate, origin at film hole center, m
X/D = dimensionless streamwise coordinate
Z = lateral coordinate, m
Z/D = dimensionless coordinate in lateral direction
k = thermal conductivity, W/m/K
α = injection angle of the coolant fluid, deg
$\eta_{ad,la}$ = lateral averaged adiabatic film cooling effectiveness
ρ = fluid density, kg/m^3

Subscripts

c = coolant fluid
cr = crossflow
i = impingement
∞ = free-stream fluid
Pl = plenum

References

[1] Goldstein, R. J., 1971, ''Film Cooling,'' *Advances in Heat Transfer*, **7**, Hartnett, J. P., and Irving, T. F., eds., Academic Press.
[2] Ardey, S., and Fottner, L., 1998, ''A Systematic Study of the Aerodynamics of Leading Edge Film Cooling on a Large Scale High Pressure Turbine Cascade,'' ASME Paper No. 98-GT-434.
[3] Chernobrovkin, A., and Lakshminarayana, B., ''Numerical Simulation and Aerothermal Physics of Leading Edge Film Cooling,'' ASME Paper No. 98-GT-504.
[4] Leylek, J. H., and Zerkle, R. D., 1994, ''Discrete-Jet Film Cooling: A Comparison of Computational Results With Experiments,'' ASME J. Turbomach., **116**, pp. 358–368.
[5] Papell, S. S., 1984, ''Vortex Generating Flow Passage Design for Increased Film-Cooling Effectiveness and Surface Coverage,'' NASA Technical Memorandum 83617, prepared for National Heat Transfer Conference, Aug. 5–8.
[6] Sinha, A. K., Bogard, D. G., and Crawford, M. E., 1991, ''Film-Cooling Effectiveness Downstream of a Single Row of Holes With Variable Density Ratio,'' ASME J. Turbomach., **113**, pp. 442–449.
[7] Walters, D. K., and Leylek, J. H., 2000, ''A Detailed Analysis of Film-Cooling Physics: Part I—Streamwise Injection With Cylindrical Holes,'' ASME J. Turbomach., **122**, pp. 102–112.
[8] Wilfert, G., 1994, ''Experimentelle und numerische Untersuchungen der Mischungsvorgänge zwischen Kühlfilmen und Gitterströmung an einem hochbelasteten Turbinenegitter,'' Ph.D. Thesis, Uni-Bundeswehr München.
[9] Vogel, D. T., Wilfert, G., and Fottner, L., 1995, ''Numerical and Experimental Investigation of Film Cooling From a Row of Holes at the Suction Side of a Highly Loaded Turbine Blade,'' ISABE Paper, **2**, p. 1121.
[10] Vogel, D. T., 1998, ''Numerical Investigation of the Influence of Specific Vortex Generation on the Mixing Process of Film Cooling Jets,'' ASME Paper No. 98-GT-210.
[11] Thole, K., Gritsch, M., Schulz, A., and Wittig, S., 1998, ''Flowfield Measurements for Film-Cooling Holes With Expanded Exits,'' ASME J. Turbomach., **120**, pp. 327–336.
[12] Thole, K., Gritsch, M., Schulz, A., and Wittig, S., 1998, ''Flowfield Measurements for Film-Cooling Holes With Expanded Exits,'' ASME J. Turbomach., **120**, pp. 327–336.
[13] Gritsch, M., Schulz, A., and Wittig, S., 1998, ''Heat Transfer Coefficient Measurement of Film-Cooling Holes With Expanded Exits,'' ASME Paper No. 98-GT-28.
[14] Berhe, M. K., and Patankar, S. V., 1996, ''A Numerical Study of Discrete-Hole Film Cooling,'' ASME Paper No. WA/HAT-8.
[15] Burd, S. W., and Simon, T. W., 1997, ''The Influence of Coolant Supply Geometry on Film Coolant Exit Flow and Surface Adiabatic Effectiveness,'' ASME Paper No. 97-GT-25.
[16] Lutum, E., and Johnson, B. V., 1999, ''Influence of the Hole Length-to-Diameter Ratio on Film Cooling With Cylindrical Holes,'' ASME J. Turbomach., **121**, pp. 209–216.
[17] Wilfert, G., and Fottner, L., 1996, ''The Aerodynamic Mixing Effect of Discrete Cooling Jets With Mainstream Flow on a Highly Loaded Turbine Blade,'' ASME J. Turbomach., **118**, pp. 468–478.

Aerothermal Investigations of Mixing Flow Phenomena in Case of Radially Inclined Ejection Holes at the Leading Edge

Dieter E. Bohn
Professor and Director,
Institute of Steam and Gas Turbines,
Aachen University of Technology,
Templergraben 55,
D-52056 Aachen, Germany

Karsten A. Kusterer
Research Engineer,
B&B-AGEMA,
Jülicher Strasse 338,
D-52070 Aachen, Germany

A leading edge cooling configuration is investigated numerically by application of a three-dimensional conjugate fluid flow and heat transfer solver, CHT-flow. The code has been developed at the Institute of Steam and Gas Turbines, Aachen University of Technology. It works on the basis of an implicit finite volume method combined with a multi-block technique. The cooling configuration is an axial turbine blade cascade with leading edge ejection through two rows of cooling holes. The rows are located in the vicinity of the stagnation line, one row on the suction side, the other row is on the pressure side. The cooling holes have a radial ejection angle of 45 deg. This configuration has been investigated experimentally by other authors and the results have been documented as a test case for numerical calculations of ejection flow phenomena. The numerical investigations focus on the aerothermal mixing process in the cooling jets and the impact on the temperature distribution on the blade surface. The radial ejection angles lead to a fully three-dimensional and asymmetric jet flow field. Within a secondary flow analysis, the cooling fluid jets are investigated in detail. The secondary flow fields include asymmetric kidney vortex systems with one dominating vortex on the back side of the jets. The numerical and experimental data show a respectable agreement concerning the vortex development. [S0889-504X(00)00102-1]

Introduction

Intensive cooling of blades and vanes in modern gas turbines is required to guarantee an economically acceptable lifespan of the components in contact with the hot gas. The maximum turbine inlet temperature is limited by the permissible material temperature of the first row of vanes. In particular, the leading edge of a turbine blade or vane is exposed to very high temperatures. Therefore, film cooling configurations have been investigated for several years. Concerning the CFD research in this subject, a bibliography (1971–1996) of the most important publications can be found in a study by Kercher [1]. Former numerical investigations focus on the development of the well-known kidney vortices [2,3], in the case of flat plate cooling [4], and cooling fluid ejection on the suction side [5]. Numerical studies of leading edge ejection have been performed by Martin and Thole [6]. Compound-angle ejection leads to an asymmetric vortex system. A detailed numerical analysis of the film cooling physics in case of a flat plate has been executed recently by McGovern and Leylek [7]. The numerical work of Baier et al. [8] focuses on the influence of the laterally inclined jets on film cooling in the case of a suction side ejection.

In the case of leading edge ejection with a showerhead configuration under real flow conditions in gas turbines, few numerical studies have been presented. In a numerical investigation of a showerhead cooling configuration by Hall et al. [9], it was observed that effects caused by secondary flows could lead to a lift-off of the cooling jet.[1] Former numerical results of Bohn and Kusterer [11] dealt with a detailed cooling jet analysis in the case of a nonlateral leading edge ejection in a turbine blade cascade.

Cooling Configuration

The configuration investigated is a turbine blade cascade with two rows of ejection holes, one on the pressure side and the other one on the suction side, in the vicinity of the leading edge. The configuration was experimentally investigated by Ardey and Fottner [12–14] in a high speed cascade wind tunnel. The facility operates continuously in a large pressurized tank. Figure 1 shows the configuration in a mean section of the ejection holes with radial angle of 90 deg (streamwise ejection). The geometric data of the cascade and the main flow parameters are shown in Table 1. In the configuration investigated the radial angle for both rows of holes is 45 deg (lateral ejection). In the case of a streamwise ejection, a comparison of experimental and numerical data regarding the primary flow phenomena results have been presented by the authors [15].

In order to investigate the secondary flow field in the jets, the experimental researchers [13,14] have carried out three-dimensional hot wire measurements and two-dimensional laser-2-

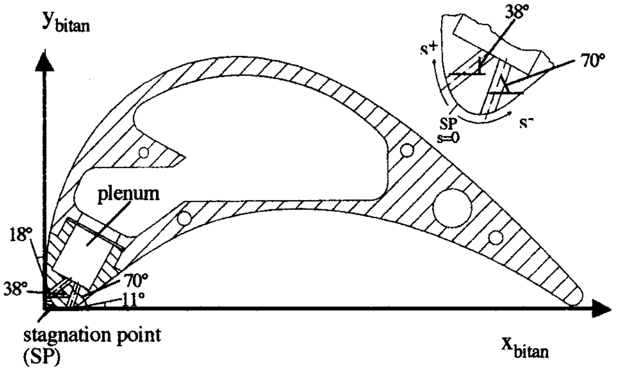

Fig. 1 Blade geometry

---

[1] Recent numerical studies of a showerhead-cooled turbine vane including plenum and several rows of cooling holes have been presented by Garg and Rigby [10]. They documented the complex flow field near the hole exits and in the hole pipes.

Contributed by the International Gas Turbine Institute and presented at the 44th International Gas Turbine and Aeroengine Congress and Exhibition, Indianapolis, Indiana, June 7–10, 1999. Manuscript received by the International Gas Turbine Institute February 1999. Paper No. 99-GT-198. Review Chair: D. C. Wisler.

Table 1 Cascade geometry and parameters

chord length:	L	= 250 mm
vane height:	H	= 300 mm
pitch ratio:	t/L	= 0.714
staggering angle:	β_S	= 73.0°
cascade aerodynamics:		
inlet Mach number	Ma_1	= 0.37
inlet Re number	Re_1	= 371000
inlet flow angle	α_1	= 43°
inlet turbulence intensity	Tu_1	= 5%
isentropic exit Ma number	Ma_{2is}	= 0.95
isentropic exit Re number	Re_{2is}	= 695000
exit flow angle	β_2	= 28.3°
AGTB-B2 cooling configuration (holes):		
position s/L SS:		0.02
position s/L PS:		-0.03
streamwise ejection angle SS γ_s:		110°
streamwise ejection angle PS γ_s:		120°
radial ejection angle SS γ_r:		45°
radial ejection angle PS γ_r:		45°
hole diameter D:		3.00 mm
hole length SS:		5.88*D
hole length PS:		5.88*D
pitch ratio of holes:		5
number of holes/row:		20

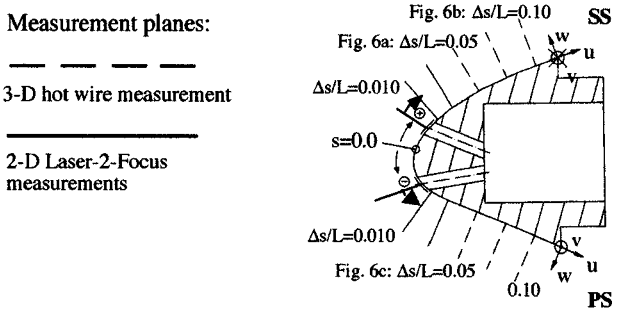

Fig. 2 Experimental measurement planes

focus measurements in planes perpendicular to the cascade blade surface as indicated in Fig. 2.

Numerical Method

The numerical scheme of the code works on the basis of an implicit finite volume method combined with a multiblock technique. The physical domain is divided into separate blocks and the full, compressible, three-dimensional Navier–Stokes equations are solved in the fluid blocks. The governing equations for the conservative variables are formulated in arbitrary, body-fitted coordinates in order to allow the simulation of complex geometries. The conservation equations are discretized implicitly to the first order in time making use of the Newton method [16]. Upwind discretization is used for the inviscid fluxes [17]. The viscous fluxes are approximated using central differences. The resulting system of linear equations is solved by a Gauss–Seidel point iteration scheme, allowing high vectorization on present-day computers. The closure of the conservation equations is provided by the algebraic eddy-viscosity turbulence model by Baldwin and Lomax [18].

Computational Grid and Boundary Conditions

At first, structured two-dimensional grids consisting of six blocks are generated (Fig. 3) using an elliptic grid generation procedure. The internal flow calculation includes the plenum region (block 6) and the ejection holes (4 and 5). The boundary conditions of the cooling fluid inlet are prescribed at the plenum inlet face. Due to the multiblock method, the outflow conditions at the hole exits depend on the external flow calculation in the main block 1. Since the investigated blade is part of a plane cascade, the three-dimensional grid for blocks 1–3 and 6 is obtained by stacking the two-dimensional grids in the radial direction, taking the changing geometry in the different grid planes at the hole inlets and exits into account (Fig. 3). The three-dimensional discretization of the radially inclined ejection holes is not as easy as for the other blocks. Here, the shapes of the intersection curves of the cylindrical shaped ejection holes with the vane surface are derived from a three-dimensional CAD program. The three-dimensional grid of the AGTB-B2 configuration consists of approximately 665,000 grid points using 63 grid planes including 27 planes for the ejection holes (Fig. 3). In the radial direction, periodic boundary conditions are used.

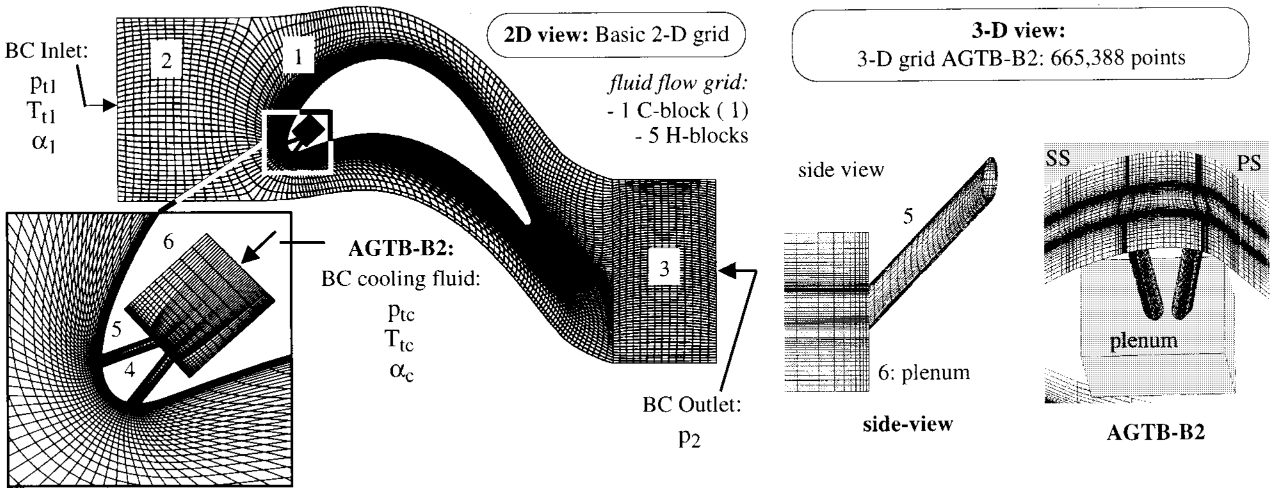

Fig. 3 Three-dimensional numerical grids of the AGTB-B2 configuration (multiblock grid)

Table 2 Boundary conditions

flow property	AGTB-B2
blowing ratio	1.1
total pressure $p_{t,1}$	19585 N/m^2
total temperature $T_{t,1}$	303.15 K
main flow angle α_1	43°
static pressure p_2	14980 N/m^2
cooling fluid inlet conditions	
total pressure $p_{t,c}$	22020 N/m^2
$(T_{t,c} / T_{t,1})$ aerodynamic	1
$(T_{t,c} / T_{t,1})$ aerothermal	0.5

Table 3 Blowing ratios

M_{SS}		M_{PS}	
experiment 0.99	calculation (aerodynamic) 1.030	experiment 1.11	calculation (aerodynamic) 1.150
experiment (no experiment)	calculation (aerothermal) 1.415	experiment (no experiment)	calculation (aerothermal)) 1.592

The boundary conditions (BC) at the cascade inlet and outlet are taken from the experimental test case [14] and are listed in Table 2. The blowing ratio is defined as the ratio of the mass flow densities of cooling flow to main flow:

$$M=(\rho c)_c/(\rho c)_1 \tag{1}$$

The blowing ratio given in Table 3 is the averaged blowing ratio of all ejection holes of both the suction side row and the pressure side row of holes.

Results

Part A: Aerodynamic Calculation

1 Blowing Ratios. Table 3 gives a comparison of the experimentally determined and the calculated blowing ratios for the ejection holes. In the experiments, direct measurement of the single blowing ratios was not possible. The blowing ratios given by the experimenters have been calculated out of the solution of a complex equation system based on measured data [14]. The numerical values are the result of an averaging of the flow values at the half-length of the ejection holes. One has to keep in mind that the flow values in the holes are only calculated from the prescribed boundary conditions. The comparison of the data shows that the numerical values are always close to the experimental values. The errors are within a 4 percent range. Taking into account an experimental error range and the indirect determination method of the values, the results are respectable. A reason for the deviations are the neglected three-dimensional effects by the side walls.

2 Pressure Distribution. Figure 4 gives a comparison of the experimental and the calculated values of the static pressure distributions in the midplanes of the ejection holes. The coincidence of the numerical and experimental data is very good on the pressure side and the rear part of the suction side. In the front part of the suction side, the pressure is somewhat overestimated in the calculation. For the AGTB-B2 configuration, the minimum pressure on the suction side is slightly lower than in the experiment. Differences between experimental data and computational data can be explained by neglecting the influence of three-dimensional flow phenomena due to the endwall effects in the calculation. The long cascade inflow channel in the experiments leads to the development of a thick side wall boundary layer. Thus, the development of a horseshoe vortex and a passage vortex in the cascade is the consequence. They influence the pressure distribution on the blade surface.

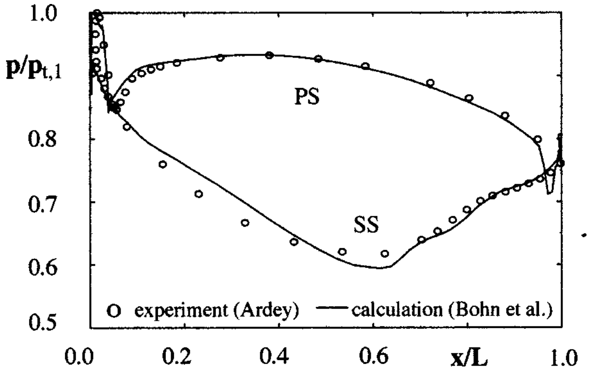

Fig. 4 Pressure distribution (AGTB-B2)

3 Ejection Jets

3.1 Ejection jet paths. Figure 5 gives an overview of the ejection jet paths on the suction side and the pressure side of the cascade blade. Due to the lateral ejection, the jets show a deviation from the streamwise direction which depends on main flow velocities on the blade surface. The deviation of the pressure side jet at the trailing edge is eight bore hole diameters, which is twice the deviation of the suction side jet.

3.2 Suction side jet (AGTB-B2). The lateral ejection leads to an asymmetric counter-rotating vortex system Ω_1 with a dominating vortex (Fig. 6(*a*), Ω_{1-b}) at the lee side of the jet. This vortex is generated by main flow material streaming over the jet and into the wake region behind the jet where it whirls up. This process leads to a transportation of main flow material underneath the jet from the lee side.

In contrast to the symmetric case (AGTB-B1) a second vortex system development [11] is prevented. Therefore, the lift-off of the jet is reduced. Figure 6(*b*) gives a comparison of computationally and experimentally [14] determined secondary flows in the indicated investigation plane at $\Delta s/L=0.1$. The flow characteristics are in good agreement. The w/D position of the vortex core is calculated at $w/D\cong0.95$ (experiment: $w/D\cong0.85$). For the v/D

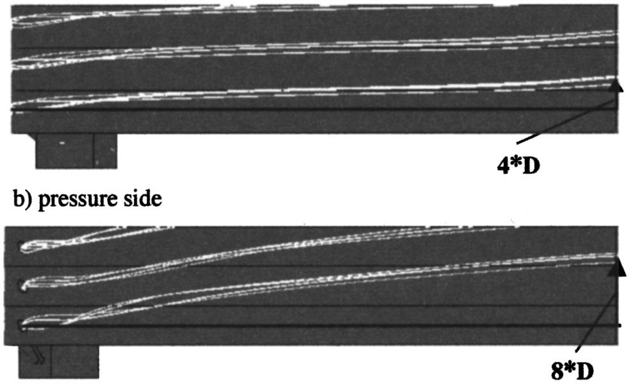

Fig. 5 Path of ejection jets

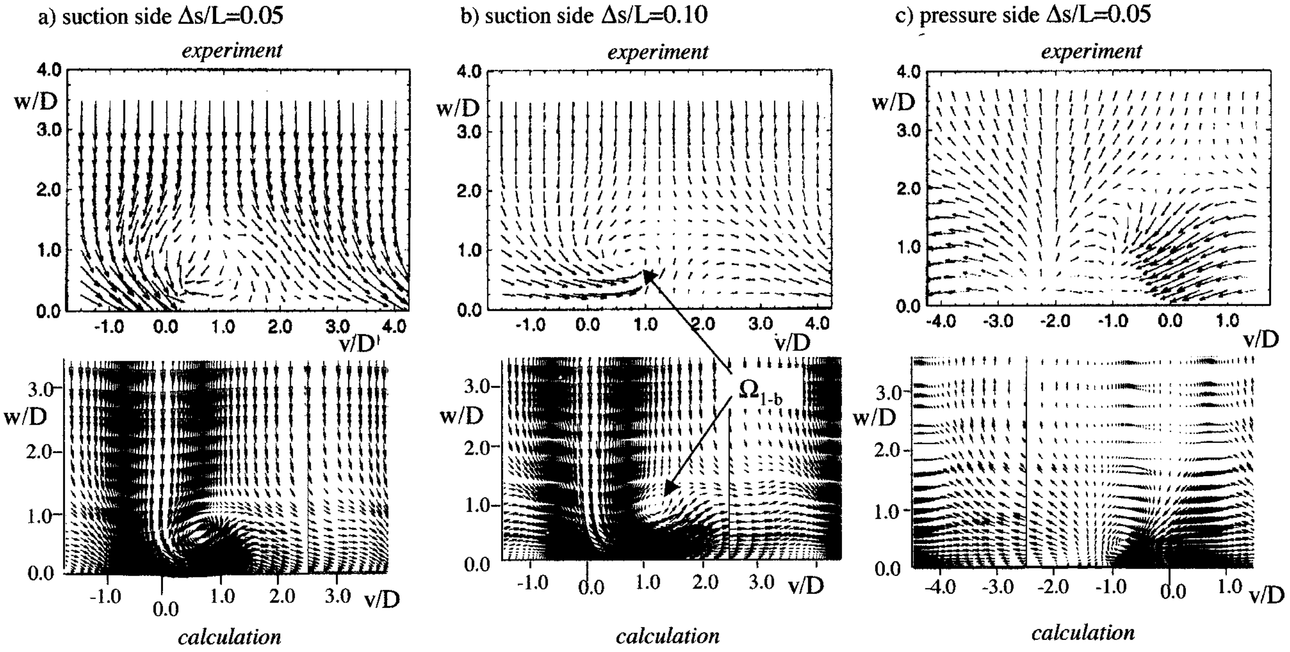

Fig. 6 Comparison of experimental and calculational secondary flow field in the ejection jets

position of the vortex, the calculated deviation from the streamwise direction is greater ($v/D \cong 1.1$) than in the experiment ($v/D \cong 0.8$). Here, the influence of passage secondary flow phenomena (passage vortices) in the experiment is the likely reason.

3.3 Pressure side jet (AGTB-B2). In this case, the secondary flow vortices in the flow recirculating area behind the ejection exit (AGTB-B1, [11]) are nonexistent. Instead of these, an asymmetric vortex system is created analogously to the suction side jet. Figure 6(*c*) gives the comparison of the experimental and numerical data in the indicated investigation planes. Due to the greater deviation of the pressure side jet, the investigation planes do not reveal the vortex structure as they are not located perpendicular to the jet main direction. Nevertheless, the comparison shows a good agreement of the basic phenomena.

Part B: Aerothermal Calculation

4 Blowing Ratio. Due to the changed boundary conditions for the cooling fluid ($T_{t,c}/T_{t1}=0.5$), the blowing ratios are higher in the case of the aerothermal calculation. For the aerothermal calculation, the new values can be obtained from Table 3.

5 Cooling Fluid/Hot Gas Mixing. Figure 7 shows the temperature distribution in the flow field at the leading edge. The cutting plane is located in the midplane of the hole exits. On both sides, the temperature of the cooling fluid is still very low ($0.55 > T/T_{\text{ref}} > 0.5$) when the fluid leaves the holes. However, due to the mixing process with hot gas, the core temperature of the jets rises quickly. The jet core temperature itself will be lower than the temperatures displayed in Fig. 7 because the jets are not ejected streamwise. Thus, the jet core temperatures will be investigated in different sections of the three-dimensional jet flow field later on.

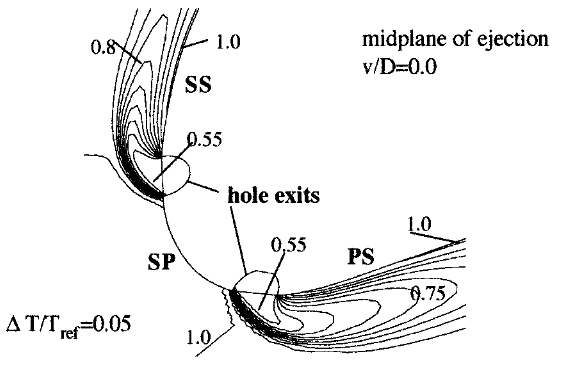

Fig. 7 Temperature field at the leading edge

On the pressure side, the jet penetrates the main flow region deeper, as the pressure side blowing ratio is higher than for the suction side hole. Due to the higher blowing ratio, the core temperature increase in the jet is not as fast as on the suction side. A disadvantageous cooling flow behavior can be detected on both sides: The cooling jets are only in weak contact with the blade surface, leading to a very fast increase in the adiabatic surface temperature. Thus, the adiabatic cooling efficiency of this type of configuration is very low. Higher blowing ratios will lead to an even worse situation as the jets will lose wall contact completely when penetrating the main flow region deeper.

5.1 Suction side jet. If one looks more closely at the development of the cooling fluid/hot gas mixing in the jets, it can be shown that the processes are similar on the suction side and pressure side. This contrasts the symmetric case with streamwise ejection [11] where additional mixing vortices can be found. Figures 8 and 9 show that in the lateral ejection case the jet is completely dominated by the large vortex of the asymmetric vortex pair. The vortex at the front of the jet is always very small and vanishes when the complete jet is rotating with the dominating vortex. Figure 8(*a*) shows for the suction side that there is still a high temperature gradient in the outer jet region at a small distance behind the ejection hole. One part of the suction side jet is still in contact with the blade surface. The asymmetric vortex pair leads to the deformation of the jet core, which has moved quickly out of the midplane ($v/D=0.0$). Figure 8(*b*) shows that the suction side jet is hardly in touch to the wall and that flow mixing leads to a fast increase in the core temperature in between a small distance behind the ejection hole. Later on (Fig. 8(*c*)) the further increase in the core temperature is much more moderate.

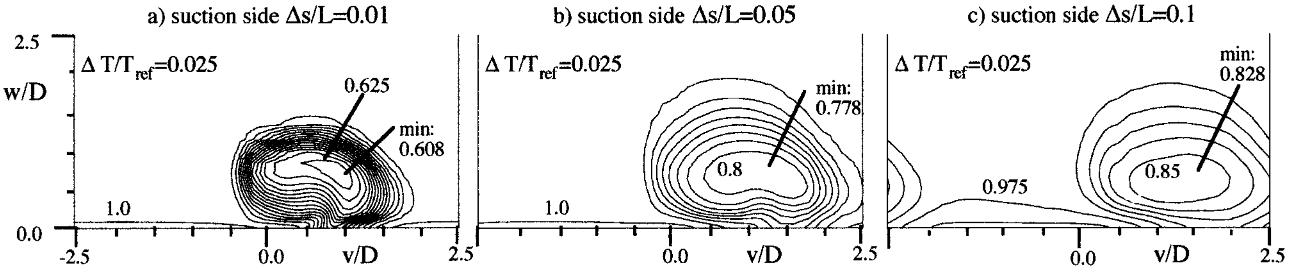

Fig. 8 Temperature field in suction side jet

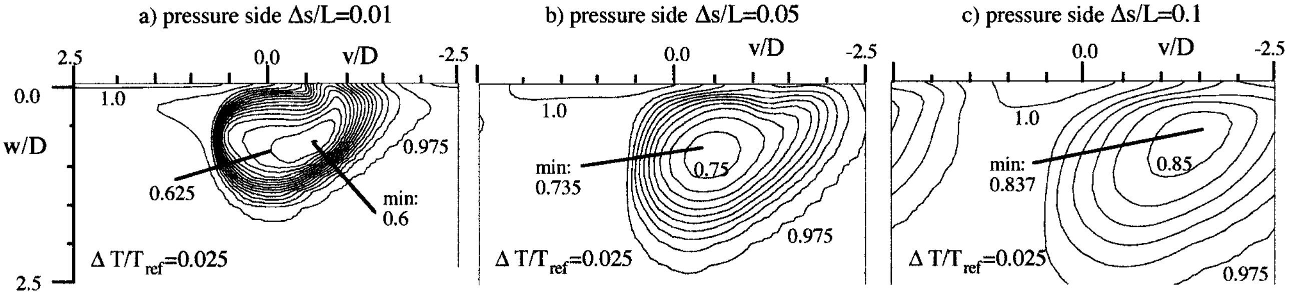

Fig. 9 Temperature field in pressure side jet

5.2 Pressure side jet. The situation on the pressure side is principally the same as on the suction side. The dominating vortex of the pressure side jet is stronger and even more effective than in the suction side jet. Due to the higher blowing ratio of the pressure side hole, the jet penetrates the main flow field deeper. Thus, the surface contact of the pressure side jet is less than the contact of the suction side jet (Fig. 9). The curvature of the profile on the pressure side is stronger than on the suction side in the leading edge region. Therefore, in this region flow acceleration and flow velocities are higher than on the suction side directly behind the ejection hole. Thus, the displacement of the pressure side jet is less than the displacement of the suction side jet in the small distance behind the ejection holes (compare Figs. 9(*b*) and 8(*b*). Later, the displacement of the pressure side jet will catch up with the development on the suction side (Figs. 9(*c*) and 8(*c*)).

Conclusions

Complex numerical three-dimensional investigations of the aerothermal ejection jet phenomena in case of a lateral leading edge ejection have been undertaken. The numerical results of the pressure distribution and the jet secondary flow phenomena correspond well with the experimental data. The jet flow field is dominated by one large vortex, which is generated on the lee side of the jet as a part of an asymmetric vortex pair. The numerical investigations have shown that the cooling jets are only in weak contact with the blade surface. Thus, the cooling efficiency is reduced distinctly. The reason for this behavior is to be found in the deep penetration of the jets and the consequent transportation of hot gas material under the jets by the dominating vortex.

Nomenclature

D = hole diameter, mm
L = chord length, mm
M = blowing ratio
T = temperature, K
c = velocity, m/s
p = pressure, N/m^2
s = blade surface coordinate
t = spacing, mm
u, v, w = Cartesian coordinates (surface oriented), mm
x = Cartesian coordinate (axial direction), mm
α, β = flow angles, deg
γ_r, γ_s = ejection angles, deg
ρ = density, kg/m^3

Subscripts

bitan = bitangential coordinates
c = cooling air conditions
t = total
1 = at inlet
2 = at exit

References

[1] Kercher, D. M., 1998, ''A Film-Cooling CFD Bibliography: 1971–1996,'' Int. J. Rot. Mach., **4**, No. 1, pp. 61–72.
[2] Bergeles, G., Gosman, A. D., and Launder, B. E., 1976, ''The Prediction of Three-Dimensional Discrete-Hole Cooling Processes,'' ASME J. Heat Transfer, **98**, pp. 379–386.
[3] Leylek, J. H., and Zerkle, R. D., 1994, ''Discrete-Jet Film Cooling: A Comparison of Computational Results With Experiments,'' ASME J. Turbomach., **116**, pp. 358–368.
[4] Walters, D. K., and Leylek, J. H., 2000, ''A Detailed Analysis of Film-Cooling Physics: Part I—Streamwise Injections With Cylindrical Holes,'' ASME J. Turbomach., **122**, pp. 102–112.
[5] Vogel, D. T., Wilfert, G., and Fottner, L., 1995, ''Numerical and Experimental Investigations of Film Cooling From a Row of Holes at the Suction Side of a Highly Loaded Turbine Blade,'' ISABE 95-7103.
[6] Martin C. A., and Thole K. A., 1997, ''A CFD Benchmark Study: Leading Edge Film-Cooling With Compound Angle Injection,'' ASME Paper No. 97-GT-297.
[7] McGovern, K. T., and Leylek, J. H., 2000, ''A Detailed Analysis of Film Cooling Physics: Part II—Compound-Angle Injection With Cylindrical Holes,'' ASME J. Turbomach., **122**, pp. 113–121.
[8] Baier, R.-D., Broichhausen, K.-D., Fritsch, G., and Koschel, W., 1997, ''Systematic Study on the Fluid Dynamical Behavior of Streamwise and Laterally Inclined Jets in Crossflow,'' ASME Paper No. 97-GT-98.
[9] Hall, J. E., Topp, D. A., and Delaney, R. A., 1994, ''Aerodynamic/Heat Transfer Analysis of Discrete Site Film-Cooled Turbine Airfoils,'' AIAA Paper No. 94-3070.
[10] Garg, V. K., and Rigby, D. L., 1999, ''Heat Transfer on a Film-Cooled Blade—Effect of Hole Physics,'' Int. J. Heat Fluid Flow, **20**, pp. 10–25.
[11] Bohn, D., and Kusterer, K., 1999, ''Blowing Ratio Influence on Jet Mixing Flow Phenomena at the Leading Edge,'' AIAA Paper No. 99-0670.
[12] Ardey, S., and Fottner, L., 1997, ''Flow Field Measurements on a Large Scale

Turbine Cascade With Leading Edge Film Cooling by Two Rows of Holes,'' ASME Paper No. 97-GT-524.

[13] Ardey, S., and Fottner, L., 1998, ''A Systematic Experimental Study on the Aerodynamics of Leading Edge Film Cooling on a Large Scale High Pressure Turbine Cascade,'' ASME Paper No. 98-GT-434.

[14] Ardey S., 1998, ''3D-Messung des Strömungsfeldes um die filmgekühlte Vorderkante einer Referenzschaufel,'' Ph.D. Thesis, University of the Armed Forces Munich.

[15] Bohn, D., Becker, V., Kusterer, K., Ardey S., and Fottner, L., 1997, ''The Influence of Slot-Ejection and Showerhead Ejection on the 3-D. Flow Field of a Film-Cooled Turbine Blade Under Consideration of Side Wall Effect,'' ISABE 97-7162.

[16] Schmatz, M. A., 1988, ''Three-Dimensional Viscous Flow Simulations Using an Implicit Relaxation Scheme,'' Notes on Numerical Fluid-Mechanics (NNFM), **22**, Vieweg, Braunschweig, 226–242.

[17] Eberle, A., Schmatz M. A., and Bissinger, N., 1990, ''Generalized Flux Vectors for Hypersonic Shock-Capturing,'' AIAA Paper No. 90-0390.

[18] Baldwin, B. S., and Lomax, H., 1978, ''Thin Layer Approximation and Algebraic Model for Separated Turbulent Flows,'' AIAA Paper No. 78-257.

Shuye Teng
Dong Kee Sohn[1]
Je-Chin Han
Turbine Heat Transfer Laboratory,
Department of Mechanical Engineering,
Texas A&M University,
College Station, TX 77843-3123

Unsteady Wake Effect on Film Temperature and Effectiveness Distributions for a Gas Turbine Blade

The film effectiveness and coolant jet temperature profile on the suction side of a gas turbine blade were measured using a transient liquid crystal and a cold-wire technique, respectively. The blade has only one row of film holes near the gill hole portion on the suction side of the blade. Tests were performed on a five-blade linear cascade in a low-speed wind tunnel. The mainstream Reynolds number based on cascade exit velocity was 5.3×10^5. Upstream unsteady wakes were simulated using a spoke-wheel type wake generator. Coolant blowing ratio was varied from 0.6 to 1.2. Wake Strouhal number was kept at 0 and 0.1. Results show that unsteady wake reduces film cooling effectiveness. Results also show that film injection enhances local heat transfer coefficient while the unsteady wake promotes earlier boundary-layer transition. The development of coolant jet temperature profiles could be used to explain the film cooling performance.
[S0889-504X(00)00402-5]

Introduction

A continuing trend toward higher gas turbine inlet temperatures has resulted in higher heat loads on turbine components. Hence, sophisticated cooling techniques must be employed to cool the components to maintain the performance requirements. Film cooling through discrete holes is used as a method of external cooling on turbine blades. Many studies have presented heat transfer measurements on turbine blades with film cooling. Nirmalan and Hylton [1] and Abuaf et al. [2] studied heat transfer on film cooled turbine vanes. Camci and Arts [3] studied heat transfer on film cooled turbine blades. Takeishi et al. [4] compared the film cooling effectiveness values for a stationary cascade under 4 percent mainstream turbulence intensity and for a rotor blade using the heat-mass transfer analogy. Ito et al. [5] and Haas et al. [6] studied the effect of coolant density on film cooling effectiveness on turbine blades under low mainstream turbulence levels. Ames [7] reported the influence of high free-stream turbulence on turbine vane heat transfer coefficient and film effectiveness distributions.

The effect of unsteady wakes produced by upstream vane trailing edges has a strong effect on the rotor blade surface heat transfer coefficient distributions. Several studies have focused on the effect of unsteady wakes on the downstream blade heat transfer coefficient distributions without film cooling. They all reported that unsteady wakes enhanced turbine blade heat transfer and caused earlier and longer laminar–turbulent boundary-layer transition on the suction surface. Few studies have focused on the effect of unsteady wakes on film cooled turbine blades. Abhari and Epstein [8] conducted heat transfer experiments on a film-cooled transonic turbine stage in a short-duration turbine facility. They concluded that film cooling reduces the time-averaged heat transfer by about 60 percent on the suction surface compared to the uncooled rotor blade. However, the effect is relatively low on the pressure surface. Ou et al. [9] and Mehendale et al. [10] simulated unsteady wake conditions over a linear turbine blade cascade with film cooling. They concluded that heat transfer coefficients increase and film cooling effectiveness values decrease with an increase in unsteady wake strength.

A few previous studies have measured detailed heat transfer coefficients on turbine blades with film cooling. Vedula and Metzger [11] presented a transient liquid crystal technique for detailed measurements of both heat transfer coefficients and film cooling effectiveness over a flat surface with one row of simple angle injection holes. Ekkad et al. [12,13] presented detailed heat transfer coefficient and film cooling effectiveness distributions on a flat surface with different compound angle injections and two coolant densities. Based on the same technique, Du et al. [14,15] reported the detailed film cooling measurements over a film cooled turbine blade under the effect of upstream unsteady wakes. They concluded that unsteady wake slightly enhances Nusselt numbers but significantly reduces film cooling effectiveness on a film-cooled blade surface as compared to a film-cooled blade without unsteady wake. Drost and Bölcs [16] also reported detailed heat transfer coefficient and film effectiveness distributions on a turbine vane using a transient liquid crystal technique.

The measurement of coolant jet temperature field using a cold wire is well described in the study of Kohli and Bogard [17]. Their study has focused on temperature measurements in a film cooling flow field on the flat plate. A high-frequency-response temperature sensor was used, which provided information about film cooling flow in terms of actual turbulence levels and probability density functions of the thermal field. They concluded that film cooling jets tend to lift off the surface with higher blowing ratio and lateral injection yields a more uniform distribution of effectiveness immediately downstream of injection. Sohn et al. [18] also used the same technique to measure the coolant jet temperature fields on a cylindrical leading edge film cooling model. The film cooling jet behavior could be characterized by the result of the film coolant temperature measurement.

The present study uses a transient liquid crystal technique to measure the distributions of heat transfer coefficient and film cooling effectiveness, and a cold wire to measure film cooling jet temperature fields. The effects of upstream unsteady wake and coolant-to-mainstream blowing ratio are presented. The study has been focused on only one row of film holes near the suction-side gill hole portion. This single-row film cooling model isolates up-

---

[1] Visiting scholar from Turbo and Power Machinery Research Center, Department of Mechanical Engineering, Seoul National University, Seoul, 151-742, Korea.

Contributed by the International Gas Turbine Institute and presented at the 44th International Gas Turbine and Aeroengine Congress and Exhibition, Indianapolis, Indiana, June 7–10, 1999. Manuscript received by the International Gas Turbine Institute February 1999. Paper No. 99-GT-172. Review Chair: D. C. Wisler.

stream effect and eliminates the interaction of several rows of film cooling jets. It provides a better understanding of a single row of coolant jet behavior over the suction surface of a turbine blade. The combined results of film cooling jet temperature field measurement with the detailed film effectiveness and heat transfer coefficient measurement on the suction surface present a clear picture of coolant jet behavior under upstream unsteady wake condition. It helps us look into the interaction between coolant jet and mainstream, which affects coolant jet temperature contour, film effectiveness, and heat transfer coefficient distribution. It also provides a good database for film cooling computational model development.

Experimental Apparatus

Figure 1(*a*) shows the schematic of the test section and camera locations. The test apparatus consists of a low-speed wind tunnel with an inlet nozzle, a linear turbine blade cascade with the test blade in the center, and a suction-type blower. The wind tunnel is designed to accommodate for the 107.49 deg turn of the blade cascade. The mean velocity increases 2.5 times from inlet of the cascade to exit. The test apparatus was described in detail by Ou et al. [9]. A spoked wheel type wake generator, similar to the one used by Ou et al. [9], simulated the upstream unsteady wake. The error caused by using nonparallel rotating rods with a linear blade cascade was small and was discussed by Ou et al. [9]. The blade configuration, scaled up five times. produces a velocity distribution typical of an advanced high-pressure turbine blade row. The cascade has five blades, each with an axial chord length of 17 cm and radial span of 25.2 cm. The blade spacing is 17.01 cm at the cascade inlet and the throat-to-blade span ratio is 0.2. Du et al. [14] have presented the local-to-exit velocity ratio distribution around the blade as well as the instantaneous velocity, ensemble-averaged velocity and ensemble-averaged turbulence profiles at the cascade inlet under the effect of upstream unsteady wakes. The velocity on the suction side accelerates to about $X/SL = 0.5$ ($V/V_2 = 110$ percent) and then decelerates slightly until the exit. At the film hole location, V/V_2 is about 68 percent, the momentum thickness δ_2 is about 9×10^{-4} m and the momentum thickness Reynolds number is about 200 for steady flow. The unsteady wakes are actually velocity deficiencies caused by the blockage of mainstream flow by the rotating rods. The ensemble-averaged turbulence intensity profiles show that intensity could be as high as 20 percent inside the wake. The time mean averaged turbulence is about 10.4 percent. For cases without unsteady wake effect, the time mean averaged turbulence is about 0.7 percent.

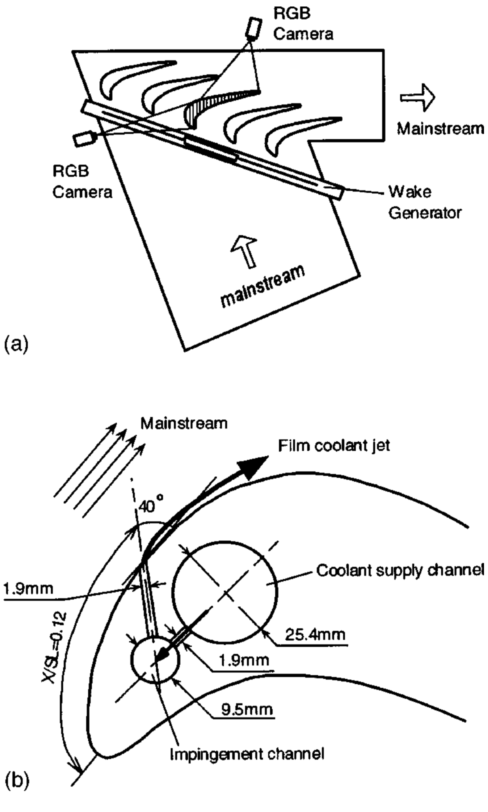

Fig. 1 (*a*) **Five-blade cascade with center blade coated with liquid crystal and viewed by two cameras;** (*b*) **a two-dimensional view of the film-cooled blade model**

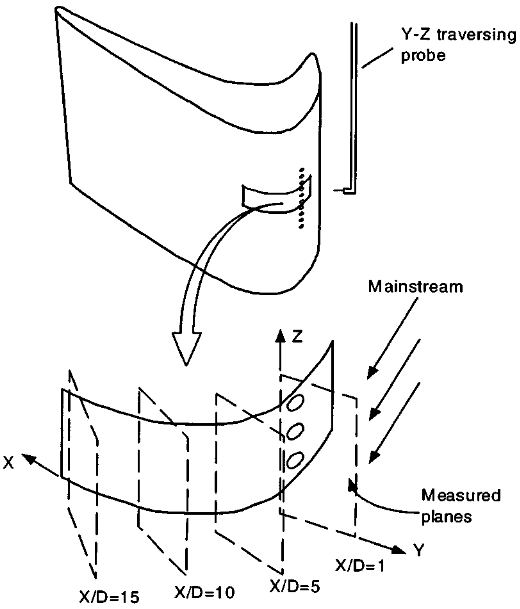

Fig. 2 Measurement planes at selected locations with a cold-wire probe

Figure 1(*b*) presents a two-dimensional view of the film cooled turbine blade model. There is one cavity used to supply coolant to the row of film holes on the suction side. The film holes, 1.905 mm in diameter and 10.16 mm apart from one another ($P/D = 5.3$), have a radial angle of 90 deg and a tangential angle of 40 deg. The film hole length is 15 mm ($L/D = 7.9$). Flow rate is controlled by a flowmeter. The heated coolant flow is passed through a solenoid-controlled three-way diverter valve before the flow enters the coolant cavity inside the blade. The solenoid-controlled valve is connected to a switch that triggers the heated coolant flow into the cavity at the instant the transient test is initiated.

The film temperature distributions are measured at $X/D = 1$, 5, 10, 15 from the centerline of the film cooling holes as shown in Fig. 2. The measuring plane is perpendicular to the oncoming mainstream. When measuring film temperature field, the blade model is not heated and only the coolant is heated and ejected. The coolant has been heated to maintain a temperature difference from free-stream at about 18°C. The temperature field is measured using a cold-wire system [18]. The cold-wire system includes a tungsten wire probe, 5 μm in diameter and 1.5 mm in length, and a temperature bridge. The temperature bridge is designed to restrict the current applied to the wire at less than 1 mA to ensure negligible sensitivity to velocity. The wire current is typically maintained at about 70 μA. The frequency response of the cold-wire is about 800 Hz. The signal from the cold-wire system is directed to an A/D converter installed in a PC. The A/D converter has 12-bit resolution and maximum gain of 8. Resulting temperature measurement accuracy is 0.1°C.

The liquid crystal coated surface area is 7.2 cm wide and the data acquisition area is 2.5 cm wide along the midspan region of the test blade. In film cooling measurements, the test blade surface is heated uniformly using a heater box [14]. The blade surface temperature is monitored using embedded thermocouples during heating. The uniformity of surface temperature with heating is within ±1.2°C. An interpolation scheme was used to further reduce the temperature variation in the initial surface temperature to within ±0.2°C. In the present study, the blade surface is heated to a temperature above liquid crystal blue color (37.2°C). The mainstream air is turned on by starting the suction-type blower. When the blower reaches the stable test flow conditions, the heater box is raised to expose the hot blade to the room temperature mainstream air within 0.1 s. When the heater box completely clears the blade height, the liquid crystal data acquisition system is automatically triggered. The liquid crystal color change time is measured using a high-precision image processing system. The system consists of two cameras individually connected to a color frame grabber board in the PC and a monitor. Software is used to measure the time of color change of liquid crystals. During one test, only one camera is operational. Hence, we require two different runs with two different camera locations to measure one set of data on the suction side for a particular condition. Details on the image processing system were presented by Du et al. [14]. The image processing system consists of an RGB camera, monitor and a PC with color frame grabber board.

Data Analysis

A well-established cold-wire technique was used to measure the detailed temperature and temperature fluctuation profiles on the blade suction side. The technique is similar to that described by Sohn et al. [18]. The mean temperature fields are presented as a nondimensional temperature defined similar to film effectiveness, i.e., $\theta=(T-T_m)/(T_c-T_m)$. The temperature fluctuation is normalized as $\theta'=T'/(T_c-T_m)$. Here, T' represent the root mean squared temperature fluctuation. 1200 data points are measured at each measurement plane at different X/D locations. The sampling rate is 10,000 Hz. At each data point. 36,864 samples are acquired and averaged to get time-averaged and fluctuation temperature.

A transient liquid crystal technique was used to measure the detailed heat transfer coefficients and film cooling effectiveness on the blade suction surface. The technique is similar to the one described by Du et al. [14]. A one-dimensional transient conduction model into a semi-infinite solid with convective boundary condition is assumed. The solution for surface temperature is obtained as

$$\frac{T_w-T_i}{T_m-T_i}=\left[1-\exp\left(\frac{h^2\alpha t}{k^2}\right)\operatorname{erfc}\left(\frac{h\sqrt{\alpha t}}{k}\right)\right] \tag{1}$$

where T_w is the wall temperature when liquid crystals change to red from green (32.7°C) at time t, T_i is the initial surface temperature, T_m is the oncoming mainstream flow temperature, and α and k are the thermal diffusivity and conductivity of the blade material, respectively. The heat transfer coefficient is obtained from Eq. (1). For film cooling tests, the mainstream temperature (T_m) in Eq. (1) is replaced by the local film temperature (T_f), which is a mixture of the coolant (T_c) and mainstream temperatures. The film temperature is defined in terms of η, which is the film cooling effectiveness.

$$\eta=\frac{T_f-T_m}{T_c-T_m}, \quad \text{or} \quad T_f=\eta T_c+(1-\eta)T_m \tag{2}$$

For the film cooling test, we obtain an equation similar to Eq. (1):

$$\frac{T_w-T_i}{T_f-T_i}=\frac{T_w-T_i}{\eta T_c+(1-\eta)T_m-T_i}=\left[1-\exp\left(\frac{h^2\alpha t}{k^2}\right)\operatorname{erfc}\left(\frac{h\sqrt{\alpha t}}{k}\right)\right] \tag{3}$$

Two similar transient tests are run to obtain the heat transfer coefficient (h) and film cooling effectiveness (η). In the first test, the blade surface is heated and the coolant and the mainstream temperatures are nearly the same. In this case, there is only one unknown, h, in the equation. For the second test, the coolant is heated to a temperature close to blade initial temperature. The calculated local heat transfer coefficient from the first test is substituted in the equation to obtain the local film cooling effectiveness. The methodology is described in detail by Du et al. [14]. Equation (3) is solved at each point on the blade surface (16,600 points) to obtain the detailed heat transfer coefficient and film cooling effectiveness distributions.

The uncertainty in the coolant jet temperature field measurement using cold-wire was estimated to be 5.8 percent. The uncertainty in the film cooling effectiveness measurement includes the additional uncertainties in heat transfer coefficient measurement and was estimated to be about 6.8 percent. The uncertainty in the immediate vicinity of the hole (less than 1 diameter around the hole) and close to the blade trailing edge could be as high as 17 percent due to invalidation of the semi-infinite model assumption.

Results and Discussion

Experiments were performed at a cascade exit Reynolds number of 5.3×10^5. The corresponding flow velocity at the cascade

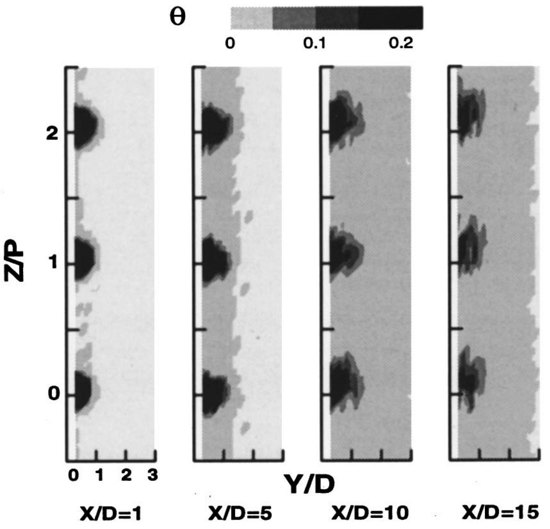

(a) time averaged temperature

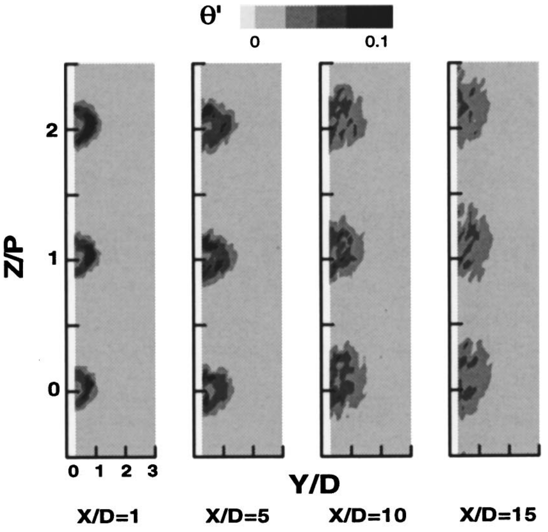

(b) temperature fluctuation

Fig. 3 Film temperature field at different locations for the case of $M=0.8$ and without wake effect ($S=0$)

exit was 50 m/s. Air as coolant was tested at blowing ratios of 0.6, 0.8, and 1.2 for no rod no wake cases ($S=0$, $\overline{Tu}=0.7$ percent) and cases with wake ($S=0.1$, $\overline{Tu}=10.4$ percent).

Coolant Jet Temperature Field Measurements

Effect of Unsteady Wake. Figures 3 and 4 present the result of heated coolant jet temperature profile development for the cases of $M=0.8$, with and without wake effect ($S=0.0$ and $S=0.1$, respectively). Temperature profiles are measured at planes at $X/D=1$, 5, 10, and 15 along the streamwise direction. Due to the delicacy of cold wire, we could not approach it very close to the blade wall surface (in the Y direction). The closest measurement location is about 0.5 mm away from the surface ($Y \geqslant 0.5$ mm, $Y/D \geqslant 0.25$). Temperature contours dilute as the heated coolant jet moves away from the eject location due to mixing between heated jet and cold free-stream air for both steady and unsteady flow cases. However, the unsteady cases dilute faster. Higher mean temperature (θ) can be seen at the center of the heated jet trajectory. Both the strength and the area of this central hotter region are also reduced along the streamwise direction. There is no significant interference between two adjacent coolant jets. Higher temperature fluctuation (θ') can be found at the mixing region of the jet and the free-stream, where the mean temperature varies greatly. The fluctuation intensity is also gradually weakened along the streamwise direction. The results show that the unsteady wake produces slightly higher temperature fluctuations than the steady flow case. Meanwhile, at the same locations, the case with wake effect has larger areas of temperature fluctuations than the case without. This indicates that the unsteady wake has expanded the mixing region by bringing more free-stream air into it and thus enhanced the diffusion of the jet.

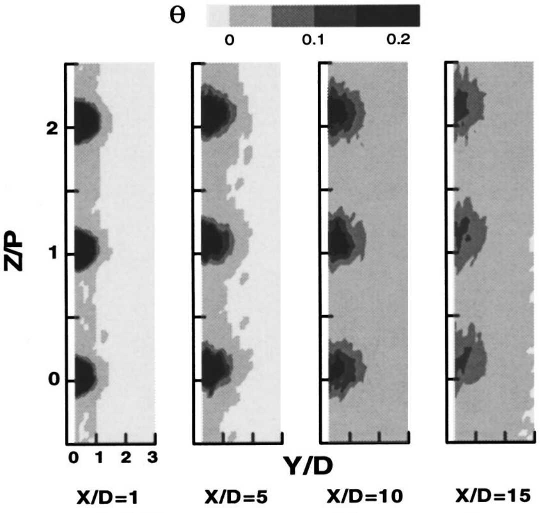

(a) time averaged temperature

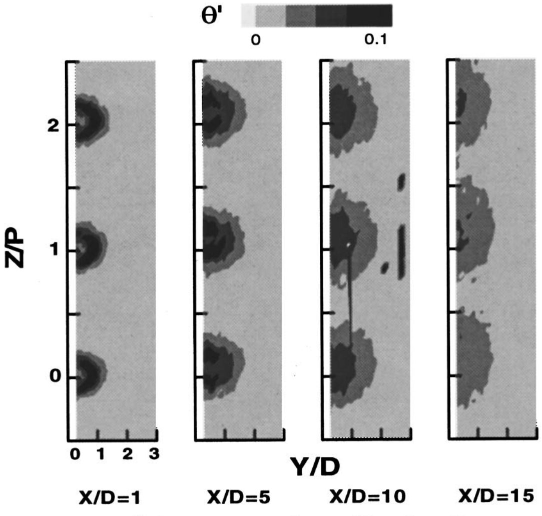

(b) temperature fluctuation

Fig. 4 Film temperature field at different locations for the case of $M=0.8$ and with wake effect ($S=0.1$)

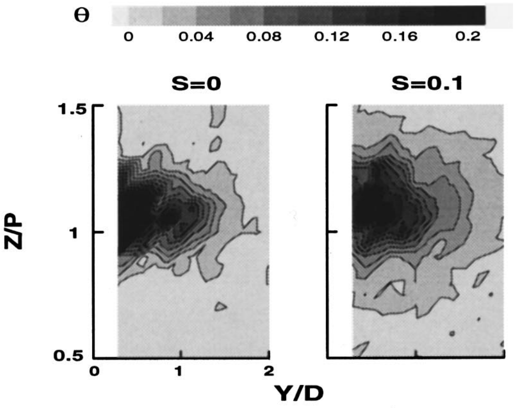

(a) time averaged temperature

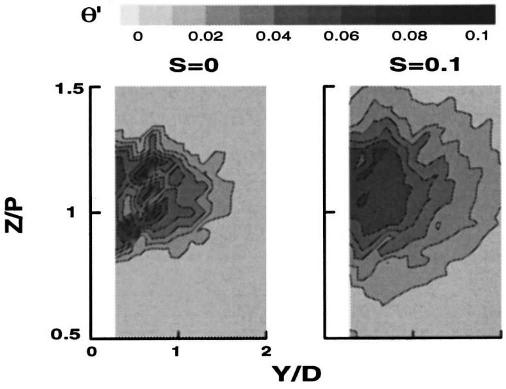

(b) temperature fluctuation

Fig. 5 Detailed film temperature contour at $X/D=10$ for the cases of $M=0.8$, without and with wake effect

Figure 5 shows the enlarged coolant jet temperature contours at $X/D=10$ for both steady and unsteady cases of a blowing ratio of $M=0.8$. For the case with unsteady wake effect, both the coolant jet mean temperature (θ) and temperature fluctuation (θ') contour have been expanded to a larger area. The dimensionless mean temperature at jet center is 0.27 for the steady case and is reduced to 0.19 for the unsteady case. The central hotter region of the coolant jet for the case with wake effect is smaller than that of the case without wake effect and it has somewhat drifted away from the blade surface. The temperature fluctuation level is of the same range (from 0 to 0.08) for both cases, but the unsteady case has a much larger temperature fluctuation area. All this implies that the unsteady wake enhances the mixing between the heated coolant jet and the cold free-stream, and more heated jet is diffused into the free-stream.

Effect of Blowing Ratio. Figure 6 presents the result of enlarged coolant jet contours for two different blowing ratios ($M=0.8$ and $M=1.2$) at location $X/D=10$ and without wake effect ($S=0$). The dimensionless mean temperature (θ) at jet center is 0.27 for the case $M=0.8$ and is reduced to 0.15 for the case $M=1.2$. For the case $M=0.8$, we observe a fairly large center re-

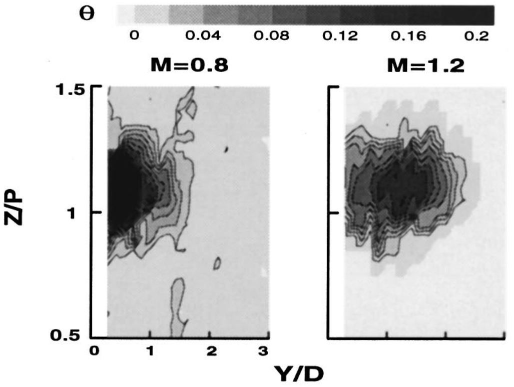

(a) time averaged temperature

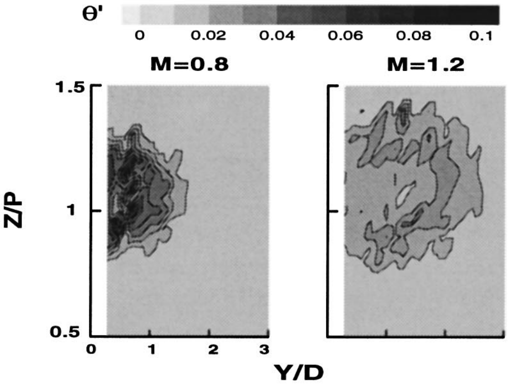

(b) temperature fluctuation

Fig. 6 Effect of blowing ratio on film temperature field ($S=0$, $X/D=10$)

gion of higher mean temperature, and the jet center is still attached to the blade surface. For the case $M=1.2$, the central hotter region is smaller than the case $M=0.8$ and the coolant jet has lift off the blade surface and is barely attached to the wall. Only part of the periphery of the jet has touched the blade wall. This indicates that the higher the blowing ratio, the further the jet would lift off the blade surface, which reduces the film cooling coverage. The case $M=1.2$ has a much larger temperature fluctuation area than the case $M=0.8$, but the temperature fluctuation level is decreased due to its lower jet temperature. The temperature fluctuation range is from 0 to 0.05 for the case $M=1.2$, and from 0 to 0.08 for the case $M=0.8$. All this shows that for the higher blowing ratio, there is more mixing between the heated coolant jet and the cold main stream. The coolant jet dilutes faster as the jet goes away along the streamwise direction.

Film Cooling Measurements

Effect of Unsteady Wake on Film Cooling Effectiveness. Figure 7 presents the detailed film cooling effectiveness distributions for air injection at three different blowing ratios ($M=0.6$, 0.8, 1.2) with and without unsteady wakes, respectively. Since there are no film cooling holes at leading edge of the blade, the film streaks start where the row of film cooling holes (the only row of holes in this study) is located. From Fig. 7, one can see that the film streaks extend along the streamwise direction fairly straightly. The streaks are gradually weakened the further they extend away from the film cooling holes. The film cooling effectiveness between streaks is very low due to the lack of spanwise mixing of jets, which we can also clearly observe from the coolant jet temperature contour measurements. For cases without the effect of unsteady wakes, the streaks remain clearly evident downstream of the injection holes, except for the very high blowing ratio of 1.2, in which the jet has apparently lifted off from the blade surface because of its high momentum. With the effect of unsteady wake, the turbulence level in the free-stream is higher. The figure shows that the streaks are evidently weakened but expanded further down in the streamwise direction. Observation of coolant jet temperature contour tells us that, due to the effect of unsteady wake, the coolant jet has more mixing with the mainstream, which widens the jet streak yet weakens the cooling jet much faster than the cases without unsteady wake.

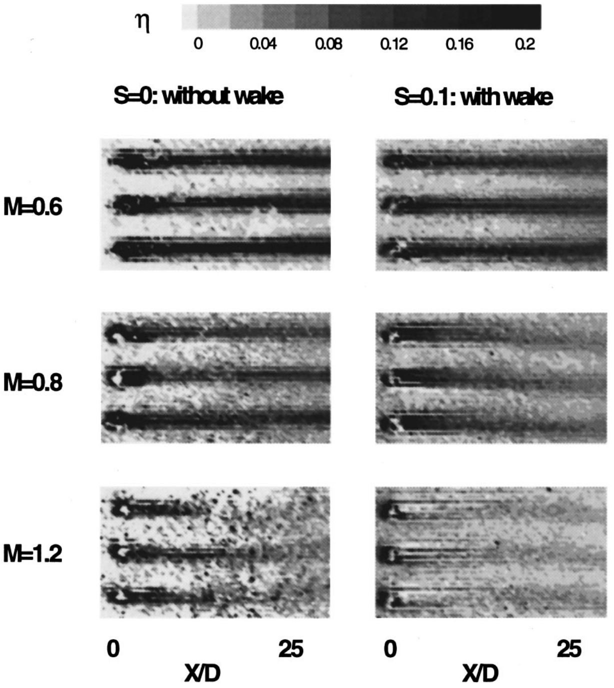

Fig. 7 Effect of unsteady wake and blowing ratio on detailed film cooling effectiveness distribution

In Fig. 8, the film cooling effectiveness distribution along film hole centerline shows that centerline film effectiveness decreases along the streamwise direction due to the continuous mixing between coolant jet and mainstream. The higher the blowing ratio, the lower its centerline film effectiveness at the same location. Among all the cases, the case $M=0.6$ and without wake effect has the highest centerline effectiveness. It has a high value of 0.33 at the location right behind the film hole and then decreases to and remains at about 0.2 afterwards. Addition of unsteady wake decreases the centerline film effectiveness for the same blowing ratios. Compared to the case $M=0.8$, unsteady wake has a greater effect on the case of lower ($M=0.6$) and higher blowing ratios ($M=1.2$), especially at the region right behind the film hole, where both of the latter two cases have a sharp drop in centerline effectiveness.

In the spanwise-averaged film effectiveness distribution shown in Fig. 8, for blowing ratios of 0.6 and 0.8, film cooling effectiveness with the effect of unsteady wake is significantly lower than that without unsteady wake at areas immediately downstream of the film cooling holes. However, this trend does not last long. Starting from $X/D=5$, the spanwise-averaged cooling effectiveness with wake effect is about the same as that without wake effect. The possible explanation for this phenomenon is that before $X/D=5$, the wake effect is mainly manifested in the reduction of the spanwise-averaged effectiveness; after $X/D=5$, another aspect of wake effect, expansion of the coolant jet to cover more blade surface area, begins to show its beneficial part and thus keeps the spanwise-averaged effectiveness from decreasing.

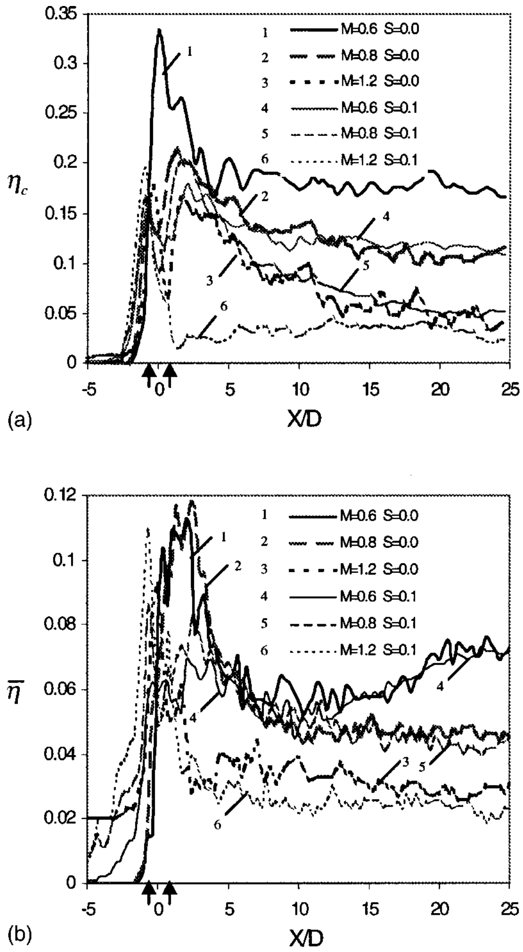

Fig. 8 Film cooling effectiveness distribution: (*a*) along film hole centerline; (*b*) spanwise-averaged

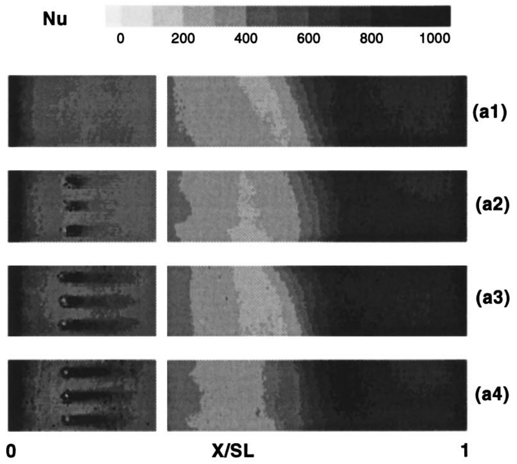

(a) S=0.0, no film hole and M=0.6, 0.8, 1.2

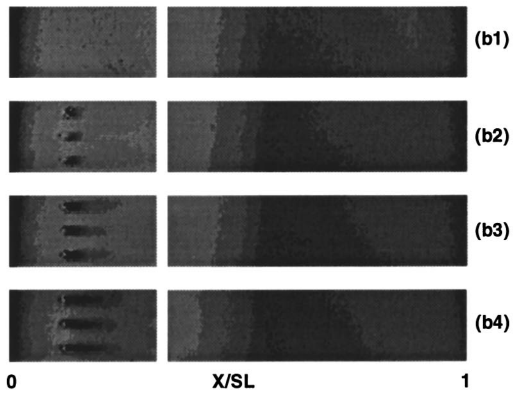

(b) S=0.1, no film hole and M=0.6, 0.8, 1.2

Fig. 9 Detailed Nusselt number distribution for cases at different blowing ratios, with and without wake effect

For a blowing ratio of 1.2, the spanwised cooling effectiveness with wake effect is generally only slightly lower than that without wake effect. In this case, the expanding of the coolant jet will not make much difference because the jet has lifted off the blade surface anyway. So the wake effect is mainly the decrease of the film cooling effectiveness.

All this indicates that unsteady wake has a strong effect on the film cooling effectiveness distributions. Without unsteady wake, the film cooling jets protect the surface better within limited areas. Addition of unsteady wake causes disturbances in the mainstream, which results in more mixing between the mainstream and coolant jets. This results in two effects: On the one hand, the film coolant jet has been diluted and produced smaller cooling effectiveness; on the other hand, the film coolant jet has been expanded along the spanwise direction and more area is covered by film cooling, and thus could contribute to the increase of spanwise-averaged cooling effectiveness. However, generally, unsteady wake has caused the film cooling effectiveness to decrease.

Effect of Unsteady Wake on Nusselt Number. Figure 9(a1)–(a4) are for cases without wake effect and (b1)–(b4) for cases with wake effect. Among them, (a1) and (b1) are for the smooth surface and the other three in each group have blowing ratios of 0.6, 0.8, and 1.2. Unlike the film effectiveness distribution measurements, here we have gathered data on the whole suction surface in order to get information on the film cooling jet's effect on the blade surface heat transfer right behind the film cooling holes as well as its effect on boundary-layer transition.

For a smooth surface without wakes (case a1), the Nusselt numbers drop rapidly from the leading edge to about $X/SL=0.5$ on the suction surface and then increase again due to boundary-layer transition to turbulent flow. For a smooth surface with wakes (case b1), the Nusselt numbers also decrease along the streamwise direction but transition occurs much earlier ($X/SL=0.25$) for this case than for case a1. Also, its spanwise-averaged Nusselt number is higher than that of case a1 before the transition begins.

With film cooling, the Nusselt numbers at locations right behind the film cooling holes increase significantly and traces of high Nusselt numbers are formed right behind the holes. The higher the blowing ratio, the longer this trace of highly increased Nusselt numbers. Due to the film injection, boundary-layer transition occurs slightly earlier in cases a2 to a4 than in case a1. As soon as boundary transition begins, the Nusselt numbers increase at about the same rate as in case a1, and they keep increasing much further down the blade before they begin to decrease again. The same is true for cases with both film cooling and unsteady wake effect, as we compare the cases b2 to b4 with case b1. However, as we have noticed, no matter with or without film cooling, the addition of an unsteady wake has caused boundary transition to occur significantly earlier than the cases without unsteady wake. Also, for cases with wake effect, the streaks of high Nusselt numbers right after the film holes are a little shorter compared with cases without wake effect. The reason for this is that, due to the unsteady wake, the cooling jet is diluted faster along the streamwise direction than in cases without unsteady wake.

Figure 10 presents the spanwise-averaged Nusselt number distributions for both steady and unsteady flow with wake effect. The small arrows indicate where the film injection is. The results for

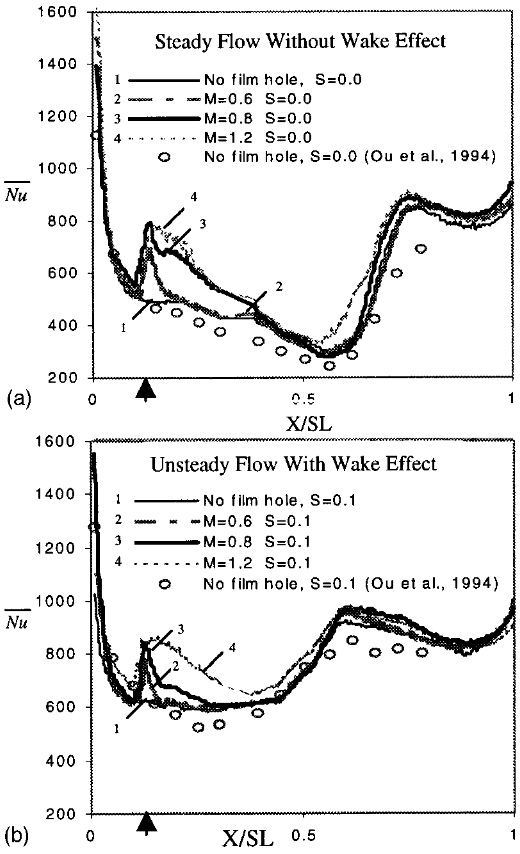

Fig. 10 Spanwise-averaged Nusselt number distribution for: (*a*) steady flow; (*b*) unsteady flow with wake effect

the smooth surface blade with and without wake are in good agreement with those for the same cases from Ou et al. [9], who used the thin-foil-thermocouple technique to study the heat transfer over a model turbine blade. The figure shows that, for both cases with and without unsteady wake, the spanwise-averaged Nusselt number shows a peak increase right downstream of the jet ejection location. It then decreases along the streamwise direction till it reaches the boundary-layer transition location, where it begins to increase again to reach its second peak value. The second peak value is higher than the first one. However, for the cases with wake effect, the spanwise-averaged Nusselt number does not drop as low as the cases without wake effect before it begins to increase again due to much earlier boundary-layer transition. In Fig. 10 we also observe that, the higher the blowing ratio, the greater both of its peak values. Blowing ratio has a comparatively greater effect on the first peak value. Higher blowing ratio pushes the transition front only slightly ahead. The blowing ratio effect is very small compared to the effect of unsteady wake as far as the boundary-layer transition is concerned.

It indicates that film cooling enhances the surface heat transfer along the blade while the unsteady wake causes earlier boundary-layer transition. However, the results show that both film cooling and wake effect do not have much effect on the maximum spanwise-averaged Nusselt number (the second peak value at the end of boundary-layer transition) achieved on the suction surface.

Conclusions

Detailed film effectiveness, heat transfer coefficient, and coolant jet temperature profile on the suction side of a film-cooled blade were measured and presented under the effects of upstream unsteady wakes. The blade has only one row of holes near the gill hole portion on the suction side. Results are presented at a cascade exit Reynolds number of 5.3×10^5 for cases without and with wake. Coolant blowing ratio was varied from 0.6 to 1.2. Wake Strouhal number was kept at 0 and 0.1. The conclusions based on the experimental results are:

1 The development of coolant jet temperature and its fluctuation profiles provides better understanding of the film cooling process and can be used to explain the film cooling performance.

2 Unsteady wake reduces film cooling effectiveness of the film cooled blade.

3 Film injection in the laminar boundary-layer region enhances the local heat transfer coefficient up to 60 percent right after ejection. The magnitude of film-induced heat transfer enhancement decreases along the blade and diminishes near the flow transition location.

4 Unsteady wake promotes earlier boundary-layer transition and enhances heat transfer on the suction surface for conditions with and without film cooling.

5 Unsteady wake plays a predominate role in determining the boundary-layer transition location. Single-row of film injection does not affect much on the location of boundary-layer transition.

Acknowledgments

This paper was prepared with the support of the NASA-Lewis Research Center under grant number NAG3-1656. The NASA technical team is Dr. Philip E. Poinsatte and Dr. Raymond Gaugler. Their support is greatly appreciated. Financial support from Seoul National University to Dr. Dong Kee Sohn is acknowledged.

Nomenclature

C_x = blade axial chord length=17 cm
d = wake generator rod diameter
D = film hole diameter
h = local heat transfer coefficient
k = thermal conductivity of blade material=0.159 W/m·°C
k_{air} = thermal conductivity of mainstream air
L = film cooling delivery length
M = coolant-to-mainstream mass flux ratio or blowing ratio$=\rho_c V_c/\rho_m V$
n = number of rods on wake generator
N = speed of rotating rods
Nu = local Nusselt number based on axial chord$=hC_x/k_{\mathrm{air}}$
$\overline{\mathrm{Nu}}$ = spanwise-averaged Nusselt number
P = film hole pitch
Re = Reynolds number based on exit velocity and axial chord$=V_2C_x/v$
S = wake Strouhal number$=2\pi Ndn/(60V_1)$
SL = streamwise length on the suction surface=33.1 cm
t = liquid crystal color change time
T_c = coolant temperature
T_f = film temperature
T_i = initial temperature of blade surface
T_m = mainstream temperature
T_w = liquid crystal color change from green to red
V_1 = cascade inlet velocity
V_2 = cascade exit velocity
X = streamwise distance from centerline of film cooling holes
Y = radial distance from blade surface
α = thermal diffusivity of blade material$=0.135\times10^{-6}$ m^2/s
δ_2 = local momentum thickness
η = local film cooling effectiveness
$\overline{\eta}$ = spanwise-averaged film cooling effectiveness
ν = kinematic viscosity of cascade inlet mainstream air
ρ_c = coolant density
ρ_m = mainstream flow density

References

[1] Nirmalan, V., and Hylton, L., 1990, ''An Experimental Study of Turbine Vane Heat Transfer With Leading Edge and Downstream Film Cooling,'' ASME J. Turbomach., **112**, pp. 477–487.

[2] Abuaf, N., Bunker, R., and Lee, C. P., 1995, ''Heat Transfer and Film Cooling Effectiveness in a Linear Airfoil Cascade,'' ASME Paper No. 95-GT-3.

[3] Camci, C., and Arts, T., 1990, ''An Experimental Convective Heat Transfer Investigation Around a Film-Cooled Gas Turbine Blade,'' ASME J. Turbomach., **112**, pp. 497–503.

[4] Takeishi, K., Aoki, A., Sato, T., and Tsukagoshi, K., 1992, ''Film Cooling on a Gas Turbine Rotor Blade,'' ASME J. Turbomach., **114**, pp. 828–834.

[5] Ito, S., Goldstein, R. J., and Eckert, E. R. G., 1978, ''Film Cooling of a Gas Turbine Blade,'' ASME J. Eng. Power, **100**, pp. 476–481.

[6] Haas, W., Rodi, W., and Schönung, B., 1992, ''The Influence of Density Difference Between Hot and Coolant Gas on Film Cooling by a Row of Holes: Predictions and Experiments,'' ASME J. Turbomach., **114**, pp. 747–755.

[7] Ames, F. E., 1998, ''Aspects of Vane Film Cooling With High Turbulence: Part I—Heat Transfer; Part II—Adiabatic Effectiveness,'' ASME J. Turbomach., **120**, pp. 768–784.

[8] Abhari, R. S., and Epstein, A. H., 1994, ''An Experimental Study of Film Cooling in a Rotating Transonic Turbine,'' ASME J. Turbomach., **116**, pp. 63–70.

[9] Ou, S., Han, J. C., Mehendale, A. G., and Lee, C. P., 1994, ''Unsteady Wake Over a Linear Turbine Blade Cascade With Air and CO_2 Film Injection: Part I—Effect on Heat Transfer Coefficients,'' ASME J. Turbomach., **116**, pp. 721–729.

[10] Mehendale, A. B., Han, J. C., Ou, S., and Lee, C. P., 1994, ''Unsteady Wake Over a Linear Turbine Blade Cascade With Air and CO_2 Film Injection: Part II—Effect on Film Effectiveness and Heat Transfer Distributions,'' ASME J. Turbomach., **116**, pp. 730–737.

[11] Vedula, R. J., and Metzger, D. E., 1991, ''A Method for Simultaneous Determination of Local Effectiveness and Heat Transfer Distributions in Three-Temperature Convection Situations,'' ASME Paper No. 91-GT-345.

[12] Ekkard, S. V., Zapata, D., and Han, J. C., 1997, ''Heat Transfer Coefficients Over a Flat Surface With Air and CO_2 Injection Through Compound Angle Holes Using a Transient Liquid Crystal Image Method,'' ASME J. Turbomach., **119**, No. 3, pp. 580–586.

[13] Ekkard, S. V., Zapata, D., and Han, J. C., 1997, ''Film Effectiveness Over a Flat Surface With Air and CO_2 Injection Through Compound Angle Holes Using a Transient Liquid Crystal Image Method,'' ASME J. Turbomach., **119**, No. 3, pp. 587–593.

[14] Du, H., Han, J. C., and Ekkard, S. V., 1998, ''Effect of Unsteady Wake on Detailed Heat Transfer Coefficient and Film Effectiveness Distributions for a Gas Turbine Blade,'' ASME J. Turbomach., **120**, pp. 808–817.

[15] Du, H., Ekkad, S. V., and Han, J., 1999, ''Effect of Unsteady Wake With Trailing Edge Coolant Ejection on Film Cooling Performance for a Gas Turbine Blade,'' ASME J. Turbomach., **121**, pp. 448–453.

[16] Drost, U., and Bölcs, A., 1999, ''Investigation of Detailed Film Cooling Effectiveness and Heat Transfer Distributions on a Gas Turbine Airfoil,'' ASME J. Turbomach., **121**, pp. 233–242.

[17] Kohli, A., and Bogard, D. G., 1998, ''Fluctuating Thermal Field in the Near-Hole Region for Film Cooling Flows,'' ASME J. Turbomach., **120**, pp. 86–91.

[18] Sohm, D. K., Teng, S., and Han, J. C., 1998, ''Film Temperature and Effectiveness Measurements on a Cylindrical Leading Edge Film Cooling Model,'' *Heat Transfer 1998, Proc. of 11th IHTC*, **6**, pp. 571–576, Aug. 23–28, Kyongju, Korea.

A Three-Dimensional Coupled Internal/External Simulation of a Film-Cooled Turbine Vane

James D. Heidmann
NASA Lewis Research Center,
Cleveland, OH 44135

David L. Rigby
Dynacs Engineering Co., Inc.,
Brookpark, OH 44142

Ali A. Ameri
AYT Corporation,
NASA Lewis Research Group,
Cleveland, OH 44135

A three-dimensional Navier–Stokes simulation has been performed for a realistic film-cooled turbine vane using the LeRC-HT code. The simulation includes the flow regions inside the coolant plena and film cooling holes in addition to the external flow. The vane is the subject of an upcoming NASA Lewis Research Center experiment and has both circular cross-sectional and shaped film cooling holes. This complex geometry is modeled using a multiblock grid, which accurately discretizes the actual vane geometry including shaped holes. The simulation matches operating conditions for the planned experiment and assumes periodicity in the spanwise direction on the scale of one pitch of the film cooling hole pattern. Two computations were performed for different isothermal wall temperatures, allowing independent determination of heat transfer coefficients and film effectiveness values. The results indicate separate localized regions of high heat flux in the showerhead region due to low film effectiveness and high heat transfer coefficient values, while the shaped holes provide a reduction in heat flux through both parameters. Hole exit data indicate rather simple skewed profiles for the round holes, but complex profiles for the shaped holes with mass fluxes skewed strongly toward their leading edges. [S0889-504X(00)02802-6]

Introduction

Film cooling is commonly used in advanced turbine designs to produce a buffer layer of relatively cool air between the turbine blade and the hot free-stream gas. The great majority of film cooling studies involve use of a flat plate as an idealization of the actual environment of a film-cooled turbine blade. Early research of this type is summarized by Goldstein [1]. These early studies describe the general behavior of film cooling on a flat plate and define the parameters applied to its description: film effectiveness and heat transfer coefficient. Subsequent research on flat plate film cooling has typically focused on a specific aspect of the problem. Gritsch et al. [2] and Thole et al. [3] have studied flow exiting holes with expanded exits, also known as shaped holes. The results have shown shaped holes to have flow characteristics much different from round holes. A series of papers by Walters and Leylek [4], McGovern and Leylek [5], Hyams and Leylek [6], and Brittingham and Leylek [7] provided a detailed computational study of progressively more complex film cooling geometries, including hole shape and orientation. Of particular interest to the present study is the conclusion of Hyams and Leylek [6] that laterally diffused film holes provide the best film coverage of the shaped hole designs studied. Leylek and Zerkle [8] were among the first to assess the effect of accounting for the presence of a plenum in a computational study. A jetting effect was identified wherein a low-momentum region is produced behind the sharp entrance corner of a film hole.

Ito et al. [9] explained the balance that exists between static pressure forces and coolant jet momentum and how this determines film cooling performance on a curved surface. Low-momentum cooling jets perform better on the suction side, while high-momentum jets do better on the pressure side. Mick and Mayle [10] showed through experiment that leading edge film cooling, also known as showerhead film cooling, reduces heat flux over the entire flat test body for moderate blowing ratios, despite large increases in heat transfer coefficient in the leading edge region. Garg and Gaugler [11] computationally demonstrated the profound effect of film hole exit velocity and temperature profile variations on blade surface heat transfer. One of the goals of the present study is thus to describe these profiles accurately for use in new models.

Several computational studies have included plenum effects in realistic blade geometries, most notably Garg and Rigby [12], Bohn et al. [13], and Choi [14]. Choi modeled a film-cooled vane using an overlapped grid with a fine mesh near the coolant hole and plenum and a coarse global mesh. Hole exit profiles were not published. Bohn et al. [13] modeled a showerhead film-cooled turbine vane and included conjugate conduction effects in the blade. However, the film holes were oriented normal to the blade surface, unlike the angled holes of an actual turbine blade. Garg and Rigby [12] were the first to model a film-cooled turbine blade with angled showerhead holes and plenum three dimensionally and present hole exit profiles of momentum and stagnation temperature. Simulations of this type have typically been limited to a single idealized plenum and have considered only circular cross-sectional holes due to the inherent geometrical complexity of the problem.

Relatively few experimental studies on realistic film-cooled turbine blades have been published in the open literature. One such study was performed by Hylton et al. [15] for a turbine vane similar to the one of the present study. Suction surface, pressure surface, and showerhead film cooling holes were present. Surface temperature data was collected downstream of the cooling holes at midspan, and a finite element solution was used to obtain the internal temperature field and associated wall heat fluxes. No data were recorded in the insulated portion of the vane containing the film cooling holes.

The present study seeks to model a realistic film-cooled turbine vane computationally. The simulation accounts for actual three-dimensional vane geometry including plena and film holes. Both film effectiveness and heat transfer coefficient are computed on the entire vane surface and will be compared with future experimental results on the same geometry. The observation of computed three-dimensional flow phenomena including hole exit profiles is used to interpret the computed performance of this film cooling design and to suggest simplified models for characterizing

---

Contributed by the International Gas Turbine Institute and presented at the 44th International Gas Turbine and Aeroengine Congress and Exhibition, Indianapolis, Indiana, June 7–10, 1999. Manuscript received by the International Gas Turbine Institute February 1999. Paper No. 99-GT-186. Review Chair: D. C. Wisler.

the film hole exit properties. Inclusion in the design of the various generic types of film cooling—showerhead, suction, pressure, shaped holes—allows extrapolation of the flow phenomena and accompanying interpretations to other film cooling designs.

Vane Geometry and Numerical Grid

The turbine vane of this study is based on an Allied-Signal film-cooled engine design. The present computation models an upcoming NASA Lewis Research Center experiment, which will be performed in a linear cascade. The geometry of this test vane is based on the engine vane midspan coordinates, and is scaled up by a factor of 2.943 to allow matching of engine exit Mach number (0.876) and exit Reynolds number (2.9×10^6 based on true chord) with atmospheric inlet conditions. The resultant test vane has a true chord of 0.206 m. The computation of this study is a true prediction and is being used to help design the experiment, as well as to provide data as a ''numerical test cell,'' pending experimental verification. Since the test vane is of constant cross section, only one spanwise pitch of the film hole pattern is discretized, with periodicity enforced at each end. This simplification assumes no effect of endwalls, but greatly reduces the number of grid points required to model the vane.

As shown in Fig. 1, the vane has two plena, which feed 12 rows of film cooling holes as well as trailing-edge ejection slots, all of which is modeled by the grid. Since the experiment will have no trailing edge ejection, this flow is blocked in the computation although future computational studies may incorporate this feature. Table 1 provides geometric data for each row of film holes. Figure 2 shows the definitions of α and β. Streamwise angles are defined as positive away from the geometric leading edge.

All rows have circular cross-sectional holes except for rows 1–4, which have shaped holes. These holes are expanded in both the lateral and downstream directions in an attempt to achieve better film coverage. The expansion angle on each side of the holes and on the downstream edge is 10 deg. Rows 5–10 consist of compound-angle holes in the showerhead region with an inclination of 60 deg, in the spanwise direction. Rows 11 and 12 have a spanwise pitch equal to two-thirds of the spanwise pitch of rows 1–10, so the overall vane spanwise pitch covers three holes each in rows 11 and 12, and two holes each in rows 1–10. In rows 1–10, the holes are in a staggered arrangement, so it was necessary to split some holes on the spanwise periodic boundary.

A multiblock grid approach is adopted to model this complex geometry, in which a system of locally structured grid blocks is generated in a globally unstructured assembly. This multiblock system is generated in the present study by the grid generation program GridPro™ [16]. This program produces a body-fitted multiblock grid with hexahedral cells and full face-matching blocks. The present grid was initially composed of 2298 blocks, which were merged to produce a grid consisting of 140 blocks using the method of weakest descent as described in Rigby [17] and Rigby et al. [18]. The grid is composed of 1.2×10^6 computational cells. Algebraic clustering produces a y^+ value of less than 1.0 at the first grid point away from the wall at all locations.

Table 1 Film-cooling hole geometric parameters

row	s/c	type	p/d	α (deg)	β (deg)
1	-0.447	shaped, staggered pressure side	4.06	65.5	0
2	-0.385	shaped, staggered pressure side	4.06	62.9	0
3	-0.182	shaped, staggered pressure side	4.06	63.8	0
4	-0.142	shaped, staggered pressure side	4.06	61.4	0
5	-0.053	round, staggered showerhead	4.06	6.2	60
6	-0.032	round, staggered showerhead	4.06	2.7	60
7	-0.011	round, staggered showerhead	4.06	0.9	60
8	0.011	round, staggered showerhead	4.06	0.9	60
9	0.033	round, staggered showerhead	4.06	2.9	60
10	0.054	round, staggered showerhead	4.06	4.4	60
11	0.116	round, aligned suction side	2.71	44.5	0
12	0.157	round, aligned suction side	2.71	47.0	0

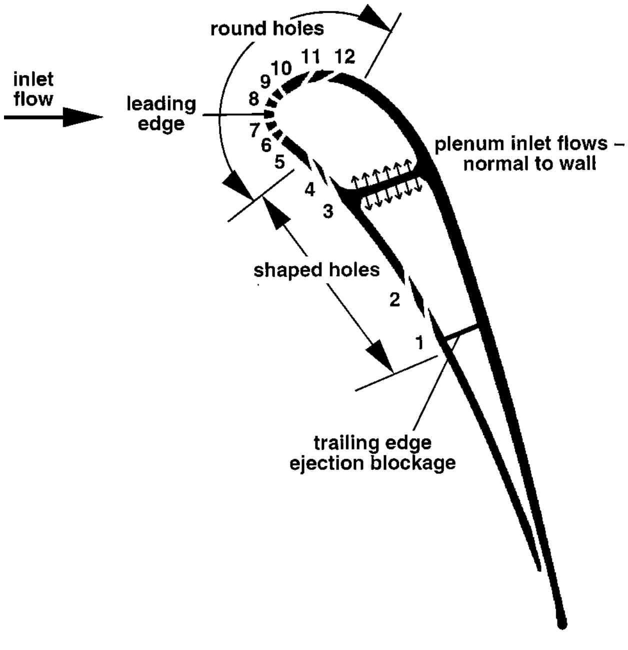

Fig. 1 Vane cross section and film hole row numbers

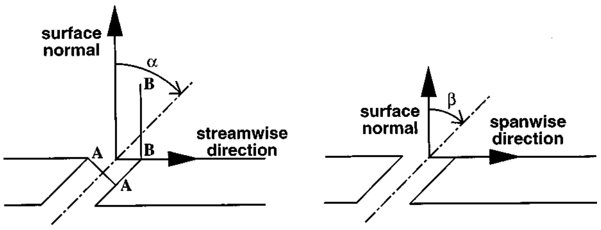

a) streamwise angles

b) spanwise angles

Fig. 2 Film hole angles

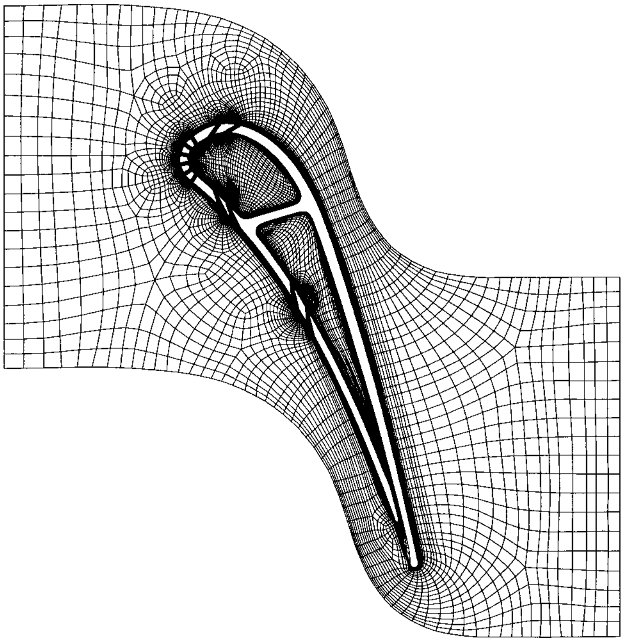

Fig. 3 Blade-to-blade view of multiblock computational grid

Several calculations were performed for varying wall spacings, and it was found that further reductions produced little change in the solution. The grid consists of 20 cells across both the inlet and outlet boundaries, 60 cells on the periodic boundary, over 200 cells around the vane, and 44 cells from the vane to the periodic boundary. These values are consistent with good computational practice. A blade-to-blade view of the computational grid is shown in Fig. 3.

Figure 4 shows the grid in the leading edge region of the vane. The faithful discretization of the shaped holes should be noted, as well as the ability of the multiblock grid to transition from a very fine structure near locations of complex geometry such as film holes to a coarser structure far from the holes. In addition, the clustered viscous grids abut all wall boundaries without extending into the flow field. These features would be impossible for a single-block grid on even modestly complex geometries, and serve to greatly reduce the number of grid points necessary to adequately resolve the geometry.

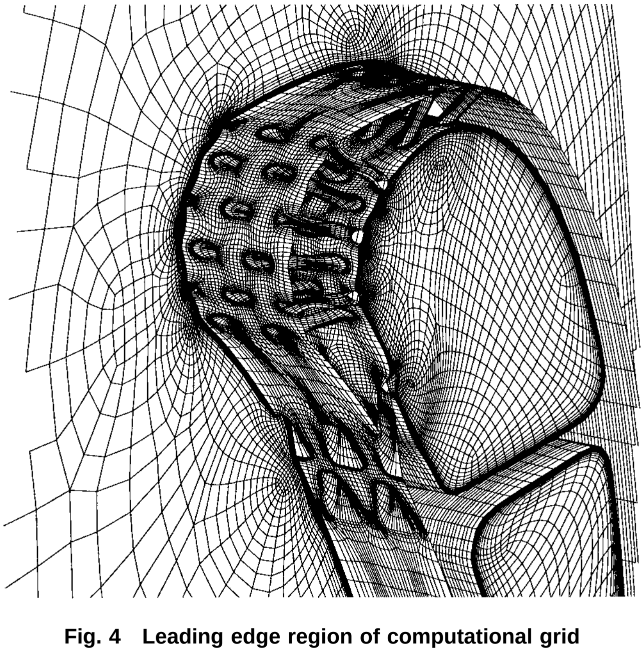

Fig. 4 Leading edge region of computational grid

Computational Method

The simulations in this study were performed using a multiblock computer code called LeRC-HT, previously known as TRAF3D.MB [19], which is based on a single block code designed by Arnone et al. [20]. This code is a general-purpose flow solver designed for simulations of flows in complicated geometries. The code solves the full compressible Reynolds-averaged Navier–Stokes equations using a multistage Runge–Kutta-based multigrid method. It uses the finite volume method to discretize the equations. The code uses central differencing together with artificial dissipation to discretize the convective terms. The overall accuracy of the code is second order. The present version of the code [17,21,22] employs the $k-\omega$ turbulence model developed by Wilcox [23,24], with subsequent modifications by Menter [25] as implemented by Chima [26]. The $k-\omega$ turbulence model is desirable because it does not require specification of distance to the wall. Such a specification is difficult for complex geometries requiring multiblock grids, such as is considered in the present study. Accurate heat transfer predictions are possible with the code because the model integrates to the walls and no wall functions are used. Rather, the computational grid is generated to be sufficiently fine near walls to produce a y^+ value of less than 1.0 at the first grid point away from the wall. For heat transfer a constant value of 0.9 for turbulent Prandtl number, Pr_t, is used. A constant value of $\mathrm{Pr}=0.72$ is used. Laminar viscosity is a function of temperature through a 0.7 power law [27] and c_p is taken to be a constant.

The free-stream inlet flow to the vane is at an angle of 0 deg to the axial direction, with all temperatures and pressures normalized by the inlet stagnation values of 294 K and 101 kPa, respectively. The inlet turbulence intensity is 8.0 percent and the turbulence scale is 15.0 percent of vane true chord. These values were based on preliminary experimental turbulence grid designs. Other inflow quantities are set by means of the upstream-running Riemann invariant. The vane downstream exit flow is defined by imposing a constant normalized static pressure of 0.576, which was empirically determined to yield the design exit Mach number of 0.876. Periodicity was enforced in both the blade-to-blade and spanwise directions based on vane and film hole pitches, respectively.

To maintain a true periodic solution, inflow to the plena was provided by defining a region of each plenum wall as an inlet and introducing uniform flow normal to the wall. These regions lie on either side of the internal wall that separates the two plena as shown in Fig. 1. The experiment will have spanwise flow in the plenum, but bleed of the plenum flow into the film holes results in a spanwise-varying mass flow rate and static pressure, which would violate spanwise periodicity. Modeling this spanwise plenum flow was attempted computationally, but was abandoned when numerical instabilities prevented convergence. The inflow stagnation temperature to the plena was 0.5, the velocity was fixed to the constant value required to provide the design mass flow rate to each plenum, and static pressure was extrapolated from the interior. The inflow patch for each plenum was defined to be sufficiently large to yield very low inlet velocities (Mach number <0.05), allowing each plenum to approximate an ideal plenum.

All solid walls were given a no-slip boundary condition in addition to a fixed temperature. The isothermal wall boundary condition extended to all wall surfaces, including the film hole surfaces and plenum surfaces, so heat transfer in the plena and film holes occurs and provides a stagnation temperature profile in the jet exiting each hole. Two solutions were generated with wall temperatures (T_w) of 0.7 and 0.8, respectively. The predicted wall heat flux distributions (q''_w) from these solutions were used to solve simultaneously for adiabatic wall temperature (T_{aw}) and Stanton number based on adiabatic wall temperature ($\mathrm{St}_{\mathrm{aw}}$) using

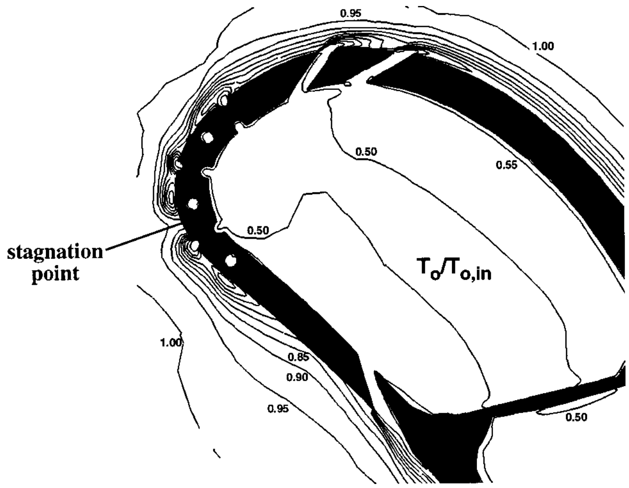

Fig. 5 Stagnation temperature contours on plane of fixed span

Eq. (1), under the assumption that T_{aw} and St_{aw} are independent of T_w. Having solved for T_{aw}, film effectiveness (η) was found by Eq. (2) and Stanton number based on inlet stagnation temperature (St_{in}) was found using Eq. (3) for the 0.7 wall temperature case:

$$St_{aw}=\frac{q''_w}{(\rho V c_p)_{in}(T_{aw}-T_w)} \tag{1}$$

$$\eta=\frac{T_{in}-T_{aw}}{T_{in}-T_c} \tag{2}$$

$$St_{in}=\frac{q''_w}{(\rho V c_p)_{in}(T_{in}-T_w)} \tag{3}$$

T_{in} is the inlet stagnation temperature, T_c is the coolant temperature, and ρ, V, and c_p are the density, velocity, and specific heat of the free-stream inlet. St_{aw} is a dimensionless heat transfer coefficient and may be thought of as the heat transfer coefficient that would result for a coolant flow at the same temperature as the free stream. St_{in} is the dimensionless overall heat transfer coefficient, and is simply proportional to local wall heat flux for the $T_w = 0.7$ case. The wall temperature of 0.7 is considered the baseline case because it most closely matches the temperature of an isothermal cooled turbine vane. Volumetric flow data and wall heat fluxes are given for this case. A third calculation was performed for a smooth vane with no film holes or plenum at a wall temperature of 0.7. The results of this calculation were used to normalize the film-cooling predictions.

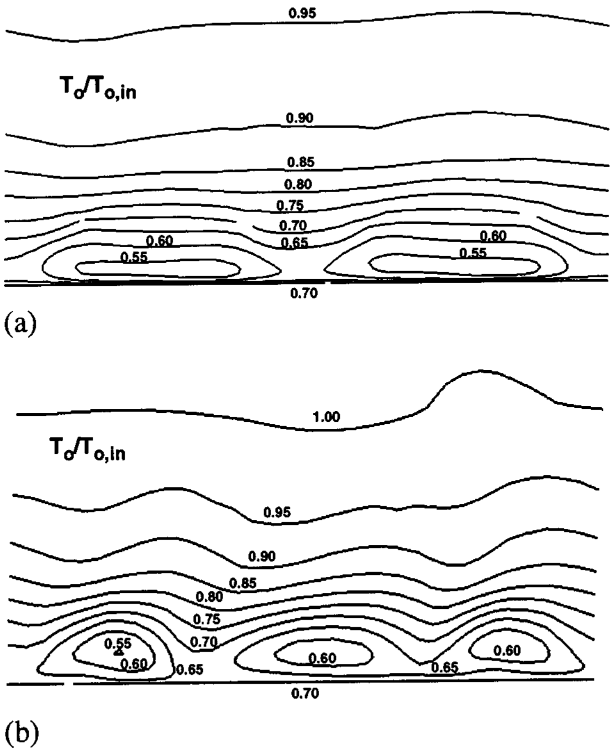

Fig. 6 Stagnation temperature contours on plane normal to streamwise direction through film hole trailing edges: (*a*) row 3—pressure side (shaped holes); (*b*) row 12—suction side (round holes)

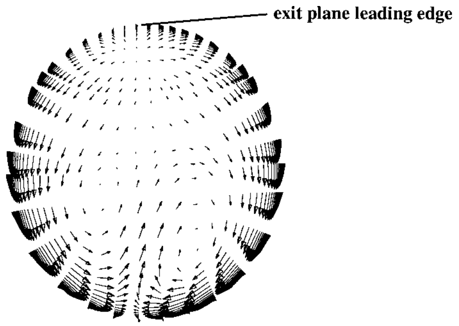

(a) plane A–A in Figure 2(a)

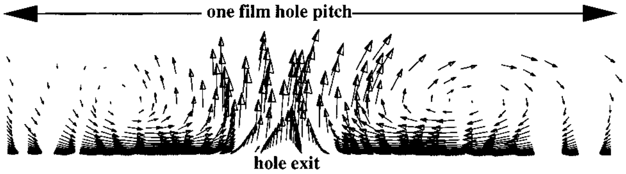

(b) plane B–B in Figure 2(a)

Fig. 7 Projected velocity vectors for row 12—suction side (round holes); (*a*) plane A–A in Fig. 2(*a*); (*b*) plane B–B in Fig. 2(*a*)

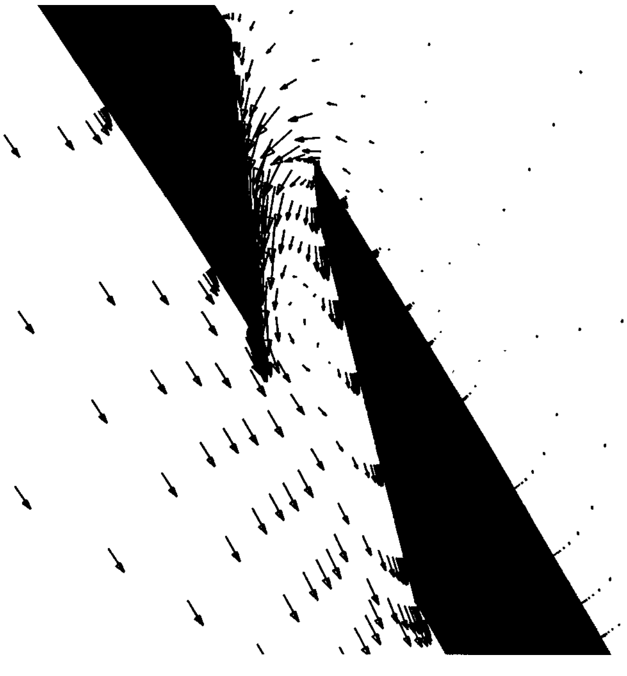

Fig. 8 Momentum vectors along hole centerline in row 2

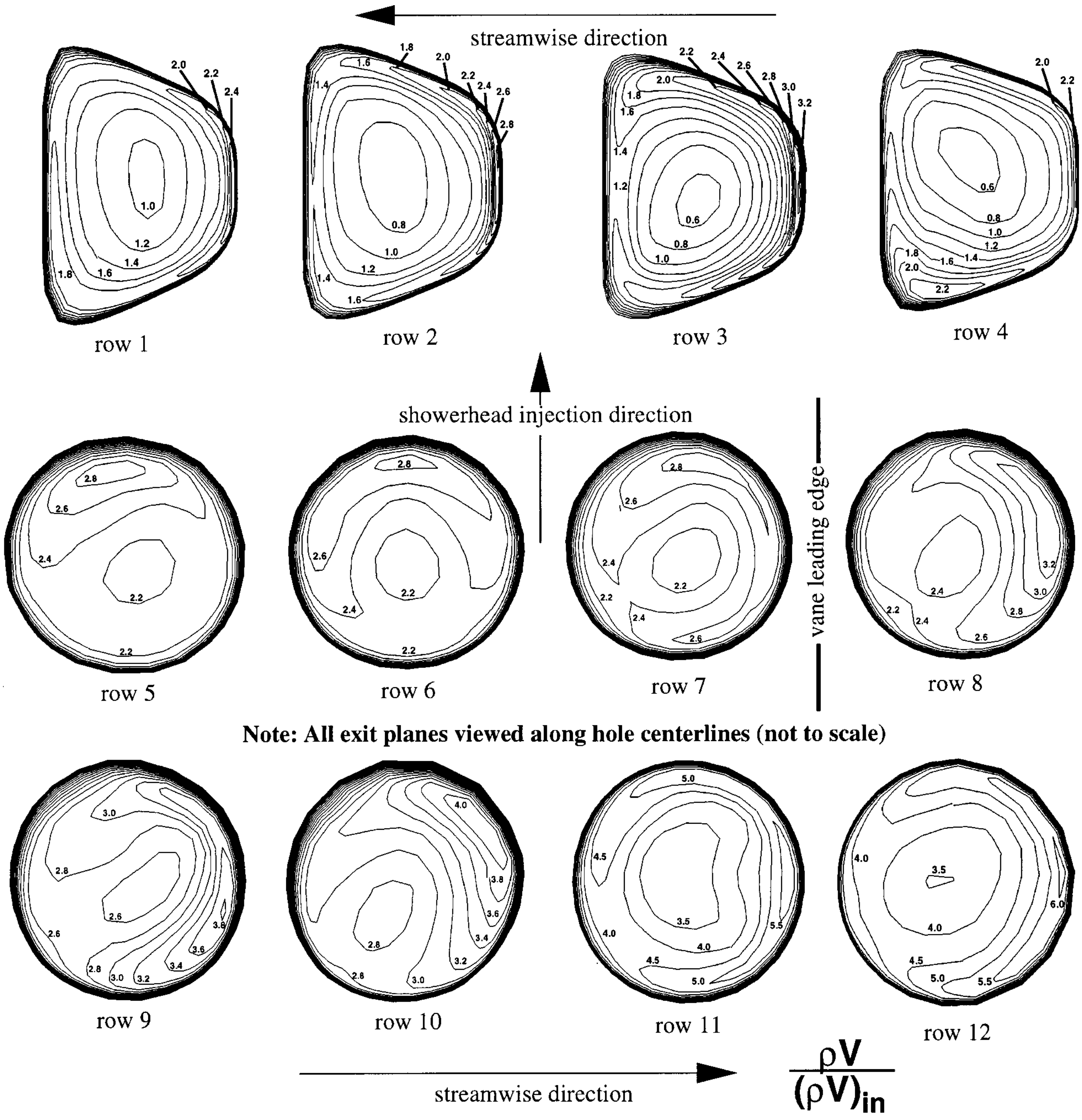

Fig. 9 Film hole exit momentum magnitude profiles

Computations were performed in parallel fashion on the NASA Ames Research Center CRAY J90 cluster using eight processors. Approximately 80 J90 hours (20 equivalent C90 hours) were required to reach convergence for each calculation. The computations were considered converged when changes to the heat flux after an additional 300 iterations were no longer noticeable either in contour plots or in graphs of span-averaged data versus surface distance. This typically occurred after density residuals had been reduced by more than three orders of magnitude.

Computational Results

In lieu of experimental data, the computational results will initially focus on flow physics and detailed phenomena, which experiments have difficulty resolving. These results will then be reduced to averaged quantities more amenable to comparison with future data. Computational results are organized into four types of data: volumetric flow quantities, integrated flow quantities, surface quantities, and span-averaged surface quantities.

Figure 5 shows the stagnation temperature on a fixed-span plane through the centerline of the central suction side film holes. It is immediately evident that the stagnation line intersects this plane between rows 6 and 7 (the second and third showerhead rows from the pressure side) since the high-temperature isotherms approach the vane. The free stream impinges at this point, diverting the cooling flow from these rows to opposite sides of the vane. A thinning of the thermal boundary layer is also evident on the pressure side, just upstream of the shaped holes. This will manifest itself as an increase in heat flux at this location. A thermal boundary layer is present inside the plenum and film holes due to the isothermal boundary condition there. The resultant stagnation temperature profile in the film jets is of great interest, as is the velocity profile. Both will be showcased later in this report.

Figure 6 illustrates the differing behavior of the suction side

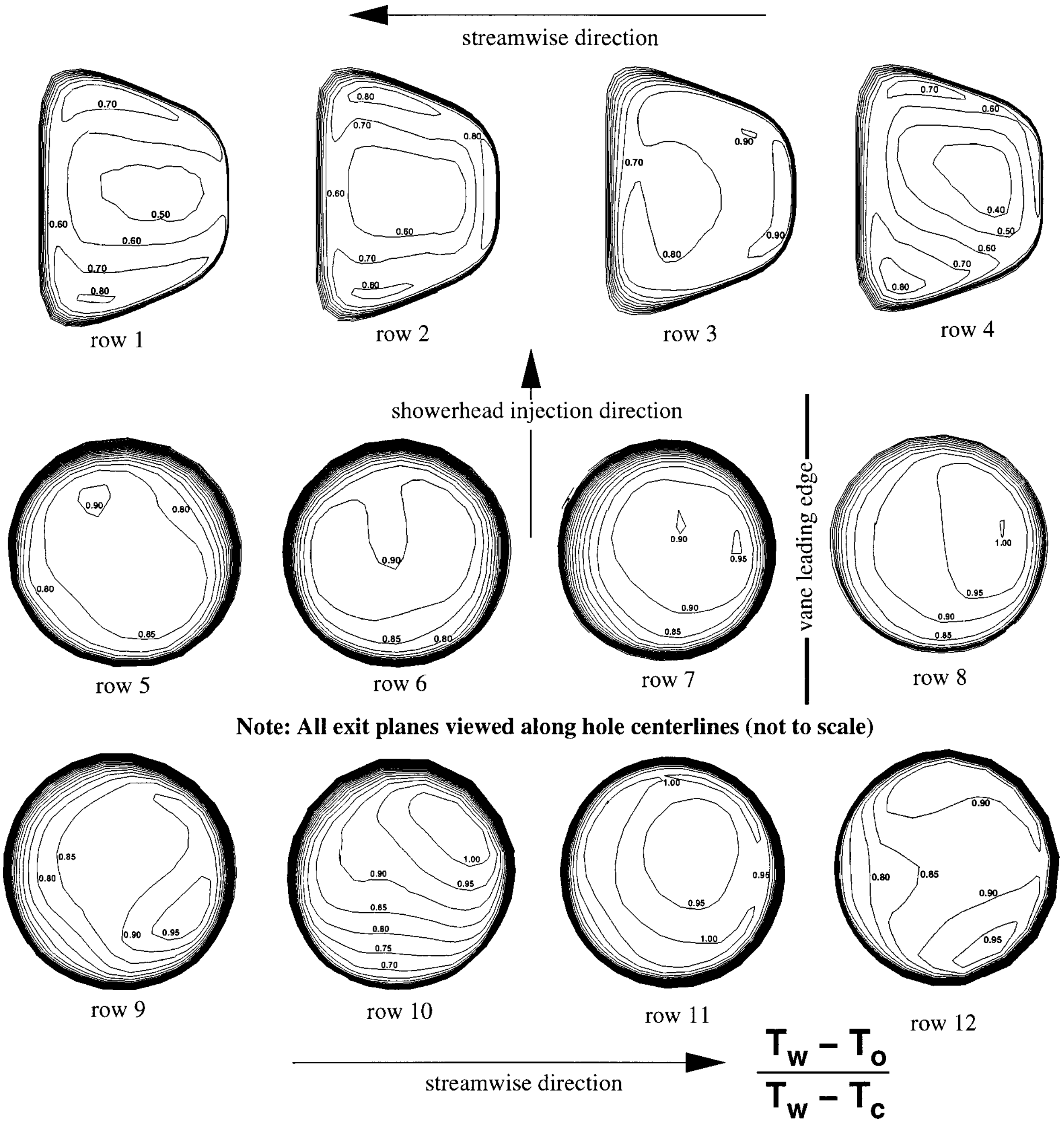

Fig. 10 Film hole exit stagnation temperature profiles

round holes and the pressure side shaped holes. In Figs. 6(*a*) and 6(*b*), the stagnation temperature is shown on normal planes just downstream of rows 3 and 12, respectively. As expected, the shaped holes exhibit improved spreading of the coolant flow in the spanwise direction. It is also evident that the thermal mixing region is somewhat thicker on the pressure side as expected due to lower free-stream velocities. On an uncooled blade, this lowers heat transfer because of smaller temperature gradients and associated heat transfer coefficients. However, on a film-cooled blade, the film effectiveness may suffer on the pressure side due to enhanced coolant diffusion. In fact, the design of this vane reflects this, as the improved performance of the shaped holes is needed on the pressure side to offset a more rapid decay of film effectiveness. Also worth noting is the spanwise skewing of the outer thermal boundary layer on the suction side due to its larger share of spanwise flow from the showerhead holes.

Figure 7 shows projected velocity vectors on planes near a hole in row 12. The planes are defined in Fig. 2(*a*). A pair of counterrotating vortices inside the film hole can be seen in Fig. 7(*a*). These are caused by a jetting effect as described by Leylek and Zerkle [8]. The plenum flow makes a sharp turn around the downstream edge of the hole inlet, causing a jet to form that impinges on the upstream side of the hole. This impingement results in a counterrotating pair of vortices, which distribute the mass flux along the sides of the hole. Figure 7(*b*) shows a different pair of counterrotating vortices outside the film hole, which are produced by the viscous action of the exiting film jet on the surrounding fluid. These vortices encourage entrainment of hot free-stream gas and separation of the cooling jet from the wall. The jetting action that produces the vortices inside the film holes is illustrated in Fig. 8 for a hole in row 2. This behavior is present in some form for all holes, but the shape, angle, length, blowing rate, and location of

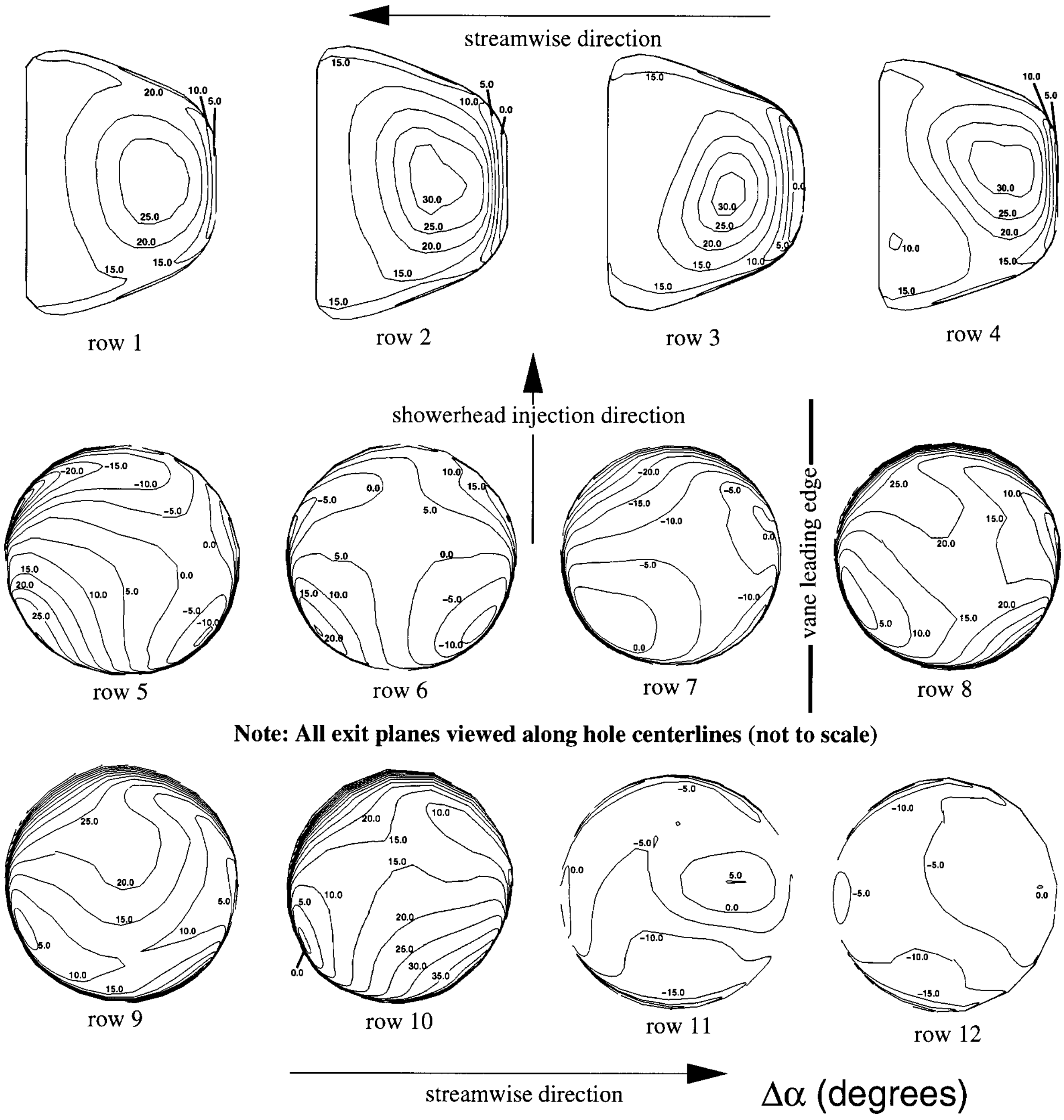

Fig. 11 Film hole exit streamwise angle profiles

the hole all have an effect on the flow profiles exiting the hole. An understanding of the jetting effect is required to describe hole exit profiles adequately.

To define the characteristics of flow exiting each row of holes, it is necessary to present those flow properties that have the most fundamental impact on the external flow and are usable in simplified models. The stagnation temperature is directly related to the external heat transfer and is thus presented. The flow is represented by the momentum magnitude and two flow angles. Streamwise and spanwise flow angle deviation from the hole centerline are chosen to represent the flow direction since film hole exit flow is often assumed to be at the hole geometric angle in the absence of detailed data. While other quantities such as pressure and turbulence values are also important, they are not presented in interests of brevity. Figure 9–12 present these profiles. In these figures, the hole exit plane at the blade surface is shown for one hole in each row, rotated to be viewed along the hole axis. While small variations exist from hole to hole in a given row, they are small compared to the row to row differences. The shaped holes are scaled to appear approximately the same size as the round holes.

Figure 9 shows contours of momentum magnitude. These plots are normalized by the vane inlet momentum. For the shaped holes, a sharp maximum in momentum occurs along the upstream edge of the hole, with elevated levels also near the sides and downstream edge of the hole. The center of the shaped holes is a very low-momentum region. This behavior results from the aforementioned jetting effect. The spanwise and downstream expansion of the shaped holes greatly increase the flow area and correspondingly decrease the momentum in the downstream portion of the holes. The circular holes, on the other hand, have a much more uniform momentum distribution. The maximum value for these holes depends on the external pressure variation as well as the hole orientation. The jetting effect and counterrotating vortices occur as for the shaped holes, but the momentum distribution is

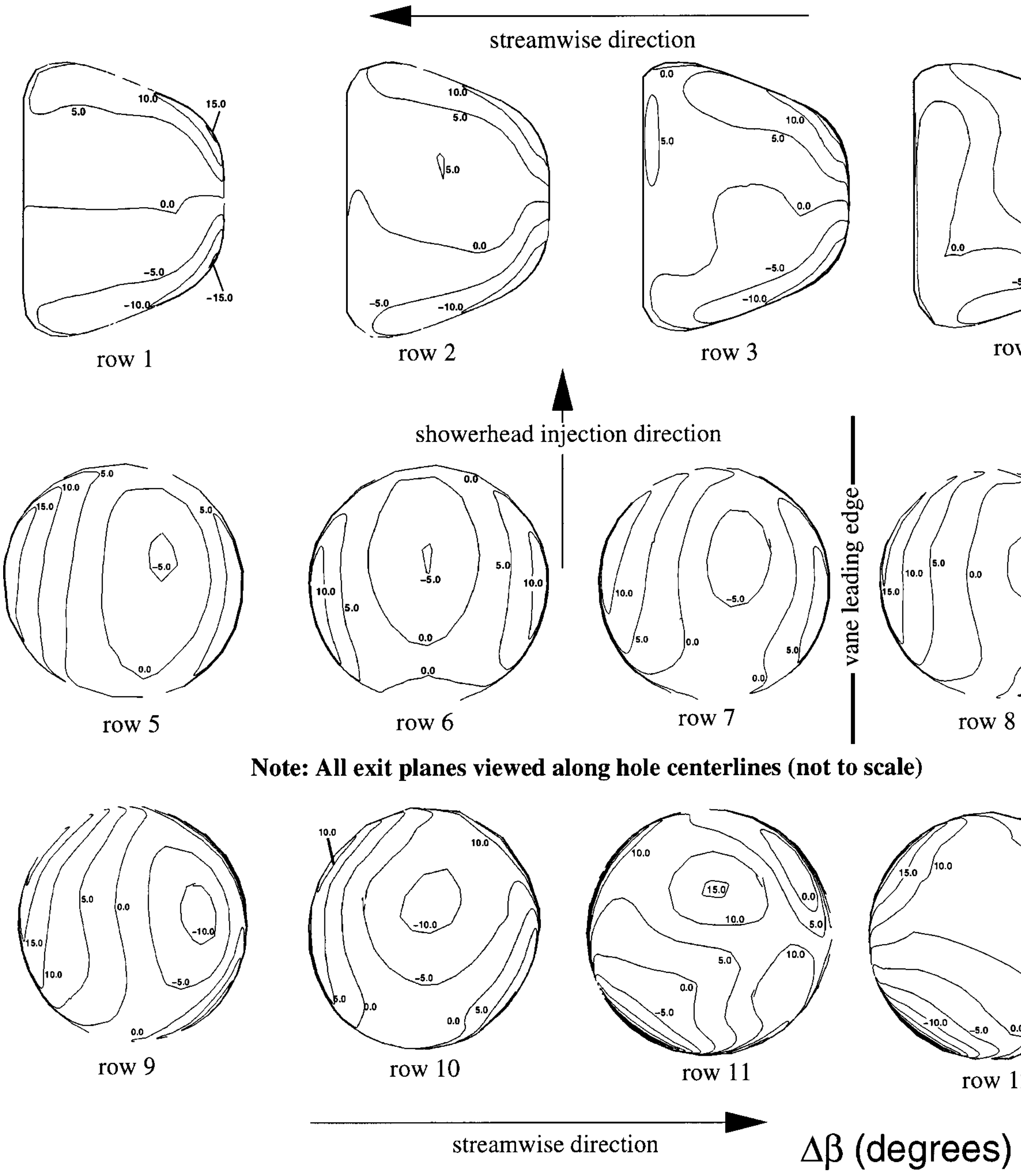

Note: All exit planes viewed along hole centerlines (not to scale)

Fig. 12 Film hole exit spanwise angle profiles

more uniform because of the lack of spanwise and downstream expansion. The holes in the stagnation region (rows 5–7) have a maximum momentum near their trailing edge, while the suction side showerhead holes (rows 8–10) have a maximum momentum skewed toward the downstream direction because of the decreasing external static pressure. The suction side holes (rows 11 and 12) are quite skewed toward the downstream direction, although high-momentum remnants can be seen near their leading edge due to the high momentum associated with these holes. The combined effect produces an inverted momentum profile, where the maximum values lie in a ring around the lower momentum region in the center of the hole.

Figure 10 shows the stagnation temperature profiles for each row of holes. These plots are normalized by the plenum inlet and wall temperatures. Temperatures closer to the plenum inlet temperature tend to occur at locations of high momentum because this fluid has been influenced less by the warmer plenum and hole walls. Because of this phenomenon, it should be possible to correlate the stagnation temperature with momentum, much as it is for a fully developed channel flow with heat transfer. It would then only be necessary to model the hole exit momentum to obtain both parameters. The higher temperatures near the center of the shaped holes result from the low momentum, which allows the warmer external flow to approach the hole exit plane, as seen also in Fig. 5.

Figure 11 presents profiles of streamwise flow angle relative to the hole geometric streamwise angle. Positive values represent deflections away from the vane leading edge. The low-momentum regions of the shaped holes show large streamwise deflections in the streamwise direction due to the downstream diffusion of the hole. In fact, the flow in this region is nearly parallel to the vane surface. This observation is corroborated by Fig. 8. The shaped holes also exhibit a thin region of flow nearly aligned with the hole angle at the upstream edge. This coincides with the high-

Table 2 Film-cooling hole row-averaged flow parameters

row	$M=(m/A_h)/(\rho V)_{in}$	$T_{o,ave}/T_{o,in}$
1	2.36	0.536
2	2.08	0.525
3	2.79	0.525
4	2.47	0.526
5	2.02	0.525
6	1.99	0.519
7	2.16	0.519
8	2.25	0.518
9	2.69	0.516
10	2.75	0.514
11	3.41	0.513
12	3.66	0.527

momentum region of Fig. 9, and indicates that a large fraction of the mass flux in the shaped holes occurs in this region. It may thus be possible to model the flow from these shaped holes as if it were issuing from a thin slot with an inviscid boundary condition immediately downstream representing the low flux region near the hole center.

The behavior of the showerhead holes (rows 5–10) in Fig. 11 is easily explainable in terms of the counterrotating vortices associated with the jetting effect. For all these holes, clockwise and counterclockwise vortices exist on the left and right sides of the hole, respectively, as viewed in Fig. 11. Thus the flow at the bottom of each hole is away from the centerline, while the opposite is true at the top. As the holes get farther from the stagnation line such as at rows 9 and 10, the flow from the entire hole is deflected downstream, but the vortex effect is still present and is superimposed on the overall deflection angle. Rows 11 and 12 exhibit very little gradient in streamwise deflection angle, and generally have a small deflection toward the leading edge due to the large jetting effect associated with their high momentum.

Figure 12 presents contours of spanwise deflection angle, defined as flow spanwise angle relative to the hole geometric spanwise angle. Here deflection angles in the showerhead injection direction are positive. The shaped holes have a simple behavior, with flow moving away from the centerline due to spanwise diffusion, although row 4 exhibits a skewed profile due to deflection from the showerhead holes. The showerhead holes again are subject to the vortex behavior, with flow tending to move away from the showerhead injection direction along the centerline and toward it on the edges. A similar effect can be inferred in the suction side holes of rows 11 and 12, with a deflection toward the showerhead direction caused by the showerhead flow, especially in row 11.

Table 2 presents row-averaged mass flux and stagnation temperature ratios for each row of holes. The mass flux ratios are given in relation to the upstream mass flux. For shaped holes, the mass flux is based on their circular inlet cross section. It can be seen that the suction side holes have the highest mass flow rate because of their low exit static pressure. Although the mass flux ratio seems high for the suction side holes, their mass flux ratio based on local rather than inlet free-stream mass flux is actually about 1.1. The lowest mass flux ratios occur near the stagnation region (rows 5–7) due to the high exit static pressure. The stagnation temperatures are slightly above the plenum inlet temperature of 0.5 due to heat transfer in the plenum and hole pipes. The deviation from 0.5 correlates generally with the amount of plenum wall heat transfer area surrounding each row.

Figures 13–15 present local wall heat transfer data for the leading edge region of the vane. The spanwise variations are greatest on this portion of the vane. Span-averaged results will be presented for the entire vane. Figure 13 presents the wall heat flux nondimensionalized as overall Stanton number for a wall temperature of 0.7. It should be noted that overall Stanton number may be either positive (heat flux into the vane) or negative (heat flux from vane to flow) because the wall temperature is between the free-stream and coolant temperatures. The largest heat flux occurs along the stagnation line, between rows 6 and 7, where coolant is not present. Heat flux is also high in streaks between jets on the suction side portion of the showerhead region, and between the holes in the first row of shaped holes on the pressure side. While knowledge of heat flux is important, it is more illuminating to know the relative contributions to heat flux of film effectiveness (adiabatic wall temperature) and heat transfer coefficient. The second solution for wall temperature of 0.8 allows determination of St_{aw} and T_{aw} through Eq. (1) by assuming St_{aw} to be the same for both solutions at all locations. Film effectiveness is then simply found by Eq. (2).

Film effectiveness is the primary determinant of heat flux, and is shown on the vane surface in Fig. 14. The stagnation line and the region near row 4 exhibit a low film effectiveness, which simply means the driving temperature for heat transfer is near the free-stream temperature. This is consistent with the behavior shown in Fig. 13. However, the high heat flux region near rows 9 and 10 in Fig. 13 is not accompanied by a low film effectiveness. For an explanation of this behavior, the heat transfer coefficient data must be examined, shown in Fig. 15 nondimensionalized as adiabatic wall Stanton number. A pronounced maximum in St_{aw} is apparent in the very location of the high heat flux, which explains its existence. Here the driving temperature for heat transfer is not much above the wall temperature, but the intense mixing associated with the showerhead jets interacting with the accelerating free stream causes the heat flux to increase. An interesting phenomenon occurs downstream of the suction side film holes. Although the heat transfer coefficient is high in the regions of high vorticity shown in Fig. 7(*b*), the driving temperature for heat transfer is below the wall temperature as shown in Fig. 14, resulting in large negative heat flux (Fig. 13). This illustrates the dependence of wall heat flux on wall temperature. Film effectiveness and heat transfer coefficient are independent of wall temperature by this model.

Figures 16–18 present the span-averaged film effectiveness, Stanton numbers, and Stanton number ratios, respectively. Span-averages near film holes exclude the hole exit planes. The locations of film hole centerlines are shown by vertical dashed lines. The high Stanton numbers on the pressure side trailing edge result from both low film effectiveness and high heat transfer coefficient. The vane is designed for trailing edge coolant ejection which was not considered in this simulation. This highlights the necessity of using this method of cooling. However, the primary focus of this study is the film cooling performance of the twelve existing film cooling rows.

In Fig. 17, a high overall Stanton number at the stagnation line is apparent, but this occurs over a very short streamwise distance, and its effects would likely be mitigated in a conducting metal vane. A region that seems to be of more concern is that between the showerhead holes and the first row of holes on the pressure side. This represents the largest integrated heat flux in the forward portion of the vane. It results from the fact that most of the showerhead coolant goes to the suction side. The adiabatic wall Stanton number is not tremendously high in this region, but the film effectiveness is quite low, indicating a lack of coolant coverage, as shown in Figs. 14 and 16. This phenomenon is exhibited to a

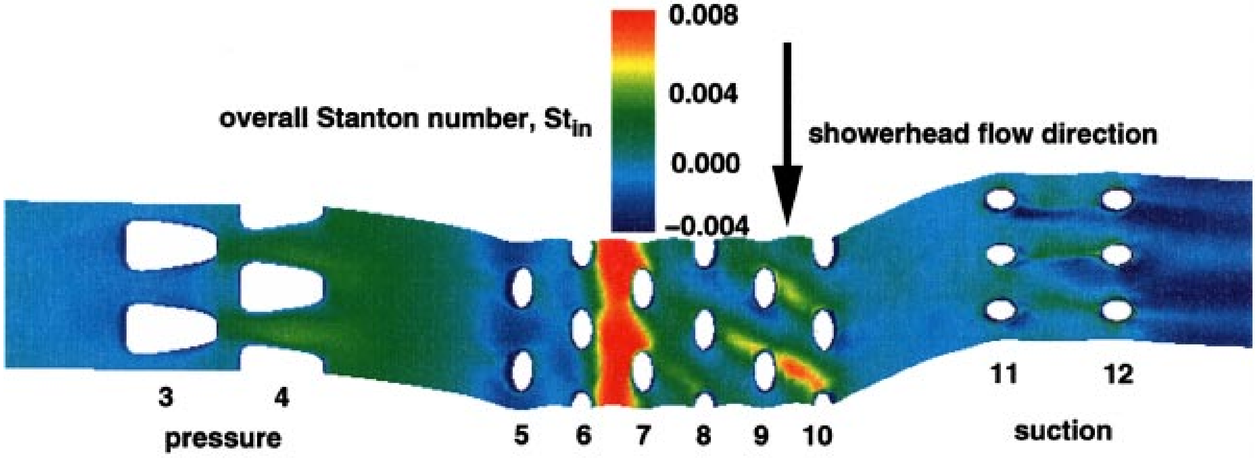

Fig. 13 Overall Stanton number values near vane leading edge

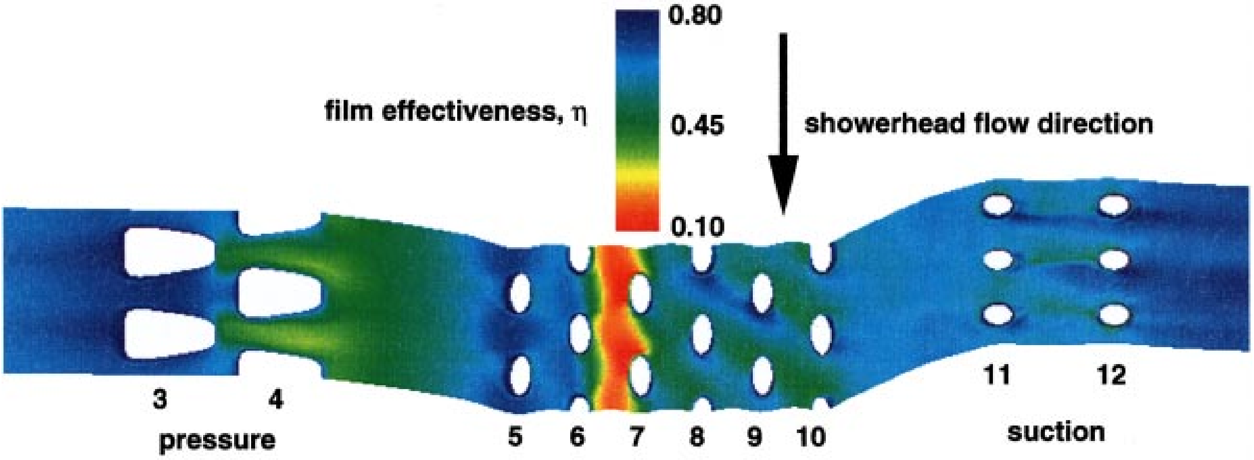

Fig. 14 Film effectiveness values near vane leading edge

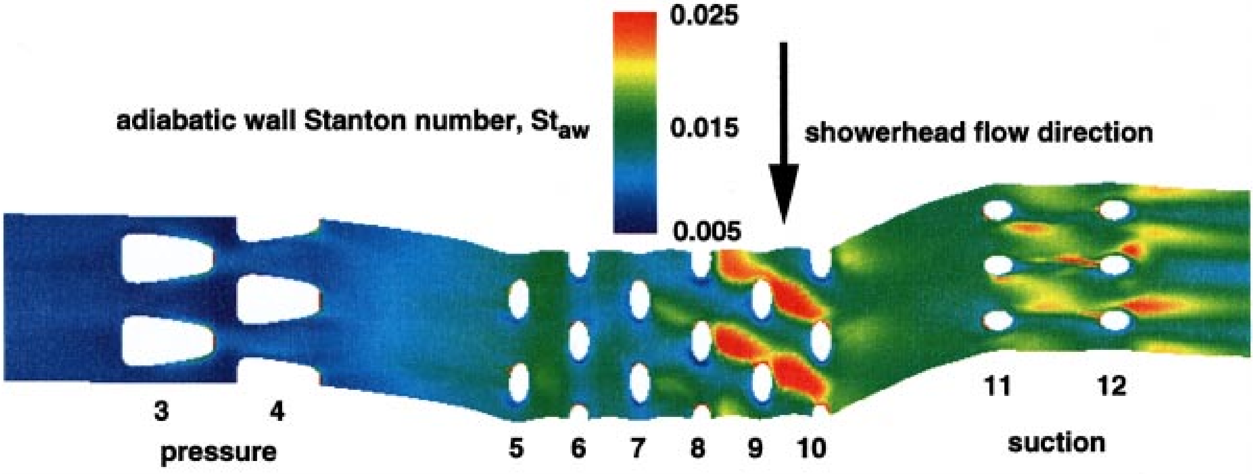

Fig. 15 Adiabatic wall Stanton number values near vane leading edge

lesser extent just upstream of the last two rows on the pressure side. A region of very high overall Stanton number is predicted on the aft portion of the suction side. Unlike the pressure side, this behavior would not be affected by inclusion of trailing edge coolant ejection in this constant wall temperature prediction. However, in a conducting vane, the high-velocity internal coolant flow associated with trailing edge ejection should keep temperatures low in the thin aft portion of the vane.

As noted previously, the suction side film holes provide a region of large negative heat flux. The film effectiveness actually

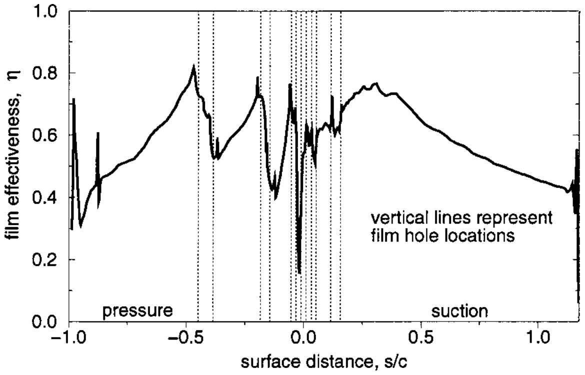

Fig. 16 Span-averaged film effectiveness

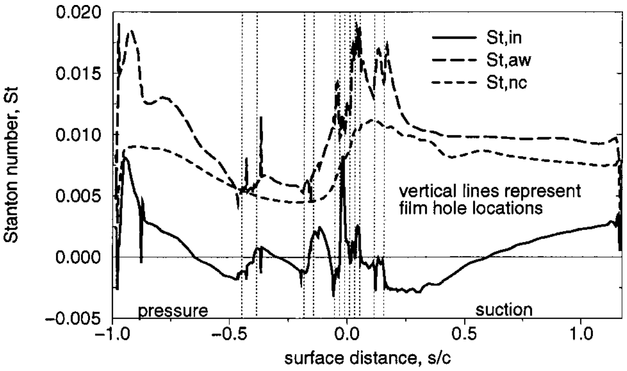

Fig. 17 Span-averaged Stanton numbers

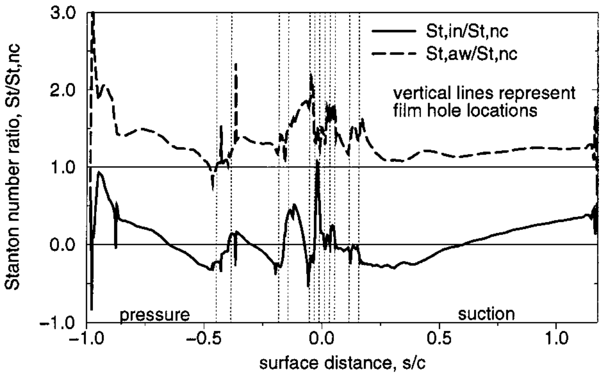

Fig. 18 Span-averaged Stanton number ratios

peaks some distance downstream of the last row of holes, indicating a small jet separation and reattachment. This is unlike the pressure side rows, where a sharp maximum in film effectiveness is reached at the hole exit followed by a rapid decrease. This rapid decrease accounts for the small region of positive heat flux between the two sets of pressure side holes, but the effect is mitigated by the very low heat transfer coefficient provided by the shaped holes.

Figure 18 shows both the overall and adiabatic wall Stanton numbers normalized by the Stanton number for the smooth vane calculation with no coolant. The adiabatic wall Stanton number is greater than 1.0 at nearly all locations, indicating that the presence of film cooling increases heat transfer coefficient over the entire vane. The ratio dips below 1.0 downstream of the last pressure side row due to the low-velocity flow exiting the diffusing holes. The overall Stanton number ratio is less than 1.0 at nearly all locations, indicating that the film-cooled vane heat flux is everywhere less than for the uncooled vane, as expected. The only small exception occurs right at the stagnation point, where the ratio barely exceeds 1.0 due to the very low film effectiveness and enhanced heat transfer coefficient in this region.

Summary and Conclusions

A computational study has been performed on a realistic film-cooled turbine vane in anticipation of an upcoming experimental study of the same geometry. Much detailed information has been extracted from the simulations. The two solutions at different isothermal wall temperatures have allowed independent determination of film effectiveness and heat transfer coefficient on the vane surface. Film effectiveness values are shown to be the primary determinant of wall heat flux for a particular wall temperature, although variations in heat transfer coefficient also play a role. Low film effectiveness values are predicted along the stagnation line and just upstream of the first row of pressure side holes due to the absence of coolant flow and flow mixing, respectively. High heat transfer coefficient values on the downstream portions of the showerhead region augment heat flux values and are due to the intense mixing associated with the interaction of accelerating free-stream flow and showerhead injection. High heat transfer coefficients near the suction side holes are again due to the intense mixing in this region, but here cooling is enhanced for the baseline wall temperature because of the high film effectiveness. Comparison with a smooth vane, no coolant case indicates that the presence of film cooling almost universally lowers heat flux despite increasing heat transfer coefficient over virtually the entire vane.

Detailed information from the film hole flows is shown in the form of hole exit profiles. All holes exhibit the expected jetting behavior reported by Leylek and Zerkle [8]. The peak mass flux is influenced by both external static pressure variations and the hole orientation. For the circular cross section holes, this peak tends to be skewed both toward the downstream direction and toward the injection angle of the hole. The suction side holes exhibit the greatest skewing because these two effects are in the same direction. The shaped holes exhibit a complex behavior with an intense local maximum in mass flux near the leading edge of the hole. The center of the hole contributes very little mass flux, while the sides and trailing edge supply coolant that has followed the hole wall around from the leading edge. The shaped holes are effective in producing a low-velocity, uniform film layer. All holes exhibit a relatively flat stagnation temperature profile except for the centers of the shaped holes, where the negligible mass flux allows greater influence of the hotter free stream.

The round holes have exit profiles of momentum and stagnation temperature that could be generalized, allowing external vane computations to model their flow. The complex flow in the shaped holes makes it difficult to generalize their exit properties for input to an external vane calculation, but the more spanwise-uniform flow they produce, especially in a staggered arrangement, could be modeled by a two-dimensional wall function or modified slot flow with downstream inviscid wall condition.

Nomenclature

A_h = hole circular cross-sectional area
c = vane true chord
c_p = specific heat
d = film hole diameter
h = heat transfer coefficient
m = hole mass flow rate
M = mass flux ratio $=(m/A_h)/(\rho V)_{\text{in}}$
Pr = Prandtl number
Pr_t = turbulent Prandtl number
p = film hole spanwise pitch
q'' = wall heat flux
s = streamwise distance from leading edge
St = Stanton number

T = temperature
V = velocity
α = streamwise film hole angle
$\Delta\alpha$ = streamwise flow deviation
β = spanwise film hole angle
$\Delta\beta$ = spanwise flow deviation
η = film effectiveness
ρ = density

Subscripts

av = row-average quantity
aw = adiabatic wall conditions
c = plenum supply conditions
in = free-stream inlet conditions
nc = smooth vane, no coolant case
o = stagnation conditions
w = isothermal wall conditions

References

[1] Goldstein, R. J., 1971, ''Film Cooling,'' Adv. Heat Transfer, **7**, pp. 321–379.
[2] Gritsch, M., Schulz, A., and Wittig, S., 1998, ''Adiabatic Wall Effectiveness Measurements of Film-Cooling Holes With Expanded Exits,'' ASME J. Turbomach., **120**, pp. 549–556.
[3] Thole, K., Gritsch, M., Schulz, A., and Wittig, S., 1998, ''Flowfield Measurements for Film-Cooling Holes With Expanded Exits,'' ASME J. Turbomach., **120**, pp. 327–336.
[4] Walters, D. K., and Leylek, J. H., 2000, ''A Detailed Analysis of Film-Cooling Physics: Part I—Streamwise Injection With Cylindrical Holes,'' ASME J. Turbomach., **122**, pp. 102–112.
[5] McGovern, K. T., and Leylek, J. H., 2000, ''A Detailed Analysis of Film Cooling Physics: Part II—Compound-Angle Injection With Cylindrical Holes,'' ASME J. Turbomach., **122**, pp. 113–121.
[6] Hyams, D. G., and Leylek, J. H., 2000, ''A Detailed Analysis of Film Cooling Physics: Part III—Streamwise Injection With Shaped Holes,'' ASME J. Turbomach., **122**, pp. 122–132.
[7] Brittingham, R. A., and Leylek, J. H., 2000, ''A Detailed Analysis of Film Cooling Physics: Part IV—Compound-Angle Injection With Shaped Holes,'' ASME J. Turbomach., **122**, pp. 133–145.
[8] Leylek, J. H., and Zerkle, R. D., 1994, ''Discrete-Jet Film Cooling: A Comparison of Computational Results With Experiments,'' ASME J. Turbomach., **116**, pp. 358–368.
[9] Ito, S., Goldstein, R. J., and Eckert, E. R. G., 1978, ''Film Cooling of a Gas Turbine Blade,'' ASME J. Eng. Power, **100**, pp. 476–481.
[10] Mick, W. J., and Mayle, R. E., 1988, ''Stagnation Film Cooling and Heat Transfer, Including its Effect Within the Hole Pattern,'' ASME J. Turbomach., **110**, pp. 66–72.
[11] Garg, V. K., and Gaugler, R. E., 1997, ''Effect of Velocity and Temperature Distribution at the Hole Exit on Film Cooling of Turbine Blades,'' ASME J. Turbomach., **119**, pp. 343–351.
[12] Garg, V. K., and Rigby, D. L., 1998, ''Heat Transfer on a Film Cooled Blade—Effect of Hole Physics,'' ASME Paper No. 98-GT-404.
[13] Bohn, D. E., Becker, V. J., and Rungen, A. U., 1997, ''Experimental and Numerical Conjugate Flow and Heat Transfer Investigation of a Shower-Head Cooled Turbine Guide Vane,'' ASME Paper No. 97-GT-15.
[14] Choi, D., 1993, ''A Navier–Stokes Analysis of Film Cooling in a Turbine Blade,'' AIAA Paper No. 93-0158.
[15] Hylton, L. D., Nirmalan, V., Sultanian, V. K., and Kaufman, R. M., 1988, ''The Effects of Leading Edge and Downstream Film Cooling on Turbine Vane Heat Transfer,'' NASA CR-182133.
[16] Program Development Corporation, 1997, ''GridPro™/az3000-User's Guide and Reference Manual,'' White Plains, NY.
[17] Rigby, D. L., 1996, ''Method of Weakest Descent for Automatic Block Merging,'' *15th International Conference on Numerical Methods in Fluid Dynamics*, Monterey, CA, June.
[18] Rigby, D. L., Steinthorsson, E., and Coirier, W. J., 1997, ''Automatic Block Merging Using the Method of Weakest Descent,'' AIAA Paper No. 97-0197.
[19] Steinthorsson, E., Liou, M. S., and Povinelli, L. A., 1993, ''Development of an Explicit Multiblock/Multigrid Flow Solver for Viscous Flows in Complex Geometries,'' Paper No. AIAA-93-2380.
[20] Arnone, A., Liou, M.-S., and Povinelli, L. A., 1991, ''Multigrid Calculation of Three-Dimensional Viscous Cascade Flows,'' AIAA Paper No. 91-3238.
[21] Rigby, D. L., Ameri, A. A., and Steinthorsson, E., 1997, ''Numerical Prediction of Heat Transfer in a Channel With Ribs and Bleed,'' ASME Paper No. 97-GT-431.
[22] Ameri, A., Rigby, D. L., and Steinthorsson, E., 1998, ''Effect of Squealer Tip on Rotor Heat Transfer and Efficiency,'' ASME J. Turbomach., **120**, pp. 753–759.
[23] Wilcox, D. C., 1994, *Turbulence Modeling for CFD*, DCW Industries, Inc., LaCanada, CA.
[24] Wilcox, D. C., 1994, ''Simulation of Transition With a Two-Equation Turbulence Model,'' AIAA J., **32**, No. 2, pp. 247–255.
[25] Menter, F. R., 1993, ''Zonal Two-Equation $k-\omega$ Turbulence Models for Aerodynamic Flows,'' AIAA Paper No. 93-2906.
[26] Chima, R. V., 1996, ''A $k-\omega$ Turbulence Model for Quasi-Three-Dimensional Turbomachinery Flows,'' NASA TM-107051.
[27] Schlichting, H., 1979, *Boundary Layer Theory*, 7th ed., McGraw-Hill, New York, pp. 312–313.

Mist/Steam Cooling in a Heated Horizontal Tube—Part 1: Experimental System

Tao Guo[1]
Ting Wang[2]
J. Leo Gaddis
Department of Mechanical Engineering,
Clemson University,
Clemson, SC 29634

To improve the airfoil cooling significantly for the future generation of advanced turbine systems (ATS), a fundamental experimental program has been developed to study the heat transfer mechanisms of mist/steam cooling under highly superheated wall temperatures. The mist/steam mixture was obtained by blending fine water droplets (3∼15 μm in diameter) with the saturated steam at 1.5 bars. Two mist generation systems were tested by using the pressure atomizer and the steam-assisted pneumatic atomizer, respectively. The test section, heated directly by a DC power supply, consisted of a thin-walled (∼0.9 mm), circular stainless steel tube with an ID of 20 mm and a length of 203 mm. Droplet size and distribution were measured by a phase Doppler particle analyzer (PDPA) system through view ports grafted at the inlet and the outlet of the test section. Mist transportation and droplet dynamics were studied in addition to the heat transfer measurements. The experiment was conducted with steam Reynolds numbers ranging from 10,000 to 35,000, wall superheat up to 300°C, and droplet mass ratios ranging from 1∼6 percent. [S0889-504X(00)02402-8]

Introduction

Closed-loop steam cooling has been adopted by two major gas turbine manufacturers for their heavy-frame advanced turbine system (ATS) engines [1–3]. The major advantage of closed-loop steam cooling is that it can eliminate the need for film cooling. According to Bannister [4], as the turbine inlet temperature (TIT) is raised to 1400°C (∼2600 F), excessive film cooling is the major obstacle to a further increase in gas turbine thermal efficiency because as the cooling air is injected from the airfoil into the main hot gas flow, it interferes with the main flow field and subsequently causes aerodynamic and thermal losses. Meanwhile, less air is available for combustion and therefore the work output will be reduced. Furthermore, excessive film cooling will force the combustion temperature to be raised and further compound the issue of reducing NO_x and controlling emissions.

As a result, using the closed-loop steam cooling scheme allows a higher thermal efficiency than using air film cooling [5]. However, there are still many technical challenges to overcome. One of the most challenging problems is that a very large amount of steam will be needed [3,6]. The reason is that to eliminate film cooling, the coolant side heat transfer coefficient must be greatly increased to about 8000–10,000 W/m^2 K. To reach this, a very high steam Reynolds number and thus a very high steam flow rate must be maintained. Drawing this large amount of steam out from the bottom steam cycle would decrease the thermal efficiency of the bottom steam turbines since the normal steam expansion process would be interrupted [7]. Furthermore, high steam flow rate will significantly increase the pressure losses.

In this study, the concept of closed-loop steam/mist cooling is proposed to alleviate some of the abovementioned problems. Basically, better heat transfer performance can be expected for the following reasons: (*a*) Due to the latent heat of evaporation, the water droplets serve as numerous heat sinks in the mist/steam flow. This results in a higher effective specific heat for the mist/steam mixture. Consequently, the mean bulk temperature of the mist/steam flow will be lower than that of the corresponding single-phase steam flow. Besides, a larger heat transfer coefficient h can be achieved because a steeper temperature gradient near the wall is maintained; (*b*) previous studies on air/solid-particle flow have shown that the heat transfer performance of the single-phase air flow can be enhanced up to 100 percent by injecting solid particles into the air flow [8] due to particle-fluid interactions; and (*c*) due to the evaporation of the liquid droplets, there are momentum, heat, and mass transfer between the droplets and the steam flow. These interactions are expected to induce mixing and turbulence inside the steam main flow and the boundary layer and increase the heat transfer rate. As a result, for mist/steam cooling, the steam mass flow rate can be greatly reduced to reach the same heat transfer performance as the single steam flow.

As a first step toward using mist/steam cooling, an experimental system under low pressure (1.5 bar) and low heat flux conditions, instead of high-pressure and high-heat-flux conditions as in a real gas turbine environment, has been set up in the laboratory. Four test conditions have been performed: a horizontal tube, a 180 deg curved tube [9], impingement jets on a flat surface, and impingement jets on a curved surface. In this paper, only the results for the horizontal tube are reported.

Previous Work

The current study focuses on the heat transfer of mist/steam internal flow in a heated horizontal tube under high wall superheat. Although there are numerous investigations on the one-component, two-phase water/steam flow such as the post-dryout dispersed flow heat transfer or the two-component, two-phase mist/air flow, no experimental studies can be found in the open literature of internal mist/steam flow where the mist is generated by atomizing water and then injected into the steam under controlled conditions.

Previous studies in these two related areas, namely, the post-dryout dispersed flow and the two-component two-phase mist/air internal flow, have provided guidance to the current study. Both have a dispersed liquid phase flowing within a gas phase, as in the case of the mist/steam flow. The main difference between the post-dryout dispersed flow and the present mist/steam flow is the different inlet conditions. The droplet size and distribution as well as the liquid mass fraction at the critical heat flux (CHF) point for post-dryout flow depend on the flow conditions prior to the CHF

---

[1] Current address: GE Power Systems, Schenectady, NY 12301.

[2] Current address: Energy Conversion and Conservation Center, University of New Orleans, New Orleans, LA 70148-2220.

Contributed by the International Gas Turbine Institute and presented at the 44th International Gas Turbine and Aeroengine Congress and Exhibition, Indianapolis, Indiana, June 7–10, 1999. Manuscript received by the International Gas Turbine Institute February 1999. Paper No. 99-GT-144. Review Chair: D. C. Wisler.

point and are usually difficult to control. The inlet conditions for the mist/steam internal flow are controlled mainly by the atomizing system; the droplet size and distribution as well as the liquid mass fraction and liquid temperature are systematically controlled. The droplets in the post-dryout flow are usually generated from the breakup and entrainment of liquid layers and the droplet sizes are quite large. The radial temperature profile is more developed in the post-dryout flow than in the current flow in which the mist/steam mixture is introduced homogeneously into a highly heated test section.

The difference between mist/air flow and mist/steam flow is that they are thermodynamically different. Mist/air is a two-component two-phase flow where the evaporation process of the water droplets is controlled by the partial pressure of the water vapor in the air, not by the total pressure of the mixture. Mist/steam is a one-component two-phase flow in which the evaporation process of the water droplets is controlled by the steam pressure. Generally, under the same pressure and the same temperature, the droplets within mist/air flow are more likely to evaporate than those within mist/steam flow. For example, for mist/steam flow under saturated pressure and temperature, no evaporation would occur. However, for mist/air flow under the same pressure and temperature, if the air is dry, the water droplets would be in a superheated state and evaporate immediately because the partial pressure of the vapor is lower than the saturated pressure.

Experimental Facility

A schematic of the overall experimental facility is shown in Fig. 1(*a*). Basically, the experimental setup consists of four systems: the steam system, the water system, the atomizing system, and the test section.

Steam System. The piping details of the steam system are shown in Fig. 1(*b*). It consists of a low-pressure steam subsystem and a high-pressure steam subsystem.

Low-Pressure Subsystem. This subsystem supplies the needed main steam flow. The saturated steam at 8.5 bar (120 psi) is extracted from the existing high-pressure steam pipeline. It first passes through a strainer and then enters a regulatory system where its pressure is reduced to about 1.6 bar (25 psi). A *desuperheater* is designed to cool the superheated steam to a nearly saturated state by injecting water droplets into the steam flow using a pressure-type atomizing nozzle that is directly connected to tap water. Any carryover of liquid from the desuperheater is then removed by a low-pressure filter to obtain essentially clean and dry saturated steam. The filter consists of 48 porous stainless steel tubes 1.8 m (6 ft) in length and 1.3 cm (0.5 in.) in diameter. The pore size of the metal tube is 0.5 μm. The steam flow rate to the mixing chamber is measured by an orifice flow meter. For safety measures, a relief valve with a maximum pressure rating of 2 bar (30 psi) combined with a burst plate with a bursting pressure of 1.6 bar (24 psi) is installed between the filter and the flow meter.

High-Pressure Subsystem. A high pressure (approximately 8.5 bar) steam subsystem furnishes the energy source for the ''steam-assist'' pneumatic atomizer (see below for more information) to generate mist from water. The steam flow rate (approximately 0.001 kg/s) is monitored by another orifice flow meter. Similar to the low-pressure subsystem, a single high-pressure filter tube keeps the atomizer from being clogged. Three disk-type steam traps are used to channel out the condensation inside the desuperheater, the low-pressure filter, and the high-pressure filter.

Water System. Two water systems have been designed for two different atomizing systems. The *low-pressure water system*, used for the ''steam-assist'' pneumatic atomizer, is illustrated in Fig. 1(*a*), where the reverse-osmosis-filtered water is placed into a PVC tank pressurized by high-pressure nitrogen and compressed to approximately 5 bar (70 psi). A rotameter is used to measure the water flow (approximately 1 GPH) before it enters the atomizer. For the pressure atomizers, a *high-pressure water system* is designed where the filtered tap water is compressed to a pressure of up to 68 bar (1000 psi) by a high pressure pump.

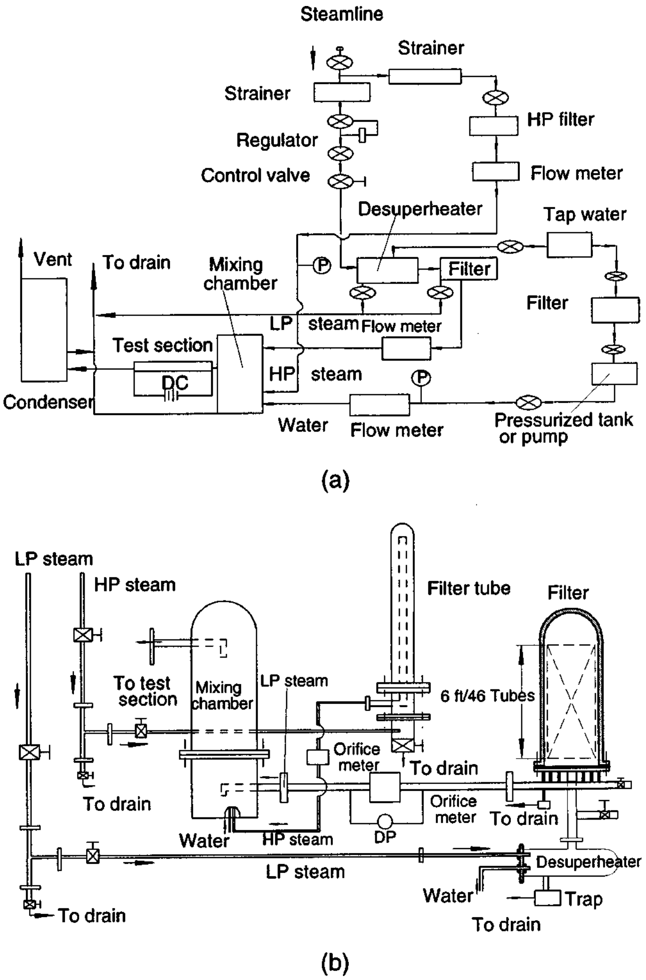

Fig. 1 Diagrams of the experimental system: (*a*) flow chart; (*b*) layout of the experimental facility

Atomizing System. The atomizing system is designed to generate the needed steam/fine water-droplet flow for the test section.

Atomizers. Different kinds of atomizers have been reviewed and compared [10]. Based on the review, two kinds of atomizer, the pneumatic atomizer and the pressure atomizer, were chosen as for the current application. It should be noted that pneumatic atomizers are usually designed as ''air-assist'' atomizers where the compressed air is used. In the present study, high-temperature, high-pressure steam instead of the compressed air is used. Thus corrosive-resistant materials are required and the spray characteristic from the atomizer is expected to be changed due to the heat transfer between the steam and the liquid.

Mixing Chamber. A mixing chamber blends mist from the atomizer with a controlled amount of saturated vapor. The bottom part of the mixing chamber contains the atomizer. The atomizer jet directly impinges on the main stream flow of the low-pressure steam (Fig. 1(*b*)). The top part of the mixing chamber serves as the blender. The mixture exits from the top of the mixing chamber and goes into the horizontal test section. Excessive condensation inside the mixing chamber is channeled out by a disc-type steam trap installed at the bottom of the mixing chamber.

Atomizing Systems. To decide on the best atomizer for the current experiment, two mist generation systems were tested. The first mist generation system uses the pneumatic atomizer with steam and water as the working fluids. The second mist generation system uses the pressure atomizer with high-pressure water (1000 psi). The droplet size and distributions are measured at the exit of the mixing chamber. For the pneumatic atomizer, only very small droplets (0~10 μm) exist at the exit of the mixing chamber. For the pressure atomizer, relatively larger droplets (10–40 μm) follow the main steam flow and exit. As a result, the pressure atomizer system is adopted in this study because the mean droplet size (3~4 μm in diameter) and the droplet mass ratio (less than 1 percent of the main steam flow) from the pneumatic atomizer are less ideal for heat transfer enhancement. See Part 2 for details.

Test Section. The test section schematic is shown in Fig. 2. The main part of the test section consists of a thin wall, welded, circular stainless steel tubing. The OD of the tubing is 22.2 mm (7/8 in.), the wall thickness is 0.889 mm (0.035 in.), and the length is about 177.8 mm (8 in.). The main features of the test section include:

- A tube with an outer diameter of 22.2 mm was selected for three reasons: (1) This is a typical air cooling hole size in some of the current industrial gas turbines; (2) the tubes used in many previous experiments [11,12] were too small to remove the liquid film formed near the entrance region of the test sections; and (3) it is large enough to measure easily the particle sizes and velocity distribution.
- Welded instead of seamless tube is used because welded tube is made from a flat plate and provides a more uniform wall thickness. This is important for providing uniform local Joule heating.
- Thin wall tubing is used to minimize axial heat conduction losses. The wall thickness of the test section varies within 0.025 mm (1/1000 in.). Thus, the variation of the electrical resistance and consequently the heat deposition is within 3 percent of uniformity.

The test section is heated by a high-current DC power supply system rated at 5.6 kW at 750 A and 7.5 V. Copper wires with electrodes on the ends connect the power supply to the test section. To isolate the test section from the possible short circuits, the test section is mounted on a wooden table. In addition, at both ends of the test section, reinforced dielectric silicone tubes are used to connect to the other parts of the experimental system.

To prevent excessive formation of liquid film through condensation on the inlet of the test section, a preheater heats the tube immediately before the test section to a temperature 1~2 F above the saturation temperature. The steam/water droplet mixture coming out of the test section is condensed in a condenser and led into the drainage. Between the test section and the condenser, a ball valve controls the backpressure of the steam.

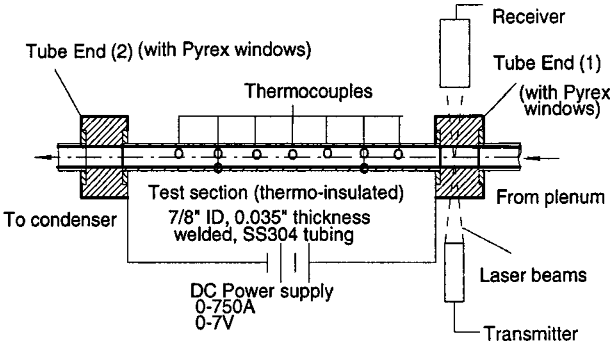

Fig. 2 Design of the test section

Droplet Size Measurements

Particle size and its distribution play an essential role in steam/mist heat transfer. A large number of particle sizing methods have been developed and reviewed by Swithenbank et al. [13]. For the current study, different kinds of particle sizing methods were reviewed and compared and the phase Doppler particle analyzer (PDPA) was decided to be the best choice.

PDPA System. PDPA [14,15] is based on the concept of light-scattering interferometry and uses an optical transmitting system similar to conventional Laser-Doppler velocimetry (LDV). As shown in Fig. 3, the laser beam is split into two beams of equal intensity which are then focused to a point of intersection (the measuring volume). A receiver is usually placed 30 deg off the plane of the transmitting beams. Particles passing the measuring volume scatter light independently from each beam. The scattered light then interferes to form a fringe pattern in the plane of the receiver lens. This fringe pattern is imaged to a set (usually three) of detectors in the receiver to measure the temporal frequency (for velocity measurement) and spatial frequency (relative to phase shift, for particle size measurement) of the scattered light. Thus, unlike conventional interferometric techniques where particle size is determined by measuring the visibility of the Doppler signal, PDPA measures the relative phase shift of the Doppler signal directly as a linear function of the droplet diameter. As such, PDPA measurements are dependent on the wavelength of the scattered light, which is not easily affected by environmental conditions. Visibility, on the other hand, is directly related to the intensity of the Doppler signal, which is sensitive to background noise.

For the PDPA system, the laser transmitting fiberoptic probe has a focal length of 350 mm and a beam waist diameter of 115 μm. The beam spacing for the probe is 50 mm. The focal length of the receiver for the PDPA system is 500 mm. A 4W water-cooled argon laser was used.

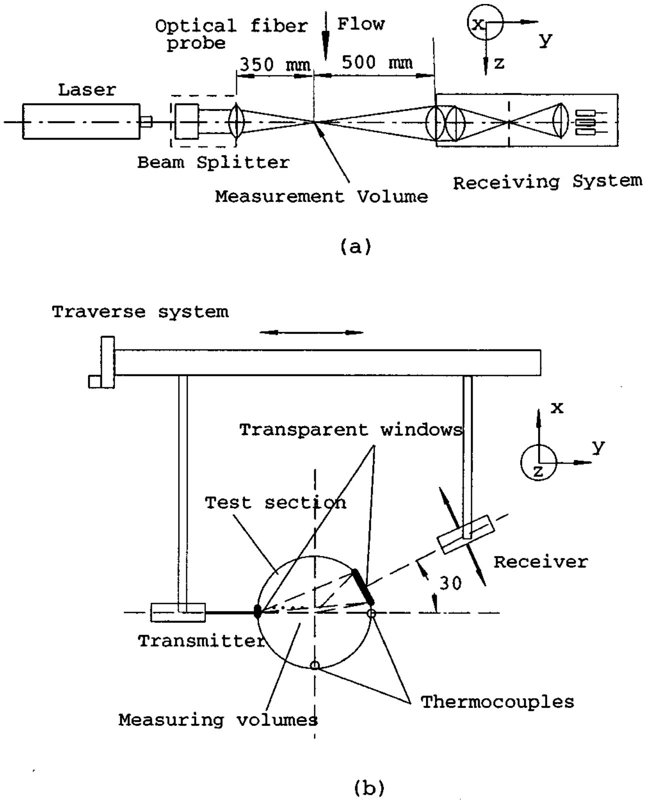

Fig. 3 PDPA measurement arrangement: (*a*) top view; (*b*) side view

Approach of This Study. Droplet size measurement is a major challenge. No measurements are made within the test section because it is thermally insulated. Measurements inside unheated, noninsulated transparent tubing are also difficult. One difficulty arises when laser beams pass through the wall of the transparent circular tubing. The optical paths of the laser beams are changed by the surface curvature and the refraction of light. Thus, the focal point is affected. Another difficulty is that the scattered light caused by the laser beam bouncing on the inner wall surface proves to be a large background noise source to the measured signal. To overcome this, specially designed flat Pyrex windows are used as the optical ports on two tube-end blocks. The size of the transparent windows (1 mm in width and 10 mm in length) is large enough to let the transmitting and receiving laser beams pass through, but small enough to avoid disturbance to the flow field and to reduce heat losses through the windows. The current design is a compromise between the minimum flow interference and the feasibility of fabrication. To prevent steam from leaking behind the glass window, EPDM O-rings that can stand high temperature (up to 280°C) seal the Pyrex window and the tube end.

To overcome the difficulty associated with the light scattering inside the tube, the inner surface of the endblocks and the test section are painted with high temperature black paint, and a through hole (2×4 mm) in alignment with the incident laser beam is opened on the endblock so as to let the laser beam exit the tube directly. The arrangement of the PDPA system is shown in Fig. 3(*b*).

Verification of the PDPA System. The PDPA system was verified against Polymer Latex particles (manufactured by Duke Scientific Corp.) of known sizes. These particles, with moderately low standard deviations, are microspheres with a density of 1.05×10^3 kg/m^3 and a light refraction index of 1.59 at 590 nm. The verification process was performed by putting the Polymer Latex particles into a transparent container filled with water and moved across the PDPA measuring volume at a constant speed. Five different particle sizes from $3\sim22$ μm were used. The measured particle sizes from PDPA agree very well with the actual particle sizes.

Instrumentation

Temperature Measurement. The temperatures are measured by Omega gage 30 (0.2546 mm in diameter) iron/constantan thermocouples with braided fiberglass insulation, which are monitored by a FLUKE data logger. The thermocouples, along with the data logger, were calibrated against a standard resistance temperature device (RTD) system by attaching the thermocouple junctions to a copper block and placing them in a furnace.

Wall Temperature of the Test Section. To eliminate the possible electrical voltage drop across the thermocouple junctions due to the DC Joule heating, the test section is first wrapped with a thin layer (<0.1 mm) of mica tape (a dielectric tape with insignificant temperature drop across the tape thickness, manufactured by Cogebi, Inc.). Then, seven thermocouples, with one inch spacing along the tube axis, are mounted onto the external surface of the test section using Omega CC high temperature cement, which has a thermal conductivity of 0.5 W/mK and a dielectric constant of 6.

Detailed thermocouple arrangement for the test section is shown in Fig. 2. Note two more thermocouples are off the line of all the others to check circumferential heating uniformity. Temperatures are also measured at (*a*) inlet and outlet of the test section, (*b*) exit of the mixing chamber, and (*c*) inlet of the low pressure steam orifice flow meter.

Flow Measurement

Steam Flow Rate. Two orifice flow meters are used for the high-pressure steam system and the low-pressure steam system with pressure transmitters from Dwyer (diaphragm type of 630A series). Pigtail siphon tubes are used as the intermediate parts between the orifice pressure ports and the transmitter inputs to trap the condensate of steam and to avoid direct contact of steam to the transmitter. The uncertainties for the flow measurement are estimated to be less than 4 percent.

Water Flow Rate. The water flow coming into the atomizer is measured by an Omega rotameter FL-112, which is calibrated in-situ by using the catch-and-weigh method. The uncertainty of the rotameter for measuring the water flow is estimated to be less than 5 percent for a typical flow of 15 kg/h.

Pressure Measurement. Steam pressure is measured by standard pressure gages at inlets of the low-pressure filter and the high-pressure filter, and the outlets of the low-pressure filter and the high-pressure filter.

Heating Power. The heating power is calculated from the electrical current and voltage across the test section. The current is obtained by measuring the voltage across the shunt (with a pure resistance of $1.3333\times10^{-4}\,\Omega$) of the power supply. The uncertainty for the heating power is estimated to be less than 3 percent of a typical heat flux of 10,000 W/m^2.

Droplet Size Measurement. As discussed previously, droplet sizes are measured at the centerline of both the inlet and outlet of the test section. It is noted that PDPA has a point size measurement volume and measures the droplet size, velocity, and droplet number density during a certain period of time. To obtain the droplet size distribution, the PDPA system is traversed along the radial direction of the test section tube by a special traverse system, which synchronizes the movements of the transmitter and receiver.

Mean Droplet Sizes. The most important droplet characteristic is the mean diameter. This diameter can be evaluated in various ways. The most commonly used mean diameter is the arithmetic mean diameter (d_{10}). Other commonly used mean diameters are the area mean diameter (d_{20}), volume mean diameter (d_{30}), and the sauter mean diameter (d_{32}), which represents the ratio of volume to area.

If all the droplets are of the same size, then $d_{10}=d_{20}=d_{30}=d_{32}=d$. For droplets with different sizes, d_{10} among all the mean diameters has the smallest value, while d_{32} has the largest. Generally, d_{10} represents the diameters of most droplets, d_{32} represents the diameters of large droplets. For example, if we have 10 spherical droplets with 9 of them having diameters of 1, and 1 having a diameter of 10, then $d_{10}=1.9$, $d_{20}=3.3$, $d_{30}=4.7$, and $d_{32}=9.3$.

Droplet Volume Flux. The volume flux is the volume of droplets passing a unit cross-sectional area per unit time (e.g., cm^3/s cm^2). It is obtained in PDPA by summing all the volumes of the droplets measured over an interval of time:

$$V'=\frac{\pi}{6}nd_{30}^3/t_0/A_0 \tag{1}$$

where t_0 is the elapsed time for the measurement and A_0 is the sampling cross-sectional area. The droplet mass flux can be obtained by simply multiplying the volume flux by the droplet material density.

Experimental Procedure

The experimental runs for two-phase mist/steam flow heat transfer were conducted in the following sequence. For each run, the main steam flow rate was fixed. The test section was first heated with a certain heat flux and the wall temperature distribution of the test section for steam only was measured. After this, a certain amount of water was added into the main steam flow through the atomizing system, and the wall temperatures for the

Table 1 Results of *n*th-order uncertainty analysis

Independent variable	Nominal value	Uncertainty of imprecision	Uncertainty of unsteadiness	Uncertainty of calibration	Nth order Uncertainty %
T_w (F)	400	0.05	2.0	0.5	1.2
Orifice flow meter (LP) kg/s	27.0	0.0	1.35	0.81	5.5
Pressure transducer (LP) mA	10.0	0.005	0.2	0.2	2.6
Orifice flow meter (HP) kg/s	1.7	0.0	0.085	0.085	0.4
Pressure transducer (HP) mA	10	0.005	0.5	0.5	0.4
Rotameter scale	15	0.5	0.5	0.05	4.7
Uncertainty for steam flow	Nominal flow: LP steam: 27.0 kg/hr, HP steam: 1.7 kg/hr Total steam flow: 28.7 kg/hr				6.1
Uncertainty for water flow	Nominal water flow rate: 4.5 kg/hr				4.7

two-phase mist/steam flow were measured. This concluded one case for this specific run. Then for a different case, a different heat flux value was applied and the above procedure was repeated. For another experimental run, the main steam flow rate was changed, and the aforementioned process was repeated.

Experimental Conditions. The experiment was performed under the following conditions: The Reynolds numbers for the main steam flow range from 10,000 to 35,000; the liquid droplet mass ratios range from 1~6 percent; the wall heat fluxes range from 3000~25,000 W/m^2 (with the highest wall superheat up to 300°C). The average droplet diameter d_{10} at the inlet of the test section is around 6 μm. Totally, nine experimental runs have been conducted. Generally, the increase of the main steam Reynolds number from inlet to outlet due to droplet evaporation in each run is small (less than 6 percent) because of the relatively low droplet mass ratios in all the cases.

Data Reduction

The objective of this experimental program is to measure the heat transfer between the heated test section and the two-phase mist/steam mixtures, and to compare with the results of the corresponding one-phase steam only heat transfer. For a single-phase flow, the heat transfer coefficient can be obtained by

$$h_o(z)=\frac{q''(z)}{T_w(z)-T_m(z)} \tag{2}$$

where q'' is the wall heat flux, T_w is the local wall temperature, and T_m is the fluid (mist/steam mixture) bulk temperature at the same wall location.

For the current two-phase flow, the heat transfer coefficient for the mist/steam flow can *typically* be calculated by using the steam saturation temperature at the inlet of the test section as the reference temperature ($T_{\mathrm{sat,in}}$). That is,

$$h_{1,\mathrm{mist}}(z)=\frac{q''(z)}{T_w(z)-T_m}\approx\frac{q''(z)}{T_w(z)-T_{\mathrm{sat,in}}} \tag{3}$$

where $q''(z)$ is the local wall heat flux and $T_w(z)$ is the local wall temperature for two-phase mist/steam flow.

The reason for using the inlet saturation temperature as the reference temperature in Eq. (3) is that in most experimental cases, the steam flow at the center of the tube has an average temperature that is close to the saturation temperature (though near the wall the steam is superheated) due to the short test section used. Considering that the pressure drop along the test section is small and T_{sat} along the test section is very close to $T_{\mathrm{sat,in}}$, $T_{\mathrm{sat,in}}$ is thus used in Eq. (3).

By definition, $h_{1,\mathrm{mist}}$ is intended to reflect the driving potential more realistically in the mist flow per se. However, when evaluating the *heat transfer enhancement* by comparing with the steam-only results, use of T_{sat} as the sink temperature will not render a fair comparison because using T_{sat} implicitly buries the effects introduced by the merits of liquid droplets. Therefore, it is felt to make a fair evaluation of the cooling enhancement, the mist effects should be removed from the T_{sat} and be lumped into the h value by replacing T_{sat} with T_m of the steam-only condition for each corresponding case. This definition is designated as $h_{2,\mathrm{mist}}$:

$$h_{2,\mathrm{mist}}(z)=\frac{q''(z)}{T_w(z)-T_m} \tag{4}$$

The cooling enhancement is finally evaluated as $h_{2,\mathrm{mist}}/h_0$ instead of $h_{1,\mathrm{mist}}/h_0$.

Wall Temperature. Since the temperature drop across the wall is negligible (less than 1 K) compared to the absolute values of the temperature difference between the wall and the steam saturation temperature (300 K), the thermocouple measurements are directly used in the data reduction process.

Heat Flux. The local heat flux of the test section is determined by dividing the heating power for the test section by the inner surface area of the test section. Three corrections of the local heat flux are made to obtain the net local heat flux. The first correction accounts for the variation of electrical resistivity with temperature for the test section material (SS304). In this study, the variation of electrical resistance of the test section with temperature has been observed to be less than 5 percent. The second correction accounts for the backside heat loss from the test section to the ambient through the insulation. A simple one-dimensional heat conduction model is used to estimate the heat loss. The variation of the heat transfer coefficient due to the effect of backside heat loss is found to be less than 0.3 percent. The third correction is to account for axial conduction heat loss from the ends of the test section to the endblocks. It has been found that less than 2 percent of all the heating power may be lost from the two ends of the test section.

Uncertainty Analysis

An uncertainty analysis identifies large uncertainty sources and assists in planning for experimental procedures. The uncertainty analysis is based on the theories of Kline [16] and Moffat [17] and closely follows the method used by Wang and Simon [18] and will not be detailed here. The results of the uncertainty analysis are summarized in Table 1. The detailed analysis is documented in Guo [10].

Acknowledgments

The authors would like to thank Graver Separations (Wilmington, DE) for donating the steam filters for the experiment. We also want to thank Mee Industries, Inc. (El Monte, CA), for donating the pressure atomizers and the high-pressure pump. We appreciate the help from X. Li in setting up the test facility. This research is sponsored by the U.S. Department of Energy under the contract DOE/AGTSR 95-01-SR-034, and is managed by Dr. N. Holcombe at the Federal Energy Technology Center and by Dr. D. Fant at the South Carolina Energy Research and Development Center.

Nomenclature

A = cross-sectional area
C = droplet mass concentration
C_p = specific heat
d = droplet diameter
D = deposition rate
D_{ch} = channel diameter
d_{10} = droplet arithmetic mean diameter
d_{20} = droplet surface mean diameter
d_{30} = droplet volume mean diameter
d_{32} = droplet Sauter mean diameter
E = entrainment rate
h_0 = heat transfer coefficient for single-phase flow
h_{mist} = heat transfer coefficient for mist/steam flow
h_{lg} = latent heat of the liquid
H = heating factor $= q''/(\text{Re}\, m_r)$
k = thermal conductivity
m_r = droplet mass flow ratio
n = number of samples
Nu = Nusselt number $= hD_{ch}/k$
Pr = Prandtl number
q'' = heat flux
R = electric resistance
Re = Reynolds number $= UD_{ch}/\nu$
T_{sat} = saturation temperature of steam
T_w = wall temperature
TIT = Turbine Inlet Temperature
U = mean flow velocity
V, V_p = particle (droplet) velocity
V^* = $(\tau_w/\rho)^{0.5}$
V_{dep} = deposition velocity
V_{dep}^+ = V_{dep}/V^*
y = perpendicular distance from test wall surface
δ = boundary layer thickness
δ_1 = thermal boundary layer thickness
λ = friction coefficient $= 0.3164/\text{Re}^{0.25}$
ν = kinematic viscosity
ρ = density
μ = dynamic viscosity
τ_p = particle relaxation time $= \rho_p d_p^2/(18\rho_g \nu_g)$
τ_{p+} = particle relaxation time $= \tau_p V^{*2}/\nu_g$
τ_w = wall shear stress

Subscripts

g = gas or vapor phase
l = liquid phase
p = particle or droplet
sat = saturation
w = wall

References

[1] Van der Lindea, S., 1992, ''Advanced Turbine Design Program,'' in: *Proc. Ninth Annual Coal-Fueled Heat Engines, Advanced Pressurized Fluid-Bed Combustion (PFBC), and Gas Stream Cleanup Systems Contractors Reviewing Meeting*, Oct. 27–29, Morgantown, WV, pp. 215–227.

[2] Bannister, R. L., and Little, D. A., 1993, ''Development of Advanced Gas Turbine System,'' in: *Proc. Joint Contractor Meeting: FE/EE Advanced Turbine System Conference; FE Fuel Cells and Coal-Fired Heat Engine Conference*, Aug. 3–5, Morgantown, WV, pp. 3–15.

[3] Mukavetz, D. W., Wenglarz, R., Nirmalan, N., and Daehler, T., 1994, ''Advanced Turbine System (ATS) Turbine Modification for Coal and Biomass Fuels,'' in: *Proc. of the Advanced Turbine System Annual Program Review Meeting*, Nov. 9–11, ORNL/Arlington, VA, pp. 91–95.

[4] Bannister, R. L., Cheruvu, N. S., Little, D. A., and McQuiggan, G., 1995, ''Development Requirements for an Advanced Gas Turbine System,'' ASME J. Turbomach., **117**, pp. 724–733.

[5] Farmer, R., and Fulton, K., 1995, ''Design 60% Net Efficiency in Frame 7/9H Steam-Cooled CCGT,'' Gas Turbine World, May–Jun, pp. 12–20.

[6] Mukherjee, D., 1984, ''Combined Gas Turbine and Steam Turbine Power Station,'' Patented by ABB, U.S. Patent No. 4424668.

[7] Alff, R. K., Manning, G. B., and Sheldon, R. C., 1978, ''The High Temperature Water Cooled Gas Turbine in Combined Cycle With Integrated Low BTU Gasification,'' Combustion, **49**, pp. 27–34.

[8] Chen, J. C., and Costigan, 1992, ''Review of Post-Dryout Heat Transfer in Dispersed Two Phase Flow,'' *Post-Dryout Heat Transfer*, Hewitt, G. F., et al. eds., CRC Press, Inc., FL, pp. 1–37.

[9] Guo, T., Wang, T., and Gaddis, J., 1999, ''Mist/Steam Cooling in a 180-Degree Tube,'' presented at the *National Heat Transfer Conference*, Albuquerque, NM, Aug. 14–17.

[10] Guo, T., 1998, ''Mist/Steam Cooling in a Heated Horizontal Tube,'' Ph.D Dissertation, Mechanical Engineering Department, Clemson University, Clemson, SC.

[11] Mori, Y., Hijikata, K., and Yasunaga, T., 1982, ''Mist Cooling of Very Hot Tubules With Reference to Through-Hole Cooling of Gas Turbine Blades,'' Int. J. Heat Mass Transf., **25**, No. 9, pp. 1271–1278.

[12] Janssen, J. M., Florschuetz, L. W., and Fizdon, J. P., 1986, ''Heat Transfer to Two-Phase Air/Water Mixtures Flowing in Small Tubes With Inlet Disequilibrium,'' NASA CR 175076.

[13] Swithenbank, J., Cao, J., and Hamidi, A. A., 1991, *Spray Diagnostics by Laser Diffraction Combustion Measurement*, Chigier, N., ed., Hemisphere Publishing Co.

[14] Bachalo, W. D., 1980, ''Method for Measuring the Size and Velocity of Spheres by Dual-Beam Light Scatter Interferometry,'' Appl. Opt., **19**, No. 3, pp. 363–372.

[15] Bachalo, W. D., and Houser, M. J., 1984, ''Phase Doppler Spray Analyzer for Simultaneous Measurements of Drop Size and Velocity Distributions,'' Opt. Eng. (Bellingham), **23**, No. 5, pp. 583–597.

[16] Kline, S. J., 1985, ''The Purposes of Uncertainty Analysis,'' ASME J. Fluids Eng., **107**, pp. 153–160.

[17] Moffat, R. J., 1985, ''Using Uncertainty Analysis in the Planning of an Experiment,'' ASME J. Fluids Eng., **107**, pp. 173–178.

[18] Wang, T., and Simon, T. W., 1989, ''Development of a Special-Purpose Test Surface Guided by Uncertainty Analysis,'' J. Thermophys. Heat Transfer, **3**, No. 1, pp. 19–26.

Mist/Steam Cooling in a Heated Horizontal Tube—Part 2: Results and Modeling

Tao Guo[1]
Ting Wang[2]
J. Leo Gaddis
Department of Mechanical Engineering,
Clemson University,
Clemson, SC 29634

Experimental studies on mist/steam cooling in a heated horizontal tube have been performed. Wall temperature distributions have been measured under various main steam flow rates, droplet mass ratios, and wall heat fluxes. Generally, the heat transfer performance of steam can be significantly improved by adding mist into the main flow. An average enhancement of 100 percent with the highest local heat transfer enhancement of 200 percent is achieved with 5 percent mist. When the test section is mildly heated, an interesting wall temperature distribution is observed: The wall temperature increases first, then decreases, and finally increases again. A three-stage heat transfer model with transition boiling, unstable liquid fragment evaporation, and dry-wall mist cooling has been proposed and has shown some success in predicting the wall temperature of the mist/steam flow. The PDPA measurements have facilitated better understanding and interpreting of the droplet dynamics and heat transfer mechanisms. Furthermore, this study has shed light on how to generate appropriate droplet sizes to achieve effective droplet transportation, and has shown that it is promising to extend present results to a higher temperature and higher pressure environment. [S0889-504X(00)02502-2]

PDPA Measurement

Throughout the experimental program, the droplet size and distribution, droplet mean velocity, and volume flux were measured. These measurements not only facilitated the understanding of the droplet dynamics and the heat transfer mechanisms, but also served to check the validity of the experimental data.

It is desirable for a mist-generating system to provide controllable and predictable droplet size and distribution at the inlet of the test section; however, these are affected by many factors, such as the atomizing system, the mixing chamber design, and the deposition of droplets during the mist transportation process. The measurement of the droplet size and distribution is indispensable in identifying the problems and revealing physical mechanisms associated with mist generation.

Effects of Mixing Chamber. The spraying characteristic of an atomizer in an unconfined environment is different from that in a confined space because of the interactions between the spraying jet and the adjacent surfaces. Therefore, the droplet size and distribution at the exit of the mixing chamber are expected to deviate from those measured for a free jet and strongly depend on the design of the mixing chamber. To investigate the effects of the current mixing chamber on the mist generation, droplet size and distribution at the exit of the mixing chamber have been measured and compared with those measured in an unconfined environment.

Figures 1(*a*) and 1(*b*) show the results for the pressure atomizer and the air-assist pneumatic atomizer, respectively. For both types of atomizer, the average droplet diameters at the exit of the mixing chamber decrease 30∼40 percent from those of the corresponding free jets. The mixing chamber serves as a filter where large droplets are generally trapped inside the mixing chamber. The design of the mixing chamber and the configuration of the atomizers within the mixing chamber need further systematic investigation to obtain more precise control of the liquid droplet size and distribution.

Effects of Atomizer Type. To decide the appropriate atomizer for the current experimental program, two mist generation systems have been designed and tested. The first mist generation system uses the pneumatic atomizer with steam and water as the working fluids. The atomizer is installed at the center of the bottom flange of the mixing chamber. The droplet size is measured at the exit of the mixing chamber. Generally, for the pneumatic atomizer, only very small droplets (0∼10 μm in diameter) exist at the exit of the mixing chamber, as shown in Fig. 2(*a*). It is believed that the spray jet from the pneumatic atomizer is so vigorous that most large droplets are impinged on the wall and trapped inside the mixing chamber. The pneumatic atomizer is less ideal for the current experiment because the droplet mass ratio obtained from the current pneumatic atomizer system is too small (less than 1 percent of total steam flow) to affect the heat transfer.

The second mist generation system uses the pressure atomizer with high-pressure water (1000 psi) as the working fluid. Since

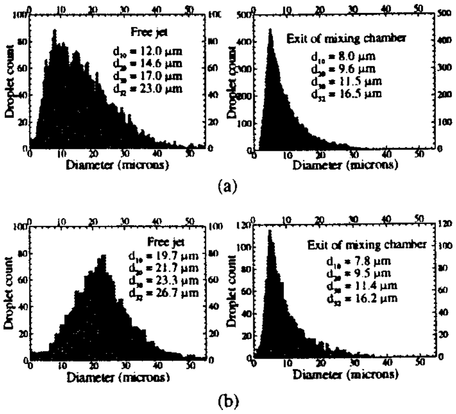

Fig. 1 Effect of mixing chamber on droplet size measurement: (*a*) pressure atomizer; (*b*) air-assist atomizer

---

[1] Current address: GE Power Systems, Schenectady, NY 12309.

[2] Current address: Energy Conversion and Conservation Center, University of New Orleans, New Orleans, LA 70148-2220.

Contributed by the International Gas Turbine Institute and presented at the 44th International Gas Turbine and Aeroengine Congress and Exhibition, Indianapolis, Indiana, June 7–10, 1999. Manuscript received by the International Gas Turbine Institute February 1999. Paper No. 99-GT-145. Review Chair: D. C. Wisler.

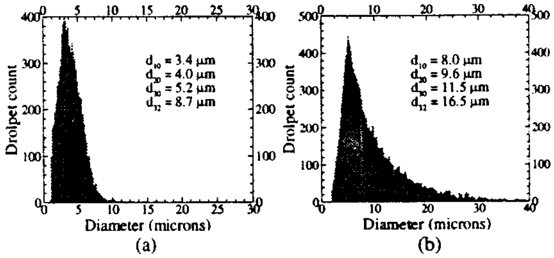

Fig. 2 Effect of atomizer type on droplet size distribution (measured at the exit of the mixing chamber): (*a*) steam-assist atomizer; (*b*) pressure atomizer

the pressure atomizer has a mild spray jet, relatively larger droplets (10–40 μm in diameter) follow the main steam flow and exit the mixing chamber, as shown in Fig. 2(*b*). Obviously, the average droplet size and the droplet mass ratio from the pressure atomizer system are larger than those for the pneumatic atomizer system. As a result, the pressure atomizer system is adopted in this study.

Effects of Transportation Length. Since there is a starting length (~0.5 m) connecting the mixing chamber and the heated test section, the droplet size measurement at the exit of the test section (when it is unheated) can provide useful information about droplet transportation. Figure 3(*a*) represents the droplet size and distribution at the exit of the mixing chamber, and Fig. 3(*b*) is at the exit of the *unheated* test section. The droplet size is generally smaller at the exit of the test section than at the exit of the mixing chamber. This implies that larger droplets are lost during the transportation due to the deposition mechanisms to be discussed later in detail.

Effect of Main Steam Flow. The transportation of droplets from the mixing chamber to the test section is also affected by the main steam flow rates. Figure 4 shows the changes of the mean droplet size at the exit of the *unheated* test section under different main steam flow rates in terms of Reynolds numbers, with all other parameters being fixed. It is obvious that as the main steam flow increases, the mean droplet size also increases. This is understandable because larger main steam flow induces larger drag between the droplets and the steam, and bigger droplets can thus be entrained out of the mixing chamber.

Droplet Evaporation. The effect of heat flux on droplet evaporation was investigated by measuring the droplet size and distribution at the exit of the test section. The measurement was performed in the following way: Under a certain main steam flow, the test section was first heated with the highest heat flux. Then the PDPA system was traversed to the desired position, and the size measurement was taken. With the measuring volume of the PDPA system being fixed, the heat flux to the test section was reduced, and subsequent PDPA measurements were conducted.

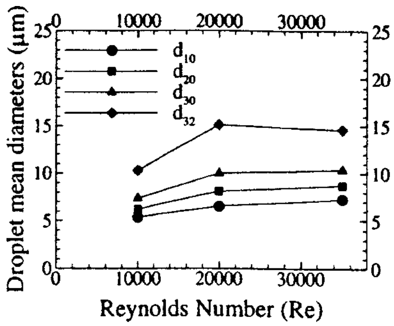

Fig. 4 Effect of main steam flow on droplet size distribution (unheated test section)

This gave the change of droplet size at a fixed location under a fixed steam flow rate but with different heat fluxes.

Local Droplet Mean Diameter. At a fixed measuring point in the test section outlet, the changes in the mean diameter of the droplets under different heat fluxes are shown in Fig. 5. It is interesting to notice that as the heat flux increases, the local droplet mean diameter increases also. At first, this seems unexpected because usually the droplet sizes are expected to become smaller in a heated test section due to evaporation. However, the current measurements indicate that inside the heated test section, smaller droplets are more susceptible to the wall heat transfer and will evaporate quickly. Larger droplets, on the other hand, may not be evaporated when they are subject to the same amount of wall heat transfer and most of them can remain intact at the exit of the relatively short test section. The diminishing number of droplets can be seen from the decreasing data rates of the PDPA measurement as the heat flux increases. So statistically speaking, the droplet sizes increase.

Steam Superheat. Although the steam temperature inside the test section cannot be easily obtained in this study, PDPA has been used to identify if the steam and the droplets are in thermal equilibrium in the heated test section.

It is expected that for a certain mist/steam flow over the total length of the heated test section, a maximum amount of liquid will be evaporated at the end of the tube if thermal equilibrium is achieved between the steam and the droplets. Suppose that the available heat flux is q'', and if this heat flux is used totally for evaporation (not for steam superheat), then the maximum evaporation rate of the droplets can be obtained as:

$$m_{\max}=\frac{Q}{h_{\text{lg}}}=\frac{\pi D_{\text{ch}}Lq''}{h_{\text{lg}}}$$

Comparing this $m_{\max}$ with all the experimental cases, it has been found that, for the cases of low main steam flow (Re =10,000) and low droplet mass ratio (~1 percent), $m_{\max}$ is larger than the available droplet mass flow, i.e., all the liquid droplets in

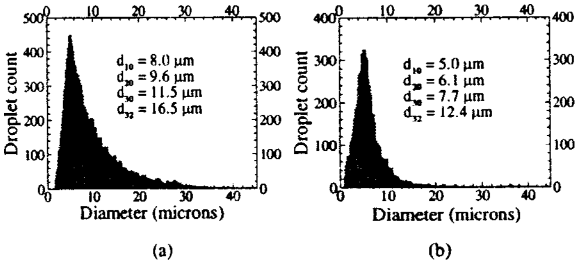

Fig. 3 Effect of unheated transportation length on droplet size measurement: (*a*) mixing chamber exit; (*b*) unheated test section exit

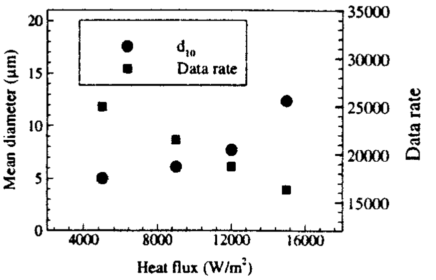

Fig. 5 Effect of heat flux on mean droplet size

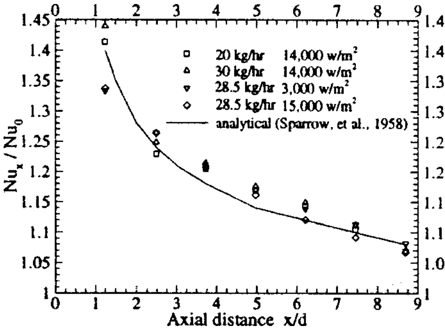

Fig. 6 Comparison of experimental and analytical results in the test section for steam-only flow

these cases should have been evaporated if there was thermal equilibrium between the steam and the droplets. However, the PDPA measurements indicate that in all the experimental cases, there are still large numbers of droplets existing at the exit of the test section. This implies that a certain amount of heat must have superheated the steam, and thus thermal nonequilibrium exists between the steam and the droplets within the test section. This is expected because it always takes a finite time to vaporize a droplet and it also takes time for the thermal boundary layer to diffuse toward the core. For example, it takes about 0.014 s for the 5°C superheated steam to vaporize a 4 μm water droplet by using Ranz and Marshall's correlation [1]. This can be translated into a flying distance of 1.2 times the length of the test section if the steam velocity is 14 m/s.

Heat Transfer Results for One-Phase Steam Flow

Experimental runs with steam as the only working fluid were performed first. These runs not only served as the basis for future comparison with mist/steam flow heat transfer, but also provided an opportunity to qualify the performance of the test section. The measured Nusselt numbers ($\mathrm{Nu}=hD_{\mathrm{ch}}/k$) under various heat fluxes and flow rates (Reynolds numbers) are shown in Fig. 6.

Since the current test section is relatively short ($l/d=8$), the Nusselt numbers decrease along the test section as expected in the thermal entrance region. This is different from the case of fully developed single-phase turbulent flow where the Nusselt number is constant under the constant heat flux condition. Shown also in Fig. 6 are the analytical heat transfer results for the single-phase thermal entrance region obtained by Sparrow et al. [2]. Generally, it can be seen that the current experimental results (except for the first point of data at $x/D_{\mathrm{ch}}=1$) agree within ±3 percent with the analytical result. This qualifies the experimental setup and instrumentation of this study. A correlation has been developed based on the current experimental data for single-phase steam-only flow:

$$\mathrm{Nu}_z=\mathrm{Nu}_\infty\left[1+\frac{1.25}{(z/D_{\mathrm{ch}})^{1.34}}\right] \tag{1}$$

$$\mathrm{Nu}_\infty=0.023\,\mathrm{Re}^{0.8}\,\mathrm{Pr}^{0.3} \tag{2}$$

where Nu_z is the Nu number at any z location, and Nu_∞ is the Nusselt number for the thermally fully developed flow.

Heat Transfer Results for Two-Phase Mist/Steam Flow

Wall Temperature Distribution. Figures 7, 8, and 9 show the measured wall temperature distributions of the test section for two-phase mist/steam flow under various steam Re numbers, wall heat fluxes, and mist/steam mass ratios. In particular, each figure gives the temperature distributions for various heat fluxes under a fixed Reynolds number and a fixed mist/steam mass ratio, along with the corresponding temperature distribution for single-phase steam-only flow for comparison.

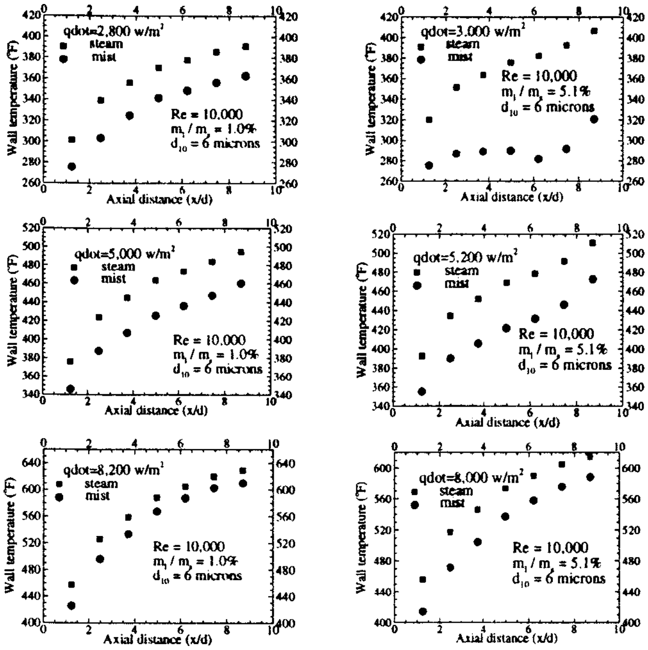

Fig. 7 Comparison of wall temperature variations between steam-only and mist for low steam flow

Figure 7 shows the results of wall temperature measurements at Re=10,000 with mist/steam mass ratios of ~1 and ~5 percent respectively. The effect of adding water droplets into the steam flow on heat transfer is obvious. Generally, a decrease of local wall temperature of 11°C~22°C (20~40°F) can be seen for the case of ~1 percent mist mass ratio. By increasing the mist mass ratio to ~5 percent, the local wall temperature is seen to have a decrease of 40°C~100°C (104~212°F).

Similar results are observed for the cases of higher main steam flows. Figure 8 shows the results of wall temperature measurements at Re=20,000 with mist/steam mass ratios of ~1 and ~5

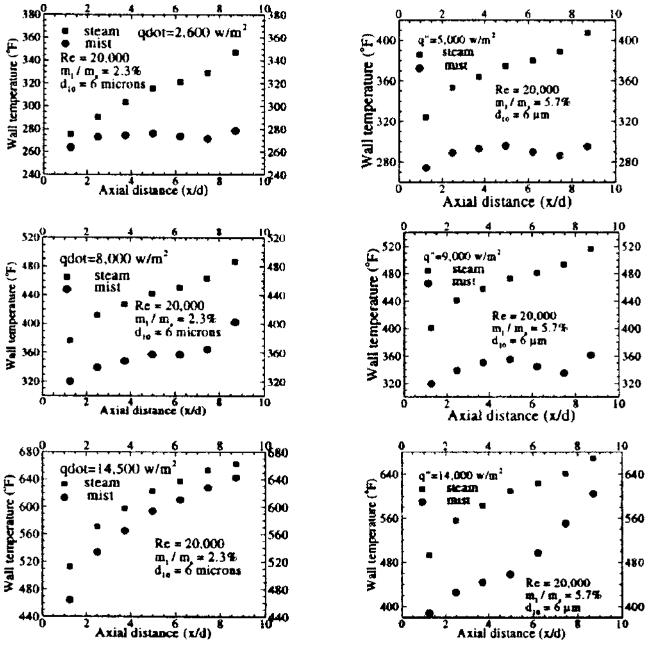

Fig. 8 Comparison of wall temperature variations between steam-only and mist flow for medium steam flow

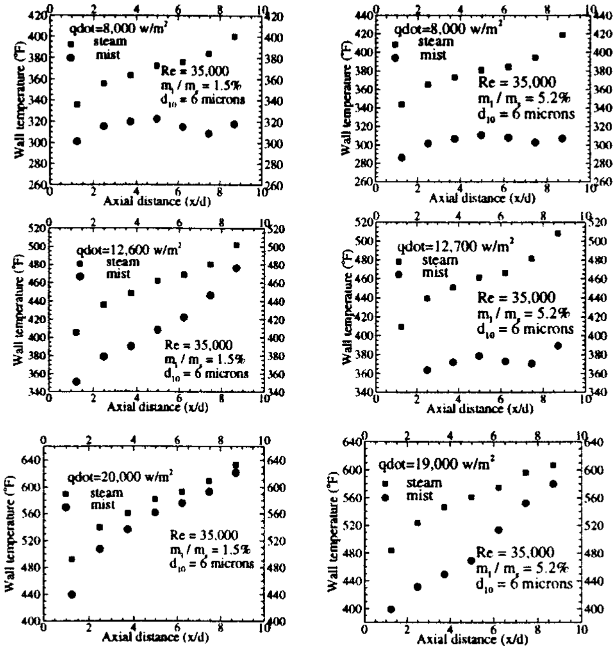

Fig. 9 Comparison of wall temperature variations between steam-only and mist flow for high steam flow

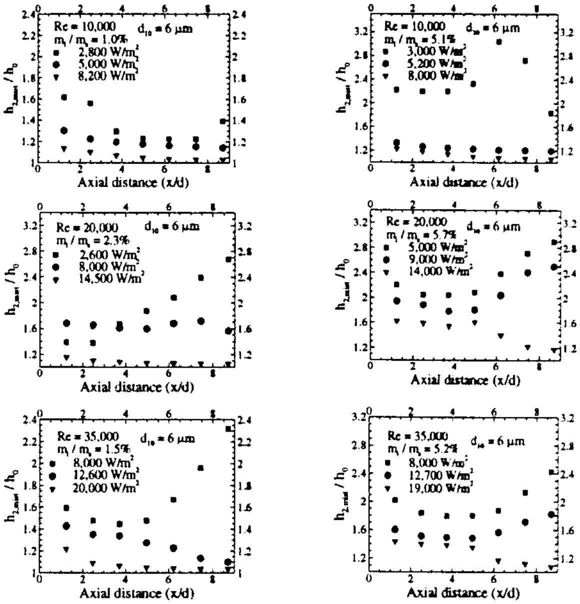

Fig. 10 Effect of heat flux on heat transfer enhancement for mist flow

percent, respectively. Figure 9 shows the results at Re=35,000. In both cases, a significant decrease in wall temperature (44~83°C or 111~180°F) is detected under low to medium heat flux conditions. Besides, these figures also show that under the same heat flux and droplet mass ratio, as the main steam flow rate (Re number) increases, the heat transfer enhancement also increases.

Based on the wall temperature measurements, it can be seen that heat transfer enhancement decreases as the heat flux increases. This is expected because as the heat flux increases, the wall temperature also increases. As the wall temperature becomes higher and higher, fewer and fewer droplets can contact the wall surface. Therefore, the ''quench'' effect due to direct contact between the droplets and the wall reduces. The major heat transfer path in such a case is by steam convection, with the heat transfer enhancement coming from (*a*) a lower steam bulk temperature and (*b*) a progressively increasing steam mass flow rate resulting from the added steam mass from droplet evaporation inside the steam flow.

An interesting observation from the wall temperature measurements is that when the test section is mildly heated (i.e., high main steam flow with low/medium heat flux and high droplet mass ratio), the wall temperature exhibits an ''up-down-up'' characteristic (see Fig. 8, for example): The wall temperature for mist/steam flow increases first, then decreases, and finally increases again. This indicates that the heat transfer rate at the entrance region of the heated test section decreases initially, then it is significantly enhanced in a short region downstream before a reduction in heat transfer enhancement takes place.

One plausible explanation for this phenomenon is that, after an initial heating-up process, most of the droplets start to evaporate somewhere downstream of the inlet. The evaporation of droplets causes a local increase of the main steam flow rate which, in turn, locally enhances the heat transfer. However, the possible increase of the steam flow rate (due to droplet evaporation) is too small (less than 5 percent in present study) to have so large an effect on heat transfer. Also, the possibility of the nonuniform wall heating due to the nonuniformity of the wall thickness is removed since the wall thickness is measured to be within 3 percent of nonuniformity. Therefore, other heat transfer mechanisms must have played their roles in contributing to this heat transfer enhancement. Further discussions of this subject will be given later.

Heat Transfer Coefficient Distribution. Figure 10 shows the effect of heat fluxes for different droplet mass ratios (~1 and ~5 percent) under different main steam flow rates. The *y* axis represents the ratio of the heat transfer coefficient of mist/steam flow over that for single-phase steam flow. By observing all the subplots in Fig. 10, it is obvious that the heat transfer coefficient ratio (or enhancement) decreases with the increase of heat flux under the same main steam flow rate and droplet mass ratio.

Figure 11 shows the effects of droplet mass ratios on heat transfer enhancement for different main steam Reynolds numbers (10,000, 20,000, and 35,000, respectively) under different heat fluxes. It can be seen that the heat transfer coefficient ratios increase with an increase of the droplet mass ratio under the same Reynolds number and heat flux.

Figure 12 shows the effects of Reynolds number for different droplet mass ratio (1~2 and 5~6 percent, respectively) under different heat fluxes. By observing Fig. 12, it can be found that the heat transfer coefficient ratios increase with the increase of Reynolds number under the same droplet mass ratio and heat flux.

In all the cases, the heat transfer coefficient ratio (enhancement) for mist/steam flow is larger than 1, which means that the heat transfer enhancement is achieved by adding mist into the steam flow. The highest local enhancement achieved so far is 200 percent ($h_{\mathrm{mist}}/h_0 = 300$ percent).

Flow and Heat Transfer Mechanisms of Mist/Steam Mixture

As indicated before, an interesting ''up-down-up'' wall temperature distribution has been found to be the characteristic for mist/steam flow when the wall is mildly heated. Attention has thus been directed to further understanding the droplet dynamics. It is believed that the understanding of the droplet dynamics purely from the interaction between fluid and solid particles (without involving heat transfer and droplet size change) serves as the foundation for the understanding of more complex conditions involving droplet evaporation. To initiate the investigation, the following droplet dynamics mechanisms are briefly reviewed.

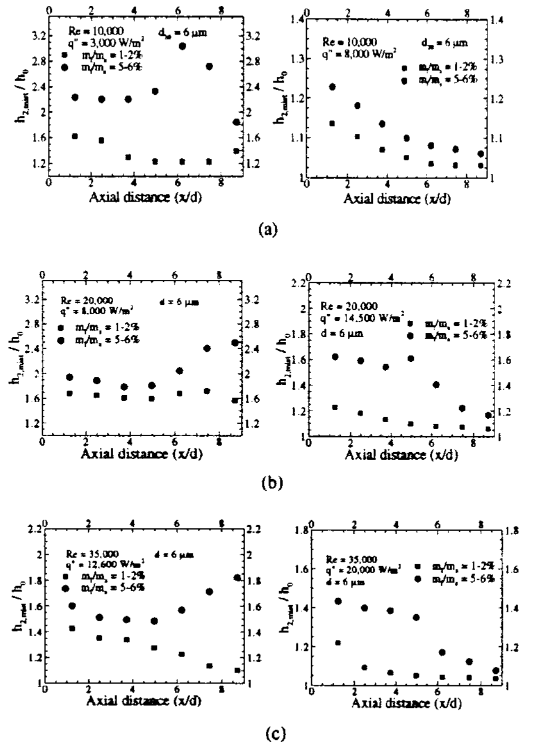

(a)

(b)

(c)

Fig. 11 Effect of droplet mass ratio on heat transfer enhancement for mist flow: (*a*) low steam (Re=10,000); (*b*) medium steam (Re=20,000); (*c*) high steam (Re=35,000)

Unheated Section: Deposition and Entrainment

Droplet Deposition. The understanding and prediction of the deposition of small particles suspended in a turbulent gas flow onto an adjacent surface is of great interest in applications such as pollution control, gas cleaning, design of industrial reactors, and transport of droplets in two-phase flow systems. Abundant articles and papers have been published in this research area, for example, Liu and Agarwal [3]; Johansen [4]; and Papavergos and Hedley [5], to name a few.

Many mechanisms can contribute to the deposition of particles. The particles can deposit onto the wall by particle inertia, gravitational settling, diffusion, space charge precipitation, etc. [3]. For neutrally charged particles suspended in a turbulent pipe flow, the major deposition mechanisms are Brownian diffusion [3], turbulent diffusion [5], turbophoresis force [6] and lift force [6], assuming that the gravitational force is negligible. Detailed discussions on each of these forces can be found in Guo [7].

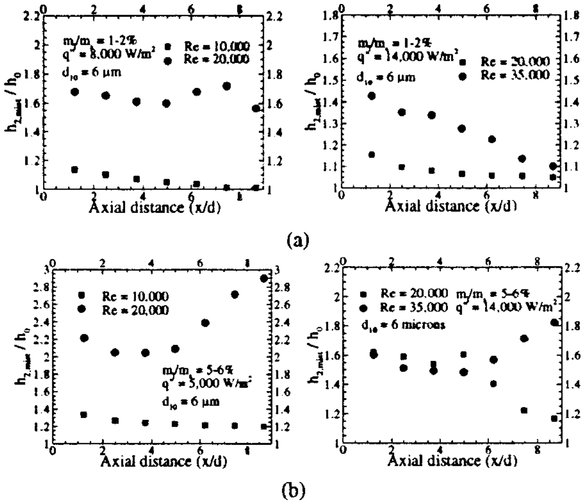

(a)

(b)

Fig. 12 Effect of mist steam flow on heat transfer enhancement for mist flow: (*a*) low droplet mass ratio (1~2 percent); (*b*) high droplet mass ratio (5~6 percent)

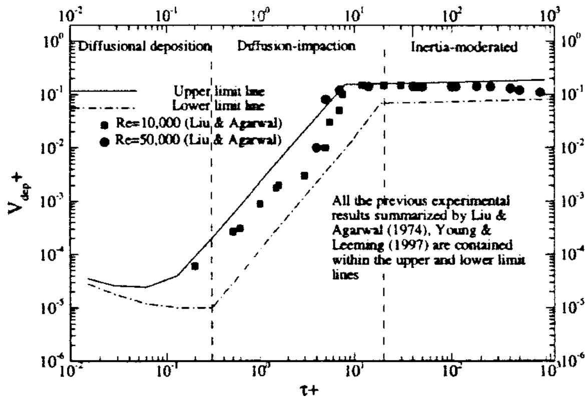

Fig. 13 Droplet deposition from fully developed turbulent pipe flow

Many experimental studies investigated the mechanisms of particle deposition inside a turbulent flow. Figure 13 is a summary of the previous experimental results on particle deposition [3,6]. This figure shows the rate of particle deposition onto the wall of a circular pipe as a function of particle size, using non-dimensionalized variables. The definition of the dimensionless deposition velocity is $V^+_{\rm dep}=V_{\rm dep}/V^*$, where $V_{\rm dep}$ is the absolute deposition velocity of the particles onto the surface, and V^* is the friction velocity $V^*=(\tau_w/\rho_g)^{0.5}$. The dimensionless particle relaxation time τ_{p+} is defined as $\tau_{p+}=\tau_p V^*/\nu_g$, where ν_g is the kinematic viscosity of the gas, and τ_p is the particle relaxation time with $\tau_p=\rho_p d_p^2/(18\rho_g\nu_g)$. Apparently, τ_{p+} increases as either the particle size or the main flow velocity increases.

The deposition curves of Fig. 13 are usually divided into three regimes: the ''diffusion-deposition'' regime, the ''diffusion-impaction'' regime, and the ''inertia-moderated'' regime.

''Diffusion-deposition'' regime ($\tau_{p+}=0.1\sim0.2$). In the diffusion-deposition regime, the particle sizes are usually small and the particle motion in this region is totally controlled by diffusion (both Brownian diffusion and turbulent diffusion).

''Diffusion-impaction'' regime ($0.1\sim0.2<\tau_{p+}<10\sim20$). In this regime, a significant increase in the deposition rate of several orders of magnitude is observed when τ_{p+} (or the particle diameter) increases. The particle sizes are moderately large in this regime and the particle deposition is controlled by both the diffusion and the particle inertia.

''Inertia-moderated'' regime ($\tau_{p+}>10\sim20$). In this regime, the particle deposition is controlled totally by the forces related to the particle inertia (turbophoresis force and lift force). In general, the deposition rate is high but decreases slightly as the particle size increases. This is largely because the increase in particle inertia results in a decrease in response to the main flow turbulence.

Entrainment. When the liquid film from the deposition process reaches a certain thickness, the liquid film will be broken up by the main flow and a certain amount of liquid will be reentrained into the main flow. The entrainment rate E (kg m^{-2} s^{-1}) can be calculated from the following correlation [8]:

$$\frac{E}{m_g}=5.75\times10^{-5}\left[(m_{\rm lf}-m_{\rm lfc})^2\frac{D_{\rm ch}\rho_l}{\sigma\rho_g^2}\right]^{0.316}\quad \text{for } m_{\rm lf}>m_{\rm lfc} \qquad (3)$$

where σ is the surface tension of the liquid phase, m_g the gas mass flux, $m_{\rm lf}$ the liquid film flow rate (referred to the total cross section of the pipe), and m_{lfc} the critical film flow rate for the onset of entrainment, which is given by the following relationship [8]:

$$\frac{m_{\mathrm{lfc}} D_{\mathrm{ch}}}{\mu_l} = \mathrm{Re}_{\mathrm{lfc}} = \exp\left(5.8504 + 0.4249 \frac{\mu_g}{\mu_l} \sqrt{\left(\frac{\rho_l}{\rho_g}\right)} \right) \tag{4}$$

Before the mist/steam mixture flows into the heated test section, it first passes through an ''unheated'' tube which connects the test section and the mixing chamber. The unheated section is actually 1~2 F superheated due to the heating of the guard heaters near the inlet of the test section. In this unheated section, the droplet motion is controlled by fluid mechanics. Basically, most droplets will be accelerated and reach terminal speed. Some droplets might coalesce into larger ones; some large droplets might break up into smaller ones. Many droplets will deposit on the wall due to gravity, gradient diffusion, lift force, or turbulent interaction. As a result, a thin layer of liquid film will accumulate on the wall surface. Usually, the liquid film is relatively thin. However, if the droplet concentration is large and the tube is long, the liquid film may grow thicker. As the liquid film grows thicker, the shear force between the main steam flow and the liquid film would eventually break up the liquid film. Entrainment of liquid droplets into the main flow would thus occur. Eventually, the thickness of the liquid film will be balanced by the steam shear force, droplet deposition, and break-up of the liquid film on the steam–water interface.

Prediction of Liquid Film Thickness Formed by Droplet Deposition. A model has been proposed in this study to predict the droplet deposition rate and the liquid film thickness in a turbulent pipe flow when the droplet size and main flow rate are the known parameters. In this model, the deposition velocity is calculated based on the experimental data (Fig. 13) of Liu and Agarwal [3], i.e.,

$$V_{\mathrm{dep}}^{+} = (6\times 10^{-4})\tau_{p+}^{2} \qquad \tau_{p+} < 10 \tag{5a}$$

$$V_{\mathrm{dep}}^{+} = 0.1 \qquad \tau_{p+} > 10 \tag{5b}$$

The deposition rate D ($\mathrm{kg\,m^{-2}\,s^{-1}}$) is calculated by the following equation:

$$D = V_{\mathrm{dep}} C \tag{5c}$$

where C ($\mathrm{kg\,m^{-3}}$) is the droplet concentration and V_{dep} is the deposition velocity.

The local liquid film flow rate m_{lf} ($\mathrm{kg\,m^{-2}\;s^{-1}}$) in the pipe can be obtained by integrating the following equation:

$$\frac{dm_{\mathrm{lf}}}{dz} = \frac{4}{D_{\mathrm{ch}}}(D - E) \tag{6}$$

where D and E are the deposition and entrainment rates, respectively. D is calculated from Eq. (5) and E is calculated from Eqs. (3) and (4).

Once the liquid film flow rate is known, the liquid film thickness can be estimated as follows. Let U_m represent the mean flow velocity, and the shear stress at the gas-liquid interface can be calculated as: $\tau_{\mathrm{lg}} = (1/8)\lambda\rho_g U_m^2$, where λ is the friction coefficient, $\lambda = 0.3164/\mathrm{Re}^{0.25}$. Assume that a linear velocity distribution exists across the film thickness, then we have: $\tau_{\mathrm{lg}} = \tau_w = \mu_l\,(u/y)$, where u is the velocity of the liquid film at position y, which is the distance from the wall.

The liquid film flow rate can be obtained by integrating the following equation:

$$m_{\mathrm{lf}} = \int_0^{\delta} \rho_l \cdot u \cdot \pi D_{\mathrm{ch}} dy = \int_0^{\delta} \rho_l \cdot \pi D_{\mathrm{ch}} \frac{\tau_w}{\mu_l} y \cdot dy \tag{7}$$

By equating Eqs. (3) and (7), the film thickness δ can be obtained. Figure 14 shows the predicted liquid film flow rate and the film thickness using this model for droplet/steam flow under the following conditions: pipe diameter=2 cm, pipe length=70 cm, steam velocity=25 m/s, average droplet size=7.7 μm, and inlet droplet mass concentration $C_0 = 0.038\,\mathrm{kg/m^3}$. Based on this figure, it is shown that at the end of the pipe, approximately 50 percent of all the droplets have deposited onto the wall. The thickness of the liquid film at the end of the pipe is around 30 μm and the corresponding liquid film flux with respect to the cross-sectional area of the tube is 0.35 $\mathrm{kg/m^2 s}$. This is an important information, which serves as the inlet boundary conditions of the test section and is used later for interpretation of the experimental results.

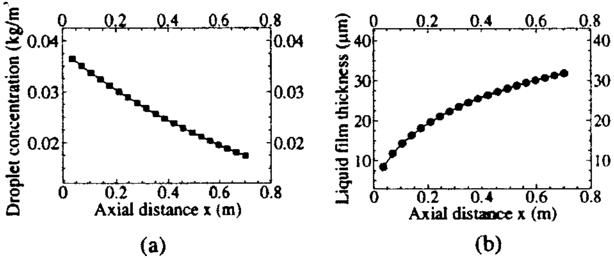

Fig. 14 Calculated droplet deposition film thickness for current study: (*a*) droplet concentration; (*b*) deposited liquid film thickness

Heated Test Section: A Three-Stage Heat Transfer Model. In the heated section, the droplet motion is affected by both the fluid mechanics and the heat transfer. The deposition mechanisms mentioned in the previous section still control the droplet deposition rate. However, since there is a steep temperature gradient near the wall (the turbulent thermal boundary layer), the droplet motion in this layer is also affected by the thermal reaction force or the thermophoresis force [9,10] which resists the droplet motion toward the wall. As a result, the overall deposition rate in the heated test section is smaller than that in the unheated section.

Generally, the heat transfer mechanisms of a vapor-liquid mixture adjacent to a heated surface can be classified as nucleate boiling, film boiling, and transition boiling. It has been reported [11] that if the wall superheat is higher than the *critical value* of 28°C (50°F), the direct contact between the liquid film and the wall surface no longer exists because the momentum of the rapidly evaporating vapor between the liquid and the wall surface forms a steam cushion which prevents the liquid from ''wetting'' the surface. This is the so-called ''film boiling'' where the heat transfer coefficient is almost equal to that for dry steam. If the wall superheat is lower than 28°C but well above the saturation temperature, the liquid film will contact the wall surface intermittently, depending on the local wall temperature. This is the so-called ''transition boiling'' where the heat transfer coefficient can be three to six times larger than that for dry steam [12]. It should be noted that the critical value 28°C for wall superheat is a function of pressure, droplet size and flow parameters. In many cases, it can be well above 28°C [12].

The heat transfer mechanisms of the mist/steam mixture in the current heated test section are more complicated. As indicated before, a liquid film always exists at the inlet of the current heated test section due to the droplet deposition in the upstream unheated section. The heat transfer performance of the mist/steam flow in the heated section is greatly affected by the existence of the liquid film. It has been observed that if the wall is severely heated, the wall temperature will increase monotonically along the flow direction, as expected in the case of constant wall heat flux. However, if the wall is mildly heated, an unusual ''up-down-up'' wall temperature distribution has been detected. As discussed earlier, the sole increase of the mean flow rate due to the evaporated liquid is not sufficient to increase the heat transfer to 100 percent. It is obvious that other heat transfer mechanisms exist for the mist/steam flow in the current heated section. A three-stage heat

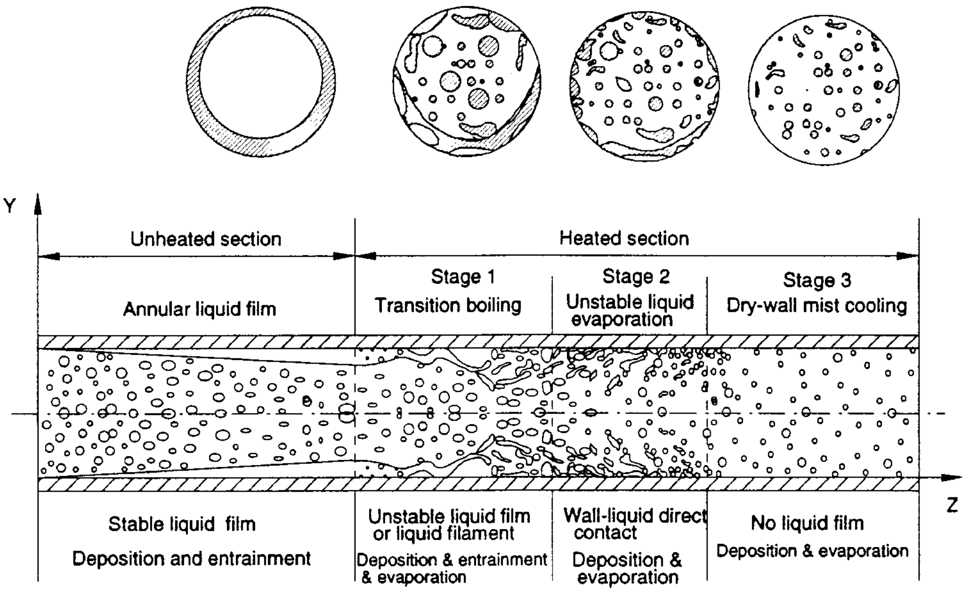

Fig. 15 Three-stage heat transfer model

transfer model has thus been proposed to explain the ''specific'' wall temperature distribution in the current study (Fig. 15).

Stage One: Transition Boiling. The flow pattern of the mist/steam mixture at the inlet of the heated section is that the fine water droplets are carried along by the main steam flow in the core region with a thin liquid film formed by deposition moving on the wall surface. As the mist/steam mixture enters the heated test section, whether or not the deposited liquid film can directly contact the wall depends on the degree of wall superheat. If the wall is heated with a relatively low heat flux (but still with significant wall superheat), the liquid film tends to contact the wall intermittently and transition boiling will occur. The features of the mist/steam heat transfer in this stage are further described below.

It is believed that the wall surface is not fully wetted by the liquid film because if the wall were fully wetted, the wall temperature should have been measured at the saturation temperature since the mass of the liquid film is sufficient to quench the wall to the saturation temperature. However, since the wall temperature data indicate significant wall superheat (20~100°F), it is concluded that part of the liquid film may intermittently detach from the wall due to the evaporating vapor pockets. Then the liquid film may become discontinuous and be broken up into fragments or large droplets by the ejection of bursting vapor pockets and by the shear force imposed from the main flow. The interaction between the liquid fragments and the main flow tends to move some of the liquid toward the wall and sweep some of the fragments downstream.

Stage Two: Unstable Liquid Evaporation With Large Droplets Deposition. In this unstable liquid evaporation stage, the heat transfer coefficient is very high for the following reasons:

- As the mist/steam mixture proceeds along the heated wall, the liquid film or fragments become thinner, smaller, and finger-like. Most liquid fragments will be confined within the near-wall region, while some fragments will be able to reach the wall surface due to the interactions between the liquid and the main flow. To some point, the liquid film or fragments become so thin that when they contact the wall, they can be completely evaporated by the supplied local heat flux. In other words, the evaporation process takes place in such a way that the vapor generated from evaporation can directly diffuse into the main flow without being trapped, in contrast to the case of conventional film boiling. Since there is no vapor layer between the wall and the liquid fragments, the liquid remnants or large droplets *swept down* from upstream (stage one) are able to penetrate the thermal boundary layer and reach the wall, and thus, heat transfer can be enhanced.
- The vapor flow rate (thus the convection between the vapor and the wall) increases at this heat transfer stage due to liquid evaporation.

It should be noted that Nirmalan et al. [13] used a similar concept (where they called it the flash evaporation) to design their experiment of mist/air cooling of gas turbine vane blades.

Stage Three: Dry-Wall Mist Cooling. Further down the heated test section, the liquid film is totally absent and the wall temperature is highly superheated. This is the mist cooling stage where the direct contact between the remaining droplets and the wall is minimal. There are three major ways that the droplets can affect the heat transfer. First, the latent heat of droplets provides additional energy sink to absorb energy. Second, the main steam flow can maintain a relatively lower temperature and hence the local temperature gradient is increased. Third, the droplet motion and evaporation can disturb the thermal boundary layer and increase mixing which, in turn, can improve the steam flow heat transfer. This third effect can be seen from the heat transfer enhancement for solid particles [11]. In general, the mist heat transfer coefficient is much higher than that for single-phase steam flow.

Wall Temperature Prediction

According to Eq. (3) in Part 1, the wall temperature for the two-phase mist/steam flow can be calculated as:

$$T_w = T_{\mathrm{sat,in}} + q''/h_{1,\mathrm{mist}} \tag{8}$$

where $T_{\mathrm{sat,in}}$ and q'' are known parameters.

Using the present data, a method is developed to predict the wall temperature distribution for mist/steam flow within a heated tube.

Heating Factor *H*. Based on the measured wall temperature data, it is observed that the wall temperature distribution is greatly affected by the heat flux and the flow conditions. When the wall is ''severely'' heated, the measured wall temperature increases monotonically, indicating that the first two stages of the proposed three-stage heat transfer model are very short. If the wall is ''mildly'' heated, the wall temperature distribution clearly exhibits the ''up-down-up'' feature.

Table 1 Heating factor values for the current experimental cases

Heating Factor $H = q'' / (\mathrm{Re}\ m_r)$			
		Droplet mass ratio 1~2 %	Droplet mass ratio 5~6 %
Re = 35,000	20,000 W/m^2	57	11
	12,700 W/m^2	36	7
	8,000 W/m^2	23	4
Re = 20,000	14,500 W/m^2	36	14
	8,000 W/m^2	20	9
	2,600 W/m^2	7	5
Re = 10,000	8,200 W/m^2	82	16
	5,000 W/m^2	50	11
	3,000 W/m^2	30	6

It is thus necessary to differentiate the degree of wall heating in order to predict the wall temperature distribution. A heating factor, *H*, is then introduced here as:

$$H=\frac{q''}{\mathrm{Re}\ m_r} \tag{9}$$

where q'' is the heat flux (W/m^2), Re is the main steam flow Reynolds number, and m_r is the liquid droplet over steam mass ratio.

If H is smaller than a critical value H_{cr}, then the wall is considered to be mildly heated. If H is larger than the critical value H_{cr}, then the wall is severely heated. Based on the experimental results of this study, the critical heating factor H_{cr} is approximately at 25 (see Table 1). Note that H has a unit of W/m^2. The physical reasoning for using this heating factor is based on that (*a*) a certain amount of heat flux is required to maintain the wall superheated at a critical value (say 28°C) to keep the wall unwetted; and (*b*) since this critical value of wall superheat may vary from case to case and is not easy to control, for designers' convenience, H is used by inputting q'', Re, and m_r, which are the parameters easiest to obtain.

Prediction of Wall Temperature. Under a certain main steam Reynolds number, mist/steam mass ratio (m_r), and wall heat flux (q''), the following procedure is adopted to predict the wall temperature distribution:

- Calculate the heating factor H. If $H > H_{\mathrm{cr}} = 25$, then the wall is severely heated, and the wall temperature increases monotonically. In such a case, choose $h_{\mathrm{mist}} = (1\sim2)\ h_0$ (h_0 is the heat transfer coefficient for single-phase steam flow and is calculated from Eqs. (1) and (2)). T_w can be obtained from Eq. (8).
- If the heating factor $H < H_{\mathrm{cr}} = 25$, the wall temperature distribution is expected to have the ''up-down-up'' feature. In such a case, the wall temperature distribution can be predicted by employing the aforementioned deposition and entrainment correlations, combined with the proposed three-stage heat transfer model under the following assumptions for the heat transfer coefficient between the mist/steam flow and the heated test section:

$$h_{\mathrm{mist}} = (3\sim4)h_0 \quad \text{for stage 1}$$

$$h_{\mathrm{mist}} = (5\sim6)h_0 \quad \text{for stage 2}$$

$$h_{\mathrm{mist}} = (1\sim2)h_0 \quad \text{for stage 3.}$$

Specifically, the following steps are followed:

- Calculate the liquid film thickness δ_0 and the liquid film mass flow rate m_{lf0} at the exit of the unheated section as the inlet condition for the heated section based on the above discussed deposition/entrainment models. The effect of the thermal reaction force on droplet deposition is neglected. The results will be used as the inlet condition for the heated test section.

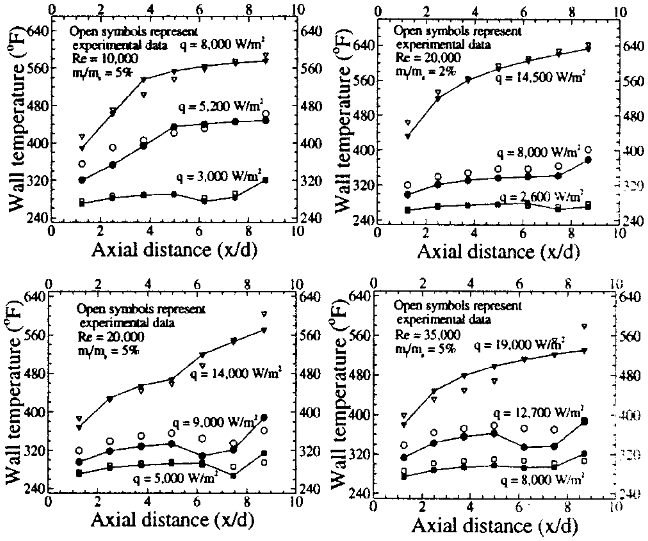

Fig. 16 Predicted wall temperature distributions by using the three-stage heat transfer model

- In the heated test section, the local change of the mass flow rate of the liquid film is calculated by integrating the following equation:

$$dm_{\mathrm{lf}} = \frac{4}{D_{\mathrm{ch}}}\left(D - E - \frac{q''}{h_{\mathrm{lg}}}\right)dz \tag{10}$$

with the initial condition of $z=0$, $m_{\mathrm{lf}} = m_{\mathrm{lf0}}$.

- Choose an appropriate heat transfer coefficient correlation based on the updated liquid film flow rate. The current adopted way is to simply choose, based on the measured wall temperature distribution, two critical values of m_{lf} from the calculated m_{lf} curve: $m_{\mathrm{lf,cr1}}$ and $m_{\mathrm{lf,cr2}}$. If $m_{\mathrm{lf}} < m_{\mathrm{lf,cr1}}$, then the heat transfer coefficient is taken as that for first-stage transition boiling, i.e., $h_{\mathrm{mist}} = (3\sim4)\ h_0$. If $m_{\mathrm{lf,cr1}} < m_{\mathrm{lf}} < m_{\mathrm{lf,cr2}}$, then the heat transfer coefficient is taken as that for second-stage unstable liquid evaporation with large droplet deposition, i.e., $h_{\mathrm{mist}} = (5\sim6)\ h_0$. If $m_{\mathrm{lf}} > m_{\mathrm{lf,cr2}}$, then the heat transfer coefficient is taken as that for third-stage pure mist cooling, i.e., $h_{\mathrm{mist}} = (1\sim2)\ h_0$.
- Calculate the local wall temperature using Eq. (8).

Figure 16 shows the predicted wall temperature distributions using the current three-stage heat transfer model compared with the measured wall temperature distributions. Generally, it can be seen that the predicted wall temperature agrees reasonably well in most cases with the measured wall temperatures.

It should be noted that in the current prediction method, the values of $m_{\mathrm{lf,cr1}}$ and $m_{\mathrm{lf,cr2}}$ are chosen based only on the present experimental results. Further systematic heat transfer studies on mist/steam flow are required in order to develop general correlations for $m_{\mathrm{lf,cr1}}$ and $m_{\mathrm{lf,cr2}}$.

Applicability of Present Study to Real Gas Turbines. An observation from the wall temperature measurements (Figs. 7, 8, and 9) is that the cooling enhancement at the highest heat flux value for each fixed Reynolds number is lower than 20 percent. This may raise the concern that as the heat flux reaches a very high value (such as those in the real gas turbine applications where the heat flux is about 20~40 times higher and the steam pressure is about 25 times higher than in the current experiment), very little cooling enhancement might be obtained by using mist/steam cooling. However, by closely examining the heat transfer measurements, it can be seen that the cooling enhancement at the highest heat flux does improve when the main steam Reynolds number increases. For example, the average cooling enhancement at $q''=8000\ \mathrm{W/m^2}$ increases from 20 percent at Re=10,000 to 50 percent at Re=20,000. Similar results can be observed for other cases. This indicates that in real gas turbine applications where the Reynolds number is 20~30 times higher than the current experimental value, the turbine blade could still be effectively cooled by mist/steam mixture. Besides, under real engine conditions, the steam density will increase approximately 14 times while the liquid density will decrease approximately 15 percent. Heavier steam could sustain more volume of the liquid droplets, so this would translate into an increase of approximately 16 times more liquid volume (or more droplets) in the high-pressure engine condition with the same amount of liquid mass and liquid droplet size distributions as in the laboratory. More droplets would imply better cooling. Other favorable changes at real engine conditions include 2.8 times better steam thermal conductivity and 10 percent better steam specific heat *Cp*. Unfavorable changes include 24 percent reduction of latent heat and 100 percent increase of steam dynamic viscosity. Future studies are required to verify the validity of mist/steam heat transfer enhancement in high-temperature and high-pressure conditions.

Conclusions and Recommendations

The following conclusions are made from this study:

- The design of the mixing chamber has a direct effect on the droplet size and distribution. Generally, the current mixing chamber serves as a filter where large droplets are trapped inside the mixing chamber.
- Droplet transportation is an important aspect of obtaining desirable droplet size and distribution. Droplets larger than 15 μm are mostly lost during the transportation, due to the deposition mechanisms.
- Usually, as the main steam flow increases, the mean droplet size measured at the test section also increases.
- As the heat flux increases, the local droplet mean diameter increases too. This indicates that inside the heated test section, smaller droplets are more susceptible to the wall heat transfer and evaporate quickly.
- Thermal nonequilibrium exists between the steam and the droplets within the test section.
- The heat transfer performance of steam can be significantly improved by adding mist into the main flow. An average enhancement of 100 percent with the highest heat transfer enhancement of 200 percent is achieved with 5 percent mist.
- When the test section is mildly heated, an interesting wall temperature distribution is observed: The wall temperature for the mist/steam flow increases first, then decreases, and finally increases again. A three-stage heat transfer model, which incorporates different heat transfer mechanisms for the internal mist/steam flow, has been proposed to explain this phenomenon.
- When the test section is severely heated, the wall temperature for the mist/steam flow increases monotonically. No three-stage heat transfer behavior is observed.
- The heat transfer enhancement increases as either the main flow rate or the droplet mass ratio increases.
- The heat transfer enhancement decreases as the wall heat flux increases.
- A heating factor is proposed to aid the design and prediction.

Acknowledgments

This research is sponsored by the U.S. Department of Energy under the contract DOE/AGTSR 95-01-SR-034 with Clemson University. This program is managed by Dr. Norman Holcombe at the Federal Energy Technology Center and by Dr. Dan Fant of Advanced Gas Turbine System Research at the South Carolina Energy Research and Development Center.

References

[1] Ranz, W. E., and Marshall, W. R., 1952, ''Evaporation From Drops, Part I and II,'' Chem. Eng. Prog., **48**, Nos. 3 and 4, pp. 141–146.

[2] Sparrow, E. M., Hallman, T. M., and Siegel, R., 1958, ''Turbulent Heat Transfer in the Thermal Entrance Region of a Pipe With Uniform Heat Flux,'' Appl. Sci. Res., **7**, Section A, pp. 47–52.

[3] Liu, B. Y. H., and Agarwal, J. K., 1974, ''Experimental Observation of Aerosol Deposition in Turbulent Flow,'' Aerosol Sci. **5**, pp. 145–155.

[4] Johansen, S. T., 1991, ''The Deposition of Particles on Vertical Walls,'' Int. J. Multiphase Flow, **17**, No. 3, pp. 355–376.

[5] Papavergos, P. G., and Hedley, A. B., 1984, ''Particle Deposition Behavior From Turbulent Flows,'' Chem. Eng. Res. Des., **62**, pp. 275–293.

[6] Young, J., and Leeming, A., 1997, ''A Theory of Particle Deposition in Turbulent Pipe Flow,'' J. Fluid Mech., **340**, pp. 129–159.

[7] Guo, T., 1998, ''Mist/Steam Cooling in a Heated Horizontal Tube,'' Ph.D Dissertation, Mechanical Engineering Department, Clemson University.

[8] Hewitt, G. F., and Govan, A. H., 1990, ''Phenomenological Modeling of Nonequilibrium Flows With Phase Change,'' Int. J. Heat Mass Transf., **33**, No. 2, pp. 229–242.

[9] Ganic, E. N., 1976, ''Post Critical Heat Flux Heat Transfer,'' Ph.D. Dissertation, MIT.

[10] Talbot, L. et al., 1980, ''Thermophoresis of Particles in a Heated Boundary Layer,'' J. Fluid Mech., **101**, pp. 737–758.

[11] Chen, J. C., and Costigan, G., 1992, ''Review of Post-Dryout Heat Transfer in Dispersed Two Phase Flow,'' *Post-Dryout Heat Transfer*, Hewitt, G. F., et al., eds., CRC Press Inc., FL, pp. 1–37.

[12] Tong L. S. and Tang, Y. S., 1997, *Boiling Heat Transfer and Two-Phase Flow*, Taylor & Francis, Washington, DC.

[13] Nirmalan, N. V., Weaver, J. A., and Hylton, L. D., 1998, ''An Experimental Study of Turbine Vane Heat Transfer With Water–Air Cooling,'' ASME J. Turbomach., **120**, No. 1, pp. 50–62.

Local Swirl Chamber Heat Transfer and Flow Structure at Different Reynolds Numbers

C. R. Hedlund[1]
Mem. ASME

P. M. Ligrani
Professor.
Mem. ASME

Convective Heat Transfer Laboratory,
Department of Mechanical Engineering,
University of Utah,
Salt Lake City, UT 84112

Local flow behavior and heat transfer results are presented from two swirl chambers, which model passages used to cool the leading edges of turbine blades in gas turbine engines. Flow results are obtained in an isothermal swirl chamber. Surface Nusselt number distributions are measured in a second swirl chamber (with a constant wall heat flux boundary condition) using infrared thermography in conjunction with thermocouples, energy balances, and in situ calibration procedures. In both cases, Reynolds numbers Re based on inlet duct characteristics range from 6000 to about 20,000. Bulk helical flow is produced in each chamber by two inlets, which are tangent to the swirl chamber circumference. Important changes to local and globally averaged surface Nusselt numbers, instantaneous flow structure from flow visualizations, and distributions of static pressure, total pressure, and circumferential velocity are observed throughout the swirl chambers as the Reynolds number increases. Of particular importance are increases of local surface Nusselt numbers (as well as ones globally averaged over the entire swirl chamber surface) with increasing Reynolds number. These are tied to increased advection, as well as important changes to vortex characteristics near the concave surfaces of the swirl chambers. Higher Re also give larger axial components of velocity, and increased turning of the flow from each inlet, which gives Görtler vortex pair trajectories greater skewness as they are advected downstream of each inlet. [S0889-504X(00)00502-X]

Introduction

Improving the efficiencies of gas turbine engines requires the use of higher turbine inlet temperatures, which in turn requires better schemes for cooling turbine components located just downstream of the combustion chamber. Recent years have seen increased attention devoted to both internal cooling schemes, as well as external schemes (such as film cooling) for this purpose. Internal schemes are advantageous since they often require smaller fractions of compressor air, and because they do not produce the aerodynamic penalties associated with film cooling. In fact, such methods are sometimes's used to reduce or eliminate the need to employ film cooling. However, the design of internal cooling methods must consider internal pressure drop penalties as well as the augmentation of surface heat transfer coefficients. This is the motivation of the present investigation. Here, heat transfer and flow structure are investigated in a swirl chamber that models the passages used to cool the leading edges of turbine airfoils employed in gas turbine engines used for power generation.

The first use of swirl in tube flows to augment surface heat transfer rates relative to flows without swirl is described by Kreith and Margolis [1]. Following that study, a variety of devices and geometries were developed to induce swirl in internal flows. Date [2] and Hong and Bergles [3] employ twisted tape inserts. Sampers et al. [4], Li and Tomita [5], and Kok et al. [6] use rotating vanes, blades, propellers, or honeycombs near tube entrances in adiabatic flows. Glezer et al. [7–9], Hedlund [10], Hedlund et al. [11], Moon et al. [12], and Khalatov and Zagumennov [13] employ tangential jets from wall slots or ducts to induce large-scale swirling in internal tube flows. Other recent experimental investigations examine fluid mechanics in swirl chambers with single-phase flow, wall injection, and no heat transfer [14–18. Gambill and Bundy [19], Bergles [20], Razgaitis and Holman [21], Papadopouios et al. [22], and Hedlund [10] provide surveys of recent swirl flow investigations.

The present study is different from other recent swirl chamber investigations (i.e., [11]) because spatially resolved distributions of local Nusselt numbers, instantaneous flow structure, and distributions of static pressure, total pressure, and circumferential velocity are provided as the Reynolds number varies. Emphasis is placed on *local* flow structure. Because such data are given for different Reynolds numbers, heat transfer and flow characteristics can be extrapolated to Reynolds numbers higher than those investigated. As such, the present study extends the results described by Hedlund et al. [11], who consider *local* flow structure at only one Reynolds number. Here, local heat transfer and flow structure are presented for locations throughout the swirl chamber at three different Reynolds numbers (based on inlet duct characteristics) of about 6000, 12,000, and 18,000. Instantaneous flow structure is described from flow visualizations conducted at Reynolds numbers ranging from 3000 to 19,000. Particular attention is devoted to characteristics near swirl chamber inlets, since this is where Görtler vortex pairs, shear layer vortices, and thermal boundary layers begin to develop. Here, important changes occur as the Reynolds number varies, which affect flow behavior and characteristics throughout the swirl chamber.

Experimental Apparatus and Procedures

Swirl Chamber for Heat Transfer Measurements. A schematic of the swirl chamber used for heat transfer measurements is shown in Fig. 1(*a*). The coordinate system is shown in Fig. 1(*b*). The air used within the swirl chamber is circulated in a closed-loop by a Dayton 5CO87-80CFM induced draft blower, which forces air through the facility, starting with a series of three large 1 m square plenums. A Bonneville crossflow heat exchanger is located between two of these plenums, and is cooled with liquid nitrogen at flow rate appropriate to give the desired air temperature at the exit of the heat exchanger. As the air exits the heat exchanger, it enters the third plenum, from which the air passes

---

[1] Present address: GE Corporate Research and Development, ES-119, Schenectady, NY 12309.

Contributed by the International Gas Turbine Institute and presented at the 44th International Gas Turbine and Aeroengine Congress and Exhibition, Indianapolis, Indiana, June 7–10, 1999. Manuscript received by the International Gas Turbine Institute February 1999. Paper No. 99-GT-164. Review Chair: D. C. Wisler.

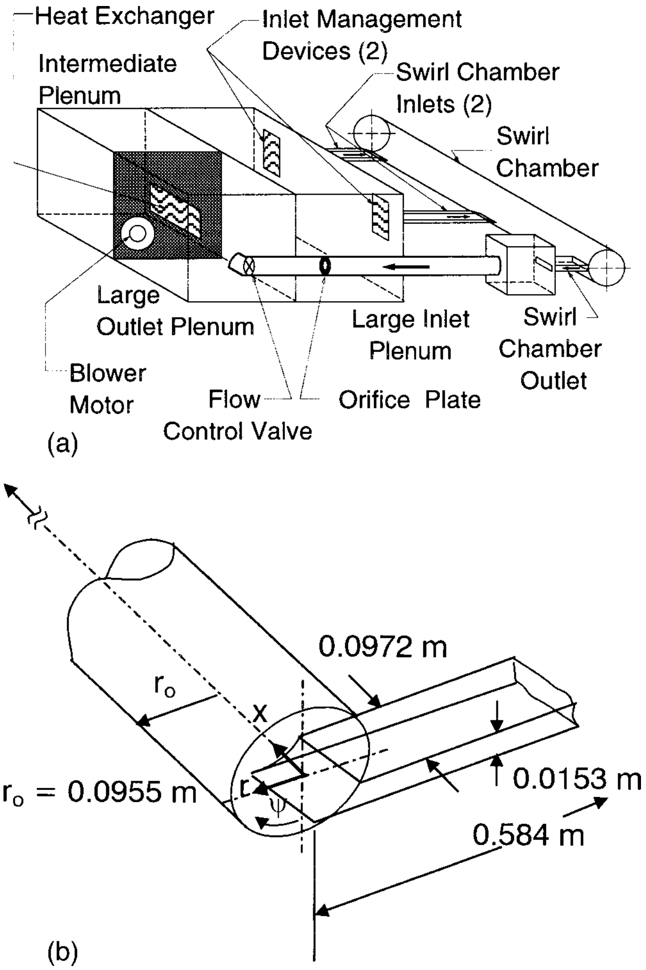

Fig. 1 Swirl chamber used for heat transfer measurements: (*a*) schematic diagram; (*b*) coordinate system

into one of two rectangular bell mouth inlets, each followed by a honeycomb, two screens, and a two-dimensional 10:1 contraction ratio nozzle. Each of the two nozzles leads to a rectangular cross-sectional inlet duct 21.7 hydraulic diameters in length, connected to the principal swirl chamber cylinder so that one surface is tangent to the cylinder inner circumference. Inlet duct 1 extends axially from $x/r_0=0$ to $x/r_0=1$, and inlet duct 2 extends axially from $x/r_0=7$ to $x/r_0=8$. Both inlet ducts are tangent to the swirl chamber at $\psi=0$ deg. Each $0.0972\,\mathrm{m}\times0.0153\,\mathrm{m}$ inlet duct is 0.584 m long, with a 0.0264 m hydraulic diameter. The pressure used to supply the intakes of the two inlets (at laboratory ambient pressure) is kept the same, just as in the application. Consequently, the flow rates in the two inlets depend upon the static pressure variation in the main swirl chamber cylinder just downstream of each inlet duct.

The cylinder length is 1.43 m, and its inner and outer radii are 0.0955 m and 0.1015 m, respectively. Because the ratio of the radial extent of the inlet duct to the radius of curvature of the swirl chamber is 0.160, the curvature near cylinder walls is considered to be ''strong.'' With this arrangement, the flow has important axial and circumferential components of velocity, and the overall flow pattern through the cylinder is similar to a helix. The exit duct from the cylinder is oriented in a radial/axial plane near the end of the swirl chamber cylinder at a location along the cylinder farthest from the inlet ducts. This 0.195-m-long exit duct is then connected to a 0.305 m square plenum, which is followed by a pipe containing a valve and an orifice plate, used to regulate and measure the air flow rate, respectively. This pipe is then connected to the same large plenum adjoining the blower inlet.

All exterior and many interior surfaces of the facility are insulated with 2 to 3 layers of 2.54 cm thick, Elastomer Products black neoprene foam insulation ($k=0.038\,\mathrm{W/m\,K}$) to minimize heat losses. Calibrated copper-constantan thermocouples are located between the three layers of insulation located outside of the main cylinder of the swirl chamber to determine conduction losses. Between the first layer and the 0.635-cm-thick acrylic cylinder of the chamber are 11 custom-made Electrofilm etched-foil heaters (each encapsulated between two thin layers of Kapton) to provide a constant heat flux boundary condition on the concave test surface. The acrylic cylinder contains 30 copper-constantan thermocouples, and its inner surface is adjacent to the air stream. Each of these thermocouples is located 0.0508 cm just below this surface to provide measurements of local surface temperatures, after correction for thermal contact resistance and temperature drop through the 0.0508 cm thickness of acrylic. Contact resistance and temperature drop through the wall are determined experimentally (in a separate set of tests) from calibrated thermocouple junction temperatures as the surface temperature is measured simultaneously using calibrated liquid crystals. The temperature difference is then correlated as a function of surface heat flux. Acrylic is chosen because of its low thermal conductivity ($k=0.16\,\mathrm{W/m\,K}$ at 20°C) to minimize axial and circumferential conduction along the test surface, and thus minimize ''smearing'' of spatially varying temperature gradients along the test surface. Acrylic also works well for infrared imaging because its surface emissivity ranges from 0.60 to 0.65. The power to each foil heater is controlled and regulated by a separate variac power supply. Energy balances, performed on each heated segment of the swirl chamber cylinder, then allow determination of local magnitudes of the convective heat flux.

The mixed-mean temperature of the air entering the swirl chamber is measured using five calibrated copper-constantan thermocouples spread across the cross section of each inlet duct, just downstream of each nozzle. These locations are chosen for these measurements because temperature and velocity profiles are uniform across the duct, allowing simple determination of local mixed-mean temperatures. Mixed-mean temperature at each entrance to the cylinder is then determined after accounting for conduction losses through each inlet duct. All measurements are obtained when the swirl chamber is at steady state, achieved when each of the temperatures from the 30 thermocouples (on the swirl chamber surface) vary by less than 0.1°C over a 10 minute period.

Local Nusselt Number Measurement. Spatially resolved temperature distributions along the swirl chamber concave surface are determined using infrared imaging in conjunction with thermocouples, energy balances, digital image processing, and in situ calibration procedures. To accomplish this, the infrared radiation emitted by the heated interior surface of the swirl chamber is captured using a VideoTherm 340 Infrared Imaging Camera, which operates at infrared wavelengths from 8 μm to 14 μm. Temperatures, measured using the 30 calibrated, copper-constantan thermocouples distributed along the swirl chamber surface adjacent to the flow, are used to perform the in situ calibrations simultaneously as the radiation contours from surface temperature variations are recorded.

This is accomplished as the camera views the test surface through a custom-made, cylindrical zinc-selenide window (which transmits infrared wave lengths between 6 and 17 μm). Reflection and radiation from surrounding laboratory sources are minimized using an opaque shield which covers the camera lens and the zinc selenide window. Frost build-up on the outside of the window is eliminated using a small heated air stream. The window is located on a segment of the swirl chamber, which is either rotated or relocated axially so that the camera can view different portions of the interior surface of the swirl chamber. At least two, and as many as five, thermocouple junction locations are present in any field viewed by the camera. The exact spatial locations and pixel locations of these thermocouple junctions and the coordinates of a 12.7 cm×12.7 cm field of view are known from calibration maps obtained prior to measurements. During this procedure, the camera is focused, and rigidly mounted and oriented relative to the test surface in the same way as when radiation contours are recorded.

With these data, gray scale values at pixel locations within video taped images from the infrared imaging camera are readily converted to temperatures. Because such calibration data depend strongly on camera adjustment, the same brightness, contrast, and aperture camera settings are used to obtain the experimental data. The in situ calibration approach rigorously and accurately accounts for these variations.

Images from the infrared camera are recorded as 8-bit gray scale images on commercial videotape using a Panasonic AG-1960 video recorder. Images are then digitized using NIH Image v1.60 software, operated on a Power Macintosh 7500 computer. Subsequent software is used to perform coordinate transformations to correct for nonrectangular, ''stretched,'' or distorted recorded images because of camera perspective or because camera lens orientation is not normal to the curved target surface. This software also converts each of 256 possible gray scale values to temperature at each pixel location using calibration data, and then determines values of local Nusselt numbers. Thermal conductivity in the Nusselt number is based on the average of the local wall temperature and the temperature of the air at the nearest upstream inlet. Contour plots of local surface temperature and Nusselt number (in ''unrolled'' planar, Cartesian coordinates) are prepared using DeltaGraph v4.0 software. Each individual image covers a 300 pixel by 300 pixel area. Data from 42 of these images are combined to produce the data presented in Fig. 9. Hedlund [10] and Hedlund et al. [11] provide additional details.

Total Pressure, Static Pressure, and Mean Velocity Components. A United Sensor DC-250-24-CD five-hole pressure probe, and a five-hole pressure probe manufactured at the University of Utah, each with a conical-shaped sensing head of 6.35 mm diameter, are used to obtain time-averaged surveys of total pressure, static pressure, and the three mean velocity components. Procedures for calibration and measurement are described by Ligrani et al. [23,24]. To obtain the surveys, the probe is mounted on an automated two-dimensional traverse, and inserted into the chamber through slots lined with foam to prevent air leakage. Outputs of the five-hole probe are connected to five Validyne DP103-06 pressure transducers, which measure differential pressures up to 2.5 mm of water. Signals from each transducer are then processed using Celesco CD10D Carrier-Demodulators. Voltages from the Carrier-Demodulators are acquired using Hewlett-Packard 44422A data acquisition cards installed in a Hewlett-Packard 3497A data acquisition control unit. This control unit, the Superior Electric type M092-FD310 Mitas stepping motors on the two-dimensional traverse, a Superior Electric Modulynx Mitas type PMS085-C2AR controller, and a Superior Electric Modulynx Mitas type PMS085-D050 motor drive are controlled by a Hewlett-Packard 362 Series computer. Contour plots of measured quantities are generated using a polynomial interpolating technique (within DeltaGraph software) between data points. In each survey plane, data points are spaced either 0.51 cm or 1.27 cm apart. Hedlund [10] and Hedlund et al. [11] provide additional details, including descriptions of the second isothermal swirl chamber employed for these measurements as well as flow visualization.

Flow Visualization. The smoke injection for flow visualization is used to identify vortex structures. Smoke from burning mesquite wood in a specially designed smoke generator is injected into the facility one of two ways: (*i*) into the inlet bell mouth, prior to conditioning the flow, using a cylindrical manifold with a row of small tubes which produce an array of quiescent, laminar jets of smoke, or (*ii*) through the cylinder wall through one of the slots lined with foam. In either case, the smoke forms into a single thin layer next to the concave surface of the swirl chamber cylinder as it enters the flow. The smoke in this layer is neutrally buoyant in laboratory air, very dense, and has fairly uniform particle size distribution. As the smoke is advected downstream, the secondary flows that accompany Görtler vortex development cause the smoke to be rearranged in patterns that show the locations and distributions of the Görtler vortices. Smoke patterns are illuminated at different Re in one axial–radial plane using thin planes (or sheets) of light. Images are recorded using a Dage-MTI CCD72 camera and control box with a Computar, Inc., 12.5 mm, F1.8 lens, connected to a Panasonic AG-1960 type four-head, multiplex video cassette recorder. Images recorded on videotape (taken individually or in sequence) are then processed and digitized using Apple Video processing and capture software employed on a Macintosh Power PC computer. Images are then enhanced, further processed, and arranged for printing using the same computer. Additional details are provided by Hedlund [10].

Uncertainty Estimates

Uncertainty estimates are based on 95 percent confidence levels, and determined using procedures described by Moffat [25]. Uncertainty of temperatures measured with thermocouples is ±0.15°C. Spatial and temperature resolutions achieved with the infrared imaging are 0.8 mm and 0.8°C, respectively. This magnitude of temperature resolution is due to uncertainty in determining the exact locations of thermocouples with respect to pixel values used for the in situ calibration. Nusselt number uncertainty is then about ±9.4, or ±7.8 percent for a nominal Nusselt number value of 120. Reynolds number uncertainty is ±200, or about ±1.7 percent for Re equal to 12,000. The uncertainties of total pressure and static pressure (relative to atmospheric pressure) in Pa are ±0.15 and ±0.08, respectively. The uncertainty for the circumferential velocity is ±0.03 m/s. In percent, total pressure, static pressure, and circumferential velocity uncertainties are about ±4.0 (3.75 Pa), ±4.0 (2.00 Pa), and ±2.5 (1.2 m/s), respectively (where typical nominal values are given in parentheses).

Experimental Results and Discussion

Flow Visualization Results. Flow visualization results are presented in Fig. 2, which show the effects of varying Reynolds number in a single axial-radial plane within the swirl chamber. Figure 3 shows the imaging location at $10.0 \leqslant x/r_0 \leqslant 11.2$ and $\psi = 130$ deg. In Fig. 2, the swirl chamber interior surface (at $r/r_0 = 1$) appears as a horizontal white line near the bottom of each image. The circumferential component of velocity is oriented out of the page. The axial dimension x increases from the right edge of each image to the left edge. The radial coordinate ranges from $r/r_0 = 0.7$ at the top of each image to $r/r_0 = 1.0$ at the bottom.

As Reynolds number increases in Fig. 2, the number of Görtler vortex pairs across the span of each image generally tends to increase, and sizes of Görtler vortex pairs generally tend to decrease. The Görtler pairs also become more diffuse and distorted as Re increases both because the smoke becomes more diffuse and because the flow phenomena become more unsteady. At the lower range of Reynolds numbers, Re=3150–8290, two to four Görtler vortex pairs appear across the span of each visualization image. These Görtler pairs remain in approximately the same axial locations as Re increases to 9390–10,370. For higher Re from 9390 to 18,520, numerous smaller Görtler vortices are evident. Both the smaller, more active Görtler pairs and the larger, less active vortex pairs are evident in the swirl chamber at Re=9390–18,520. Interactions between the large and small vortex pairs occur as the vortices split, merge, appear, and disappear. The interactions between the large Görtler vortex pairs and the smaller, more active Görtler vortices become more frequent and intense as Re increases. At the swirl chamber location visualized in Fig. 2, distor-

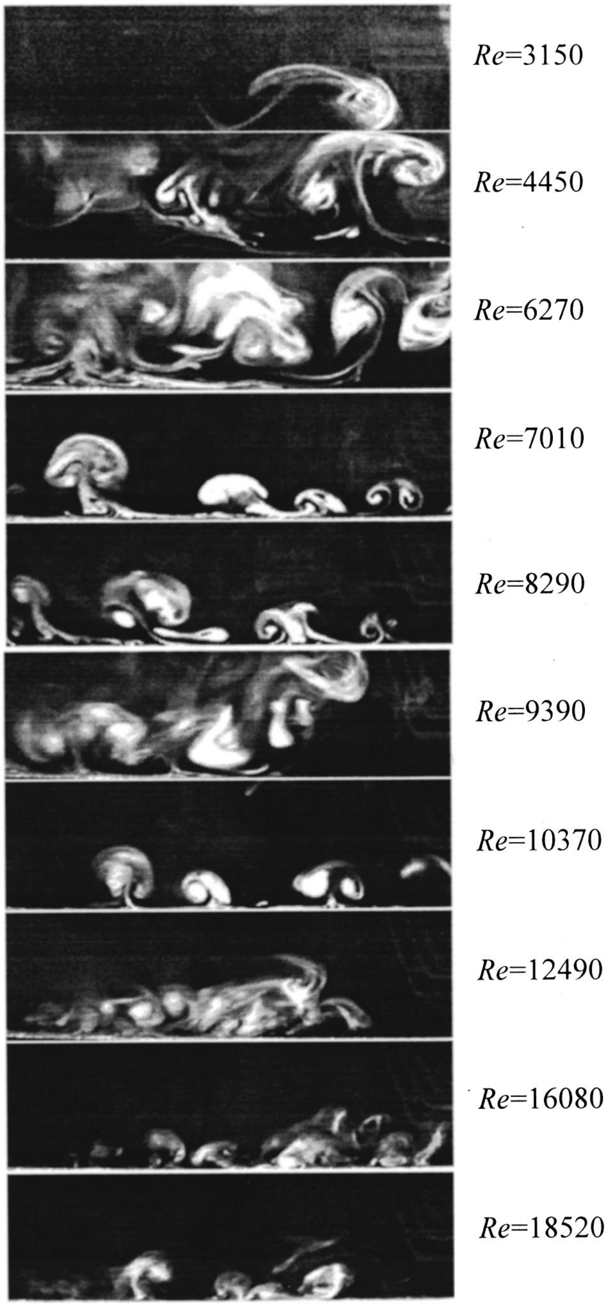

Fig. 2 Visualizations of flow behavior downstream of inlet 2, at $10.0 \leqslant x/r_0 \leqslant 11.2$ and $\psi = 130$ deg

tions of the Görtler vortices, as well as the size of the Görtler vortices, are much larger than observed near the swirl chamber inlets [10]. At Re from 3150 to 6270, individual vortex pairs often fill the entire radial extent of the image in Fig. 2, thus extending over r/r_0 as large as 0.30.

Variations of Static Pressure, Total Pressure, and Circumferential Velocity. Figures 4–6 present local distributions of time-averaged static pressure $P_s - P_a$, total pressure $P_t - P_a$, and circumferential velocity $\overline{u_\psi}$, respectively, for Reynolds numbers of 18,000, 12,000, and 6000. Corresponding $\overline{V}$ are about 12.5 m/s, 8.3 m/s, and 4.2 m/s, respectively. Corresponding $\overline{U}$ (downstream of the second inlet) are then 1.30 m/s, 0.86 m/s, and 0.43 m/s, respectively. Data are thus arranged to illustrate the changes to flow structure that result as the Reynolds number is varied. All data are presented for axial-radial planes at $\psi = 90$ deg for $0 < r/r_0 < 1$. Data at each Re in Figs. 4–6 are obtained throughout seven axial-radial plane segments over $0.15 \leqslant x/r_0 \leqslant 14.65$. Even though no data are provided in the gaps between these adjacent segments, the data within all of the surveyed regions provide a good picture of flow behavior throughout the swirl chamber at $\psi = 90$ deg.

Figures 4(*a–c*) show static pressure distributions for all three Re, which are highest with the largest spatial variations near inlet 1 at $0.0 < x/r_0 < 1$ and $0.8 < r/r_0 < 1.0$, and near inlet 2, at $7.0 < x/r_0 < 8.0$ and $0.8 < r/r_0 < 1.0$. Static pressures then generally decrease with increasing x/r_0 and decreasing r/r_0 as one moves away from each inlet. Larger variations of static pressure are also evident near $14 < x/r_0 < 15$ as flow turns to exit the swirl chamber through the radially oriented outlet. Spatial variations in $P_s - P_a$ are larger at Re=18,000 than at Re of 12,000 or 6000, when compared at the same location.

Figures 5 and 6 show that variations of total pressure $P_t - P_a$ and circumferential velocity $\overline{u_\psi}$ are much higher near inlets 1 and 2 than at other locations in the swirl chamber. This is due to the jets from the swirl chamber inlets and secondary flows, particularly Görtler vortex pairs (such as the ones shown in Fig. 2), which move lower pressure, slower fluid from the region near the swirl chamber wall at $r/r_0 = 1$ to locations away from the wall. Spatial variations of $P_t - P_a$ and $\overline{u_\psi}$ generally tend to increase as Re increases in Figs. 5 and 6, when compared at the same location. The convoluted contour lines located away from the inlets in Figs. 4(*c*), 5(*c*), and 6(*c*) indicate very small variations of measured quantities with spatial location.

Figure 7 shows static pressure, total pressure, and circumferential velocity data from Figs. 4–6, after each quantity is radially averaged over $0 < r/r_0 < 1$. The data are arranged to show variations of these quantities along the length of the swirl chamber as the Reynolds number changes. Static pressure and total pressure are non-dimensionalized using $\rho \overline{U}^2/2$ in Figs. 7(*a*) and 7(*b*). Circumferential velocity $\overline{u_\psi}$ is nondimensionalized using $\overline{U}$ in Fig. 7(*c*).

In Figs. 7(*a*) and 7(*b*), nondimensional static pressure and nondimensional total pressure each collapse onto a single curve for Re of 12,000 and 18,000 when the swirl chamber flow is fully

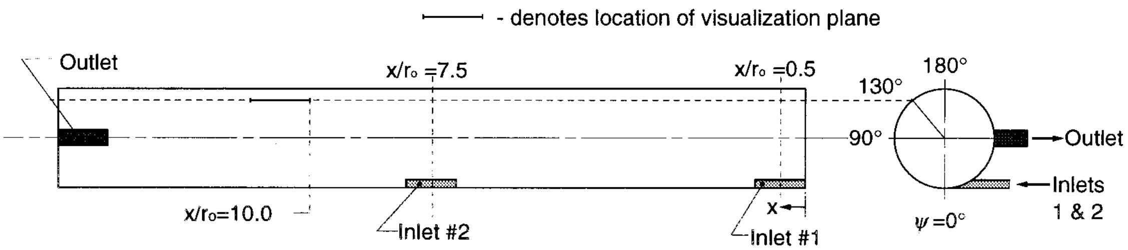

Fig. 3 Schematic of swirl chamber geometry showing flow visualization location at $10.0 \leqslant x/r_0 \leqslant 11.2$ and $\psi = 130$ deg

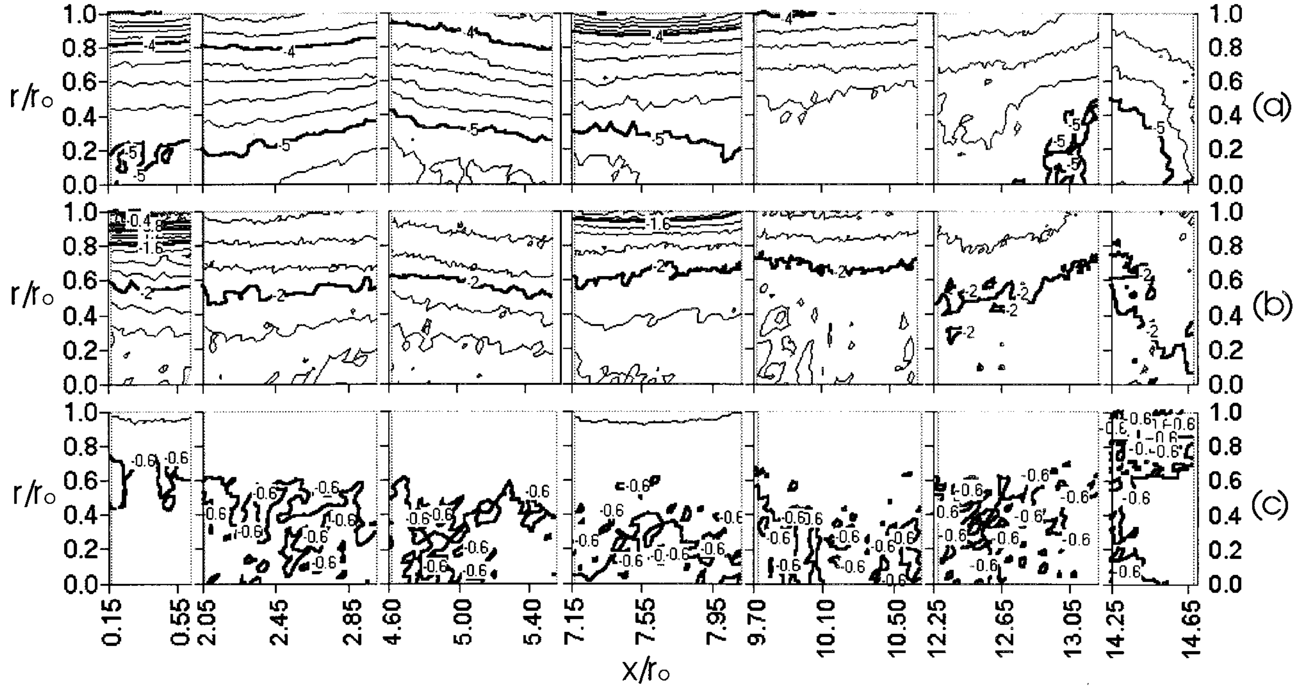

Fig. 4 Distribution of static pressure P_t-P_a (Pa) at $\psi=90$ deg for Re of: (*a*) 18,000, (*b*) 12,000, and (*c*) 6000; spacings between adjacent contour lines: (*a*) 0.2 Pa, (*b*) 0.1 Pa, and (*c*) 0.1 Pa

turbulent. Radially averaged nondimensional static pressures at these Re are relatively constant versus axial location, except near the exit duct at $14<x/r_0<15$. Radially averaged nondimensional total pressures for Re of 12,000 and 18,000 are highest near inlet 1, and then decrease as x/r_0 increases, until the region near inlet 2, where $P_t-P_a/(\rho\overline{U}^2/2)$ increases slightly. Total pressures at these Re then decrease from inlet 2 to the exit. Figures 7(*a*) and 7(*b*) also show nondimensional static and total pressures at Re $=6000$ which are lower (with larger streamwise variations) than values measured at higher Re, when compared at the same x/r_0.

The profiles of radially averaged nondimensional circumferential velocity $\overline{u_\psi}/\overline{U}$ in Fig. 7(*c*) generally increase with increasing Re, when compared at the same x/r_0. The largest changes with x/r_0 are present when Re$=6000$, rather than when Re is 12,000 or

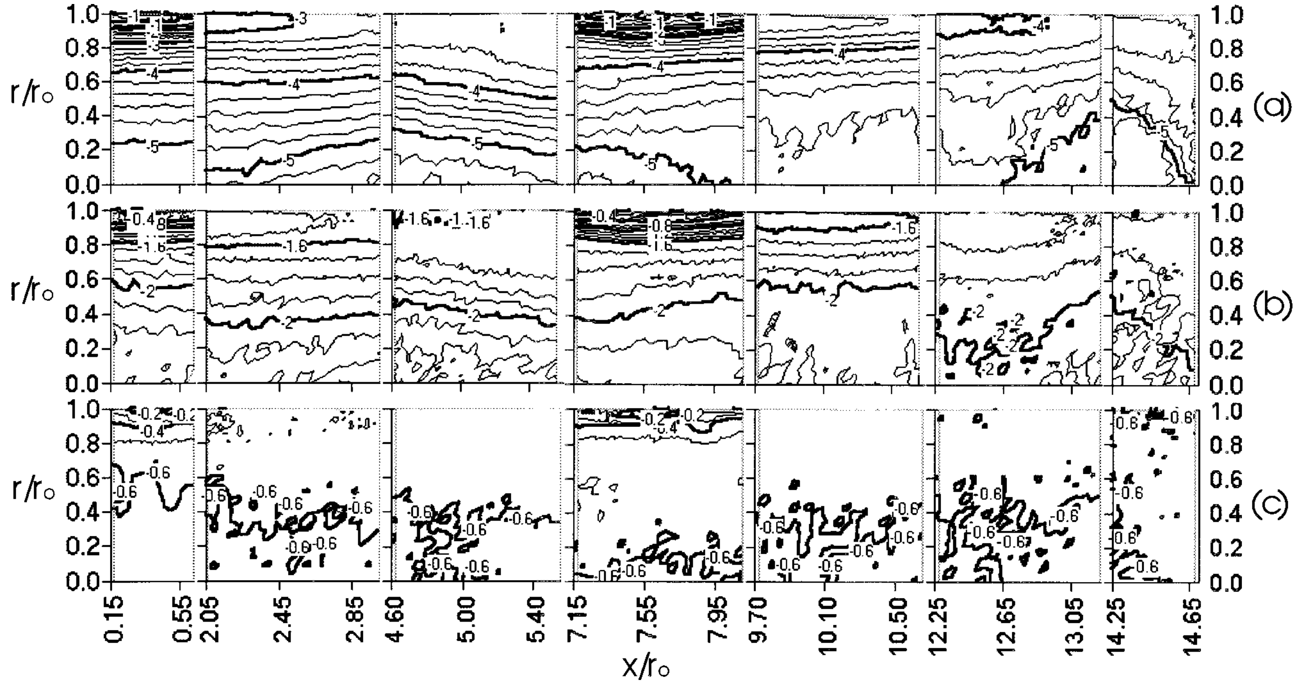

Fig. 5 Distributions of total pressure P_t-P_a (Pa) at $\psi=90$ deg for Re of (*a*) 18,000, (*b*) 12,000, and (*c*) 6000; spacings between adjacent contour lines: (*a*) 0.2 Pa, (*b*) 0.1 Pa, and (*c*) 0.1 Pa

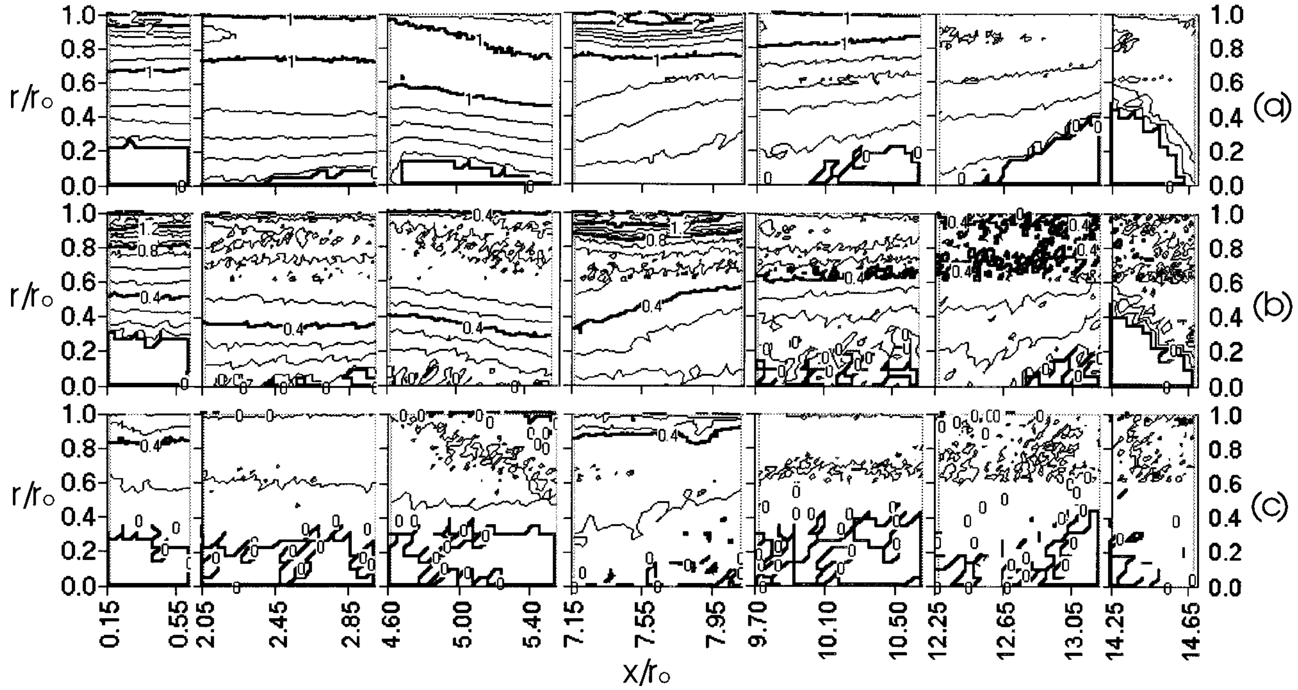

Fig. 6 Distribution of circumferential component of velocity u_ψ (m/s) at $\psi=90$ deg for Re of: (*a*) 18,000, (*b*) 12,000, and (*c*) 6000; spacings between adjacent contour lines: (*a*) 0.2 m/s, (*b*) 0.1 m/s, and (*c*) 0.2 m/s

18,000. Such changes with Reynolds number are due to different relative influences of inertial and viscous effects in the swirl chamber.

Figure 8 shows profiles of static pressure, total pressure, and circumferential velocity (normalized in the same way as in Fig. 7), as they vary with r/r_0, arranged to illustrate the influences of Reynolds number. Each symbol represents data from Figs. 4–6, which have been averaged over small axial regions near inlets 1 and 2. Closed symbols represent data averaged over $0.15 \leq x/r_0 \leq 0.65$ (near inlet 1), and open symbols represent data averaged over $7.15 \leq x/r_0 \leq 8.15$ (near inlet 2).

Regardless of the averaging region or Reynolds number, each profile in Fig. 8 is highest near the swirl chamber wall at $r/r_0 = 1$, then decreases as r/r_0 decreases. The profiles of total pressure and circumferential velocity also show local maxima at or near $r/r_0 = 0.95$. Such characteristics are due to the relatively high momentum fluid in the wall jets which emerge from each inlet. Profiles of static pressure and total pressure, measured at Re $=6000$, are lower than profiles measured at higher Re, when compared at the same r/r_0. Normalized circumferential velocity data show a similar trend when $r/r_0 > 0.6$. Most of the static pressure, total pressure, and circumferential velocity profiles averaged just downstream of inlet 1 (over $0.15 \leq x/r_0 \leq 0.65$) are similar to the profiles averaged just downstream of inlet 2 (over $7.15 \leq x/r_0 \leq 8.15$). The most important exception occurs in the normalized circumferential velocity data when $r/r_0 < 0.6$. For those experimental conditions, velocities measured downstream of inlet 2 are significantly higher than velocities measured downstream of inlet 1. This indicates increased large-scale rotation of fluid throughout the swirl chamber, especially at locations closer to the centerline axis, as the flow advects downstream in the positive x/r_0 direction.

Local Nusselt Number Behavior Throughout the Swirl Chamber. Figure 9 shows local Nusselt numbers as they vary along the entire interior concave surface of the swirl chamber (in "unrolled," Cartesian coordinates) for Re=6100. These data are given to illustrate local Nusselt number variations at one Reynolds

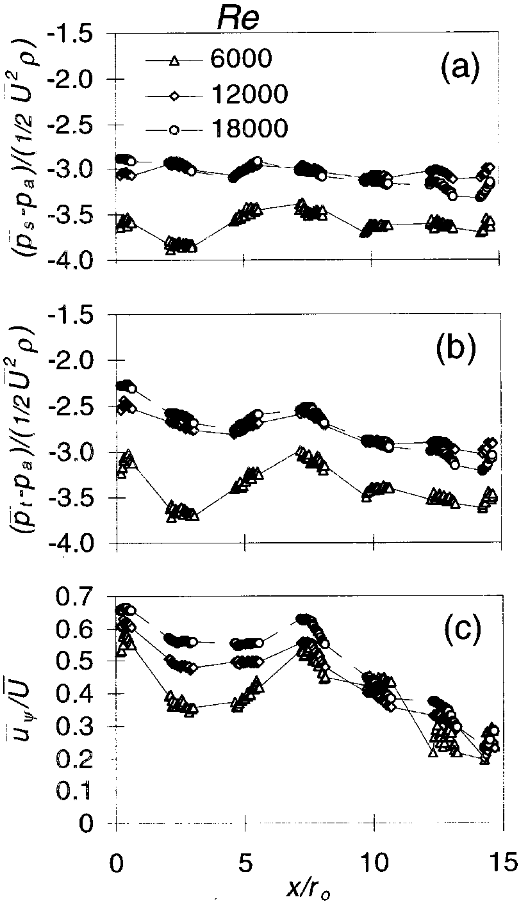

Fig. 7 Nondimensional radially averaged profiles of: (*a*) static pressure, (*b*) total pressure, and (*c*) circumferential velocity, for $\psi=90$ deg and Re of 6000, 12,000, and 18,000. Data are averaged over $0.0 \leq r/r_0 \leq 1.0$.

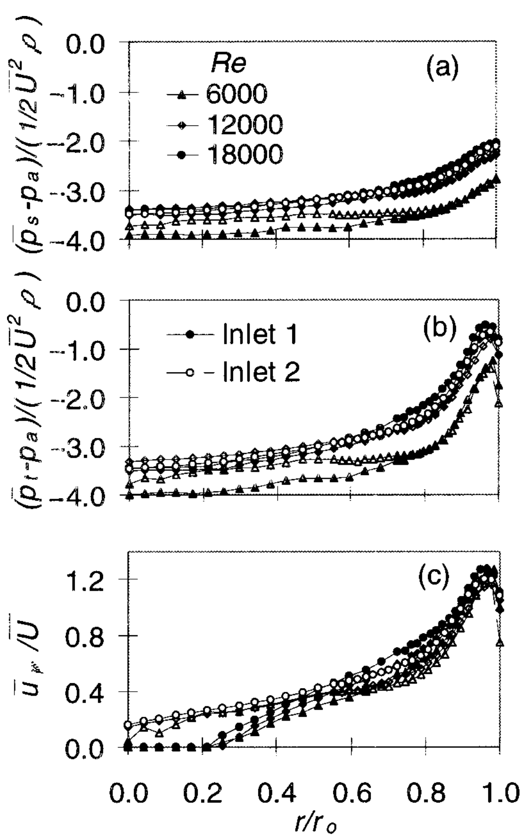

Fig. 8 Nondimensional axially averaged profiles of: (*a*) static pressure, (*b*) total pressure, and (*c*) circumferential velocity, for $\psi=90$ deg and Re of 6000, 12,000, and 18,000. Solid data points represent data averaged over $0.15\leq r/r_0\leq 0.65$, and open data points represent data averaged over $7.15\leq x/r_0\leq 8.15$.

number. Three different shaded regions denote surface areas where no data are provided. Light gray regions at $x/r_0=0-1$ and $x/r_0=7-8$ correspond to inlet duct openings. White regions at $x/r_0=0-1$ and $x/r_0=7-8$ indicate locations of unused tangential ducts, each fitted with a contoured plug, which matches the interior curved surface of the swirl chamber. The dark gray region at $x/r_0=14-15$ corresponds to the radial exit duct of the swirl chamber.

The largest Nusselt number variations, as well as the largest Nu magnitudes in Fig. 9, are observed around the entire swirl chamber circumference from $\psi=0$ deg to $\psi=360$ deg, near the two tangential inlets at $x/r_0=0-1$, and $x/r_0=7-8$. As x/r_0 increases to become greater than 1.5, Nu values initially decrease and then become more uniform in the circumferential direction. Nusselt numbers are then nearly constant in both circumferential and axial directions for $2.8<x/r_0<6.0$ and $0\text{ deg}<\psi<360\text{ deg}$. At $x/r_0=6.0$, influences of inlet 2 begin to affect the flow, and Nu values increase as x/r_0 increases from 6.0 to 7.0. Surface Nusselt numbers subsequently begin to vary in both axial and circumferential directions at slightly larger x/r_0, near inlet 2. As x/r_0 becomes greater than 8.4–9.0, the flow leaves the vicinity of inlet 2, and Nusselt numbers become more axially and circumferentially uniform.

Local Nusselt Number Behavior Near Swirl Chamber Inlets. Local Nusselt number distributions and corresponding infrared images, measured just downstream of inlets 1 and 2, are presented in Figs. 10 and 11, respectively. To illustrate the effects of changing Reynolds number, data are given for Re of 6100, 12,150, and 19,200, which correspond to Re_D of 2270, 4510, and 7130, respectively. The data in Figs. 10 and 11 thus provide amplified views of portions of plots such as the one shown in Fig. 9. Each contour plot in Fig. 10 extends circumferentially from $\psi=0$ deg, the point at which each inlet duct is tangent to the swirl chamber, to $\psi=80$ deg, and axially over $0<x/r_0<1.1$. In Fig. 11, the same ψ range is used, however, x/r_0 ranges from 6.8 to 8.2. The experimental arrangement used to obtain the data presented in Figs. 10 and 11 is shown in Fig. 12.

A common feature of the data for each Re in Figs. 10 and 11 is the presence of a region of locally lower Nu (which corresponds to a lighter patch in each infrared image), immediately downstream of each inlet, shown in the bottom portion of each figure. These oval regions of relatively low Nu are seen in approximately the same locations for each Re. These Nusselt numbers are lower than ones just downstream because Görtler vortices do not begin to develop until $\psi>22-40$ deg.

Curved, lighter colored "stripes" are also evident in Figs. 10 and 11. Lighter-colored regions in each infrared image correspond to higher surface temperatures and lower Nu, whereas darker re-

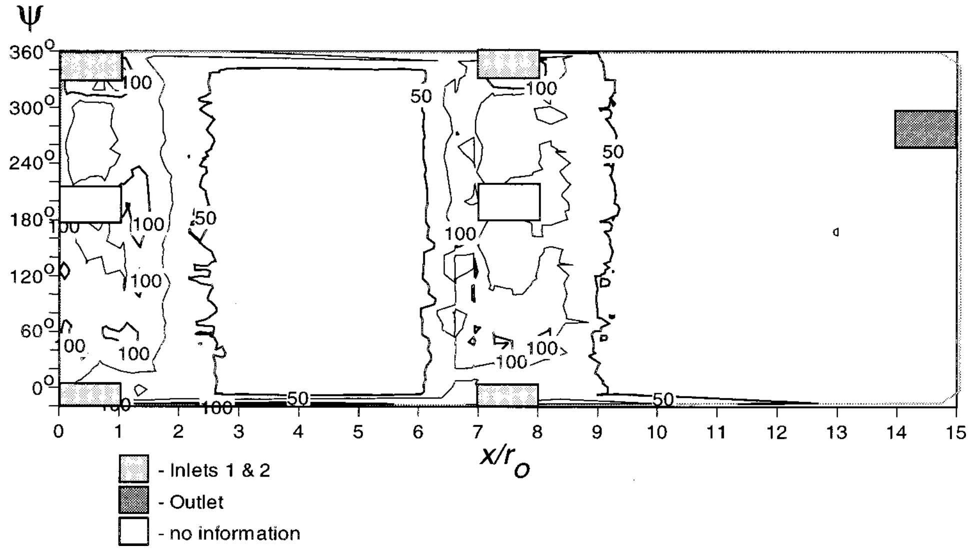

Fig. 9 Local Nusselt number distribution over the entire interior surface of swirl chamber for Re of 6100 and $T_i/T_w=0.95$

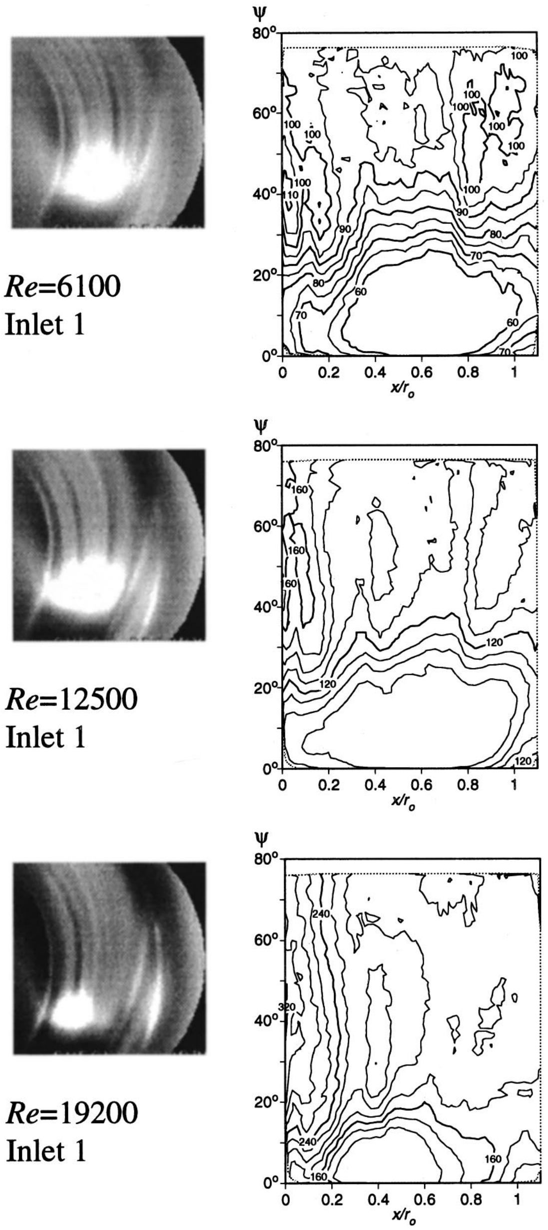

Fig. 10 Local Nusselt number distributions near inlet 1 for Re of 6100, 12,500, and 19,200

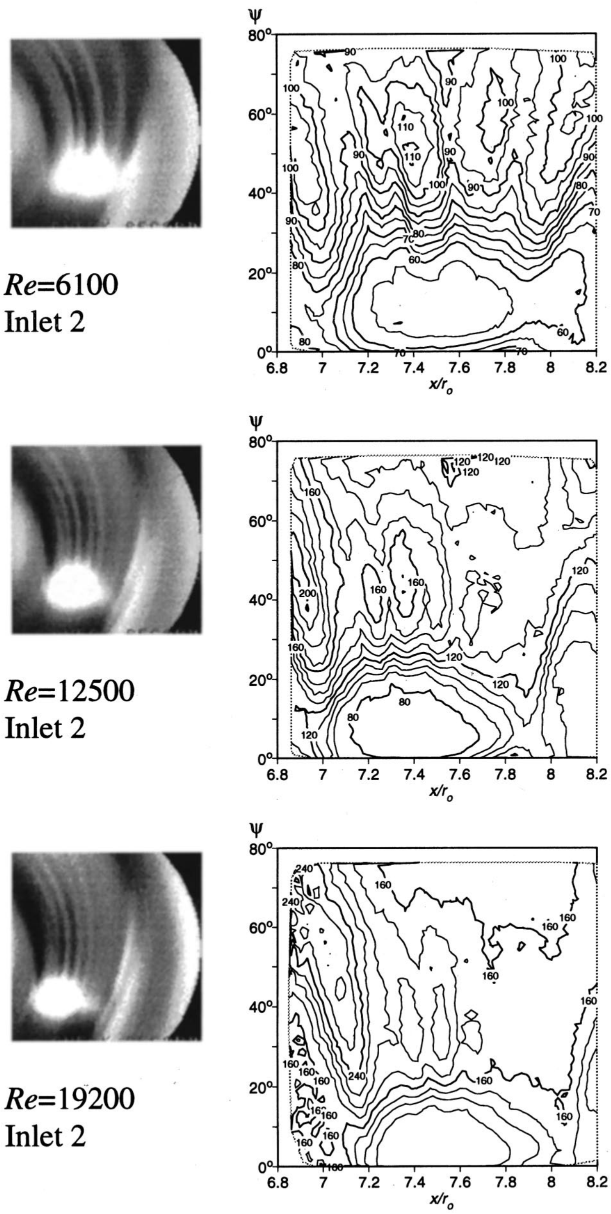

Fig. 11 Local Nusselt number distributions near inlet 2 for Re of 6100, 12,500, and 19,200

gions indicate lower surface temperatures and higher Nu. Each Görtler vortex pair produces an upwash region and a downwash region. In the upwash region between the two vortices comprising each Görtler pair, higher temperature air from near the wall is moved away from the wall, producing a light stripe as the vortex pair advects in the positive ψ direction. Each Görtler pair also has a downwash region on each side, in which lower temperature air is moved toward the wall, producing darker stripes (and higher local Nu) as the vortices advect in the positive ψ direction. Light and dark curved stripes due to Görtler vortex pairs are seen near inlet 1 in Fig. 10 at $0.2<x/r_0<0.9$ and $30\ \mathrm{deg}<\psi<70\ \mathrm{deg}$, and near inlet 2 in Fig. 11 at $7.1<x/r_0<8.0$ and $30\ \mathrm{deg}<\psi<80\ \mathrm{deg}$.

Also common to all of the data sets in Figs. 10 and 11 are regions where local Nusselt numbers are augmented at smaller x/r_0 locations on the left-hand sides of each plot, and at larger x/r_0 locations on the right-hand sides. These are located at $x/r_0<0.2$ and $0.8<x/r_0<1.2$ just downstream of inlet 1, and at 6.8

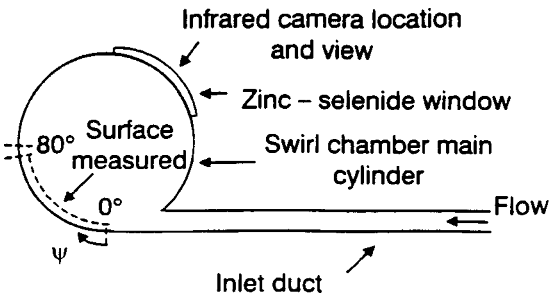

Fig. 12 Experimental arrangement used to obtain the data presented in Figs. 10 and 11

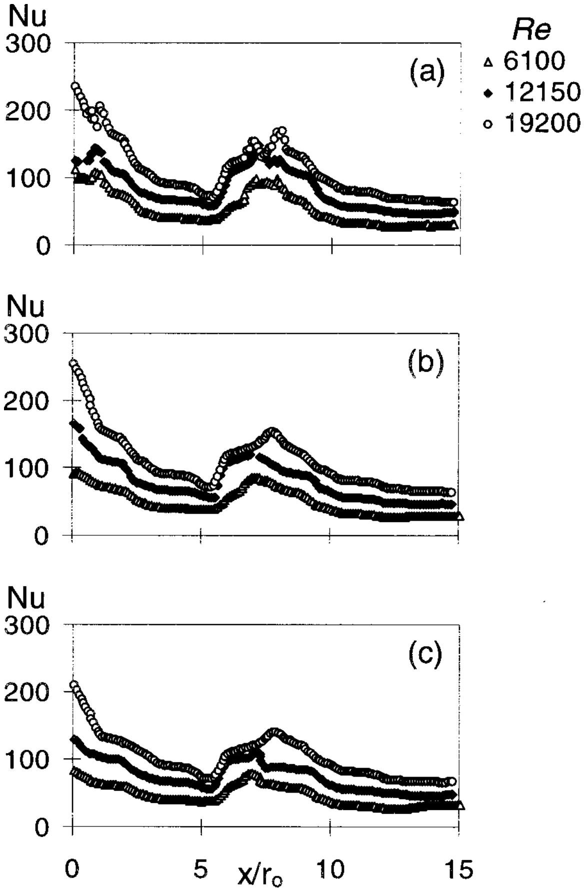

Fig. 13 Local Nusselt numbers at fixed circumferential locations as they vary with normalized axial distance for Re of 6100, 12,150, and 19,200: (*a*) $\psi=30$ deg, (*b*) $\psi=90$ deg, and (*c*) $\psi=150$ deg

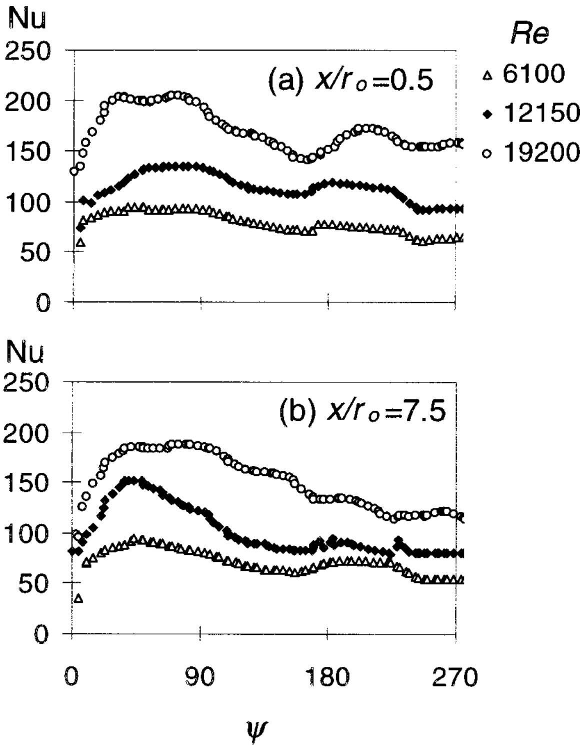

Fig. 14 Local Nusselt numbers at fixed axial locations as they vary with circumferential angle for Re of 6100, 12,150, and 19,200: (*a*) $x/r_0=0.5$ near inlet 1, and (*b*) $x/r_0=7.5$ near inlet 2

$<x/r_0<7.2$ and $8.0<x/r_0<8.3$ just downstream of inlet 2. These local Nu augmentations are due to vortices in the shear layers, which form on both sides of the jets that emanate from each inlet duct. The shear layers are quite strong because of the differences in velocities between the jets and the slower swirl chamber fluid which are encountered on each side.

Figures 10 and 11 also show important changes as Reynolds number is varied. First, local Nusselt number magnitudes at particular swirl chamber locations generally increase with Reynolds number. In addition, the positions and orientations of local Nusselt number streaks and infrared image ''stripes'' change with Re. For example, at Re equal to 12,500 and 19,200, Nusselt number streaks due to Görtler vortex pairs are most apparent at x/r_0 smaller than 0.6–0.8 in Fig. 10 and at x/r_0 smaller than 7.6 in Fig. 11. In contrast, well-contrasted Görtler streaks are also apparent at larger x/r_0 when Re is 6100. Such changes are due to increased turning of the flow from each inlet. This occurs by increasing amounts as Re increases and the axial components of velocity become larger, which gives Görtler vortex pair trajectories larger angles with respect to fixed values of ψ.

Axial Development of Local Nusselt Numbers. Figure 13 presents local Nu data as they vary with x/r_0 at fixed values of ψ of 30, 90, and 150 deg. These data are given for three Reynolds numbers, and are determined from distributions like the one shown in Fig. 9. Figure 13 shows that Nusselt numbers increase with increasing Re when compared at the same x/r_0, and that Nu values are highest near each inlet at $x/r_0=0-1$ and 7–8. The near-inlet Nusselt number peaks are due to vortex unsteadiness like that evidenced in Fig. 2. The development of and interactions between Görtler vortices, and between Görtler vortices and shear layer vortices, also play important roles since these vortices increase mixing between warmer fluid near the wall and cooler fluid from the inlet jet. Higher Nu near each inlet are also due to development of new thermal boundary layers just downstream of each inlet duct. As a result, local Nusselt numbers near inlet 1 are slightly higher than Nu near inlet 2 at all three Re investigated. Local Nusselt numbers in Fig. 13 decrease with x/r_0 downstream of each inlet, before becoming approximately constant at $x/r_0=4-5$ and $x/r_0=12-15$.

Circumferential Development of Local Nusselt Numbers. Figure 14 shows local Nusselt numbers as they vary with circumferential position ψ, for two axial locations, $x/r_0=0.5$ (near inlet 1) and $x/r_0=7.5$ (near inlet 2). Data are given for Re of 6100, 12,150, and 19,200. For each value of ψ, Nusselt numbers increase with increasing Re, because of larger advection. Nu values also increase as ψ increases from 0 deg to 45–80 deg, then decrease slowly as ψ increases further to 270 deg at each Reynolds number. These variations at ψ from 0 to 80 deg are due to the same phenomena that augment local Nusselt numbers at x/r_0 of 1–2 and 7–8 in Fig. 13.

Globally Averaged Nusselt Numbers. Figure 15 presents Nusselt number data averaged over the entire swirl chamber interior surface ($0<x/r_0<15$ and 0 deg$<\psi<$360 deg), as dependent upon Re_D. This type of Reynolds number (based on swirl chamber diameter) is employed so that the present data can be compared to results presented by Glezer et al. [7], which are also included in Fig. 15. Globally averaged Nusselt numbers in this figure increase as Re_D increases. The data are well represented using an equation of the form

$$\overline{\mathrm{Nu}}=0.27\cdot \mathrm{Re}_D^{0.65} \tag{1}$$

which is valid for $2000<\mathrm{Re}_D<80{,}000$.

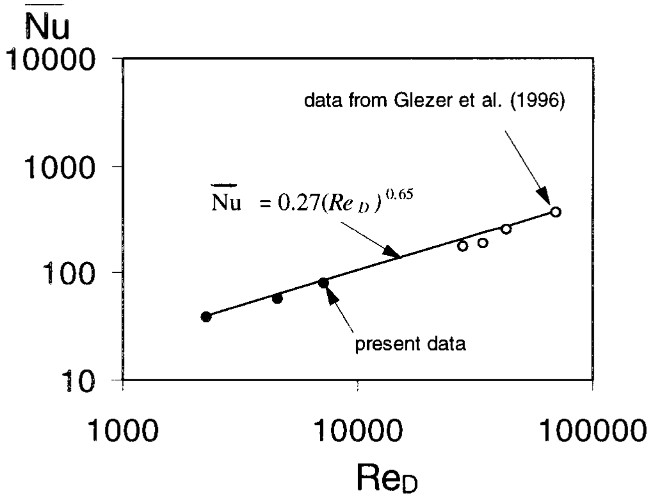

Fig. 15 Globally averaged Nusselt numbers, averaged over $0 < x/r_0 < 15$ and $\psi = 0-360$ deg

Summary and Conclusions

Local flow behavior and heat transfer results are presented from two swirl chambers at Reynolds numbers based on inlet duct characteristics from 6000 to 19,600. Flow results are obtained in an isothermal swirl chamber. Surface Nusselt number distributions are measured in a second swirl chamber (with a constant wall heat flux boundary condition) using infrared thermography, in conjunction with thermocouples, energy balances, and in situ calibration procedures. Bulk helical flow is produced in each chamber by two inlets which are tangent to the swirl chamber circumference.

Important changes of surface heat transfer and flow structural characteristics are observed as the Reynolds number varies. Local surface Nusselt numbers (as well as ones spatially averaged over the entire swirl chamber surface) increase with increasing Reynolds number (both Re and Re_D) throughout the swirl chamber. Particularly important changes are observed just downstream of each inlet, where Nusselt numbers are locally augmented compared to other locations. Here, ''stripe-like'' spatial variations of Nusselt numbers develop due to Görtler vortex pairs, as well as vortices that form in the shear layers on the sides of the jets just downstream of each inlet. Heat transfer coefficient enhancements at these locations are tied to the development of new thermal boundary layers, and the behavior and characteristics of the vortices, as evidenced by flow visualizations. These include intense vortex secondary flows, vortex unsteadiness, interactions between vortices, and vortex induced mixing between warmer fluid near the wall and cooler fluid from the inlet jet. Axially averaged profiles, as well as local values of normalized total pressure, static pressure, and circumferential velocity, also show augmented values with large spatial variations just downstream of each inlet. Local maxima in total pressure and circumferential velocity distributions are evident in these regions at r/r_0 of about 0.95.

Nusselt number increases with increasing Re are due to increased advection, as well as important changes to vortex characteristics near the concave surfaces of the swirl chambers. As the Reynolds number increases, flow visualization results show that Görtler vortex pairs generally become more numerous as their sizes decrease. Vortex pair interactions are more frequent and intense, and increasingly involve vortices of different size. As the flow becomes increasingly turbulent, unsteady disturbances result in greater distortion and diffusion of the flows within and near the vortices. These are accompanied by larger axial components of velocity, and increased turning of the flow from each inlet, which gives Görtler vortex pair trajectories larger angles with respect to fixed values of ψ. Important changes with Reynolds number are also evident in radially averaged distributions of nondimensional static pressure, total pressure, and circumferential velocity. When compared at the same x/r_0, each of these quantities increases with increasing Re when Re is less than 8000–10,000. The profiles of static and total pressure then collapse together on the same curve at higher Re.

Acknowledgments

The work presented in this paper was performed as a part of the Advanced Turbine System Technology Development Project, sponsored both by the U.S. Department of Energy and Solar Turbines, Inc. Dr. Boris Glezer and Dr. Hee-Koo Moon are acknowledged for many valuable discussions on the research.

Nomenclature

D = swirl chamber inner diameter
D_H = hydraulic diameter of inlet duct
h = heat transfer coefficient
k = thermal conductivity
Nu = Nusselt number$=hD/k$
P = pressure
r = radial coordinate, measured from swirl chamber centerline
r_0 = swirl chamber radius
Re = Reynolds number based on inlet duct characteristics $=D_H\overline{V}/\nu$
Re_D = Reynolds number based on swirl chamber diameter and average axial velocity$=D\overline{U}/\nu$
T_i = inlet air temperature
T_w = temperature of air adjacent to swirl chamber wall
$\overline{V}$ = average inlet duct velocity
$\overline{U}$ = axial bulk velocity in swirl chamber averaged over radial/circumferential planes
$\overline{u}_\psi$ = time-averaged circumferential velocity
x = axial coordinate measured from swirl chamber end plate
ν = kinematic viscosity
ρ = density
ψ = swirl chamber circumferential location

Subscripts

a = ambient value
i = swirl chamber inlet value
s = static value
t = total or stagnation value
w = wall value

Superscripts

$\overline{\ }$ = spatially averaged

References

[1] Kreith, F., and Margolis, D., 1959, ''Heat Transfer and Friction in Turbulent Vortex Flow,'' Appl. Sci. Res., **8**, pp. 457–473.
[2] Date, A. W., 1974, ''Prediction of Fully Developed Flow in a Tube Containing a Twisted-Tape,'' Int. J. Heat Mass Transf., **17**, pp. 845–859.
[3] Hong, S. W., and Bergles, A. E., 1976, ''Augmentation of Laminar Flow Heat Transfer in Tubes by Means of Twisted-Tape Inserts,'' ASME J. Heat Transfer, **98**, pp. 251–256.
[4] Sampers, W. F. J., Lamers, A. P. G. G., and Van Steenhoven, A. A., 1992, ''Experimental and Numerical Analysis of a Turbulent Swirling Flow in a Tube,'' ICHEME Symposium Series, **2**, No. 129, pp. 765–771.
[5] Li, H., and Tomita, Y., 1994, ''Characteristics of Swirling Flow in a Circular Pipe,'' ASME J. Fluids Eng., **116**, pp. 370–373.
[6] Kok, J. B. W., Rosendal, F. J. J., and Brouwers, J. J. H., 1993, ''LDA-Measurements on Swirling Flows in Tubes,'' SPIE Laser Anemometry Advances and Applications, **2052**, pp. 721–728.
[7] Glezer, B., Moon, H.-K., and O'Connell, T., 1996, ''A Novel Technique for the Internal Blade Cooling,'' ASME Paper No. 96-GT-181.
[8] Glezer, B., Lin, T., and Moon, H.-K., 1997, ''An Improved Turbine Cooling System,'' U.S. Patent No. 5603606.
[9] Glezer, B., Moon, H.-K., Kerrebrock, J., Bons, J., and Guenette, G., 1998,

''Heat Transfer in a Rotating Radial Channel With Swirling Internal Flow,'' ASME Paper No. 98-GT-214.

[10] Hedlund, C. R., 1998, ''Heat Transfer and Flow Behavior in a Swirl Chamber With Helical Flow,'' Ph.D. dissertation, University of Utah.

[11] Hedlund, C. R., Ligrani, P. M., Moon, H.-K., and Glezer, B., 1998, ''Heat Transfer and Flow Phenomena in a Swirl Chamber Simulating Turbine Blade Internal Cooling,'' ASME J. Turbomach., **121**, pp. 804–813.

[12] Moon, H.-K., O'Connell, T., and Glezer, B., 1998, ''Heat Transfer Enhancement in a Circular Channel Using Lengthwise Continuous Tangential Injection,'' *Proceedings of the International Heat Transfer Congress*, Seoul, South Korea.

[13] Khalatov, A. A., and Zagumennov, I. M., 1990, ''Heat Transfer and Fluid Dynamics Near Flat Surfaces in Confined Swirling Flows,'' *Proceedings of the Ninth International Heat Transfer Conference*, Jerusalem, Israel, pp. 329–334.

[14] Kumar, R., and Conover, T., 1993, ''Flow Visualization Studies of a Swirling Flow in a Cylinder,'' Exp. Therm. Fluid Sci., **7**, pp. 254–262.

[15] Dong, M., and Lilley, D. G., 1993, ''Parameter Effects on Flow Patterns in Confined Turbulent Swirling Flows,'' *Computer Modeling, Cofiring and NOx Control*, ASME FACT-Vol. 17, pp. 17–21.

[16] Bruun, H. H., Fitouri, A., and Khan, M. K., 1993, ''The Use of a Multiposition Single Yawed Hot-Wire Probe for Measurements in Swirling Flow,'' *Thermal Anemometry*, ASME FED-Vol. 167, pp. 57–65.

[17] Fitouri, A., Khan, M. K., and Bruun, H. H., 1995, ''A Multiposition Hot-Wire Technique for the Study of Swirling Flows in Vortex Chambers,'' Exp. Therm. Fluid Sci., **10**, pp. 142–151.

[18] Chang, F., and Dhir, V. K., 1994, ''Turbulent Flow Field in Tangentially Injected Swirl Flows in Tubes,'' Int. J. Heat Fluid Flow, **15**, No. 5, pp. 346–356.

[19] Gambill, W. R., and Bundy, R. D., 1962, ''An Evaluation of the Present Status of Swirl-Flow Heat Transfer,'' ASME Paper No. 62-HT-42.

[20] Bergles, A. E., 1969, ''Survey and Evaluation of Techniques to Augment Convective Heat and Mass Transfer,'' Int. J. Heat Mass Transf., **1**, pp. 331–413.

[21] Razgaitis, R., and Holman, J. P., 1976, ''A Survey of Heat Transfer in Confined Swirling Flows,'' *Future Energy Production Systems*, *Heat and Mass Transfer Processes*, Academic Press, New York, **2**, pp. 831–866.

[22] Papadopoulos, P., France, D. M., and Minkowycz, W. J., 1991, ''Heat Transfer to Dispersed Swirl Flow of High-Pressure Water With Low Wall Super Heat,'' Exp. Heat Transfer, **4**, pp. 153–169.

[23] Ligrani, P. M., Singer, B. A., and Baun, L. R., 1989, ''Miniature Five-Hole Pressure Probe for Measurement of Three Mean Velocity Components in Low Speed Flow,'' J. Phys. [E], **22**, No. 10, pp. 868–876.

[24] Ligrani, P. M., Singer, B. A., and Baun, L. R., 1989, ''Spatial Resolution and Downwash Velocity Corrections for Multiple-Hole Pressure Probes in Complex Flows,'' Experiments in Fluids, **7**, No. 6, pp. 424–426.

[25] Moffat, R. J., 1988, ''Describing the Uncertainties in Experimental Results,'' Exp. Therm. Fluid Sci., **1**, No. 1, pp. 3–17.

The Measurement of Local Wall Heat Transfer in Stationary U-Ducts of Strong Curvature, With Smooth and Rib-Roughened Walls

Hector Iacovides

David C. Jackson

George Kelemenis

Brian E. Launder
Fellow ASME

UMIST,
Department of Mechanical Engineering,
Manchester, M60 1QD, United Kingdom

The paper presents some of our recent experimental investigations of convective heat transfer in flow through stationary passages relevant to gas turbine blade-cooling applications. The main objective of this effort is to produce local heat transfer data for CFD validation. Local Nusselt number measurements in flows through round-ended ***U****-bends of square cross section, with and without artificial wall roughness, are presented. Our earlier LDA measurements of flows through these passages are first briefly reviewed and then the liquid-crystal technique for the measurement of local wall heat transfer inside passages of complex geometries is presented. Tightly curved* ***U****-bends generate strong secondary motion and cause flow separation at the bend exit, which substantially raise turbulence levels. Wall heat transfer is significantly increased, especially immediately downstream of the* ***U****-bend, where it is over two times higher than in a straight duct. The local heat transfer coefficient around the perimeter of the passage is also found to vary considerably because of the curvature-induced secondary motion. The introduction of surface ribs results in a further increase in turbulence levels, a reduction in the size of the curvature-induced separation bubble, and a complex flow development after the bend exit with additional separation regions along the outer wall. Heat transfer levels in the straight sections are more than doubled by the introduction of ribs. The effects of the bend on the overall levels of Nusselt number are not as strong as in the smooth* ***U****-bend, but are still significant. The effects of the bend on the perimetral variation of local heat transfer coefficients within the ribbed downstream section are also substantial.*
[S0889-504X(00)00802-3]

1 Introduction

The demand for improvements in the efficiency and power output of gas turbines has led engine designers continuously to seek to raise operating temperatures. In order to preserve the structural integrity of rotating blades, elaborate cooling systems have been evolved in which relatively cool air is extracted from the compressor and, through the central shaft, is fed to cooling passages inside the turbine blades and nozzle guide vanes. The flow inside these cooling passages is complex and highly three dimensional, influenced by the presence of sharp **U**-bends and artificial rib-roughness, and also by the rotation of the blades. In order to optimize the cooling process, the engine designer needs to have accurate information on the detailed flow development and its effects on local wall heat transfer. Because of the geometric complexities of the cooling passages and the presence of rotation, most of the experimental heat transfer data that initially emerged, such as Han [1,2] and Lau et al. [3,4], though of considerable value, were nevertheless confined to averaged values. Studies such as these demonstrated the enhancement in heat transfer that can be achieved through the introduction of ribs, and the accompanying increase in pressure loss and also the effects of rib spacing, rib size, the angle between the ribs and the flow direction, and Reynolds number. More recent studies, such as those of Taslim et al. [5] and Rau et al. [6], have also produced measurements of the local Nusselt number in ribbed passages of various geometries and tried to explain how the local flow development influences the local thermal behavior. Such detailed data on local flow and heat transfer are crucial to the development of a clear understanding of the hydrodynamic and thermal behavior in such passages and also to the development and validation of numerical flow solvers that can be reliably used for the simulation of blade cooling flows and the consequent thermal stresses that arise. What is especially important as far as CFD validation is concerned is to have both local flow and thermal data for the same passage geometries. It is the second of these two areas, the provision of local flow and thermal data for validation of numerical flow solvers, that provides the motivation for the work reported here.

This investigation forms part of a more extensive experimental effort in our group [7], aimed at producing local flow and heat transfer data for CFD-validation data for idealized blade-cooling passages under stationary and rotating conditions. As shown in Fig. 1, we here focus on the thermal development through stationary, round-ended **U**-bends of strong curvature of square cross section, both with smooth walls and with the inner and outer walls of the straight sections roughened with staggered ribs of square cross section. Placing the ribs along the inner and outer walls, instead of the two flat walls of the passage, is perhaps the most severe departure from the practice followed in real blade-cooling passages. Because, however, the main objective of our work is to provide data for CFD validation, we elected to start our investigations of ribbed passages by placing ribs along the inner and outer walls in order to preserve the geometric and flow symmetry, thereby reducing grid size requirements in subsequent numerical computations. The presence of strong curvature and rib roughness still leads to the development of most of the important flow features

---

Contributed by the International Gas Turbine Institute and presented at the 44th International Gas Turbine and Aeroengine Congress and Exhibition, Indianapolis, Indiana, June 7–10, 1999. Manuscript received by the International Gas Turbine Institute February 1999. Paper No. 99-GT-254. Review Chair: D. C. Wisler.

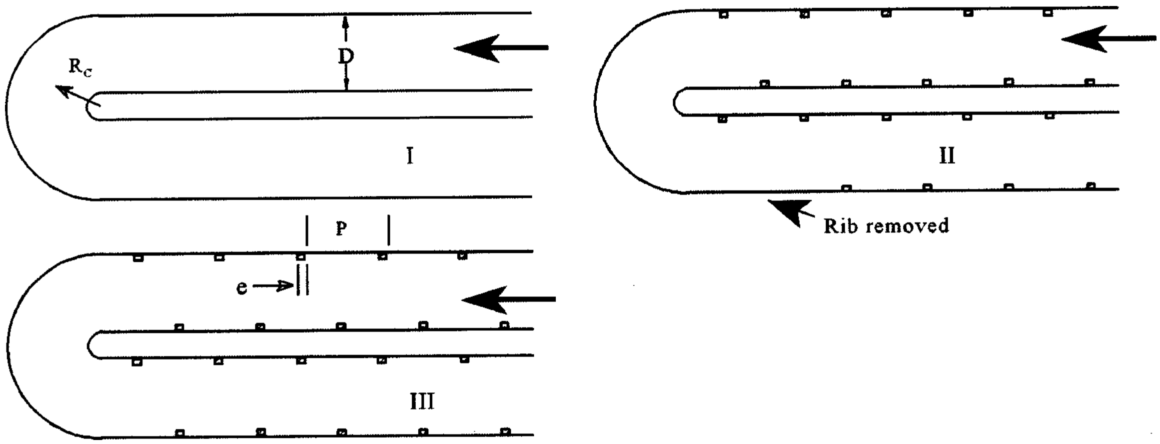

Fig. 1 Cases investigated

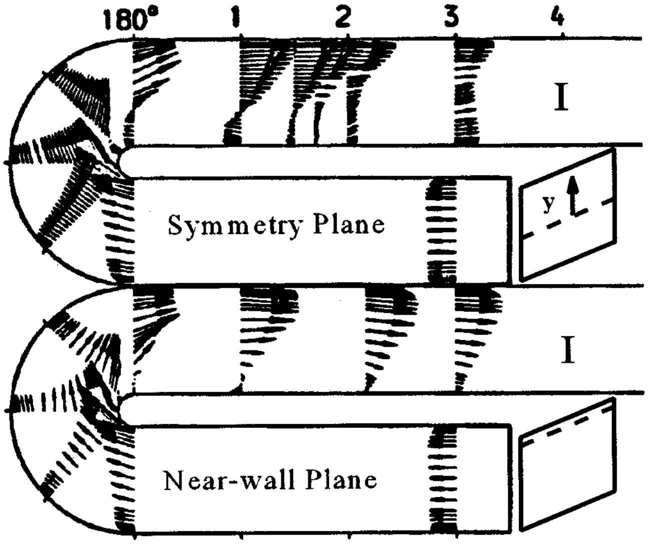

Fig. 2 LDA measurements for case I [8]

found in real blade-cooling passages. The local flow development through these passages has been the subject of earlier investigations in our group, such as Cheah et al. [8] and Iacovides et al. [9,10]. As can be seen in Fig. 2, for the passage with smooth walls the LDA measurements [8] revealed that the flow development is dominated by the strong streamwise pressure gradients at the bend entry and exit. A separation bubble is formed along the inner wall halfway around the bend which extends to about two diameters in the straight downstream section. Because of the flow separation, turbulence levels are greatly increased at the bend exit. As can also be seen in Fig. 2, due to the curvature-induced secondary motion, the flow on the midplane and on a parallel plane close to the flat wall are very different.

The introduction of ribs [9,10] naturally increases turbulence in the straight sections. This results in the delay of flow separation along the inner wall of the bend. As seen in Fig. 3, Case III, downstream of the bend, as the faster fluid along the outer wall encounters the first rib, a large separation bubble is formed along the outer wall, behind the first rib. Consequently the length of the separation bubble along the inner wall is reduced. Removal of the first downstream rib from the outer wall, Case II in Fig. 1, displaces the outer-wall separation bubble further downstream and reduces its size. This is accompanied by an increase in the length of the separation bubble along the *inner* wall however.

The thermal measurements have been obtained using air as the working fluid. As shown in Fig. 4, an open-loop system is employed, with a fan drawing air into the experimental model

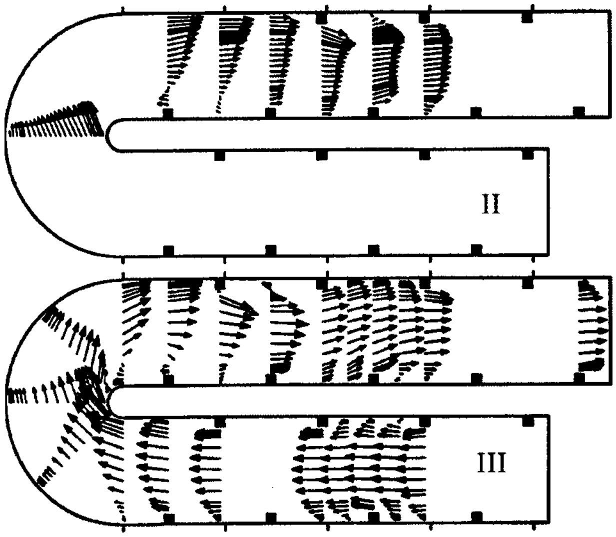

Fig. 3 LDA measurements along the duct symmetry plane for cases II and III [9,10]

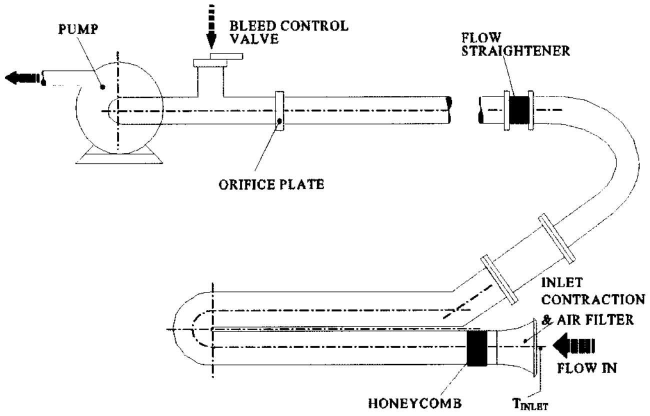

Fig. 4 Apparatus

through a contracting inlet section and a combination of fine wire meshes and a honeycomb section, placed there to ensure uniform and symmetric entry conditions.

Here heat-transfer measurements that we have recently obtained using the liquid-crystal technique are reported and, through comparisons with the earlier LDA measurements, the mechanisms by which the flow development influences wall heat transfer are discussed.

2 Apparatus

The working section is connected to the fan through a long orifice plate section, used to measure the mass flow rate.

The experimental model is made of 10-mm-thick perspex. The passage has a square cross section with a diameter of 50 mm. The ratio between the bend mean radius and the duct diameter, R_C/D_h, is 0.65 and the upstream and downstream straight sections are ten diameters long. The ribs, for cases II and III are of a square cross section. The ratio between the rib height and the duct diameter, e/D_h, is 0.1 and the rib spacing, P/e, is 10. In both the upstream and the downstream sections the ribs closest to the bend are at a distance of $0.45D_h$ from the bend entry and exit.

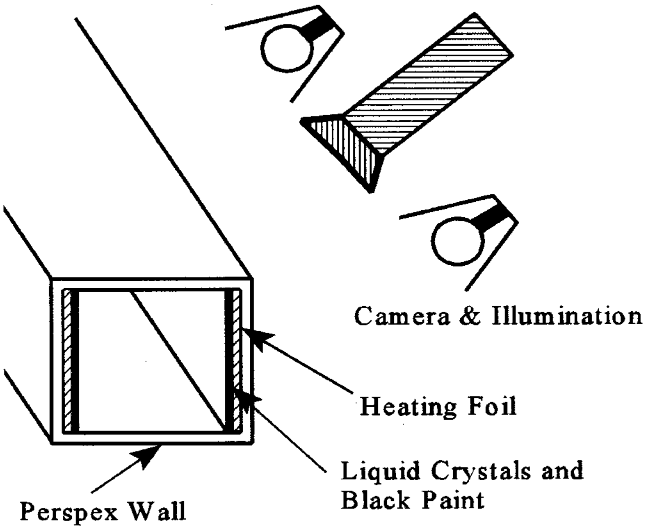

Fig. 5 Heating and viewing arrangements

3 Heat Transfer Measurements

As is well documented [11,12], the molecular structure of thermochromic liquid crystals, over a certain temperature range, depends on temperature. Changes in molecular structure in tum affect the wavelength of visible light absorbed by the liquid crystals and hence, over a certain temperature range, the color of the liquid crystals can be used to determine their temperature. In heat transfer experiments where air is the working fluid, most groups have adopted the transient liquid-crystal technique, in which the surface under investigation is covered with a layer of liquid crystals and is exposed to a hot air stream. As the surface temperature gradually rises from the initial ambient conditions, the movement of the color contours of the liquid crystals along the surface is monitored. Then, at each location along the surface, from the time needed for the wall temperature to rise from its initial value to that of the crystal-color-change temperature, the solution of the one-dimensional transient heat-conduction equation produces the value of the heat transfer coefficient, *h*. In this study, however, because of our intention to employ this technique subsequently in experiments in rotating passages using water as the working fluid, the steady-state technique was employed. To the best of our knowledge, use of this technique was first reported by Cooper et al. [13]. This is because in water, due to the higher coefficients of heat transfer involved, the thermal time constant ($\tau \equiv \rho_w c_{pw} k_w / h^2$) is too short to measure accurately.

The internal surfaces of the inner and outer walls of the experimental model are covered with a 0.013-mm-thick, electrically heated, stainless steel foil, which provides a constant-heat-flux thermal boundary condition. The ribs were made of perspex and the heating foil underneath the ribs was short circuited. The rib surfaces could thus be considered as thermally insulated. A thin layer of liquid crystals is then applied over the surface of the heating foil. Once steady thermal conditions are reached, the resulting contours of the yellow color are also contours of known wall temperature, determined through a prior calibration, under conditions of uniform wall heat flux. Electrical measurements provide the wall heat flux, q_w and from the overall energy balance, the fluid bulk temperature, T_B, can also be determined:

$$mc_p(dT_B/dz) = Pq_w \tag{1}$$

where *m* is the mass flow rate, *z* the streamwise direction, and *P* the heated perimeter.

The local Nusselt number along each color contour can then be calculated, since

$$\mathrm{Nu} \equiv (q_w D_h)/[k(T_W - T_B)] \tag{2}$$

By repeating this procedure for a number of heating rates, detailed mapping of the local Nusselt number over each heated wall can be constructed.

The liquid crystals employed were micro-encapsulated crystals manufactured by Merck, with a nominal color-change band between 29.5°C and 31°C, for the entire visible spectrum, and a nominal change of 0.1°C across the yellow color, which was used to determine the wall temperature. At each heating rate, the image of the resulting color contours was recorded using a CCD camera at a 45 deg angle as shown in Fig. 5, digitized and stored on a PC. As the recent work of Farina and Moffat [14] has shown, provided that the viewing and illumination angles are the same, as in this study, then there is no shift in the wavelength of the light reflected by the liquid crystals. In any event, the crystals were calibrated under exactly the same illumination and viewing conditions as those of the experiment. In order to minimize heat losses, the experimental model was covered with thermal insulation. The thermal insulation of the top wall was removed for only the few seconds needed for the camera to record the image. The digitized image was then converted into a hue-saturation-and-intensity format and the pixels with a hue value corresponding to that of the yellow color were identified. Software developed for this study then corrected the coordinates of the selected pixels accounting for distortions caused by the camera lens and angle. The information from each image was thus reduced to provide the coordinates of the constant-wall-temperature contour. The value of *h* along the contour line was then calculated, using Eqs. (1) and (2). Finally, the contour lines produced by different heating rates were brought together and, through interpolation, the continuous variation of the Nusselt number over the heated surface was produced. Side-averaged values of the Nusselt number were also subsequently computed. Error analysis using the method of Kline and McKlintock [15] indicates that the uncertainty in the local Nusselt number is ±7.4 percent and in the side-averaged values ±5.5 percent. The analysis took into account uncertainties in the determination of the wall and inlet temperatures, the location of the color contours, the electrical current, the resistivity and thickness of the heating foil, the mass flow rate, and the duct diameter. Preliminary tests showed that heat losses contributed an uncertainty of well below 1 percent because the duct was covered with a 2 in. foam insulation.

While in real blade-cooling passages the cooling fluid would remove thermal energy from all four walls, in these experiments only the inner and outer walls have been heated. This does not, however, diminish the usefulness of the data in CFD validation, or invalidate any conclusions reached on how the flow development influences wall heat transfer.

Ideally the heat transfer pattern should be symmetric about the center plane of the duct, $y=0$. While contour lines, discussed in the next section, are not perfectly symmetric, the main anomalies occur in regions where Nu is not changing rapidly, so discrepancies associated with the asymmetric contours are not important.

4 Results and Discussion

Three sets of data are presented, one for each of the three geometries shown in Fig. 1, all at a Reynolds number of 95,000.

4.1 Case I. The local Nusselt number measurements in the **U**-bend with smooth walls, Fig. 6, provide an opportunity to assess the effects of strong curvature on heat transfer. In the upstream section, Nusselt-number levels along both walls are fairly uniform and close to the value returned by the Dittus–Boelter correlation:

$$\mathrm{Nu}=0.023\,\mathrm{Re}^{0.8}\mathrm{Pr}^{0.4} \tag{3}$$

Within the **U**-bend heat transfer levels rise along the outer wall, with the maximum level at each axial location occurring at the centerline of the outer wall. The general rise in Nusselt number is consistent with the flow acceleration along the outer wall, as shown in Fig. 2. Within the bend the higher heat transfer levels along the centerline of the outer wall are probably caused by the secondary motion, which causes relatively cool fluid from near the duct center to impinge along the centerline of the outer wall. This fluid heats up as it moves out to the corner regions, leading to a reduction in the heat transfer coefficient in the two corners. Downstream of the bend, along the outer wall, heat transfer coefficients continue to rise, reaching a maximum value more than twice that prevailing upstream, at about three diameters after the bend exit. As can be seen in [2], the location of the maximum Nusselt number coincides with the region where the highest turbulence levels along the outer wall have been measured. Beyond this point, as the flow along the outer wall starts to slow down and the turbulence levels begin to reduce, Nusselt numbers also start to diminish. Even after six diameters from the bend exit, however, the Nusselt number is still more than 50 percent higher than that upstream. Along the inner wall, Nusselt number levels rise very rapidly after the bend exit, reaching their maximum values, similar to those along the outer wall, about two diameters after the exit, which is very close to the reattachment point, Fig. 2. In contrast to the measured distribution along the outer wall, along the inner wall, the Nusselt numbers in the corner regions are higher than those on the centerline. This is also consistent with the curvature-induced secondary motion which, along the thermally insulated top and bottom walls, transports relatively cool fluid to the corner regions of the inner wall. As this fluid moves toward the duct center, it is heated and also slowed down by the inner wall, causing a strong reduction in wall heat transfer. At about three diameters downstream of the bend, the variation in Nusselt number between the centerline and the corner regions, at the inner wall, is about 60 percent. As the flow begins to recover after re-attachment, Nusselt number levels along the inner wall begin to decrease, though, as for the outer wall, even after six diameters from the bend exit, they are still significantly higher than those of the upstream region. The strong streamwise changes in the mean flow and the rise in turbulence levels caused by the tight **U**-bend thus lead to substantial increases in the heat transfer coefficient. Moreover, curvature-induced secondary motion, as well as contributing to the increase in wall heat transfer, also influences the distribution of the local Nusselt number on the inner and outer walls. The influence of the bend on heat transfer is still significant after six diameters from the bend exit.

4.2 Case II. The effects of rib-roughness on heat transfer can be seen in the Nusselt number contours of Fig. 7. In the upstream section, there appear to be enough rib intervals for thermal conditions to repeat themselves over each interval. Nusselt numbers become highest in the middle of each rib interval, by which point, according to the LDA data of Fig. 3, the flow has re-attached, after separating behind the upstream rib. Nusselt number levels in the corner regions are higher than in the center of each wall, probably because the top and bottom walls are thermally insulated. The actual levels of the heat transfer coefficient are typically twice as high as those in the smooth **U**-bend (Case I). This substantial increase must be related to the high levels of turbulence caused by the presence of ribs, shown in the measurements of Iacovides et al. [9]. Within the bend, heat transfer coefficients display a monotonic rise along the outer wall but, in contrast to the smooth **U**-bend, Nusselt number levels along the centerline are higher than those in the corners. The levels of Nu along the outer wall are higher than the corresponding levels for the smooth **U**-bend, but not as high as the highest levels encountered in the ribbed upstream sections. Downstream of the bend,

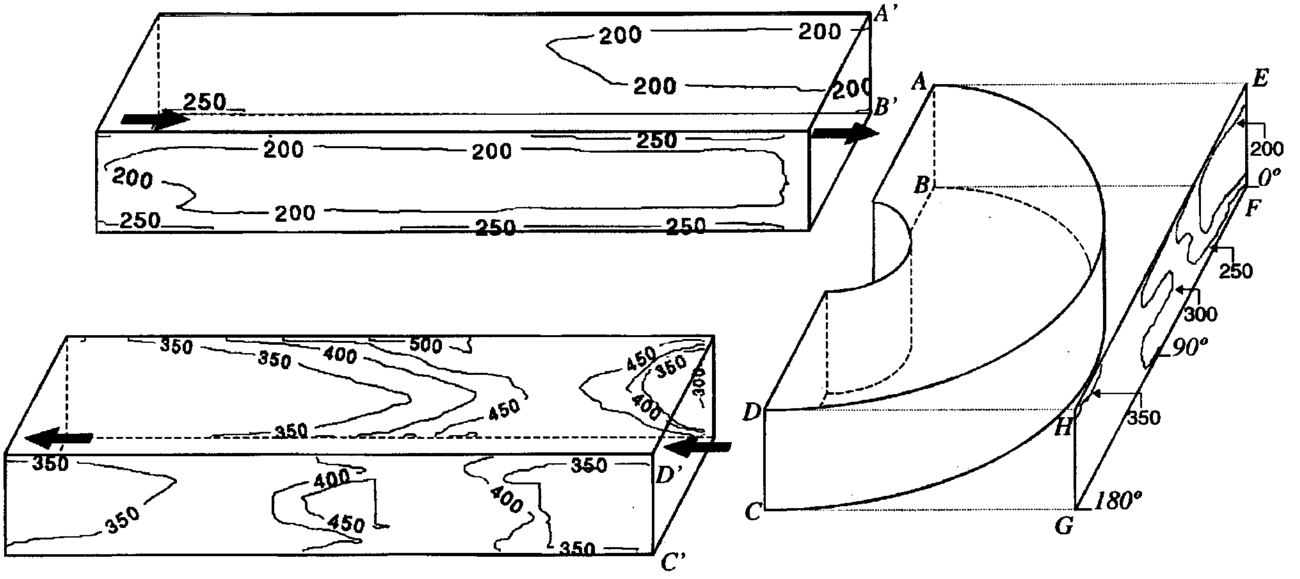

Fig. 6 Nusselt number contours for the smooth U-bend, case I; Re=95,000 and Pr=0.71

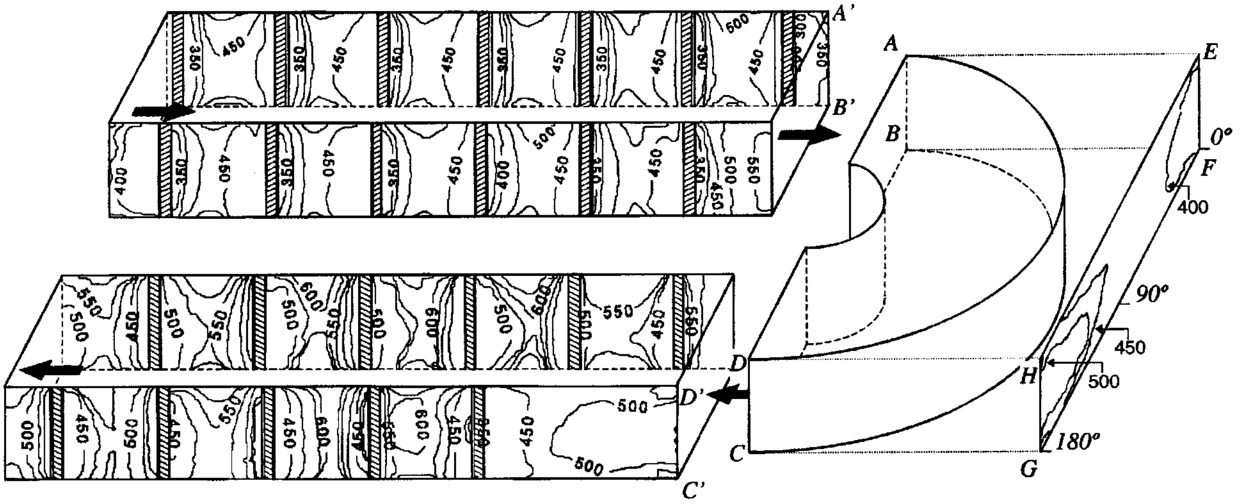

Fig. 7 Nusselt number contours for the ribbed U-bend, case II; Re=95,000 and Pr=0.71

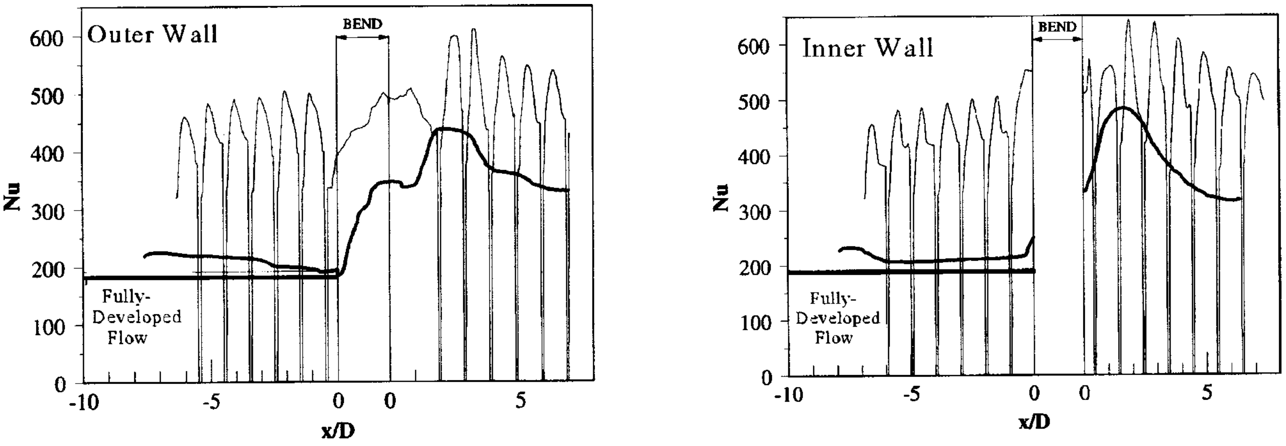

Fig. 8 Axial variation of side-averaged Nusselt number of smooth and a rib-roughened U-bend, cases I and II; ━━: smooth duct; —— ribbed duct

along the outer wall, Nu levels fall after the first diameter, where, as shown in Fig. 3, the flow along the outer wall starts to decelerate. Over the first downstream rib interval along the outer wall, where a large separation bubble is generated, the Nusselt number rises to levels higher than those encountered upstream of the bend. Heat transfer coefficients gradually fall, over the subsequent rib intervals, tending toward the levels measured in the upstream section. Along the inner wall, over the first downstream rib interval, which is partially within the region of bend-induced separation, heat transfer levels are especially high in the corner regions. Over the two subsequent rib intervals, the Nusselt number rises even further, to levels higher than those along the outer downstream wall. Beyond the third downstream rib, heat transfer coefficients begin to fall toward those of the upstream sections.

The overall effect of the **U**-bend and of the ribs on wall heat transfer, can be more easily assessed through the plots of the side-averaged Nusselt numbers, shown in Fig. 8. As expected, the introduction of ribs raises the levels of the heat transfer coefficient in the upstream section by more than a factor of 2. The round-ended **U**-bend still influences heat transfer levels downstream of the bend, especially along the inner wall, but its effects are not as strong as in the smooth **U**-bend.

4.3 Case III.

Finally the local Nusselt measurements of Fig. 9 show how the inclusion of an additional rib along the outer downstream wall, at a distance of 0.95 diameters from the bend exit, affects wall heat transfer. Some of the images for the higher heating rates were, unfortunately, lost and consequently some regions have not been fully mapped. In these regions, shown as shaded in Fig. 9, the Nusselt number reaches values that are higher than those indicated by the levels of the contours present.

Along the outer wall, differences in the thermal behavior between Cases II and III begin to appear over the second half of the bend, where the additional downstream rib causes an earlier rise in the Nusselt number. After the bend, because the first downstream rib is now closer to the bend, the reduction in Nusselt number after the first diameter is eliminated. Over the first rib interval, now one diameter closer to the bend, the Nusselt number is higher than for Case II and the distribution is different, with the highest levels occurring at the downstream end of the interval. This must be caused by the larger separation bubble over the first rib interval in Case III. Beyond the first rib interval along the outer wall, the thermal behavior becomes similar to that of Case II.

Along the inner wall, while the Nusselt number distribution is similar to that for Case II, over the first two rib intervals the levels are about 10 percent higher. The changes observed are consistent with the changes that the additional rib causes to the flow development, Fig. 3. As shown in Iacovides et al. [9], this enhancement in heat transfer in comparison with the smooth **U**-bend), is

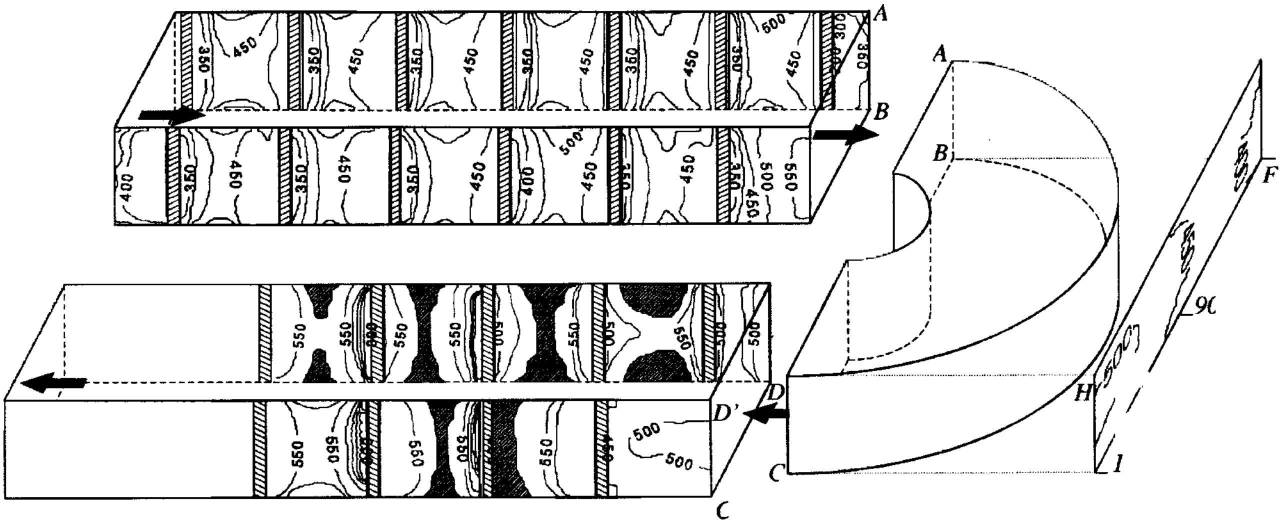

Fig. 9 Nusselt number contours for the ribbed U-bend, case III; Re=95,000 and Pr=0.71

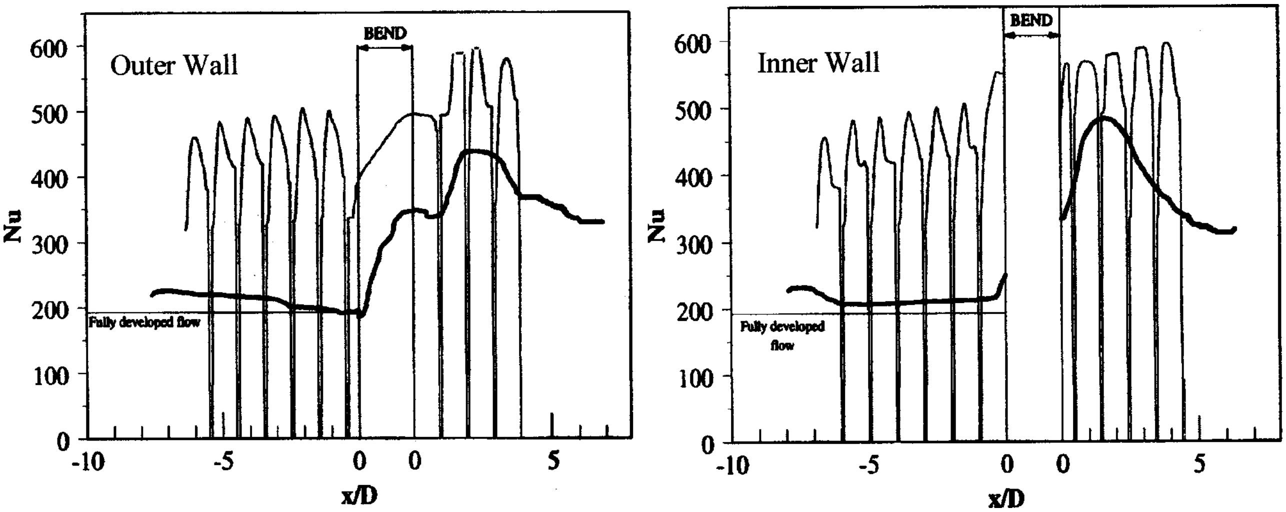

Fig. 10 Axial variation of side-averaged Nusselt number of a smooth and a rib-roughened U-bend, cases I and III; ——: smooth duct; —— ribbed duct

achieved at the expense of doubling the drop is static pressure, for a **U**-bend with 8-diam-long upstream and downstream sections.

The effects of the extra downstream rib are also seen in the plots of the side-averaged Nusselt number, shown in Fig. 10.

5 Concluding Remarks

The results presented provide data for local wall heat transfer in idealized blade cooling passages that should be useful for CFD code validation. The data have also revealed how, in strongly curved and ribbed passages, the flow development influences wall heat transfer.

In flows through smooth **U**-bends, the main flow features are the flow separation from the inner wall at the bend exit, which as Iacovides et al. [9] have shown, substantially increases turbulence levels, and the curvature-induced secondary motion. The enhanced mixing of the fluid, caused by the mean motion (separation and secondary motion) as well as the increased turbulence, raise the Nusselt number through the bend, with the peak values, more than twice as high as those upstream, along both the inner and outer walls, reached between two and three diameters after the bend exit. Moreover, the secondary motion induces strong perimetral variations in Nusselt number, around 60 percent along both the inner and outer walls. Bend effects on heat transfer remain appreciable even beyond seven diameters from the exit.

The introduction of ribs substantially raises turbulence levels, which, for the case of the round-ended **U**-bend, reduces the size of the separation bubble along the inner wall. The flow development downstream of the bend becomes very complex, as the flow, highly distorted by the bend, encounters ribs along the inner and outer walls. It is also found to be sensitive to the distance of the first downstream ribs to the bend exit. Wall heat transfer is substantially raised within the bend and also within the upstream and downstream sections. While the effects of the **U**-bend on heat transfer levels are not as strong as in the case with smooth walls, they are nevertheless still significant. Furthermore, the effects of the bend on the perimetral variation in Nusselt number after the bend exit are also highly evident. Moreover, the rather steep streamwise variation of Nusselt number in the space between ribs suggests that, even though the blade as a whole is more effectively cooled by surface ribbing, important thermal stresses may nevertheless be encountered.

The nonlinear nature of the laws that govern the fluid motion lead to the development of complex flow patterns in blade cooling passages, which can neither be anticipated nor deduced by simply combining the separate effects of rotation, strong curvature and rib roughness. Detailed experimental data, or use of reliable flow solvers, is thus necessary to determine local Nusselt numbers of the quality needed for modern design.

Acknowledgments

Funding for the work presented has been provided by the EPSRC, ABB (Switzerland), EDF (France), EGT, and Rolls-Royce plc. The authors gratefully acknowledge both the financial support and expert technical advice received. The authors also acknowledge technical support provided by Mr. D. Cooper, Mr. J. Hosker, and Mr. M. Jackson. Authors' names are listed alphabetically.

Nomenclature

c_p = specific heat capacity
D_h = hydraulic diameter
e = rib height
h = coefficient of wall heat flux $\equiv q_w/(T_w - T_B)$
k = thermal conductivity
m = mass flow rate through the passage
Nu = Nusselt number $\equiv hD_h/k$
P = duct perimeter or rib spacing
Pr = fluid Prandtl number
R_c = bend radius of curvature
Re = flow Reynolds number $\equiv W_B D_h/\nu$
q = heat flux per unit area
T = temperature
W = axial velocity
z = main flow direction
ν = fluid kinematic viscosity
ρ = density
τ = thermal time constant of duct wall

Subscripts

B = bulk
w = wall

References

[1] Han, J. C., 1984, ''Heat Transfer and Friction in Channels With Two Opposite, Rib-Roughened Walls,'' ASME J. Heat Transfer, **106**, pp. 774–781.
[2] Han, J. C., 1988, ''Heat Transfer and Friction Characteristics in Rectangular Channels With Rib Turbulators,'' ASME J. Heat Transfer, **110**, pp. 321–328.
[3] Lau, S. C., McMillin, R. D., and Han, J. C., 1991, ''Turbulent Heat Transfer and Friction in a Square Channel With Discrete Rib Turbulators,'' ASME J. Turbomach., **113**, pp. 360–366.
[4] Lau, S. C., Kukreja, R. T., and McMillin, R. D., 1992, ''Turbulent Heat Transfer in a Square Channel With Staggered Discrete Ribs,'' AIAA J. Thermophys., **6**, No. 1, pp. 171–173.
[5] Taslim, M. E., Li, T., and Kercher, D. M., 1996, ''Experimental Heat Transfer and Friction in Channels Roughened With Angled, V-Shaped, and Discrete Ribs on Two Opposite Walls,'' ASME J. Turbomach., **118**, pp. 20–28.
[6] Rau, I., Cakan, M., Moeller, D., and Arts, T., 1998, ''The Effect of Periodic Ribs on Local Aerodynamic and Heat Transfer Performance of a Straight Cooling Channel,'' ASME J. Turbomach., **120**, pp. 368–375.
[7] Iacovides, H., Jackson, D. C., Kelemenis, G., Launder, B. E., and Yuan, Y.-M., 1998, ''Recent Progress in the Experimental Investigation of Flow and Local Wall Heat Transfer in Internal Cooling Passages of Gas-Turbine Blades,'' *Proceedings of the 2nd EF Conference on Turbulent Heat Transfer*, pp 7.14–7.28, Manchester, UK.
[8] Cheah, S. C., Iacovides, H., Jackson, D. C., Ji, H. H., and Launder, B. E., 1996, ''LDA Investigation of the Flow Development Through Rotating **U**-Ducts,'' ASME J. Turbomach., **118**, pp. 590–596.
[9] Iacovides, H., Jackson, D. C., Ji, H., Kelemenis, G., Launder, B. E., and Nikas, K., 1998, ''LDA Study of the Flow Development Through an Orthogonally Rotating **U**-Bend of Strong Curvature and Rib-Roughened Walls,'' ASME J. Turbomach., **120**, pp. 366–391.
[10] Iacovides, H., Jackson, D. C., Launder, B. E., and Yuan, Y. M., 1999, ''An Experimental Study of a Rib Roughened Rotating **U**-Bend Flow,'' J. Eng. Thermal Fluid Sci., **19**, pp. 151–159.
[11] Baughn J. W., and Yan, X., 1992, ''Local Heat Transfer Measurements in Square Ducts With Transverse Ribs,'' *Enhanced Heat Transfer*, ASME HTD-Vol. 202, pp. 1–7.
[12] Jones, T. V., Wang Z., and Ireland, P. T., 1992, ''Liquid Crystal Techniques,'' presented at the International Symposium on Heat Transfer in Turbomachinery (ICHMT), Athens, Greece.
[13] Cooper, T. E., Field, R. J., and Meyer, J. F., 1975, ''Liquid Crystal Thermography and Its Application to the Study of Convective Heat Transfer,'' ASME J. Heat Transfer, **97**, pp. 442–450.
[14] Farina, D. J., and Moffat, R. J., 1994, ''A System for Making Temperature Measurements Using Thermochromic Liquid Crystals,'' Report No. HMT-48, Thermoscience Division, Department of Mechanical Engineering, Stanford University.
[15] Kline, A. B., and McClintock, C. D., 1953, ''Calculating Uncertainty in Single-Sample Experiments,'' *Mechanical Engineering*, Jan., pp. 3–8.